



# DMFT: From Infinite Dimensions to Real Materials

Eva Pavarini, Erik Koch, Alexander Lichtenstein, and Dieter Vollhardt (Eds.)



Forschungszentrum Jülich GmbH  
Institute for Advanced Simulation

**Lecture Notes of the Autumn School on  
Correlated Electrons 2018**

Eva Pavarini, Erik Koch, Alexander Lichtenstein, and Dieter Vollhardt (Eds.)

# **DMFT: From Infinite Dimensions to Real Materials**

Autumn School organized by  
the Institute for Advanced Simulation  
at Forschungszentrum Jülich  
17 – 21 September 2018

Schriften des Forschungszentrums Jülich  
Modeling and Simulation

Band / Volume 8

ISSN 2192-8525

ISBN 978-3-95806-313-6

Bibliografische Information der Deutschen Nationalbibliothek.  
Die Deutsche Nationalbibliothek verzeichnet diese Publikation in der  
Deutschen Nationalbibliografie; detaillierte Bibliografische Daten  
sind im Internet über <http://dnb.d-nb.de> abrufbar.

Herausgeber  
und Vertrieb: Forschungszentrum Jülich GmbH  
Zentralbibliothek, Verlag  
52425 Jülich  
Tel.: +49 2461 61-5368  
Fax: +49 2461 61-6103  
E-Mail: [zb-publikation@fz-juelich.de](mailto:zb-publikation@fz-juelich.de)  
[www.fz-juelich.de/zb](http://www.fz-juelich.de/zb)

Umschlaggestaltung: Forschungszentrum Jülich GmbH

Druck: Schloemer & Partner GmbH, Düren

Copyright: Forschungszentrum Jülich 2018

Schriften des Forschungszentrums Jülich  
Reihe Modeling and Simulation, Band / Volume 8

ISSN 2192-8525  
ISBN 978-3-95806-313-6

Vollständig frei verfügbar über das Publikationsportal des Forschungszentrums Jülich (JuSER) unter  
[www.fz-juelich.de/zb/openaccess](http://www.fz-juelich.de/zb/openaccess)



This is an Open Access publication distributed under the terms of the [Creative Commons Attribution License 4.0](https://creativecommons.org/licenses/by/4.0/),  
which permits unrestricted use, distribution, and reproduction in any medium, provided the original work is properly cited.



# Contents

## Preface

1. From Infinite Dimensions to Real Materials  
*Dieter Vollhardt*
2. From Materials to Models: Deriving Insight from Bands  
*Ole Andersen*
3. Effective Electron-Electron Interaction in Many-Electron Systems  
*Ferdi Aryasetiawan*
4. The Foundations of Dynamical Mean-Field Theory  
*Marcus Kollar*
5. Cluster Extensions of Dynamical Mean-Field Theory  
*Michael Potthoff*
6. Charge Self-Consistency in Correlated Electronic Structure Calculations  
*Frank Lechermann*
7. LDA+DMFT: Multi-Orbital Hubbard Models  
*Eva Pavarini*
8. Determining Orbital Wavefunctions using  
Core-Level Non-Resonant Inelastic X-Ray Scattering  
*Hao Tjeng*
9. DMRG for Multiband Impurity Solvers  
*Hans Gerd Evertz*
10. Quantum Monte Carlo Methods for Fermion-Boson Problems  
*Fakher Assaad*
11. Analytic Continuation of Quantum Monte Carlo Data  
*Erik Koch*
12. Introduction to Diagrammatic Approaches  
*Hartmut Hafermann*
13. Dynamical Mean-Field and Dynamical Cluster Approximation Based  
Theory of Superconductivity  
*Thomas Maier*
14. Quantum Criticality and Superconductivity in Diagrammatic Extensions of DMFT  
*Karsten Held*
15. Correlated Electrons out of Equilibrium: Non-Equilibrium DMFT  
*Martin Eckstein*

## Index



# Preface

Since the beginning of quantum mechanics, emergent many-body phenomena represent the grand-challenge in theoretical condensed-matter physics. Indeed, static mean-field approaches fail to capture even the simplest many-body effects, while diagrammatic techniques generally fail in the regime characteristic of strong correlations. The introduction of dynamical mean-field theory (DMFT) has revolutionized this field. Two insights paved the way to this paradigm shift. The first is that in the limit of infinite dimensions all contributions to the self-energy become local. The second is that the locality of the self-energy makes it possible to build a new type of mean-field theory, dynamical in nature, by mapping a correlated lattice problem onto a self-consistent quantum-impurity model. In the last decades, thanks to advances in model building combined with the development of flexible and numerically exact quantum-impurity solvers, DMFT was successfully linked with ab-initio density-functional techniques, making it the method of choice for the investigation of correlated electron materials.

This year's school covers the most important aspects of the DMFT approach to real materials. Lectures range from the basics to advanced topics, covering the DFT+DMFT method, non-local extensions of DMFT, advanced quantum impurity solvers, the calculation of dynamical response functions, and the description of correlation effects out of equilibrium. The goal of the school is to introduce advanced graduate students and up to this modern method for the realistic modeling of strongly correlated matter.

A school of this size and scope requires support and help from many sources. We are very grateful for all the financial and practical support we have received. The Institute for Advanced Simulation at the Forschungszentrum Jülich and the Jülich Supercomputer Centre provided the major part of the funding and were vital for the organization of the school and the production of this book. The Center for Electronic Correlations and Magnetism at the University of Augsburg offered housing support for the lecturers and some of the students, while the Institute for Complex Adaptive Matter (ICAM) provided travel grants for selected international speakers and participants.

The nature of a school makes it desirable to have the lecture notes available when the lectures are given. This way students get the chance to work through the lectures thoroughly while their memory is still fresh. We are therefore extremely grateful to the lecturers that, despite tight deadlines, provided their manuscripts in time for the production of this book. We are confident that the lecture notes collected here will not only serve the participants of the school but will also be useful for other students entering the exciting field of strongly correlated materials.

We are grateful to Mrs. H. Lexis of the Verlag des Forschungszentrum Jülich and to Mrs. N. Daivandy of the Jülich Supercomputer Centre for providing their expert support in producing the present volume on a tight schedule. We heartily thank our students and postdocs who helped with proofreading the manuscripts, often on quite short notice: Julian Mußhoff, Esmaeel Sarvestani, and Qian Zhang.

Finally, our special thanks go to Dipl.-Ing. R. Hölzle for his invaluable advice on the innumerable questions concerning the organization of such an endeavor, and to Mrs. L. Snyders for expertly handling all practical issues.

Eva Pavarini, Erik Koch, Alexander Lichtenstein, and Dieter Vollhardt

August 2018



# 1 From Infinite Dimensions to Real Materials

Dieter Vollhardt

Center for Electronic Correlations and Magnetism

University of Augsburg

## Contents

<b>1</b>	<b>From materials to models</b>	<b>2</b>
1.1	The long way to a model for ferromagnetism in $3d$ transition metals . . . . .	2
1.2	Electronic correlations . . . . .	4
1.3	The Hubbard model . . . . .	4
<b>2</b>	<b>Mean-field theories</b>	<b>6</b>
2.1	Infinite dimensions . . . . .	6
2.2	Weiss mean-field theory for the Ising model . . . . .	7
2.3	Hartree mean-field theory for the Hubbard model . . . . .	8
<b>3</b>	<b>Gutzwiller variational method</b>	<b>10</b>
3.1	Gutzwiller approximation . . . . .	10
3.2	Brinkman-Rice transition . . . . .	11
3.3	Systematic derivation of the Gutzwiller approximation? . . . . .	12
<b>4</b>	<b>Lattice fermions in infinite dimensions</b>	<b>13</b>
4.1	Simplifications of diagrammatic many-body perturbation theory . . . . .	13
4.2	The Hubbard model in $d = \infty$ . . . . .	15
<b>5</b>	<b>Dynamical mean-field theory (DMFT)</b>	<b>19</b>
5.1	The self-consistent DMFT equations . . . . .	19
5.2	Characteristic features of the DMFT . . . . .	21
<b>6</b>	<b>From models back to materials: DFT+DMFT</b>	<b>22</b>
6.1	Metallic ferromagnetism . . . . .	23
6.2	Electronic correlations and lattice stability of solids: paramagnetic Fe . . . . .	25
<b>7</b>	<b>Conclusions and outlook</b>	<b>27</b>

## 1 From materials to models

In view of the great complexity of nature, scientific explanations of natural phenomena can only be found by appropriate simplifications, namely through idealization and abstraction (“reduction”). This requires modelling. Models are supposed to take into account the most important features of a complicated object or process, neglecting features which are considered less important. This has been an extremely successful approach in science, especially in physics. Take, for example, a steam engine in a power plant. Many aspects of the functional principle of such a large and technically complicated machine can already be understood in terms of a simple mechanical model consisting of a cylinder and piston, and using the concept of temperature, pressure, and volume. For a long time mechanical models were thought to be indispensable for an understanding of physical phenomena. Indeed, in 1861 Maxwell, the founding father of the highly elegant theory of electromagnetism, introduced a mechanical model of electromagnetism [1] based on vortices in a molecular medium, which looks rather bizarre to us today. Although it helped Maxwell to explain the displacement current, the molecular vortex model did not turn out to be useful to understand electromagnetism and was soon abandoned. This shows that models have to prove their usefulness over the course of time – otherwise they will be discarded.

### 1.1 The long way to a model for ferromagnetism in *3d* transition metals

When it comes to materials and the explanation of their properties the question again arises what kind of models to use. One of the most famous properties of solids which is known for a very long time already [2] is ferromagnetism, in particular in magnetite ( $\text{Fe}_3\text{O}_4$ ) and elemental iron (Fe). What is a good model to understand ferromagnetism? A crucial step in the development of a microscopic theory of ferromagnetism in solids was the model of magnetic domains proposed by Weiss [3] in 1906, where he postulated the alignment of elementary magnets due to the existence of a “molecular field”, also referred to as “Weiss mean field”. But what is the origin of this peculiar field?

Starting from the interaction between neighboring elementary magnets the Ising model [4] was formulated almost 20 years later to provide a microscopic explanation of the molecular field. Ising solved the one-dimensional problem, found that a phase transition does not occur, and concluded (incorrectly) that this was also the case in three dimensions. The Ising model is a classical spin model. Earlier it had been shown by Bohr (1911) and van Leeuwen (1919) that magnetism is actually a quantum effect. Therefore another important step in the development of a theory of ferromagnetism was Heisenberg’s formulation of a quantum spin model in 1928 [5]. The Heisenberg model explains the Weiss molecular field as the result of a quantum mechanical exchange process. But this model includes only the spin degree of electrons, i.e., describes localized electrons.

In 1929 Bloch [6] pointed out that such a model cannot explain ferromagnetism as observed in *3d* transition metals such as iron, cobalt and nickel, and that an appropriate model had to

include the *itineracy* of the electrons, i.e., their wave nature, which in a solid leads to electronic bands. However, the conditions for ferromagnetism which he obtained for free electrons were unrealistic.<sup>1</sup> Obviously one has to go beyond free electrons and take also their mutual *interaction* into account. This immediately leads to an enormously difficult many-body problem, which is made especially complicated by the fermionic nature of the electrons, their long-range Coulomb interaction, their high density in the metallic state, and the presence of a periodic lattice potential. Attempts by Slater [8] in 1936 to explain ferromagnetism in Ni by including the Coulomb interaction within Hartree-Fock theory were not successful. In particular, the screening of the bare Coulomb repulsion was a difficult issue. It became clear that one had to include genuine correlation effects within well-defined approximations.<sup>2</sup> This implies two intimately connected problems: the formulation of a sufficiently simple model of correlated electrons which unifies the competing approaches by Heisenberg and Bloch (namely the picture of localized and itinerant electrons, respectively), and its solution within more or less controlled approximations. Progress in this direction was slow. One reason certainly was that in the nineteen-thirties and forties nuclear physics attracted more attention than solid-state physics, with a very specific focus of research during the 2nd World War. But apart from that, the sheer complexity of the many-body problem itself did not allow for quick successes. High hurdles had to be overcome, both regarding the development of appropriate mathematical techniques (field-theoretic and diagrammatic methods, Green functions, etc.) and physical concepts (multiple scattering, screening of the long-range Coulomb interaction, quasiparticles and Fermi liquid theory, electron-phonon coupling, superconductivity, metal-insulator transitions, disorder, super-exchange, localized magnetic states in metals, etc.).<sup>3</sup>

At the Washington Conference on Magnetism, held at the University of Maryland on September 2-6, 1952, the conceptual problems regarding a theory of ferromagnetism in  $3d$  transition metals were discussed in detail. This resulted in a series of articles in the Reviews of Modern Physics, including papers by Slater [11], Wohlfarth [12], and van Vleck [13], which summarized the understanding of this fundamental problem at that time. But in spite of great progress in many areas of condensed matter physics a microscopic model for metallic ferromagnetism, or of interacting electrons in general, did not emerge until 1963, when a model for correlated lattice electrons was proposed independently by Gutzwiller [14], Hubbard [15], and Kanamori [16]. All three wanted to explain ferromagnetism in  $3d$  transition metals. This model is now called “Hubbard model” and is the fundamental theoretical model for electronic correlations in solids.

---

<sup>1</sup>For a historical review of the development of the quantum-mechanical theory of metals from 1928 to 1933, which describes the conceptual problems of that time, see Ref. [7].

<sup>2</sup>Apparently Wigner [9] was the first who tried to calculate the contribution of the mutual electronic interaction to the ground state energy relative to the Hartree-Fock result, which he called “correlation energy”.

<sup>3</sup>A discussion of the many-body problem and of some of the important developments up to 1961 can be found in the lecture notes and reprint volume by Pines [10].

## 1.2 Electronic correlations

The concept of electronic correlations plays a very important role in modern condensed matter physics. It refers to electronic interaction effects which cannot be explained within a static mean-field picture and which therefore go beyond results obtained by factorization approximations such as Hartree or Hartree-Fock mean-field theory. Correlation effects are particularly strong in materials with partially filled  $d$  and  $f$  electron shells and narrow energy bands, as in the  $3d$  transition metals or the rare-earths and their compounds.

Electronic correlations in solids lead to the emergence of complex behavior, resulting in rich phase diagrams. In particular, the interplay between the spin, charge, and orbital degrees of freedom of the correlated  $d$  and  $f$  electrons with the lattice degrees of freedom leads to a cornucopia of correlation and ordering phenomena including heavy fermion behavior [17], high temperature superconductivity [18], colossal magnetoresistance [19], Mott metal-insulator transitions [20], and Fermi liquid instabilities [21]. Such properties are not only of interest for fundamental research but also have a great potential for technological applications. Namely, the great sensitivity of correlated electron materials with respect to changes of external parameters such as temperature, pressure, electromagnetic fields, and doping can be employed to develop materials with useful functionalities [22]. Consequently there is a great need for the development of appropriate models and theoretical investigation techniques which allow for a comprehensive, and at the same time reliable, exploration of correlated electron materials [23–25].

## 1.3 The Hubbard model

The single-band Hubbard model [14–16] is the simplest microscopic lattice model for interacting electrons in a solid such as  $3d$  electrons in transition metals [26]. The Hamiltonian consists of two terms, the kinetic energy  $\hat{H}_0$  and the interaction energy  $\hat{H}_{\text{int}}$  (in the following operators are denoted by a hat):

$$\hat{H} = \hat{H}_0 + \hat{H}_{\text{int}} \quad (1a)$$

$$\hat{H}_0 = \sum_{\mathbf{R}_i, \mathbf{R}_j} \sum_{\sigma} t_{ij} \hat{c}_{i\sigma}^{\dagger} \hat{c}_{j\sigma} = \sum_{\mathbf{k}, \sigma} \varepsilon_{\mathbf{k}} \hat{n}_{\mathbf{k}\sigma} \quad (1b)$$

$$\hat{H}_{\text{int}} = U \sum_{\mathbf{R}_i} \hat{n}_{i\uparrow} \hat{n}_{i\downarrow} \equiv U \hat{D}. \quad (1c)$$

Here  $\hat{c}_{i\sigma}^{\dagger}$  ( $\hat{c}_{i\sigma}$ ) are creation (annihilation) operators of fermions with spin  $\sigma$  at site  $\mathbf{R}_i$  (for simplicity denoted by  $i$ ),  $\hat{n}_{i\sigma} = \hat{c}_{i\sigma}^{\dagger} \hat{c}_{i\sigma}$ , and  $\hat{D}$  is the operator of total double occupation of the lattice sites. The Fourier transform of the kinetic energy in (1b), where  $t_{ij}$  is the amplitude for hopping between sites  $i$  and  $j$ , involves the dispersion  $\varepsilon_{\mathbf{k}}$  and the momentum distribution operator  $\hat{n}_{\mathbf{k}\sigma}$ . A schematic picture of the Hubbard model is shown in Fig. 1.

In the Hubbard model the Coulomb interaction between two electrons is assumed to be so strongly screened that it can be described as a purely local interaction which occurs only *on* a



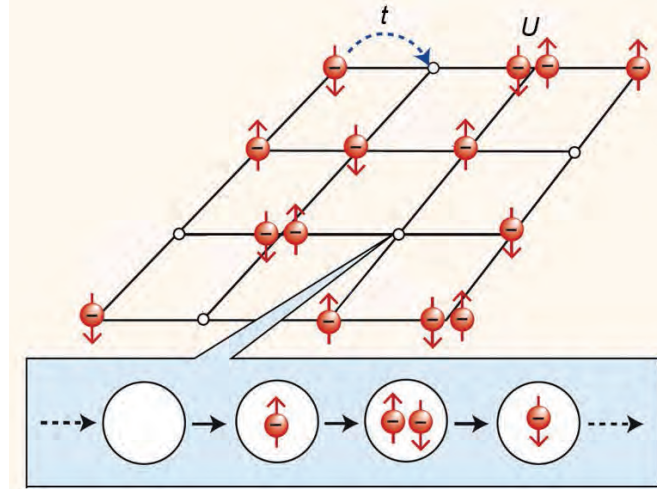


**Fig. 1:** Schematic illustration of interacting electrons in a solid described by the Hubbard model. The ions enter only as a rigid lattice, here represented by a square lattice. The electrons, which have mass, negative charge, and spin ( $\uparrow$  or  $\downarrow$ ), are quantum particles which move from one lattice site to the next with a hopping amplitude  $t$ . Together with the lattice structure this determines the band structure of the non-interacting electrons. The quantum dynamics leads to fluctuations in the occupation of lattice sites as indicated by the sequence: a lattice site can either be unoccupied, singly occupied ( $\uparrow$  or  $\downarrow$ ), or doubly occupied. When two electrons meet on a lattice site, which is only possible if they have opposite spin because of the Pauli exclusion principle, they encounter a local interaction  $U$ .

lattice site.<sup>4</sup> In view of the Pauli principle the interaction is therefore only possible if the two electrons have opposite spin. A direct interaction between electrons with equal spin direction, e.g., on neighboring sites, is not described by the model, but can be easily included. The interaction is therefore completely independent of the lattice structure and spatial dimension of the system. This property distinguishes it from other model interactions since it has no classical counterpart. The kinetic energy  $\hat{H}_0$  is diagonal in momentum space and reflects the wave nature of the electrons, while the interaction energy  $\hat{H}_{\text{int}}$  is diagonal in position space and characterizes their particle nature.

The physics described by the Hubbard model is clearly very different from that of bare electrons with a long-range Coulomb interaction. Therefore the Hubbard model is far from obvious. Its formulation required fundamentally new insights as explained in section 1.1. In particular, screening is a basic ingredient of the many-body problem of metals.

As discussed above, the Hubbard model was originally introduced to provide a microscopic explanation of ferromagnetism in 3d transition metals [14–16]. How should this model be able to do that? In fact, the interaction energy is lowest (zero) when double occupation of lattice sites is fully suppressed, i.e., when the spins of electrons are ferromagnetically aligned. From the point of view of the interaction alone one can therefore expect the ground state to be ferromagnetic for sufficiently strong repulsion  $U$ . However, this argument neglects the kinetic

<sup>4</sup>In particular, the Hubbard model applies to lattice fermions with a point interaction, such as cold atoms in optical lattices where the bare interaction is indeed extremely short-ranged [27, 28]; see section 5.2.2.

energy. While the lattice structure and spatial dimension do not affect the Hubbard interaction at all, they play a very important role for the kinetic energy since they determine the structure of the density of states of the non-interacting electrons. This is especially important for the stabilization of ferromagnetism and will be discussed in more detail in section 6.1.

In spite of the extreme simplifications made by the Hubbard model in comparison with interacting electrons in a real solid, it still cannot be solved analytically, except in dimension  $d = 1$  for nearest-neighbor hopping [29]. For dimensions  $d = 2, 3$ , approximations are required.<sup>5</sup> Here “mean-field theories” play a particularly important role.

## 2 Mean-field theories

In the statistical theory of classical and quantum-mechanical systems a rough, overall description of the properties of a model can often be obtained within a mean-field theory. While in the full many-body model a particle or spin experiences a complicated, fluctuating field generated by the other particles or spins, in a mean-field theory this fluctuating field is approximated by an average (“mean”) field. Usually, but not always, the full interaction problem then reduces to an effective, single-particle problem — a self-consistent field theory.

A mean-field theory can often be constructed by letting some variable or parameter become large (in fact, infinite), whereby fluctuations are suppressed. Depending on the model this can be the length of the spins  $S$ , the spin degeneracy  $N$ , the spatial dimension  $d$ , or the coordination number  $Z$ , i.e., the number of nearest neighbors of a lattice site.<sup>6</sup> Mean-field theories obtained in such a limit, supplemented if possible by an expansion in the inverse of the large parameter, can provide valuable insights into the fundamental properties of a model. Perhaps the best-known mean-field theory in many-body physics is the Weiss molecular-field theory for the Ising model [31]. It is a prototypical “single-site mean-field theory” which becomes exact in the limit of infinite coordination number  $Z$  or infinite dimensions  $d$ .

### 2.1 Infinite dimensions

The meaning of “infinite dimensions” needs some explanation. Already in  $d = 3$  the coordination number can be quite large, e.g.,  $Z = 6$  for a simple cubic lattice,  $Z = 8$  for a bcc lattice and  $Z = 12$  for an fcc-lattice, making its inverse,  $1/Z$ , rather small. It is then interesting to investigate whether the limit  $Z \rightarrow \infty$  leads to some simplifications. For a hypercubic lattice, obtained by generalizing the simple cubic lattice in  $d = 3$  to arbitrary dimensions, one has  $Z = 2d$ . The limit  $d \rightarrow \infty$  is then equivalent to  $Z \rightarrow \infty$ .

<sup>5</sup>In view of the complexity of the many-body problem in condensed matter theory, progress in this field relies on making good approximations. As Peierls wrote: “... *the art of choosing a suitable approximation, of checking its consistency and finding at least intuitive reasons for expecting the approximation to be satisfactory, is much more subtle than that of solving an equation exactly*” [30].

<sup>6</sup>For regular lattices both a dimension  $d$  and a coordination number  $Z$  can be defined. The coordination number  $Z$  is then determined by the dimension  $d$  and the lattice structure. But there exist other lattice-like structures, such as the Bethe lattice, which cannot be associated with a physical dimension  $d$ , although a coordination number  $Z$  is well-defined.

It is interesting to note that investigations in statistical mechanics based on the simplifications arising in the limit of infinite coordination number  $Z$  or dimension  $d$  do not go far back. In fact,  $Z$  originally denoted the number of spins in the *range* of the interaction [32]. In this case the limit  $Z \rightarrow \infty$  describes an infinitely long-ranged interaction.<sup>7</sup> Since a particle or spin at a given site then interacts with infinitely many other particles or spins (which are all “neighbors”), this limit was referred to as “limit of infinite dimensions” or “limit of high density” [32]. It was found that the Weiss mean-field theory for the Ising model becomes exact in this limit. Starting with Fisher and Gaunt [33] in 1964 the Ising model and other classical models were investigated on general  $d$ -dimensional simple hypercubic lattices. Now  $Z$  is really the coordination number, i.e., the number of nearest neighbors, as we use it today, with  $Z = 2d$ . For the Ising model the limit of infinitely long-ranged spin coupling  $J$  and the limit of infinite dimensions  $d$  both yield the same result, namely the Weiss mean-field theory.

## 2.2 Weiss mean-field theory for the Ising model

The Hamiltonian for the Ising model with nearest-neighbor coupling between two classical spins is given by

$$H = -\frac{1}{2} J \sum_{\langle \mathbf{R}_i, \mathbf{R}_j \rangle} S_i S_j, \quad (2)$$

where we assume ferromagnetic coupling ( $J > 0$ ) and summation over nearest-neighbor sites. This can also be written as

$$H = \sum_{\mathbf{R}_i} h_i S_i, \quad (3)$$

where now every spin  $S_i$  interacts with a local field

$$h_i = -J \sum_{\mathbf{R}_j}^{(i)} S_j \quad (4)$$

produced by the spins on nearest-neighbor sites; here the superscript  $(i)$  implies summation over the nearest-neighbor sites of  $\mathbf{R}_i$ . In the Weiss mean-field theory the spin interaction in (2), or the interaction of a spin with the local field in (3), are decoupled, i.e.,  $H$  is replaced by a mean-field Hamiltonian

$$H^{\text{MF}} = h_{\text{MF}} \sum_{\mathbf{R}_i} S_i + E_{\text{shift}}. \quad (5)$$

Now a spin  $S_i$  interacts only with a global (“molecular”) field

$$h_{\text{MF}} \equiv \langle h_i \rangle = -JZS, \quad (6)$$

---

<sup>7</sup>This limit can be even used in one-dimensional particle models, in which case the equation of state reduces to the van der Waals equation [31].

where  $\langle \rangle$  indicates the thermal average,  $\langle S_i \rangle \equiv S$ ,  $E_{\text{shift}} = \frac{1}{2} L J Z \langle S \rangle^2$  is a constant energy shift, and  $L$  is the number of lattice sites. Formally this result can be obtained by employing the factorization

$$\langle (S_i - S)(S_j - S) \rangle = 0, \quad (7)$$

whereby correlated fluctuations of spins at sites  $\mathbf{R}_i$  and  $\mathbf{R}_j$  are neglected. In the limit  $Z \rightarrow \infty$  the coupling constant  $J$  needs to be rescaled as

$$J \rightarrow \frac{J^*}{Z}, \quad J^* = \text{const} \quad (8)$$

for  $h_{\text{MF}}$ , and thereby the energy, to remain finite. In this limit the factorization (7), and hence the replacement of (2) by the mean-field Hamiltonian (5), becomes exact [32, 34]. Eq. (5) implies that in the limit  $Z \rightarrow \infty$  fluctuations of a finite number of spins in the “bath” of surrounding neighbors become unimportant, such that the surrounding of any site is completely described by a single mean-field  $h_{\text{MF}}$ . Hence the Hamiltonian becomes purely local

$$H^{\text{MF}} = \sum_{\mathbf{R}_i} H_i + E_{\text{shift}}, \quad (9)$$

where  $H_i = h_{\text{MF}} S_i$ . Thereby the problem reduces to an effective single-site problem. The value of  $S$  (the “magnetization”) is determined by the self-consistent Curie-Weiss or Bragg-Williams equation

$$S = \tanh(\beta J^* S), \quad (10)$$

where  $\beta = 1/(k_B T)$  and the self-consistency condition (6) was used. The scaling (8) is typical for localized spin models.

The Weiss mean-field theory is seen to become exact in the limit of infinite coordination number  $Z$  or dimension  $d$ . In this case  $1/Z$  or  $1/d$  serve as a small parameter which can be used to improve the mean-field theory systematically. The Weiss mean-field theory contains no unphysical singularities, is applicable for all values of the input parameters (temperature and/or additional external magnetic field), and is diagrammatically controlled [35]. Therefore it is often viewed as a prototypical mean-field theory in statistical mechanics.

## 2.3 Hartree mean-field theory for the Hubbard model

Lattice fermion models such as the Hubbard model are much more complicated than localized spin models. Therefore the construction of a mean-field theory with the comprehensive properties of the Weiss mean-field theory for the Ising model will be more complicated, too.

The simplest static mean-field theory for the Hubbard model is the Hartree approximation [36–38]. To clarify the shortcomings of this mean-field theory we proceed as in the derivation of the Weiss mean-field theory for the Ising model and factorize the interaction term. To this end we rewrite the Hubbard interaction in the form of (3), i.e., we let an electron with spin  $\sigma$  at site  $\mathbf{R}_i$  interact with a local field  $\hat{h}_{i\sigma}$  produced by an electron with opposite spin on that site<sup>8</sup>

<sup>8</sup>This field is described by an operator and therefore has a dynamics.

$$\hat{H}_{\text{int}} = \sum_{\mathbf{R}_i} \sum_{\sigma} \hat{h}_{i\sigma} \hat{n}_{i\sigma}, \quad (11)$$

where  $\hat{h}_{i\sigma} = \frac{1}{2}U\hat{n}_{i-\sigma}$ . As in the derivation of the Weiss mean-field theory we now factorize the two-particle interaction in (11), i.e., we replace  $\hat{H}$  by

$$\hat{H}^{\text{MF}} = \hat{H}_{\text{kin}} + \sum_{\mathbf{R}_i, \sigma} \langle \hat{h}_{i\sigma} \rangle \hat{n}_{i\sigma} + E_{\text{shift}}. \quad (12)$$

Now a  $\sigma$ -electron at site  $\mathbf{R}_i$  interacts only with a local, *static* field (a c-number)

$$\langle \hat{h}_{i\sigma} \rangle = \frac{1}{2}U n_{-\sigma}, \quad (13)$$

where  $n_{-\sigma} = \langle \hat{n}_{i-\sigma} \rangle$  is the global density of  $(-\sigma)$ -electrons. The above decoupling of the operators corresponds to the Hartree approximation,<sup>9</sup> which assumes

$$\langle (\hat{n}_{i\sigma} - n_{\sigma})(\hat{n}_{i-\sigma} - n_{-\sigma}) \rangle = 0, \quad (14)$$

whereby correlated fluctuations *on* the site  $\mathbf{R}_i$  are neglected.

It is important to note that although (12) is now a one-particle problem it still cannot be solved exactly, since, in principle, the potential (the static mean field  $\langle \hat{h}_{i\sigma} \rangle$ ) may vary from site to site. This is a new feature due to the quantum-mechanical kinetic energy, which enters as an additional term in the Hamiltonian.

The Hartree approximation becomes exact in the weak-coupling limit ( $U \rightarrow 0$ ) and/or the low-density limit ( $n \rightarrow 0$ ). But how about  $d \rightarrow \infty$ ? Does it become exact in this limit for all input parameters (temperature, density, interaction strength)? The answer is clearly no: the Hubbard interaction is purely local and hence independent of the spatial dimensions. Although the factorizations (7) and (14) are mathematical identical, the physics they imply is very different. Namely, (7) describes the decoupling of a spin from a bath of infinitely many neighboring spins in which fluctuations do indeed become unimportant in the limit  $d \rightarrow \infty$ , while (14) corresponds to the decoupling of an electron from *one* other electron (with opposite spin) on the same site. For strong repulsion  $U$  double occupation of a lattice site is energetically unfavorable and is therefore suppressed. In this situation the local correlation function  $\langle \hat{n}_{i\uparrow} \hat{n}_{i\downarrow} \rangle$  must not be factorized, since otherwise correlation phenomena are immediately eliminated. It is therefore clear that the Hartree decoupling, which factorizes the local quantum dynamics, can never become exact in any dimension or for any coordination number, since  $\langle \hat{n}_{i\uparrow} \hat{n}_{i\downarrow} \rangle \neq \langle \hat{n}_{i\uparrow} \rangle \langle \hat{n}_{i\downarrow} \rangle$ , unless  $U \rightarrow 0$  and/or  $n \rightarrow 0$ . Hence the nature of the Hartree mean-field theory for spin- $\frac{1}{2}$  electrons with on-site interaction is very different from the Weiss mean-field theory for spins with nearest-neighbor coupling.

---

<sup>9</sup>Since the Hubbard interaction acts only between electrons with opposite spin on the same lattice site an exchange (Fock) term does not arise.

### 3 Gutzwiller variational method

Another useful but very different approximation scheme for quantum many-body systems, which has a long and successful history in theoretical many-body physics [39], makes use of variational wave functions. Starting from a many-body trial wave function the energy expectation value is calculated and then minimized with respect to physically motivated variational parameters. Although variational wave functions usually yield only approximate results, they have several advantages: they are physically intuitive, can be custom tailored to a particular problem, and can be used even when standard perturbation methods fail or are inapplicable.

For the analytic investigation of the electronic correlation model which Gutzwiller [14] had introduced (and which was later named after Hubbard), he had also proposed a very simple variational wave function. This “Gutzwiller wave function” introduces correlations into the wave function for non-interacting particles via a purely local correlation factor in real space, which is constructed from the double occupation operator  $\hat{D}$  as

$$|\Psi_G\rangle = g^{\hat{D}} |\text{FG}\rangle \quad (15a)$$

$$= \prod_{\mathbf{R}_i} (1 - (1 - g)\hat{D}_i) |\text{FG}\rangle. \quad (15b)$$

Here  $|\text{FG}\rangle$  is the wave function of non-interacting fermions (Fermi Gas),  $g$  is a variational parameter with  $0 \leq g \leq 1$ , and  $\hat{D}_i = \hat{n}_{i\uparrow}\hat{n}_{i\downarrow}$  is the operator of double occupation of lattice site  $\mathbf{R}_i$ , which monitors the interaction on that site. The projector  $g^{\hat{D}}$  globally reduces the amplitude of those spin configurations in  $|\text{FG}\rangle$  which have too many doubly occupied sites for given repulsion  $U$ . The limit  $g = 1$  describes the non-interacting case, while  $g \rightarrow 0$  corresponds to strong coupling (usually  $U \rightarrow \infty$ ). The Gutzwiller wave function can be used to calculate the expectation value of an operator, e.g., the ground state energy  $\bar{E}(g, U)$  of the Hubbard model, using the Hamiltonian (1). By computing the minimum of  $\bar{E}(g, U)$ , the variational parameter  $g$  is determined as a function of the interaction parameter  $U$ .

#### 3.1 Gutzwiller approximation

In general the evaluation of expectation values cannot be performed exactly. Therefore Gutzwiller introduced a non-perturbative approximation scheme which allowed him to obtain an explicit expression for the ground state energy of the Hubbard model [14, 40]; for details see Refs. [41, 24]. The Gutzwiller approximation is based on the counting of classical spin configurations and is therefore a quasiclassical approximation. The idea behind the approximation can be illustrated by calculating the norm  $\langle \Psi_G | \Psi_G \rangle$ . In configuration space the ground state of the Fermi gas can be written as

$$|\text{FG}\rangle = \sum_D \sum_{\{i_D\}} A_{i_D} |\Psi_{i_D}\rangle, \quad (16)$$

where  $|\Psi_{i_D}\rangle$  is a spin configuration with  $D$  doubly occupied sites and  $A_{i_D}$  is the corresponding probability amplitude. The sum extends over the whole set  $\{i_D\}$  of different configurations with

the same  $D$ , and over all  $D$ . For a system with  $L$  lattice sites and  $N_\sigma$   $\sigma$ -electrons the number  $N_D$  of different configurations in  $\{i_D\}$  is given by the combinatorial expression

$$N_D = \frac{L!}{L_\uparrow! L_\downarrow! D! E!}, \quad (17)$$

where  $L_\sigma = N_\sigma - D$ , and  $E = L - N_\uparrow - N_\downarrow + D$  are the numbers of singly occupied and empty sites, respectively. Since  $|\Psi_{i_D}\rangle$  is an eigenstate of  $\hat{D}$ , the norm of  $|\Psi_G\rangle$  reads

$$\langle \Psi_G | \Psi_G \rangle = \sum_D g^{2D} \sum_{\{i_D\}} |A_{i_D}|^2. \quad (18)$$

In the Gutzwiller approximation spatial correlations between the spins of the electrons are neglected. The probability  $|A_{i_D}|^2$  is then the same for all configurations of electrons on the lattice, i.e., is given by the classical combinatorial result for uncorrelated particles

$$|A_{i_D}|^2 = P_\uparrow P_\downarrow, \quad (19)$$

where  $P_\sigma = 1/\binom{L}{N_\sigma} = N_\sigma! (L - N_\sigma)! / L! \simeq n_\sigma^{N_\sigma} (1 - n_\sigma)^{L - N_\sigma}$ , with  $n_\sigma = N_\sigma / L$ , is the probability for an arbitrary configuration of  $\sigma$ -electrons. In this case (18) reduces to

$$\langle \Psi_G | \Psi_G \rangle = P_\uparrow P_\downarrow \sum_D g^{2D} N_D. \quad (20)$$

In the thermodynamic limit the sum in (20) is dominated by its largest term corresponding to a value  $D = \bar{D}$ , where  $\bar{D}$  is determined by

$$g^2 = \frac{\bar{d}(1 - n_\uparrow - n_\downarrow + \bar{d})}{(n_\downarrow - \bar{d})(n_\uparrow - \bar{d})}, \quad (21)$$

where  $\bar{d} = \bar{D}/L$ . Eq. (21) has the form of the law of mass action, where the correlation parameter  $g^2$  rather than the Boltzmann factor regulates the dynamical equilibrium between the concentrations of singly occupied sites on one side of this “chemical reaction” and that of doubly occupied sites and holes on the other.<sup>10</sup> The calculation of the expectation values of the kinetic and the interaction energy of the Hubbard model proceeds similarly [41]. We will later see that the Gutzwiller approximation leads to the correct results for the expectation value of an operator calculated in terms of the Gutzwiller wave function in the limit  $d = \infty$ .

### 3.2 Brinkman-Rice transition

The results of the Gutzwiller approximation [14,40] describe a correlated, normal-state fermionic system at zero temperature whose momentum distribution has a discontinuity  $q$  at the Fermi level, with  $q = 1$  in the non-interacting case, which is reduced to  $q < 1$  by the interaction as in a Landau Fermi liquid. In 1970 Brinkman and Rice [43] observed that in the case of a half-filled

<sup>10</sup>In fact, eq. (21), with  $g^2$  replaced by the Boltzmann factor  $e^{-\beta U}$ , is the exact result for the Hubbard model with infinite-range hopping [42].

band ( $n_{\uparrow} = n_{\downarrow} = 1/2$ ) the Gutzwiller approximation describes a transition at a finite critical interaction strength  $U_c$  from an itinerant to a localized state, where lattice sites are singly occupied and the discontinuity  $q$  vanishes. This “Brinkman-Rice transition” therefore corresponds to a correlation induced (Mott) metal-insulator transition. They argued [43] that the inverse of  $q$  can be identified with the effective mass of Landau quasiparticles,  $q^{-1} = m^*/m \geq 1$ , which diverges at  $U_c$ .

The results obtained with the Gutzwiller approximation are physically very reasonable. In fact, in the nineteen-seventies and eighties it was the only approximation scheme which was able to describe a Mott metal-insulator transition at a finite value of the interaction *and* was in accord with basic properties of Landau Fermi liquid theory.<sup>11</sup> This was confirmed by a detailed investigation of the assumptions and implications of the Gutzwiller approximation which I published in 1984 [41], and in which I showed that the Gutzwiller-Brinkman-Rice theory was not only in qualitative [46], but even in good quantitative agreement with experimentally measured properties of normal-liquid  $^3\text{He}$ ; for a discussion see section 3 in Ref. [47].

### 3.3 Systematic derivation of the Gutzwiller approximation?

The results of the Gutzwiller approximation are clearly mean-field-like since, for example, the kinetic energy of the correlated system is obtained by renormalizing the kinetic energy of non-interacting single-particle states  $(\mathbf{k}, \sigma)$  by an overall factor  $q$ . This is also one of the reasons why the results obtained for the Hubbard lattice model have a much wider range of applicability, i.e., can even be used to understand liquid  $^3\text{He}$  [41, 48]. However, the validity of the Gutzwiller approximation was still unclear in 1984. In particular, it was not known how to improve this approximation — after all it was based on the calculation of *quantum-mechanical* matrix elements from the most probable *classical* spin configurations. The question was, whether the Gutzwiller approximation could be derived in a controlled way, for example by calculating expectation values of operators with the Gutzwiller wave function using quantum many-body perturbation theory in a well-defined limit, or by some other method of quantum many-body theory. This question was answered a few years later, when the Gutzwiller approximation was re-derived in two different ways: as a slave-boson mean-field theory [49]<sup>12</sup> and in the limit of infinite spatial dimensions [52], as will be discussed below.

<sup>11</sup>Other well-known approximation schemes, in particular those proposed by Hubbard, did not have these important properties: in the Hubbard-I approximation [15], which interpolates between the atomic limit and the non-interacting band, a band gap exists for any  $U > 0$  (so there is no Mott transition at all), while the Hubbard-III approximation [44] corresponds to the coherent potential approximation [45] for disordered systems, in which case the Fermi surface volume is not conserved.

<sup>12</sup>Kotliar and Ruckenstein [50] formulated a functional integral representation of the Hubbard and Anderson models in terms of auxiliary bosons, whose simplest saddle-point approximation (“slave-boson mean-field theory”) reproduces exactly the results of the Gutzwiller approximation [49]. Thus they showed that the results of the Gutzwiller approximation can also be obtained without the use of the Gutzwiller variational wave function.



## 4 Lattice fermions in infinite dimensions

The expectation values of the kinetic and the interaction energy of the Hubbard model (1) in terms of the Gutzwiller wave function can, in principle, be calculated within diagrammatic many-body perturbation theory for arbitrary dimensions  $d$ . Introducing a new analytic approach in which the expectation values were expressed by sums over different lattice sites, Walter Metzner and I showed that these calculations can be greatly simplified [51, 52].<sup>13</sup> Thereby we were able to calculate the diagrams analytically to all orders in  $d = 1$ , which led to analytic results for the ground-state energy for arbitrary density  $n$  and interaction strength  $U$  [51, 52].<sup>14</sup> In  $d > 1$  analytic calculations to all orders were not possible. But by evaluating individual diagrams numerically in dimensions as high as  $d = 15$  we observed that in  $d = \infty$  the values of these diagrams could equally be obtained if momentum conservation at a vertex was neglected, i.e., if the momenta carried by the lines of a diagram were assumed to be independent. When summed over all diagrams this approximation gave exactly the results of the Gutzwiller approximation [52]. Thus the Gutzwiller approximation had been derived systematically within quantum many-body perturbation theory in the limit of infinite spatial dimensions. Apparently the limit  $d \rightarrow \infty$  was not only useful for the investigation of spin models, but also for fermions.

### 4.1 Simplifications of diagrammatic many-body perturbation theory

The simplifications of the diagrammatic many-body perturbation theory in the limit  $d \rightarrow \infty$  are due to a collapse of irreducible diagrams, which implies that only local diagrams remain [57, 58]. In particular, the irreducible self-energy is then completely local (Fig. 2). To understand this diagrammatic collapse let us consider diagrams where lines correspond to one-particle density matrices,  $g_{ij,\sigma}^0$ , as they enter in the calculation of expectation values with the Gutzwiller wave function (nevertheless the following arguments are equally valid for the one-particle Green function  $G_{ij,\sigma}^0(\omega)$ <sup>15</sup>). The one-particle density matrix may be interpreted as the amplitude for transitions between sites  $\mathbf{R}_i$  and  $\mathbf{R}_j$ . The square of its absolute value is therefore proportional to the *probability* for a particle to hop from  $\mathbf{R}_j$  to a site  $\mathbf{R}_i$ . In the case of nearest-neighbor sites on a lattice with coordination number  $Z$  this implies  $|g_{ij,\sigma}^0|^2 \sim \mathcal{O}(1/Z)$ . For nearest-neighbor

<sup>13</sup>The resulting diagrams have the same form as Feynman diagrams in many-body perturbation theory (due to the locality of the interaction they are identical to those of a  $\Phi^4$  theory), but a line corresponds to a one-particle density matrix  $g_{ij,\sigma}^0 = \langle \hat{c}_{i\sigma}^\dagger \hat{c}_{j\sigma} \rangle_0$  and not to a one-particle propagator  $G_{ij,\sigma}^0(\omega)$  since in the variational approach there is no dynamics.

<sup>14</sup>Correlation functions can also be calculated analytically in  $d = 1$  [53, 54] and provide further insights into the properties of the Gutzwiller wave function. For example, the result for the spin-spin correlation function show that in the strong coupling limit the Gutzwiller wave function describes spin correlations in the nearest-neighbor, isotropic Heisenberg chain extremely well and coincides with the exact solution of the spin-1/2 antiferromagnetic Heisenberg chain with an exchange interaction falling off as  $1/r^2$  [55, 56]; for a discussion see section 4.1 in Ref. [47].

<sup>15</sup>This follows directly from  $g_{ij,\sigma}^0 = \lim_{t \rightarrow 0^-} G_{ij,\sigma}^0(t)$  and the fact that the scaling properties do not depend on the time evolution and the quantum-mechanical representation. The Fourier transform of  $G_{ij,\sigma}^0(\omega)$  also preserves this property. For this reason the same results as those obtained in the calculation with the Gutzwiller wave function hold: all connected one-particle irreducible diagrams collapse in position space, i.e., are purely diagonal in  $d = \infty$ .

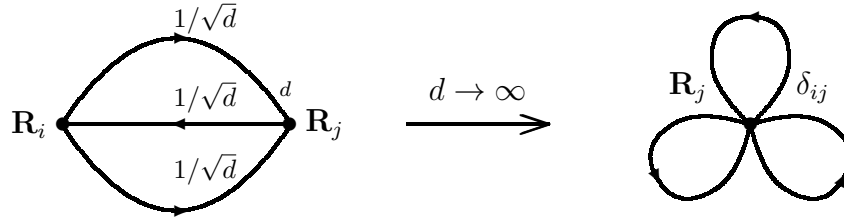


**Fig. 2:** Collapse of the irreducible self-energy diagram for the Hubbard model in second-order perturbation theory in  $U$  in the limit  $d \rightarrow \infty$ .

sites  $\mathbf{R}_i$  and  $\mathbf{R}_j$  on a hypercubic lattice (where  $Z = 2d$ ) one therefore finds for large  $d$  [57, 58]

$$g_{ij,\sigma}^0 \sim \mathcal{O}\left(\frac{1}{\sqrt{d}}\right). \quad (22)$$

For general  $i, j$  one obtains [58, 59]

$$g_{ij,\sigma}^0 \sim \mathcal{O}\left(1/d^{\|\mathbf{R}_i - \mathbf{R}_j\|/2}\right). \quad (23)$$

Here  $\|\mathbf{R}\| = \sum_{n=1}^d |R_n|$  is the length of  $\mathbf{R}$  in the “New York metric”, where particles only hop along horizontal or vertical lines, never along a diagonal; for further discussions of diagrammatic simplifications see Ref. [60].<sup>16</sup>

For non-interacting electrons at  $T = 0$  the expectation value of the kinetic energy is given by

$$E_{\text{kin}}^0 = -t \sum_{\langle \mathbf{R}_i, \mathbf{R}_j \rangle} \sum_{\sigma} g_{ij,\sigma}^0. \quad (24)$$

On a hypercubic lattice the sum over nearest neighbors leads to a factor  $\mathcal{O}(d)$ . In view of the  $1/\sqrt{d}$  dependence of  $g_{ij,\sigma}^0$  it is therefore necessary to scale the nearest-neighbor hopping amplitude  $t$  as

$$t \rightarrow \frac{t^*}{\sqrt{d}}, \quad t^* = \text{const.}, \quad (25)$$

since only then the kinetic energy remains finite for  $d \rightarrow \infty$ . The same result is obtained in a momentum-space formulation.<sup>17</sup> It is important to bear in mind that, although  $g_{ij,\sigma}^0 \sim 1/\sqrt{d}$

<sup>16</sup>Gebhard [61] showed that it is possible to calculate with the Gutzwiller wave function in the limit  $d = \infty$  even without diagrams. Thereby he re-derived the full set of static saddle-point equations of the slave-boson approach and provided a direct connection between the slave-boson mean-field theory [49] and the diagrammatic calculation of expectation values in terms of the Gutzwiller wave function in  $d = \infty$  [57, 58]. The approach was generalized by him and collaborators to multi-band Hubbard models into a “Gutzwiller density functional theory” which can be used to describe the effect of correlations in real materials [62, 63].

<sup>17</sup>This can be seen by calculating the density of states of non-interacting particles. For nearest-neighbor hopping on a  $d$ -dimensional hypercubic lattice  $\varepsilon_{\mathbf{k}}$  has the form  $\varepsilon_{\mathbf{k}} = -2t \sum_{i=1}^d \cos k_i$  (here and in the following we set Planck’s constant  $\hbar$ , Boltzmann’s constant  $k_B$ , and the lattice spacing equal to unity). The density of states corresponding to  $\varepsilon_{\mathbf{k}}$  is given by  $N_d(\omega) = \sum_{\mathbf{k}} \delta(\omega - \varepsilon_{\mathbf{k}})$ , which is the probability density for finding the value  $\omega = \varepsilon_{\mathbf{k}}$  for a random choice of  $\mathbf{k} = (k_1, \dots, k_d)$ . If the momenta  $k_i$  are chosen randomly,  $\varepsilon_{\mathbf{k}}$  is the sum of  $d$  many independent (random) numbers  $-2t \cos k_i$ . The central limit theorem then implies that in the limit  $d \rightarrow \infty$  the density of states is given by a Gaussian, i.e.,  $N_d(\omega) \xrightarrow{d \rightarrow \infty} \frac{1}{2t\sqrt{\pi d}} \exp\left[-\left(\frac{\omega}{2t\sqrt{d}}\right)^2\right]$ . Only if  $t$  is scaled with  $d$  as in (25) does one obtain a non-trivial density of states  $N_{\infty}(\omega)$  in  $d = \infty$  [38, 57] and thus a finite kinetic energy.

vanishes for  $d \rightarrow \infty$ , the particles are not localized, but are still mobile. Indeed, even in the limit  $d \rightarrow \infty$  the off-diagonal elements of  $g_{ij,\sigma}^0$  contribute, since particles may hop to  $d$  many nearest neighbors with amplitude  $t^*/\sqrt{d}$ .

A rescaling of the microscopic parameters of the Hubbard model with  $d$  is only required in the kinetic energy, since the interaction term is independent of the spatial dimension. Altogether this implies that only the Hubbard Hamiltonian with a rescaled kinetic energy

$$\hat{H} = -\frac{t^*}{\sqrt{d}} \sum_{\langle \mathbf{R}_i, \mathbf{R}_j \rangle} \sum_{\sigma} \hat{c}_{i\sigma}^\dagger \hat{c}_{j\sigma} + U \sum_{\mathbf{R}_i} \hat{n}_{i\uparrow} \hat{n}_{i\downarrow} \quad (26)$$

has a non-trivial  $d \rightarrow \infty$  limit where both the kinetic energy and the interaction contribute equally. Namely, it is the *competition* between the two terms which leads to interesting many-body physics.

#### 4.1.1 Is there a unique $d \rightarrow \infty$ limit for the Hubbard model?

The motivation for the scaling discussed above deserves a more detailed discussion: To obtain a physically meaningful mean-field theory for a model, its internal or free energy has to remain finite in the limit  $d$  or  $Z \rightarrow \infty$ . While for the Ising model the scaling  $J \rightarrow J^*/Z$ ,  $J^* = \text{const.}$ , is rather obvious, this is not so for more complicated models. Namely, fermionic or bosonic many-particle systems are usually described by a Hamiltonian with several non-commuting terms, e.g., a kinetic energy and an interaction, each of which is associated with a coupling parameter, usually a hopping amplitude and an interaction, respectively. In such a case the question of how to scale these parameters has no unique answer since this depends on the physical effects one wishes to explore. The scaling should be performed such that the model remains non-trivial and that its internal or free energy stays finite in the  $d, Z \rightarrow \infty$  limit. Here “non-trivial” means that not only  $\langle \hat{H}_0 \rangle$  and  $\langle \hat{H}_{\text{int}} \rangle$  but also the *competition*, expressed by  $\langle [\hat{H}_0, \hat{H}_{\text{int}}] \rangle$ , should remain finite. In the case of the Hubbard model it would be possible to scale the hopping amplitude as in the Weiss mean-field theory, i.e.,  $t \rightarrow t^*/Z$ ,  $t^* = \text{const.}$ , but then the kinetic energy would be reduced to zero in the limit  $d, Z \rightarrow \infty$ , making the resulting model uninteresting (but not unphysical) for most purposes. For the bosonic Hubbard model the situation is even more subtle, since the kinetic energy has to be scaled differently depending on whether it describes the normal or the Bose-Einstein condensed fraction; for a discussion see Ref. [64]. Hence, in the case of a many-body system described by a Hamiltonian with several terms, the solution in the limit  $d \rightarrow \infty$  depends on the scaling of the model parameters.

## 4.2 The Hubbard model in $d = \infty$

In our 1989 paper [57] Walter Metzner and I had shown (i) that the diagrammatic collapse of diagrams which occurs in the limit  $d \rightarrow \infty$  leads to great simplifications in quantum many-body perturbation theory and (ii) that the Hubbard model, when scaled properly, stills describes nontrivial correlations among the fermions. This is already apparent from the evaluation of the second-order diagram in Goldstone perturbation theory for the correlation energy at weak

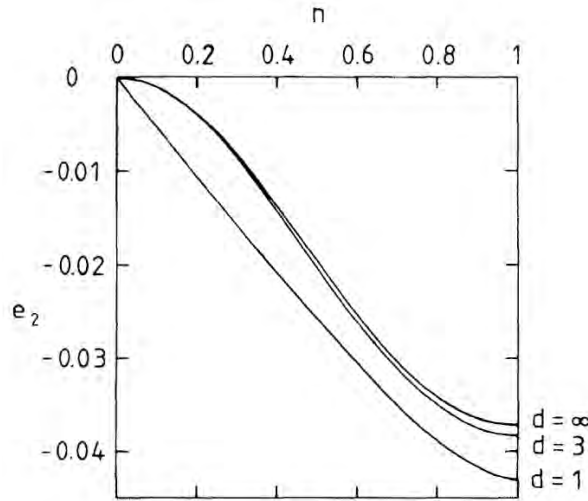


**Fig. 3:** Correlation energy of the Hubbard model in second-order Goldstone perturbation theory in  $U$  (in units of  $2U^2/|\varepsilon_0|$ ) vs. density  $n$  for dimensions  $d = 1, 3, \infty$ . Here  $\varepsilon_0$  is the kinetic energy for  $U = 0$  and  $n = 1$ ; adapted from Ref. [57].

coupling [57]. Namely, the nine-dimensional integral in  $d = 3$  over the three internal momenta reduces to a single integral in  $d = \infty$ , implying that in  $d = \infty$  the calculation is simpler than in any other dimension. More importantly, the numerical results obtained in  $d = \infty$  turn out to be very close to those in  $d = 3$  and therefore provide a computationally simple, but quantitatively reliable approximation (Fig. 3).

These results clearly showed that microscopic calculations for correlated lattice fermions in  $d = \infty$  dimensions were useful and very promising. Further insights followed quickly:

(i) Müller-Hartmann [65] proved that in infinite dimensions only local interactions remain dynamical, that the proper self-energy becomes momentum independent<sup>18</sup>

$$\Sigma_\sigma(\mathbf{k}, \omega) \stackrel{d \rightarrow \infty}{\equiv} \Sigma_\sigma(\omega), \quad (27)$$

and that therefore typical Fermi liquid features are preserved [66] (for a discussion see section 4.2.3),

(ii) Schweitzer and Czycholl [71] demonstrated that calculations for the periodic Anderson model also become much simpler in high dimensions, and

(iii) Brandt and Mielsch [72] derived the exact solution of the Falicov-Kimball model for infinite dimensions by mapping the lattice problem onto a solvable atomic problem in a generalized,

<sup>18</sup>This result may be understood as follows [67, 68]: The interaction between particles influences their motion. This effect is described by a complex, spatially dependent, and dynamical field — the self-energy  $\Sigma_\sigma(\mathbf{k}, \omega)$ . When a lattice has a very large number of nearest neighbors the *spatial* dependence of this field becomes increasingly unimportant and vanishes completely in  $d = \infty$ , as in the Weiss mean-field theory. So the field becomes a *mean field* in position space but retains its full dynamics. In this respect there is a direct analogy to non-interacting electrons in the presence of static (“quenched”) disorder, where the self-energy also becomes purely local ( $\mathbf{k}$  independent) in the limit  $d \rightarrow \infty$  (“coherent potential”). The coherent potential approximation [45] is a single-site theory where a particle moves through an effective medium described by the self-energy  $\Sigma_\sigma(\omega)$  and becomes exact in  $d = \infty$  [69, 70]. It should be noted that the coherent potential in the case of the Hubbard model in the limit  $d \rightarrow \infty$  is more complicated due to the interaction between the particles (see section 5.1).

time-dependent external field.<sup>19</sup> They also indicated that such a mapping was, in principle, also possible for the Hubbard model.

Due to the property (27) the most important obstacle for diagrammatic calculations in finite dimensions  $d \geq 1$ , namely the integration over intermediate momenta, is removed. At the same time the limit  $d \rightarrow \infty$  does not affect the *dynamics* of the system. Hence, in spite of the simplifications in position or momentum space, the many-electron problem retains its full dynamics in  $d = \infty$ .

#### 4.2.1 Interactions beyond the on-site interaction

In the case of more general interactions than the Hubbard interaction, e.g., nearest-neighbor interactions such as

$$\hat{H}_{nn} = \sum_{\langle \mathbf{R}_i, \mathbf{R}_j \rangle} \sum_{\sigma\sigma'} V_{\sigma\sigma'} \hat{n}_{i\sigma} \hat{n}_{j\sigma'} \quad (28)$$

the interaction constant has to be scaled, too, in the limit  $d \rightarrow \infty$ . Since (28) has the form of a classical interaction, the scaling known from the Ising model

$$V_{\sigma\sigma'} \rightarrow \frac{V_{\sigma\sigma'}^*}{Z} \quad (29)$$

is required [65]. Therefore in the limit  $d \rightarrow \infty$  non-local contributions reduce to their Hartree equivalent and only the Hubbard interaction remains dynamical, as discussed in section 2.3.

#### 4.2.2 One-particle propagator

Due to the  $\mathbf{k}$ -independence of the irreducible self-energy, (27), the one-particle propagator of an interacting lattice fermion system (“lattice Green function”) is given by

$$G_{\mathbf{k},\sigma}(\omega) = \frac{1}{\omega - \varepsilon_{\mathbf{k}} + \mu - \Sigma_{\sigma}(\omega)}. \quad (30)$$

We note that the  $\mathbf{k}$ -dependence of  $G_{\mathbf{k}}(\omega)$  comes entirely from the energy dispersion  $\varepsilon_{\mathbf{k}}$  of the *non-interacting* particles. This means that in a homogeneous system described by the propagator

$$G_{ij,\sigma}(\omega) = L^{-1} \sum_{\mathbf{k}} G_{\mathbf{k},\sigma}(\omega) e^{i\mathbf{k} \cdot (\mathbf{R}_i - \mathbf{R}_j)} \quad (31)$$

its local part,  $G_{ii,\sigma} \equiv G_{\sigma}$ , is given by

$$G_{\sigma}(\omega) = L^{-1} \sum_{\mathbf{k}} G_{\mathbf{k},\sigma}(\omega) = \int_{-\infty}^{\infty} d\varepsilon \frac{N_0(\varepsilon)}{\omega - \varepsilon + \mu - \Sigma_{\sigma}(\omega)}, \quad (32)$$

where  $N_0(\varepsilon)$  is the density of states of the non-interacting system. In the paramagnetic phase we can suppress the spin index. The spectral function of the interacting system (also often called density of states) is then given by

$$A(\omega) = -\frac{1}{\pi} \text{Im} G(\omega + i0^+). \quad (33)$$

---

<sup>19</sup>Alternatively, it can be shown that in the limit  $Z \rightarrow \infty$  the dynamics of the Falicov-Kimball model reduces to that of a non-interacting, tight-binding model on a Bethe lattice with coordination number  $Z = 3$  which can thus be solved analytically [73].

### 4.2.3 Consequences of the $k$ -independence of the self-energy: Fermi liquid behavior

The  $k$ -independence of the self-energy allows one to make contact with Fermi liquid theory [66]. At  $T = 0$  the one-particle propagator (30) takes the form

$$G_{\mathbf{k}}(\omega) = \frac{1}{\omega - \varepsilon_{\mathbf{k}} + E_F - \Sigma(\omega)}. \quad (34)$$

In general, i.e., even when  $\Sigma$  has a  $k$ -dependence, the Fermi surface is defined by the  $\omega = 0$  limit of the denominator of (34)

$$\varepsilon_{\mathbf{k}} + \Sigma_{\mathbf{k}}(0) = E_F. \quad (35a)$$

According to Luttinger and Ward [74] the volume within the Fermi surface is not changed by interactions, provided the latter can be treated in perturbation theory. This is expressed by

$$n = \sum_{\mathbf{k}\sigma} \Theta(E_F - \varepsilon_{\mathbf{k}} - \Sigma_{\mathbf{k}}(0)), \quad (35b)$$

where  $n$  is the particle density and  $\Theta(x)$  is the step function. The  $k$ -dependence of  $\Sigma_{\mathbf{k}}(0)$  in (35a) implies that, in spite of (35b), the shape of the Fermi surface of the interacting system will be quite different from that of the non-interacting system (except for the rotationally invariant case  $\varepsilon_{\mathbf{k}} = f(|\mathbf{k}|)$ ). By contrast, for lattice fermion models in  $d = \infty$ , where  $\Sigma_{\mathbf{k}}(\omega) \equiv \Sigma(\omega)$ , the Fermi surface itself, and hence the enclosed volume, is not changed by the interaction. The Fermi energy is simply shifted uniformly from its non-interacting value  $E_F^0$  to  $E_F = E_F^0 + \Sigma(0)$ , to keep  $n$  in (35b) constant. Thus  $G(0)$ , the  $\omega = 0$  value of the local lattice Green function, and of the spectral function  $A(0) = -\frac{1}{\pi} \text{Im } G(i0^+)$  are not changed by the interaction at all. This “pinning behavior” is well-known from the single-impurity Anderson model [75]. A renormalization of  $N(0)$  can only come from a  $k$ -dependence of  $\Sigma$ .

For  $\omega \rightarrow 0$  the self-energy has the property [66]

$$\text{Im } \Sigma(\omega) \propto \omega^2, \quad (35c)$$

which implies Fermi liquid behavior. The effective mass of the quasiparticles

$$\frac{m^*}{m} = 1 - \left. \frac{d\Sigma}{d\omega} \right|_{\omega=0} \quad (35d)$$

$$= 1 + \frac{1}{\pi} \int_{-\infty}^{\infty} d\omega \frac{\text{Im } \Sigma(\omega + i0^-)}{\omega^2} \geq 1 \quad (35e)$$

is seen to be enhanced. In particular, the momentum distribution

$$n_{\mathbf{k}} = \frac{1}{\pi} \int_{-\infty}^0 d\omega \text{Im } G_{\mathbf{k}}(\omega) \quad (36)$$

has a discontinuity at the Fermi surface, given by  $n_{k_F^-} - n_{k_F^+} = (m^*/m)^{-1}$ , where  $k_F^{\pm} = k_F \pm 0^+$ .

## 5 Dynamical mean-field theory (DMFT)

The diagrammatic simplifications of many-body perturbation theory in infinite spatial dimensions provide the basis for the construction of a comprehensive mean-field theory for lattice fermions which is diagrammatically controlled and whose free energy has no unphysical singularities. The construction is based on the scaled Hamiltonian (26). The self-energy is then momentum independent, but retains its frequency dependence and thereby describes the full many-body dynamics of the interacting system.<sup>20</sup> The resulting theory is mean-field-like *and* dynamical and hence represents a *dynamical mean-field theory* (DMFT) for lattice fermions, which is able to describe genuine correlation effects as will be discussed next.

### 5.1 The self-consistent DMFT equations

The DMFT equations were derived in 1991/92 by Janiš [67] and Georges and Kotliar [76] in different ways: (i) as a generalization of the coherent potential approximation [67],<sup>21</sup> and (ii) by mapping the lattice electron problem onto a single-impurity Anderson model with a self-consistency condition [76]; the latter mapping was also employed by Jarrell [77]. For a detailed discussion of the two derivations see Ref. [60]. Both derivations make use of the fact that in  $d = \infty$  lattice fermion models with a local interaction effectively reduce to a single site embedded in a dynamical mean field provided by the other fermions as illustrated in Fig. 4. Although the DMFT equations derived within the coherent potential approximation approach and by the mapping onto a self-consistent single-impurity Anderson model, respectively, are identical, the latter approach was immediately adopted by the community since it connects with the well-studied theory of quantum impurities and the Kondo problem [75], for whose solution efficient numerical codes such as the quantum Monte-Carlo (QMC) method [78] had already been developed and were readily available. For this reason the single-impurity based derivation of the DMFT immediately became the standard approach. For a detailed derivation see the review by Georges, Kotliar, Krauth, and Rozenberg [79]; an introductory presentation can be found in Ref. [80]. The foundations of the DMFT will be discussed at this Autumn School in the lecture by M. Kollar.

The self-consistent DMFT equations are given by

(I) the *local propagator*  $G_\sigma(i\omega_n)$ , which is expressed by a functional integral as

$$G_\sigma(i\omega_n) = -\frac{1}{\mathcal{Z}} \int \prod_\sigma \mathcal{D}c_\sigma^* \mathcal{D}c_\sigma c_\sigma(i\omega_n) c_\sigma^*(i\omega_n) \exp(-S_{\text{loc}}) \quad (37)$$

with the partition function

$$\mathcal{Z} = \int \prod_\sigma \mathcal{D}c_\sigma^* \mathcal{D}c_\sigma \exp(-S_{\text{loc}}) \quad (38)$$

<sup>20</sup>This is in contrast to Hartree(-Fock) theory where the self-energy is merely a static potential.

<sup>21</sup>In the coherent potential approximation quenched disorder acting on non-interacting electrons is averaged and produces a mean field, the “coherent potential”. For the Hubbard model in  $d = \infty$  the infinitely many fluctuating fields generated by the Hubbard-Stratonovich transformation of the Hubbard interaction represent “annealed” disorder acting on non-interacting electrons which, after averaging, produces a mean field, the self-energy [68].

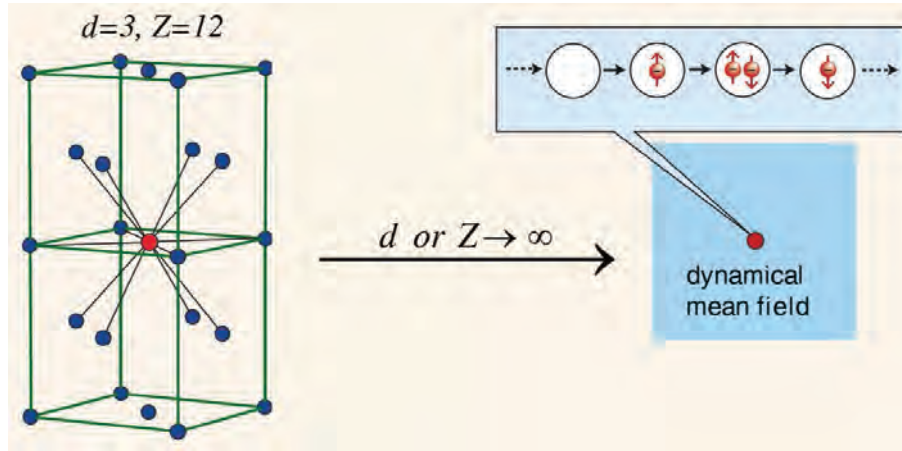


**Fig. 4:** In the limit  $d$  or  $Z \rightarrow \infty$  the Hubbard model effectively reduces to a dynamical single-site problem which may be viewed as a lattice site embedded in a  $\mathbf{k}$ -independent, dynamical fermionic mean field. Electrons can hop from the mean field onto this site and back, and interact on the site as in the original Hubbard model (see Fig. 1). The local propagator (i.e., the return amplitude) and the dynamical mean field are the most important quantities in this limit.

and the local action

$$S_{\text{loc}} = - \int_0^\beta d\tau_1 \int_0^\beta d\tau_2 \sum_\sigma c_\sigma^*(\tau_1) \mathcal{G}_\sigma^{-1}(\tau_1 - \tau_2) c_\sigma(\tau_2) + U \int_0^\beta d\tau c_\uparrow^*(\tau) c_\uparrow(\tau) c_\downarrow^*(\tau) c_\downarrow(\tau). \quad (39)$$

Here  $\mathcal{G}_\sigma$  is the effective local propagator (also called “bath Green function”, or “Weiss mean field”)<sup>22</sup> which is defined by a Dyson equation

$$\mathcal{G}_\sigma(i\omega_n) = \left( (G_\sigma(i\omega_n))^{-1} + \Sigma_\sigma(i\omega_n) \right)^{-1}. \quad (40)$$

Furthermore, by identifying the local propagator (37) with the Hilbert transform of the lattice Green function

$$G_{\mathbf{k}\sigma}(i\omega_n) = \frac{1}{i\omega_n - \varepsilon_{\mathbf{k}} + \mu - \Sigma_\sigma(i\omega_n)} \quad (41)$$

(which is exact in  $d = \infty$  [79]) one obtains

(II) the *self-consistency condition*

$$G_\sigma(i\omega_n) = \frac{1}{L} \sum_{\mathbf{k}} G_{\mathbf{k}\sigma}(i\omega_n) = \int_{-\infty}^{\infty} d\varepsilon \frac{N(\varepsilon)}{i\omega_n - \varepsilon + \mu - \Sigma_\sigma(i\omega_n)} \quad (42)$$

$$= G_\sigma^0(i\omega_n - \Sigma_\sigma(i\omega_n)). \quad (43)$$

In (42) the ionic lattice enters only through the density of states of the non-interacting electrons. Eq. (43) illustrates the mean-field character of the DMFT equations particularly clearly: the local Green function of the interacting system is given by the non-interacting Green function  $G_\sigma^0$  at the renormalized energy  $i\omega_n - \Sigma_\sigma(i\omega_n)$ , which corresponds to the energy measured relative to the mean-field energy  $\Sigma_\sigma(i\omega_n)$  of the surrounding dynamical fermionic bath.

<sup>22</sup>In principle, both the local functions  $\mathcal{G}_\sigma(i\omega_n)$  and  $\Sigma_\sigma(i\omega_n)$  can be viewed as a dynamical mean field since both appear in the bilinear term of the local action (39).



### 5.1.1 Solution of the self-consistent DMFT equations

The self-consistent DMFT equations can be solved iteratively: starting with an initial guess for the self-energy  $\Sigma_\sigma(i\omega_n)$  one obtains the local propagator  $G_\sigma(i\omega_n)$  from (42) and thereby the bath Green function  $\mathcal{G}_\sigma(i\omega_n)$  from (40). This determines the local action (39) which is needed to compute a new value for the local propagator  $G_\sigma(i\omega_n)$  from (37). By employing the old self-energy a new bath Green function  $\mathcal{G}_\sigma$  is calculated and so on, until convergence is reached. It should be stressed that although the DMFT corresponds to an effectively local problem, the propagator  $G_{\mathbf{k}}(\omega)$  *does* depend on the crystal momentum  $\mathbf{k}$  through the dispersion relation  $\varepsilon_{\mathbf{k}}$  of the non-interacting electrons. But there is no additional momentum-dependence through the self-energy, since this quantity is local within the DMFT.

Solutions of the self-consistent DMFT equations require the extensive application of numerical methods, in particular quantum Monte-Carlo simulations [77, 79, 81], the numerical renormalization group [82], the Lanczos method [83], and other techniques [79].

## 5.2 Characteristic features of the DMFT

In the DMFT the mean field is dynamical, whereby local quantum fluctuations are fully taken into account, but is spatially independent because of the infinitely many neighbors of every lattice site. The only approximation of the DMFT when applied in  $d < \infty$  is the neglect of the  $\mathbf{k}$ -dependence of the self-energy (“single-site DMFT”). The DMFT provides a comprehensive, non-perturbative and thermodynamically consistent approximation scheme for the investigation of correlated lattice models at all interaction strengths. It describes fluctuating moments and the renormalization of quasiparticles and is especially valuable for the study of correlation problems at intermediate couplings.

The DMFT allows one to define electronic correlations in such a way that they can be tested experimentally, for example, by electron spectroscopies. Namely, correlations lead to transfer of spectral weight and to a finite lifetime of quasiparticles through the real and imaginary part of the dynamic self-energy, respectively. This is particularly useful for understanding and characterizing the correlation-induced metal-insulator transition.

### 5.2.1 The Mott-Hubbard metal-insulator transition

The correlation driven transition between a paramagnetic metal and a paramagnetic insulator, first discussed by Mott [84, 85] and now referred to as Mott- or Mott-Hubbard metal-insulator transition, is one of the most intriguing phenomena in condensed matter physics [86, 20]. This transition is a consequence of the quantum-mechanical competition between the kinetic energy of the electrons and their local interaction  $U$ . Namely, the kinetic energy prefers the electrons to be mobile (a wave effect) which leads to doubly occupied sites and thereby to interactions between the electrons (a particle effect). For large values of  $U$  the doubly occupied sites become energetically very costly. The system can reduce its total energy by localizing the electrons. Hence the Mott transition is a localization-delocalization transition [80]. While the Gutzwiller-

Brinkman-Rice approach [41] gives a good description of the quasiparticle behavior, it cannot reproduce the upper and lower Hubbard bands. Here the DMFT has been extremely valuable since it provided detailed insights into the nature of the Mott-Hubbard metal-insulator transition for all values of the interaction  $U$  and temperature  $T$  [79, 87, 80, 60].

### 5.2.2 Cold atoms in optical lattices

The investigation of correlation phenomena in cold atoms in optical lattices is a fascinating field of current research [28]. While the Hubbard model with its strictly local interaction is a strong approximation for electrons in solids, the model can describe cold atoms in optical lattices very accurately since the interaction between the atoms is indeed extremely short ranged. Here the DMFT has also been extremely useful. In fact, experiments with cold atoms in optical lattices have shown that the DMFT leads to reliable results even for finite-dimensional systems [88].

## 6 From models back to materials: DFT+DMFT

It took several decades to develop many-body techniques to study and understand at least the basic principles of the Hubbard model and the physics it describes. During that time first-principles investigations of correlated materials were out of reach. Electronic properties of solids were mainly studied within density-functional theory (DFT) [89, 90], e.g., in the local density approximation (LDA) [91], the generalized gradient approximation (GGA) [92], or using the so-called LDA+ $U$  method [93]. These approaches are able to describe the phase diagrams of many simple elements and semiconductors, and even of some insulators, quite accurately. Moreover, they often allow one to correctly predict the magnetic, orbital, and crystal structures of solids where the equilibrium structures are determined by the simultaneous optimization of the electron and lattice systems [94–96]. However, these methods usually fail to describe the correct electronic and structural properties of electronically correlated paramagnetic materials since they miss characteristic features of correlated electron systems, e.g., heavy quasiparticle behavior and Mott physics.

This changed dramatically with the advent of the DMFT. The computational scheme obtained by merging DFT with DMFT, now referred to as DFT+DMFT (or more explicitly as LDA+DMFT, GGA+DMFT, etc.), provides a powerful new method for the calculation of the electronic, magnetic, and structural properties of correlated materials from first principles [97–103]. The DFT+DMFT approach is able to describe and explain the effect of finite temperatures, including thermally driven phase transitions, in real materials. By overcoming the limitations of conventional band-structure methods, it opened up new vistas for fully microscopic investigations of the structural properties of strongly correlated systems, and has already led to many important insights into the properties of strongly correlated materials.

To illustrate the power of the DFT+DMFT approach and, at the same time, stay in line with the historically motivated discussion of correlated electron physics in section 1, I will limit the following presentation to elemental iron (Fe). Iron has been known for its extraordinary

magnetic and metallurgical properties for several thousand years already [2]. Since iron is the main constituent of the Earth's core it is also of great interest in geophysics [104].<sup>23</sup> More information about the DFT+DMFT approach can be found in the lecture notes of the Autumn Schools in 2011 and 2014 [25]. A detailed presentation will be given by E. Pavarini in her lecture during this Autumn School.

## 6.1 Metallic ferromagnetism

The Hubbard model had been introduced in 1963 in the attempt to explain ferromagnetism in  $3d$  metals such as Fe, Co, and Ni [14–16]. But the resulting many-body problem turned out to be so hard to solve that it was uncertain for a long time whether the Hubbard model would be able to fulfill the expectations. Studies of the stability of ferromagnetism in the Hubbard model are made difficult not only by the fact that investigations have to be performed at intermediate coupling strengths, but also by the delicate dependence of the kinetic energy on the lattice structure, orbital overlap (determining the hopping amplitudes), and electronic density. It is well-known from Hartree-Fock-type approximations that the shape of the density of states of non-interacting electrons plays a very important role for ferromagnetism. Indeed, a peak at one of the band edges as in the case of the fcc-lattice is known to be favorable for ferromagnetism. This is supported by the observation that Co and Ni, having a non-bipartite hcp and fcc lattice structure, respectively, show a full magnetization, while bcc Fe is only partially magnetized (for a discussion with detailed references see Ref. [106]).

Investigations of the stability of metallic ferromagnetism on fcc-type lattices within DMFT were first performed by Ulmke [107]. For a generalized fcc lattice in  $d = \infty$  and at an intermediate interaction strength of  $U = 4$ , he found ferromagnetic solutions around quarter filling ( $n \simeq 0.5$ ), with the susceptibility  $\chi_F$  obeying a Curie-Weiss law (Fig. 5). Below  $T_c$  the magnetization  $M$  grows rapidly, reaching more than 80% of the fully polarized value ( $M_{max} = n = 0.58$ ) at the lowest temperature (30% below  $T_c$ ). It is remarkable that the data points  $M(T)$  in Fig. 5 are consistent with a Brillouin function (dashed curve) with the same critical temperature of  $T_c = 0.05$  and an extrapolated full polarization at  $T = 0$ . So a Curie-Weiss-type static susceptibility with Brillouin-function-type magnetization, and a non-integer magneton number as in  $3d$  transition metals are seen to coexist. These two features were usually thought to arise from seemingly contrasting physical effects: the former to localized spins, and the latter to itinerant electrons. However, these conclusions were derived from static mean-field-type approximations such as the Weiss mean-field theory for spin models and Hartree-Fock mean-field theory for electrons. Now we understand that these features appear naturally also in correlated electronic systems, where they are generated by the quantum dynamics of the many-electron problem. Within DMFT the seemingly paradoxical behavior of the magnetization and the susceptibility in band ferromagnets is resolved without difficulty.

<sup>23</sup> Iron is also vital for the human body, in particular in the production of blood. Many-body effects in the kernel of hemoglobin were recently found to be essential to explain the binding of CO and O<sub>2</sub> to heme [105].

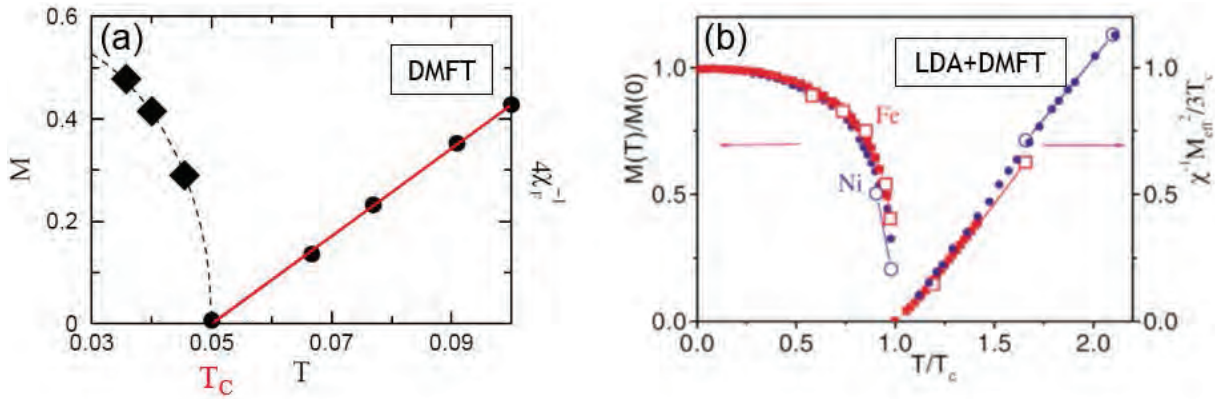


**Fig. 5:** Magnetization and inverse ferromagnetic susceptibility calculated (a) by DMFT for the one-band Hubbard model on a generalized fcc lattice in  $d = \infty$  at  $U = 4$  and  $n = 0.58$  (adapted from Ref. [107]), and (b) by LDA+DMFT for Fe (open squares) and Ni (open circles), where the results are compared with experimental results for Fe (squares) and Ni (circles); adapted from Ref. [108]). For details see text.

Shortly thereafter Lichtenstein, Katsnelson and Kotliar [108] obtained the first finite-temperature results for the magnetic properties of elemental Fe and Ni within the *ab initio* LDA+DMFT approach. The temperature dependence of the magnetization and of the inverse ferromagnetic susceptibility of Fe and Ni explain the experimental data remarkably well.<sup>24</sup> The shape of the curves agrees with that obtained by Ulmke for the Hubbard model on fcc-type lattices within DMFT [107]. This demonstrates that the Hubbard model is indeed able to explain fundamental features of ferromagnetism in 3d metals such as Fe and Ni. Moreover the microscopic origin of the exchange couplings in ferromagnetic bcc Fe was recently clarified using the DFT+DMFT scheme [109].

The critical behavior of the magnetization and of the inverse susceptibility observed in Refs. [107, 108] is clearly mean-field-like. Since the DMFT is derived from the Hubbard model in the limit  $d = \infty$  this does not come unexpected. Deviations from mean-field exponents will be due to non-local effects which go beyond single-site DMFT. The critical properties of the Hubbard model will be discussed in the lecture by K. Held during this Autumn School.

<sup>24</sup>The temperature scale is in units of  $T/T_C$ . The actual Curie temperatures  $T_C$  for Fe(Ni) were obtained as 1900(700) K [108] and are in reasonable agreement with the experimental values 1043(631) K. The fact that the calculated values are higher than the experimental values is not surprising since the single-site nature of the DMFT cannot capture the reduction of  $T_C$  due to spin waves with finite wavelengths.

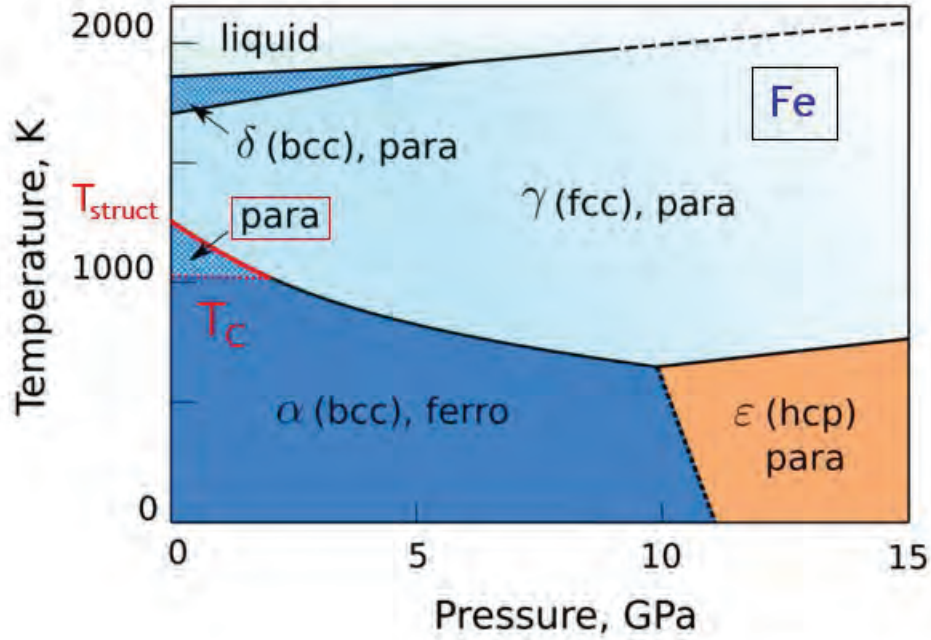


**Fig. 6:** Schematic temperature-pressure ( $T$ - $p$ ) phase diagram of iron; adapted from Ref. [110].

## 6.2 Electronic correlations and lattice stability of solids: paramagnetic Fe

Iron exhibits a rich phase diagram with at least four allotropic forms (Fig. 6). At ambient conditions iron is ferromagnetic and has a bcc crystal structure ( $\alpha$  phase). Upon heating above the Curie temperature  $T_C \sim 1043$  K,  $\alpha$  iron becomes paramagnetic, but remains in its bcc crystal structure. Only when the temperature is increased above  $T_{\text{struct}} \sim 1185$  K does  $\alpha$  iron exhibit a structural phase transition to a fcc structure ( $\gamma$  phase). Clearly iron is a complicated material where magnetic order and correlation effects play an important role; for a discussion see [111, 112]. In spite of intensive research on iron its electronic and lattice properties are still not sufficiently understood.

### 6.2.1 Lattice stability and phonon spectra near the $\alpha$ -to- $\gamma$ transition

State-of-the-art band structure methods provide a qualitatively correct description of various electronic and structural properties of iron [113]. For example, these methods provide a good quantitative understanding of the equilibrium crystal structure and the lattice dynamical properties of the ferromagnetic  $\alpha$  phase. However, applications of these techniques to describe, for example, the  $\alpha$ -to- $\gamma$  phase transition in iron, do not lead to satisfactory results. They predict a simultaneous transition of the structure and the magnetic state at the bcc-to-fcc phase transition while, in fact, the bcc-to-fcc phase transition occurs only about 150 K above  $T_C$ . Moreover, the elastic and dynamical stability of the bcc phase is found to depend sensitively on the value of the magnetization. For example, in the absence of a magnetization, standard band-structure methods predict bcc iron to be unstable [114]. We now understand that the stability of paramagnetic bcc iron is due to the presence of local moments above  $T_C$  which cannot be treated realistically by conventional band-structure techniques.

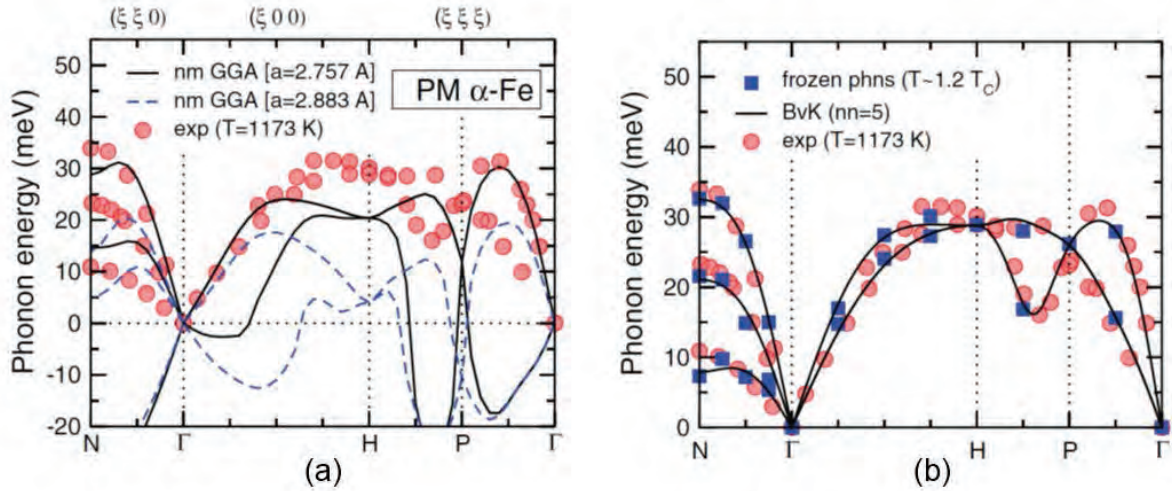


**Fig. 7:** Phonon dispersion curves and corresponding phonon density of states of paramagnetic bcc Fe as calculated within (a) the non-magnetic GGA and (b) GGA+DMFT. The results are compared with neutron inelastic scattering measurements at 1173 K; adapted from Ref. [117].

This problem has been overcome by employing the DFT+DMFT approach which allows one to study correlated materials both in the long-range ordered and the paramagnetic state [115–118, 110, 111]. The DFT+DMFT method naturally accounts for the existence of local moments above  $T_C$  and provides a good quantitative description of the properties of  $\alpha$  iron. In particular, DFT+DMFT studies of the equilibrium crystal structure and phase stability of iron at the  $\alpha$ -to- $\gamma$  phase transition found that the bcc-to-fcc phase transition indeed takes place at a temperature well above the magnetic transition, at about  $1.3 T_C$ , in agreement with experiment [110].

In view of the crucial importance of electronic correlations for the phase stability of  $\alpha$  iron Leonov *et al.* [117] also computed the phonon dispersion relations of paramagnetic iron near the bcc-to-fcc phase transition (Fig. 7). For this purpose the DFT+DMFT approach implemented with the frozen-phonon method was employed [117]. To evaluate the phonon frequencies for arbitrary wave vectors in the Brillouin zone, lattice dynamical calculations were performed on the basis of a Born-von Kármán model with interactions expanded up to the 5-th nearest-neighbor shell. The calculated phonon dispersions of the bcc phase of iron show the typical behavior of a bcc metal with an effective Debye temperature  $\sim 458$  K. The phonon frequencies are overall positive, implying mechanical stability of the bcc lattice structure at  $\sim 1.2 T_C$ , i.e., well above the Curie temperature, in agreement with experiment. This corrects the results obtained with the non-magnetic GGA which finds the bcc lattice to be dynamically unstable even for the equilibrium lattice constant  $a = 2.883$  Å. These results clearly demonstrate the crucial importance of electronic correlations for an explanation of the thermodynamic and the lattice dynamical stability of the paramagnetic bcc phase of iron [117]. Overall, the structural phase stability, equilibrium lattice constant, and phonon frequencies of bcc iron obtained by DFT+DMFT are in remarkably good agreement with the experimental data which were taken at nearly the same reduced temperature  $T/T_C$  [119]. Results obtained for the lattice stability of Fe at even higher temperatures are discussed in Refs. [117, 111].

## 7 Conclusions and outlook

By now the dynamical mean-field theory (DMFT) has developed into a versatile method for the investigation of electronic systems with strong correlations. It provides a comprehensive, non-perturbative and thermodynamically consistent approximation scheme for the investigation of finite-dimensional systems, in particular for dimension  $d = 3$ , and is particularly useful for the study of problems where perturbative approaches fail. For this reason the DMFT has now become the standard mean-field theory for fermionic correlation problems. The generalization of this approach and its applications is currently a subject of active research. Non-local extensions of the DMFT play a particularly important role [120, 81, 121]; see also the lecture by H. Hafermann during this Autumn School. They make it possible to study and explain correlation effects which occur on the scale of several lattice constants. Furthermore, investigations of inhomogeneous bulk systems and of internal and external inhomogeneities, such as surfaces and interfaces [122–127], lead to an improved understanding of correlation effects in thin films and multi-layered nanostructures. This is particularly desirable in view of the novel functionalities of these structures and their possible applications in electronic devices.

The study of correlated electrons out of equilibrium using the DMFT has become yet another fascinating new research area. Non-equilibrium DMFT is able to explain, and even predict, the results of time-resolved experiments [128] and will be discussed in the lecture by M. Eckstein during this Autumn School.

In particular, the combination of the DMFT with methods for the computation of electronic band structures (“DFT+DMFT”) has led to a conceptually new theoretical framework for the realistic study of correlated materials.

The development of a comprehensive theoretical approach which allows for a quantitative understanding and prediction of correlation effects in materials, ranging from complex inorganic materials all the way to biological systems, is one of the great challenges for modern theoretical physics. The lecture notes of the “Autumn Schools on Correlated Electrons” held at the Forschungszentrum Jülich since 2011 provide an excellent introduction into this very active field of research [25].

## References

- [1] J.C. Maxwell, *Phil. Mag.* **90**, 11 (1861)
- [2] D.C. Mattis: *The Theory of Magnetism I: Statics and Dynamics* (Springer, Berlin, 1988)
- [3] P. Weiss, *Comptes Rendus* **143**, 1136 (1906)
- [4] E. Ising, *Z. Phys.* **31**, 253 (1925)
- [5] W. Heisenberg, *Z. Phys.* **49**, 619 (1928)
- [6] F. Bloch, *Z. Phys.* **57**, 545 (1929)
- [7] L. Hoddeson, G. Baym, and M. Eckert, *Rev. Mod. Phys.* **59**, 287 (1987)
- [8] J.C. Slater, *Phys. Rev.* **49**, 537 (1936)
- [9] E. Wigner, *Phys. Rev.* **46**, 1002 (1934)
- [10] D. Pines: *The Many-Body Problem* (W.A. Benjamin, Reading, 1962)
- [11] J.C. Slater, *Rev. Mod. Phys.* **25**, 199 (1953)
- [12] E.P. Wohlfarth, *Rev. Mod. Phys.* **25**, 211 (1953)
- [13] J.H. Van Vleck, *Rev. Mod. Phys.* **25**, 220 (1953)
- [14] M.C. Gutzwiller, *Phys. Rev. Lett.* **10**, 159 (1963)
- [15] J. Hubbard, *Proc. Roy. Soc. London A* **276**, 238 (1963)
- [16] J. Kanamori, *Prog. Theor. Phys.* **30**, 275 (1963)
- [17] N. Grewe and F. Steglich, in K.A. Gschneidner Jr. and L. Eyring (eds.): *Handbook on the Physics and Chemistry of Rare Earths*, Vol. 14 (North Holland, Amsterdam, 1991) p. 343
- [18] J.R. Schrieffer (ed.): *Handbook of High-Temperature Superconductivity* (Springer, Berlin, 2007)
- [19] E. Dagotto: *Nanoscale Phase Separation and Colossal Magnetoresistance* (Springer, Berlin, 2002)
- [20] M. Imada, A. Fujimori, and Y. Tokura, *Rev. Mod. Phys.* **70**, 1039 (1998)
- [21] H. v. Löhneysen, A. Rosch, M. Vojta, and P. Wölfle, *Rev. Mod. Phys.* **79**, 1015 (2007)
- [22] Y. Tokura, *Physics Today*, July 2003, p. 50
- [23] P. Fulde: *Electron Correlations in Molecules and Solids* (Springer, Berlin, 2002)



- [24] P. Fazekas: *Lecture Notes on Electron Correlation and Magnetism* (World Scientific, Singapore, 1999)
- [25] The “Lecture Notes of the Autumn Schools on Correlated Electrons” which have been edited by E. Pavarini, E. Koch and various co-editors since 2011 provide comprehensive and up-to-date information about electronic correlations in models and materials and about theoretical techniques for their investigation:  
<https://www.cond-mat.de/events/correl.html>
- [26] A. Montorsi (ed.): *The Hubbard Model — A Reprint Volume* (World Scientific, Singapore, 1992)
- [27] D. Jaksch, C. Bruder, J.I. Cirac, C.W. Gardiner, and P. Zoller, *Phys. Rev. Lett.* **81**, 3108 (1998)
- [28] I. Bloch, J. Dalibard, and W. Zwerger, *Rev. Mod. Phys.* **80**, 885 (2008)
- [29] E. Lieb and F.Y. Wu, *Phys. Rev. Lett.* **20**, 1445 (1968)
- [30] R. Peierls, *Contemp. Physics* **21**, 3 (1980)
- [31] R.J. Baxter: *Exactly Solved Models in Statistical Mechanics* (Academic Press, London, 1982)
- [32] R. Brout, *Phys. Rev.* **118**, 1009 (1960)
- [33] M.E. Fisher and D.S. Gaunt, *Phys. Rev.* **133**, A224 (1964)
- [34] C.J. Thompson, *Commun. Math. Phys.* **36**, 255 (1974)
- [35] C. Itzykson and J.-M. Drouffe: *Statistical Field Theory* (Cambridge University Press, Cambridge, 1989)
- [36] W. Langer, M. Plischke, and Mattis, *Phys. Rev. Lett.* **23**, 1448 (1969)
- [37] K. Dichtel, R.J. Jelitto, and H. Koppe, *Z. Phys.* **246**, 248 (1971)
- [38] U. Wolff, *Nucl. Phys. B* **225**, 391 (1983)
- [39] J. Bardeen, L.N. Cooper and J.R. Schrieffer; *Phys. Rev.* **108**, 1175 (1957); E. Feenberg: *Theory of Quantum Fluids* (Academic, New York, 1969); R.P. Feynman: *Statistical Physics* (Benjamin, Reading, 1972); C.M. Varma and Y. Yafet, *Phys. Rev. B* **13**, 2950 (1976); V.R. Pandharipande and R.B. Wiringa, *Rev. Mod. Phys.* **51**, 821 (1979); R.B. Laughlin, *Phys. Rev. Lett.* **50**, 1395 (1983); O. Gunnarsson and K. Schönhammer, *Phys. Rev. B* **28**, 4315 (1983); P.W. Anderson, P.A. Lee, M. Randeria, T.M. Rice, N. Trivedi, and F.C. Zhang, *J. Phys.: Condens. Matter* **16** R755–R769 (2004)
- [40] M.C. Gutzwiller, *Phys. Rev.* **137**, A1726 (1965)

- [41] D. Vollhardt, Rev. Mod. Phys. **56**, 99 (1984)
- [42] P.G.J. van Dongen and D. Vollhardt, Phys. Rev. B **40**, 7252 (1989)
- [43] W.F. Brinkman and T.M. Rice, Phys. Rev. B **2**, 4302 (1970)
- [44] J. Hubbard, Proc. Roy. Soc. London A **281**, 401 (1964)
- [45] R.J. Elliott, J.A. Krumhansl, and P.L. Leath, Rev. Mod. Phys. **46**, 465 (1974)
- [46] P.W. Anderson and W.F. Brinkman, in K.H. Bennemann and J.B. Ketterson (eds.): *The Physics of Liquid and Solid Helium*, Part II (Wiley, New York, 1978), p. 177
- [47] D. Vollhardt: *From Gutzwiller Wave Functions to Dynamical Mean-Field Theory*, in E. Pavarini, E. Koch, D. Vollhardt, A. Lichtenstein (eds.): *DMFT at 25: Infinite Dimensions, Modeling and Simulation*, Vol. 4 (Forschungszentrum Jülich, 2014) <https://www.cond-mat.de/events/correl14/manuscripts/vollhardt.pdf>
- [48] D. Vollhardt, P. Wölfle, and P.W. Anderson, Phys. Rev. B **35**, 6703 (1987)
- [49] G. Kotliar and A.E. Ruckenstein, Phys. Rev. Lett. **57**, 1362 (1986)
- [50] For an account by Andrei Ruckenstein of the developments leading to the formulation of the Kotliar-Ruckenstein slave-boson MFT see <https://www.aspenphys.org/aboutus/history/presidentialalessays/ruckenstein.html>
- [51] W. Metzner and D. Vollhardt, Phys. Rev. Lett. **59**, 121 (1987)
- [52] W. Metzner and D. Vollhardt, Phys. Rev. B **37**, 7382 (1988);  
Erratum: Phys. Rev. B **39**, 12339 (1989)
- [53] F. Gebhard, and D. Vollhardt, Phys. Rev. Lett. **59**, 1472 (1987)
- [54] F. Gebhard and D. Vollhardt, Phys. Rev. B **38**, 6911 (1988)
- [55] F.D.M. Haldane, Phys. Rev. Lett. **60**, 635 (1988)
- [56] B.S. Shastry, Phys. Rev. Lett. **60**, 639 (1988)
- [57] W. Metzner and D. Vollhardt, Phys. Rev. Lett. **62**, 324 (1989)
- [58] W. Metzner, Z. Phys. B **77**, 253 (1989)
- [59] P.G.J. van Dongen, F. Gebhard, and D. Vollhardt, Z. Phys. **76**, 199 (1989)
- [60] D. Vollhardt, in A. Avella and F. Mancini (eds.): *Lectures on the Physics of Strongly Correlated Systems XIV, AIP Conference Proceedings*, Vol. 1297 (American Institute of Physics, Melville, 2010) p. 339; <http://arxiv.org/abs/1004.5069v3>

- [61] F. Gebhard, Phys. Rev. B **41**, 9452 (1990)
- [62] J. Bünemann, F. Gebhard, and W. Weber, Found. of Physics **30**, 2011 (2000)
- [63] T. Schickling, J. Bünemann, F. Gebhard, and W. Weber, New J. Phys. **16**, 93034 (2014)
- [64] K. Byczuk and D. Vollhardt, Phys. Rev. B **77**, 235106 (2008)
- [65] E. Müller-Hartmann, Z. Phys. B **74**, 507 (1989)
- [66] E. Müller-Hartmann, Z. Phys. B **76**, 211 (1989)
- [67] V. Janiš, Z. Phys. B **83**, 227 (1991)
- [68] V. Janiš and D. Vollhardt, Int. J. Mod. Phys. **B6**, 731 (1992)
- [69] R. Vlaming and D. Vollhardt, Phys. Rev. B **45**, 4637 (1992)
- [70] V. Janiš and D. Vollhardt, Phys. Rev. B **46**, 15712 (1992)
- [71] H. Schweitzer and G. Czycholl, Solid State Comm. **69**, 171 (1989)
- [72] U. Brandt and C. Mielsch, Z. Phys. B **75**, 365 (1989)
- [73] P.G.J. van Dongen and D. Vollhardt, Phys. Rev. Lett. **65**, 1663 (1990)
- [74] J.M. Luttinger and J.C. Ward, Phys. Rev. **118**, 1417 (1960)
- [75] A.C. Hewson: *The Kondo Problem to Heavy Fermions* (Cambridge University Press, Cambridge, 1997)
- [76] A. Georges and G. Kotliar, Phys. Rev. B **45**, 6479 (1992)
- [77] M. Jarrell, Phys. Rev. Lett. **69**, 168 (1992)
- [78] J.E. Hirsch and R.M. Fye, Phys. Rev. Lett. **56**, 2521 (1986)
- [79] A. Georges, G. Kotliar, W. Krauth, and M.J. Rozenberg, Rev. Mod. Phys. **68**, 13 (1996)
- [80] G. Kotliar and D. Vollhardt, Phys. Today **57**, 53 (2004)
- [81] E. Gull, A.J. Millis, A.I. Lichtenstein, A.N. Rubtsov, M. Troyer, P. Werner, Rev. Mod. Phys. **83**, 349 (2011)
- [82] R. Bulla, T.A. Costi, and Th. Pruschke, Rev. Mod. Phys. **80**, 395 (2008)
- [83] E. Koch: *The Lanczos Method*, in  
E. Pavarini, E. Koch, D. Vollhardt, and A.I. Lichtenstein (eds.)  
*The LDA+DMFT approach to strongly correlated materials*  
Modeling and Simulation, Vol. 1 (Forschungszentrum Jülich, 2011)

- [84] N.F. Mott, *Rev. Mod. Phys.* **40**, 677 (1968)
- [85] N.F. Mott: *Metal–Insulator Transitions* (Taylor and Francis, London, 1990), 2nd edition
- [86] F. Gebhard: *The Mott Metal-Insulator Transition* (Springer, Berlin, 1997)
- [87] N. Blümer: *Metal-Insulator Transition and Optical Conductivity in High Dimensions* (Shaker Verlag, Aachen, 2003)
- [88] U. Schneider, L. Hackermüller, S. Will, Th. Best, I. Bloch, T.A. Costi, R.W. Helmes, D. Rasch, A. Rosch, *Science* **322**, 1520 (2008)
- [89] P. Hohenberg and W. Kohn, *Phys. Rev. B* **136**, 864 (1964)
- [90] W. Kohn and L.J. Sham, *Phys. Rev.* **140**, A1133 (1965)
- [91] R.O. Jones, O. Gunnarsson, *Rev. Mod. Phys.* **61**, 689 (1989)
- [92] J.P. Perdew, K. Burke, M. Ernzerhof, *Phys. Rev. Lett.* **77**, 3865 (1996)
- [93] V.I. Anisimov, J. Zaanen, O.K. Andersen, *Phys. Rev. B* **44**, 943 (1991)
- [94] S. Baroni, S. de Gironcoli, A.D. Corso, P. Giannozzi, *Rev. Mod. Phys.* **73**, 515 (2001)
- [95] P. Blaha, K. Schwarz, G. Madsen, D. Kvasnicka, J. Luitz: *WIEN2k, An Augmented Plane Wave + Local Orbitals Program for Calculating Crystal Properties.* (Karlheinz Schwarz, TU Wien, 2001)
- [96] G. Kresse, J. Hafner, *Phys. Rev. B* **47**, 558 (1993)
- [97] V.I. Anisimov, A.I. Poteryaev, M.A. Korotin, A.O. Anokhin, G. Kotliar, *J. Phys.: Condens. Matt.* **9**, 7359 (1997)
- [98] A.I. Lichtenstein, M.I. Katsnelson, *Phys. Rev. B* **57**, 6884 (1998)
- [99] K. Held, I.A. Nekrasov, G. Keller, V. Eyert, N. Blümer, A.K. McMahan, R.T. Scalettar, T. Pruschke, V.I. Anisimov, and D. Vollhardt, *Psi-k Newsletter* **56**, 65 (2003); reprinted in *Phys. Status Solidi B* **243**, 2599 (2006)
- [100] G. Kotliar, S.Y. Savrasov, K. Haule, V.S. Oudovenko, O. Parcollet, C.A. Marianetti, *Rev. Mod. Phys.* **78**, 865 (2006)
- [101] K. Held, *Adv. Phys.* **56**, 829 (2007)
- [102] M.I. Katsnelson, V. Yu. Irkhin, L. Chioncel, A.I. Lichtenstein, and R.A. de Groot, *Rev. Mod. Phys.* **80**, 315 (2008)
- [103] D. Vollhardt and A.I. Lichtenstein (eds.): *Dynamical Mean-Field Approach with Predictive Power for Strongly Correlated Materials* *Eur. Phys. J. Spec. Top.* **226** (2017)

- [104] S. Tateno, K. Hirose, Y. Ohishi, Y. Tatsumi, *Science* **330**, 359 (2013); A. Hausoel, M. Karolak, E. Şaşıoğlu, A. Lichtenstein, K. Held, A. Katanin, A. Toschi, G. Sangiovanni, *Nature Comm.* **8**, 16062 (2017)
- [105] C. Weber, D.D. O'Regan, N.D.M. Hine, P.B. Littlewood, G. Kotliar, M.C. Payne, *Phys. Rev. Lett.* **110**, 106402 (2013)
- [106] D. Vollhardt, N. Blümer, K. Held, M. Kollar, J. Schlipf, M. Ulmke: *Z. Phys. B* **103**, 283 (1997); D. Vollhardt, N. Blümer, K. Held, M. Kollar, J. Schlipf, M. Ulmke, J. Wahle: *Advances In Solid State Physics* 38, p. 383 (Vieweg, Wiesbaden 1999)
- [107] M. Ulmke: *Euro. Phys. J. B* **1**, 301 (1998)
- [108] A.I. Lichtenstein, M.I. Katsnelson, G. Kotliar, *Phys. Rev. Lett.* **87**, 067205 (2001)
- [109] Y.O. Kvashnin, R. Cardias, A. Szilva, I. Di Marco, M.I. Katsnelson, A.I. Lichtenstein, L. Nordström, A.B. Klautau, O. Eriksson, *Phys. Rev. Lett.* **116**, 217202 (2016)
- [110] I. Leonov, A.I. Poteryaev, V.I. Anisimov, D. Vollhardt, *Phys. Rev. Lett.* **106**, 106405 (2011)
- [111] I. Leonov, A.I. Poteryaev, Y.N. Gornostyrev, A.I. Lichtenstein, M.I. Katsnelson, V.I. Anisimov, D. Vollhardt, *Sci. Rep.* **4**, 5585 (2014)
- [112] J. Kuneš, I. Leonov, P. Augustinský, V. Křápek, M. Kollar, and D. Vollhardt, *Eur. Phys. J. Spec. Top.* **226**, 2641 (2017)
- [113] D.J. Singh, W.E. Pickett, H. Krakauer, *Phys. Rev. B* **43**, 11628 (1991); S.V. Okatov, A.R. Kuznetsov, Y.N. Gornostyrev, V.N. Urtsev, M.I. Katsnelson, *Phys. Rev. B* **79**, 094111 (2009); F. Körmann, A. Dick, B. Grabowski, T. Hickel, J. Neugebauer, *Phys. Rev. B* **85**, 125104 (2012)
- [114] H.C. Hsueh, J. Crain, G.Y. Guo, H.Y. Chen, C.C. Lee, K.P. Chang, and H.L. Shih, *Phys. Rev. B* **66**, 052420 (2002)
- [115] A.I. Lichtenstein, M.I. Katsnelson, and G. Kotliar, *Phys. Rev. Lett.* **87**, 067205 (2001)
- [116] A.A. Katanin, A.I. Poteryaev, A.V. Efremov, A.O. Shorikov, S.L. Skornyakov, M.A. Korotin, V.I. Anisimov, *Phys. Rev. B* **81**, 045117 (2010)
- [117] I. Leonov, A.I. Poteryaev, V.I. Anisimov, D. Vollhardt, *Phys. Rev. B* **85**, R020401 (2012)
- [118] L.V. Pourovskii, J. Mravlje, M. Ferrero, O. Parcollet, I.A. Abrikosov, *Phys. Rev. B* **90**, 155120 (2014)
- [119] J. Neuhaus, W. Petry, A. Krimmel, *Physica B* **234-236**, 897 (1997)
- [120] Th. Maier, M. Jarrell, Th. Pruschke, and M.H. Hettler, *Rev. Mod. Phys.* **77**, 1027 (2005)

- [121] K. Held: *Dynamical Vertex Approximation*, in  
E. Pavarini, E. Koch, D. Vollhardt, A. Lichtenstein (eds.):  
*DMFT at 25: Infinite Dimensions Modeling and Simulation*, Vol. 4  
(Forschungszentrum Jülich, 2014)
- [122] M. Potthoff and W. Nolting, Phys. Rev. B **59**, 2549 (1999)
- [123] R.W. Helmes, T.A. Costi, and A. Rosch, Phys. Rev. Lett. **100**, 056403 (2008)
- [124] M.J. Han, X. Wang, C.A. Marianetti, and A.J. Millis, Phys. Rev. Lett. **107**, 206804 (2011)
- [125] J.K. Freericks, *Transport in multilayered nanostructures — The dynamical mean-field approach*, 2nd edition (Imperial College Press, London, 2016)
- [126] T. Yoshida and N. Kawakami, Phys. Rev. B **95**, 045127 (2017)
- [127] I. Di Marco, A. Held, S. Keshavarz, Y.O. Kvashnin, and L. Chioncel,  
Phys. Rev. B **97**, 035105 (2018)
- [128] H. Aoki, N. Tsuji, M. Eckstein, M. Kollar, T. Oka, and P. Werner,  
Rev. Mod. Phys. **86**, 779 (2014)

# 2 From Materials to Models: Deriving Insight from Bands

Ole Krogh Andersen

Max-Planck-Institut für Festkörperforschung  
Stuttgart

## Contents

<b>1</b>	<b>Introduction</b>	<b>2</b>
<b>2</b>	<b>Periodic system of the elements</b>	<b>2</b>
<b>3</b>	<b>Band structures of the elemental metals</b>	<b>7</b>
3.1	Separating structure and potential . . . . .	7
3.2	Force theorem, pressures, and structures . . . . .	16
3.3	Band magnetism . . . . .	20
3.4	Fermi surfaces and mass renormalizations . . . . .	28
<b>4</b>	<b>Post 1986</b>	<b>29</b>
4.1	ARPES . . . . .	30
4.2	Static and dynamical mean-field approximations . . . . .	31
4.3	Transition-metal oxides (TMOs) . . . . .	32
4.4	Elemental metals . . . . .	35

## 1 Introduction

In contrast to most other lectures in this Autumn-School series on Correlated Electrons, this one will deal little with recent theories of how to describe and compute observables for correlated materials, but mostly with insights derived a while ago from bands, not even quasiparticle excitations, but merely Hohenberg-Kohn-Sham eigenvalues, Kohn's "bastards of DFT". After scanning through previous year's lectures and recent papers, I felt that this might not be entirely inappropriate.

## 2 Periodic system of the elements

The most fundamental chemical insight ever derived from one-electron energies is Bohr's theory of the periodic system of the elements [1]. I therefore found it appropriate to start with a reminder about the electronic structure of atoms (see also Refs. [2–5]).

Materials are made of atoms, and atoms are (almost) round. The electronic structure of an atom can therefore be constructed from atomic orbitals,  $\varphi_l(\varepsilon_{nl}, r) Y_{lm}(\hat{\mathbf{r}}) \chi_\sigma(s)$ , which are the solutions of the one-electron Schrödinger equation in the spherically symmetric, self-consistent potential,  $v(r)$ , from the attractive protons in the nucleus and the repulsive (other) electrons in the atomic shells.  $\chi_\sigma(s)$  are the spin functions which are the eigenfunctions of  $\hat{s}_z$ ,  $Y_{lm}(\hat{\mathbf{r}})$  are the spherical harmonics which are eigenfunctions of  $\hat{l}^2$  and  $\hat{l}_z$ , and the radial functions satisfy the radial Schrödinger equations,

$$-(r\varphi_l(\varepsilon_{nl}, r))'' = (\varepsilon_{nl} - v_l(r)) r\varphi_l(\varepsilon_{nl}, r), \text{ with } v_l(r) \equiv v(r) + l(l+1)/r^2 \quad (1)$$

(in atomic Rydberg units) with the boundary conditions that  $\varphi(r)$  be regular at the origin and vanish at infinity. The potentials  $v(r) = v_s(r)$  and  $v_d(r)$  are shown in Fig. 3 for a neutral Pt atom in weak lines.

For given  $l$ , the solutions of (1) are numbered in order of increasing energy,  $\varepsilon_{nl}$ , by the principal quantum number,  $n$ , which takes the values  $l+1, l+2, \dots$ , because with this convention, the energy levels for a Coulomb potential,  $-2Z/r$ , are independent of  $l$  and given by  $\varepsilon_{nl} = -(Z/n)^2$ , Bohr's formula from 1913, before quantum mechanics. The radial functions decay at large distances as  $\exp(-Zr/n)$  and the number of nodes in the radial function is  $n-l-1$ .

For a neutral atom with  $Z$  protons in the nucleus and  $Z$  electrons in the shells, the effective charge defined in terms of the self-consistent potential through:  $Z_{\text{eff}}(r) \equiv -rv(r)/2$ , decreases from the value  $Z$ , towards 1 as  $r$  increases from 0 to  $\infty$  due to the screening by the (other) electrons. As a consequence, the  $2(2l+1)$ -degeneracy of the attractive Coulomb potential is lifted and the perturbation by the repulsive centrifugal potential,  $l(l+1)/r^2$ , will cause the one-electron energies for the same  $n$  to increase with  $l$ :  $\varepsilon_{ns} < \varepsilon_{np} < \varepsilon_{nd} < \dots$ . Whereas the order of the  $s$ - and  $p$ -energies is always such that  $\varepsilon_{ns} < \varepsilon_{np} < \varepsilon_{(n+1)s}$ , the order of the  $d$ -energies is such that  $\varepsilon_{(n+1)s} < \varepsilon_{nd}$  when the  $nd$ -shell is empty, and such that  $\varepsilon_{np} < \varepsilon_{nd} < \varepsilon_{(n+1)s}$  when the  $nd$ -shell is full. Analogously,  $\varepsilon_{nd} < \varepsilon_{(n-1)f}$  when the  $(n-1)f$ -shell is empty, and  $\varepsilon_{(n-1)d} < \varepsilon_{(n-1)f} < \varepsilon_{nd}$  when the  $(n-1)f$ -shell is full.



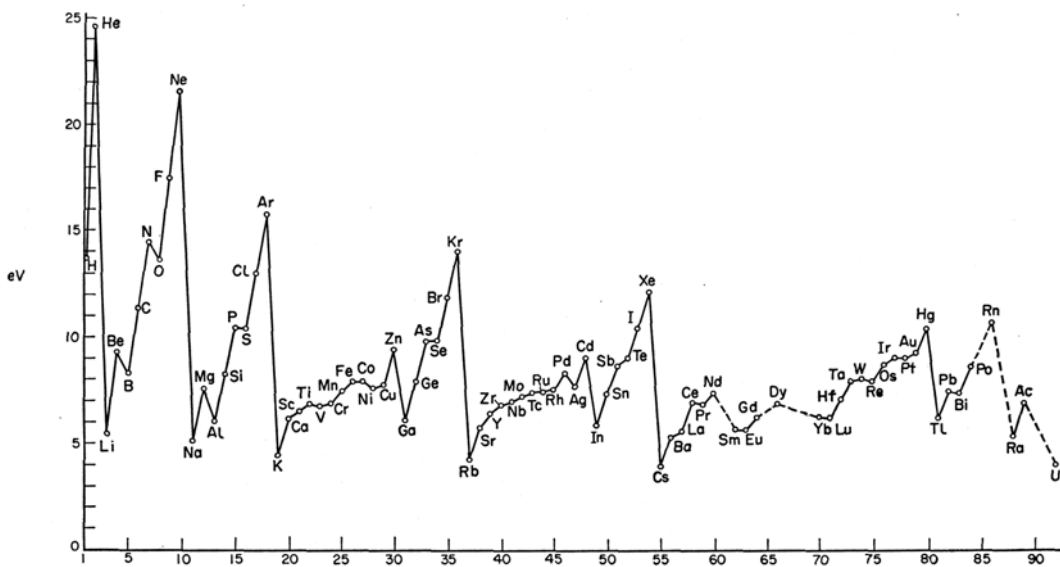
Li <sup>3</sup> Be <sup>4</sup>		Periodic Table, with the Outer Electron Configurations of Neutral Atoms in Their Ground States										B <sup>5</sup>	C <sup>6</sup>	N <sup>7</sup>	O <sup>8</sup>	F <sup>9</sup>	Ne <sup>10</sup>
2s	2s <sup>2</sup>	The notation used to describe the electronic configuration of atoms and ions is discussed in all textbooks of introductory atomic physics. The letters <i>s</i> , <i>p</i> , <i>d</i> , . . . signify electrons having orbital angular momentum 0, 1, 2, . . . in units $\hbar$ ; the number to the left of the letter denotes the principal quantum number of one orbit, and the superscript to the right denotes the number of electrons in the orbit.										2s <sup>2</sup> 2p	2s <sup>2</sup> 2p <sup>2</sup>	2s <sup>2</sup> 2p <sup>3</sup>	2s <sup>2</sup> 2p <sup>4</sup>	2s <sup>2</sup> 2p <sup>5</sup>	2s <sup>2</sup> 2p <sup>6</sup>
Na <sup>11</sup>	Mg <sup>12</sup>											Al <sup>13</sup>	Si <sup>14</sup>	P <sup>15</sup>	S <sup>16</sup>	Cl <sup>17</sup>	Ar <sup>18</sup>
3s	3s <sup>2</sup>											3s <sup>2</sup> 3p	3s <sup>2</sup> 3p <sup>2</sup>	3s <sup>2</sup> 3p <sup>3</sup>	3s <sup>2</sup> 3p <sup>4</sup>	3s <sup>2</sup> 3p <sup>5</sup>	3s <sup>2</sup> 3p <sup>6</sup>
K <sup>19</sup>	Ca <sup>20</sup>	Sc <sup>21</sup>	Ti <sup>22</sup>	V <sup>23</sup>	Cr <sup>24</sup>	Mn <sup>25</sup>	Fe <sup>26</sup>	Co <sup>27</sup>	Ni <sup>28</sup>	Cu <sup>29</sup>	Zn <sup>30</sup>	Ga <sup>31</sup>	Ge <sup>32</sup>	As <sup>33</sup>	Se <sup>34</sup>	Br <sup>35</sup>	Kr <sup>36</sup>
4s	4s <sup>2</sup>	3d 4s <sup>2</sup>	3d <sup>2</sup> 4s <sup>2</sup>	3d <sup>3</sup> 4s <sup>2</sup>	3d <sup>5</sup> 4s <sup>2</sup>	3d <sup>5</sup> 4s <sup>2</sup>	3d <sup>6</sup> 4s <sup>2</sup>	3d <sup>7</sup> 4s <sup>2</sup>	3d <sup>8</sup> 4s <sup>2</sup>	3d <sup>10</sup> 4s <sup>2</sup>	3d <sup>10</sup> 4s <sup>2</sup>	4s <sup>2</sup> 4p	4s <sup>2</sup> 4p <sup>2</sup>	4s <sup>2</sup> 4p <sup>3</sup>	4s <sup>2</sup> 4p <sup>4</sup>	4s <sup>2</sup> 4p <sup>5</sup>	4s <sup>2</sup> 4p <sup>6</sup>
Rb <sup>37</sup>	Sr <sup>38</sup>	Y <sup>39</sup>	Zr <sup>40</sup>	Nb <sup>41</sup>	Mo <sup>42</sup>	Tc <sup>43</sup>	Ru <sup>44</sup>	Rh <sup>45</sup>	Pd <sup>46</sup>	Ag <sup>47</sup>	Cd <sup>48</sup>	In <sup>49</sup>	Sn <sup>50</sup>	Sb <sup>51</sup>	Te <sup>52</sup>	I <sup>53</sup>	Xe <sup>54</sup>
5s	5s <sup>2</sup>	4d 5s <sup>2</sup>	4d <sup>2</sup> 5s <sup>2</sup>	4d <sup>4</sup> 5s <sup>2</sup>	4d <sup>5</sup> 5s <sup>2</sup>	4d <sup>6</sup> 5s <sup>2</sup>	4d <sup>7</sup> 5s <sup>2</sup>	4d <sup>8</sup> 5s <sup>2</sup>	4d <sup>10</sup> 5s <sup>2</sup>	4d <sup>10</sup> 5s <sup>2</sup>	4d <sup>10</sup> 5s <sup>2</sup>	5s <sup>2</sup> 5p	5s <sup>2</sup> 5p <sup>2</sup>	5s <sup>2</sup> 5p <sup>3</sup>	5s <sup>2</sup> 5p <sup>4</sup>	5s <sup>2</sup> 5p <sup>5</sup>	5s <sup>2</sup> 5p <sup>6</sup>
Cs <sup>55</sup>	Ba <sup>56</sup>	La <sup>57</sup>	Hf <sup>72</sup>	Ta <sup>73</sup>	W <sup>74</sup>	Re <sup>75</sup>	Os <sup>76</sup>	Ir <sup>77</sup>	Pt <sup>78</sup>	Au <sup>79</sup>	Hg <sup>80</sup>	Tl <sup>81</sup>	Pb <sup>82</sup>	Bi <sup>83</sup>	Po <sup>84</sup>	At <sup>85</sup>	Rn <sup>86</sup>
6s	6s <sup>2</sup>	5d 6s <sup>2</sup>	4f <sup>14</sup> 5d <sup>2</sup> 6s <sup>2</sup>	5d <sup>3</sup> 6s <sup>2</sup>	5d <sup>4</sup> 6s <sup>2</sup>	5d <sup>5</sup> 6s <sup>2</sup>	5d <sup>6</sup> 6s <sup>2</sup>	5d <sup>9</sup> 6s <sup>2</sup>	5d <sup>9</sup> 6s <sup>2</sup>	5d <sup>10</sup> 6s <sup>2</sup>	5d <sup>10</sup> 6s <sup>2</sup>	6s <sup>2</sup> 6p	6s <sup>2</sup> 6p <sup>2</sup>	6s <sup>2</sup> 6p <sup>3</sup>	6s <sup>2</sup> 6p <sup>4</sup>	6s <sup>2</sup> 6p <sup>5</sup>	6s <sup>2</sup> 6p <sup>6</sup>
Fr <sup>87</sup>	Ra <sup>88</sup>	Ac <sup>89</sup>															
7s	7s <sup>2</sup>	6d 7s <sup>2</sup>	Ce <sup>58</sup> 4f <sup>2</sup> 6s <sup>2</sup>	Pr <sup>59</sup> 4f <sup>3</sup> 6s <sup>2</sup>	Nd <sup>60</sup> 4f <sup>4</sup> 6s <sup>2</sup>	Pm <sup>61</sup> 4f <sup>5</sup> 6s <sup>2</sup>	Sm <sup>62</sup> 4f <sup>6</sup> 6s <sup>2</sup>	Eu <sup>63</sup> 4f <sup>7</sup> 6s <sup>2</sup>	Gd <sup>64</sup> 4f <sup>7</sup> 5d 6s <sup>2</sup>	Tb <sup>65</sup> 4f <sup>8</sup> 6s <sup>2</sup>	Dy <sup>66</sup> 4f <sup>10</sup> 6s <sup>2</sup>	Ho <sup>67</sup> 4f <sup>11</sup> 6s <sup>2</sup>	Er <sup>68</sup> 4f <sup>12</sup> 6s <sup>2</sup>	Tm <sup>69</sup> 4f <sup>13</sup> 6s <sup>2</sup>	Yb <sup>70</sup> 4f <sup>14</sup> 6s <sup>2</sup>	Lu <sup>71</sup> 4f <sup>14</sup> 5d 6s <sup>2</sup>	
			Th <sup>90</sup> - 6d <sup>2</sup> 7s <sup>2</sup>	Pa <sup>91</sup> 5f <sup>2</sup> 6d 7s <sup>2</sup>	U <sup>92</sup> 5f <sup>3</sup> 6d 7s <sup>2</sup>	Np <sup>93</sup> 5f <sup>4</sup> 7s <sup>2</sup>	Pu <sup>94</sup> 5f <sup>6</sup> 7s <sup>2</sup>	Am <sup>95</sup> 5f <sup>7</sup> 7s <sup>2</sup>	Cm <sup>96</sup> 5f <sup>7</sup> 6d 7s <sup>2</sup>	Bk <sup>97</sup>	Cf <sup>98</sup>	Es <sup>99</sup>	Fm <sup>100</sup>	Md <sup>101</sup>		Lw <sup>103</sup>	

Fig. 1: Periodic Table of the Elements. From Ref. [6].

If we now occupy the orbitals, of which there are  $2(2l+1)$  per  $nl$ -subshell, with  $Z$  electrons in order of increasing energy, we recover the Periodic Table, which has one entry for each value of  $Z$  increasing in steps of 1 along one row after the other (Fig. 1). The rows are numbered by the period,  $n$ , which is the principal quantum number of the outermost  $s$ -electron. As  $Z$  increases, the first term of the radial potential,  $-2Z_{\text{eff}}(r)/r + l(l+1)/r^2$ , in Eq. (1) deepens and counteracts the repulsive second term such that bound states occur if  $Z \geq 5$  (B), 21 (Sc), and 58 (Ce), for  $l=1, 2$ , and 3, respectively. This leads to the insertion of the  $p$ -,  $d$ -, and  $f$ -series, whereby the length of the period (number of one-electron states in the  $n$ -shell) becomes  $2(l_{\text{max}}+1)^2$ .

In the columns are the elements with similar chemical properties, and Fig. 1 gives the configuration, i.e., the numbers of electrons in the outer shells for the ground states of the neutral atoms. With increasing  $l$ , the radial potential-well becomes more narrow and with it, the region where  $\varepsilon_{nl} > v_l(r)$ , i.e., which is classically-allowed (see Fig. 3). This increased localization of the orbitals with higher  $l$  leads to their decreased chemical activity and, hence, the very similar chemical properties of the rare earths and of the actinides which are exclusively associated with their outer  $s$ -,  $p$ -, and possibly  $d$ -electrons.

When, in the process of filling the  $nl$ -subshell, we move from one element to the next, the added  $nl$ -electron will partly screen out the added proton. Specifically, the increase of  $Z_{\text{eff}}(r)$  is 1 for  $r$  in the region near the nucleus which is classically forbidden [ $v_l(r) > \varepsilon_{nl}$ ] for an  $nl$ -electron,



**Fig. 2:** First ionization potentials as a function of  $Z$ . From Ref. [2].

trails off in the classically-allowed region, and vanishes outside. Hence,  $\varepsilon_{nl}$  will fall a bit, and  $\varphi_l(\varepsilon_{nl})$  will contract.

When the filling of the  $nl$ -subshell is completed and we start to fill into the next,  $n'l'$ -subshell, the increase of  $Z_{\text{eff}}(r)$  by unity does not start to trail off before  $r$  reaches the region allowed for an  $n'l'$ -electron. If  $n' \geq n$ , this is outside the region of an  $nl$ -electron and  $\varepsilon_{nl}$  will therefore drop sharply and  $\varphi_l(\varepsilon_{nl})$  contract rapidly, the  $nl$ -shell thereby starts to become part of the core. The Fermi level,  $\varepsilon_F$ , will jump up, from  $\varepsilon_{nl}$  to  $\varepsilon_{n'l'}$ . This is what happens most dramatically when going from  $ns^2 np^6$  to  $ns^2 np^6 (n+1)s^1$ , i.e., from an inert gas to an alkali metal, and far less dramatically when going from  $ns^2$  to  $ns^2 np^1$ , i.e., from Be to B, from Mg to Al, from Zn to Ga, from Cd to In, and from Hg to Tl. In the last three cases the upwards jumps are larger because, here, also the full  $(n-1)d^{10}$  shell contracts. This shell structure is clearly seen in Fig. 2 showing for increasing  $Z$  the experimental first ionization potential. In theory, this is the ground-state energy of the positive ion minus that of the neutral atom. Neglecting multiplet effects and using the transition-state potential [7], it is simply  $-\varepsilon_F$ .

For an  $nd$ -shell,  $\varepsilon_{nd}$  continues to drop after the  $nd$  band is full, i.e., when going from  $nd^{10}(n+1)s^1$  to  $nd^{10}(n+1)s^2$ , i.e., from Cu to Zn, from Ag to Cd, and from Au to Hg. This is because the  $(n+1)s$  shell contracts as it gets filled and drags the  $nd$  shell along.

The abrupt behaviors observed when we start to fill into the  $n'l'$ -subshell do not occur if  $n' < n$ , because now  $\varphi_{l'}(\varepsilon_{n'l'})$  lies inside  $\varphi_l(\varepsilon_{nl})$ . This is the case at the beginning of a transition series when going from  $ns^2$  to  $ns^2 (n-1)d^1$ , i.e., from Ca to Sc, from Sr to Y, from Ba to La, or from Ra to Ac. Filling the more localized  $(n-1)d$ -shell, e.g., going from  $ns^2 (n-1)d^1$  to  $ns^2 (n-1)d^2$ , hardly influences the  $ns$  energies and orbitals,  $\varepsilon_{ns}$  and  $\varphi_s(\varepsilon_{ns})$ . As  $\varepsilon_{(n-1)d}$  gradually drops, it will therefore at some stage reach  $\varepsilon_{ns}$  whereby some of the electrons in the  $ns$ -shell may be transferred into the  $(n-1)d$ -shell. After the filling of the  $(n-1)d$ -shell has been completed, the filling of the  $ns$  shell will be resumed. The same holds for  $\varepsilon_{nd}$  and  $\varphi_d(\varepsilon_{nd})$  when filling the  $(n-1)f$ -shell in lanthanide or actinide series.

The positions and widths of the  $sp$ - and  $d$ -bands in the elemental, closely-packed transition metals follow the same trends as the one-electron energies and orbitals described above. Also the relative positions of O  $p$ -bands and transition-metal  $d$ -bands in transition-metal oxides are roughly in accord with the ionization potentials in Fig. 2. Periodic Tables of the elements containing information about bands in solids may be found in Refs. [8–12] and [4].

The relativistic effects may for the purpose of conceptual simplicity and with little loss of accuracy be included by *formally* using the Pauli Hamiltonian,

$$H = -\nabla^2 + v(r) - \frac{1}{c^2} \left( (\varepsilon - v(r))^2 + v'(r) \frac{\partial}{\partial r} - \frac{v'(r)}{r} 2\hat{\mathbf{s}} \cdot \hat{\mathbf{l}} \right). \quad (2)$$

Of the relativistic terms ( $\propto c^{-2}$ ) the two first, the mass-velocity and the Darwin term are diagonal in the  $lm\sigma$ -representation and may therefore be included in the radial equation for  $\varphi_l(\varepsilon, r)$ . But the last, the spin-orbit(SO)-coupling term is not diagonal because

$$\langle l'm' | 2\hat{\mathbf{s}} \cdot \hat{\mathbf{l}} | lm \rangle = \begin{pmatrix} m \delta_{m'm} & \sqrt{(l+m)(l-m+1)} \delta_{m'(m-1)} \\ \sqrt{(l-m)(l+m+1)} \delta_{m'(m+1)} & -m \delta_{m'm} \end{pmatrix} \delta_{l'l} \quad (3)$$

in the  $\uparrow, \downarrow$ -representation. Since the atom is round,  $\hat{j} \equiv \hat{\mathbf{l}} + \hat{\mathbf{s}}$  is conserved, so that  $\hat{l}^2$ ,  $\hat{s}^2$ ,  $\hat{j}_z$ , and  $\hat{j}^2$ , are good quantum numbers whose eigenvalues are specified by respectively  $l$ ,  $s = \frac{1}{2}$ ,  $\mu = m \pm \frac{1}{2}$ , and  $j = l \pm \frac{1}{2}$ . From:

$$j(j+1) = \hat{j} \cdot \hat{j} = \hat{\mathbf{l}} \cdot \hat{\mathbf{l}} + \hat{\mathbf{s}} \cdot \hat{\mathbf{s}} + 2\hat{\mathbf{s}} \cdot \hat{\mathbf{l}} = l(l+1) + 3/4 + 2\hat{\mathbf{s}} \cdot \hat{\mathbf{l}}$$

we then see that

$$2\hat{\mathbf{s}} \cdot \hat{\mathbf{l}} = -(1 + \kappa) = \begin{cases} l & \text{when } j = l + \frac{1}{2} \\ -(l+1) & \text{when } j = l - \frac{1}{2} \end{cases}.$$

Changing to the Pauli spinor representation,  $\varphi_\kappa(\varepsilon, r) Y_{\kappa\mu}(\hat{\mathbf{r}}\sigma)$ , the radial equation for  $r \varphi_\kappa(\varepsilon, r)$  is (1), but with

$$\frac{1}{c^2} \left( (\varepsilon - v(r))^2 - \frac{v''(r)}{2} - \frac{v'(r)}{r} + (1 + \kappa) \frac{v'(r)}{r} \right) \quad (4)$$

subtracted from the potential,  $v(r)$ .

The relativistic terms are seen to have their origin in the regions close to the nuclei where the velocity of the electron is high. Hence, they increase with increasing probability that the electron is near the nucleus; that is, with increasing  $Z$  (approximately  $\propto Z^2$ ) for a given  $nl$ -shell, and with decreasing  $n$  and  $l$  for a given  $Z$ . The first term in Eq. (4), which is caused by the increase of the electron's mass with velocity, is always lowering its energy. The second term, which may be interpreted as the correction of the electron's potential energy due to its finite extent of the order of the Compton wavelength  $h/m_0c$ , raises the energy of  $s$ -electrons, but is negligible for higher  $l$ . Those two first terms are by far the largest. They can be treated essentially exactly by exchanging the radial Schrödinger equation (1) by the radial *scalar* Dirac equation, which is like the perturbative Pauli equation (4), but without its last, SO-coupling term [13]. That

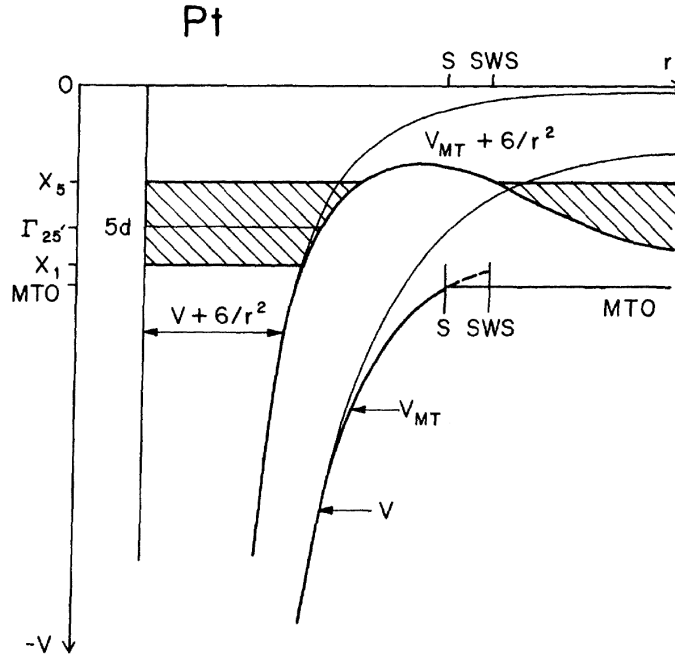


**Fig. 3:** Energies,  $\varepsilon_{5d}$ , and potentials,  $v(r)$  and  $v_d(r)$ , entering the radial Schrödinger equation (1) for atomic and fcc Pt in respectively weak and solid lines. The potentials are lined up close to the nucleus. MTO is the MT zero. S and SWS are respectively the MT and the WS radius. The latter is denoted  $s$  in the following.  $1 \text{ Ry} = 13.6 \text{ eV}$ . From Ref. [15].

term,  $\xi \hat{\mathbf{s}} \cdot \hat{\mathbf{l}}$ , is then added as in the Pauli Hamiltonian (2), but the parameter,  $\xi_l(\varepsilon)$ , is obtained accurately from the proper two coupled radial Dirac-equations [14]. The transition-metal band edges and the SO coupling parameters for the  $nd$ -bands shown respectively in Figs. 7 and 10 in the next section were calculated using the radial Dirac equations.

Finally, a brief reminder about the many-electron wavefunctions and energies of atoms: The configurations given in the Periodic Table specify the occupations of the open  $nl$ -subshells. Due to the  $2(2l+1)$ -fold  $m$ - and  $\sigma$ -degeneracy of such a shell, several Slater determinants corresponding to the various possible occupancies of  $m$  and  $\sigma$  may be formed for this configuration. Since the Hamiltonian is invariant to all rotations, the proper linear combinations of Slater determinants are those which correspond to definite values of  $\hat{L}^2$ ,  $\hat{L}_z$ ,  $\hat{S}^2$ , and  $\hat{S}_z$ , and the energy of such an  $L$ - $S$  term, designated  $^{2S+1}L$ , is independent of  $M_L$  and  $M_S$ . The terms differ in energy by intra-atomic Coulomb energies, i.e. eVs. The  $(2L+1)(2S+1)$ -fold degeneracy of a term will be lifted by the SO coupling, in the presence of which  $L$ ,  $S$ ,  $J$ , and  $M_J$ , rather than  $L$ ,  $S$ ,  $M_L$ , and  $M_S$ , are good quantum numbers. Here  $J$  is the quantum number for the length of  $\hat{\mathbf{J}} \equiv \hat{\mathbf{L}} + \hat{\mathbf{S}}$ . An atomic level is thus designated by the symbol  $^{2S+1}L_{2J+1}$ , and the levels of a given term form its *multiplet* structure.

For a given configuration the state of the lowest total energy usually follows from the three *Hund rules* which dictate that one should first choose the maximum value of  $S$  consistent with the Pauli principle, then the maximum value of  $L$ , and finally the minimum value,  $|L - S|$ , of  $J$  if the shell is less than half full, and the maximum value,  $|L + S|$ , of  $J$  if the shell is more than half full.

### 3 Band structures of the elemental metals

Referring to Walter Harrison’s textbook [4] for a more comprehensive view, I shall concentrate on the elements in the left part of the periodic table. This part includes the one with  $d$ - and  $f$ -electron elements. They become either superconducting (“itinerant”) or magnetic (“localized”) at low temperature. A table reorganized in such a way that this separation becomes clearly visible and exhibits the elements of particular interest, namely those (Ce-Pr, Pu-Am, Mn-Fe, Rh-Co, Pd-Ni) around the border line, was reproduced as Fig. 1 in Richard Martin’s lecture notes and discussed there [16].

#### 3.1 Separating structure and potential

The structures of the alkali, alkaline earth, transition, noble, rare-earth, and most actinide metals are close- or closely packed with 12 (fcc, hcp, dhcp) or 8 (bcc) nearest neighbors at ambient temperature and pressure. The Wigner-Seitz (WS) cells are regular polyhedra with 12 or 8 faces and – as “seen” by an  $s$ -,  $p$ -, or  $d$ -electron with at most 4 orbital lobes – they are almost spherical, and so is the crystal potential,  $V(\mathbf{r})$ , inside a WS cell. If we approximate this potential by a superposition of spherically symmetric potential wells,  $v(r)$ , centered at the atomic sites:  $V(\mathbf{r}) \approx \sum_{\mathbf{R}} v(|\mathbf{r} - \mathbf{R}|)$ , each well can have short range. If we force it to vanish outside the sphere inscribed the WS cell, this forces the crystal potential to take the form of a muffin-tin (MT). Such potentials are used to generate the basis sets in the Korringa-Kohn-Rostocker (KKR) and (linear) augmented plane-wave (L)APW methods of band theory [5, 17]. By being able to handle slightly overlapping potential wells, muffin-tin orbitals (EMTOs, LMTOs, or NMTOs) are, individually, more accurate than APWs [18].

The full lines in Fig. 3 show  $v(r)$  and  $v_d(r)$  for the MT potential in fcc Pt, lined up near the nucleus with the weak lines showing those potentials in a neutral Pt atom. In elementary, closely-packed solids where the WS cells are neutral and nearly spherical,  $v(r)$  bends over towards the value of the self-potential,  $-2/s$ , because the charge which in the neutral atom was outside the WS sphere is compressed into it [19]. Adding now the centrifugal repulsion, we see that  $v_d(r)$  – rather than confining  $\varphi_d(\varepsilon_{5d}, r)$  as in the atom – develops a barrier through which the  $5d$  states in the solid can leak out, thus causing the atomic  $5d$ -level to broaden into a band (cross-hatched).

To understand the details of this, we need to consider how  $\varphi_l(\varepsilon, r)$  depends on  $\varepsilon$  in the neighborhood of the atomic eigenvalue,  $\varepsilon_{nl}$ , as dictated by the radial equation (1) and the shape of  $v_l(r)$ . This is illustrated in Fig. 2 of Ref. [18]. The aim is to find the energies for which we can join linear combinations of partial waves,  $\sum_{Rlm} \varphi_l(\varepsilon, r_R) Y_{lm}(\widehat{\mathbf{r}}_R) c_{Rlm}$  [notation:  $\mathbf{r}_R \equiv \mathbf{r} - \mathbf{R}$  and  $r_R \equiv |\mathbf{r}_R|$ ], with different  $lm$  and  $\mathbf{R}$  smoothly across the boundaries of the WS cells and thus form solutions of the Schrödinger equation for the solid. If it is a crystal with one atom per cell, the linear combinations in neighboring cells separated by a translation  $\mathbf{t}$  should merely differ by the Bloch phase  $\exp(i\mathbf{k} \cdot \mathbf{t})$ . This is how Wigner and Seitz posed the band-structure problem, but it proved difficult to solve in that way. However, the generalized WS rules, used in the renormalized-atom approach [19], stating that there will be a band of  $l$ -character extending

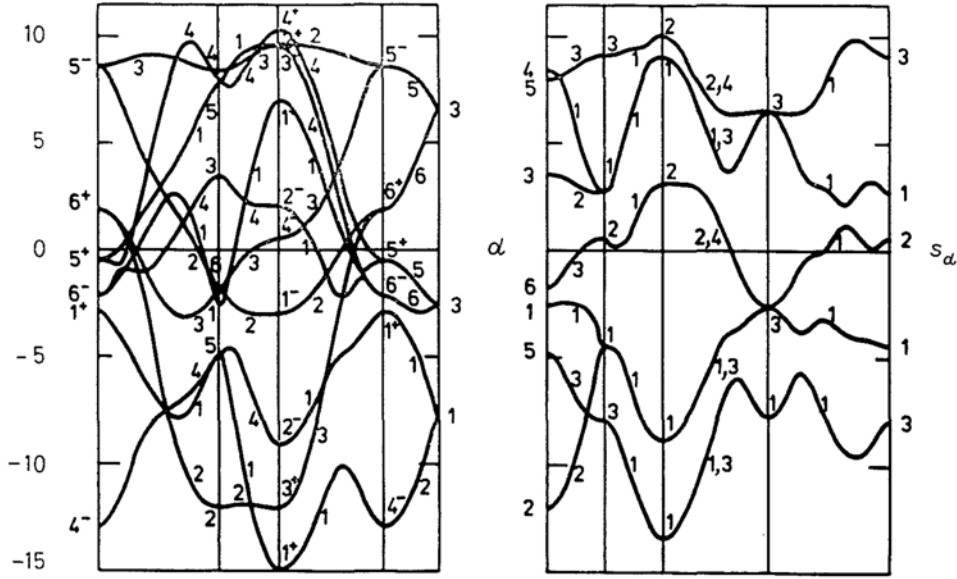


**Fig. 4:** Bare canonical  $d$ -bands, i.e., the eigenvalues of  $S_{R'l'm',Rlm}(\mathbf{k})$ , for the hcp structure with  $c/a = \sqrt{8/3}$ . From Ref. [12].

from the energy,  $B_l$ , where  $\varphi_l(r)$  comes in flat to the WS sphere, i.e.,  $\varphi'_l(B_l, s) = 0$ , to the energy,  $A_l$ , where  $\varphi_l(r)$  has a node at the sphere, i.e.,  $\varphi_l(A_l, s) = 0$ , have proved quite accurate and most useful.

The atomic-sphere approximation (ASA) [20] solved the problem to the extent that charge- and spin-selfconsistent – and thus DFT – calculations could be carried out. It specified anisotropic  $\mathbf{k}$ -dependent boundary conditions for the radial logarithmic derivatives on the WS sphere,

$$D_l(\varepsilon) \equiv D\{\varphi_l(\varepsilon, s)\} \equiv \frac{s\varphi'_l(\varepsilon, s)}{\varphi_l(\varepsilon, s)}, \quad (5)$$

by the set of linear, homogeneous equations

$$\sum_{lm} \left( S_{l'm',lm}(\mathbf{k}) - P_{l'}(\varepsilon) \delta_{l'l} \delta_{m'm} \right) c_{lm} = 0 \quad (6)$$

for the coefficients,  $c_{lm}$ , of the local partial-wave expansions. In the diagonal of the secular matrix are  $l$ -dependent, ever-increasing potential functions of energy, which are

$$P_l(\varepsilon) \equiv 2(2l+1) \frac{D_l(\varepsilon) + l + 1}{D_l(\varepsilon) - l} \approx \frac{\varepsilon - C_l}{\Delta_l} \left[ 1 + \gamma_l \frac{\varepsilon - C_l}{\Delta_l} \right]^{-1} \equiv \frac{1}{\gamma_l} \frac{\varepsilon - C_l}{\varepsilon - V_l}, \quad (7)$$

in terms of the ever-decreasing logarithmic-derivative functions (5). In fact,  $dD_l(\varepsilon)/d\varepsilon = -\langle \varphi_l^2(\varepsilon) \rangle / s\varphi_l^2(\varepsilon, s)$ , as follows from partial integration of  $\langle \varphi(\varepsilon') | -\nabla^2 + v(r) - \varepsilon | \varphi(\varepsilon) \rangle = 0$  and  $\varepsilon' \rightarrow \varepsilon$ . On the right-hand side of the approximation (7), the potential functions are parametrized in terms of potential parameters for the center of the  $l$ -band,  $C_l$ , its width,  $\Delta_l$ , and its distortion,  $\gamma_l$ , or, alternatively, the square-well pseudopotential parameters,  $V_l \equiv C_l - \Delta_l/\gamma_l$ , and the band-mass parameters,  $\mu_l$  and  $\tau_l$  ( $= 1$  for free electrons), to be defined in Eq. (11).

The matrix  $S_{l'm',lm}(\mathbf{k})$  is the bare canonical structure matrix, which depends on the Bloch vector  $\mathbf{k}$ , but is independent of the energy and the scale of the lattice. Each diagonal block,  $S_{lm',lm}(\mathbf{k})$ , can be diagonalized, once and for all, yielding the so-called canonical bands,  $S_{li}(\mathbf{k})$ , which upon scaling via  $P_l(\varepsilon)$  become the unhybridized  $l$ -bands,  $\varepsilon_{li}(\mathbf{k})$ . In Fig. 4 we show the ten canonical  $d$ -bands for the hcp structure with two atoms per primitive cell, the most common structure of the elemental metals. Obviously, the detail displayed here is way beyond the WS rules, which merely state that the  $l$ -band extends from  $D_l = 0$  to  $-\infty$ , which rescales to  $P_l$  extending from  $-2(2l+1)(l+1)/l$  to  $2(2l+1)$ , i.e., from  $-15$  to  $+10$  for the  $d$ -band, from  $-12$  to  $+6$  for the  $p$ -band, and from  $-\infty$  to  $+2$  for the  $s$ -band. This agrees surprisingly well with the more accurate values taken at the edges of the canonical bands, albeit less well in the more open bcc structure. This may be seen in Figs. 4 and 5, and in Refs. [8, 10–12]. The center of gravity of a canonical band, i.e., its first moment integrated over the Brillouin zone, is zero, and so is its average for any  $\mathbf{k}$ -point, except for the canonical  $s$ -band, and for the  $p$ -bands at  $\mathbf{k}=\mathbf{0}$ .

Knowledge of the potential parameters, tables of which may also be found in Refs. [8, 10, 11] and with most detail in [12], allows one to construct the unhybridized energy bands by placing them at the respective energies,  $C_l$ , scaling them by,  $\Delta_l$ , and distorting them by  $\gamma_l$ . Finally, the  $s$ -,  $p$ -, and  $d$ -bands belonging to the same irreducible representation (the numbers in Fig. 4) should be allowed to hybridize by taking the off-diagonal blocks of the structure matrix into account. This is illustrated in Fig. 6, but since the distortion of the  $s$ -band and its hybridization with the  $p$ -band are relatively large, thus developing into a nearly free-electron like  $sp$ -band, the unhybridized bands shown here were defined with respect to the *screened* structure matrix:  $S^\gamma \equiv S[1 - \gamma S]^{-1}$ . The quantities in this screening equation are matrices and  $\gamma$  is diagonal. In the  $\gamma$ -representation, the one-electron Hamiltonian takes the simple, orthogonal tight-binding form [12, 22]

$$H_{R'l'm',Rlm}^\gamma(\mathbf{k}) = \sqrt{\Delta_{R'l'}} S_{R'l'm',Rlm}^\gamma(\mathbf{k}) \sqrt{\Delta_{Rl}} + C_{R'l'} \delta_{R'l'} \delta_{m'm}. \quad (8)$$

For completeness we have included an index,  $R$ , labelling the sites,  $\mathbf{R}$ , of the atoms in the primitive cell. For the hcp structure considered in Fig. 4, the two sites are identical, so that the potential parameters are independent of  $R$ , but the dimension of structure matrix is doubled.

The ASA brought the realization that the bewilderingly complication of the band structures of  $d$ - and  $f$ -band materials is primarily of *structural* origin and can be expressed as canonical bands or hopping integrals. The *potential* and, hence, the approximations for exchange and correlation, merely decide the positions and widths of – and the hybridizations between – these  $s$ -,  $p$ -,  $d$ -, and possibly  $f$ -bands. This partly explained why a standard potential construction could work so well for Fermi surfaces and low-energy excitations [10, 23]. The original KKR method, *has* the form (6), but its structure matrix has long  $|\mathbf{R}' - \mathbf{R}|$ -range end thereby depends strongly on energy so that obtaining the band structure,  $\varepsilon_j(\mathbf{k})$ , requires a complicated search for the roots of a secular determinant.

The insight leading to the ASA (6) was that the relevant energies,  $\varepsilon$ , are less than  $\sim 2$  Ry above the potential,  $-2/s$ , in the region between the atoms (Fig. 3), whereby the corresponding wavelengths,  $\lambda \equiv 2\pi/\kappa \gtrsim 2\pi/\sqrt{2}$  a.u., exceed typical interstitial distances in closely packed mate-

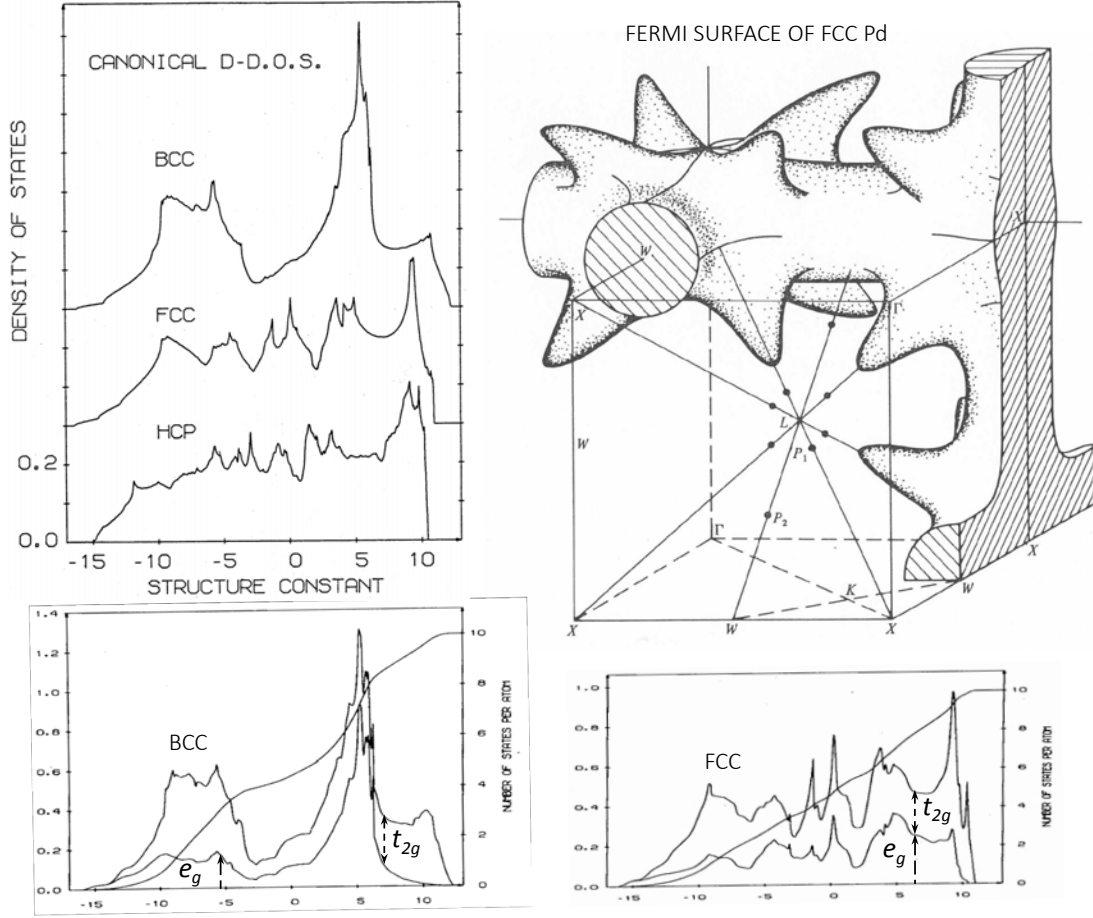


**Fig. 5:** Densities of states (DOS) for the bcc, fcc, and hcp ( $c/a = \sqrt{8/3}$ ) bare canonical d-bands and their separation into  $e_g$  and  $t_{2g}$  projections for the bcc (bottom left) and fcc (bottom right) structures. From Ref. [8]. The open, heavy-hole FS-sheet in fcc Pd. The van Hove singularities caused by the saddlepoints in this 5th band at  $P_1$  and  $P_2$ , lying respectively 2 and 13 mRy below  $\varepsilon_F$ , bracket the large DOS peak at the top of the fcc d-bands. From Ref [15]. A tiny hole pocket (not shown) caused by spin-orbit splitting at L existed in the calculation and was observed later [21].

rials, and therefore need not be accurate. Similarly, partial waves with  $l \lesssim 3$  cannot distinguish between touching and slightly overlapping MT spheres. The simplest choice was therefore to join a solution of the *Laplace equation* smoothly onto the partial wave at the WS radius:

$$\frac{\varphi_l(\varepsilon, r)}{\varphi_l(\varepsilon, s)} = \frac{D_l(\varepsilon) + l + 1}{2l + 1} \left(\frac{r}{s}\right)^l + \frac{l - D_l(\varepsilon)}{2l + 1} \left(\frac{r}{s}\right)^{-l-1}$$

and then subtract the function which is irregular at infinity

$$\chi_l(\varepsilon, r) \equiv \varphi_l(\varepsilon, s) \begin{cases} \frac{\varphi_l(\varepsilon, r)}{\varphi_l(\varepsilon, s)} - \frac{D_l(\varepsilon) + l + 1}{2l + 1} \left(\frac{r}{s}\right)^l & \text{for } r \leq s \\ \frac{l - D_l(\varepsilon)}{2l + 1} \left(\frac{r}{s}\right)^{-l-1} & \text{for } r \geq s \end{cases} \quad (9)$$

to obtain a regular function which decays as an electrostatic  $2^l$ -pole field. This is essentially the 1st-generation MTO whose tail is trivial to expand around other sites, thus giving rise to



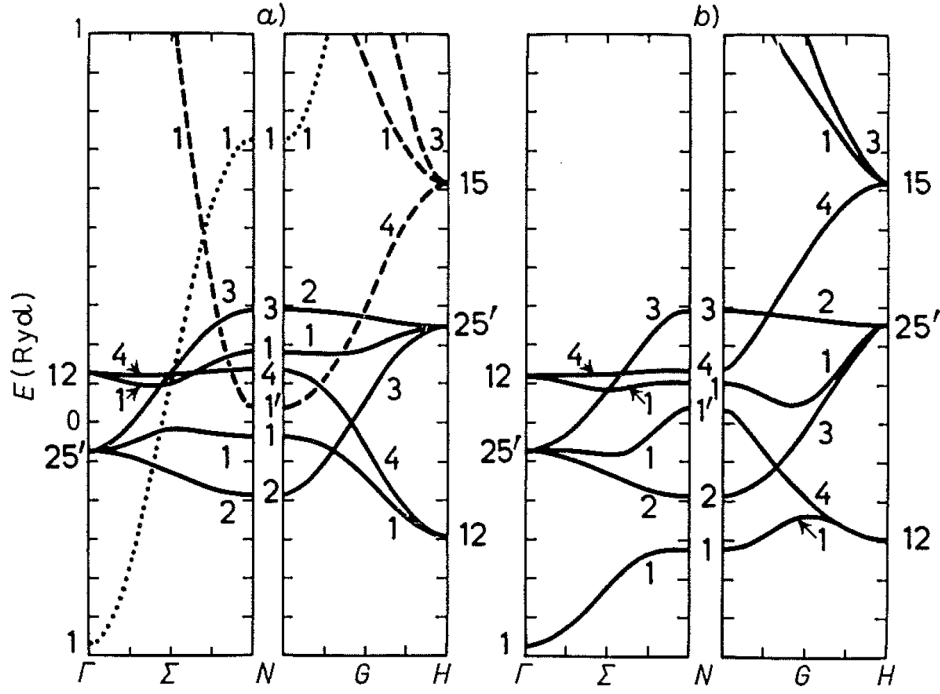


**Fig. 6:** *Bcc vanadium.* a): Unhybridized  $s$ (dotted)-,  $p$ (stippled)-, and  $d$ (full)-energy bands,  $C_l + \Delta_l S_{li}^\gamma(\mathbf{k})$ . b): Hybridized bands. Here,  $\gamma_s = 0.425$ ,  $\gamma_p = 0.0907$ , and  $\gamma_d = 0.0095$ . From Ref. [12].

the canonical structure matrix. Expressed in real space as two-center hopping integrals between two MTOs at distance  $d$ , with the  $z$ -axis chosen along the inter-atomic vector,  $\mathbf{R} - \mathbf{R}'$ , and  $M$  being the common azimuthal quantum number,

$$S_{l'lM} = (-1)^{l'+M+1} (l' + l)! 2 \sqrt{\frac{2l' + 1}{(l' + M)! (l' - M)!}} \sqrt{\frac{2l + 1}{(l + M)! (l - M)!}} \left(\frac{s}{d}\right)^{l'+l+1}. \quad (10)$$

For 1st-generation MTOs the two-center Slater-Koster integrals [24] take the factorized form  $V_{l'lM} = \sqrt{\Delta_{R'l'm'}} S_{l'lM-m'} \sqrt{\Delta_{Rlm}}$ . For a general direction of the  $z$ -axis, e.g., the global  $z$ -axis in a crystal, the bare structure matrix is given analytically in Ref. [14]. Using the real-valued cubic harmonics listed on pp. 7.38/39 in Ref. [24], instead of the spherical harmonics, the bare canonical two-center integrals are given in Table II of Ref. [25], which – with  $V_{l'lM}$  as given above – is identical with those in Ref. [24].

The condition that a linear combination of MTOs solves the Schrödinger equation is then, that inside any sphere  $R'$  and for any  $l'm'$ , the sum of the *tails* from all other sites *cancel* the artificial, regular Laplace solution in Eq. (9). Despite the extreme simplicity of expression (10), the long range of the bare  $s$ - and  $p$ -MTOs (9) is for most purposes unpractical, and this is the reason why *screened* Laplace solutions were chosen for the tails of the 2nd-generation MTOs [12, 22].

Fig. 7 shows the behavior of the Fermi level and the DFT-LDA band edges,  $A_d$ ,  $B_d$ ,  $B_s$ , and  $B_p$  across the  $3d$   $4sp$ ,  $4d$   $5sp$ , and  $5d$   $6sp$  series with respect to the zero of electrostatic potential in the infinite solid. The  $sp$ -bands are so wide that their tops,  $A_s$  and  $A_p$ , are beyond the frame of the figure. The most significant trends follow from the filling of the subshells, like for the

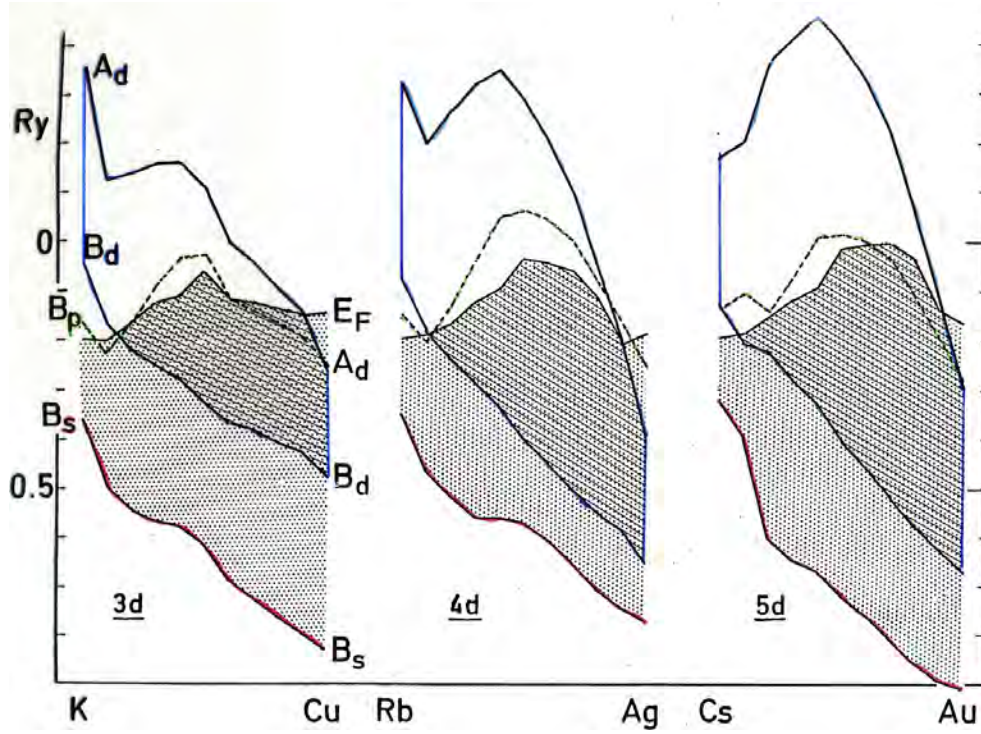


**Fig. 7:** Band edges in the elemental, close-packed  $(n-1)d ns np$  metals.  $B_i$  bottoms of the  $s$  (red),  $p$  (green), and  $d$  (blue) bands.  $A_d$  (dark blue) top of the  $d$  band.  $E_F$  (black) Fermi level. The filled part of the  $sp$  and  $d$  bands are respectively dotted and cross hatched. The zero of energy is the electrostatic potential at the WS sphere. Lu rather than La was taken as the 3d 5d metal. DFT-LDA and LMTO were used in the calculations. From Table III in Ref. [12].

elements (Figs. 1 and 2): First, and most dramatically, the filling of the  $ns$  band going from the alkalis to the alkaline earths causing  $B_s$ ,  $B_p$ , and  $B_d$  to drop sharply and the  $ns$  orbital to contract. Subsequently, the gradual development of the  $(n-1)d$ -band from being empty and free-electron like in the alkali- and alkaline earths, to being an occupied semi-core band beyond Cu, Ag, and Au, i.e., in Zn, Cd, and Hg. When going from the alkaline earths to the first transition metal,  $B_p$  and  $B_d$  move below the Fermi level, but while  $B_d$  and  $B_s$  continue to drop,  $B_p$  moves up again and more or less stays slightly above  $\varepsilon_F$  throughout the transition series. The shape and occupation of the nearly-free-electron  $ns np$ -band thus stay fairly constant. The Fermi level follows a parabolic, downwards curving trend which results from the combined effects of filling-up the  $d$ -band and lowering its center of gravity. The internal work function,  $-\varepsilon_F$ , differs by the surface dipole from the external work function, which experimentally increases from 3.1 eV in Y to 5.5 eV in Pd, as an example, while  $-\varepsilon_F$  merely increases by 0.4 eV from 2.3 to 2.8 eV. The experimental ionization potential for atoms shown in Fig. 2 increases from 6.5 to 8.5 eV [26].

Included in the LDA energies in Fig. 7 is the solid-state effect that the filling of first the  $ns$ - and then the  $(n-1)d$ -bands causes the lattice to contract (Fig. 8) and this, itself, causes the bands to broaden. The broadening is most visible for the  $d$ -bands whose bandwidth,  $A_d - B_d = 25\Delta_d$ , and reaches its maximum at respectively V, Nb, and Ta. Going from one period to the next,

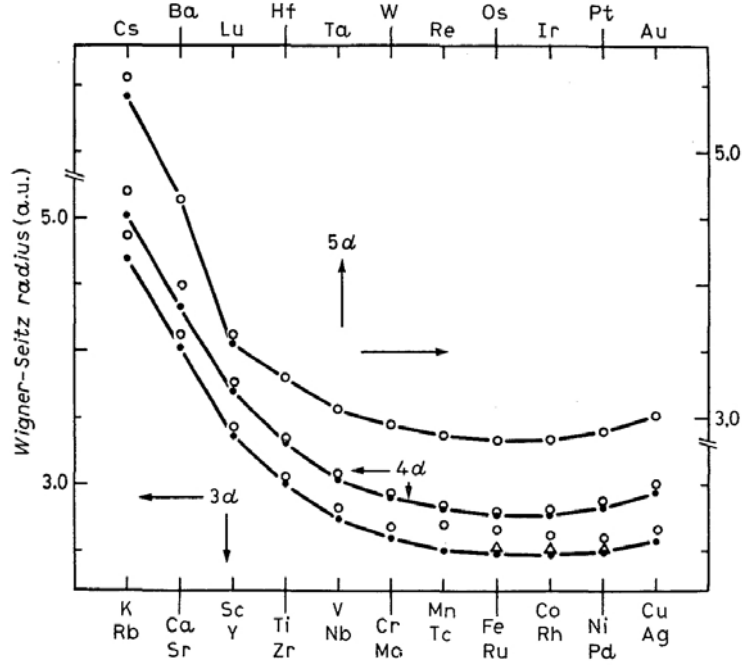


**Fig. 8:** Equilibrium WS radii for the elemental alkali, transition, and noble metals. Open dots are the experimental values. The line and the full dots are the results [12] of LDA LMTO [14,26] calculations. The open triangles are LSD calculations for Fe, Co, and Ni. From Ref. [12].

i.e., increasing  $n$ , makes the orbitals expand and with them, the lattice and the bandwidths. Now, the energy of an electron, free with respect to a flat potential  $V_s (\equiv B_s)$  is purely kinetic, and its band therefore scales like  $s^2$ . In Fig 9, we therefore plot for the  $4d5sp$  series the filled free-electron bandwidth  $s^2(\varepsilon_F - V_s)$ , which is seen to be more constant than  $\varepsilon_F$  in Fig. 7. The  $s^2(C_d - V_s)$ -measure of  $d$ -band position, together with the inverse of the mass at the center of the  $d$ -band, Eq. (11), clearly exhibit the drop and narrowing of the  $d$ -band with respect to the  $sp$ -band. Fig. 9 finally shows the behavior of the square-well pseudopotentials  $V_l$ , and the inverse of the band masses,  $\tau_l$ , at the respective  $V_l$

$$\frac{1}{\mu_l} \equiv s^2 \Delta_l = \frac{1}{2} s^3 \varphi_l^2(C_l, s) \quad \text{and} \quad \frac{1}{\tau_l} = \frac{1}{2l+3} s^3 \varphi_l^2(V_l, s). \quad (11)$$

These inverse masses are proportional to the respective probability amplitudes at the WS sphere, i.e., between the atoms. Since the partial waves are normalized to unity in the WS sphere, this means that, had the partial wave been as in the atom, the band mass would be proportional to the (re)normalization integral over the WS sphere [19]. The bottom of the  $5s$ -band lies well above the  $4f$ -pseudopotential which, itself, is close to the potential  $\sim -2/s$  at the WS sphere. Moreover, the  $5s$ -mass is significantly smaller than unity and attains a minimum, as do  $(V_f - V_s) s^2$  and  $(-2/s - V_s) s^2$ , near the middle of the series. This means that the  $5s$ -electron is excluded from the core region (orthogonalization hole). For a further discussion of this point and other trends in the  $4d5sp$  series see Ref. [9].

The relativistic corrections (4) originate close to the nuclei and are negligible between the atoms. But this does not mean that their effects in solids are the same as in atoms: In the ASA we may, initially, normalize the solution,  $\varphi_l(\varepsilon, r)$ , of the radial equation to have the same behavior

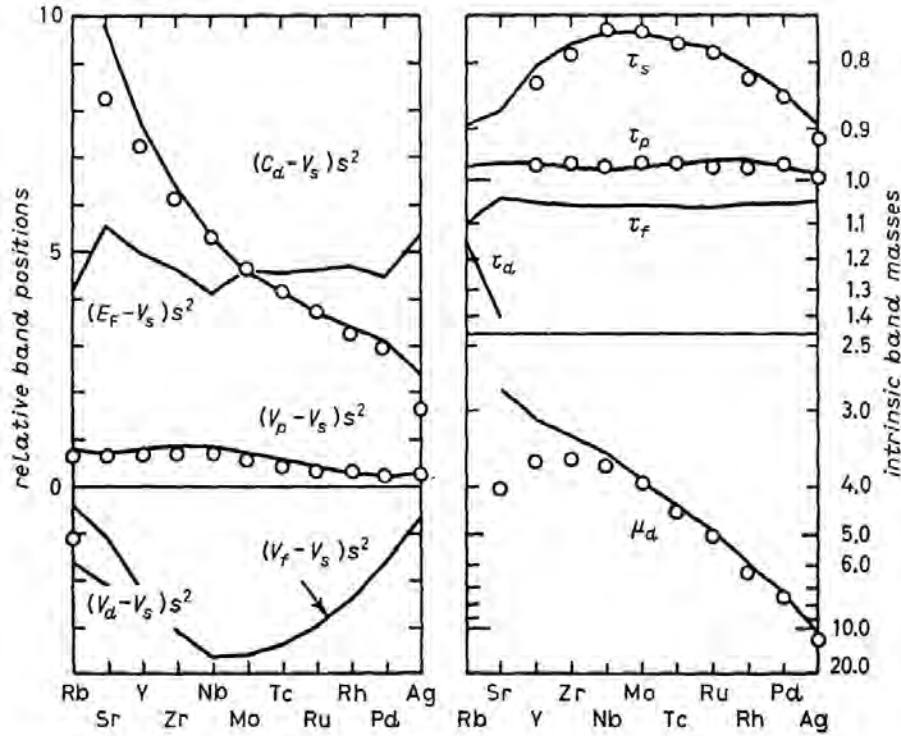


**Fig. 9:** Band positions relative to the bottom of the  $s$ -band,  $B_s=V_s$ , in dimensionless units, and intrinsic band masses,  $\tau_l$  and  $\mu_d$ , on a reciprocal scale, in the  $4d\ 5sp$ -series; see text. Open circles from the Mattheiss-Slater [27] construction (from Ref. [8]) and full lines from the LDA [26] (from Ref. [10, 12]). For Rb, Sr, and Ag, the LDA yield Fermi surfaces in better agreement with experiments.

near a given nucleus, i.e., integrate the radial equation outwards with the same initial condition regardless of the surroundings and the energy. In the solid,  $\varphi_l(\varepsilon, r)$  must then be (*re*)normalized to inside the WS sphere [see, e.g., Eq. (11)], and this makes the magnitudes of the relativistic effects *larger* in the solid than in the atom by a factor of approximately  $1/(1 - q_{nl})$ , where  $q_{nl}$  is the fraction of the *atomic*  $nl$ -electron which lies outside the WS sphere. This fraction is about 0.5 for  $s$ -electrons and less than 0.1 for  $d$ -electrons. The partial-wave renormalization furthermore causes the magnitude of the relativistic effects in the solid to increase from the bottom ( $B_l$ ) to the top ( $A_l$ ) of the band, and this increase is nearly a factor two! The width of the  $l$ -band is thereby decreased by the relativistic shifts, but increased by the SO splitting. When going beyond the ASA, such renormalization effects are described by the overlap of the MTOs (see Fig. 3 in Ref. [18]).

Of the relativistic corrections, the shifts are the most important and they have been included in, e.g., Figs. 7 and 9. The downwards shift of the center of the  $ns$ -band (due to the mass-velocity minus Darwin terms) with respect to the center of the  $(n-1)d$  band (due to mass-velocity),  $C_{ns} - C_{(n-1)d}$ , is about 15 mRy, 75 mRy, and 250 mRy in the middle of the  $3d$ -,  $4d$ -, and  $5d$ -series, respectively. As a result, the number of non- $d$ -electrons increases from  $1.50 \pm 0.10$  e/atom in the  $3d$ - and  $4d$ -series to  $1.75 \pm 0.15$  in the  $5d$ -series. Here, the smaller/larger number refers to the beginning/end of the series. Note also that the bottom,  $B_p$ , of the  $p$ -band is occupied in the second half of the  $3d$ - and  $5d$ -, but not in the  $4d$ -series.

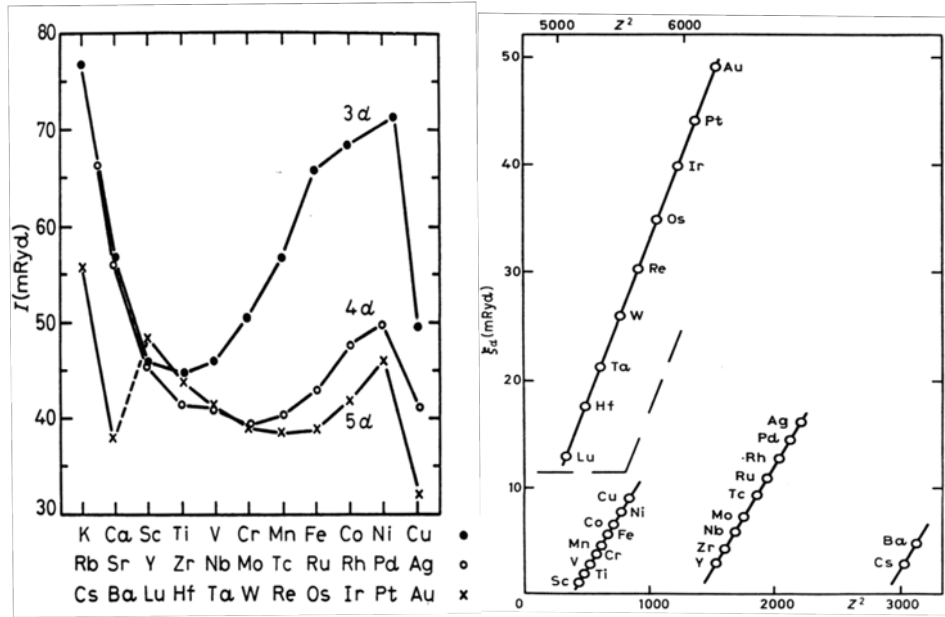


**Fig. 10:** Left: LSD [26] Stoner parameter,  $I$ , at  $\varepsilon_F$  calculated [12] with the LMTO method and using the procedure of Janak [28]. Right: Spin-orbit coupling parameter  $\xi_d$  ( $C_d$ ) for the center of the  $d$ -band in elemental transition metals as a function of  $Z^2$ . Note that  $\xi_d(\varepsilon)$  increases by about a factor 2 from the bottom to the top of the  $d$ -band. From Ref. [12].

The SO coupling parameters shown in Fig. 10 are typically one order of magnitude smaller than the relativistic shifts. Moreover, for crystals with inversion symmetry, the SO coupling cannot split the two spin bands and therefore gives rise to splittings of first order in  $\xi$  only in small regions of  $k$ -space near points of degeneracy. SO coupling is important near the top of the  $d$ -bands where the bands have  $t_{2g}$  character (see Fig. 5).

The abrupt increase in the size of the relativistic effects seen in Figs. 7 and 10 between the 2nd (Ba) and 3rd (Lu)  $5d$ -elements is caused by the jump of  $Z$  due to the insertion of the 14 Lanthanides. All of those are, contrary to the case for the atoms (Fig. 1), trivalent  $5d$ -metals ( $4f^n 5d^1 6s^2$ ) with the exceptions of divalent Eu ( $4f^7 6s^2$ ) and Ce ( $4f^x 5d^{2-x} 6s^2$ ), whose  $\alpha$ - $\gamma$  transition was discussed by Richard Martin in last year's lecture notes [16]. In this connection it should be mentioned that the actinides are  $5f^n 6d^1 7s^2$ -metals whose  $5f$ -electrons are itinerant in the first- and localized in the second part of the series.

In the 60ies and 70ies, energy bands computed using the standard, non-selfconsistent, Mattheiss-Slater construction of the crystal potential [27] were found to give surprisingly good agreement between experimental and computed Fermi surfaces, and useful optical spectra for nearly all elemental metals in the  $4d$ - and  $5d$ -series [10]. When in the late 70ies and early 80ies it became possible to perform selfconsistent DFT calculations [9, 10, 29–31], it turned out that one and the same local exchange-correlation potential [26] not only gave “bastard” bands which were nearly identical with those obtained with the Mattheiss-Slater construction (see Fig. 9), but also gave what DFT was designed for: good total energies, or rather: good total-energy differences, e.g., lattice constants, structures, trends, and last, but not least, Car-Parrinello molecular dynamics [10, 12, 31–33]. Towards the end of the 80ies DFT was accepted in a large part of the condensed-matter community and rapidly spreading beyond [23].

### 3.2 Force theorem, pressures, and structures

The cohesive properties (at  $T=0$ ) can be computed from the total-energy. But this provides little insight, because it is expressed in terms of largely cancelling quantities, the selfconsistently calculated Coulomb energies of the electron-electron and proton-proton repulsions and of the electron-proton attraction, plus the kinetic energy of the electrons. However, the cohesive properties only involve total-energy *differences* and these are given to *first* order by the difference of the one-electron energies calculated for *frozen* one-electron potentials (i.e., the difference of kinetic energies avoids double counting of the e-e interactions) plus the difference of Madlung energies. This so-called force theorem was originally proved within the LDA in Refs. [10, 34, 35]. With appropriate definitions it holds in general, but only to 1st order [36]. In the following, I shall illustrate this by application to pressure-volume relations and crystal structures of the closely-packed elemental metals.

#### 3.2.1 Partial pressures

Neglecting the zero-point motion of the nuclei, the pressure,  $\mathcal{P}$ , which must be applied in order to keep the crystal in equilibrium at a given volume,  $\mathcal{V}$ , is the change of the total energy with uniform compression (see top left part of Fig. 11). In terms of the equation of state,  $\mathcal{P}(\mathcal{V})$ , the equilibrium atomic volume,  $\mathcal{V}_0 = (4\pi/3) s_0^3$ , is determined by  $\mathcal{P}(\mathcal{V}_0) = 0$ , the bulk modulus by  $\mathcal{B} = -d\mathcal{P}/d \ln \mathcal{V}|_{\mathcal{V}_0}$  and the cohesive energy per atom by

$$E_{\text{coh}} = - \int_{\mathcal{V}_0}^{\infty} \mathcal{P} d\mathcal{V} = - \int_{s_0}^{\infty} 3\mathcal{P}\mathcal{V} d(\ln s),$$

where  $s_0$  is the equilibrium WS radius. With the force theorem, the pressure is most conveniently calculated by “peeling the skin off” the self-consistent, cellular potential, moving the frozen potentials together in the compressed structure, and recalculating the sum of the one-electron energies. To the change of the latter, should finally be added the change of electrostatic energy between the cells. I.e.

$$3\mathcal{P}\mathcal{V} \equiv - \frac{dE_{\text{tot}}}{d \ln s} = - \sum_{i\mathbf{k}}^{\text{occ}} \frac{\delta \varepsilon_i(\mathbf{k})}{\delta \ln s} - \frac{\delta \text{Mad}}{\delta \ln s}, \quad (12)$$

where  $\delta$  indicates the derivative for frozen potentials in the first term and frozen charge densities in the second [36]. For closely-packed elemental solids, the latter may often be neglected so that only the one-electron energies remain.

In the ASA (6), only the logarithmic-derivative functions (5) change because they must be re-evaluated at an infinitesimally smaller WS radius. What happens to the band edges,  $B_l$  and  $A_l$ , may be understood from the bottom left part of Fig. 11, where the bonding and antibonding partial waves,  $\varphi_l(B_l, r)$  and  $\varphi_l(A_l, r)$ , are shown for cases where  $B_l$  and  $A_l$  lie above the value  $v_l(s)$  of the effective potential at the sphere (dotted) and where they lie below (full) [see Fig. 3]. In the dotted case, the region between the atoms is classically allowed so that, according to the radial Schrödinger equation (1),  $r\varphi_l(\varepsilon, r)$  curves towards the  $r$ -axis, whereas in the full,

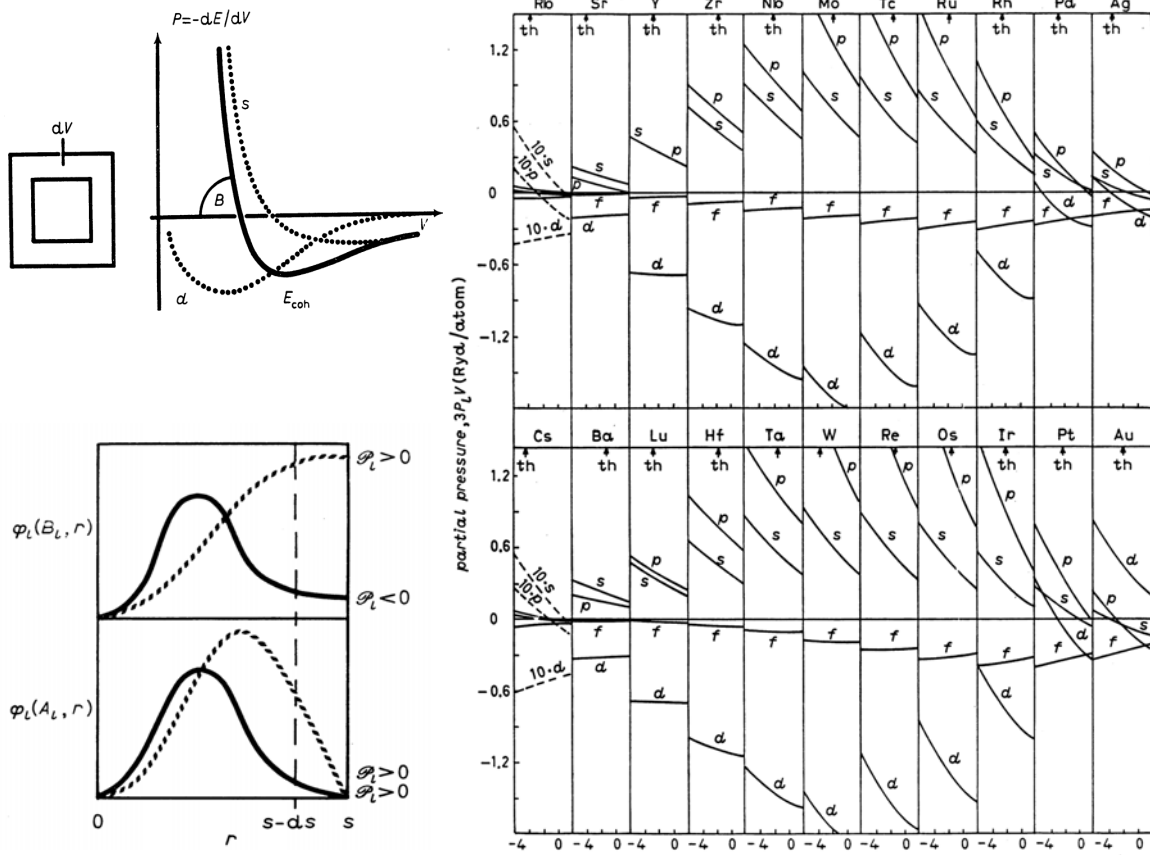


**Fig. 11:** Top left: Total and partial pressure-volume curves (schematic). The bulk modulus is the slope of the curve, the equilibrium volume is the intersection with the volume axis, and the cohesive energy is the area below the curve from the intersection to infinity. Bottom left: Radial wave functions (normalized for  $r \rightarrow 0$ ),  $\varphi_l(r)$ , at the bottom ( $B_l$ ) and top ( $A_l$ ) of the  $l$ -band. The dotted/full lines are for cases where  $B_l$  and  $A_l$  are above/below the effective potential,  $v_l(s)$ , at the WS sphere. The sign of the partial pressure,  $\mathcal{P}_l$ , is indicated. Right: Partial pressures calculated with LDA LMTO [12] for the 5sp 4d and 6sp 5d series as functions of the percentage deviation from the experimental WS radius at zero pressure. The calculated deviations are indicated by “th”. From Ref. [12].

classically forbidden case,  $r\varphi_l(\varepsilon, r)$  curves away from the axis and the electron must tunnel out of the WS sphere in order to get to a neighboring atom.

Now, under compression we need to re-install the bonding/antibonding boundary conditions at  $s-ds$  and to use the fact proved below Eq. (7), that the logarithmic derivative is an ever-decreasing function of energy. From Fig. 11 we see that if  $s$  is classically allowed, the slope  $\varphi'_l(B_l, s-ds)$  is positive, so that in order to re-install the zero-slope condition, we must *increase* the energy, i.e., the bottom of the  $l$ -band goes up upon compression, and this means that it adds to the pressure,  $\mathcal{P}_l(B_l)$ , i.e., will tend to press the nuclei apart. This is the case for electrons in bonding states at the bottom of broad bands such as  $s$  and  $p$ , because their centrifugal repulsion vanishes, or is small, and because the bandwidth is proportional to  $[-dD_l(\varepsilon)/d\varepsilon]^{-1} = s\varphi_l^2(\varepsilon, s)/\langle\varphi_l^2(\varepsilon)\rangle$ , the probability of being *at* the sphere. If, on the other hand, the interstitial

region is classically forbidden,  $\varphi'_l(B_l, s - ds)$  is negative and the bottom of the  $l$ -band therefore goes down in energy upon compression. Its contribution to the pressure is negative, i.e., the *bonding electrons at the bottom of narrow bands* are attractive, they tend to keep the nuclei together. This is the case for transition-metal  $d$ -bands. At the top of an  $l$ -band, the slope  $\varphi'_l(A_l, s - ds)$  is always negative, so that in order to re-install the  $\varphi_l(A_l, s) = 0$  condition, we must always increase the energy, and this means that the antibonding electrons at the top of an  $l$ -band are always repulsive, i.e., press the nuclei apart.

The right-hand side of Fig. 11 shows for the metals in the  $4d$ - and  $5d$ -series the partial pressures as functions of the percentage deviation of  $s$  from the experimental low-temperature values. The values where the total pressure vanishes, the theoretical WS radii, are indicated by arrows. The experimental and theoretical absolute values were shown in Fig. 8. The picture of the bonding emerging is that the  $d$ -electrons contract the crystal against the repulsion from the “more free”  $sp$ -electrons. This attraction increases until the bonding states in the lower part of the  $d$ -band are full and filling of the antibonding states in the upper part starts. In Au, the  $d$ -electrons are seen to be repulsive (hard core repulsion) while in Ag, they are still attractive. We also note that the bulk moduli in the  $6sp5d$ -series are larger than those in  $5sp4d$ -series. Had it been possible to decompose the pressures according to an  $spd$ -set of local orbitals, rather than partial waves, the small attractive  $f$ -pressures would have been associated with the tails of these orbitals.

The ASA pressure relation was originally derived from the virial theorem and we can get to the form given by Pettifor [37] by using the radial Schrödinger equation (1) to express the derivative,  $\delta D_l(\varepsilon)/\delta \ln s$ , of the logarithmic-derivative function (5) as

$$-s \left( \frac{s \varphi'}{\varphi} \right)' = -s \frac{(s \varphi)''}{\varphi} + \frac{s \varphi'}{\varphi} + \left( \frac{s \varphi'}{\varphi} \right)^2 = \left( \varepsilon - v_l(s) \right) s^2 + D(\varepsilon) \left( D(\varepsilon) + 1 \right).$$

Note in passing, that since  $D_l(D_l + 1) = (D_l + l + 1)(D_l - l)$ , the contribution to the pressure by not only electrons at the bottom,  $B_l$ , but also at the center,  $C_l$ , of the band, and at the energy,  $V_l$ , of the square-well pseudopotential is proportional to  $\varepsilon - v_l(s)$ . Now, the energy,  $\varepsilon_l(D)$ , corresponding to the boundary condition  $D$  at  $s$ , i.e., the function inverse to  $D_l(\varepsilon)$ , is

$$-\frac{\delta \varepsilon_l(\varepsilon)}{\delta \ln s} = -\frac{\delta D_l(\varepsilon)}{\delta \ln s} \left( \frac{dD_l(\varepsilon)}{d\varepsilon} \right)^{-1} = \left( (\varepsilon - v_l(s)) s^2 + (D_l(\varepsilon) + 1) D_l(\varepsilon) \right) s \varphi_l^2(\varepsilon, s)$$

where  $\varphi_l(\varepsilon, r)$  is normalized to 1 in the WS sphere. Multiplication by the  $l$ -projected DOS and integration up to the Fermi level yields Pettifor's pressure relation. The form (12) is more intelligible and, using the Hamiltonian (8) or the full LMTO version, requires the  $\delta \ln s$ -derivatives of the potential parameters given analytically in, e.g., Ref. [12].

### 3.2.2 Structures

The structural sequence for the non-magnetic transition metals at low temperature and ambient pressure is: hcp (Sc, Y, Lu), hcp (Ti, Zr, Hf), bcc (V, Nb, Ta), bcc (Cr, Mo, W), hcp (Tc, Rs), hcp (Ru, Os), fcc (Rh, Ir), and fcc (Ni, Pd, Pt). Already in the late 60ies [39], it had been pointed out that this reflects a trend in the sum of the one-electron energies, but the force theorem made the



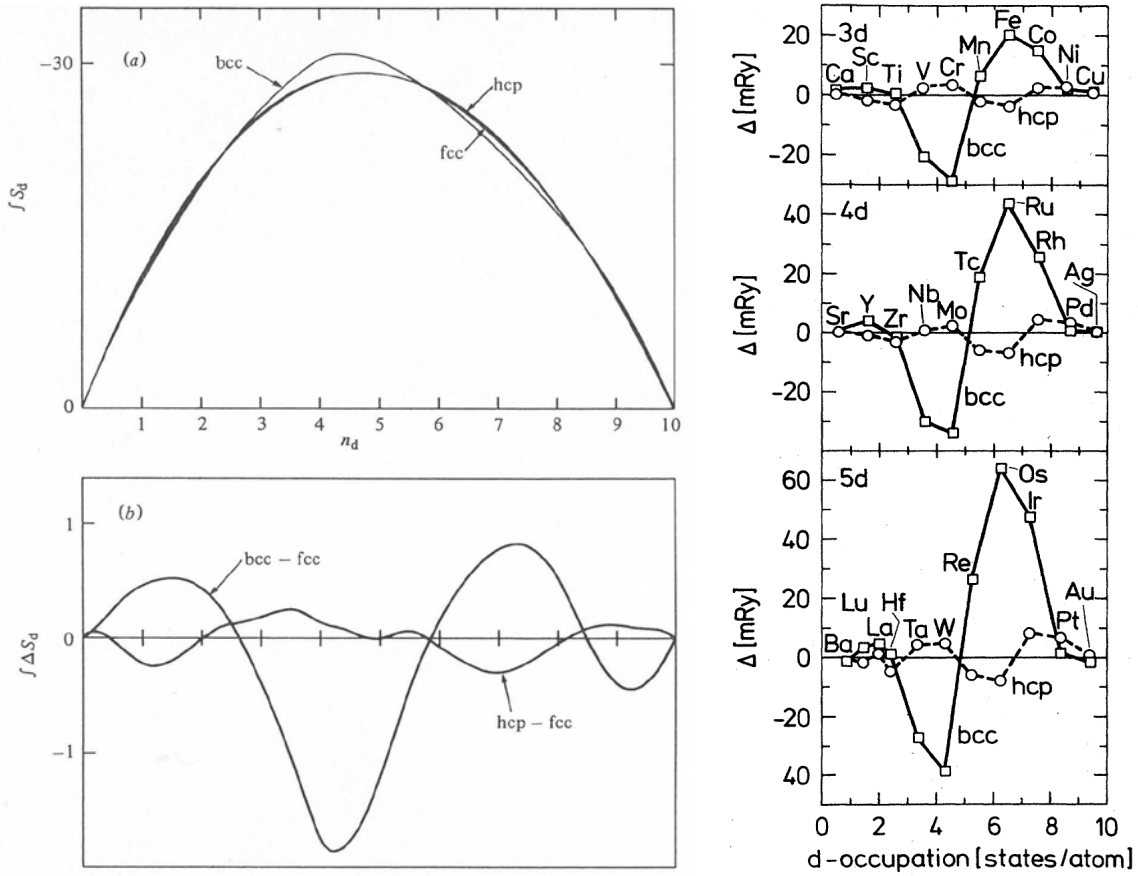


**Fig. 12:** Left: (a) First moment of the canonical  $d$ -band density of states in Fig. 5 as function of its occupancy,  $n_d$ . Note that negative values are upwards so that the curve resembles that of the cohesive energy. (b) The bcc-fcc and hcp-fcc structural differences, now with positive moments upwards. From Refs. [30, 10]. Right: Structural energy differences calculated by LDA-LMTO for the 4sp 3d, 5sp 4d and 6sp 5d series at the experimental equilibrium volumes and plotted as functions of the calculated number of  $d$ -electrons. From Ref. [38].

computational procedure accurate and more generally applicable. Now, if we assume that the difference between the closely-packed structures, at conserved atomic volume, is a 1st-order effect, we can use the force theorem with the same atomic-sphere potential in all structures, and if we use the ASA, the Madelung energy vanishes because the spheres are neutral. If we finally neglect the  $s$ - and  $p$ -bands and consider merely the bare, canonical  $d$ -bands, the structural energy difference in units of  $\Delta_d$  is simply the difference between the 1st canonical moments,

$$\int^{S(n_d)} S N_d(S) dS, \quad \text{with } n_d \equiv \int^{S(n_d)} N_d(S) dS,$$

shown to the left in Fig. 12 as a function of the number,  $n_d$ , of bare, unhybridized  $d$ -electrons per atom. The canonical densities of states,  $N_d(S)$ , were shown in Fig. 5 and  $S(n_d)$  is the canonical Fermi level. As mentioned before, the 1st moment of a bare canonical band always vanishes when the band is full. Had  $N_d(S)$  in Fig. 5 been rectangular, the first moment would have been a parabola resembling the behavior of the cohesive energy as a function of the  $d$ -band filling [40]. But now, the structural differences shown at the bottom of Fig. 12 clearly reproduce the observed

structural sequence. The characteristic two-peak structure in the bcc DOS, makes this structure stable for materials with the Fermi level in the gap between the peaks. By properly including the  $s$ - and  $p$ -bands and the hybridization with them, as well as the Madelung- and the so-called combined-correction to the ASA, i.e., by doing proper LDA-LMTO calculations, Skriver [38] obtained the results shown in the right-hand panel. Independent, exhaustive LAPW total-energy calculations [41] for merely bcc and fcc Cr, Mo, and W agree within 2 mRy with Skriver's results, thus confirming his approach. But also the ten-times-smaller energy differences between the hcp and fcc metals, having merely different stackings along (111) and, hence,  $N_d(S)$ -shapes, give structures in agreement with experiments. Skriver also considered La, Ce, and Lu, as well as Th and Pa. In fact, of the 39 non-magnetic cases studied, only for Na, Au, Yb, and Pa, the correct structure was less stable than the one calculated.

Using the same methodology as Skriver, McMahan and Moriarty studied the pressure-induced phase transitions between the closely-packed structures of Na, Mg, Al, and Si, and found these transitions to be driven by the hybridization of the occupied  $sp$ -bands with the bottom of the  $3d$ -band moving down with pressure. Earlier, and in a similar way, Duthie and Pettifor [42] had explained the Lanthanide structural sequence: hcp, Sm-type, double-hcp, fcc, observed for decreasing atomic number and increasing pressure as a result of the increasing population of the falling  $5d$ -band.

### 3.3 Band magnetism

The generalization of DFT to a spin-DFT [26, 43] was a first step in “helping” the density functional, through symmetry breaking, to treat exchange and correlation more accurately than in the LDA, which merely uses the xc-energy density,  $\epsilon_{xc}(\rho)$ , calculated for the homogeneous electron gas as a function of its density. In spin-DFT, the independent variable is the space-diagonal matrix element of the first-order density matrix,  $\rho(\mathbf{r}\sigma, \mathbf{r}\sigma')$ , and the self-consistency condition for the one-electron potential in the Schrödinger equation, which generates the density as:

$$\rho(\mathbf{r}\sigma, \mathbf{r}\sigma') \equiv \sum_k \theta(\epsilon_F - \epsilon_k) \psi_k^*(\mathbf{r}\sigma) \psi_k(\mathbf{r}\sigma'), \quad (13)$$

is given by

$$V(\mathbf{r}\sigma, \mathbf{r}\sigma') = V_{\text{ext}}(\mathbf{r}\sigma, \mathbf{r}\sigma') + V_C(\mathbf{r}) + V_{xc}(\mathbf{r}\sigma, \mathbf{r}\sigma'). \quad (14)$$

Here,  $V_{\text{ext}}$  is the Coulomb potential of the protons plus an external spin-dependent potential, such as:  $-\text{sgn}(\sigma)\mu_B\mathcal{H}$  with  $\text{sgn}(\uparrow) = \pm$ , from a uniform magnetic field,  $V_C$  is the classical Coulomb potential from all electrons, and  $V_{xc}(\mathbf{r}\sigma, \mathbf{r}\sigma')$  is the exchange-correlation potential. In case the potential (14) has translational symmetry, the state-label  $k$  is  $i\mathbf{k}$ . The density generated self-consistently from this potential minimizes the total-energy functional.

In its local approximation (LSD), spin-DFT uses  $\epsilon_{xc}(\rho_\uparrow, \rho_\downarrow)$  for a homogeneous electron gas subject to a homogeneous magnetic field which creates a density,  $\rho = \rho_\uparrow + \rho_\downarrow$ , and a spin density,  $m = \rho_\uparrow - \rho_\downarrow$ . The corresponding exchange-correlation potential is diagonal in spin and equals  $\partial(\rho \epsilon_{xc}(\rho_\uparrow, \rho_\downarrow))/\partial\rho_\sigma \equiv \mu_{xc\sigma}(\rho_\uparrow, \rho_\downarrow)$ . Expansion around the non spin-polarized values,  $\rho_\uparrow = \rho_\downarrow = \rho/2$ , i.e., in powers of  $m$  yields  $\epsilon_{xc}(\rho_\uparrow, \rho_\downarrow) = \epsilon_{xc}(\rho) + \epsilon_{xc}''(\rho) m^2/4 + \mathcal{O}(m^3)$ , and,

hence, for the exchange-correlation potential

$$\mu_{xc\uparrow\downarrow}(\rho, m) = \mu_{xc}(\rho) \pm m \rho \epsilon''_{xc}(\rho)/2 + \mathcal{O}(m^2). \quad (15)$$

Here,  $\mu_{xc}$  and  $\epsilon''_{xc}(\rho)$  are both *negative*, so that increasing  $m = \rho_{\uparrow} - \rho_{\downarrow}$  lowers the potential seen by a  $\uparrow$ -electron and rises it for a  $\downarrow$ -electron, i.e., exchange tends to align the spins. This leads to Hund's 1st rule for degenerate levels (an open shell) in atoms and since the Pauli principle prevents multiple occupation, level-separation works against spin-polarization.

### 3.3.1 Ferromagnetism

For a para- or ferromagnet (without SO coupling) in the presence of a uniform magnetic field, which provides the Zeeman splitting  $\pm\mu_B\mathcal{H}$ , the band-structure problem decouples into separate Schrödinger equations (14), one for each direction of spin. By filling the states to a common Fermi level (13) and solving selfconsistently, the zero-temperature spin-magnetizations,  $m = \langle m(\mathbf{r}) \rangle$ , the uniform susceptibilities,  $\mu_B dm/d\mathcal{H}$ , and magnetic contributions to the cohesive properties may be computed [30].

This was done in the mid-70ies using the ASA [29] and the results were interpreted in terms of Stoner theory with the exchange constant,  $I$ , obtained from the Stoner equation:  $C_{d\downarrow} - C_{d\uparrow} = mI + 2\mu_B\mathcal{H}$  using the computed magnetization and splitting of the centers of the  $d$ -bands. Gunnarsson [44] used the spin-splitting of the xc-potential to order  $m$  in Eq. (15) and treated it by 1st-order perturbation theory on top of the paramagnetic bands. Hence, the band-splitting is

$$\varepsilon_{j\downarrow}(\mathbf{k}) - \varepsilon_{j\uparrow}(\mathbf{k}) = \langle \psi_{j\mathbf{k}}(\mathbf{r}) | -\rho(\mathbf{r}) \epsilon''_{xc}[\rho(\mathbf{r})] m(\mathbf{r}) | \psi_{j\mathbf{k}}(\mathbf{r}) \rangle + 2\mu_B\mathcal{H} \approx mI + 2\mu_B\mathcal{H}. \quad (16)$$

In the last approximation, the  $j\mathbf{k}$ -dependence of  $I$  was neglected. Janak [28] evaluated  $I$  from essentially the same expression with the expectation value taken as the average over the paramagnetic Fermi surface. This is appropriate when subsequently filling the exchange-split bands (16) to a common Fermi level in order to get, first, the magnetization and, then, the splitting,  $m/N(\varepsilon_F)$ , by dividing  $m$  by the paramagnetic DOS per spin. Equating this splitting with the approximation (16), yields Stoner's expression for the exchange-enhanced spin-susceptibility

$$\chi \equiv \mu_B m / \mathcal{H} = 2\mu_B^2 N(\varepsilon_F) \left(1 - IN(\varepsilon_F)\right)^{-1}. \quad (17)$$

The values of  $I$  obtained for Fe, Ni, Rh, Ir, Pd, and Pt from LSD ASA calculations of  $C_{d\downarrow} - C_{d\uparrow}$  [29,30] and from approximation (16) agree within a few percent. The trends apparent in Fig. 10 were explained by Gunnarsson [44] for the late transition metals plus V, and by Janak [28] for the entire  $3d$  and  $4d$  series, although in considerably less detail. The dominating trend that  $I$  decreases with increasing  $Z$  and, hence, with increasing  $\rho$ , is due to  $\epsilon_{xc}$  being dominated by  $\epsilon_x \propto \rho^{1/3}$ , so that the kernel behaves like  $-\rho \epsilon''_x \propto \rho^{-2/3} = (4\pi/3)^{2/3} r_s^2$ , which decreases with  $\rho$ . For understanding that in a given series,  $I$  rises again until it drops sharply at the noble metals, we use the ASA, i.e., take  $-\rho(\mathbf{r}) \epsilon''_{xc}[\rho(\mathbf{r})]$  and  $m(\mathbf{r})$  to be spherically symmetric, and

expand  $\psi_{j\mathbf{k}}(\mathbf{r})$  on the FS in partial waves. Since only partial waves with the same  $l$  contribute to  $I$  as defined in (16), we get

$$I \sim s \int_0^1 (r_s(r)/r)^2 \left( \alpha (r\varphi_{sp}(\varepsilon_F, r))^2 + (1 - \alpha) (r\varphi_d(\varepsilon_F, r))^2 \right)^2 d(r/s), \quad (18)$$

leaving out constants and using  $\epsilon_x$  instead of  $\epsilon_{xc}$ .

The form (18) with  $\alpha = 0$  is the one discussed by Gunnarsson for the transition metals [44]. He showed that the factor  $(r_s(r)/r)^2$ , apart from its general decrease with  $Z$ , for  $Z$  given and  $r$  increasing, increases outside the last core  $np$ -shell, i.e., for  $r \gtrsim 0.3s$ , and peaks for  $r \sim 0.8s$ . This peaking is the combined result of the general increase of  $r_s(r)$  with  $r$  and the filling of the  $nd$ -shell, whose charge-density peaks for  $r \lesssim 0.5s$ . One factor  $(r\varphi_d(\varepsilon_F, r))^2$  in (18) comes from  $|\psi_{j\mathbf{k}}(\mathbf{r})|^2$  and the other from  $m(\mathbf{r})/m$ . The product,  $(r\varphi_d(\varepsilon_F, r))^4$ , is very strongly peaked at a value  $r \lesssim 0.5s$ , which moves towards the edge of the  $np$ -shell as the Fermi level moves towards the top,  $A_d$ , of the  $d$ -band (Fig. 7) where  $(r\varphi_d(A_d, r))^4$  vanishes smoothly for  $r$  approaching  $s$ . This behavior of the integrand  $(r_s(r)/r)^2 (r\varphi_d(\varepsilon_F, r))^4$  explains the increase of  $I$  through the second half of a transition series (Fig. 10).

Prior to the filling of a  $d$ -shell, i.e., for the alkali-, alkaline-earth, and rare-earth metals,  $(r_s(r)/r)^2$  merely increases monotonically with  $r$ , once it is outside the core, and its value at the WS sphere is approximately given by  $nr_s^3(s) = 1$ , where  $n = 1, 2, 3$  is the number of valence electrons (Fig. 19 in Ref. [12]). The contribution to  $I$  of the  $sp$ -electrons is taken care of in Eq. (18) by  $\alpha \equiv N_{sp}(\varepsilon_F) (N_{sp}(\varepsilon_F) + N_d(\varepsilon_F))^{-1}$ , the relative  $sp$ -character on the Fermi surface. For  $n_{sp} = n = 1$  and 2, the factor  $(r\varphi_{sp}(\varepsilon_F, r))^4$ , is the only one relevant, and it is fairly constant in the outer part of the WS sphere. The decrease of  $I$  for  $n$  increasing from 1 to 2, thus follows the factor-  $2^{-2/3}$  decrease of  $r_s^2(s)$ . How, upon entering a transition series, this decreasing trend is taken over by the increasing trend at the end of the series, is described by Eq. (18) with  $\alpha$  decreasing from 1 to 0 and  $r_s(r)$  developing the above-mentioned  $d$ -peak. Finally, the relatively low  $I$ -values for the noble metals is due to the  $sp$ -character on the FS jumping from about 10 to 50% for Cu and Ag, and to 70% for Au.

If we use the approximate Stoner equation (16) for a ferromagnet, the condition for spin self-consistency is that the integral over the paramagnetic DOS (per spin) over the energy range  $mI + 2\mu_B \mathcal{H}$  equals the magnetization  $m$ . Since the number of electrons,  $n_\uparrow + n_\downarrow$ , must be kept constant,  $m/2$  spins must be moved from above the paramagnetic Fermi level,  $\varepsilon_F$ , to below. This is illustrated in the left-hand panel of Fig. 13 using the unhybridized, canonical bcc  $d$ -DOS shown in Fig. 5, which is a good approximation for the  $d$ -projected DOS,  $N_d(\varepsilon)$ , in paramagnetic bcc Fe (see Fig. 7 in Ref. [8]). Insight to the workings of this self-consistency condition is provided by the construction from  $N_d(\varepsilon)$  of a function,  $\bar{N}(n, m)$ , which is the DOS per spin, averaged around the Fermi level corresponding to an occupancy of  $n/2$  spins, over a range corresponding to  $m$  spins. I.e.: for an assumed  $m$ , we move the Fermi level up and down in the rigid DOS until the integral is respectively increased and decreased by  $m/2$ . With  $\Delta$  being the splitting between these two Fermi levels,  $\bar{N}(n, m) \equiv m/\Delta$ . This band-structure function is shown as a function of  $m$  at the bottom. Since, for paramagnetic Fe where  $n_d=6.5$ ,  $\varepsilon_F$  is a

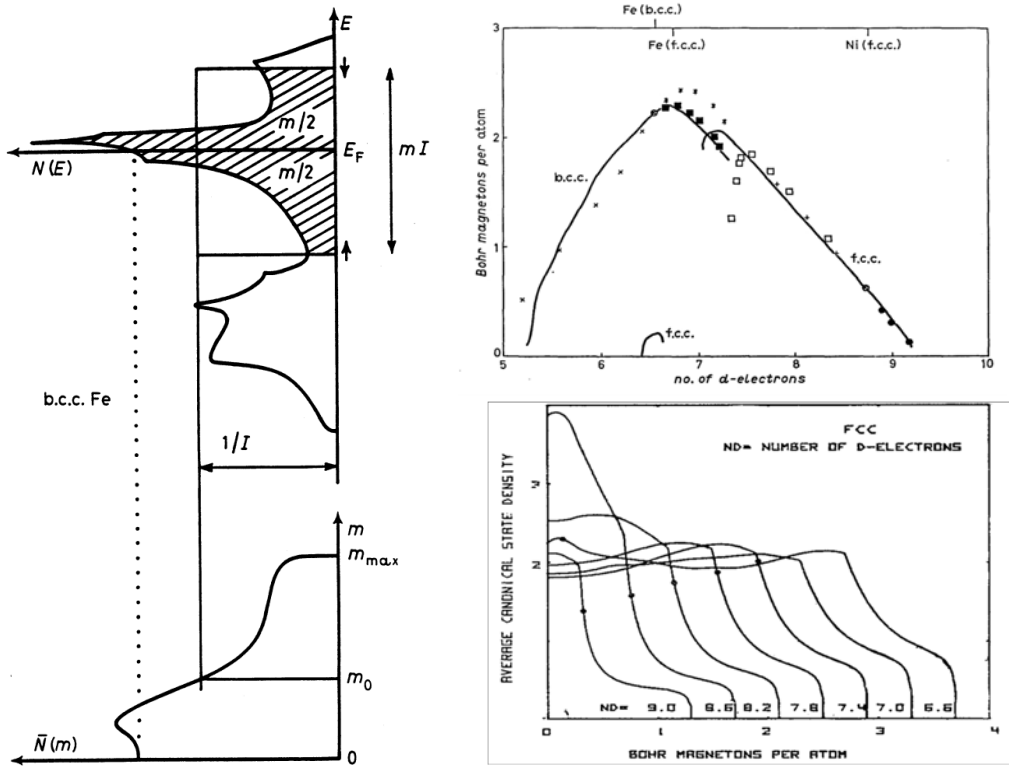


**Fig. 13:** Left: Stoner construction for ferromagnetism using the canonical, bcc d-DOS in Fig. 5 for Fe. Dotted/full line:  $I = 0/65$  mRy (from Ref. [12]). Right bottom: Canonical fcc  $\bar{N}(n_d, m)$  for varying  $n_d$  as functions of  $m$ . The dots are at the crossing with  $1/I$  at normal pressure. The reason why  $m_{\max}$  is not exactly  $10 - n_d$  is that the d-projected DOS for fcc Pd, rather than the fcc canonical d-band in Fig. 5 was used [30]. Right top: Slater-Pauling curve showing the magnetization,  $m$ , as a function of d-band occupation,  $n_d$ . The full curves were calculated with the procedure shown to the left and below using the experimental structures (hcp taken as fcc) and with  $I$  and  $n_d$  interpolated between the values calculated for Fe, Co, and Ni. Experimental values were obtained for the pure metals and intermetallic alloys ( $\bullet$  NiCu,  $+$  CoNi,  $\cdot$  FeCo,  $\square$  NiFe fcc,  $\blacksquare$  NiFe (bcc),  $\times$  FeCr). From Ref. [30].

bit below the big bcc DOS peak,  $\bar{N}_d(6.5, m)$  starts to increase from  $N(\varepsilon_F)$  for  $m$  increasing, but as soon as  $\varepsilon_{F\downarrow}$  has passed above the top of the peak,  $\bar{N}(n, m)$  drops and eventually hits the plateau caused by the  $t_{2g}$  states at the top of the  $d$ -band (see Fig. 5).  $\bar{N}$  finally vanishes when all  $m_{\max} \sim 3.5$  holes at the top of the  $d$ -band are filled. Knowledge about the interaction,  $I$ , and with  $\mathcal{H}=0$ , allows us to find the selfconsistent value of  $m$  as the solution of:  $\bar{N}(n, m) = I^{-1}$ . We see that  $I \sim 67$  mRy does not suffice to split  $\varepsilon_{F\downarrow}$  beyond the edge of the  $t_{2g}$  plateau and  $\varepsilon_{F\uparrow}$  below the bottom of the pseudogap. So Fe is not, like fcc Ni and hcp Co, a strong ferromagnet, but has a moment of  $m=2.2 \mu_B/\text{atom}$  with 54%  $e_g$  character [8], as may be imagined from Fig. 5 and which is in good agreement with the experimental 53%. Similarly, for fcc Ni the Stoner condition with  $I=73$  mRy and  $n_d=8.7$  yields a moment of  $0.68 \mu_B/\text{atom}$  with only 24%  $e_g$ -character, also in agreement with the experimental 19% [45]. The canonical fcc  $\bar{N}(8.5, m)$  shown in Fig. 13 at the bottom to the right (turned by  $90^\circ$  with respect to the bcc  $\bar{N}(6.5, m)$  to

the left) is approximately the one appropriate for Ni, and the dot marks the crossing with  $I^{-1}$ . In the right-hand, upper part of Fig. 13, we show in full line the ferromagnetic moments,  $m$ , as functions of  $n_d$ , calculated as shown on the left-hand side using the experimental structures (hcp taken as fcc) and with  $I$  and  $n_d$  interpolated between the values calculated for Fe, Co, and Ni. This so-called Slater-Pauling curve is compared with experimental values (dots) for the pure metals and intermetallic alloys. So-called strong ferromagnets are those with  $\varepsilon_{F\downarrow}$  split above the top of the  $d$ -band and thus have  $m = 10 - n_d$ . The late fcc and hcp metals have high  $I$ -values (Fig. 10), and the high peak in the  $d$ -DOS at  $n_d=8.5$  (Fig. 5) keeps the average DOS,  $\bar{N}(n_d, m)$ , above  $I^{-1}$  for all  $m \lesssim 10 - n_d$  and for  $n_d$  decreasing from 10 to about 7.2. (Fig. 13 bottom right). At that point,  $I^{-1}$  gets above  $\bar{N}(n_d, m)$  for all  $m$ . This drop of  $m$  happens also for the real alloys, but at a slightly larger  $n_d$ . For  $n_d$  decreasing below 7.3, the structure changes from fcc (hcp) to bcc and the Fermi level enters the large peak in the bcc DOS and thereby makes  $\bar{N}(n_d, m)$  reach above  $I^{-1}$ . By  $n_d=6.5$ , we have the situation of bcc Fe illustrated to the left in the figure. For  $n_d$  decreasing further,  $I^{-1}$  increases and  $\varepsilon_F$  moves down-hill on the low-energy side of the large peak, whereby  $\bar{N}(n_d, m)$  flattens out, and by  $n_d \sim 5.2$ , it is entirely below  $I^{-1}$ .

With pressure, mainly the band-width parameter  $\Delta_d$  in the Hamiltonian (8) changes; increasing approximately like  $s^{-5}$  (note the difference between  $\Delta_d$  and the exchange splitting  $\Delta$ ). This means that if  $\bar{N}(n, m)$  refers to the canonical  $S$ - or  $S^\gamma$ -scale, the self-consistency condition becomes:  $\bar{N}(n, m) = \Delta_d(s)/I$ , whereby the  $\bar{N}$  vs.  $m$  curves at the bottom of Fig. 13 become pressure vs.  $m$  curves (see Fig. 5 in Ref. [30]). Under pressure, bcc Fe thus loses its moment gradually. Had we constructed  $\bar{N}(6.5, m)$  using the hcp and fcc DOS curves shown in Fig. 5,  $\bar{N}$  would with  $m$  increasing from 0, start off from a somewhat lower value than for bcc Fe, but then stay constant, because the canonical DOS for the hcp and fcc structures are fairly flat around  $n_d=6.5$ , until dropping to zero near 3.5. For fcc and  $n_d=6.6$ , this is shown in the bottom right-hand part of Fig. 13. This means that, since for hcp and fcc Fe  $\bar{N}(n, 0)$  is slightly larger than  $\Delta_d/I$  at normal pressure, this changes as  $\Delta_d$  is increased by a slight lattice compression, and the moment vanishes abruptly (hcp) or within a small pressure range (fcc) (Figs. 4-6 in Ref. [30]).

Had it not been for its ferromagnetism, Fe would not have been bcc, but hcp like Ru and Os with  $n_d \sim 6.5$ . This is clearly seen in Fig. 12 on the right-hand side and at the bottom to the left. The top-left “bond-energy” curve can be used for each direction of spin in bcc Fe to realize that its bond energy, the value at  $n_d = 6.5$  of the chord connecting the values at  $6.5 \mp m$ , is *lower* (the sum of one-electron kinetic energies is higher) than those of hcp and fcc paramagnetic Fe. The energy gain comes from the exchange energy,  $-m^2 I/4$ . Compression reduces  $m$  as explained above, and the point where gain of exchange energy equals the cost in kinetic energy gives the critical value of the moment for which the structural phase transition occurs. The observed phase transition from bcc ferromagnetic to hcp non-magnetic Fe, occurs at a pressure of 100 kbar when  $m$  and  $s$  have both been reduced by a few per cent. (Actually, the stability of ferromagnetic bcc Fe over non-magnetic hcp Fe is marginal and depends on the DFT used [46]).

The loss of kinetic energy associated with magnetism may in Stoner theory be described as contribution to the pressure given by:

$$3\mathcal{P}_{d\text{magn}}\mathcal{V} = -\frac{\delta \ln \Delta_d}{\delta \ln s} \int_0^m \frac{m' dm'}{2\bar{N}(n, m)} - \frac{1}{\mu_d} (m^2 I + 2\mu_B \mathcal{H}). \quad (19)$$

Here,  $-\delta \ln \Delta_d / \delta \ln s \sim 5$  and  $\mu_d^{-1} = s^2 \Delta_d$  was shown in Fig. 9. From Fig. 8, we realize that the magnetic metals do have relatively large WS radii (open dots), but that LSD calculations (open triangles) for Fe, Co, and Ni only account for a fraction of these anomalies.

Turning now to fcc Ni under pressure, we need the canonical fcc  $\bar{N}(8.7, m)$ -curve, but shall use  $\bar{N}(8.5, m)$  which is shown at the bottom right-hand side of Fig. 13 as a proxy. We see that the dot marking its crossing with  $\Delta_d/I$  at zero pressure, can be raised by the large factor  $\sim 2.4$ , before reaching the peak at  $m \sim 0$ , which is the one in the canonical DOS caused by the saddle-points  $P_1$  and  $P_2$  in the 5th band (Fig. 5). 2.4 is the factor by which the  $d$ -bandwidth ( $\propto \Delta_d$ ) can be increased before an fcc ferromagnet (FM) with 8.5  $d$ -electrons loses its moment. Since Ni under pressure keeps its fcc structure, it also keeps its moment up to several Mbars because  $d \ln \Delta_d / d \ln s \sim -5$ ,  $\mathcal{B} \sim 2$  Mbar, and  $\partial \mathcal{B} / \partial \mathcal{P} \sim 4$  [29].

If we now increase the saturation moment from the  $0.6 \mu_B$  of Ni ( $0.8 \mu_B$  for the proxy) by decreasing the number of  $d$ -electrons, i.e. moving up the Slater-Pauling curve in Fig. 13 and the Fermi level moving down the low-energy side of the canonical fcc DOS peak and into the u-shaped valley in Fig. 5, the fcc  $\bar{N}(n_d, m)$ -curves lose their peak and become flat once the valley is entered. This happens when  $n_d \sim 8$ . From the values of  $\bar{N}(n_d, 0)$ , we see that the bottom of the valley is reached when  $n_d \sim 7.4$ , and that by  $\sim 6.6$  the Fermi level has moved up so high on the low-energy side of the valley that the DOS exceeds  $\Delta_d/I$  and a FM with a low moment becomes stable. The large-moment FMs exist as long as the high DOS peak at  $n_d = 8.6$  continues to raise the average  $\bar{N}(n_d, m)$  above  $\Delta_d/I$ , which happens until  $n_d$  falls below 7.3. The  $8 \gtrsim n_d \gtrsim 6.5$  region is that of the Invar alloys which keep their atomic volume constant over a useful range of temperatures. In the early 60ies, this was explained as the effect of competing large-moment large-volume and low-moment low-volume states [47]. With pressure, the  $\Delta_d/I$ -dots move up their respective fcc  $\bar{N}(n_d, m)$ -curves in Fig. 13. We see that the initial slope,  $-dm/d\mathcal{P}$ , stays constant until  $n_d = 7.4$ , but that the pressure where the moment disappears in a 1st-order transition, corresponding to the  $\Delta_d/I$ -line touching the maximum of  $\bar{N}(n_d, m)$ , falls rapidly as we move away from Ni.

On exhibit at the entrance to the mineralogical museum in Copenhagen is a 20 tons iron-nickel meteorite found at Cape York in Greenland. It consists of a bcc and an fcc phase with a common orientation throughout the entire meteorite, which therefore seems to have been a single crystal in the mother asteroid. The fcc phase (taenite) has been found to be a simple, ordered FeNi alloy consisting of alternating (100) layers of Fe and Ni, which disorders by heating to 750 K for 50 hours [48]. This demonstrates that the meteorite has not –since its formation in the parent planet– been reheated to a temperature above 730 K for longer than 50 hours.

Attempting to get “insight” to the properties of the Earth’s inner core, we [49] performed a proper LSD calculation for taenite resulting in Fig 14. In the ferromagnetic DOS, we see the  $\uparrow$

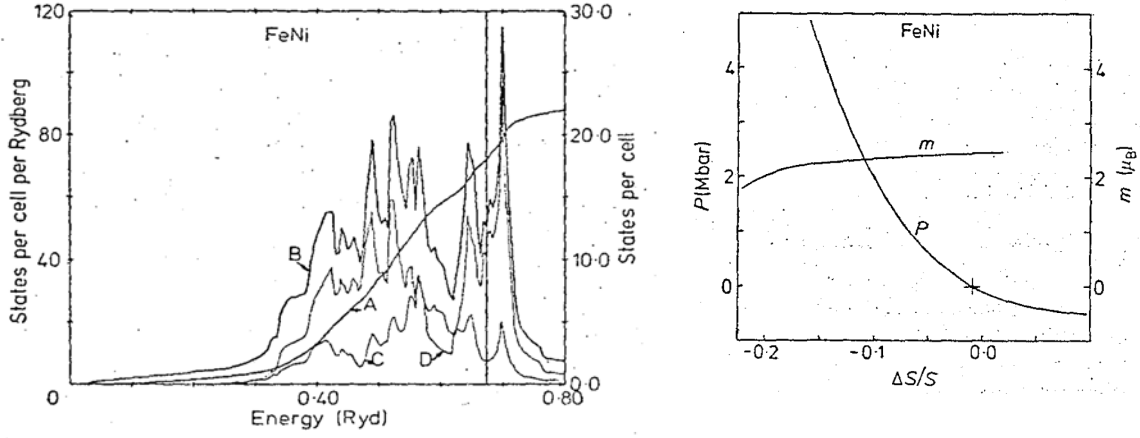


**Fig. 14:** Results of LSD LMTO calculation for fcc FeNi (taenite). Left: Number(A)- and density(B) of states per FeNi. Fe(C)- and Ni(D)-projected DOS. Right: FM magnetization and Pressure as functions of the relative deviation of the WS radius from its experimental value at 1 kbar. From Ref. [49].

and  $\downarrow$  fcc peaks, split on either side of  $\varepsilon_F$ , and we also see that the Fe(C)- and Ni(D)-projected DOS share these peaks, but with the dominant weight on Fe, because  $C_d$  lies higher- and  $\Delta_d$  is broader in Fe than in Ni. Most remarkable: The FM magnetization stays robustly above  $2 \mu_B$  for pressures up to 5 Mbar (causing a 15% compression of  $s$ ). Using, instead, the rigid-band picture and  $\bar{N}(7.7, m)$  in Fig. 13,  $m$  would drop significantly already at a 20% reduction of  $\Delta_d/I$ , i.e. at a mere 4% reduction of  $s$ . So apparently, taenite is special. We were fascinated by the thought that the earth's core could be a ferromagnet, but 40 years ago we did not know how to treat fluctuations at high temperatures.

For more recent LSD calculations of the spin and *orbital* moments in Fe, Co, and Ni, see Ref. [50].

### 3.3.2 Spin spirals

One may go beyond collinear spin-polarization by allowing the direction of spin-quantization to depend on  $\mathbf{r}$ , or simpler and more relevant for magnetic order, on the site,  $\mathbf{t}$ . Let us consider the case where all spin-quantization axes lie in the same plane, i.e., not on a cone. Provided that spin-orbit coupling (causing magnetic anisotropy) is neglected, it does not matter which plane we take. We choose the  $xy$ -plane and let  $\phi(\mathbf{t})$  give the direction of spin on site  $\mathbf{t}$ . With the matrix for hopping from site  $\mathbf{t}$  and spin  $\sigma$  to site  $\mathbf{t}'$  and spin  $\sigma'$  being  $h_{\mathbf{t}\mathbf{t}'}\delta_{\sigma\sigma'}$  in the *global* spin frame, it becomes:

$$\tilde{h}_{\mathbf{t}\sigma, \mathbf{t}'\sigma'} = \left\{ \begin{array}{cc} \uparrow & \cos \frac{\phi(\mathbf{t}') - \phi(\mathbf{t})}{2} & i \sin \frac{\phi(\mathbf{t}') - \phi(\mathbf{t})}{2} \\ \downarrow & i \sin \frac{\phi(\mathbf{t}') - \phi(\mathbf{t})}{2} & \cos \frac{\phi(\mathbf{t}') - \phi(\mathbf{t})}{2} \end{array} \right\} h_{\mathbf{t}\mathbf{t}'}$$

in the *local* frame. Here,  $h_{\mathbf{t}\mathbf{t}'}$  could be the ASA Hamiltonian (6),  $H_{\mathbf{t}'\mathbf{t}m', \mathbf{t}lm}^\gamma$ , before Fourier-summing it to  $\mathbf{k}$ -space. Including the exchange splitting,  $\Delta(\mathbf{t})$ , the total one-electron Hamilto-



nian in the *local* frame is therefore

$$\tilde{H}_{\mathbf{t}\sigma,\mathbf{t}'\sigma'} = \begin{array}{cc} & \begin{array}{c} \uparrow \\ \downarrow \end{array} \\ \begin{array}{c} \uparrow \\ \downarrow \end{array} & \begin{array}{cc} -\frac{\Delta(\mathbf{t})}{2}\delta_{\mathbf{t},\mathbf{t}'} + \cos\frac{\phi(\mathbf{t}')-\phi(\mathbf{t})}{2}h_{\mathbf{t}\mathbf{t}'} & i\sin\frac{\phi(\mathbf{t}')-\phi(\mathbf{t})}{2}h_{\mathbf{t}\mathbf{t}'} \\ i\sin\frac{\phi(\mathbf{t}')-\phi(\mathbf{t})}{2}h_{\mathbf{t}\mathbf{t}'} & \frac{\Delta(\mathbf{t})}{2}\delta_{\mathbf{t},\mathbf{t}'} + \cos\frac{\phi(\mathbf{t}')-\phi(\mathbf{t})}{2}h_{\mathbf{t}\mathbf{t}'} \end{array} \end{array},$$

$h_{00}$  is the on-site orbital Hamiltonian.  $\Delta(\mathbf{t})$  is an orbital matrix, which is approximately diagonal, with  $\Delta$  in the  $d$ -block, possibly with different  $e_g$  and  $t_{2g}$  elements, and zero in the  $sp$ -blocks. With  $\Delta$  positive,  $\uparrow$  will be the majority spin.

If the sites,  $\mathbf{t}$ , now form a lattice and all atoms are equivalent, i.e. we have 1 atom per translational cell, then  $h_{\mathbf{t}\mathbf{t}'} = h(\mathbf{t}' - \mathbf{t})$ . If also  $\Delta(\mathbf{t})$  and  $\phi(\mathbf{t}') - \phi(\mathbf{t})$  are translationally invariant, i.e. equal to respectively  $\Delta$  and  $\phi(\mathbf{t}' - \mathbf{t})$ , then the Hamiltonian,  $\tilde{H}_{\mathbf{t}\sigma,\mathbf{t}'\sigma'} = \tilde{H}(\mathbf{t}' - \mathbf{t})_{\sigma,\sigma'}$ , is translationally invariant and therefore diagonal in the Bloch representation

$$\tilde{H}(\mathbf{k})_{\sigma,\sigma'} = \begin{array}{cc} & \begin{array}{c} \uparrow \\ \downarrow \end{array} \\ \begin{array}{c} \uparrow \\ \downarrow \end{array} & \begin{array}{cc} -\frac{\Delta}{2} + \sum_{\mathbf{t}} e^{i\mathbf{k}\cdot\mathbf{t}} \cos\frac{\phi(\mathbf{t})}{2}h(\mathbf{t}) & i\sum_{\mathbf{t}} e^{i\mathbf{k}\cdot\mathbf{t}} \sin\frac{\phi(\mathbf{t})}{2}h(\mathbf{t}) \\ i\sum_{\mathbf{t}} e^{i\mathbf{k}\cdot\mathbf{t}} \sin\frac{\phi(\mathbf{t})}{2}h(\mathbf{t}) & \frac{\Delta}{2} + \sum_{\mathbf{t}} e^{i\mathbf{k}\cdot\mathbf{t}} \cos\frac{\phi(\mathbf{t})}{2}h(\mathbf{t}) \end{array} \end{array}.$$

The hopping matrix,  $h(\mathbf{t})$  becomes  $h(\mathbf{k})$ , e.g.  $H_{l'm',lm}^\gamma(\mathbf{k})$ , in the Bloch representation. For a *spin spiral* of wave-vector  $\mathbf{q}$ ,

$$\phi(\mathbf{t}) \equiv \mathbf{q} \cdot \mathbf{t}, \quad (20)$$

we therefore get

$$2\tilde{H}(\mathbf{q},\mathbf{k})_{\sigma,\sigma'} = \begin{array}{cc} & \begin{array}{c} \uparrow \\ \downarrow \end{array} \\ \begin{array}{c} \uparrow \\ \downarrow \end{array} & \begin{array}{cc} -\Delta + h(\mathbf{k} + \mathbf{q}) + h(\mathbf{k}) & h(\mathbf{k} + \mathbf{q}) - h(\mathbf{k}) \\ h(\mathbf{k} + \mathbf{q}) - h(\mathbf{k}) & \Delta + h(\mathbf{k} + \mathbf{q}) + h(\mathbf{k}) \end{array} \end{array}$$

where we have redefined  $\mathbf{k}$  to have its origin at  $-\mathbf{q}/2$ . This representation in which the local exchange splitting,  $\Delta$ , appears in the diagonal and the hopping difference in the off-diagonal, is the natural one when  $\Delta$  is large and  $\mathbf{q}$  is small. However, a unitary transformation brings the Hamiltonian into the simplest form

$$\tilde{H}(\mathbf{q},\mathbf{k}) = \begin{array}{ccc} & (\uparrow - \downarrow)/\sqrt{2} & (\uparrow + \downarrow)/\sqrt{2} \\ (\uparrow - \downarrow)/\sqrt{2} & h(\mathbf{k}) & \frac{\Delta}{2} \\ (\uparrow + \downarrow)/\sqrt{2} & \frac{\Delta}{2} & h(\mathbf{k} + \mathbf{q}) \end{array}, \quad (21)$$

where the paramagnetic bands are in the diagonal and  $\Delta$  is in the off diagonal. For small  $\Delta$ , this form is the natural one.

We recapitulate: All spins have been chosen to lie in the same plane, which in the absence of spin-orbit coupling is arbitrary. In all planes perpendicular to  $\mathbf{q}$ , all spins are identical, but as we progress by  $\mathbf{t}$  in the plane, they turn by the angle  $\mathbf{t} \cdot \mathbf{q}$ . For  $\mathbf{q}=0$ , we get back to the FM Hamiltonian (but doubly degenerate). If in the  $xy$ -plane the lattice is square with lattice

constant 1,  $\mathbf{q}=(\pi, 0)$  gives an antiferromagnet (AF) with stripe-order and  $\mathbf{q}=(\pi, \pi)$  an AF with checkerboard-order.

Incommensurability is *no* complication as long as SO coupling is neglected. We simply must have the same Abelian group in configuration and spin space. In configuration space, the generators of this group are the primitive lattice translations. In spin space, they are the primitive lattice translations, times turning the axes of spin quantization by a fixed angle: Subject yourself (being either a charge or a spin) to such an operation, look around, and you cannot see that you moved. It is of course essential that only the direction, and not magnitude of the magnetization changes. The band structure in the presence of the spin spiral has lost the crystalline point-group symmetry, but the number of states remains 1 per primitive cell and BZ, i.e.: the problem can be solved for any  $\mathbf{q}$  without increasing the size of the primitive cell. This is all not obvious and I believe that Sadratskii was the first who realized it [51].

The reduction to the Stoner model has the conceptual advantage of cutting the self-consistency loop into a band-structure part, which for a given spin order,  $\mathbf{q}$ , site, and orbital-dependent exchange-splitting field,  $\Delta$ , yields the site and orbital-dependent spin-moments,  $m(\mathbf{q})$ , plus a self-consistency condition which states that  $m(\mathbf{q})/\Delta = I^{-1}$ . The band-structure part gives insight into the complicated static response,  $\chi(\mathbf{q}) \equiv m(\mathbf{q})/\Delta$ , of the non-interacting system, and not only in the linear regime [52].

### 3.3.3 Local exchange couplings

The *spatial* dependence of the magnetic coupling in metals, i.e. the change in total energy upon turning the direction of one spin with respect that of a neighbor is needed to calculate for instance Curie temperatures and magnon spectra. By considering infinitesimal spin rotations rather than spin flips, Lichtenstein and Katsnelson could use the force theorem locally and derived an elegant expression for the second derivative of the total energy in terms of the one-electron Green function,  $[(\varepsilon - i0) \delta_{RR'} \delta_{ll'} \delta_{mm'} - H_{Rlm, R'l'm'}^\gamma]^{-1}$ . Their expression has become a standard tool for complex magnetic systems and made it possible to simulate magnetic properties of real materials via *ab initio* spin models [53–55].

## 3.4 Fermi surfaces and mass renormalizations

For the elemental metals in the 4*d*- and 5*d*-series the Fermi surfaces (FSs) calculated using LDA (or Mattheiss-Slater) agree with de-Haas-van-Alphen (dHvA) measurements of the extremal areas of the cyclotron orbits on the FS to an accuracy better than what corresponds to a 15 mRy-shift in the position of the *d*- with respect to the non-*d* bands [10]. For the fcc late 5*d*- and 4*d*-metals [15], the agreement is even beyond 5 mRy – and best for Pt and Pd where over 80% of the DOS at the Fermi level,  $N(\varepsilon_F)$ , is contributed by the large, 5th-band *d*-hole sheet shown in Fig. 5, the same, which in combination with the larger Stoner *I* (Fig. 10) and the smaller 3*d*-bandwidth is responsible for the FM in fcc Ni.

Pd is nearly ferromagnetic and its uniform, static spin-susceptibility (17) is enhanced by a Stoner factor  $\sim 10$ , over the Pauli value, which is proportional to  $N(\varepsilon_F)$  like the electronic-

specific heat coefficient. In the late 60ies it had been suggested [56] that such ferromagnetically correlated, paramagnetic (PM) spin fluctuations would be detrimental for the singlet Cooper pairs formed via the electron-phonon interaction and, hence, could be the reason why Pd does not become a superconductor at low temperature like e.g. its neighbor Ir. Moreover, the interaction of the conduction electrons with these spin fluctuations would lead to an enhancement of the electronic mass and specific-heat coefficient, initially estimated –using a spherical FS– to be a factor 4. Comparison of the measured specific-heat coefficients with  $N(\varepsilon_F)$  for the above-mentioned calculated band structures gave mass enhancements of 1.37 for Ir, 1.44 for Rh, 1.63 for Pt, and 1.66 for Pd [15]. Experimental results for the cyclotron masses (energy-derivatives of the extremal areas on the FS) did not exist for Ir, and dHvA for Rh only gave masses for the smaller orbits. They exceed the calculated band masses by factors around 1.1, except for the largest orbit where the mass enhancement was 1.3. So, presumably, the mass-enhancement for the large, 5th-band sheet, which for Rh and Ir is  $\Gamma$ -centered and closed, is the 1.44 obtained from the specific heat. Also for Pd, no masses could be detected from orbits around the 5th-band sheet, but only from a smaller  $d$ -like sheet and the large  $sp$ -like sheet. In all those cases, the masses exceeded those calculated by factors 1.5-1.7, which is consistent with the factor 1.66 obtained from the specific heat. For Pt, masses from several orbits on all three sheets could be measured and were found to be enhanced by factors of 1.44, 1.45, and 1.54 for the orbits on the  $sp$ -sheet, and by 1.30, 1.68, and 1.72 for those on the large  $d$ -hole sheet; thus consistent with the specific heat enhancement. In the 80ies, this was supported by more detailed experiments and analyses [57]. In conclusion, a mass enhancement of  $\sim 1.4$  was attributed to the electron-phonon interaction ( $\lambda_{ep} \sim 0.4$ ) [58]. This agreed with McMillans estimate for the superconductor Ir and with rigid-MT calculations of  $\lambda_{ep}$  in the early 80ies, and with S.Y. and D.Y. Savrasov's DFT linear-response calculations [59] in the mid 90ies. The remaining mass-enhancement in Pd was attributed to the PM spin fluctuations ( $\lambda_{e-sf} \sim 0.25$ ). The results of the first spin-fluctuation calculation using LDA bands to calculate e.g.  $\chi(\mathbf{q}, \mathbf{q}', \omega)$  [60] and of Savrasov's linear-response calculations from the late 90ies [61] agreed with this small value.

For the exchange-split FS of ferromagnetic bcc Fe, dHvA experiments [62] found surprisingly good agreement with the FS calculated with LSD [63], e.g., the sum of- and difference between- the numbers,  $n_{\uparrow}=5.08$  and  $n_{\downarrow}=2.93$ , extracted from the extremal areas agree closely with the number of electrons, 8, and Bohr magnetons, 2.12. The mass-enhancements, found to range between 1.5 and 3.0, were larger than for, e.g., Pd.

## 4 Post 1986

The discoveries beginning in 1986 of high-temperature superconducting materials (HTSCs) which without doping are AF insulators –as is the case for cuprates– or AF metals –in case of iron pnictides and chalcogenides– caused enormous interest in the role of AF-correlated spin fluctuations as mediators of the superconductivity [64–67].

In the ruthenates, depending on the distortion of the  $\text{RuO}_6$ -octahedra building these corner-sharing perovskites [68, 69], not only AF- but also FM spin fluctuations exist. This was shown

by Mazin and Singh by demonstrating, first, that the diverse magnetic properties of the 3D ruthenates,  $\text{SrRuO}_3$ ,  $\text{CaRuO}_3$ , and  $\text{Sr}_2\text{YRuO}_6$  follow from the Stoner band-picture as consequences of differences in oxygen positions and Ru-O-Ru hopping paths (Ca makes the oxygen octahedra rotate and Y blocks the paths). In these materials the detailed lattice structure is thus crucial for the magnetic properties. Next, they found 2D  $\text{Sr}_2\text{RuO}_4$  to have strong FM spin fluctuations causing susceptibility- and mass renormalizations, as well as a critical temperature for triplet  $p$ -wave-pairing superconductivity, which agreed quantitatively with observations. The subsequent experimental observation of AFM in  $\text{Ca}_2\text{RuO}_4$ , lead Mazin and Singh to calculate the susceptibility of  $\text{Sr}_2\text{RuO}_4$  for all  $\mathbf{q}$ -vectors. That revealed competing AF spin fluctuations (confirmed later by neutron scattering), and concomitant singlet  $d$ -wave pairing. This, finally, led them to suggest that the actual superconducting ground state of  $\text{Sr}_2\text{RuO}_4$  is determined by a competition between the  $p$ - and  $d$ -wave-pairing states [70].

## 4.1 ARPES

The intensive interest in HTSC lead to a development of angle-resolved photo-electron spectroscopy (ARPES) which, by the end of the millennium, was able to observe single-particle excitations from the occupied bands with 2-meV accuracy and  $0.2^\circ$  angular resolution and thereby, in some people's view, obviated the need for band-structure calculations. But of course, ARPES has problems of its own, such as surface-, final-state, and matrix-element effects [71].

After much smoke had cleared, the LDA FSs predicted a decade earlier for the HTSCs in their normal state usually turned out to be correct, e.g. for the  $\text{YBa}_2\text{Cu}_3\text{O}_7$  FS with sheets from the two plane-bands and the chain-band [72–74]. This being settled –more or less– the challenge was –and remains– to observe how the bands get from  $k_F$ , where they agree with the LDA, but have a smaller, renormalized slope to join the LDA bands again, deeper down, below the Fermi level. These are the effects of the real part of the self-energy describing the interactions with e.g. phonons and spin-fluctuations. The imaginary part produces broadening. The mass renormalization is a measure of the strength of the interaction, and the energy over which this  $\zeta$ -shaped anomaly (kink) occurs, is determined by the energy-spectrum of the interacting boson. For phonons, this energy is the Debye energy, for spin-fluctuations it is wider, but less well known. And then, there are competing phases. To observe and understand what happens to the anomaly when entering the superconducting state is the holy grail, so let us therefore leave the HTSC and return to Pd.

For fcc Pd, it has been possible with polarization-dependent, high-resolution ARPES to study the self-energy effects of the  $sp$ -like band along  $\Gamma\text{K}$ , where the large  $d$ -sheet (Fig. 5) is avoided [75]. The anomaly was found to be 20 meV below  $\varepsilon_F$ , in agreement with the Debye energy, and the renormalization of the Fermi velocities were found to yield  $\lambda_{ep}=0.39\pm0.05$  in agreement with the above-mentioned, previous studies. For this  $sp$ -like band, it was estimated that  $\lambda_{ee}\sim0.02$ . Analysis of the anomaly indicated a possible contribution from PM spin-fluctuations down to  $100\pm50$  meV below  $\varepsilon_F$ , and that  $\lambda_{e-sf}\sim0.06$  for the  $sp$ -like band.

## 4.2 Static and dynamical mean-field approximations

LSD worked surprisingly well for the elemental metals. Even for the actinides and the transition-metal oxides, CaO through NiO, it reproduced the onset of antiferromagnetism and the associated large lattice expansion upon passing the middle of the series [34]. But LSD failed to reproduce the proper band gap, by an order of magnitude in MnO and NiO, and FeO and CoO were even metals! However, it was not until 5 years later when LSD was applied unwisely to the Mott insulator NiO [76], and another 4 years when it failed to reproduce the antiferromagnetism – a ground-state property – in undoped  $\text{La}_2\text{CuO}_4$  –  $I$  being  $\sim 5$  times too small – that the failures became widely recognized [77].

This then gave birth to the self-energy-corrected (SIC) LDA [78], a proper DFT which, however, gave bad bands, and the LDA+ $U$  which, like LSD, helped the functional, but by using Hubbard  $U$  instead of Stoner  $I$  in a static mean-field approximation [79, 80]. Values of  $U$ , the properly screened, on-site Coulomb integral, had previously been calculated by constrained LDA [81, 82] for use in the Anderson impurity model whose Coulomb repulsion is merely on the impurity site [83]. LDA+ $U$  works successfully for insulators with spin- or orbital order [84–87], but the description of (finite-temperature) paramagnetic Mott-insulating states, or of spectra of correlated metals are entirely out of reach. This problem is related to the dynamical nature of electron correlations not accounted for in static mean-field approximations.

In 1989, Metzner and Vollhardt [88] had observed that the single-band Hubbard model with Coulomb repulsion,  $U$ , between two electrons on the same site and integral,  $t$ , for hopping between nearest-neighbor sites becomes far more tractable, while preserving much of its interesting correlation physics, if taken at infinite dimensions (after appropriate scaling). Moreover, the correlation energy in the weak-coupling limit turns out to be nearly the same for  $D=\infty$ , as for  $D=3$ . Hence, the  $D=\infty$ -Hubbard model seemed to be not only simple, but also realistic.

(Although two decades earlier, I had set out to provide many-body theorists with a simple way to obtain realistic band structures and had exploited, that in metals there are usually far more neighbors than lobes in a  $d$ -orbital, had I come across Ref. [88], I could not have cared less. This is the danger of having no training in many-body physics).

Georges and Kotliar [89] soon realized that the  $D=\infty$ -Hubbard model can be mapped exactly onto the Anderson impurity model –supplemented by a self-consistency condition for the energy-dependent (dynamical) coupling to the non-interacting medium. Hence, the quasiparticle peak of the Hubbard model may arise self-consistently from the Kondo resonance of the impurity model [90]. So what they achieved was to construct a mean-field picture of the Hubbard model which becomes exact as  $D \rightarrow \infty$ , and to provide an idea about how to solve the  $D=\infty$ -Hubbard model. The immediate question was whether the  $D=\infty$ -Hubbard model at half filling exhibits a metal-insulator Mott transition in the high-temperature, paramagnetic phase, i.e. whether, upon increasing  $U$ , the quasiparticle peak will develop into a gap by transfer of weight to the lower and upper Hubbard bands. The affirmative answer was found within months by Georges and Krauth who solved the Anderson impurity problem numerically and, independently, also by Rozenberg, Zang, and Kotliar. This dynamical mean-field approximation

(DMFT) is what eventually opened the door for theoretical treatment of correlated electrons in real materials [91,92].

(Although we had, for the impurity model, been computing realistic Coulomb integrals and hybridization-functions, and for alloys had been computing band structures using the coherent-potential approximation [93], we did not get the idea to combine them).

By suggesting the so-called LDA++ scheme, Lichtenstein and Katsnelson [94] proposed how model Hamiltonians of strongly correlated materials could be derived from DFT and thereafter solved by techniques like the Hubbard-I approximation or DMFT [95]. Together with an independent, simultaneous contribution by Anisimov, Kotliar *et al.* [96], this work marks the birth of the LDA+DMFT scheme which brings numerical LDA realism to DMFT [97].

But since that is at the heart of this series of autumn schools, I will proceed with a short description of a few of the applications in which I happened to be involved.

### 4.3 Transition-metal oxides (TMOs)

The TM  $sp$ -orbitals are far more extended than its  $d$ -orbitals, and in the oxides, the former therefore hybridize stronger with the O  $2p$  orbitals than the latter. This pushes the TM  $sp$ -bands up, above the top of the  $d$ -bands, and can formally be neglected. For most transition-metal oxides, the  $d$ -bands lie completely above the O  $2p$  bands (see Fig. 2), and the hybridization between them splits the  $d$ -bands into e.g.  $t_{2g}$ - and  $e_g$ -subbands [69,98].

#### 4.3.1 Wannier Orbitals

Since it makes the chemistry and physics intelligible, and because DMFT requires a small basis set of correlated single-particle orbitals [100], it has become customary to project out of the Rydbergs-wide DFT Band structure a set (or sets) of so-called maximally localized Wannier functions, which span for instance the O  $2p$  and the TM  $d$ -bands, and, hence, have the TM  $sp$ -orbitals folded down into the tails of mainly the O  $2p$  orbitals, or merely the  $e_g$ -band with the tails of the O  $2p$ - as well as those of the  $sp$ - and  $t_{2g}$ -orbitals on the TM neighbors folded in.

We prefer to generate such Wannier orbitals (WOs) *directly*, as symmetrically orthonormalized, minimal basis sets of NMTOs [18]. These are like linear MTOs (LMTOs), which use a linear  $\{\varphi(r), \dot{\varphi}(r)\}$ -expansion of the energy dependence of the partial waves. If the downfolding is massive and the range of the MTOs therefore long and their energy dependence strong, the expansion needs to be of higher than linear order, hence of order  $N > 1$ .

The WOs can also be used to form intelligible tight-binding (TB) models [98, 101]. For the HTSCs, we [102] for instance found the empirical trend (Fig. 4 in Refs. [103] or [104]) that the transition temperature,  $T_{c \text{ max}}$ , for optimal doping increases with the ratio  $t'/t$  between the 2nd and 1st-nearest-neighbor hopping integrals in a massively downfolded, half-full one-band model (Cu  $d^{9-x}$ ). The connection between  $t'/t$  and the chemistry, i.e. the structures and compositions of the 15 different families of HTSCs whose  $t'/t$  are shown in the figure, we have understood: These hopping integrals are between effective Cu  $3d_{x^2-y^2}$  orbitals sitting on a

square lattice with primitive translations  $(1, 0)$  and  $(0, 1)$ , and with each Cu connected by oxygens at  $(\frac{1}{2}, 0)$  and  $(0, \frac{1}{2})$ . The  $t$ -hop is along  $x$ , from  $d_{x^2-y^2}$  at  $(0, 0)$  to  $d_{x^2-y^2}$  at  $(1, 0)$ , via O  $p_x$  at  $(\frac{1}{2}, 0)$ , or equivalently, along  $y$ . The  $t'$ -hop is from  $(0, 0)$  to  $(1, 1)$ . In this description, all orbitals (partial waves) are thus folded down into one, effective Cu  $d_{x^2-y^2}$  orbital. But this orbital does, of course, have tails of O  $2p_x$  at  $(\pm\frac{1}{2}, 0)$  and of O  $2p_y$  at  $(0, \pm\frac{1}{2})$ , to which the hopping in an up-folded three-band model is antibonding  $pd\sigma$ . The  $t'$  hop is “around the corner” on the square  $\text{CuO}_2$  lattice, and proceeds via a so-called axial orbital which is a particular hybrid of Cu  $3d_{3z^2-1}$ , Cu  $4s$ , apical O  $2p_z$ , and whatever the latter bonds covalently to, such as La  $5d_{3z^2-1}$ . Note that the TB Hamiltonian is now up-folded to have four orbitals. Apical oxygens are those forming the apexes of the elongated  $\text{CuO}_6$  octahedron, and the  $t'/t$  trend is caused by differences in this elongation, i.e. distance to apical oxygen, and in what the  $2p_z$ -orbital on the latter binds to out there in the “doping” layers. But the physics, the correlation with  $T_{c \text{ max}}$ , remains to be understood or disproved.

In the cuprates the center of the Cu  $3d$  band is only a few eV above that of the O  $2p$  bands and the hopping between the two is so large that they form a common band. The strongest hopping integral is  $pd\sigma$  and it creates for the  $\text{CuO}_2$  plane a bonding-, a non-bonding-, and an antibonding-band spanning about 8 eV in the LDA. It is the latter band which the above-mentioned  $t, t', t''$  model describes.

### 4.3.2 Metal-insulator transition in $\text{V}_2\text{O}_3$

The theoretical Mott-transition is the one in the single-band Hubbard model investigated by Georges and Krauth, and by Rozenberg, Zang, and Kotliar. But the DMFT+LDA NMTO calculations in which I have been involved, of experimentally observed metal-insulator transitions in TMOs, all dealt with multi-band systems where the isostructural (not-symmetry breaking) metal-insulator transition was basically the opening a gap between occupied and unoccupied bands by moving them apart.

$\text{V}_2\text{O}_3$ , for instance, undergoes an isostructural phase transition from a paramagnetic metal (PM) to a paramagnetic insulator (PI) upon raising the temperature from 20° C to about 400°, the transition temperature depending on the Cr-content in the 1% range. All V atoms and all O atoms are equivalent, and since each V brings in 5 electrons and each O has two holes to be filled, there remains 2 electrons per V. The  $\text{VO}_6$  octahedra are nearly perfect and since the  $pd\sigma$  interaction is stronger than the  $pd\pi$  interaction, the more antibonding V  $3d$ -like  $e_g$  level lies above the less antibonding V  $3d$ -like  $t_{2g}$  level. As a consequence, the electronic configuration is  $\text{V } t_{2g}^2$ . All three orbitals hop to their neighbors, and with 4 formula units per primitive cell in this corundum structure, the LDA band structure is a solid mess of 12 bands, spread over 2.5 eV and 1/3 filled; a metal (see Fig. 15).

There is a slight displacement of the V ions along the 3-fold  $[111]$  axis, away from the centers of their octahedra, so that the distance between a vertical ( $\equiv 111$ )  $\text{V}_2$ -pair whose octahedra in this corundum structure share a (111) face, is slightly longer than the distance between the centers of their octahedra. The  $xy$ ,  $yz$ , and  $xz$  orbitals therefore rehybridize into one orbital,

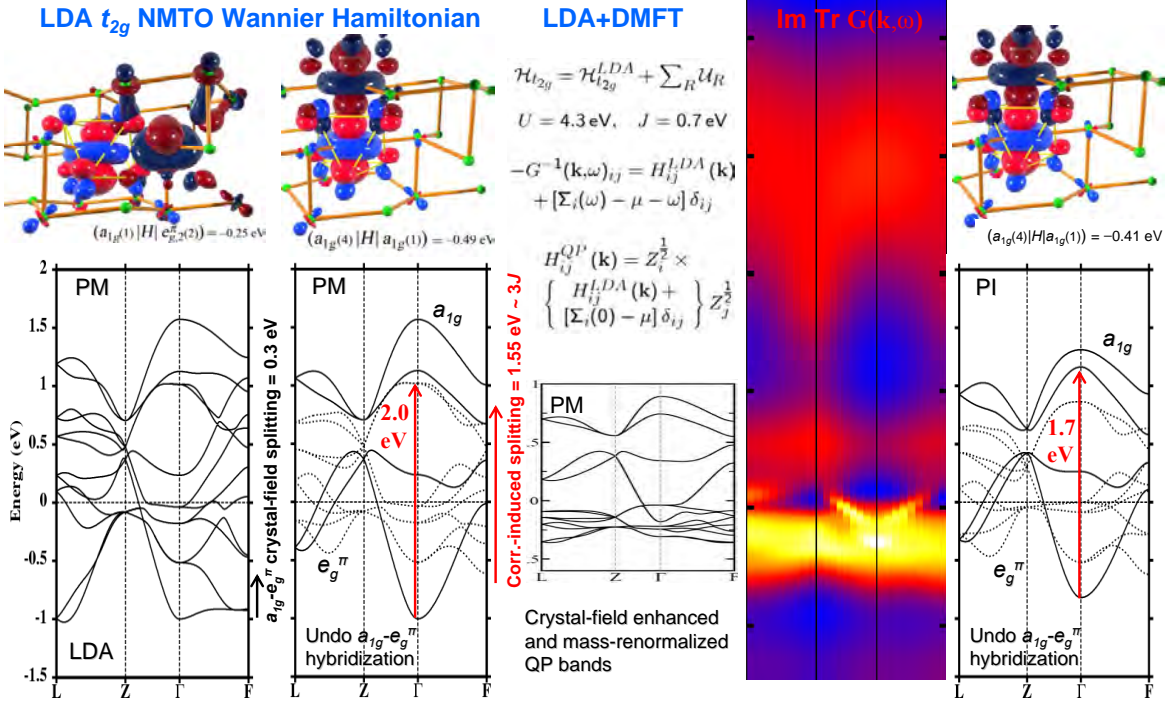


**Fig. 15:** The  $V_2O_3$  story (see text). Three first panels: *Experimental PM structure at 20° C.* 1st panel: *LDA hopping integral between effective  $a_{1g}$  (light) and  $e_g^\pi$  (dark) orbitals,  $-0.25$  eV (upper left), and between  $a_{1g}$  orbitals on the vertical pair,  $-0.49$  eV (upper right).* *LDA  $t_{2g}$  bands with- (lower left) and without (lower right) all  $a_{1g}$ - $e_g^\pi$  hops.* 2nd panel: *Input Hamiltonian, DMFT output Hamiltonian, energy-linearized quasiparticle (QP) Hamiltonian and its band structure.* 3rd panel: *DMFT spectrum.* 4th panel: *Experimental PI structure at 400° C.* *LDA hopping integral between vertical pair,  $-0.41$  eV (upper).* *LDA  $a_{1g}$ - $e_g^\pi$  unhybridized band structure (lower).* From Ref. [99].

$(xy + yz + xz) / \sqrt{3} = 3z_{111}^2 - 1$ , of symmetry  $a_{1g}$  and two degenerate orbitals of symmetry  $e_g$ , called  $e_g^\pi$ , whereby the  $t_{2g}$  level is split into an upper  $a_{1g}$  and a lower, doubly degenerate  $e_g^\pi$  level. But this trigonal crystal-field splitting is 0.3 eV, an order of magnitude smaller than the bandwidth. At the  $\Gamma$  point, the center of the Brillouin zone, where  $a_{1g}$  and  $e_g^\pi$  cannot mix, the 4  $a_{1g}$  levels are raised with respect to the 8  $e_g$  levels by the 0.3 eV. The pure  $a_{1g}$ - and  $e_g^\pi$ - band structures, obtained by setting all hopping integrals between  $a_{1g}$  and  $e_g$  orbitals to zero, shows that the bottom of the  $a_{1g}$  and the top of the  $e_g$  band are at  $\Gamma$ , so that their distance, 2.0 eV of which the trigonal splitting contributes  $-0.3$  and the hoppings 2.3 eV, can be read off the fully hybridized LDA bands.

The on-site Coulomb repulsion, however, prefers by  $3J = 2.1$  eV to have one  $\uparrow$  electron in each  $e_g$  orbital, and none in the  $a_{1g}$  orbital. And this is basically what our DMFT calculation [99] at 100° C provides: It, first of all, “spin-polarizes” the bands and moves the  $\downarrow$ -weight to a very broad, incoherent upper Hubbard band lying  $U = 4.2$  eV above the partly occupied  $\uparrow$ -band. For the latter, it then enhances the crystal-field splitting from 0.3 to 1.85 eV, whereby the  $a_{1g}$  bands essentially empties into the  $e_g^\pi$  band; the bottom of the former merely dips a 0.15 eV below the top of the latter.



With the splitting almost as large as the bandwidth, the  $a_{1g}$ - $e_g$  hopping is strongly reduced, whereby the dispersion resembles that of pure LDA  $a_{1g}$  and  $e_g$  bands. But on top of this, there are quasiparticle renormalization by factors 2.5 and 5 for respectively the  $a_{1g}$ - $e_g^\pi$ -bands, and, finally, inside the  $e_g^\pi$ -band there is strong  $e$ - $e$  scattering which makes it incoherent. The metallic quasiparticles are those on the small  $a_{1g}$  sheet of FS.

Upon increasing the temperature across the metal-insulator transition, there is an increase of the so-called umbrella distortion which changes the LDA band structure. In particular, the distortion makes the effective  $dd\sigma$  hopping integral between vertical  $V_2$  pair decrease from  $-0.49$  to  $-0.41$  eV, whereby the distance between bottom of the  $a_{1g}$  and the top of the  $e_g^\pi$  LDA bands, is reduced from 2.0 to 1.7 eV. A Coulomb-enhanced crystal-field splitting of 1.85 eV would thus suffice to separate the bands. Sure enough, the DMFT calculation with the new LDA bands for the high-temperature structure, but the values of  $U$  and  $J$  unchanged, yields a small, insulating gap. This, we felt, demystified what for more than 30 years was considered *the* Mott transition.

#### 4.4 Elemental metals

The  $e$ - $e$  interaction effects in  $V_2O_3$  are really drastic in comparison with those in Pd. Savrasov *et al.* [105] recently returned to the problem of calculating the effects on the self-energy,  $\Sigma(\omega, \mathbf{k})$ , from the interaction with the paramagnons in Pd and included the  $\mathbf{k}$ -dependence by combining the LDA with the fluctuational exchange (FLEX) approximation. By including ladder diagrams, FLEX can describe spin-fluctuations, in contrast to quasi-particle self-consistent  $GW$  (QSGW) approach (see below). As the results turned out to have only a small  $\mathbf{k}$ -dependence, they were compared with those of LDA+DMFT, and found to be in better agreement with experiments, yielding  $\lambda=0.1-0.3$  for  $U=1-2$  eV.

From ARPES for ferromagnetic bcc Fe, it was concluded in 2010 [106] that previous estimates of the  $d$ -band narrowing due to many-electron effects were too large due to neglect of SO-splitting in the LSD calculations, and of final-state transitions plus final-state broadening in the photoemission analysis. As a result, many-electron effects seem to narrow the  $d$ -band by merely 10%. In accord with the measured cyclotron masses [62] and the LSD calculations, the renormalizations of the Fermi velocities are in the range 1.5–3, presumably with  $\lambda_{ep} \sim 0.4$  like for Pd, and a similar contribution from the electron-magnon interaction. However, whereas the two latter are expected to extend down to respectively 40 and 300 meV below  $\varepsilon_F$ , the self-energy anomaly was observed down to at least 500 meV, and finally attributed to many-electron effects.

The quasi-particle self-consistent  $GW$  (QSGW) approach which has been most successful in describing weak, but  $\mathbf{k}$ -dependent correlations, was recently applied to bcc Fe and fcc Ni by Schilfsgaarde *et al.* [107]. For Fe, the agreement with the available FS data from dHvA was perfect, and the mass enhancements and the ARPES were well described. Due to its  $\Sigma(\omega)$  lacking  $\mathbf{k}$ -dependence, DMFT does less well for ARPES. QSGW gave a 25% narrowing of the  $d$ -bandwidth, but that may have been due to neglect of SO splitting as suggested in Ref. [106].

For Ni, the PM part of the QSGW bands were in excellent agreement with experiments, but the exchange splitting was overestimated by a factor 2, even more than in the LSD, and the moment was overestimated by 20% and, hence, much worse than in the LSD. This problem is known for itinerant magnets, the iron pnictides, in particular. This failure was ascribed to the inability of  $GW$  to treat spin-fluctuations, and it was demonstrated by use of QSGW+DMFT, that a reasonable, simple cure is to add an external magnetic field adjusted get the moment right. The approach by Mazin *et al.*, who adjust the Stoner  $I$ , is at least based on Moriya's fluctuation theory [108].

Friedel once asked me about the real-space reason for the double-peak in the bcc DOS, which for instance is crucial for the martensitic transformation in steels. As seen in Fig. 5, the reason is *not* a separation of  $e_g$ - and  $t_{2g}$ -characters. But what *is* seen in this figure, is that in FM bcc Fe, the FS has mostly  $t_{2g}$  character (the  $\uparrow$ -sheet exclusively) and the big peak mostly  $e_g$  character. This was recently found to have consequences for the real-space exchange interactions [109]: The  $t_{2g}$  states are itinerant and determined by FS nesting, while the  $e_g$  states form localized moments which must be treated by DMFT. Most important was the subsequent insight [110] that for both fcc and bcc structures, and throughout the  $3d$  series, the exchange coupling between an  $e_g$  orbital and a  $t_{2g}$  orbital on a near neighbor vanishes.

Most recently the *local* magnetic moments in Fe and Ni at ambient and Earth's-core conditions were studied [111] using an arsenal of methods, in particular DMFT. At normal pressure, the Curie temperature of Fe comes out about 30% too large while that of Ni is slightly too low. The authors (re-)discovered the van Hove singularities in fcc Ni and concluded that without these, Ni would not be a strong-coupling quantum magnet. Moreover: "The most important implication of our results for Ni comes from the observation that even at a pressure of hundreds of GPa (Mbars), the position and shape of these sharp features in the DOS do not change dramatically. Ni remains in its fcc structure up to even larger pressures and its magnetic moments, though smaller, are much more robust than those of Fe".

Well, in the process of substituting  $I$  with  $U$ , and static- with dynamical mean-field theory, insights from canonical band theory were apparently forgotten. In the end, AI may take over.

## References

- [1] N. Bohr, *Zeitschrift für Physik* **9**, 1 (1922); spin and exclusion principle came later: W. Pauli, *Zeitschrift für Physik* **31**, 765 (1925)
- [2] L.D. Landau and E.M. Lifshitz: *Quantum Mechanics* (Pergamon, 1965)
- [3] M. Tinkham: *Group Theory and Quantum Mechanics* (McGraw-Hill, 1964) Ch. 6
- [4] W.A. Harrison: *Electronic structure and the properties of solids* (Dover, 1989)
- [5] R.M. Martin: *Electronic Structure: Basic Theory and Practical Methods* (Cambridge University Press, 2008)
- [6] C. Kittel: *Introduction to Solid State Physics* (Wiley, 1956)
- [7] K.H. Schwarz, *Chem. Phys.* **7**, 100 (1975)
- [8] O.K. Andersen and O. Jepsen, *Physica B+C* **91**, 317 (1977)
- [9] D.G. Pettifor, *J. Phys. F: Metal Phys.* **7**, 613 (1977);  
*ibid*, **7**, 1009 (1977); *ibid* **8**, 219 (1978)
- [10] For a review, see: A.R. Mackintosh and O.K. Andersen:  
*The electronic structure of transition metals* in Ref. [113]
- [11] H.L. Skriver: *The LMTO method: muffin-tin orbitals and electronic structure* (Springer, 1984)
- [12] O.K. Andersen, O. Jepsen, and D. Glözel: *Canonical Description of the Band Structures of Metals* in Ref. [114] (where  $\gamma_l$  is named  $Q_l$ )
- [13] D.D. Koelling and B.N. Harmon, *J. Phys. C* **10**, 3107 (1977)
- [14] O.K. Andersen, *Phys. Rev. B* **12**, 3060 (1975)
- [15] O.K. Andersen and A.R. Mackintosh, *Solid State Commun.* **6**, 285 (1968);  
O.K. Andersen, *Phys. Rev. B* **2**, 883 (1970)
- [16] R.M. Martin in Ref. [119]
- [17] P.E. Blöchl in Ref. [115]
- [18] O.K. Andersen: *NMTOs and their Wannier functions* in Ref. [116]
- [19] L Hodges, R.E. Watson, and H. Ehrenreich, *Phys. Rev. B* **5**, 3953 (1972)
- [20] O.K. Andersen, *Solid State Commun.* **13**, 133 (1973)
- [21] C.R. Brown, J.P. Kalejs, F.D. Manchester, J.M. Perz, *Phys. Rev. B* **6**, 4458 (1972)

- [22] O.K. Andersen and O. Jepsen, Phys. Rev. Lett. **53**, 2571 (1984)
- [23] R.O. Jones and O. Gunnarsson, Rev. Mod. Phys. **61**, 689 (1989), Sects. IVC, VI, and VII
- [24] E. Pavarini, p. 7.40 in Ref. [118]
- [25] O.K. Andersen, W. Klose, H. Nohl, Phys. Rev. B **17**, 1209 (1978)
- [26] U. von Barth and L. Hedin, J. Phys. C: Solid St. Physics **5**, 1629 (1972)
- [27] L.F. Mattheiss, Phys. Rev. **133**, A1399 (1964)
- [28] J.F. Janak, Phys. Rev. B **16**, 255 (1977); Janak's  $I$  is half- and his DOS twice our value
- [29] J. Madsen, O.K. Andersen, U.K. Poulsen, O. Jepsen in *Magnetism and Magnetic Materials 1975*, 327 (AIP, N.Y. 1976); U.K. Poulsen, J. Kollar, O.K. Andersen, J. Phys. F **6**, L241 (1976)
- [30] O.K. Andersen, J. Madsen, U.K. Poulsen, O. Jepsen, J. Kollar, Physica **86-88 B**, 249 (1977); J. Kollar *et al.* in *Proceedings of the VIII Symposium on Electronic Structure of Metals and Alloys* (Dresden, 1978)
- [31] V.L. Moruzzi, J.F. Janak, and A.R. Williams: *Calculated Electronic Properties of Metals* (New York, Pergamon 1978)
- [32] R. Car and M. Parrinello, Phys. Rev. Lett. **55**, 2471 (1985)
- [33] M.T. Yin, and M.L. Cohen, Phys. Rev. B **26**, 5668 (1982); M.L. Cohen in Ref. [114]
- [34] O.K. Andersen, H.L. Skriver, H. Nohl, B. Johansson, Pure and Appl. Chem. **52**, 93 (1979)
- [35] V. Heine, in H. Ehrenreich, F. Seitz, D. Turnbull (Eds.): *Solid State Physics* **35** (Academic Press, N.Y. 1980)
- [36] The force theorem considers an  $N$ -particle system whose Hamiltonian is the sum of the kinetic energy, two-body particle-particle interactions, and one-body interactions with an external potential. It gives expressions for the *internal* force on all particles in a region,  $\Omega$ , which together with the force by the external potential on the particles in  $\Omega$  keeps the system in a given stationary state,  $\Phi$ . The derivation employs the variational principle with a trial function,  $\Phi + d\Phi$  obtained from  $\Phi$  by translating it rigidly from region  $\Omega$  to  $\Omega + d\mathbf{u}$ , where  $d\mathbf{u}$  is the direction of the force. The first result is that *the external force balances the kinetic force plus the two-body (e.g. electrostatic) force between the particles inside  $\Omega$  and outside  $\Omega$*  (the sum of the forces between the particles inside  $\Omega$  cancel). Here, the kinetic force is the integral over the surface of  $\Omega$  and the sum over all particles,  $j$ , of the kinetic stress tensor field,  $\overleftrightarrow{\sigma}_j(\mathbf{r})$ , which may be expressed in terms of the eigenvectors,  $\psi_{jk}(\mathbf{r})$ , and eigenvalues,  $n_{jk}$ , of the 1st-order density matrix. Transformation of the surface integral to a volume integral, transforms the kinetic force to the integral in  $\Omega$

of a kinetic force-density,  $\mathbf{F}_{\text{kin}j}(\mathbf{r})$ , expressed in terms of the occupation numbers,  $n_{jk}$ , and up to third derivatives of the natural orbitals,  $\psi_{jk}(\mathbf{r})$ . We then specialize to electrons and nuclei, and neglect the nuclear kinetic force, obtaining:

$$\mathbf{F}_{\text{kin}}(\mathbf{r}) = \frac{1}{2m} \sum_k n_k \left[ \psi_k^*(\mathbf{r}) \left\{ \vec{\nabla} \nabla^2 \psi_k(\mathbf{r}) \right\} - \left\{ \nabla^2 \psi_k(\mathbf{r}) \right\}^* \left\{ \vec{\nabla} \psi_k(\mathbf{r}) \right\} \right].$$

If we *assume* that  $\psi_k(\mathbf{r})$  satisfies a one-electron Schrödinger equation with a local, possibly state-dependent potential,  $V_k(\mathbf{r})$ , then  $\mathbf{F}_{\text{kin}}(\mathbf{r}) = \sum_k n_k |\psi_k(\mathbf{r})|^2 \vec{\nabla} V_k(\mathbf{r})$ , and we thus have the results that *the one-electron potential is that effective, external potential whose force balances the kinetic force, and the one electron energies are the eigenvalues of its Schrödinger equation*. But the exact result is the one for  $\mathbf{F}_{\text{kin}}(\mathbf{r})$  given above. The LDA potential has  $\mu_{\text{xc}}$  substituted by  $\epsilon_{\text{xc}}$  on the surface of  $\Omega$ , and this is what makes the homogeneous electron gas bind with  $s_0 \sim 4.1$  a.u. [See also Ref. [5] and J. Gräfenstein and P. Ziesche, Phys. Rev. B **53**, 7143 (1996)].

- [37] D.G. Pettifor, Commun. Phys. **1**, 141 (1976) and Refs. therein
- [38] H.L. Skriver, Phys. Rev. B **31**, 1909 (1985)
- [39] N.W. Dalton and J. Hubbard, A.E.R.E. Harwell Rep. T.P. 327 (1968);  
Dalton and R.A. Deegan, J. Phys. C **2**, 2369 (1969);  
D.G. Pettifor, J. Phys. C **3**, 367 (1970)
- [40] J. Friedel in J.M. Ziman (Ed.): *The Physics of Metals* (Cambridge University Press 1969)
- [41] L.F. Mattheiss and D.R. Hamann, Phys. Rev. **33**, 823 (1986)
- [42] J.J. Duthie and D.G. Pettifor, Phys. Rev. Lett. **38**, 564 (1977)
- [43] S.H. Vosko and J.P. Perdew, Can. J. Phys. **53**, 1385 (1975);  
O. Gunnarsson and B.I. Lundqvist, Phys. Rev. B **13**, 4274 (1976);  
W. Kohn in Ref. [114]
- [44] O. Gunnarsson, J. Phys. F **6**, 587 (1976). Figs. 5 and 6 in particular
- [45] More accurate calculations giving for all 33 elemental metals values of the potential parameters, canonical bands, ground-state properties, and their pressure derivatives may be found in Ref. [12]
- [46] P. Bagno, O. Jepsen, O. Gunnarsson, Phys. Rev. B **40**, 1997 (1989)
- [47] L. Kaufman, E.V. Clougherty, R.J. Weiss, Acta Metall. **11**, 323 (1963)
- [48] J.F. Petersen, M. Aydin, J.M. Knudsen, Phys. Lett. **62** A, 192 (1977);  
F. Albertsen, J.M. Knudsen, G.B. Jensen, Nature **273**, 453 (1978)

- [49] H.L. Skriver and O.K. Andersen, Inst. Phys. Conf Ser. No. **39**, 100 (1978)
- [50] O. Eriksson, B. Johansson, R. C. Albers, A. M. Boring, M. S. S. Brooks, Phys. Rev. B **42**, 2707 (1990)
- [51] L.M. Sandratskii, Phys. Stat. Sol. (b) **135**, 167 (1986); J. Phys. Cond. Mat. **3**, 8565 (1991)
- [52] For an application to stripe order in FeAsLaO, see O.K. Andersen and L. Boeri, Ann. Phys. **523**, 8 (2011)
- [53] A.I. Lichtenstein in Ref. [117]
- [54] A.I. Lichtenstein, M.I. Katsnelson, V.A. Gubanov, J. Phys. F: Met. Phys. **14**, L125 (1984); Solid. State Commun. **54**, 327 (1985); A.I. Lichtenstein, M.I. Katsnelson, V.P. Antopov, V.A. Gubanov, J. Magn. Magn. Mater. **54-57**, 965 (1986); *ibid*, **67**, 65 (1987)
- [55] P. Bruno, Phys. Rev. Lett. **90**, 087205 (2003); M.I. Katsnelson and A.I. Lichtenstein, J. Phys.: Condens. Matter **16**, 7439 (2004)
- [56] N.F. Berk and J.R. Schrieffer, Phys. Rev. Lett. **17**, 433 (1966); *ibid* **19**, 644 (1967)
- [57] W. Joss, L.N. Hall, G.W. Crabtree, J.J. Vuillemin, Phys. Rev. B **30**, 5637 and 5646 (1984)
- [58] R. Heid in Ref. [119]
- [59] S.Y. Savrasov and D.Y. Savrasov, Phys. Rev. B **54**, 16487 (1996)
- [60] E. Stenzel and H. Winter, J. Phys. F: Metal Phys. **16**, 1789 (1986)
- [61] S.Y. Savrasov, Phys. Rev. Lett. **81**, 2570 (1998)
- [62] G.G. Lonzarich, J. Magn. and Magn. Mater. **45**, 43 (1984); *Fermi surface studies in ferromagnets* in Ref. [113]
- [63] J. Callaway and C.S. Wang, Phys. Rev. B **16**, 2095 (1977)
- [64] W. Pickett in Ref. [117]
- [65] B. Keimer in Ref. [117]
- [66] A. Tremblay in Ref. [117]
- [67] T. Maier in Ref. [120]
- [68] D. Singh in Ref. [116]
- [69] C. Franchini in Ref. [112]
- [70] I.I. Mazin and D.J. Singh, Phys. Rev. Lett. **82**, 4324 (1999) and Refs. therein

- [71] J. Minar in Ref. [92], *ibid* M. Sing
- [72] A. Damascelli, Z. Hussain, Z.X. Shen, Rev. Mod. Phys. **75**, 473 (2003)
- [73] O.K. Andersen, A.I. Liechtenstein, O. Jepsen, and F. Paulsen, J. Phys. Chem. Solids, Vol. **56**, 1573 (1995)
- [74] V.B. Zabolotnyy, S.V. Borisenko, *et al.*, Phys. Rev. B **76**, 064519 (2007)
- [75] H. Hayashi, K. Shimada, J. Jiang, H. Iwasawa, Y. Aiura, T. Oguchi, H. Namatame, M. Taniguchi, Phys. Rev. B **87**, 035140 (2013), Fig. 4, in particular
- [76] K. Terakura, T. Oguchi, A.R. Williams, J. Kübler, Phys. Rev. B **30**, 4734 (1984)
- [77] J. Zaanen, O. Jepsen, O. Gunnarsson, A.T. Paxton, O.K. Andersen, A. Svane, Physica C **153-158**, 1636 (1988)
- [78] A. Svane and O. Gunnarsson, Phys. Rev. Lett. **65**, 1148 (1990)
- [79] V. I. Anisimov, J. Zaanen, O.K. Andersen, Phys. Rev. B **44**, 943 (1991)
- [80] V. I. Anisimov, F. Aryasetiawan. A. I. Lichtenstein, J. Phys.: Condens. Matter **9**, 767 (1997)
- [81] O. Gunnarsson, O. K. Andersen, O. Jepsen, J. Zaanen, Phys. Rev. B **39**, 1708 (1989)
- [82] V.I. Anisimov, O. Gunnarsson, Phys. Rev. B **43**, 7570 (1991)
- [83] O. Gunnarsson in Ref. [116]
- [84] A. I. Lichtenstein, V. I. Anisimov, J. Zaanen, Phys. Rev. B **52**, R5467 (1995)
- [85] M. Cococcioni in Ref. [116]
- [86] E. Pavarini in Ref. [118]
- [87] E. Pavarini in Ref. [119]
- [88] W. Metzner and D. Vollhardt, Phys. Rev. Lett. **62**, 324 (1989)
- [89] A. Georges and G. Kotliar, Phys. Rev. B **45**, 6479 (1992)
- [90] M. Fabrizio in Ref. [119]
- [91] M. Kollar in Ref. [115]
- [92] E. Pavarini, E. Koch, D. Vollhardt, and A. Lichtenstein (eds.): *DMFT at 25: Infinite Dimensions*, Modeling and Simulation Vol. 4 (Forschungszentrum Jülich, 2014), [121]

- [93] J. Kudrnovsky, N.E. Christensen, O.K. Andersen, Phys. Rev. B **43**, 5924 (1991)
- [94] A.I. Lichtenstein and M.I. Katsnelson, Phys. Rev. B **57**, 6884 (1998)
- [95] F. Lechermann in Ref. [115]
- [96] V.I. Anisimov, A.I. Poteryaev, M.A. Korotin, A.O. Anokhin, G. Kotliar, J. Phys.: Condensed Matter **9**, 7359 (1997)
- [97] A.I. Lichtenstein in Ref. [92]
- [98] E. Pavarini in Ref. [116]
- [99] A.I. Poteryaev, J.M. Tomczak, S. Biermann, A. Georges, A. I. Lichtenstein, A. N. Rubtsov, T. Saha-Dasgupta, O.K. Andersen, Phys. Rev. B **76**, 085127 (2007)
- [100] J. Kunes in Ref. [115]
- [101] W.M.C. Foulkes in Ref. [118]
- [102] E. Pavarini, I. Dasgupta, T. Saha-Dasgupta, O. Jepsen, O.K. Andersen, Phys. Rev. Lett. **87**, 047003 (2001)
- [103] E. Pavarini in Ref. [117]
- [104] see E. Pavarini in Ref. [112]
- [105] S.Y. Savrasov, G. Resta, X. Wan, Phys. Rev. B **97**, 155128 (2018)
- [106] A.L. Walter, J.D. Riley, O. Rader, New J. Phys. **12**, 013007 (2010)
- [107] L. Sponza, P. Pisanti, A. Vishina, D. Pashov, C. Weber, M. van Schilfgaarde, S. Acharya, J. Vidal, G. Kotliar, Phys. Rev. B **95**, 041112 (2017)
- [108] L. Ortenzi, I.I. Mazin, P. Blaha, L. Boeri, Phys. Rev. B **86**, 064437 (2012)
- [109] Y.O. Kvashnin, R. Cardias, A. Szilva, I. Di Marco, M.I. Katsnelson, A.I. Lichtenstein, L. Nordström, A.B. Klautau, O. Eriksson, Phys. Rev. Lett. **116**, 217202 (2016)
- [110] R. Cardias, A. Szilva, A. Bergman, I. Di Marco, M.I. Katsnelson, A.I. Lichtenstein, L. Nordström, A.B. Klautau, O. Eriksson, Y.O. Kvashnin, Sci. Rep. **7**, 4058 (2017)
- [111] A. Hausoel, M. Karolak, E. Sasioglu, A. Lichtenstein, K. Held, A. Katanin, A. Toschi, G. Sangiovanni, Nat. Commun. **10**, 1038 (2017)
- [112] E. Pavarini, E. Koch, P. Coleman (Eds.): *Many-Body Physics: From Kondo to Hubbard*, Reihe Modeling and Simulation, Vol. 5 (Forschungszentrum Jülich, 2015), [121]
- [113] M. Springford (Ed.): *Electrons at the Fermi Surface* (Cambridge UP, 1980)



- [114] F. Bassani, F. Fumi and M.P. Tosi (eds.): *Highlights of Condensed-Matter Theory*, Course LXXXIX, International School of Physics “Enrico Fermi”, Varenna, Italy, (North-Holland, 1985)
- [115] E. Pavarini, E. Koch, D. Vollhardt, and A. Lichtenstein (Eds.):  
*The LDA+DMFT approach to correlated materials*,  
Reihe Modeling and Simulation, Vol. 1 (Forschungszentrum Jülich, 2011), [121]
- [116] E. Pavarini, E. Koch, F. Anders, and M. Jarrel (Eds.): *From Models to Materials*,  
Reihe Modeling and Simulation, Vol. 2 (Forschungszentrum Jülich, 2012), [121]
- [117] E. Pavarini, E. Koch, U. Schollwöck (Eds.):  
*Emergent Phenomena in Correlated Matter*,  
Reihe Modeling and Simulation, Vol. 3 (Forschungszentrum Jülich, 2013), [121]
- [118] E. Pavarini, E. Koch, J. van den Brink, G. Sawatzky (Eds.):  
*Quantum Materials: Experiments and Theory*,  
Reihe Modeling and Simulation Vol. 6 (Forschungszentrum Jülich, 2016), [121]
- [119] E. Pavarini, E. Koch, R. Scalettar, and R. Martin (Eds.):  
*The Physics of Correlated Insulators, Metals, and Superconductors*,  
Reihe Modeling and Simulation, Vol. 7 (Forschungszentrum Jülich, 2017), [121]
- [120] E. Pavarini, E. Koch, A.I. Lichtenstein, and D. Vollhardt (Eds.):  
*DMFT — From Infinite Dimensions to Real Materials*,  
Reihe Modeling and Simulation, Vol. 8 (Forschungszentrum Jülich, 2018), [121]
- [121] <https://www.cond-mat.de/events/correl.html>



# 3 Effective Electron-Electron Interaction in Many-Electron Systems

Ferdi Aryasetiawan

Mathematical Physics, Lund University,

Professorsgatan 1, 223 63 Lund, Sweden

## Contents

<b>1</b>	<b>Introduction</b>	<b>2</b>
<b>2</b>	<b>Theory</b>	<b>3</b>
2.1	Screening and screened potential . . . . .	5
2.2	Screened Coulomb interaction . . . . .	6
2.3	Linear density response function . . . . .	7
2.4	Random phase approximation . . . . .	8
2.5	The constrained RPA method . . . . .	9
2.6	Wannier orbitals . . . . .	11
2.7	cRPA for entangled bands . . . . .	12
<b>3</b>	<b>Examples</b>	<b>12</b>
3.1	Cubic perovskite $\text{SrVO}_3$ . . . . .	12
3.2	Undoped cuprate $\text{La}_2\text{CuO}_4$ . . . . .	15
3.3	Early lanthanides series . . . . .	16
<b>4</b>	<b>Summary</b>	<b>18</b>
<b>A</b>	<b>Response functions from Green function formalism</b>	<b>19</b>

# 1 Introduction

Were it not for the electron-electron (e-e) interaction in many-electron systems such as atoms, molecules and solids, we would not observe fascinating phenomena such as superconductivity, phase transitions, magnetism and many others. At the same time, it is this electron-electron interaction that makes solving the many-electron Hamiltonian exceedingly difficult. Solving the many-electron problem is perhaps one of the general goals in condensed matter theory. Direct methods for solving the many-electron Hamiltonian by, e.g., expanding the many-electron wave function as a linear combination of Slater determinants, are however not very fruitful when the number of electrons is large ( $\sim 10^{23}$ ), which is the case in real materials. The number of Slater determinants required for a reasonably accurate solution becomes enormously large and unfeasible to handle in practice.

One successful approach for handling the many-electron problem is to first identify a subspace of the full Hilbert space in which e-e interaction plays a decisive role in determining the physical properties of interest. The basic idea is to treat the e-e interaction explicitly within the limited subspace whereas the influence of the rest of the Hilbert space is accounted for in a mean-field approximation. Thus the many-electron problem is reduced to a subspace and fortunately the size of the relevant subspace is in many cases relatively small compared to the full Hilbert space. However, the reduction of the many-electron problem to a limited subspace entails the need to renormalize the e-e interaction resulting in an effective interaction. Physically, the renormalization of the e-e interaction arises from the screening processes that have been eliminated when reducing the many-electron problem to the limited subspace.

A well-known example of an effective many-electron Hamiltonian is the Hubbard model [1], which in its simplest form is given by

$$H = -t \sum_{i \neq j, \sigma} c_{i\sigma}^\dagger c_{j\sigma} + U \sum_i n_{i\uparrow} n_{i\downarrow}. \quad (1)$$

The first term describes electron hopping with the same spin  $\sigma$  from site  $j$  to site  $i$  whereas the second term describes the interaction of electrons of opposite spin when they are on the same site  $i$ . The Hubbard model was introduced by Hubbard, Gutzwiller, and Kanamori at about the same time in the early 1960's as a phenomenological model to describe localized or semi-itinerant  $3d$  states in transition metals. It is physically feasible that the bare e-e interaction is screened so that the on-site component of the screened interaction is the most important. The Hubbard model is well suited to study the electronic structure of strongly correlated systems in which on-site electron correlations are strong, due to the localized nature of the  $3d$ - or  $4f$ -orbitals. The model describes the competition between the kinetic energy represented by the hopping term and electron repulsion represented by the  $U$  term. For the half-filled case (one electron per site), as  $U$  becomes larger than  $t$  it is energetically more favorable for the electrons to be localized on their respective sites in order to avoid the large repulsion arising from having two electrons on the same site. As  $U$  increases further, each electron is locked on its site and the system turns into a Mott insulator. Since the Hubbard model is phenomenological, it is common practice to treat  $U/t$  as a parameter.

In the simplest form there is only one orbital per site but in general there can be several orbitals per site so that the hopping parameter  $t$  and the effective e-e interaction  $U$  (the Hubbard  $U$ ) are matrices instead of single numbers

$$H = \sum_{\mathbf{R}i, \mathbf{R}'j, \sigma} t_{\mathbf{R}i, \mathbf{R}'j}^{\sigma} c_{\mathbf{R}i\sigma}^{\dagger} c_{\mathbf{R}'j\sigma} + \frac{1}{2} \sum_{\mathbf{R}, \mathbf{R}', ijkl, \sigma\sigma'} U_{ijkl}^{\sigma\sigma'}(\mathbf{R}, \mathbf{R}') c_{\mathbf{R}i\sigma}^{\dagger} c_{\mathbf{R}'j\sigma'}^{\dagger} c_{\mathbf{R}'k\sigma'} c_{\mathbf{R}l\sigma}. \quad (2)$$

A set of localized orbitals  $\{\varphi_{\mathbf{R}i\sigma}\}$  defining the annihilation and creation operators are assumed. The subscripts  $\mathbf{R}$  and  $i$  label the site and the orbital, while  $\sigma$  denotes the spin variable. The parameters  $U_{ijkl}^{\sigma\sigma'}(\mathbf{R}, \mathbf{R}')$  are the matrix elements of the effective e-e interaction  $U(\mathbf{r}, \mathbf{r}')$

$$U_{ijkl}^{\sigma\sigma'}(\mathbf{R}, \mathbf{R}') = \int d^3r d^3r' \varphi_{\mathbf{R}i}^*(\mathbf{r}) \varphi_{\mathbf{R}'j}^*(\mathbf{r}') U(\mathbf{r}, \mathbf{r}') \varphi_{\mathbf{R}'k}(\mathbf{r}') \varphi_{\mathbf{R}l}(\mathbf{r}). \quad (3)$$

We have assumed that the effective interaction is static and orbitals with the same position variable belong to the same atomic site. In general  $U$  depends on four atomic sites.

In the last couple of decades there has been an increasing interest in combining the Hubbard model with realistic band structure calculations in order to study the electronic structure of strongly correlated materials from which various physical properties can be derived. Each material is then characterized by hopping parameters  $t_{\mathbf{R}i, \mathbf{R}'j}^{\sigma}$ , which determine the underlying one-particle band structure, and by  $U_{ijkl}^{\sigma\sigma'}(\mathbf{R}, \mathbf{R}')$ , which determine the effective e-e interaction. The hopping parameters can be determined from realistic band structure calculations, commonly done within the local density approximation (LDA) [2], by a tight-binding fit. However, it is much less obvious how to determine the effective e-e interaction. If we wish to make quantitative predictions about the physical properties of a material, it is necessary to compute the matrix  $U$  from first-principles, rather than treating it as an adjustable parameter. A model Hamiltonian with adjustable parameters runs the risk of producing certain properties in good agreement with experiment not for a theoretically justifiable reason but rather due to a fortuitous cancellation between an inappropriate choice of the parameters and inaccurate theoretical approximations employed in solving the model.

The purpose of this lecture is to describe a systematic way of determining the effective e-e interaction corresponding to a chosen subspace into which the many-electron problem is down-folded. The method is quite general and it yields  $U(\mathbf{r}, \mathbf{r}'; \omega)$  so not only local but also non-local matrix elements can be extracted. Moreover, the method delivers a frequency-dependent  $U$ , which encapsulates the dynamics of the screening processes determining the effective e-e interaction in the chosen subspace. The resulting effective interaction can be used in a model Hamiltonian or in an effective-action formalism, which is then solved by using many-body techniques such as dynamical mean-field theory (DMFT) [3] and quantum Monte Carlo methods.

## 2 Theory

The determination of the Hubbard  $U$  has a long history. Perhaps the earliest attempt was made by Herring [4] who defined  $U$  as the energy cost of transferring an electron between two atoms

in a crystal. If  $E(N)$  is the energy per atom in the initial configuration with  $N$  electrons, removing an electron from a given site costs  $E(N - 1) - E(N)$  and putting the removed electron to another site costs  $E(N + 1) - E(N)$  so the total cost is then

$$\begin{aligned} U &= [E(N + 1) - E(N)] + [E(N - 1) - E(N)] \\ &= E(N + 1) - 2E(N) + E(N - 1). \end{aligned} \quad (4)$$

We are usually interested in  $U$  associated with localized orbitals such as the  $3d$ -orbitals of transition metals or the  $4f$ -orbitals of the lanthanides. If  $n_d$  labels the occupation number of a  $3d$ -orbital, treating it as a continuous variable we may write Eq. (4) as

$$U = \frac{\partial^2 E}{\partial n_d^2}. \quad (5)$$

The change in the total energy associated with the change in the occupation number is given by  $\delta E = \varepsilon_d \delta n_d$ , where  $\varepsilon_d$  is the orbital energy, so that  $U$  can be expressed as the change in the orbital energy with respect to the occupation number:

$$U = \frac{\partial}{\partial n_d} \left( \frac{\partial E}{\partial n_d} \right) = \frac{\partial \varepsilon_d}{\partial n_d}. \quad (6)$$

Early calculations of  $U$  for transition metals using this formula were made by Cox *et al.* [5]. The eigenvalues are calculated for the three different configurations  $3d^n 4s^1$ ,  $3d^{n+1} 4s^0$ ,  $3d^{n-1} 4s^2$  by solving an atomic problem self-consistently with an appropriate boundary condition at the Wigner-Seitz sphere boundary to mimic the atomic environment in the crystal. The change in the atomic wave function from configuration  $3d^n 4s^1$  to configurations  $3d^{n+1} 4s^0$  and  $3d^{n-1} 4s^2$  captures, respectively, the effects of screening arising from adding and removing an electron from the  $3d$ -shell. The result shows an almost linear increase across the  $3d$ -series from 1.3 eV for Sc to 3.3 eV for Ni. A similar approach was also employed by Herbst [6] to compute  $U$  for the  $4f$ -series.

A constrained LDA (cLDA) approach was later introduced by Dederichs *et al.* [7] who used it to compute  $U$  for Ce. The total energy as a function of the  $4f$  occupation number is given by

$$E(n_f) = \min \left\{ E[\rho(\mathbf{r})] + v_f \left( \int_{R_S} d^3r \rho_f(\mathbf{r}) - n_f \right) \right\}, \quad (7)$$

where  $R_S$  is the radius of the Wigner-Seitz sphere,  $n_f$  and  $\rho_f$  are respectively the occupation number and density of the  $4f$ -orbital and  $v_f$  is a Lagrange multiplier corresponding to the constraint that the occupation number of the  $4f$ -orbital is given by  $n_f$ . The Lagrange multiplier  $v_f$  can be interpreted as a constant projection potential that acts only on the  $4f$ -orbitals. The constraint only applies to the  $4f$ -electrons while other electrons (*spd*) within the atomic sphere as well as in the neighboring cells can relax in the self-consistency cycle to minimize the total energy. By calculating  $E(n_f)$  in Eq. (7) as a function of  $n_f$  around the unconstrained equilibrium value the Hubbard  $U$  can then be computed using the formula in Eq. (5).

The cLDA method can also be formulated using the supercell approach in which the constraint is implemented by cutting off hopping integrals from the  $3d/4f$ -orbitals in the central atom in

the supercell to neighboring atoms, thus fixing the number of the  $3d/4f$ -electrons, while other electrons can relax and screen the  $3d/4f$ -electrons [8]. Hybertsen *et al.* [9] and Cococcioni and Gironcoli [10] improved the cLDA method by taking into account the change in the kinetic energy, the latter based on linear response theory.

In this note, we will describe a different method based on the idea that the effective e-e interaction in the chosen subspace corresponding to the model Hamiltonian must be such that when it is screened by the electrons in the model, it reproduces the fully screened interaction of the real system. This suggests that screening channels associated with the model must be removed when computing  $U$  [11].

## 2.1 Screening and screened potential

The underlying concept common to methods for determining  $U$  is screening. Consider a many-electron system such as a solid in its ground state and let us apply a time-dependent external field  $V_{\text{ext}}(\mathbf{r}, t)$ . We wish to study within linear response theory how this external potential is screened by the electrons in the system. The external field induces a change in the electron density, which is given by

$$\rho_{\text{ind}}(\mathbf{r}, t) = \int d^3r' dt' R(\mathbf{r}, \mathbf{r}'; t - t') V_{\text{ext}}(\mathbf{r}', t'), \quad (8)$$

where  $R(\mathbf{r}, \mathbf{r}'; t - t')$  is the linear density response function, which depends only on the relative time  $t - t'$  since the Hamiltonian of the system is assumed to be time-independent, and it is a property of the system, independent of the applied external field  $V_{\text{ext}}$ . The induced density  $\rho_{\text{ind}}$ , in turn, generates an induced potential

$$V_{\text{ind}}(\mathbf{r}, t) = \int d^3r' v(\mathbf{r} - \mathbf{r}') \rho_{\text{ind}}(\mathbf{r}', t), \quad (9)$$

where  $v(\mathbf{r} - \mathbf{r}') = 1/|\mathbf{r} - \mathbf{r}'|$  is the Coulomb interaction. The total potential or the screened potential is then given by

$$V_{\text{scr}}(\mathbf{r}, t) = V_{\text{ext}}(\mathbf{r}, t) + V_{\text{ind}}(\mathbf{r}, t). \quad (10)$$

Using  $V_{\text{ind}}$  in Eq. (9) and  $\rho_{\text{ind}}$  in Eq. (8) we find

$$\begin{aligned} V_{\text{scr}}(\mathbf{r}, t) &= V_{\text{ext}}(\mathbf{r}, t) + \int d^3r' v(\mathbf{r} - \mathbf{r}') \rho_{\text{ind}}(\mathbf{r}', t) \\ &= V_{\text{ext}}(\mathbf{r}, t) + \int d^3r' v(\mathbf{r} - \mathbf{r}') \int d^3r'' dt' R(\mathbf{r}', \mathbf{r}''; t - t') V_{\text{ext}}(\mathbf{r}'', t'). \end{aligned} \quad (11)$$

It is convenient to work in frequency space by using the Fourier transform defined according to

$$f(\omega) = \int dt e^{i\omega t} f(t) \quad \text{and} \quad f(t) = \int \frac{d\omega}{2\pi} e^{-i\omega t} f(\omega). \quad (12)$$

Since the second term in the last line of Eq. (11) is a convolution in time, applying the Fourier transform to Eq. (11) yields

$$V_{\text{scr}}(\mathbf{r}, \omega) = V_{\text{ext}}(\mathbf{r}, \omega) + \int d^3r' d^3r'' v(\mathbf{r} - \mathbf{r}') R(\mathbf{r}', \mathbf{r}''; \omega) V_{\text{ext}}(\mathbf{r}'', \omega), \quad (13)$$

Regarding Eq. (13) as a matrix equation we have

$$V_{\text{scr}}(\omega) = [1 + vR(\omega)] V_{\text{ext}}(\omega), \quad (14)$$

which allows us to identify  $1 + vR(\omega)$  as the inverse dielectric matrix

$$\epsilon^{-1}(\omega) = 1 + vR(\omega). \quad (15)$$

## 2.2 Screened Coulomb interaction

We can now apply the general formulation in the previous section to write down the screened Coulomb interaction. As the external field we consider the instantaneous bare electron-electron interaction

$$V_{\text{ext}}(\mathbf{r}t, \mathbf{r}'t') = v(\mathbf{r} - \mathbf{r}') \delta(t - t'), \quad (16)$$

where we treat  $(\mathbf{r}', t')$  as parameters. Without loss of generality we may set  $t' = 0$ . This external field can be interpreted as an instantaneous Coulomb potential at point  $\mathbf{r}$  arising from a point charge located at  $\mathbf{r}'$ . Its Fourier transform is given by

$$V_{\text{ext}}(\mathbf{r}, \mathbf{r}'; \omega) = v(\mathbf{r} - \mathbf{r}'). \quad (17)$$

Since

$$\delta(t - t') = \int \frac{d\omega}{2\pi} e^{-i\omega(t-t')}, \quad (18)$$

the external field  $v(\mathbf{r} - \mathbf{r}') \delta(t - t')$  can also be regarded as a superposition of harmonic potentials with a common strength  $v(\mathbf{r} - \mathbf{r}')$ . From Eq. (13) the screened Coulomb interaction, which we now call  $W$ , fulfills the equation

$$\begin{aligned} W(\mathbf{r}, \mathbf{r}'; \omega) &= v(\mathbf{r} - \mathbf{r}') + \int d^3r_1 d^3r_2 v(\mathbf{r} - \mathbf{r}_1) R(\mathbf{r}_1, \mathbf{r}_2; \omega) v(\mathbf{r}_2 - \mathbf{r}') \\ &= \int d^3r'' \epsilon^{-1}(\mathbf{r}, \mathbf{r}''; \omega) v(\mathbf{r}'' - \mathbf{r}'), \end{aligned} \quad (19)$$

where we have used the definition of the inverse dielectric matrix in Eq. (15). In other words,  $W(\mathbf{r}, \mathbf{r}'; \omega) \exp(-i\omega t)$  is the screened interaction of the external field  $v(\mathbf{r} - \mathbf{r}') \exp(-i\omega t)$ . The screened Coulomb interaction  $W$  plays an important role in Green function theory since it determines the self-energy, e.g., in the Hedin equations [12–14].

We may introduce a polarization function defined as

$$\rho_{\text{ind}}(\mathbf{r}, t) = \int d^3r' dt' P(\mathbf{r}, \mathbf{r}'; t - t') V_{\text{scr}}(\mathbf{r}', t'), \quad (20)$$

i.e., as a response function but defined with respect to the screened potential given in Eq. (10).

We therefore have from Eq. (8)

$$\rho_{\text{ind}} = RV_{\text{ext}} = PV_{\text{scr}} = P(V_{\text{ext}} + V_{\text{ind}}). \quad (21)$$



Since

$$V_{\text{ind}} = v\rho_{\text{ind}} = vRV_{\text{ext}} \quad (22)$$

we obtain

$$RV_{\text{ext}} = P(1 + vR)V_{\text{ext}}. \quad (23)$$

Since  $V_{\text{ext}}$  is arbitrary, we find

$$R = P(1 + vR) = P\epsilon^{-1}. \quad (24)$$

In terms of the polarization function the screened interaction in Eq. (19) can then be written as

$$W = v + vRv = v + vP\epsilon^{-1}v = v + vPW. \quad (25)$$

Solving for  $W$  we find

$$W = [1 - vP]^{-1}v, \quad (26)$$

which allows us to identify the dielectric matrix as

$$\epsilon = 1 - vP. \quad (27)$$

### 2.3 Linear density response function

The exact expression for the linear density response function (hereafter referred to as response function) was derived by Kubo using time-dependent perturbation theory [15]. It can also be derived more conveniently using Green function theory in the interaction representation described in the Appendix. The exact expression for the time-ordered response function is given by

$$iR(1, 2) = \langle \Psi_0 | \Delta\hat{\rho}_H(2) \Delta\hat{\rho}_H(1) | \Psi_0 \rangle \theta(t_2 - t_1) + \langle \Psi_0 | \Delta\hat{\rho}_H(1) \Delta\hat{\rho}_H(2) | \Psi_0 \rangle \theta(t_1 - t_2), \quad (28)$$

where we have used the notation  $1 = (\mathbf{r}_1, t_1)$ , etc.,  $\Psi_0$  is the many-electron ground state and

$$\Delta\hat{\rho}_H(1) = \hat{\rho}_H(1) - \rho(1) \quad (29)$$

is the density fluctuation operator in the Heisenberg picture

$$\Delta\hat{\rho}_H(\mathbf{r}, t) = e^{i\hat{H}t} \Delta\hat{\rho}(\mathbf{r}) e^{-i\hat{H}t}. \quad (30)$$

$\hat{H}$  is the Hamiltonian of the many-electron system, assumed to be independent of time.

The Fourier transform of the response function is given by (see Appendix)

$$R(\mathbf{r}, \mathbf{r}'; \omega) = \sum_n \left[ \frac{\langle \Psi_0 | \Delta\hat{\rho}(\mathbf{r}) | \Psi_n \rangle \langle \Psi_n | \Delta\hat{\rho}(\mathbf{r}') | \Psi_0 \rangle}{\omega - E_n + E_0 + i\eta} - \frac{\langle \Psi_0 | \Delta\hat{\rho}(\mathbf{r}') | \Psi_n \rangle \langle \Psi_n | \Delta\hat{\rho}(\mathbf{r}) | \Psi_0 \rangle}{\omega + E_n - E_0 - i\eta} \right], \quad (31)$$

where  $\hat{H}|\Psi_n\rangle = E_n|\Psi_n\rangle$ . The term  $n = 0$ , corresponding to the ground state, is zero since  $\langle \Psi_0 | \Delta\hat{\rho}(\mathbf{r}) | \Psi_0 \rangle = 0$ .

## 2.4 Random phase approximation

For real materials it is virtually impossible to compute the exact response function, so in practice we must resort to approximations. The most successful approximation is the random phase approximation (RPA) developed by Bohm and Pines in the 1950's [16]. The RPA was originally derived from the equation of motion for the density fluctuation. Some years later Gell-Mann and Brueckner derived the RPA using a diagrammatic technique. It was later recognized that the RPA can be regarded simply as the time-dependent Hartree approximation, which can be seen most clearly within Green function theory described in the Appendix.

In the RPA, it is assumed that the density response of the many-electron system to an external perturbation is the same as the response to the screened potential,  $V_{\text{scr}} = V_{\text{ext}} + V_{\text{ind}}$ , but as if the system is non-interacting. Thus, if  $P^0$  is the non-interacting response function corresponding to some mean-field approximation for the many-electron system, then schematically

$$\rho_{\text{ind}} = RV_{\text{ext}} = P^0(V_{\text{ext}} + V_{\text{ind}}). \quad (32)$$

Since  $V_{\text{ind}} = v\rho_{\text{ind}} = vRV_{\text{ext}}$  and  $V_{\text{ext}}$  is arbitrary, we obtain

$$R = P^0 + P^0vR. \quad (33)$$

It is the same equation as Eq. (24) except that  $P$  has been replaced by  $P^0$ . The time-ordered non-interacting response function is given by (see Appendix)

$$P^0(\mathbf{r}, \mathbf{r}'; \omega) = -2 \sum_i^{\text{occ}} \sum_j^{\text{unocc}} \left( \frac{f_{ij}(\mathbf{r}, \mathbf{r}')}{\omega + (\varepsilon_j - \varepsilon_i - i\delta)} - \frac{f_{ij}^*(\mathbf{r}, \mathbf{r}')}{\omega - (\varepsilon_j - \varepsilon_i - i\delta)} \right), \quad (34)$$

where

$$f_{ij}(\mathbf{r}, \mathbf{r}') = \psi_i(\mathbf{r})\psi_j^*(\mathbf{r}')\psi_i^*(\mathbf{r})\psi_j(\mathbf{r}'). \quad (35)$$

It can also be obtained from the exact expression for the response function in Eq. (31) by using non-interacting many-electron states (single Slater determinants). The factor of two accounts for the two spin channels in the paramagnetic case and for a spin-polarized system we add up the polarization from each channel.  $\{\psi_i, \varepsilon_i\}$  are the eigenfunctions and eigenvalues of the non-interacting system, which are commonly chosen to be those of the LDA.

In practice both the polarization function and the response function are expanded according to

$$P(\mathbf{r}, \mathbf{r}'; \omega) = \sum_{\mathbf{k}\alpha\beta} B_{\mathbf{k}\alpha}(\mathbf{r}) P_{\alpha\beta}(\mathbf{k}, \omega) B_{\mathbf{k}\beta}^*(\mathbf{r}'), \quad (36)$$

where  $\{B_{\mathbf{k}\alpha}\}$  is a set of (two-particle) basis functions fulfilling the Bloch theorem

$$B_{\mathbf{k}\alpha}(\mathbf{r} + \mathbf{T}) = e^{i\mathbf{k}\cdot\mathbf{T}} B_{\mathbf{k}\alpha}(\mathbf{r}). \quad (37)$$

For example,  $B_{\mathbf{k}\alpha}(\mathbf{r}) = \exp[i(\mathbf{k} + \mathbf{G})\cdot\mathbf{r}]$ , in which the label  $\alpha$  denotes the reciprocal lattice vector  $\mathbf{G}$ . Another example is a product basis [14] based on the linear muffin-tin orbital (LMTO)

method [17]:

$$B_{\mathbf{k}\alpha}(\mathbf{r}) = \sum_{\mathbf{T}} e^{i\mathbf{k}\cdot\mathbf{T}} b_{\mathbf{R}\alpha}(\mathbf{r} - \mathbf{T}), \quad (38)$$

$$b_{\mathbf{R}\alpha}(\mathbf{r}) = \chi_{\mathbf{R}L}(\mathbf{r}) \chi_{\mathbf{R}L'}(\mathbf{r}), \quad (39)$$

where  $\chi_{\mathbf{R}L}$  is an LMTO centered at atom  $\mathbf{R}$  with angular momentum  $L$  and  $\alpha = (L, L')$ . It is worth noting that the basis  $\{B_{\mathbf{k}\alpha}\}$  is by construction complete for  $P$  and  $R$ , but it is not in general complete for  $W$ . As can be seen in Eq. (19), to expand  $W$  a complete basis for the bare Coulomb interaction is needed.

## 2.5 The constrained RPA method

Our aim is to determine the effective e-e interaction among electrons residing in a given subspace, which can represent a partially filled narrow band across the Fermi level typically originating from  $3d$ - or  $4f$ -orbitals found in strongly correlated systems. The physical assumption is that when the effective e-e interaction is screened by electrons residing in the subspace, the resulting screened interaction should reproduce the screened interaction of the full system [11]. If  $P$  is the polarization of the full many-electron system the screened interaction is given by

$$W = v + vPW. \quad (40)$$

Let  $P^d$  be the polarization of the subspace such as the  $3d$ - or  $4f$ -band in the Hubbard model. We refer to this subspace as  $d$ -subspace and the rest of the Hilbert space as  $r$ -subspace. We require that

$$W = U + UP^dW \quad (41)$$

$$= (1 - UP^d)^{-1}U \quad (42)$$

which defines  $U$  as the effective e-e interaction in the  $d$  subspace. It is given by

$$U = W(1 - P^dW)^{-1}. \quad (43)$$

Within the RPA,  $P = P^0$  as given in Eq. (34) and  $P^d$  is given by the same expression except that the single-particle wave functions are restricted to those of the  $d$ -subspace. Eq. (43) provides an operational means for computing  $U$ .

Alternatively,  $U$  can be written in a physically more transparent form. The total polarization can be decomposed according to

$$P = P^d + P^r, \quad (44)$$

which is illustrated in Fig. 1. From Eq. (26) we have [11]

$$\begin{aligned} W &= (1 - vP)^{-1}v \\ &= (1 - vP^r - vP^d)^{-1}v \\ &= ((1 - vP^r)(1 - (1 - vP^r)^{-1}vP^d))^{-1}v \\ &= (1 - (1 - vP^r)^{-1}vP^d)^{-1}(1 - vP^r)^{-1}v \end{aligned}$$

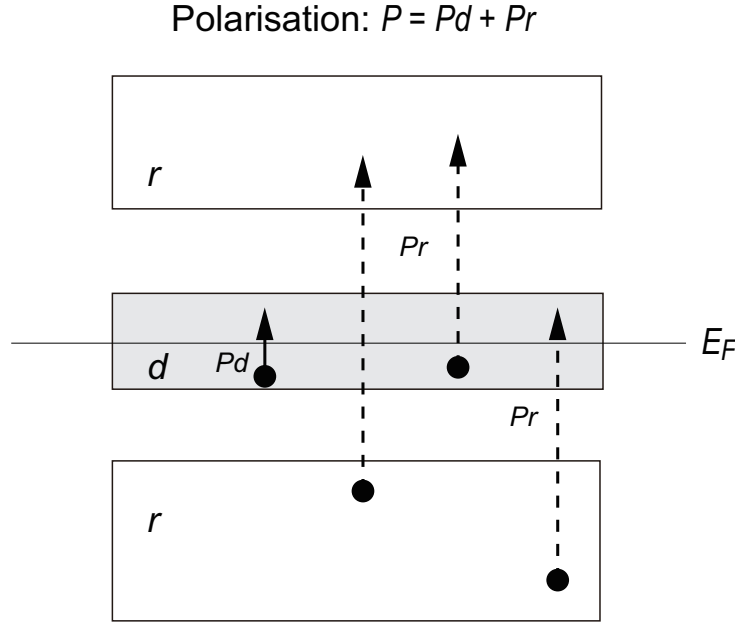


**Fig. 1:** Schematic illustration of the definitions of  $P^d$  and  $P^r$ . The former is confined to transitions inside the  $d$ -subspace whereas the latter contains both transitions inside the  $r$ -subspace as well as between the  $d$ - and  $r$ -subspaces.

Upon comparison with Eq. (42) we can verify that  $U$

$$U = (1 - vP^r)^{-1}v \quad (45)$$

$$U = v + vP^rU \quad (46)$$

which is consistent with the interpretation of  $U$  as the effective e-e interaction in the  $d$ -subspace since the bare interaction  $v$  is screened by  $P^r$ , which consists of those polarization channels that do not include the channels within the  $d$ -subspace.

Similar to the screened interaction  $W$  in Eq. (19) we may write

$$U = v + vR^rv, \quad (47)$$

where  $R^r$  satisfies

$$R^r = P^r + P^rvR^r, \quad (48)$$

$$R^r = (1 - P^rv)^{-1}P^r. \quad (49)$$

Writing out in full in position representation we obtain

$$U(\mathbf{r}, \mathbf{r}'; \omega) = v(\mathbf{r} - \mathbf{r}') + \int d^3r_1 d^3r_2 v(\mathbf{r} - \mathbf{r}_1) R^r(\mathbf{r}_1, \mathbf{r}_2; \omega) v(\mathbf{r}_2 - \mathbf{r}'). \quad (50)$$

Expanding  $R^r$  as in Eq. (36) we obtain

$$U(\mathbf{r}, \mathbf{r}'; \omega) = v(\mathbf{r} - \mathbf{r}') + \sum_{\mathbf{k}\alpha\beta} C_{\mathbf{k}\alpha}(\mathbf{r}) R_{\alpha\beta}^r(\mathbf{k}, \omega) C_{\mathbf{k}\beta}^*(\mathbf{r}'), \quad (51)$$

where

$$C_{\mathbf{k}\alpha}(\mathbf{r}) = \int d^3r_1 v(\mathbf{r} - \mathbf{r}_1) B_{\mathbf{k}\alpha}(\mathbf{r}_1). \quad (52)$$

The constrained RPA (cRPA) method provides an effective e-e interaction as a function of positions  $(\mathbf{r}, \mathbf{r}')$  and frequency  $\omega$  from which matrix elements of  $U$ , both local and non-local, needed as input in a model Hamiltonian can be extracted. Since the  $d$ -subspace usually corresponds to a partially filled narrow band across the Fermi level, as illustrated in Fig. 1,  $P^d$  contains the metallic screening whereas  $P^r = P - P^d$ , which determines  $U$ , contains no metallic screening so that  $U$  is intrinsically long range since the screening is incomplete, similar to the screened interaction in semiconductors and insulators.

## 2.6 Wannier orbitals

In most applications involving strongly correlated systems, we need to define a set of localized orbitals defining the annihilation and creation operators in the model Hamiltonian. The choice of localized orbitals is arbitrary. For example, they could be a set of pre-processed linearized muffin-tin orbitals (LMTO) [17] or a set of post-processed maximally localized Wannier orbitals [18] constructed from Bloch eigenstates generated from a band structure calculation. The Wannier function with band index  $n$  at cell  $\mathbf{R}$  is defined by

$$|\varphi_{\mathbf{R}n}\rangle = \frac{\Omega}{(2\pi)^3} \int_{BZ} d^3k e^{-i\mathbf{k}\cdot\mathbf{R}} |\psi_{\mathbf{k}n}^{(w)}\rangle, \quad (53)$$

where  $\Omega$  is the cell volume and  $|\psi_{\mathbf{k}n}^{(w)}\rangle$  is a linear combination of the eigenfunctions of a mean-field Hamiltonian

$$|\psi_{\mathbf{k}n}^{(w)}\rangle = \sum_m |\psi_{\mathbf{k}m}\rangle \mathcal{U}_{mn}(\mathbf{k}). \quad (54)$$

In practical implementations, the Kohn-Sham wavefunctions are usually used for  $|\psi_{\mathbf{k}m}\rangle$ . In the maximally localized Wannier function scheme, the coefficients  $\mathcal{U}_{mn}(\mathbf{k})$ 's are determined by minimizing the extent of the Wannier orbitals [18]

$$\Omega = \sum_n (\langle \varphi_{0n} | r^2 | \varphi_{0n} \rangle - |\langle \varphi_{0n} | \mathbf{r} | \varphi_{0n} \rangle|^2). \quad (55)$$

After defining a set of localized orbitals we now compute the matrix elements of  $U$  in these orbitals. From Eq. (51), taking the matrix elements of  $U$  as defined in Eq. (3), we obtain

$$U_{ijkl}^{\sigma\sigma'}(\mathbf{R}, \mathbf{R}'; \omega) = v_{ijkl}^{\sigma\sigma'}(\mathbf{R}, \mathbf{R}') + \sum_{\mathbf{k}\alpha\beta} \langle \varphi_{\mathbf{R}i} \varphi_{\mathbf{R}l}^* | C_{\mathbf{k}\alpha} \rangle R_{\alpha\beta}^r(\mathbf{k}, \omega) \langle C_{\mathbf{k}\beta} | \varphi_{\mathbf{R}'j}^* \varphi_{\mathbf{R}'k} \rangle, \quad (56)$$

where  $C_{\mathbf{k}\alpha}$  is defined in Eq. (52) and

$$U_{ijkl}^{\sigma\sigma'}(\mathbf{R}, \mathbf{R}'; \omega) = \int d^3r d^3r' \varphi_{\mathbf{R}i}^*(\mathbf{r}) \varphi_{\mathbf{R}'j}^*(\mathbf{r}') U(\mathbf{r}, \mathbf{r}'; \omega) \varphi_{\mathbf{R}'k}(\mathbf{r}') \varphi_{\mathbf{R}l}(\mathbf{r}). \quad (57)$$

## 2.7 cRPA for entangled bands

For isolated bands the Wannier orbitals are well defined and they reproduce the bands. However, in many applications it may happen that the narrow bands which are to be modelled are not isolated so the Wannier orbitals are not unique. For this case, we optimize  $\mathcal{U}_{mn}(\mathbf{k})$  with  $m$  limited to the states inside a chosen energy window. For a given  $\mathbf{k}$ -point the number of bands is equal to or larger than the number of  $m$ . The Wannier functions are more localized the larger the energy window, since optimization is done in a wider Hilbert space. The band structure  $\{\tilde{\psi}_{\mathbf{k}m}, \tilde{\epsilon}_{\mathbf{k}m}\}$  computed using these Wannier orbitals will not in general reproduce the original band structure.  $\{\tilde{\psi}_{\mathbf{k}m}\}$  define the  $d$ -subspace and we introduce the projection operator [19]

$$P_{\mathbf{k}} = \sum_m |\tilde{\psi}_{\mathbf{k}m}\rangle \langle \tilde{\psi}_{\mathbf{k}m}|. \quad (58)$$

We define the  $r$ -subspace as follows:

$$|\phi_{\mathbf{k}n}\rangle = (1 - P_{\mathbf{k}})|\psi_{\mathbf{k}n}\rangle, \quad (59)$$

where  $\{\psi_{\mathbf{k}n}\}$  are the original Bloch states. The states  $\{\phi_{\mathbf{k}n}\}$  are not orthonormal but they are evidently orthogonal to the  $d$ -subspace. The one-particle Hamiltonian is now calculated using  $\{\tilde{\psi}_{\mathbf{k}m}\}$  and  $\{\phi_{\mathbf{k}n}\}$  as basis functions, but as an approximation, the coupling between the  $d$ - and  $r$ -subspaces is set to zero

$$H = \begin{bmatrix} H_{dd} & 0 \\ 0 & H_{rr} \end{bmatrix}, \quad (60)$$

where  $H_{dd}$  is the Hamiltonian matrix calculated in the  $d$ -subspace, which is already diagonal,  $\{\tilde{\psi}_{\mathbf{k}m}\}$  and  $H_{rr}$  is calculated in the subspace of  $\{\phi_{\mathbf{k}n}\}$ .

The total polarization function is then computed from the new disentangled band structure obtained from the Hamiltonian in Eq. (60) and  $P^d$  is computed from  $\{\tilde{\psi}_{\mathbf{k}m}, \tilde{\epsilon}_{\mathbf{k}m}\}$ . It would seem reasonable to use the total polarization function  $P$  calculated from the original band structure but this procedure leads to oscillations in  $U$  at low energy due to the presence of low-lying polarizations not completely eliminated from  $P$  when calculating  $P^r = P - P^d$ .

## 3 Examples

In the following we will describe applications of the cRPA method to some real materials to illustrate what information can be extracted from the calculations.

### 3.1 Cubic perovskite $\text{SrVO}_3$

As a first example, we consider a prototype of a correlated metal, the cubic perovskite  $\text{SrVO}_3$ . This example has been considered before in Ref. [20] but it is included here since it provides an ideal illustration for the cRPA method. As can be seen in Fig. 2 the  $t_{2g}$ -bands cross the Fermi level and are well isolated from other bands. These three  $t_{2g}$ -bands form the  $d$ -subspace, which

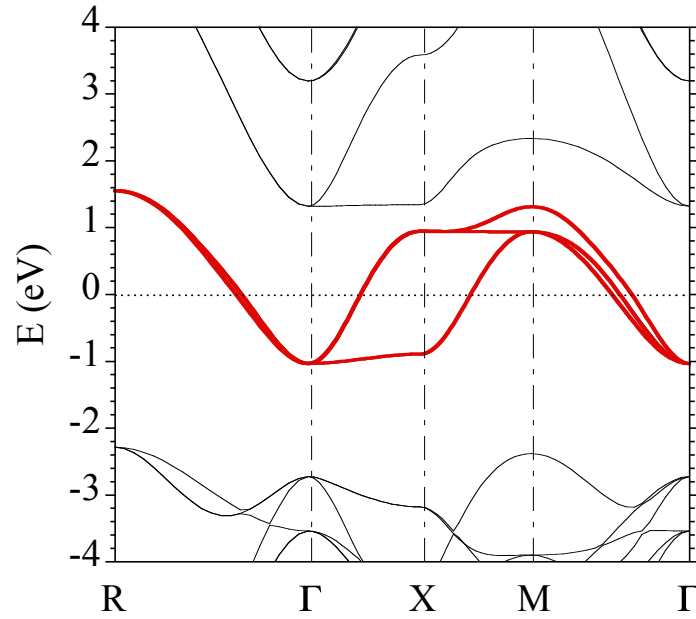


**Fig. 2:** The LDA band structure of metallic  $\text{SrVO}_3$  with cubic perovskite structure. The red lines correspond to the three  $t_{2g}$ -bands which define the  $d$ -subspace and are isolated from the rest of the bands [20].

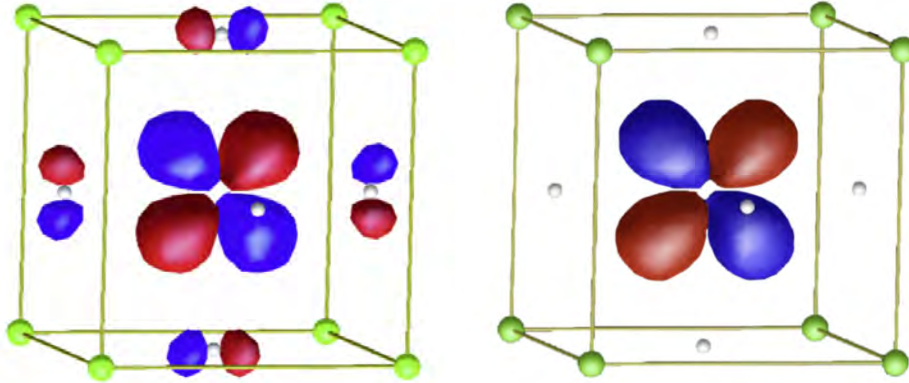


**Fig. 3:** The maximally localized Wannier functions of  $\text{SrVO}_3$  centered at vanadium of  $xy$ ,  $yz$ , or  $xz$  character. If the horizontal and vertical directions are respectively assigned to be the  $x$  and  $z$  axes the shown Wannier function corresponds to  $xz$  character. The red (blue) represents the positive (negative) contour. (Green sphere = strontium, white sphere = oxygen). Left figure: The Wannier orbital is constructed from the vanadium  $t_{2g}$ -bands only. We note that the Wannier function has tails on the oxygen sites. Right figure: The Wannier orbital is constructed from the vanadium  $(t_{2g} + e_g)$ -bands and oxygen  $p$ -bands, which makes it clearly more localized on the vanadium site compared to the one on the left figure [20].

corresponds to the Hilbert space of the Hubbard model. One of the Wannier orbitals constructed from these  $t_{2g}$ -bands is shown on Fig. 3 (left). If the  $d$ -subspace is extended to include the  $e_g$ -bands and the oxygen  $p$ -bands, the Wannier orbitals of  $t_{2g}$ -symmetry become more localized, as can be seen on the right figure of Fig. 3.

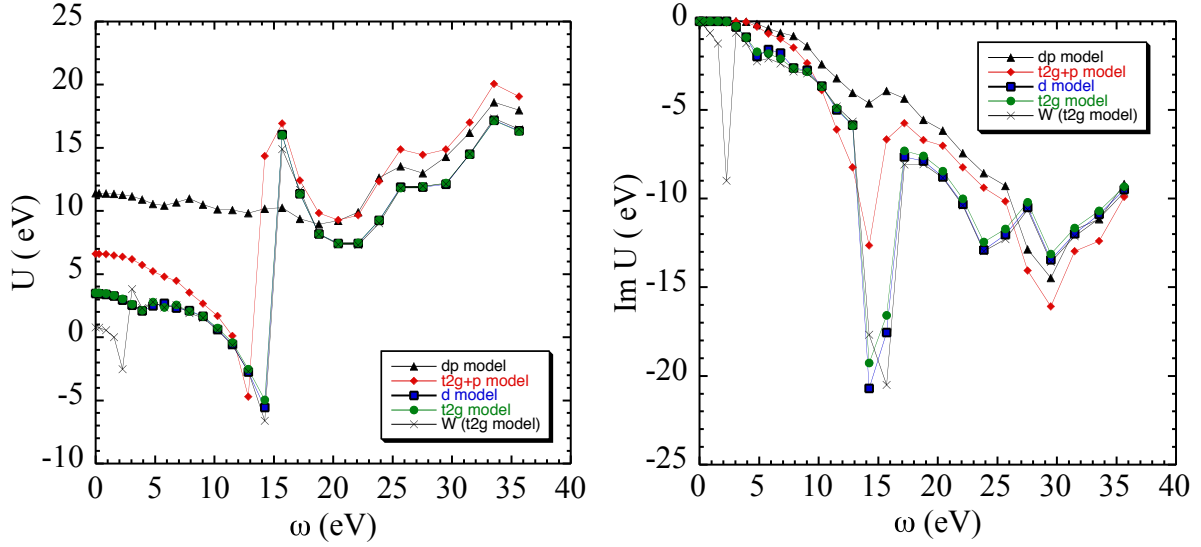


**Fig. 4:** Illustration of how the on-site Hubbard  $U = U_{iii}^{\sigma\sigma}(\mathbf{R}, \mathbf{R}; \omega)$  depends on the choice of the  $d$ -subspace indicated by the legends in the figure. The subscript  $i$  labels one of the  $t_{2g}$ -orbitals ( $xy$ ,  $yz$ , or  $xz$ ) and  $\mathbf{R}$  labels the vanadium atom.  $W$  is the fully screened interaction. The definitions of the models are summarized in Table 1 below. The left and right figures correspond respectively to the real and imaginary parts of  $U$  [20].

The on-site Hubbard  $U$  as a function of frequency for several choices of  $d$ -subspace is illustrated in Fig. 4. Several conclusions can be drawn from examining the imaginary part of  $W$  and  $U$ .  $\text{Im}(W)$  exhibits several sharp peaks, which correspond to collective excitations in the system. The peak at 2 eV arises from collective charge oscillations (plasmons) of electrons in the  $t_{2g}$ -bands whereas the peak at 15 eV corresponds to a plasmon excitation of electrons in the whole system. In the  $t_{2g}$ -model and other models, the peak at 2 eV disappears, which confirms the interpretation of it as a collective excitation of the  $t_{2g}$ -electrons since polarizations within the  $t_{2g}$ -bands are excluded in the models. We can also conclude that the 15 eV plasmon is dominated by the oxygen  $p$ -to-vanadium  $3d$  transitions since this peak disappears in the  $dp$ -model in which  $p$ -to- $d$  polarizations are excluded. The  $p$ -to- $e_g$  polarizations are apparently stronger than the  $p$ -to- $t_{2g}$  polarizations since in going from the  $t_{2g}$ -model to the  $(t_{2g} + p)$ -model, the plasmon peak at 15 eV is greatly reduced. As can be seen on the left of Fig. 4 the real part of  $U$  becomes increasingly constant as the  $d$ -subspace is enlarged and eventually it will approach the bare Coulomb interaction value, as expected.

**Table 1:** Definitions of models

model:	$t_{2g}$	$d$	$t_{2g}+p$	$dp$
$d$ - subspace:	$\text{V } t_{2g}$	$\text{V } (t_{2g} + e_g)$	$\text{V } t_{2g} + \text{O } p$	$\text{V } (t_{2g} + e_g) + \text{O } p$



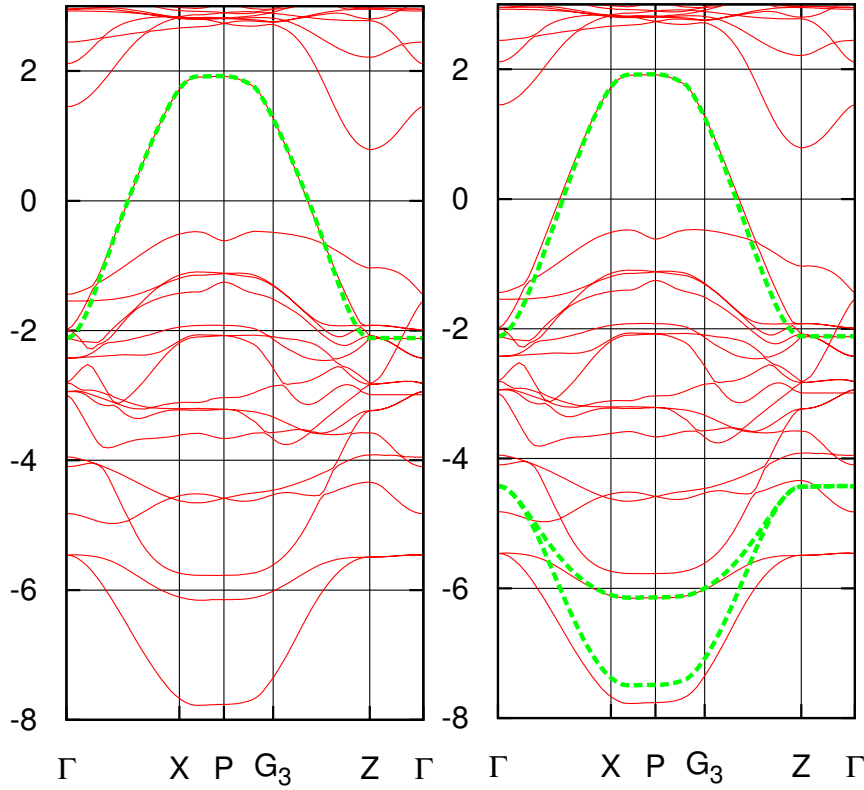


**Fig. 5:** LDA band structure of  $\text{La}_2\text{CuO}_4$ . The green dashed lines are the bands obtained from the Wannier orbitals and represent the  $d$ -subspace. Left figure: one-band model (anti-bonding  $\text{O } p_{x,y}$ - $\text{Cu } d_{x^2-y^2}$ ). Right figure: Emery's three-band model ( $\text{Cu } d_{x^2-y^2}$  and  $\text{O } p_x, p_y$ ) [21].

### 3.2 Undoped cuprate $\text{La}_2\text{CuO}_4$

The LDA band structure of  $\text{La}_2\text{CuO}_4$ , the parent compound of a prototype of high-temperature superconductors, is displayed in Fig. 5. The relevant bands arise from the copper  $d_{x^2-y^2}$  orbital and the two oxygen  $p_x$  and  $p_y$  orbitals on the  $\text{CuO}_2$  plane in which superconductivity is believed to originate. Since the bands to be modelled are not entirely isolated, the disentanglement procedure described in a previous section has been applied and the bands generated from the Wannier orbitals do not completely reproduce the original LDA bands.

The effective one-band model consists of a single orbital of  $d_{x^2-y^2}$  character at each Cu site. The three-band model includes also the two in-plane Wannier orbitals of O  $p_x/p_y$  character. Although the conduction bands in the two models look very similar the Wannier orbitals corresponding to the Cu  $d_{x^2-y^2}$  character are actually very different. In the one-band model the Cu-centered Wannier orbital is constructed from a few bands close to the Fermi energy, which leads to more delocalized Wannier orbitals than in the three-band model, in which more states are used to construct the Wannier orbitals. In the one-band model there is a one-to-one correspondence between the conduction band and the Wannier orbital of  $d_{x^2-y^2}$ -character spanning the  $d$ -subspace, while in the three-band model the conduction band is the antibonding combination of the  $p$ - and  $d$ -states and the two valence bands are the bonding and nonbonding combinations. The main  $d$ -weight is in the conduction band but there is also a small  $d$ -weight in the valence bands.

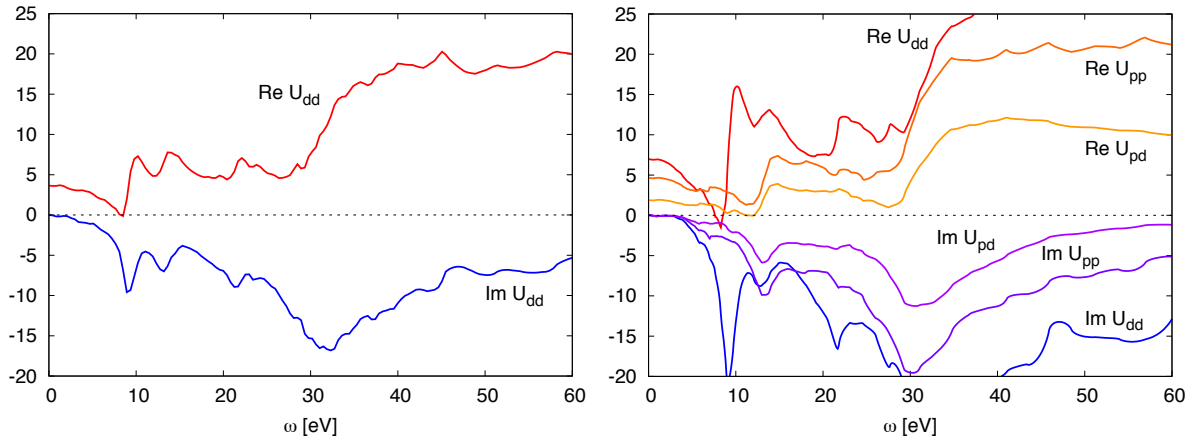


**Fig. 6:** The Hubbard  $U$  for  $\text{La}_2\text{CuO}_4$  for the one-band model (left panel) and the three-band model (right panel).  $U_{dd}$  and  $U_{pp}$  are respectively the on-site  $U$  on the copper and oxygen sites and  $U_{pd}$  is the off-site  $U$  between the copper and oxygen sites [21].

The Hubbard  $U$  for the one- and three-band models are shown in Fig. 6. It is to be noted that in both models, only transitions within the conduction band are excluded when calculating  $U$ . From the point of view of cRPA, the  $d$ -subspace is spanned by the conduction band only. The strong peak at 9 eV can be traced back to  $p$ -to- $d$  transitions corresponding to the collective charge oscillation of the oxygen  $p$ -electrons. It is interesting to note that the peak is not present in  $U_{pp}$ , indicating that the collective excitation has its main weight on the copper site [21]. A comparison between the left and right panels of Fig. 6 suggests different magnitudes of  $U$  for the two models. The reason for the larger magnitude of  $U_{dd}$  in the three-band model is due mainly to the more localized Wannier orbital. In the full three-band model in which the oxygen  $p$ -orbitals are treated as part of the  $d$ -subspace, the magnitude of  $U$  will be even larger since  $p$ -to- $d$  transitions are excluded when computing  $U$ .

Noteworthy is the significant size of the off-site  $U_{pd}$ , which evidently should not be neglected. It may, however, be sufficient to treat the effects of  $U_{pd}$  at the mean-field level.

### 3.3 Early lanthanides series

As a further example, the static  $U$  corresponding to the  $4f$ -bands of the early lanthanides series is shown in Fig. 7 (left) together with experimental estimates from XPS and BIS spectra. The cRPA values tend to be lower than the experimental estimates but noticeably follow the trend across the series rather closely and especially the jump at Eu and Gd is correctly captured [22]. The lower cRPA values are most likely due to the well known LDA problem in describing the band structure of the  $4f$ -series. Gadolinium may serve as an illustration for the problem with the LDA. In Fig. 8 the LDA  $4f$  density of states is compared with that of the LDA+ $U$ , the latter is known to be in good agreement with the experimental photoemission and inverse photoemission data. As can be seen, the LDA exchange splitting separating the occupied and unoccupied  $4f$ -bands is severely underestimated. Since the LDA  $4f$ -bands are too close to the Fermi level, cRPA calculations based on this LDA band structure overestimate screening and result in too small  $U$ . Indeed, when the band structure is calculated self-consistently within

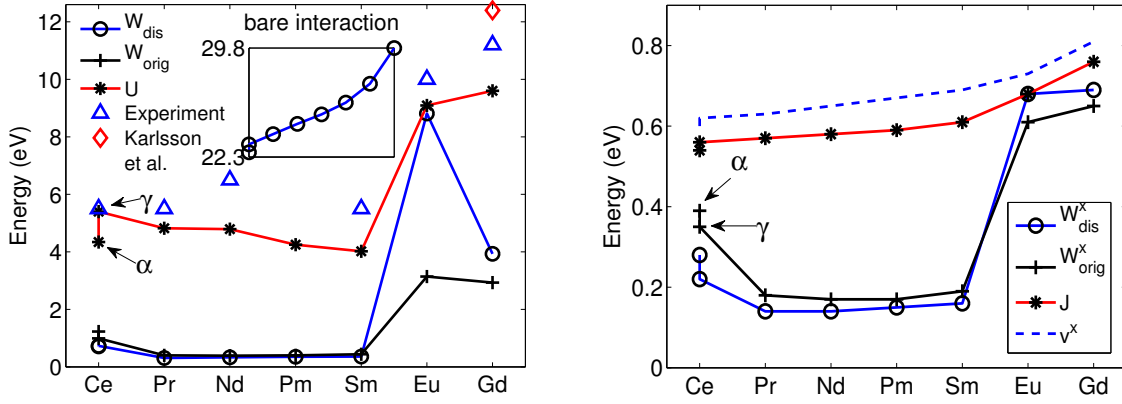


**Fig. 7:** Left: The average diagonal matrix element of the fully screened interaction  $W$  and the Hubbard  $U$  for the lanthanides at  $\omega = 0$ .  $W$  is calculated both using the original states ( $W_{orig}$ ) and the disentangled states ( $W_{dis}$ ). The experimental data are estimations of  $U$  from XPS and BIS spectra. The inset shows the average diagonal element of the bare interaction across the series. Right: The average exchange matrix element of the fully screened interaction ( $W^x$ ), the partially screened interaction ( $J$ ) and the bare interaction ( $v^x$ ) for the lanthanides [22].

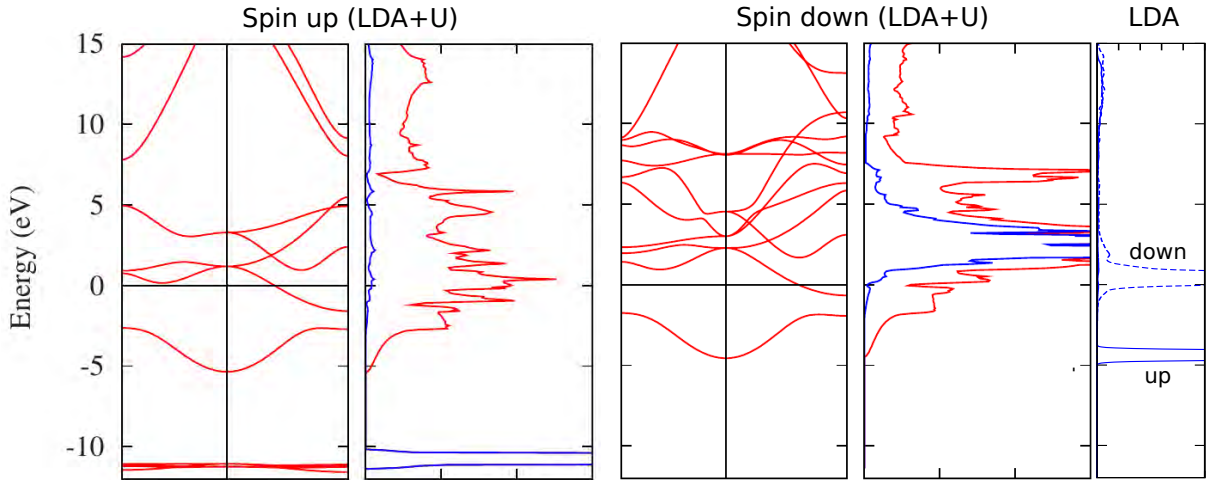


**Fig. 8:** LDA+ $U$  band structure, density of states (DOS) and partial  $f$ -DOS (blue) for gadolinium. The calculations were done using the parameters  $U = 12.4$  eV and  $J = 1.0$  eV. The experimental exchange splitting is approximately 12-13 eV. The displayed directions are  $\frac{1}{2}(1, 1, 1) \rightarrow \Gamma \rightarrow (1, 0, 0)$ . For comparison, we also show the partial  $f$ -DOS from a spin-polarized LDA calculation [23].

the LDA+ $U$  scheme, the cRPA value increases significantly and in better agreement with the experimental estimate [24]. This illustrates the importance of the one-particle part of the model Hamiltonian in capturing the correct Coulomb correlations.

In Fig. 7 (right) the exchange  $J$  across the series is also shown and compared with the bare values. It can be seen that the common procedure for approximating  $J$  by its unscreened atomic value is quite reasonable. This is as anticipated since the exchange interaction, which does not contain a  $l = 0$  charge component, is relatively immune to screening.

Since the  $4f$ -bands are entangled, as can be seen, e.g., in the case of gadolinium, the disentanglement procedure described above is also applied here. To measure quantitatively the quality of the disentangled band structure, the fully screened interactions computed using the original and disentangled band structures are compared in Fig. 7. With the exception of Eu, the small difference between the two indicates that the entangled band structure provides a good representation of the original band structure.

## 4 Summary

The reliable determination of the Hubbard  $U$  based on a realistic band structure of a given material has become feasible, allowing for a first-principles study of the electronic structure of strongly correlated materials. Theoretical calculations of the Hubbard  $U$  eliminate uncertainties and ambiguities associated with treating  $U$  as adjustable parameters. By analyzing the effects of the individual screening channels on the screened interaction, we can discern which screening channels are important, providing valuable physical insights and a guide for constructing a model Hamiltonian.

## Acknowledgments

Financial support from the Swedish Research Council (VR) is gratefully acknowledged.

## Appendix

### A Response functions from Green function formalism

The response functions can be derived from Green function by introducing a probing time-dependent field  $\varphi(\mathbf{r}, t)$  that couples to the charge density. In the presence of a time-dependent field it is convenient to work in the Dirac or interaction representation. In this representation the Green function is defined as, with the notation  $1 = (\mathbf{r}_1, t_1)$  etc.,

$$iG(1, 2) = \frac{\langle \Psi_0 | T[\hat{S} \hat{\psi}_D(1) \hat{\psi}_D(2)] | \Psi_0 \rangle}{\langle \Psi_0 | \hat{S} | \Psi_0 \rangle} \quad (61)$$

where  $\Psi_0$  is the many-electron ground state,  $\hat{\psi}_D$  is the field operator in the interaction picture

$$\hat{\psi}_D(\mathbf{r}, t) = e^{i\hat{H}t} \hat{\psi}(\mathbf{r}) e^{-i\hat{H}t}, \quad (62)$$

where  $\hat{H}$  is the many-electron Hamiltonian without the probing field  $\varphi(\mathbf{r}, t)$ . It is worth noting that in the interaction picture, the field operator does not depend on the probing field  $\varphi$ . The time-ordering operator  $T$  chronologically orders the field operators so that the operator containing the earliest time stands farthest to the right.  $\hat{S}$  is the scattering operator

$$\hat{S} = \hat{U}_D(\infty, -\infty), \quad (63)$$

where  $\hat{U}_D$  is the time-evolution operator in the interaction picture

$$\hat{U}_D(t, t') = T \exp \left( -i \int_{t'}^t d\tau \hat{\phi}(\tau) \right), \quad (64)$$

and

$$\hat{\phi}(t) = \int d^3r \hat{\rho}(\mathbf{r}, t) \varphi(\mathbf{r}, t). \quad (65)$$

The Green function satisfies the equation of motion

$$\left( i \frac{\partial}{\partial t_1} - h(1) \right) G(1, 2) - \int d3 \Sigma(1, 3) G(3, 2) = \delta(1 - 2), \quad (66)$$

where  $h$  is the one-particle part of the Hamiltonian that includes the probing field  $\varphi$  and the Hartree potential  $V_H$

$$h = -\frac{1}{2} \nabla^2 + V_{\text{ext}} + V_H + \varphi. \quad (67)$$

The time-ordered linear density response function is defined as

$$R(1, 2) = \frac{\delta \rho(1)}{\delta \varphi(2)}. \quad (68)$$

It is advantageous to work with the time-ordered response function since we are not restricted to  $t_1 > t_2$ , as in the case of the retarded version, so the functional derivative can be taken freely. The charge density can be obtained from the diagonal element of the Green function

$$\rho(1) = -iG(1, 1^+), \quad (69)$$

where  $1^+$  indicates that  $t_1^+ = t_1 + \eta$  where  $\eta$  is a positive infinitesimal. When taking the functional derivative of  $G$  with respect to the probing field  $\varphi$ , only the scattering operator  $\hat{S}$  is affected since the field operator in the interaction picture is independent of  $\varphi$ . The functional derivative of  $\hat{S}$  with respect to  $\varphi$  is given by

$$\frac{\delta \hat{S}}{\delta \varphi(2)} = \frac{\delta}{\delta \varphi(2)} T \exp \left( -i \int d1 \hat{\rho}(1) \varphi(1) \right) = -iT \left( \hat{S} \hat{\rho}(2) \right). \quad (70)$$

The response function is then

$$\begin{aligned} R(1, 2) &= \frac{\delta \rho(1)}{\delta \varphi(2)} = -i \frac{\delta G(1, 1^+)}{\delta \varphi(2)} = \frac{\delta}{\delta \varphi(2)} \frac{\langle \Psi | T \left( \hat{S} \hat{\rho}_D(1) \right) | \Psi \rangle}{\langle \Psi | \hat{S} | \Psi \rangle} \\ &= - \frac{i \langle \Psi | T \left( \hat{S} \hat{\rho}_D(2) \hat{\rho}_D(1) \right) | \Psi \rangle}{\langle \Psi | \hat{S} | \Psi \rangle} + \frac{i \langle \Psi | T \left( \hat{S} \hat{\rho}_D(1) \right) | \Psi \rangle \langle \Psi | T \left( \hat{S} \hat{\rho}_D(2) \right) | \Psi \rangle}{\langle \Psi | \hat{S} | \Psi \rangle^2} \end{aligned} \quad (71)$$

After taking the functional derivative of the density  $\rho(1) = -iG(1, 1^+)$  with respect to the applied field  $\varphi$ , we set  $\varphi = 0$ . This implies that  $\hat{S} = 1$  and the Dirac field operator becomes the Heisenberg field operator. We obtain the time-ordered linear density response function

$$iR(1, 2) = \langle \Psi | \Delta \hat{\rho}_H(2) \Delta \hat{\rho}_H(1) | \Psi \rangle \theta(t_2 - t_1) + \langle \Psi | \Delta \hat{\rho}_H(1) \Delta \hat{\rho}_H(2) | \Psi \rangle \theta(t_1 - t_2), \quad (72)$$

where the density fluctuation operator is given by

$$\Delta \hat{\rho}_H(1) = \hat{\rho}_H(1) - \rho(1). \quad (73)$$

To obtain the response function in the frequency representation we first insert a complete set of eigenstates of  $\hat{H}$  in between the density operators and use the definition of the Heisenberg operator, yielding

$$\begin{aligned} iR(1, 2) &= \sum_n \langle \Psi_0 | e^{i\hat{H}t_2} \Delta \hat{\rho}(\mathbf{r}_2) e^{-i\hat{H}t_2} | \Psi_n \rangle \langle \Psi_n | e^{i\hat{H}t_1} \Delta \hat{\rho}(\mathbf{r}_1) e^{-i\hat{H}t_1} | \Psi \rangle \theta(t_2 - t_1) \\ &\quad + \sum_n \langle \Psi_0 | e^{i\hat{H}t_1} \Delta \hat{\rho}(\mathbf{r}_1) e^{-i\hat{H}t_1} | \Psi_n \rangle \langle \Psi_n | e^{i\hat{H}t_2} \Delta \hat{\rho}(\mathbf{r}_2) e^{-i\hat{H}t_2} | \Psi_0 \rangle \theta(t_1 - t_2) \\ &= \sum_n \langle \Psi_0 | \Delta \hat{\rho}(\mathbf{r}_2) | \Psi_n \rangle \langle \Psi_n | \Delta \hat{\rho}(\mathbf{r}_1) | \Psi_0 \rangle e^{-i(E_n - E_0)(t_2 - t_1)} \theta(t_2 - t_1) \\ &\quad + \sum_n \langle \Psi_0 | \Delta \hat{\rho}(\mathbf{r}_1) | \Psi_n \rangle \langle \Psi_n | \Delta \hat{\rho}(\mathbf{r}_2) | \Psi_0 \rangle e^{-i(E_n - E_0)(t_1 - t_2)} \theta(t_1 - t_2) \end{aligned} \quad (74)$$

Performing the Fourier transform  $\int d\tau \exp(i\omega\tau) R(\tau)$ , where  $\tau = t_1 - t_2$ , yields

$$R(\mathbf{r}, \mathbf{r}'; \omega) = \sum_n \left[ \frac{\langle \Psi_0 | \Delta \hat{\rho}(\mathbf{r}) | \Psi_n \rangle \langle \Psi_n | \Delta \hat{\rho}(\mathbf{r}') | \Psi_0 \rangle}{\omega - E_n + E_0 + i\eta} - \frac{\langle \Psi_0 | \Delta \hat{\rho}(\mathbf{r}') | \Psi_n \rangle \langle \Psi_n | \Delta \hat{\rho}(\mathbf{r}) | \Psi_0 \rangle}{\omega + E_n - E_0 - i\eta} \right]. \quad (75)$$

The corresponding retarded response function, the well-known Kubo's formula, is given by

$$R^{\text{ret}}(\mathbf{r}, \mathbf{r}'; \omega) = \sum_n \left[ \frac{\langle \Psi_0 | \Delta \hat{\rho}(\mathbf{r}) | \Psi_n \rangle \langle \Psi_n | \Delta \hat{\rho}(\mathbf{r}') | \Psi_0 \rangle}{\omega - E_n + E_0 + i\eta} - \frac{\langle \Psi_0 | \Delta \hat{\rho}(\mathbf{r}') | \Psi_n \rangle \langle \Psi_n | \Delta \hat{\rho}(\mathbf{r}) | \Psi_0 \rangle}{\omega + E_n - E_0 + i\eta} \right], \quad (76)$$

which, in contrast to the time-ordered one, has all poles in the lower half plane. The response function gives information about the excitation spectrum of the system:  $\text{Im } R(\omega)$  has peaks whenever  $\omega = E_n - E_0$ , corresponding to the  $N$ -particle excitation energies.

If there is no magnetic field, i.e., if time-reversal symmetry is obeyed,

$$\langle \Psi_0 | \Delta \hat{\rho}(\mathbf{r}') | \Psi_n \rangle \langle \Psi_n | \Delta \hat{\rho}(\mathbf{r}) | \Psi_0 \rangle = \langle \Psi_0 | \Delta \hat{\rho}(\mathbf{r}) | \Psi_n \rangle \langle \Psi_n | \Delta \hat{\rho}(\mathbf{r}') | \Psi_0 \rangle \quad (77)$$

is real so that  $R$  satisfies

$$R(\mathbf{r}, \mathbf{r}'; -\omega) = R(\mathbf{r}, \mathbf{r}'; \omega), \quad (78)$$

$$R(\mathbf{r}, \mathbf{r}'; \omega) = R(\mathbf{r}', \mathbf{r}; \omega). \quad (79)$$

The response function  $R$  is the *time-ordered* response which differs from the *retarded* response  $R^{\text{ret}}$ . The two are related as

$$\text{Re } R(\omega) = \text{Re } R^{\text{ret}}(\omega), \quad (80)$$

$$\text{Im } R(\omega) \text{sgn}(\omega) = \text{Im } R^{\text{ret}}(\omega), \quad \text{sgn}(\omega) \equiv \omega/|\omega|, \quad (81)$$

valid for real  $\omega$ .

Compared with the original derivation of Kubo, the Schwinger functional derivative technique provides a simple way of deriving the response functions. We have derived the Kubo formula specifically for linear density response function. However, the method is applicable to a more general response function since any expectation value of a single-particle operator in the ground state is expressible in terms of the Green function. Moreover, higher-order density response functions can be readily worked out. For example, calculating the second-order density response function given by

$$R(1, 2, 3) = \frac{\delta^2 \rho(1)}{\delta \varphi(3) \delta \varphi(2)} = \frac{\delta R(1, 2)}{\delta \varphi(3)}, \quad (82)$$

is just a matter of inserting  $\delta \hat{S} / \delta \varphi$  at the appropriate places.

In reality, we must resort to approximations for the response function. A commonly used approximation is the RPA which can be derived from the equation of motion of the Green function in Eq. (66). We obtain after multiplying both sides of the equation by  $G^{-1}$

$$\left( i \frac{\partial}{\partial t_1} - h(1) \right) \delta(1 - 2) - \Sigma(1, 2) = G^{-1}(1, 2), \quad (83)$$

Since

$$h = -\frac{1}{2} \nabla^2 + V_{\text{ext}} + V_{\text{H}} + \varphi \quad (84)$$

we find

$$\frac{\delta G^{-1}(1, 2)}{\delta \varphi(3)} = -\delta(1 - 2) \left( \delta(1 - 3) + \frac{\delta V_H(1)}{\delta \varphi(3)} \right) - \frac{\delta \Sigma(1, 2)}{\delta \varphi(3)}. \quad (85)$$

We wish, however, to calculate  $\delta G/\delta \varphi$ , which can be obtained by using the identity

$$\int d4 \left( \frac{\delta G^{-1}(1, 4)}{\delta \varphi(3)} G(4, 2) + G^{-1}(1, 4) \frac{\delta G(4, 2)}{\delta \varphi(3)} \right) = 0, \quad (86)$$

which follows from taking the functional derivative with respect to  $\varphi$  of

$$\int d4 G^{-1}(1, 4) G(4, 2) = \delta(1 - 2). \quad (87)$$

From Eq. (86) we find

$$\frac{\delta G(1, 2)}{\delta \varphi(3)} = - \int d4 d5 G(1, 4) \frac{\delta G^{-1}(4, 5)}{\delta \varphi(3)} G(5, 2). \quad (88)$$

The response function is then

$$R(1, 2) = \frac{\delta \rho(1)}{\delta \varphi(2)} = -i \frac{\delta G(1, 1^+)}{\delta \varphi(2)} = i \int d3 d4 G(1, 3) \frac{\delta G^{-1}(3, 4)}{\delta \varphi(2)} G(4, 1^+). \quad (89)$$

Using Eq. (85) with  $\delta \Sigma/\delta \varphi = 0$  yields the RPA

$$\begin{aligned} R(1, 2) &= -i \int d3 d4 G(1, 3) \delta(3 - 4) \left( \delta(3 - 2) + \frac{\delta V_H(3)}{\delta \varphi(2)} \right) G(4, 1^+) \\ &= -i \int d3 G(1, 3) \left( \delta(3 - 2) + \frac{\delta V_H(3)}{\delta \varphi(2)} \right) G(3, 1^+). \end{aligned} \quad (90)$$

Identifying the polarization function as

$$P(1, 2) = -i G(1, 2) G(2, 1^+) \quad (91)$$

and using

$$V_H(3) = \int d4 v(3 - 4) \rho(4) \quad (92)$$

we obtain the RPA equation

$$R(1, 2) = P(1, 2) + \int d3 d4 P(1, 3) v(3 - 4) R(4, 2). \quad (93)$$

Using the convolution theorem, the Fourier transform of the polarization function becomes

$$P(\mathbf{r}, \mathbf{r}'; \omega) = -i \int \frac{d\omega'}{2\pi} G(\mathbf{r}, \mathbf{r}'; \omega + \omega') G(\mathbf{r}', \mathbf{r}; \omega'). \quad (94)$$

If we use a non-interacting Green function,

$$G^0(\mathbf{r}, \mathbf{r}'; \omega) = \sum_n^{\text{occ}} \frac{\psi_n(\mathbf{r}) \psi_n^*(\mathbf{r}')}{\omega - \varepsilon_n - i\delta} + \sum_n^{\text{unocc}} \frac{\psi_n(\mathbf{r}) \psi_n^*(\mathbf{r}')}{\omega - \varepsilon_n + i\delta}, \quad (95)$$

and perform the frequency integral, we obtain the expression in Eq. (34). The RPA is sometimes referred to as the time-dependent Hartree approximation because when calculating the response function only the change in the Hartree potential with respect to the probing field is taken into account whereas the change in the self-energy,  $\delta \Sigma/\delta \varphi$ , is neglected.



## References

- [1] J. Hubbard, Proc. Royal Soc. London A **276**, 238 (1963)
- [2] H. Jones, Rev. Mod. Phys. **87**, 897 (2015)
- [3] A. Georges, G. Kotliar, W. Krauth, and M.J. Rozenberg, Rev. Mod. Phys. **68**, 13 (1996)
- [4] C. Herring: *Exchange interactions among itinerant electrons*, Vol. 4 of G.T. Rado and H. Suhl (eds.): *Magnetism* (Academic Press, New York, 1966)
- [5] B.N. Cox, M.A. Coulthard, and P. Loyd, J. Phys. F.: Metal Physics **4**, 807 (1974)
- [6] J.F. Herbst, R.E. Watson, and J.W. Wilkins, Phys. Rev. B **17**, 3089 (1978)
- [7] P.H. Dederichs, S. Blügel, R. Zeller, and H. Akai, Phys. Rev. Lett. **53**, 2512 (1984)
- [8] O. Gunnarsson, O.K. Andersen, O. Jepsen, and J. Zaanen, Phys. Rev. B **39**, 1708 (1989)
- [9] M.S. Hybertsen, M. Schlüter, N.E. Christensen, Phys. Rev. B **39**, 9028 (1989)
- [10] M. Cococcioni and S. de Gironcoli, Phys. Rev. B **71**, 035105 (2005)
- [11] F. Aryasetiawan, M. Imada, A. Georges, G. Kotliar, S. Biermann, and A.I. Lichtenstein, Phys. Rev. B **70**, 195104 (2004)
- [12] L. Hedin, Phys. Rev. **139**, A796 (1965)
- [13] L. Hedin and S. Lundqvist in Vol. 23, H. Ehrenreich, F. Seitz, and D. Turnbull (eds.): *Solid State Physics* (Academic, New York, 1969)
- [14] F. Aryasetiawan and O. Gunnarsson, Rep. Prog. Phys. **61**, 237 (1998)
- [15] A.L. Fetter and J.D. Walecka: *Quantum Theory of Many-Particle Systems* (McGraw-Hill, New York, 1971)
- [16] D. Pines: *Elementary Excitations in Solids* (Benjamin, New York, 1963)
- [17] O.K. Andersen, Phys. Rev. B **12**, 3060 (1975)
- [18] N. Marzari and D. Vanderbilt, Phys. Rev. B **56**, 12847 (1997)
- [19] T. Miyake, F. Aryasetiawan, and M. Imada, Phys. Rev. B **80**, 155134 (2009)
- [20] Chapter 7 of E. Pavarini, E. Koch, D. Vollhardt, and A.I. Lichtenstein (eds.): *The LDA+DMFT Approach to Strongly Correlated Materials*, Reihe Modeling and Simulation, Vol. 1 (Forschungszentrum Jülich, 2011)  
<http://www.cond-mat.de/events/correl11>
- [21] P. Werner, R. Sakuma, F. Nilsson, and F. Aryasetiawan, Phys. Rev. B **91**, 125142 (2015)

- [22] F. Nilsson, R. Sakuma, and F. Aryasetiawan, Phys. Rev. B **88**, 125123 (2013)
- [23] F. Nilsson and F. Aryasetiawan, Computation **6**, 26 (2018)
- [24] K. Karlsson, F. Aryasetiawan, and O. Jepsen, Phys. Rev. B **81**, 245113 (2010)

# 4 The Foundations of Dynamical Mean-Field Theory

Marcus Kollar

Center for Electronic Correlations and Magnetism,

Institute for Physics

University of Augsburg

## Contents

<b>1</b>	<b>Introduction</b>	<b>2</b>
<b>2</b>	<b>Fermions in the limit of infinite lattice dimension</b>	<b>2</b>
<b>3</b>	<b>Consequences for many-body theory</b>	<b>6</b>
3.1	Green function, spectral function, self-energy, quasiparticles . . . . .	6
3.2	Hubbard bands and the Mott transition . . . . .	9
3.3	Diagrammatic perturbation theory . . . . .	10
3.4	Power counting in $1/d$ . . . . .	11
3.5	Local self-energy . . . . .	12
<b>4</b>	<b>Dynamical mean-field theory</b>	<b>13</b>
4.1	Path-integral representation . . . . .	13
4.2	Mapping onto effective impurity models . . . . .	14
4.3	Dynamical mean-field equations . . . . .	15
4.4	Results for the Hubbard model . . . . .	16
4.5	Results for the Falicov-Kimball model . . . . .	17
<b>5</b>	<b>Summary and outlook</b>	<b>19</b>

# 1 Introduction

In this Lecture the foundations of dynamical mean-field theory (DMFT) for interacting electrons will be reviewed along the following route. As already described in the Lecture of D. Vollhardt, the first step involves the limit of infinite lattice dimension,  $d \rightarrow \infty$ . We will discuss this limit for fermions in Sec. 2. The resulting scaling of hopping parameters with  $d$  then makes the effect of electronic interactions in Hubbard-type models more manageable, as discussed in Sec. 3. Namely, the Feynman diagrams contributing to the Green function in perturbation theory simplify, and as a result the self-energy becomes local, i.e., independent of momentum. The derivation of DMFT is then completed by mapping Hubbard-type models in infinite dimensions to single-site impurity models with a self-consistency condition (Sec. 4), which have the same self-energy but can be solved numerically. Note that other derivations of this last step are available [1–5]. Note also that the present lecture notes draw largely on a previous presentation [6]. The Hubbard model is the simplest model for describing the physics of correlated electrons, i.e., electrons which do not behave independently due to their Coulomb interaction. For a single band it can be written as

$$H = H_0 + H_1, \quad (1a)$$

$$H_0 = \sum_{ij\sigma} t_{ij} c_{i\sigma}^\dagger c_{j\sigma} = \sum_{\mathbf{k}\sigma} \varepsilon_{\mathbf{k}} c_{\mathbf{k}\sigma}^\dagger c_{\mathbf{k}\sigma}, \quad (1b)$$

$$H_1 = U \sum_i n_{i\uparrow} n_{i\downarrow}, \quad (1c)$$

where  $t_{ij}$  is the hopping amplitude from site  $i$  to  $j$ , and the dispersion relation  $\varepsilon_{\mathbf{k}}$  is its Fourier transform; for our purposes we will assume a tight-binding form. For each doubly occupied site the Hubbard interaction  $U$  is contributed to the energy of a state. To describe the electronic structure of correlated materials, more complicated models and methods are typically needed, e.g., involving several bands as obtained from density functional theory, including more complicated on-site interactions, taking retardation effects into account, reconciling a calculated charge distribution with the model parameters determined by it, nonlocal and nonequilibrium effects, and so on. For these topics we refer to the other Lectures in this book. In these contexts, as well as for (1), the goal and spirit of DMFT is to provide a controlled starting point for a reliable treatment of interactions and the induced electronic correlations.

## 2 Fermions in the limit of infinite lattice dimension

We begin with the limit of infinite spatial dimensions,  $d \rightarrow \infty$ , as introduced in Ref. [7]. First the three-dimensional simple cubic lattice is generalized to the  $d$ -dimensional hypercubic lattice in order to obtain the corresponding tight-binding dispersion for nearest-neighbor hopping. The

hypercubic lattice simply has the unit cell basis vectors

$$\begin{aligned} \mathbf{e}_1 &= (1, 0, 0, \dots, 0), \\ \mathbf{e}_2 &= (0, 1, 0, \dots, 0), \\ &\dots \\ \mathbf{e}_d &= (0, 0, 0, \dots, 1). \end{aligned} \quad (2)$$

A nearest-neighbor hopping amplitude  $t_{ij}$  and corresponding dispersion then have the form

$$t_{ij} = t(\mathbf{R}_i - \mathbf{R}_j) = \begin{cases} -t & \text{if } \mathbf{R}_i - \mathbf{R}_j = \pm \mathbf{e}_n, \\ 0 & \text{otherwise,} \end{cases} \quad (3)$$

$$\varepsilon_{\mathbf{k}} = -2t \sum_{i=1}^d \cos k_i. \quad (4)$$

We will proceed in two ways to obtain the corresponding density of states ( $L$ : number of lattice sites)

$$\rho(\omega) = \frac{1}{L} \sum_{\mathbf{k}} \delta(\omega - \varepsilon_{\mathbf{k}}). \quad (5)$$

A succinct technique is to employ the central limit theorem for probability distributions [7]. One defines random variables  $X_i = \sqrt{2} \cos k_i$  in terms of independent random variables  $k_i$ , which are independently and uniformly distributed in the interval  $[-\pi, \pi]$ . Since  $X_i$  has zero mean and unit variance, the random variable  $X_d = \frac{1}{\sqrt{d}} \sum_{i=1}^d X_i$  converges in law to a normal distributed random variable  $X$ , again with zero mean and unit variance. Here convergence in law means that the distribution function of  $X_d$  converges to the normal distribution  $\exp(-x^2/2)/\sqrt{2\pi}$ . If we then consider the density of states  $\rho(\varepsilon)$  as the distribution function of the random variable  $\sqrt{2d} t X_d$ , we see that a finite density of states is obtained only if we scale the hopping amplitude is proportional to  $d^{-1/2}$  for  $d \rightarrow \infty$ . We thus have, replacing the sum over the first Brillouin zone in (5) by an integral in the thermodynamic limit,

$$\rho(\varepsilon) = \int \frac{d^d k}{(2\pi)^d} \delta(\varepsilon - \varepsilon_{\mathbf{k}}) = \frac{1}{2\pi|t_*|} \exp\left[-\frac{\varepsilon^2}{2t_*^2}\right] \quad \text{for } t = \frac{t_*}{\sqrt{2d}}, \quad (6)$$

where  $t_*$  is independent of  $d$ . We thus obtain a Gaussian density of states with finite variance, and hence also a finite kinetic energy per lattice site. With the scaling  $t \propto 1/\sqrt{d}$  the kinetic energy and the Hubbard interaction energy thus remain of the same order of magnitude in the limit  $d \rightarrow \infty$  and hence in competition with each other. Fig. 1 depicts several densities of states for different  $d$ , showing the approach to a Gaussian for large  $d$ .

Alternatively, one can follow the idea of the proof of the central limit theorem, which uses Fourier transforms of probability distributions. We thus consider the Fourier transform of

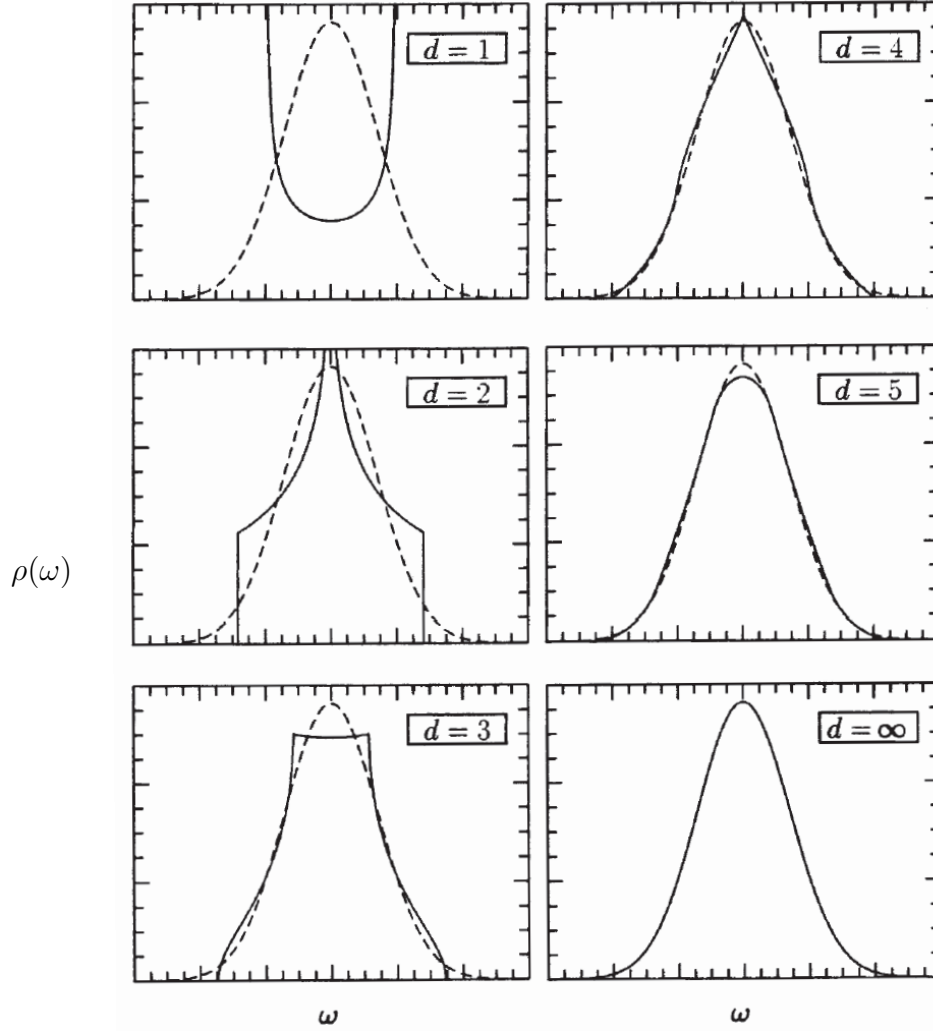


**Fig. 1:** Density of states for hopping on hypercubic lattice for several  $d$ , compared to the Gaussian that is obtained in  $d \rightarrow \infty$ . From Ref. [2].

$\rho(\varepsilon)$  [8], which separates into independent factors for each dimension,

$$\begin{aligned} \Phi(s) &= \int_{-\infty}^{\infty} d\varepsilon e^{is\varepsilon} \rho(\varepsilon) = \int \frac{d^d k}{(2\pi)^d} e^{is\varepsilon_{\mathbf{k}}} = \left[ \int_{-\pi}^{\pi} \frac{dk}{2\pi} \exp\left(-\frac{2ist_*}{\sqrt{2d}} \cos k\right) \right]^d \\ &= J_0\left(\frac{2st_*}{\sqrt{2d}}\right)^d = \left[1 - \frac{t_*^2 s^2}{2d} + \mathcal{O}\left(\frac{1}{d^2}\right)\right]^d = \exp\left[-\frac{t_*^2 s^2}{2} + \mathcal{O}\left(\frac{1}{d}\right)\right]. \end{aligned} \quad (7)$$

Here  $J_0(z)$  is a Bessel function, which has been Taylor expanded, integrated, and reexponentiated. Performing the inverse transform yields

$$\rho(\varepsilon) = \int_{-\infty}^{\infty} \frac{ds}{2\pi} e^{-is\varepsilon} \Phi(s) = \frac{1}{2\pi|t_*|} \exp\left[-\frac{\varepsilon^2}{2t_*^2} + \mathcal{O}\left(\frac{1}{d}\right)\right], \quad (8)$$

By keeping more terms in the Taylor expansion of the Bessel function one can derive further terms in an asymptotic series in powers of  $1/d$  [8].

We conclude that the nearest-neighbor hopping amplitude must be scaled with  $1/\sqrt{d}$  to obtain a meaningful large-dimensional limit. More generally, each hopping amplitude  $t_n$  must be scaled proportional to  $1/\sqrt{Z_n}$ , where the coordination number  $Z_n$  denotes the number of sites which are connected to a given site by  $t_n$ , e.g.,  $Z_1 = 2d$  for nearest-neighbor hopping and  $Z_2 = (2d - 1)2d = (Z - 1)Z$  for next-nearest-neighbor hopping on the hypercubic lattice, and so on. The density of states for a more complicated hopping matrix can also be obtained. For example, for nearest-neighbor and next-nearest-neighbor hopping a singularity develops at one of the band edges [9]. A general mapping can be constructed between the hopping matrix on the hypercubic lattice and its density of states [10, 11], which also to determine the hopping amplitudes for a given density of states.

A conceptual and practical drawback of a Gaussian density of states is that it extends up to infinite positive and negative energies  $\varepsilon$ . For other generalized lattices, such as the face-centered-hypercubic lattice [12] (which is asymmetric and has one finite band edge) or the hyperdiamond lattice [13] (for which the symmetric density of states vanishes at  $\varepsilon = 0$ ), the bandwidth is also infinite. One of the few lattices with finite bandwidth for nearest-neighbor hopping is the Bethe lattice, i.e., an infinite Cayley tree of which each node has  $Z$  nearest neighbors. This recursively defined lattice (which is not a periodic crystal lattice) has a semi-elliptic density of states with a finite bandwidth in the limit  $Z \rightarrow \infty$  for scaled nearest-neighbor hopping  $t = t_*/\sqrt{Z}$ ,

$$\rho_{\text{Bethe}}(\varepsilon) = \begin{cases} \frac{\sqrt{4t_*^2 - \varepsilon^2}}{2\pi t_*^2} & \text{for } |\varepsilon| \leq 2|t_*| \\ 0 & \text{otherwise} \end{cases}. \quad (9)$$

For comparison, for finite coordination number  $Z$ , the density of states reads  $\rho_{\text{Bethe},Z}(\varepsilon) = \rho_{\text{Bethe}}(\varepsilon) / [\frac{Z}{Z-1} - \frac{\varepsilon^2}{t_*^2/\sqrt{Z-1}}]$ . These results can be obtained, e.g., with recursive methods (see Refs. [14, 15] and references therein), which can also be used to find the density of states for longer-range hopping or to construct a set of hopping parameters yielding a given density of states.

It is rather typical for tight-binding dispersions in infinite dimensions to lead to one or both band edges at infinite energy. This is a qualitative difference to a finite-dimensional system which always has finite band edges for finite hopping amplitudes. In practice one therefore regards the simplifications following from the infinite-dimensional limit (discussed below) as independent of the dispersion, and simply uses the density of states of the finite-dimensional system of interest in the calculations. This is justified in particular for single-particle quantities into which only the dispersion  $\varepsilon_{\mathbf{k}}$  enters in infinite dimensions (but no detailed dependence on  $\mathbf{k}$ ). If necessary one can use one of the procedures, i.e., for the hypercubic [10] or Bethe lattice [14], to construct a set of hopping amplitudes that realizes a given density of states of a finite-dimensional lattice. Any density of states with finite bandwidth can be represented in infinite dimensions in this way, although long-ranged hopping amplitudes are typically required.

### 3 Consequences for many-body theory

The scaling of hopping amplitudes with negative powers of the dimension (or coordination number), discussed in the previous section, leads to simplifications in the many-body theory for Hubbard-type models such as (1). However, these simplifications will not hold at the Hamiltonian level, but rather at the level of Green functions and effective actions. We, therefore, first review some definitions and basic concepts of many-body theory that are essential for the formulation and understanding of DMFT.

#### 3.1 Green function, spectral function, self-energy, quasiparticles

The simplest dynamical quantity which measures the equilibrium properties of a correlated electron system is the electronic Green function [16–18]. A Green function  $G_{AB}$  is defined as an expectation value of operators  $A$  and  $B$  taken at different (real or imaginary) times in a thermal state, i.e., with density matrix  $\propto \exp(-\beta(H - \mu N))$  corresponding to the temperature  $T = 1/\beta$ , or possibly the ground state. Hence it measures the probability amplitude for a propagation of a particle or hole excitation in an equilibrium state if  $A$  and  $B$  are annihilation and creation operators. Note that this involves eigenstates of the Hamiltonian that differ by one in particle number, and which can describe quite different physical states in the presence of interactions.

In finite-temperature problems one uses the imaginary-time-ordered (fermionic) single-particle Green function  $G_{\alpha\beta}(\tau)$ , i.e., we put  $A = c_\alpha$ ,  $B = c_\beta^\dagger$ , with  $\alpha, \beta$  being general momentum or site indices, including also spin and orbital quantum numbers. For imaginary-time Heisenberg operators  $A(\tau) = e^{H\tau} A e^{-H\tau}$  (so that  $A^\dagger(\tau) \neq (A(\tau))^\dagger$ ), one defines

$$G_{\alpha\beta}(\tau) = -\langle T_\tau c_\alpha(\tau) c_\beta^\dagger(0) \rangle = - \begin{cases} \langle c_\alpha(\tau) c_\beta^\dagger(0) \rangle & \tau > 0 \\ -\langle c_\beta^\dagger(0) c_\alpha(\tau) \rangle & \tau \leq 0 \end{cases} \quad (10a)$$

$$= -G_{\alpha\beta}(\tau + \beta) \quad \text{for } -\beta < \tau < 0. \quad (10b)$$

(Note that in Ref. [17] the prefactor  $-1$  is not part of the definition.) The dependence only on time differences and the anti-periodicity (10b) follow from the cyclic properties of the trace and the fermionic anticommutation relations. The so-called Matsubara Green function  $G_{\alpha\beta}(i\omega_n)$  is obtained by Fourier transforming,

$$G_{\alpha\beta}(i\omega_n) = \int_0^\beta d\tau G_{\alpha\beta}(\tau) e^{i\omega_n \tau}, \quad (11)$$

$$G_{\alpha\beta}(\tau) = T \sum_{n=-\infty}^{+\infty} G_{\alpha\beta}(i\omega_n) e^{-i\omega_n \tau}, \quad (12)$$

with fermionic Matsubara frequencies  $i\omega_n = 2\pi T(n + 1/2)$ . An explicit expression for the Green function can be obtained by inserting the complete set of eigenstates of the Hamiltonian. One then obtains the spectral representation

$$G_{\alpha\beta}(i\omega_n) = \int_{-\infty}^{\infty} d\omega \frac{A_{\alpha\beta}(\omega)}{i\omega_n - \omega}, \quad (13)$$



with the spectral function  $A_{\alpha\beta}(\omega)$  given by its so-called Lehmann representation as

$$A_{\alpha\beta}(\omega) = \frac{1}{Z} \sum_{n,m} \langle n | c_{\beta}^{\dagger} | m \rangle \langle m | c_{\alpha} | n \rangle (e^{-\beta E_m} - e^{-\beta E_n}) \delta(\omega - (E_n - E_m)), \quad (14)$$

where  $Z$  is the partition function and  $E_n$  eigenvalues and  $|n\rangle$  the eigenstates of  $H - \mu N$ . We note that in particular  $A_{\alpha\alpha}(\omega) \geq 0$ . In practice the spectral or Green function can be evaluated via the Lehmann representation only for sufficiently small systems, i.e., when the many-body energy eigenvalues and eigenstates can be obtained directly. For a finite system, the spectral function (and Green function) consists of a finite sum of delta functions, but in the thermodynamic limit these functions typically become continuous just like the non-interacting density of states.

The spectral function occurs not only in the finite-temperature Matsubara Green function, but also, e.g., in the retarded Green function,

$$G_{\alpha\beta}^{\text{ret}}(\omega) = \int_{-\infty}^{\infty} d\omega' \frac{A_{\alpha\beta}(\omega')}{\omega + i0^+ - \omega'}, \quad (15)$$

which corresponds to a Green function in the time domain that involves real-time Heisenberg operators. From the pole structure it follows that

$$A_{\alpha\beta}(\omega) = -\frac{1}{\pi} \text{Im} G_{\alpha\beta}^{\text{ret}}(\omega), \quad (16)$$

and that the retarded Green function can be obtained from the Matsubara Green function by analytic continuation from  $i\omega_n$  to  $\omega + i0^+$ . (The advanced Green function, which is not discussed here, corresponds to the replacement of  $i\omega_n$  by  $\omega - i0^+$ ) Note that in a Matsubara Green function this replacement may only be done at the very end of a calculation, because the anti-periodicity in imaginary time must typically have been at work first. In view of the spectral representations (13) and (15) one often writes  $G_{\alpha\beta}(\omega)$  for both the Matsubara or retarded Green function, with the understanding that the argument is either  $i\omega_n$  for the former or  $\omega + i0^+$  for the latter, and hence is never purely real.

The indices  $\alpha, \beta, \dots$  represent lattice site or momentum  $\mathbf{k}$ , as well as spin index  $\sigma$  (and possibly orbital or band index). The real-space and momentum-space Green functions are related by a Fourier transform. Of particular importance is the local Green function

$$G_{ii\sigma}(\omega) = G_{\sigma}(\omega) = \frac{1}{L} \sum_{\mathbf{k}} G_{\mathbf{k}\sigma}(\omega), \quad (17)$$

$$A_{ii\sigma}(\omega) = A_{\sigma}(\omega) = -\frac{1}{\pi} \text{Im} G_{\sigma}(\omega + i0^+), \quad (18)$$

where translational invariance has been assumed, e.g., as in (3).

For non-interacting particles, with Hamiltonian  $H_0 - \mu N = \sum_{\mathbf{k}\sigma} (\varepsilon_{\mathbf{k}} - \mu) c_{\mathbf{k}\sigma}^{\dagger} c_{\mathbf{k}\sigma}$ , the free Green function  $G_{\mathbf{k}\sigma}^{(0)}(\omega)$  and the free density of states  $\rho(\varepsilon)$  are obtained as

$$G_{\mathbf{k}\sigma}^{(0)}(\omega) = \frac{1}{\omega + \mu - \varepsilon_{\mathbf{k}}}, \quad (19)$$

$$\rho(\omega) = A_{\sigma}^{(0)}(\omega) = \frac{1}{L} \sum_{\mathbf{k}} \delta(\omega - \varepsilon_{\mathbf{k}}). \quad (20)$$

For interacting systems the self-energy  $\Sigma_{\mathbf{k}}(\omega)$  is defined as the difference between free and interacting reciprocal Green functions:

$$G_{\mathbf{k}\sigma}(\omega)^{-1} = G_{\mathbf{k}\sigma}^{(0)}(\omega)^{-1} - \Sigma_{\mathbf{k}\sigma}(\omega), \quad (21a)$$

$$G_{\mathbf{k}\sigma}(\omega) = \frac{1}{\omega + \mu - \varepsilon_{\mathbf{k}} - \Sigma_{\mathbf{k}\sigma}(\omega)}. \quad (21b)$$

For a translationally invariant system the Green function and self-energy are diagonal in momentum space. It can also be useful instead to use a matrix notation in site indices,  $G_{ij\sigma}(i\omega_n) = (\mathbf{G})_{ij,\sigma,n}$  etc., for which

$$\mathbf{G}^{-1} = \mathbf{G}^{(0)-1} - \mathbf{\Sigma}, \quad (22a)$$

$$\mathbf{G} = \mathbf{G}^{(0)} + \mathbf{G}^{(0)} \mathbf{\Sigma} \mathbf{G}. \quad (22b)$$

Eq. (21) or (22) are referred to as the (lattice) Dyson equation.

Without interactions, single-particle excitations simply correspond to the creation or removal of a particle in an eigenstate of  $H_0$ , and as such they propagate freely through the lattice. This perfectly sharp excitation occurs as a  $\delta$ -function in the free spectral function (omitting spin indices for now),

$$A_{\mathbf{k}}^{(0)}(\omega) = \delta(\omega + \mu - \varepsilon_{\mathbf{k}}). \quad (23)$$

The situation in a many-body system with interactions is different: adding a particle or hole to an eigenstate does not give an eigenstate again, but rather a massive superposition of eigenstates. As a consequence, particle or hole excitations will usually be damped and have a finite lifetime. This is encoded in the complex (retarded) self-energy  $\Sigma_{\mathbf{k}}(\omega)$ , in terms of which the spectral function becomes

$$A_{\mathbf{k}}(\omega) = \frac{1}{\pi} \frac{\text{Im } \Sigma_{\mathbf{k}}(\omega)}{(\omega + \mu - \varepsilon_{\mathbf{k}} - \text{Re } \Sigma_{\mathbf{k}}(\omega))^2 + (\text{Im } \Sigma_{\mathbf{k}}(\omega))^2}. \quad (24)$$

This reduces to a  $\delta$ -function only if  $\text{Im } \Sigma_{\mathbf{k}}(\omega) \rightarrow 0^-$ . On the other hand, if  $\text{Im } \Sigma_{\mathbf{k}}(\omega)$  is finite and not too large, the maxima of  $A_{\mathbf{k}}(\omega)$  are located approximately at the zeros  $\omega = E_{\mathbf{k}}$  of

$$\omega + \mu - \varepsilon_{\mathbf{k}} - \text{Re } \Sigma_{\mathbf{k}}(\omega) = 0. \quad (25)$$

In the vicinity of  $E_{\mathbf{k}}$  the Green function can then be approximated to lowest order as

$$G_{\mathbf{k}}(\omega) = \frac{Z_{\mathbf{k}}(E_{\mathbf{k}})}{\omega - E_{\mathbf{k}} + i\tau_{\mathbf{k}}(E_{\mathbf{k}})^{-1}}, \quad (26a)$$

$$Z_{\mathbf{k}}(\omega) = [1 - \text{Re } \Sigma_{\mathbf{k}}(\omega)]^{-1}, \quad (26b)$$

$$\tau_{\mathbf{k}}(\omega) = [-Z_{\mathbf{k}}(\omega) \text{Im } \Sigma_{\mathbf{k}}(\omega)]^{-1}, \quad (26c)$$

where  $Z_{\mathbf{k}}$  and  $\tau_{\mathbf{k}}$  play the role of a quasiparticle weight and lifetime. In analogy to the non-interacting case, the maxima  $E_{\mathbf{k}}$  of  $A_{\mathbf{k}}(\omega)$  yield the *electronic dispersion*, i.e., the relation between crystal momentum and excitation energy, although this maximum may be quite broad.

A reliable quasiparticle picture is guaranteed in a Landau Fermi liquid close to the Fermi surface, i.e., near  $\omega = 0$ , because then  $\text{Re } \Sigma_{\mathbf{k}}(\omega)$  is linear and  $\text{Im } \Sigma_{\mathbf{k}}(\omega)$  quadratic in  $\omega$  for small frequencies at zero temperature. Near  $\omega = 0$  this leads to

$$E_{\mathbf{k}} = Z_{\mathbf{k}}(0)(\varepsilon_{\mathbf{k}} - \mu + \text{Re } \Sigma_{\mathbf{k}}(0)) , \quad (27)$$

i.e., a linear relation between non-interacting and interacting dispersion. However angle-resolved photoemission (ARPES) nowadays provides a means to measure  $A_{\mathbf{k}}(\omega)$  (times the Fermi function) even deep below the Fermi energy with high accuracy (see, e.g., Ref. [19]). Therefore the resonances given by (25) are relevant even if these excitations are not as coherent as low-energy excitations near the Fermi surface in a Landau Fermi liquid.

### 3.2 Hubbard bands and the Mott transition

Let us consider the atomic limit of the Hubbard model, i.e., no hopping,  $t_{ij} = 0$ . The Green function then becomes momentum-independent and reads

$$G_{\mathbf{k}\sigma}^{\text{at}}(\omega) = \frac{n_{-\sigma}}{\omega + \mu - U} + \frac{1 - n_{-\sigma}}{\omega + \mu} , \quad (28)$$

which corresponds to a spectral function with two  $\delta$ -peaks separated by an energy  $U$ , and the system is *insulating*, as there is no hopping at all. Next let us consider the situation for small hopping  $t_{ij}$ . Compared to the atomic limit the  $\delta$ -peaks in the spectral function will broaden, i.e., two subbands develop, the *Hubbard bands*. The nature of these subbands is quite different from that of one-electron bands in non-interacting systems. For example, the upper Hubbard band describes charge excitations on top of the filled lower Hubbard band. If the hopping is increased further, or the Hubbard interaction  $U$  decreased, these Hubbard bands will eventually overlap and the system will become metallic at a critical value  $U_c$  on the order of the bandwidth. This correlation-induced *metal-insulator transition* does not break translational invariance and is called the Mott transition [20].

When starting from the atomic limit, a standard but unreliable method to capture the Mott metal-insulator transition is the so-called Hubbard-I approximation. Here one uses the atomic self-energy, obtained from (28),

$$\Sigma_{\mathbf{k}\sigma}^{\text{at}}(\omega) = Un_{-\sigma} + U^2 \frac{n_{-\sigma}(1 - n_{-\sigma})}{\omega + \mu - U(1 - n_{-\sigma})} , \quad (29)$$

in the Dyson equation (21), which provides the Green function. However, this ad-hoc approximation exhibits several unphysical properties (discussed, e.g., in Ref. [21]). Starting from the weak-coupling side, a simple, rough picture of the Mott transition is provided by the Gutzwiller wave function (see [22] for a review), which describes a Mott insulator at half-filling when  $U$  becomes so large that all doubly occupied sites are projected out: this is the so-called Brinkman-Rice transition. These approximate understandings are quantitatively rather inaccurate. Indeed, one of the successes of DMFT has been its description of the Mott metal-insulator transition in the infinite-dimensional Hubbard model, as discussed in Sec. 4.4 below.

### 3.3 Diagrammatic perturbation theory

The self-energy, according to (22), represents the contribution to the (inverse) Green function which is due to interactions. The perturbation theory for these quantities can be organized effectively into Feynman diagrams as follows [16–18].

Feynman diagrams for single-particle Green functions (for arbitrary quadratic  $H_0$  and two-particle interaction  $H_1$ ) are built from the following pieces:

$$\text{————} = \text{non-interacting Green function line } G^{(0)}, \quad (30a)$$

$$\rangle \cdots \langle = \text{interaction vertex}, \quad (30b)$$

$$\text{====} = \text{full (interacting) Green function line } G. \quad (30c)$$

The perturbation expansion in  $H_1$  then produces a series of diagrams (unlabeled [17], and arrows omitted throughout) for the Green function

$$\text{====} = \text{————} + \text{————} \circ \text{————} + \text{————} \text{---} \text{————} + \text{————} \text{---} \text{————} \text{---} \text{————} + \text{————} \text{---} \text{————} \text{---} \text{————} + \text{————} \text{---} \text{————} \text{---} \text{————} \text{---} \text{————} + \dots \quad (31)$$

We will not review the diagrammatic rules here, but we note that each Green function line comes with a Matsubara frequency (or imaginary time) argument and a momentum (or site) argument, energy and momentum conservation holds at the interaction vertices, all variables of internal lines are integrated over, while the variables of external lines are held fixed.

Since some parts of the diagrams are repeating, one defines so-called proper self-energy diagrams, which are “one-particle irreducible” (i.e., cannot be cut in two pieces by cutting a single solid line) and have their external vertices amputated, which means that the non-interacting Green functions, which would normally be connected to external vertices, are omitted (because they already occur in other parts of the diagram). Some examples are:

$$\begin{array}{cccc} \text{proper} & \text{proper} & \text{not proper} & \text{proper} \\ \text{---} \circ \text{---} & \text{---} \text{---} \text{---} \text{---} & \text{---} \text{---} \text{---} \text{---} & \text{---} \text{---} \text{---} \text{---} \end{array} \quad (32)$$

The Dyson equation (21) can be expressed with Feynman diagrams as

$$\text{====} = \text{————} + \text{————} \text{---} \Sigma \text{---} \text{====}, \quad (33)$$

where the self-energy now has the following expansion,

$$\Sigma = \text{diagram 1} + \text{diagram 2} + \text{diagram 3} + \text{diagram 4} + \dots, \quad (34)$$

which, combined with (33), recovers (30).

This perturbation series for the self-energy has so far been written in terms of free Green functions, i.e.,  $\Sigma$  depends on the function  $G^{(0)}$  in the sense that the whole matrix  $G^{(0)}(i\omega_n)$  for all frequency arguments enters into  $\Sigma$ . In other words,  $\Sigma = \Sigma[G^{(0)}]$  is a *functional* of  $G^{(0)}$ . The diagrams for  $\Sigma[G^{(0)}]$  still contain self-energy insertions in their internal lines, i.e., some internal parts of the diagrams repeat which have already been enumerated. One can thus proceed to construct the so-called *skeleton expansion* which instead uses full (interacting) Green function lines  $G$

$$\Sigma = \text{diagram 1} + \text{diagram 2} + \text{diagram 3} + \dots \quad (35)$$

The diagrams in the skeleton expansion  $\Sigma[G]$  no longer contain self-energy insertions on the Green function lines so that each self-energy diagram does not occur more than once.

### 3.4 Power counting in $1/d$

The consequences that the scaling in the limit  $d \rightarrow \infty$  has for many-body theory [8, 23] is best discussed in terms of the Feynman diagrams for Green functions and the self-energy discussed above, in particular using the skeleton expansion.

We first consider the  $d$  dependence of  $G_{ij\sigma}(\omega)$  in the limit  $d \rightarrow \infty$ , for scaled hopping amplitudes

$$t_{ij} = t_{ij}^* d^{-\frac{1}{2} \|\mathbf{R}_i - \mathbf{R}_j\|}. \quad (36)$$

Here  $\|\mathbf{R}_i - \mathbf{R}_j\|$  is the fewest number of lattice steps that connect  $\mathbf{R}_i$  to  $\mathbf{R}_j$  on the hypercubic lattice, and hence proportional to the number of sites connected by the hopping amplitude  $t_{ij}$ , so that (36) has the correct scaling. By our construction the kinetic energy is finite in the limit  $d \rightarrow \infty$ , which can be expressed in terms of the Green function,

$$E_{\text{kin},\sigma} = \sum_{ij} t_{ij} \langle c_{i\sigma}^\dagger c_{j\sigma} \rangle = \sum_{ij} t_{ij} \int_{-\infty}^{\infty} \frac{d\omega}{2\pi i} G_{ij\sigma}(\omega) e^{i\omega 0^+} = \mathcal{O}(d^0). \quad (37)$$

Here the double sum yields a contribution of order  $L d^{\|\mathbf{R}_i - \mathbf{R}_j\|}$ . Hence we conclude

$$G_{ij\sigma}(\omega) = \mathcal{O}(d^{-\frac{1}{2} \|\mathbf{R}_i - \mathbf{R}_j\|}), \quad G_{ii\sigma}(\omega) = \mathcal{O}(d^0), \quad (38)$$

i.e., the off-diagonal Green function decays rapidly with distance, which leads to simplifications for the Feynman diagrams.

### 3.5 Local self-energy

For the discussion of the self-energy we will work with so-called Hugenholtz diagrams instead, which combine direct and exchange diagrams into a box vertex [17]. However, for the Hubbard interaction there are no exchange diagrams anyway. We thus replace

$$|i, \sigma\rangle \cdots \langle i, -\sigma| = U n_{i\uparrow} n_{i\downarrow} = \text{box vertex} \quad (39)$$

again omitting the arrows on the diagrams. We can then write the skeleton expansion as

$$\Sigma = \text{self-energy loop} + \text{two boxes connected by three lines} + \text{two boxes connected by two lines and one loop} + \dots \quad (40)$$

The skeleton expansion has the property that any two vertices are joined through Green function lines via at least three independent paths. Namely, suppose there is only one such path; then the diagram is one-particle irreducible, a contradiction. If there are only two paths, then they must run through a diagram part which is a self-energy insertion, which is also a contradiction.

Now consider an arbitrary diagram (in position space, so that the interaction vertices are labeled by lattice site vectors), in which two internal vertices labeled by  $i$  and  $j$  appear,

$$\text{Diagram with two box vertices labeled } i \text{ and } j \text{ inside an oval} \quad (41)$$

Let us hold  $i$  fixed for the moment. We now compare the case  $j \neq i$  with the case  $j = i$ . Suppose  $j \neq i$ . As discussed above, there are three independent paths from the vertex  $i$  to the vertex  $j$ . The Green function lines on these paths can thus contribute at most  $\mathcal{O}(d^{-\frac{3}{2}\|\mathbf{R}_i - \mathbf{R}_j\|})$  (or even less if there is another intermediate site  $\mathbf{R}_k$  on a path). Although the summation over  $j$  contributes a factor of order  $\mathcal{O}(d^{\|\mathbf{R}_i - \mathbf{R}_j\|})$ , on the whole, any skeleton diagram is thus suppressed at least by a factor  $\mathcal{O}(d^{-\frac{1}{2}\|\mathbf{R}_i - \mathbf{R}_j\|})$ . As an example, consider

$$\text{Diagram showing two box vertices labeled } i \text{ and } j \text{ connected by three parallel lines} \quad (42)$$

Even if the boxes without labels correspond to site  $j$ , there are three lines connecting  $i$  with  $j$  and only one summation over  $j$ .

By contrast, for  $j = i$  the Green functions are of order  $\mathcal{O}(d^0)$ , and there is no summation. We thus conclude that only the case  $i = j$  contributes in the limit  $d \rightarrow \infty$ , i.e., all diagrams in

the skeleton expansion  $\Sigma[G]$  have the same lattice site label at all their internal and external vertices. Hence the self-energy is site-diagonal (“local”),

$$\Sigma_{ij\sigma}(\omega) = \delta_{ij} \Sigma_{ii\sigma}(\omega) = \delta_{ij} \Sigma_{\sigma}(\omega), \quad (43)$$

or, equivalently, momentum-independent in  $\mathbf{k}$  space,

$$\Sigma_{\mathbf{k}\sigma}(\omega) = \Sigma_{\sigma}(\omega). \quad (44)$$

Furthermore, *the self-energy  $\Sigma_{\sigma}(\omega)$  is a functional only of the local Green function  $G_{\sigma}(\omega)$* , because all internal vertices in the skeleton expansion have the same site label.

The simple form of the self-energy has some immediate consequences also for the Green function (22), namely

$$G_{\mathbf{k}\sigma}(\omega) = \frac{1}{\omega + \mu - \varepsilon_{\mathbf{k}} - \Sigma_{\sigma}(\omega)} = G_{\mathbf{k}\sigma}^{(0)}(\omega - \Sigma_{\sigma}(\omega)). \quad (45)$$

Summing over  $\mathbf{k}$  gives us the local Green function as

$$G_{\sigma}(\omega) = \int \frac{d^d k}{(2\pi)^d} \frac{1}{\omega + \mu - \varepsilon_{\mathbf{k}} - \Sigma_{\sigma}(\omega)} \quad (46)$$

$$= \int_{-\infty}^{\infty} d\omega \frac{\rho(\varepsilon)}{\omega + \mu - \Sigma_{\sigma}(\omega) - \varepsilon}. \quad (47)$$

The last equation thus provides a relation between the local self-energy and the local Green function. It involves only the dispersion via the non-interacting density of states. This relation is one of the ingredients of DMFT, as discussed below.

## 4 Dynamical mean-field theory

As seen above, the self-energy becomes site-diagonal and thus momentum-independent in the limit  $d \rightarrow \infty$ . The last step is now to actually construct the functional  $\Sigma_{\sigma}[G_{\sigma}]$  [1–3, 24, 25], which will complete the derivation of the DMFT equations.

### 4.1 Path-integral representation

Green functions for many-body systems may be represented in a path integral representation [17]. The partition function and the imaginary-time-ordered Green function for the fermionic Hamiltonian  $H(\{c_{\alpha}^{\dagger}\}, \{c_{\alpha}\})$  can be written in terms of functional integrals over Grassmann variables

$$Z = \text{Tr} e^{-\beta(H - \mu N)} = \int_{\phi_{\alpha}(\beta) = -\phi_{\alpha}(0)} \mathcal{D}(\phi_{\alpha}^*(\tau), \phi_{\alpha}(\tau)) \exp(\mathcal{A}), \quad (48)$$

$$G_{\alpha\beta}(\tau) = \frac{1}{Z} \int_{\phi_{\alpha}(\beta) = -\phi_{\alpha}(0)} \mathcal{D}(\phi^*, \phi) \phi_{\alpha}(\tau) \phi_{\beta}^*(0) \exp(\mathcal{A}), \quad (49)$$

with the action

$$\mathcal{A} = - \int_0^\beta d\tau \left[ \sum_\alpha \phi_\alpha^* (\partial_\tau - \mu) \phi_\alpha + H(\{\phi_\alpha^*\}, \{\phi_\alpha\}) \right]. \quad (50)$$

Note that the Grassmann fields  $\phi_\alpha^*(\tau)$  and  $\phi_\alpha(\tau)$  are independent (i.e., they are not complex or Hermitian conjugates of each other, even though they represent creation and annihilation operators) and antiperiodic boundary conditions are imposed on the latter. Path-integral expressions such as (49) and (50) are actually just abbreviations for limits of expressions that are discretized in imaginary time  $\tau$ . We refer to Ref. [17] for details.

## 4.2 Mapping onto effective impurity models

It is now possible to construct an effective single-site action which matches that of the Hubbard model in infinite dimensions [24]. For this purpose let us consider an action,  $\mathcal{A} = \mathcal{A}_1 + \mathcal{A}_2$ , consisting of a quadratic part and an interaction, which only involves one lattice site

$$\mathcal{A}_1 = \int_0^\beta d\tau \int_0^\beta d\tau' \sum_\sigma c_\sigma^*(\tau) \mathcal{G}_\sigma^{-1}(\tau, \tau') c_\sigma(\tau') = \sum_{n,\sigma} c_\sigma^*(i\omega_n) \mathcal{G}_\sigma(i\omega_n)^{-1} c_\sigma(i\omega_n), \quad (51a)$$

$$\mathcal{A}_2 = -U \int_0^\beta d\tau c_\uparrow^*(\tau) c_\uparrow(\tau) c_\downarrow^*(\tau) c_\downarrow(\tau), \quad (51b)$$

with some as yet unfixed “free” Green function  $(\mathcal{G}^{-1})_{\tau,\tau'} = \mathcal{G}_\sigma^{-1}(\tau, \tau')$ , which also depends only on imaginary-time differences.

We can calculate the imaginary-time-ordered Green function of the single degree of freedom  $c$  from the action (51), and Fourier transform to Matsubara frequencies. This is abbreviated as

$$G_\sigma(i\omega_n) = \langle c_\sigma(i\omega_n) c_\sigma^*(i\omega_n) \rangle_{\mathcal{A}[\mathcal{G}]} . \quad (52)$$

Correspondingly, we define the impurity *impurity self-energy*  $\tilde{\Sigma}$  via the *impurity Dyson equation*,

$$G = [\mathcal{G}^{-1} - \tilde{\Sigma}]^{-1} . \quad (53)$$

Now consider the diagrams in the skeleton expansion of  $\tilde{\Sigma}[G]$ ,

$$\tilde{\Sigma}[G] = \text{diagram 1} + \text{diagram 2} + \text{diagram 3} + \dots , \quad (54)$$

in which of course only the single site of (51) occurs. However, since the local Hubbard interaction is the same both for the lattice Hubbard model and the single-site action, this skeleton expansion is exactly the same as that for the Hubbard model (35), i.e.,

$$\tilde{\Sigma}[G] = \Sigma[G] . \quad (55)$$

This shows that the self-energy skeleton functional  $\Sigma_\sigma[G_\sigma]$  can be obtained by solving the single-site problem (51). In the next section we discuss how to choose  $\mathcal{G}_\sigma$  appropriately.



### 4.3 Dynamical mean-field equations

Putting everything together, we arrive at three DMFT equations, which determine three unknowns: the local Green function  $G_\sigma(i\omega_n)$ , the *dynamical mean field* (or *Weiss field*)  $\mathcal{G}_\sigma(i\omega_n)$ , and the local self-energy  $\Sigma_\sigma(i\omega_n)$ :

$$G_\sigma(i\omega_n) = \langle c_\sigma(i\omega_n) c_\sigma^\dagger(i\omega_n) \rangle_{A[G]}, \quad (\text{DMFT-1})$$

$$G_\sigma(i\omega_n) = [\mathcal{G}_\sigma(i\omega_n)^{-1} - \Sigma_\sigma(i\omega_n)]^{-1}, \quad (\text{DMFT-2})$$

$$G_\sigma(i\omega_n) = \int d\varepsilon \frac{\rho(\varepsilon)}{i\omega_n + \mu - \Sigma_\sigma(i\omega_n) - \varepsilon}. \quad (\text{DMFT-3})$$

Note that the *self-consistency equation* (47) provides precisely the needed relation (DMFT-3) to fix the Weiss field  $\mathcal{G}_\sigma$ . This ensures that one solves the correct single-site problem, i.e., the one which corresponds to the Hubbard model on a lattice with density of states  $\rho(\varepsilon)$ .

A typical iterative solution then proceeds as follows: Start with some Weiss field  $\mathcal{G}_\sigma$ , obtain  $G_\sigma$  from (DMFT-1), determine  $\Sigma_\sigma$  from the impurity Dyson equation (DMFT-2), calculate  $G_\sigma$  from the self-consistency equation (DMFT-3), obtain  $\mathcal{G}_\sigma$  by using (DMFT-2) again, and repeat until convergence is reached.

One can check that the DMFT equations reproduce the correct non-interacting and atomic limits. (i) In the non-interacting case we have  $U = 0$  and thus  $\Sigma_\sigma(i\omega_n) = 0$ . Furthermore it follows from (DMFT-3) that then  $G_\sigma(i\omega_n) = G_\sigma^{(0)}(i\omega_n)$ . Finally (DMFT-2) gives  $\mathcal{G}_\sigma(i\omega_n) = G_\sigma(i\omega_n)$ , and this agrees with (DMFT-1) for  $U = 0$ . (ii) On the other hand, in the atomic limit we have  $t_{ij} = 0$  and  $\varepsilon_k = 0$ , i.e.,  $\rho(\varepsilon) = \delta(\varepsilon)$ . From (DMFT-3) we obtain  $G_\sigma(i\omega_n) = [i\omega_n + \mu - \Sigma_\sigma(i\omega_n)]^{-1}$ , and (DMFT-2) yields  $\mathcal{G}_\sigma(i\omega_n)^{-1} = i\omega_n + \mu$ , i.e.,  $\mathcal{G}_\sigma^{-1}(\tau) = -\partial_\tau + \mu$ , which agrees with (DMFT-1) for  $t_{ij} = 0$ .

For a given non-zero value of the Hubbard interaction  $U$  the Green function obtained from the local action (51) clearly represents the most difficult of the DMFT equations. To obtain the impurity Green function from it, a dynamical single-site problem must be solved, usually with numerical methods. For finite temperatures quantum and thermal averages this can be stochastically sampled with quantum Monte Carlo (QMC) methods. The older Hirsch-Fye QMC algorithm [25–27] uses a fixed imaginary time-grid, whereas the more effective continuous-time (CT) QMC [28–30] samples creation and annihilation of particles at arbitrary imaginary times. Methods that also work for zero temperature include exact diagonalization (ED) [31–33], the numerical renormalization group (NRG) [34, 35] and the density-matrix renormalization group (DMRG) [36, 37]. Several of these methods are discussed in the other lectures of this book. A number of perturbative or semianalytic methods is also available [1].

To use these “impurity solvers”, the single-site action (51) is often not used directly, but rather an impurity problem defined by a Hamiltonian is considered, usually by constructing a single-impurity Anderson model (SIAM)

$$H_{\text{SIAM}} = \sum_{\ell\sigma} \varepsilon_\ell a_{\ell\sigma}^\dagger a_{\ell\sigma} + \sum_{\ell\sigma} V_\ell (a_{\ell\sigma}^\dagger c_\sigma + c_\sigma^\dagger a_{\ell\sigma}) + U c_{\uparrow}^\dagger c_{\uparrow} c_{\downarrow}^\dagger c_{\downarrow}. \quad (56)$$

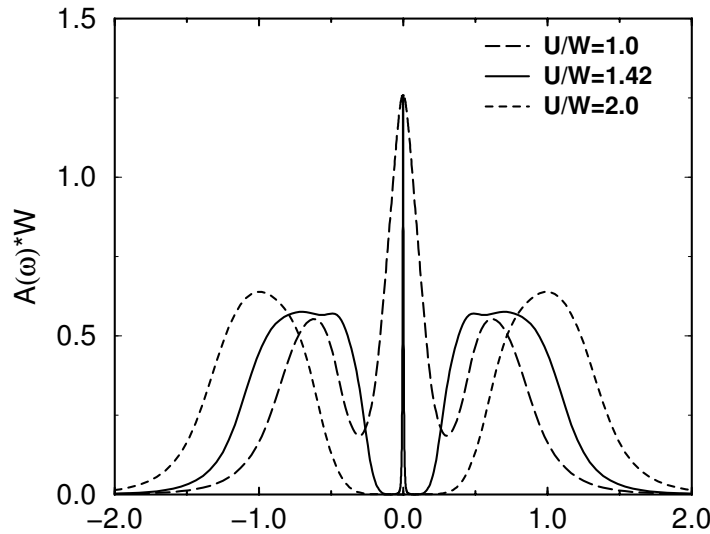


**Fig. 2:** Zero-temperature spectral function for the homogeneous phase of the Hubbard model on the Bethe lattice with nearest-neighbor hopping and bandwidth  $W = 4|t_*|$  at half-filling, evaluated with NRG. From Ref. [34].

Here the fermions  $a_{\ell\sigma}$  represent a non-interacting bath which hosts the interacting fermion  $c_\sigma$ . This bath can be at once integrated out from the action which represents  $H_{\text{SIAM}}$ , because this involves only Gaussian (path) integrals. The resulting action is then precisely of the form (51), with

$$\mathcal{G}_\sigma^{-1}(i\omega_n) = i\omega_n + \mu - \frac{1}{\pi} \int_{-\infty}^{\infty} d\omega \frac{\Delta(\omega)}{i\omega_n - \omega}, \quad \Delta(\omega) = \pi \sum_{\ell} V_{\ell}^2 \delta(\omega - \varepsilon_{\ell}), \quad (57)$$

where  $\Delta(\omega)$  is called the hybridization function. In the DMFT iteration cycle one must now find the parameters  $V_{\ell}$  and  $\varepsilon_{\ell}$  that allow a self-consistent DMFT solution. Then the SIAM has been determined which properly represents the infinite-dimensional Hubbard model in DMFT. For reference we note that the self-consistency equation (DMFT-3) yields a simple relation for nearest-neighbor hopping  $t_*$  on the Bethe lattice with density of states (9),

$$\mathcal{G}_\sigma(i\omega_n) = i\omega_n + \mu - t_*^2 G(i\omega_n). \quad (58)$$

This relation and generalizations for other types of hopping are discussed in Refs. [1, 10, 11, 14, 15].

## 4.4 Results for the Hubbard model

Some aspects of the spectrum and the DMFT phase diagram of the Hubbard model were discussed already in the Lecture of D. Vollhardt. Fig. 2 shows the zero-temperature spectral function for the homogeneous phase of the Hubbard model on the Bethe lattice with nearest-neighbor hopping and bandwidth  $W = 4|t_*|$  at half-filling, evaluated with NRG. Three values of  $U$  are shown, one in the metallic phase (three peaks in the spectral function), one close to the critical value  $U_c$ , and one for the insulating phase (with gap in the spectral function). At the

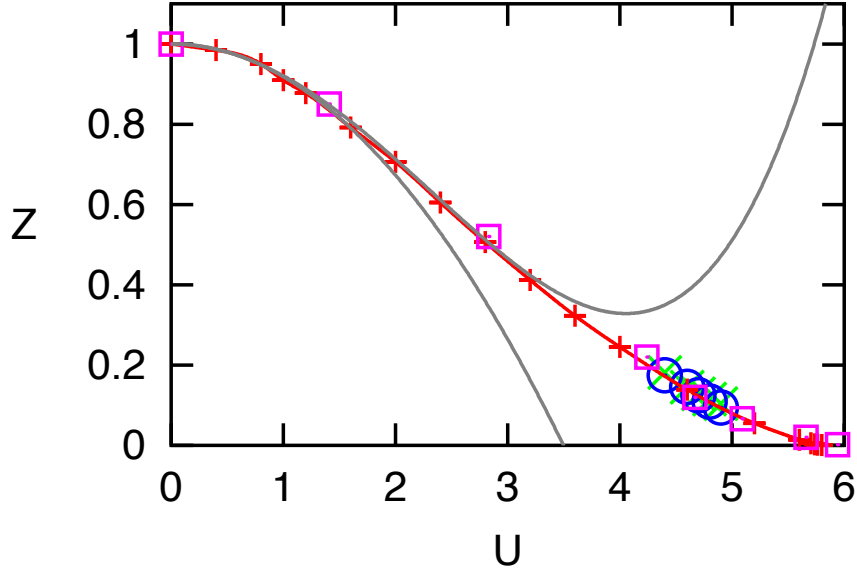


**Fig. 3:** Quasiparticle weight  $Z$  for the half-filled Hubbard model on the Bethe lattice (with  $t_* = 1$ ) in DMFT. Crosses +: NRG; squares: ED; crosses  $\times$  and circles: QMC extrapolations; lower gray line: 2nd order perturbation theory in  $U$ , upper gray line: 4th order perturbation theory in  $U$ . From Ref. [10].

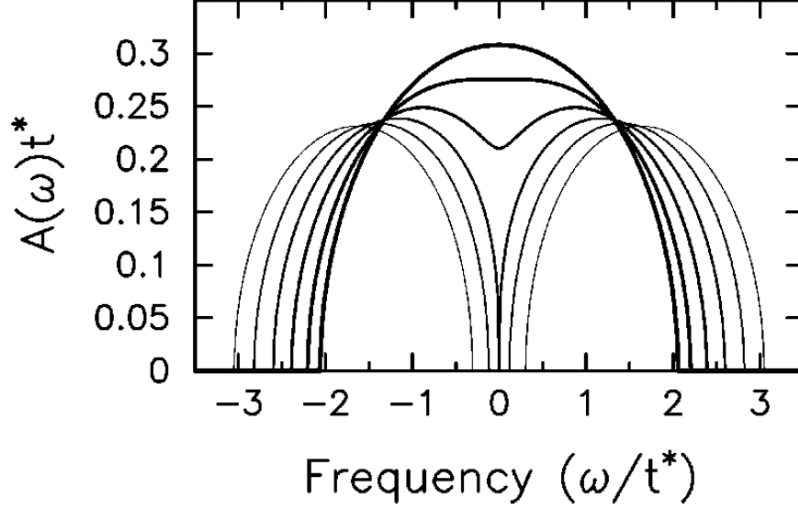
Fermi energy the spectral function has the same value for all  $U$  in the metallic phase; this is a consequence of Luttinger's theorem [8]. In the metallic phase the weight of the central peak is proportional to the Fermi liquid quasiparticle renormalization factor  $Z$  (see (27)), whereas the outer two peaks are the developing Hubbard bands. Note that the energy resolution of NRG is best near the Fermi surface, i.e., near  $\omega = 0$ . Higher-resolution DMRG calculations have shown that there is actually a more pronounced substructure at the inner edges of the Hubbard bands close to  $U_c$  [36, 37], which has been attributed to the effective interaction of so-called doublon-holon pairs [38].

Fig. 3 shows the renormalization factor  $Z$  in the limit of zero temperature obtained with various methods. It starts from  $Z = 1$  for the non-interacting case and decreases as  $U$  is increased, corresponding to the decreasing width of the central peak in the spectral function and an increasingly flatter dispersion. At  $U_c$ , the half-filled system undergoes a Mott metal insulator transition, i.e., it becomes localized and  $Z$  vanishes accordingly.

## 4.5 Results for the Falicov-Kimball model

The Falicov-Kimball model is a simplified version of the Hubbard model, in which only one of the two spin species is mobile (reabeled as  $d_i$ ), while the other (reabeled as  $f_i$ ) is not. For this model the Green function can be derived explicitly from the DMFT action [39]; higher-order Green functions can also be obtained [40, 41]. The Hamiltonian reads

$$H = \sum_{ij} t_{ij} d_i^\dagger d_j + E_f \sum_i f_i^\dagger f_i + U \sum_i d_i^\dagger d_i f_i^\dagger f_i, \quad (59)$$



**Fig. 4:** Spectral function of itinerant  $d$  electrons for the Falicov-Kimball model in DMFT for nearest-neighbor hopping on the Bethe lattice, homogeneous phase,  $n_d = n_f = 1/2$ , and  $U = 0.5, 1.0, \dots 3.0$ . From Ref. [39].

i.e., the  $d$  electrons are moving against a background of static  $f$  electrons, whose configuration is chosen such that it optimizes the free energy. In principle this makes the model quite complicated, as one needs the spectrum of  $H$  for all the possible  $f$  configurations. In dimensions  $d \geq 2$  it is known that at half-filling on a bipartite lattice checkerboard order of the  $f$  electrons appears in the ground state and persists up to a finite critical temperature [42]. Here we consider only the homogeneous phase in DMFT for simplicity.

Since there is no hopping amplitude for the  $f$  electrons, the DMFT self-consistency yields at once  $\mathcal{G}_f^{-1} = -\partial_\tau + \mu + E_f$ , as explained above for the atomic limit. The DMFT action is thus given by

$$\begin{aligned} \mathcal{A} = & \int_0^\beta d\tau \int_0^\beta d\tau' d^*(\tau) \mathcal{G}_d^{-1}(\tau, \tau') d(\tau') \\ & + \int_0^\beta d\tau f^*(\tau) (\partial_\tau - \mu + E_f) f(\tau) - U \int_0^\beta d\tau d^*(\tau) d(\tau) f^*(\tau) f(\tau). \end{aligned} \quad (60)$$

Now the  $f$  electrons can be integrated out at each lattice site, i.e., they are in the atomic limit (cf. Sec. 3.2). This leads to

$$G_d(i\omega_n) = \langle d(i\omega_n) d^*(i\omega_n) \rangle_{\mathcal{A}} = \frac{n_f}{\mathcal{G}_d(i\omega_n)^{-1} - U} + \frac{1 - n_f}{\mathcal{G}_d(i\omega_n)^{-1}}, \quad (61)$$

which must be solved together with the other two DMFT equations

$$G_d(i\omega_n) = \int_{-\infty}^{\infty} \frac{d\varepsilon \rho_d(\varepsilon)}{i\omega_n + \mu - \Sigma_d(i\omega_n) - \varepsilon}, \quad (62)$$

$$G_d(i\omega_n)^{-1} = \mathcal{G}_d(i\omega_n)^{-1} - \Sigma_d(i\omega_n). \quad (63)$$

This set of equations determines the  $d$ -electron Green function  $G_d(i\omega_n)$  for any density of states  $\rho_d(\varepsilon)$ . Analytic continuation to real frequencies shows at once that the spectra in the homogeneous phase are independent of temperature. Note that this no longer holds in the checkerboard phase). Fig. 4 shows the spectral function  $A_d(\omega)$  for several  $U$  for the Bethe lattice (with nearest-neighbor hopping  $t_* = 1$ ). In particular there is a Mott metal-insulator transition taking place at  $U_c = 2$ ; for larger  $U$  a band gap develops. Nevertheless, the transition is qualitatively different from that in the Hubbard model. For example, for the Falicov-Kimball model it can be shown from the low-energy form of the self-energy that for  $0 < U < U_c$  the metallic state is not a Landau Fermi liquid; as a consequence, the spectral function is not pinned at the Fermi surface.

It is also possible to solve for the  $d$  self-energy as a functional of the  $d$  Green function, i.e., for the skeleton expansion  $\Sigma_d[G_d]$  [21]

$$\Sigma_d(i\omega_n) = \frac{U}{2} - \frac{1}{2G_d(i\omega_n)} \pm \sqrt{\left(\frac{U}{2} - \frac{1}{2G_d(i\omega_n)}\right)^2 + \frac{Un_f}{G_d(i\omega_n)}}, \quad (64)$$

which is independent of the density of states  $\rho(\varepsilon)$ . Note that in contrast to the Hubbard model, for the Falicov-Kimball model the skeleton functional is in fact only a *function* of the Green function, i.e.,  $\Sigma_d(i\omega_n)$  depends only on  $G_d(i\omega_n)$  at the same Matsubara frequency.

## 5 Summary and outlook

In this lecture we reviewed the foundations of dynamical mean-field theory for the infinite-dimensional single-band Hubbard model, i.e., the scaling of hopping amplitudes, the local nature of the self-energy, and the mapping onto a dynamical single-site problem in an effective bath which has to be determined self-consistently. Some of the numerical approaches to the effective single-site problem, also for the multiband case, are discussed in the other lectures in this school. Also, important generalizations beyond single-site DMFT to clusters and beyond local self-energies are discussed there, which are important for the accurate description of in fact finite-dimensional systems. DMFT therefore leads not only to nonperturbative numerical solutions to Hubbard-type models in infinite dimensions, but it is also a robust starting point for approximate theories of finite-dimensional systems.

## Acknowledgment

Support of the Deutsche Forschungsgemeinschaft through the former FOR 1346 and TRR 80 is gratefully acknowledged.

## References

- [1] A. Georges, G. Kotliar, W. Krauth, and M.J. Rozenberg, *Rev. Mod. Phys.* **68**, 13 (1996)
- [2] D. Vollhardt: *Investigations of correlated electron systems using the limit of high dimensions* in: V.J. Emery (ed.): *Correlated Electron Systems* (World Scientific, 1993)
- [3] D. Vollhardt in A. Avella, F. Mancini (eds.): *Lectures on the Physics of Strongly Correlated Systems XIV*, AIP Conference Proceedings Vol. 1297 (American Institute of Physics, Melville, 2010), p. 339; arXiv:1004.5069
- [4] D. Vollhardt, K. Byczuk, and M. Kollar: *Dynamical Mean-Field Theory*, in: A. Avella and F. Mancini (eds.): *Theoretical Methods for Strongly Correlated Systems* (Springer, 2011)
- [5] A. Georges: *Dynamical Mean-Field Theory: Materials from an Atomic Viewpoint beyond the Landau Paradigm* in: E. Pavarini, E. Koch, D. Vollhardt, and A. Lichtenstein (eds.): *DMFT at 25: Infinite Dimensions, Modeling and Simulation* Vol. 4 (FZ Jülich, 2011)
- [6] M. Kollar: *Introduction to Dynamical Mean-Field Theory* in: E. Pavarini, E. Koch, A. Lichtenstein, and D. Vollhardt (eds.), *The LDA+DMFT approach to strongly correlated materials*, Modeling and Simulation Vol. 1 (Forschungszentrum Jülich, 2011)
- [7] W. Metzner and D. Vollhardt, *Phys. Rev. Lett.* **62**, 324 (1989)
- [8] E. Müller-Hartmann, *Z. Phys. B* **74**, 507 (1989)
- [9] J. Schlipf, Ph.D. Thesis, Universität Augsburg (1998)
- [10] N. Blümer, *Metal-Insulator Transition and Optical Conductivity in High Dimensions* (Shaker Verlag, Aachen, 2003)
- [11] N. Blümer and P.G.J. van Dongen: *Transport properties of correlated electrons in high dimensions* in A.C. Hewson and V. Zlatić (eds.): *Concepts in Electron Correlation* (Kluwer, 2003); arXiv:cond-mat/0303204
- [12] E. Müller-Hartmann, in E. Talik and J. Szade (eds.): *Proceedings of the V. Symposium “Physics of Metals”* (Ustroń, 1991)
- [13] G. Santoro, M. Airoidi, S. Sorella, and E. Tosatti, *Phys. Rev. B* **47**, 16216 (1993)
- [14] M. Eckstein, M. Kollar, K. Byczuk and D. Vollhardt, *Phys. Rev. B* **71**, 235119 (2005)
- [15] M. Kollar, M. Eckstein, K. Byczuk, N. Blümer, P. van Dongen, M.H. Radke de Cuba, W. Metzner, D. Tanaskovic, V. Dobrosavljevic, G. Kotliar, and D. Vollhardt, *Ann. Phys. (Leipzig)* **14**, 642 (2005)
- [16] A.L. Fetter and J.D. Walecka: *Quantum Theory of Many-Particle Systems* (McGraw-Hill, 1971)

- [17] J.W. Negele and H. Orland: *Quantum Many-Particle Systems* (Addison-Wesley, 1988)
- [18] R.D. Mattuck, *A Guide to Feynman Diagrams in the Many-Body Problem*, 2nd Edition (Dover Publications, 1992)
- [19] X.J. Zhou, T. Cuk, T. Devereaux, N. Nagaosa, and Z.-X. Shen in J.R. Schrieffer (ed.): *Handbook of High-Temperature Superconductivity: Theory and Experiment* (Springer, 2007), p. 87; arXiv:cond-mat/0604284
- [20] N.F. Mott, Proc. Phys. Soc. A (London) **62**, 416 (1947)
- [21] F. Gebhard, *The Mott Metal-Insulator Transition* (Springer, Berlin, 1997)
- [22] D. Vollhardt, Rev. Mod. Phys. **56**, 99 (1984)
- [23] E. Müller-Hartmann, Z. Phys. B **76**, 211 (1989)
- [24] A. Georges and G. Kotliar, Phys. Rev. B **45**, 6479 (1992)
- [25] M. Jarrell, Phys. Rev. Lett. **69**, 168 (1992)
- [26] M.J. Rozenberg, X.Y. Zhang, and G. Kotliar, Phys. Rev. Lett. **69**, 1236 (1992)
- [27] A. Georges and W. Krauth, Phys. Rev. Lett. **69**, 1240 (1992)
- [28] A.N. Rubtsov, V.V. Savkin, and A.I. Lichtenstein, Phys. Rev. B **72**, 035122 (2005)
- [29] P. Werner, A. Comanac, L. de' Medici, M. Troyer, and A.J. Millis, Phys. Rev. Lett. **97**, 076405 (2006)
- [30] K. Haule, Phys. Rev. B **75**, 155113 (2007)
- [31] M. Caffarel and W. Krauth, Phys. Rev. Lett. **72**, 1545 (1994)
- [32] Q. Si, M.J. Rozenberg, G. Kotliar, and A.E. Ruckenstein, Phys. Rev. Lett. **72**, 2761 (1994)
- [33] M.J. Rozenberg, G. Moeller, and G. Kotliar, Mod. Phys. Lett. B **8**, 535 (1994)
- [34] R. Bulla, Phys. Rev. Lett. **83**, 136 (1999)
- [35] R. Bulla, T.A. Costi, and Th. Pruschke, Rev. Mod. Phys. **80**, 395 (2008)
- [36] D.J. García, K. Hallberg, and M.J. Rozenberg, Phys. Rev. Lett. **93**, 246403 (2004)
- [37] M. Karski, C. Raas, and G.S. Uhrig, Phys. Rev. B **77**, 075116 (2008)
- [38] S.-S.B. Lee, J. van Delft, and A. Weichselbaum, Phys. Rev. Lett. **119**, 236402 (2017)
- [39] J.K. Freericks and V. Zlatić, Rev. Mod. Phys. **75**, 1333 (2003)

- [40] T. Ribic, G. Rohringer, K. Held, Phys. Rev. B **93** 195105 (2016)
- [41] T. Ribic, G. Rohringer, K. Held, Phys. Rev. B **95** 155130 (2017)
- [42] T. Kennedy and E.H. Lieb, Physica A **138** 320 (1986)



# **5 Cluster Extensions of Dynamical Mean-Field Theory**

Michael Potthoff

Department of Physics, University of Hamburg  
Jungiusstraße 9, D-20355 Hamburg

## **Contents**

<b>1</b>	<b>Introduction</b>	<b>2</b>
<b>2</b>	<b>Lattices, reciprocal lattices, and superlattices</b>	<b>5</b>
<b>3</b>	<b>Discrete Fourier transformations</b>	<b>7</b>
<b>4</b>	<b>Single-electron Green function</b>	<b>9</b>
<b>5</b>	<b>Local and nonlocal correlations</b>	<b>11</b>
<b>6</b>	<b>Cluster perturbation theory</b>	<b>14</b>
<b>7</b>	<b>Periodization schemes</b>	<b>16</b>
<b>8</b>	<b>Self-consistent cluster-embedding approaches</b>	<b>21</b>
<b>9</b>	<b>Discussion of selected results</b>	<b>26</b>
<b>10</b>	<b>Conclusions and open problems</b>	<b>30</b>

# 1 Introduction

Cluster extensions of dynamical mean-field theory (DMFT) are popular approximation schemes developed for systems of interacting electrons on low-dimensional lattices with local interactions to get access to their thermal equilibrium properties and to their single-electron excitations. This topic came up soon after the development of dynamical mean-field theory [1–4] and has been reviewed in a couple of papers [4–6]. Important milestones defining the field begin with the proposal for a *dynamical cluster approximation* (DCA) in 1998 [7], a cluster extension formulated in reciprocal  $k$ -space. The real-space perspective was emphasized in 2000 [8] with a cluster DMFT approach applied to the two-dimensional Hubbard model. Its formal framework is the *cellular dynamical mean-field theory* (C-DMFT), suggested in 2001 [9]. An alternative simplified cluster approach, the *variational cluster approach* (VCA) was introduced in 2003 [10]. All cluster approaches rely on a number of basic concepts, such as the many-body problem, lattice-fermion models, the mean-field idea, and the DMFT itself.

The many-body problem is a complexity problem. For a classical or quantum system consisting of a few particles the fundamental equations of motion can be solved analytically or at least numerically with machine precision. Condensed-matter theory, however, is confronted with many-particle systems, in particular with quantum systems with a macroscopic number of electrons. In these cases, to aim at the complete information on the microscopic degrees of freedom is a meaningless concept, and a quantum-statistical approach must be employed. Most of the experimentally accessible macroscopic system properties are described by thermodynamics in a phenomenological way and are derived from the underlying laws of microscopic fundamental interactions by statistical physics. The thermodynamics of a macroscopically large system of valence electrons is completely determined by a thermodynamical potential  $F(T, \mu, x)$ , which depends on temperature  $T$ , the chemical potential  $\mu$ , and other macroscopic control parameters  $x$ . Its direct computation via  $F = -T \ln Z(T, \mu, x)$  from the grand partition function  $Z(T, \mu, x) = \text{Tr} \exp(-\beta(H(x) - \mu N))$  (with  $\beta = 1/T$ ,  $k_B \equiv 1$ ) is practically impossible for generic Hamiltonians  $H(x)$  since the trace is actually a high-dimensional sum over a Fock-space basis. Hence, approximations are inevitable.

DMFT and its cluster extensions aim at a description of *strongly interacting electron systems*. The presence of interactions prohibits a simple factorization of the partition function,  $Z = \prod_k Z_k$ , into simple partition functions  $Z_k$  for the different one-particle degrees of freedom, which is known from the textbook treatment of the noninteracting Fermi gas. The Coulomb interaction, which is the relevant type of interaction for almost all interesting properties of condensed matter, must be regarded as “strong”, meaning that a perturbative theoretical approach is expected to fail. On the other hand, strongly interacting electron systems are highly interesting. Interactions are responsible for many famous collective quantum effects which only show up in interacting quantum Fermi systems in the thermodynamic limit. Some examples are the Kondo effect, i.e., the collective screening of a magnetic moment by a mesoscopically large number of valence electrons in states close to the Fermi energy [11], collective magnetism, i.e., the collective order of magnetic moments below a characteristic transition temperature [12, 13],

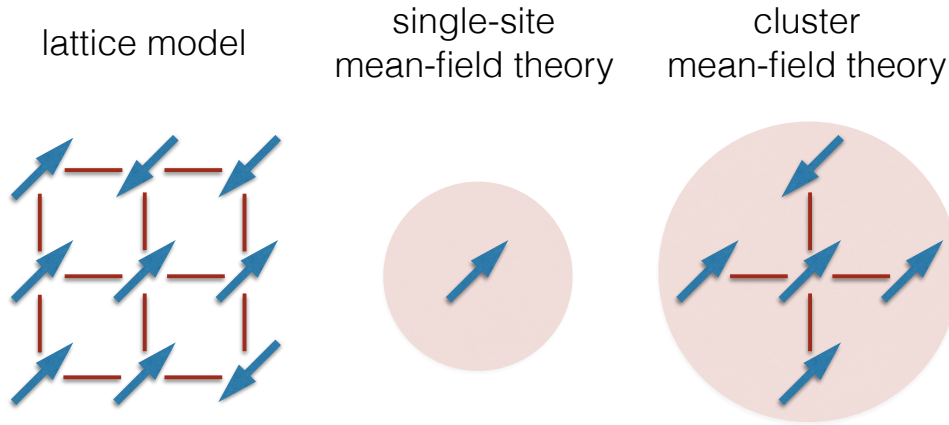


**Fig. 1:** Left: *Spin configuration of the Ising model on the square lattice.* Middle: *Ising spin in a mean field.* Right: *Configuration of an Ising-spin cluster in a mean field.*

unconventional high-temperature superconductivity [14, 15], or interaction-induced Mott insulating behavior [16]. The essence of those effects is captured with surprisingly simple lattice fermion or effective spin models, such as the Hubbard and the Heisenberg model, the Kondo-lattice model, the periodic Anderson model, other multi-orbital lattice models etc.

The *mean-field approach* to strongly interacting lattice fermion models is borrowed from the simple Weiss theory of the Ising model, see Fig. 1. For the Ising model with nearest-neighbor exchange  $J$  between spin  $S_i = \pm 1$  on the  $D = 2$ -dimensional square lattice with  $L$  sites, the left panel shows one of the  $2^L$  spin configurations which must be summed over in an exact computation of the partition function. Note that the number of configurations increases exponentially with  $L$ . The middle panel sketches the idea of a single-site mean-field theory. It takes a local point of view and picks a representative spin  $S_i$  at site  $i$  which experiences a fluctuating local field  $\sim J \sum_{j=1}^{2D} S_j$  created by the spin exchange with its  $2D$  nearest neighbors. In the mean-field approximation, this fluctuating local field is replaced by a constant mean field  $B_{\text{eff}}$ . Note that, due to the central-limit theorem, this replacement can be justified in the limit of infinite dimensions  $D \rightarrow \infty$ . The mean or Weiss field adds to a possibly nonzero physical magnetic field  $B$ . Correspondingly, the exact Ising Hamiltonian is replaced by a mean-field Hamiltonian  $H_{\text{MF}} = -(B_{\text{eff}} + B) \sum_i S_i$ . This implies a dramatic simplification of the original model as the partition function factorizes. One must merely solve the remaining impurity problem, i.e., a *single* spin coupled to a mean field or “bath”. As the bath actually represents the average nearest-neighbor spin configuration, it should be calculated from the thermal expectation value of  $S_i$ . Hence, the solution of the impurity problem and the determination of the bath must be done self-consistently, and the condition fixing the bath is therefore called the *self-consistency condition*. A mean-field theory replaces a lattice model by an impurity model where the impurity is self-consistently embedded in a bath.

Dynamical mean-field theory is in many respects the optimal mean-field theory for a lattice-fermion model like the Hubbard model as a prototype. It self-consistently maps the original

model onto a much simpler reference system which consists of a fermionic impurity, a Hubbard site, for example, which is embedded in a continuum of fermionic bath degrees of freedom. It is not surprising that this bath is much more complicated compared to the bath in the Weiss theory of the simple classical Ising model and that fixing the continuous bath requires a quite different self-consistency condition opposed to fixing a single number, namely  $B_{\text{eff}}$ , in the case of the Ising system. The formulation in fact requires a frequency-dependent one-particle Green function and thus explains the term *dynamical* mean-field theory as opposed to the static Weiss theory. The DMFT is a big landmark in the landscape of various mean-field-like approximation techniques and serves as a point of orientation, as it combines a number of attractive features: The theory is formally not restricted to certain parameter ranges, such as weak interaction, low density etc. It works without internal inconsistencies in the entire parameter regime of the model under consideration. In this sense, it is a nonperturbative theory. The DMFT can be seen as the exact theory of the lattice-fermion model in a special limit, namely for an infinite-dimensional lattice. This limit, however, must be defined carefully to keep the balance between the one- and the two-body terms in the Hamiltonian. The power of DMFT very much results from the fact that the according  $D = \infty$  models are highly nontrivial with nontrivial phase diagrams, excitation spectra, and also nontrivial real-time dynamics. Usually, however, it is employed as an approximation to treat finite-dimensional lattice models. The DMFT is able to describe spontaneous symmetry breaking and states of matter with collective order, such as magnetism, superconductivity, charge order, orbital order etc. It is a beautiful and robust theory on the formal level, which can be derived in various ways and starting from various setups. Most importantly, however, DMFT has turned out as highly successful in practice, including particularly applications to real materials which so far, on the conventional basis of density-functional theory and the local-density approximation, could not be addressed properly since strong electron correlations are essential for their observable properties.

Still, there are a couple of remaining problems which are related to the mean-field character and the local nature of the theory. For example, while DMFT is able to describe phases with long-range order, it insufficiently treats short-range correlations, particularly the feedback of short-range magnetic correlations on the one-electron Green function. It can describe two-particle correlation functions, such as the spin-structure factor or the conductivity but those do not affect the self-consistent determination of the bath. This has decisive consequences for the application to low-dimensional lattice models and can result in qualitatively wrong phase diagrams. In fact, as will be discussed later, it can spectacularly fail for models in  $D = 2$  dimensions. Furthermore, the restriction to a single-site impurity implies that the DMFT cannot describe symmetry-broken phases with nonlocal order parameters, which unfortunately includes unconventional  $d$ -wave superconductivity. DMFT also shares with all mean-field-like theories the inability to predict the correct critical behavior in the parametric vicinity of second-order phase transitions, it violates exact Ward identities and theorems such as the Mermin-Wagner theorem [17]. Clearly, DMFT cannot be the end of the story as it is approximative when applied to a finite-dimensional lattice model. What is needed here is a systematic route starting from DMFT towards the exact solution.

One idea, and this is the theme of this review and lecture, is to extend the self-consistent embedding of a single site to an embedding of a cluster consisting of several sites  $L_c$ . This is displayed in the right panel of Fig. 1. Without having detailed the precise form of a cluster extension of the DMFT, it is already clear that this is a systematic approach to the full solution. There is simply no need for a self-consistent embedding of a cluster cut out of an infinite lattice-fermion model if the cluster itself has infinite size. On the other hand, it is also obvious from the beginning that the computational effort will drastically increase with increasing  $L_c$ . The construction of a cluster DMFT should therefore be guided by the goal to achieve fast convergence for  $L_c \rightarrow \infty$ . We will see that there is more than one way to perform this construction, and we will also see some common intrinsic advantages and deficiencies of the cluster approach as such.

## 2 Lattices, reciprocal lattices, and superlattices

To develop the formal framework of cluster extensions of DMFT, we will first discuss some geometrical issues. We start with a  $D$ -dimensional Bravais lattice spanned by the basis vectors  $\mathbf{a}_1, \dots, \mathbf{a}_D$ . The points of the lattice are given by lattice vectors

$$\mathbf{R} \equiv \mathbf{R}_i = \sum_{\alpha=1}^D i_{\alpha} \mathbf{a}_{\alpha}, \quad (1)$$

where  $i = (i_1, \dots, i_D)$  with arbitrary integers  $i_{\alpha} \in \mathbb{Z}$ . For each lattice, we have a reciprocal lattice which is spanned by the basis vectors  $\mathbf{b}_1, \dots, \mathbf{b}_D$ . These are defined as the unique solution of the linear system of equations

$$\mathbf{a}_{\alpha} \mathbf{b}_{\beta} = 2\pi \delta_{\alpha\beta}. \quad (2)$$

Points in the reciprocal lattice are given by reciprocal lattice vectors

$$\mathbf{G} \equiv \mathbf{G}_j = \sum_{\beta=1}^D j_{\beta} \mathbf{b}_{\beta}, \quad (3)$$

where  $j = (j_1, \dots, j_D)$  with  $j_{\beta} \in \mathbb{Z}$ . The parallelepiped defined by the basis  $\mathbf{a}_1, \dots, \mathbf{a}_D$  is a primitive cell  $\mathcal{C}$  of the lattice, whereas  $\mathbf{b}_1, \dots, \mathbf{b}_D$  define a primitive cell of the reciprocal lattice, a reciprocal unit cell  $\mathcal{RC}$ . For their volumes we have the relation  $V_{\mathcal{C}} V_{\mathcal{RC}} = (2\pi)^D$ . Primitive cells are not unique. Another reciprocal unit cell, with higher symmetry group, is the well-known Brillouin zone ( $\mathcal{BZ}$ ).

There is a symmetry between the original and reciprocal lattice. We immediately have the identity

$$\exp(i\mathbf{G}\mathbf{R}) = 1, \quad (4)$$

and the reciprocal lattice of the reciprocal lattice is the original lattice. The reciprocal lattice can be used to expand a function  $f(\mathbf{x})$  that is lattice periodic,  $f(\mathbf{x} + \mathbf{R}_i) = f(\mathbf{x})$ , in a Fourier series

$$f(\mathbf{x}) = \sum_{\mathbf{G}} f_{\mathbf{G}} e^{i\mathbf{G}\mathbf{x}}, \quad f_{\mathbf{G}} = \frac{1}{V_{\mathcal{C}}} \int_{\mathcal{C}} d^D r f(\mathbf{x}) e^{-i\mathbf{G}\mathbf{x}}. \quad (5)$$

object, quantity	symbol, definition	properties, relations
basis spanning the lattice volume of a primitive cell lattice vectors	$\mathbf{a}_\alpha$ $V_C = \det(\{\mathbf{a}_\alpha\})$ $\mathbf{R} = \mathbf{R}_i = \sum_\alpha i_\alpha \mathbf{a}_\alpha$	$\alpha = 1, \dots, D$ $i_\alpha \in \mathbb{Z}, 1 \leq i_\alpha \leq L_\alpha$
basis vectors of reciprocal lattice volume of a reciprocal unit cell reciprocal lattice vectors	$\mathbf{b}_\beta$ $V_{RC} = \det(\{\mathbf{b}_j\})$ $\mathbf{G} = \mathbf{G}_j = \sum_\beta j_\beta \mathbf{b}_\beta$	$\mathbf{a}_\alpha \mathbf{b}_\beta = 2\pi \delta_{\alpha\beta}$ $V_{RC} = (2\pi)^D / V_C$ $j_\beta \in \mathbb{Z}, \mathbf{G}\mathbf{R} \in 2\pi\mathbb{Z}$
basis spanning the superlattice volume of a superlattice cell superlattice vectors	$\tilde{\mathbf{a}}_\alpha$ $V_{SC} = \det(\{\tilde{\mathbf{a}}_\alpha\})$ $\tilde{\mathbf{R}} = \tilde{\mathbf{R}}_i = \sum_\alpha i_\alpha \tilde{\mathbf{a}}_\alpha$	$\tilde{\mathbf{a}}_\alpha = L_{c,\alpha} \mathbf{a}_\alpha$ $V_{SC} = L_c V_C$ $i_\alpha \in \mathbb{Z}, 1 \leq i_\alpha \leq L/L_{c,\alpha}$
basis of reciprocal superlattice volume of a rec. superlattice cell reciprocal superlattice vectors	$\tilde{\mathbf{b}}_\beta$ $V_{RSC} = \det(\{\tilde{\mathbf{b}}_j\})$ $\tilde{\mathbf{G}} = \tilde{\mathbf{G}}_j = \sum_\beta j_\beta \tilde{\mathbf{b}}_\beta$	$\tilde{\mathbf{a}}_\alpha \tilde{\mathbf{b}}_\beta = 2\pi \delta_{\alpha\beta}$ $V_{RSC} = (2\pi)^D / V_{SC}$ $\tilde{\mathbf{G}}\tilde{\mathbf{R}} \in 2\pi\mathbb{Z}$
vectors spanning the system system volume	$\mathbf{A}_\alpha$ $V = \det(\{\mathbf{A}_i\})$	$\mathbf{A}_\alpha = L_\alpha \mathbf{a}_\alpha = (L/L_{c,\alpha}) \tilde{\mathbf{a}}_\alpha$ $V = L V_C$
discrete wave vectors volume element in $\mathbf{k}$ -space	$\mathbf{k}$ $\Delta^D k$	$\mathbf{k}\mathbf{A}_\alpha \in 2\pi\mathbb{Z}$ $\Delta^D k = (2\pi)^D / V$

**Table 1:** Overview of the various quantities defining the lattice and the reciprocal lattice, the system volume and the  $\mathbf{k}$ -space.

On a suitably defined Hilbert space of functions  $f(\mathbf{x})$ , this expansion results from the fact that the functions  $\exp(i\mathbf{G}\mathbf{x})$  form an orthonormal basis:  $\frac{1}{V_C} \int_C d^D r e^{-i\mathbf{G}\mathbf{x}} e^{i\mathbf{G}'\mathbf{x}} = \delta_{\mathbf{G},\mathbf{G}'}$ . A completely analogous construction can be made for functions  $g(\mathbf{p})$  with  $g(\mathbf{p} + \mathbf{G}_j) = g(\mathbf{p})$ . While one is eventually interested in the properties of a lattice-fermion model, such as the Hubbard model, on a lattice with an infinite number of lattice sites  $L$ , it is convenient to first consider a *finite* lattice and to solve the problem for  $L < \infty$ ,

$$L = L_1 \times \dots \times L_D, \quad (6)$$

and a certain finite number of fermions  $N$ , and finally to perform the thermodynamical limit  $L \rightarrow \infty$ ,  $N \rightarrow \infty$  with  $n \equiv N/L = \text{const.}$  This raises the question of boundary conditions. Excluding systems in a critical state, where system properties are infinitely susceptible to small perturbations, the precise form of the boundary conditions does not matter in the thermodynamic limit. In the case of open boundaries, the system volume is spanned by a set of vectors  $\mathbf{A}_1, \dots, \mathbf{A}_D$ , such that the system volume is  $V = \det(\mathbf{A}_1, \dots, \mathbf{A}_D)$ . We should impose consistency constraints,  $\mathbf{A}_\alpha = L_\alpha \mathbf{a}_\alpha$ , to respect the underlying lattice structure.

Periodic boundary conditions are much more convenient. Here, we identify vectors  $\mathbf{x}$  and  $\mathbf{x} + \mathbf{A}_i$ . The geometrical perspective is that the macroscopic system topology is that of a  $D$ -dimensional torus  $T^D$ . An equivalent point of view is that all real-space functions  $f(\mathbf{x})$  with  $\mathbf{x} \in \mathbb{R}^D$  respect the conditions  $f(\mathbf{x} + \mathbf{A}_i) = f(\mathbf{x})$  and, therefore, can be expanded in a Fourier series,  $f(\mathbf{x}) = \sum_{\mathbf{k}} \exp(i\mathbf{k}\mathbf{x}) f_{\mathbf{k}}$ , where the wave vectors  $\mathbf{k}$  can be seen as the reciprocal-lattice vectors of the real-space lattice spanned by  $\mathbf{A}_1, \dots, \mathbf{A}_D$ . Hence,  $\exp(i\mathbf{k}\mathbf{A}_i) = 1$ , and the volume

element in  $\mathbf{k}$  space is  $\Delta^D k = (2\pi)^D/V$ . This also implies that the number of  $\mathbf{k}$ -points in the reciprocal unit cell,  $V_{\mathcal{RC}}/\Delta^D k$ , equals the number of sites in the system  $L$ , since

$$\Delta^D k = \frac{(2\pi)^D}{V} = \frac{(2\pi)^D}{V_c} \frac{V_c}{V} = V_{\mathcal{RC}} \frac{1}{L}. \quad (7)$$

Some overview of the notations used and of the basic relations is given in table 1.

For cluster extensions of the DMFT, there is a third pair of lattice and corresponding reciprocal lattice to be considered. The original lattice of  $L$  sites is tiled into  $L/L_c$  identical clusters with a finite number of  $L_c$  sites each. Each of the identical clusters has a cluster origin, which can be chosen as a particular site in the cluster, such that all cluster origins are equivalent and form a *superlattice*. We define the primitive vectors of the superlattice  $\tilde{\mathbf{a}}_\alpha$  for  $\alpha = 1, \dots, D$ , and we impose consistency constraints, such as  $\tilde{\mathbf{a}}_\alpha = L_{c,\alpha} \mathbf{a}_\alpha$  in the most simple case, to respect the underlying lattice structure. Hence, the number of cluster sites is given by  $L_c = L_{c,1} \times \dots \times L_{c,D}$ . The volume of the unit cell of the superlattice is given by  $V_{SC} = \det(\{\tilde{\mathbf{a}}_\alpha\})$ , and we have  $V_{SC} = L_c V_c = (L_c/L)V$ .

The reciprocal superlattice consists of the vectors  $\tilde{\mathbf{G}} \equiv \tilde{\mathbf{G}}_j = \sum_\beta j_\beta \tilde{\mathbf{b}}_\beta$  and is spanned by the basis of the reciprocal superlattice  $\{\tilde{\mathbf{b}}_\beta\}$  with  $j = (j_1, \dots, j_D) \in \mathbb{Z}^D$ . The real-space consistency constraints imply that  $\tilde{\mathbf{b}}_\beta = \mathbf{b}_\beta/L_{c,\beta}$ . We have  $\exp(i\tilde{\mathbf{G}}\tilde{\mathbf{R}}) = 1$ , where  $\tilde{\mathbf{R}} \equiv \tilde{\mathbf{R}}_i = \sum_\alpha i_\alpha \tilde{\mathbf{a}}_\alpha$  are the superlattice vectors. Furthermore, the number of reciprocal superlattice vectors in the reciprocal unit cell,  $V_{\mathcal{RC}}/V_{\mathcal{RSC}}$ , is given by  $L_c$ , since

$$V_{\mathcal{RSC}} = \frac{(2\pi)^D}{V_{SC}} = \frac{(2\pi)^D}{V_c} \frac{V_c}{V_{SC}} = V_{\mathcal{RC}}/L_c. \quad (8)$$

Fig. 2 provides an example of a  $D = 2$ -dimensional lattice.

### 3 Discrete Fourier transformations

Figure 2 also demonstrates that any lattice vector

$$\mathbf{R} = \tilde{\mathbf{R}} + \mathbf{r} \quad (9)$$

can be uniquely decomposed into a vector of the superlattice  $\tilde{\mathbf{R}}$ , i.e., the position vector to the respective cluster origin, and a position vector  $\mathbf{r}$  to the respective site in the cluster, referring to the cluster origin. Note that there are  $L$  lattice points  $\mathbf{R}$ , and  $L/L_c$  clusters with  $L_c$  sites each. Vice versa, for a given wave vector  $\mathbf{k}$  there is the unique decomposition

$$\mathbf{k} = \tilde{\mathbf{k}} + \tilde{\mathbf{G}}, \quad (10)$$

where  $\tilde{\mathbf{G}}$  are the reciprocal superlattice vectors. Note that in a reciprocal unit cell there are  $L$  wave vectors  $\mathbf{k}$  and  $L_c$  reciprocal superlattice vectors  $\tilde{\mathbf{G}}$ , and there are  $L/L_c$  wave vectors  $\tilde{\mathbf{k}}$ .

Let us consider the  $L \times L$  matrix  $U$  with elements

$$U_{\mathbf{R},\mathbf{k}} = \frac{1}{\sqrt{L}} e^{i\mathbf{k}\mathbf{R}}, \quad \mathbf{k} \in \mathcal{RC}, \quad (11)$$

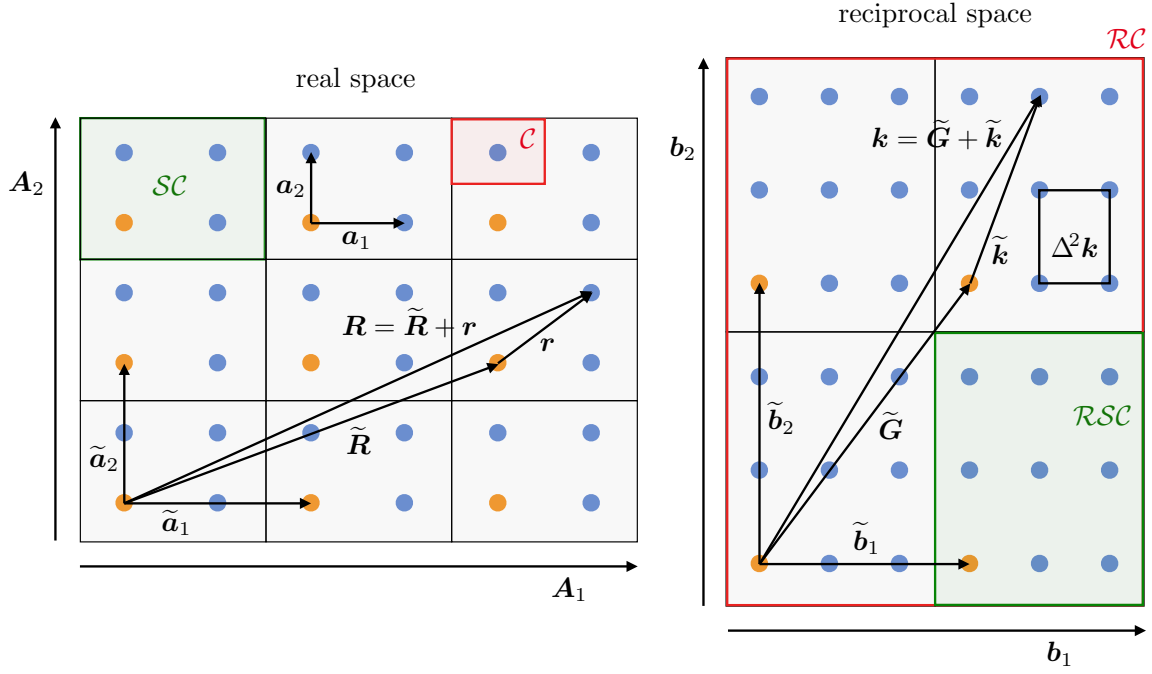


**Fig. 2:** Example of a lattice/superlattice in  $D = 2$  dimensions. Real space, left: A system consisting of  $L = 36$  sites on a square lattice with periodic boundary conditions.  $\mathcal{C}$ : unit cell.  $\mathbf{a}_1, \mathbf{a}_2$ : basis vectors of the lattice. Lines: tiling into clusters with  $L_c = 4$  sites. Orange sites: cluster origins, forming a superlattice structure of  $L/L_c = 9$  clusters.  $\mathcal{SC}$ : unit cell of the superlattice.  $\tilde{\mathbf{a}}_1, \tilde{\mathbf{a}}_2$ : superlattice basis vectors. Any lattice vector  $\mathbf{R}$  can be decomposed uniquely into a superlattice vector  $\tilde{\mathbf{R}}$  and a cluster vector  $\mathbf{r}$ .  $\mathbf{A}_1, \mathbf{A}_2$ : primitive translations defining the periodic boundary conditions and the total system size. Reciprocal space, right:  $\mathbf{b}_1, \mathbf{b}_2$  reciprocal basis spanning a reciprocal unit cell  $\mathcal{RC}$  containing  $L = 36$   $\mathbf{k}$ -points.  $\Delta^2 k = (2\pi)/V$ : volume element. The  $\mathcal{RC}$  contains  $L_c = 4$  reciprocal supercells ( $\mathcal{RSC}$ ) with  $L/L_c = 9$  wave vectors  $\tilde{\mathbf{k}}$  each. Their volume is  $V_{\mathcal{RSC}} = V_{\mathcal{RC}}/L_c$ . Any wave vector  $\mathbf{k}$  can be decomposed uniquely into a reciprocal superlattice vector  $\tilde{\mathbf{G}}$  and a wave vector  $\tilde{\mathbf{k}}$ .

and the  $L/L_c \times L/L_c$  matrix  $\mathbf{V}$  with elements

$$V_{\tilde{\mathbf{R}}, \tilde{\mathbf{k}}} = \frac{1}{\sqrt{L/L_c}} e^{i\tilde{\mathbf{k}}\tilde{\mathbf{R}}}, \quad \tilde{\mathbf{k}} \in \mathcal{RSC}, \quad (12)$$

and the  $L_c \times L_c$  matrix  $\mathbf{W}$  with elements

$$W_{\mathbf{r}, \tilde{\mathbf{G}}} = \frac{1}{\sqrt{L_c}} e^{i\tilde{\mathbf{G}}\mathbf{r}}, \quad \tilde{\mathbf{G}} \in \mathcal{RC}. \quad (13)$$

The unitary matrices  $\mathbf{U}$ ,  $\mathbf{V}$  and  $\mathbf{W}$  define discrete Fourier transformations between the respective real and reciprocal spaces. We refer to the different transformations as the lattice Fourier transformation ( $\mathbf{U}$ ), the superlattice Fourier transformation ( $\mathbf{V}$ ), and the cluster Fourier transformation ( $\mathbf{W}$ ). For example, one can straightforwardly prove that

$$\frac{1}{L} \sum_{\mathbf{R}} e^{-i(\mathbf{k}-\mathbf{k}')\mathbf{R}} = \sum_{\mathbf{R}} U_{\mathbf{k}, \mathbf{R}}^\dagger U_{\mathbf{R}, \mathbf{k}'} = \delta_{\mathbf{k}, \mathbf{k}'}, \quad \frac{1}{L} \sum_{\mathbf{k}} e^{i\mathbf{k}(\mathbf{R}-\mathbf{R}')} = \sum_{\mathbf{k}} U_{\mathbf{R}, \mathbf{k}} U_{\mathbf{k}, \mathbf{R}'}^\dagger = \delta_{\mathbf{R}, \mathbf{R}'} \quad (14)$$



and thus, for some  $\mathbf{R}$ -dependent observable  $O_{\mathbf{R}}$ ,

$$O_{\mathbf{k}} = \frac{1}{\sqrt{L}} \sum_{\mathbf{R}} e^{i\mathbf{k}\mathbf{R}} O_{\mathbf{R}}, \quad O_{\mathbf{R}} = \frac{1}{\sqrt{L}} \sum_{\mathbf{k}} e^{-i\mathbf{k}\mathbf{R}} O_{\mathbf{k}}. \quad (15)$$

Analogous relations hold for the other two cases. The formal structure of the proof is the same in all cases. Although there is a one-to-one relation between  $\mathbf{R}$  and  $(\tilde{\mathbf{R}}, \mathbf{r})$  and between  $\mathbf{k}$  and  $(\tilde{\mathbf{k}}, \tilde{\mathbf{G}})$ , the lattice Fourier transformation  $U$  involving lattice vectors  $\mathbf{R}$  cannot be decomposed into the superlattice transformation involving superlattice vectors  $\tilde{\mathbf{R}}$  and the cluster transformation involving cluster vectors  $\mathbf{r}$ , i.e.,  $U \neq VW = WV$ . We note that a quantity  $A_{\mathbf{R},\mathbf{R}'}$  which is invariant under lattice translations  $\mathbf{R}_0$ , i.e.  $A_{\mathbf{R}+\mathbf{R}_0,\mathbf{R}'+\mathbf{R}_0} = A_{\mathbf{R},\mathbf{R}'}$ , is diagonalized by  $U$ :  $(U^\dagger \mathbf{A} U)_{\mathbf{k}\mathbf{k}'} = A(\mathbf{k}) \delta_{\mathbf{k},\mathbf{k}'}$ . A quantity  $A_{\mathbf{R},\mathbf{R}'}$  which is invariant under superlattice translations  $\tilde{\mathbf{R}}_0$  as well as under cluster translations  $\mathbf{r}_0$  (i.e., which is cyclic on the cluster),  $A_{\mathbf{R}+\tilde{\mathbf{R}}_0,\mathbf{R}'+\tilde{\mathbf{R}}_0} = A_{\mathbf{R}+\mathbf{r}_0,\mathbf{R}'+\mathbf{r}_0} = A_{\mathbf{R},\mathbf{R}'}$ , is diagonalized by  $VW$ :  $(W^\dagger V^\dagger \mathbf{A} VW)_{\tilde{\mathbf{k}}\tilde{\mathbf{G}},\tilde{\mathbf{k}}'\tilde{\mathbf{G}}'} = A(\tilde{\mathbf{k}}, \tilde{\mathbf{G}}) \delta_{\tilde{\mathbf{k}},\tilde{\mathbf{k}}'} \delta_{\tilde{\mathbf{G}},\tilde{\mathbf{G}}'}$ .

## 4 Single-electron Green function

DMFT and its cluster extensions are theories based on the single-particle Green function  $G_{\mathbf{R},\mathbf{R}'}(\omega)$  which, at  $T = 0$ , for complex  $\omega \neq \mathbb{R}$  (and using units with  $\hbar = 1$ ) is defined as

$$G_{\mathbf{R},\mathbf{R}'}(\omega) = \left\langle 0 \left| c_{\mathbf{R}',\sigma}^\dagger \frac{1}{\omega - E_0 + H} c_{\mathbf{R},\sigma} \right| 0 \right\rangle + \left\langle 0 \left| c_{\mathbf{R},\sigma} \frac{1}{\omega + E_0 - H} c_{\mathbf{R}',\sigma}^\dagger \right| 0 \right\rangle. \quad (16)$$

Here,  $c_{\mathbf{R},\sigma}^\dagger$  is the creation operator of an electron with spin projection  $\sigma = \uparrow, \downarrow$  at lattice site  $\mathbf{R}$ , and  $c_{\mathbf{R},\sigma}$  is the corresponding annihilator.  $|0\rangle$  is the ground state of the Hamiltonian  $H$ , and  $E_0$  is the ground-state energy. Note that  $1/(\dots)$  stands for the operator inverse. We assume that  $H$  is spin-independent, such that the Green function is diagonal in the spin-projection indices and spin-independent. Furthermore,  $H$  shall be invariant under lattice translations,  $c_{\mathbf{R},\sigma} \rightarrow c_{\mathbf{R}+\mathbf{R}_0,\sigma}$  and  $c_{\mathbf{R},\sigma}^\dagger \rightarrow c_{\mathbf{R}+\mathbf{R}_0,\sigma}^\dagger$ . Then, the Green function is invariant under lattice translations as well,

$$G_{\mathbf{R}+\mathbf{R}_0,\mathbf{R}'+\mathbf{R}_0}(\omega) = G_{\mathbf{R},\mathbf{R}'}(\omega). \quad (17)$$

This implies that the matrix  $\mathbf{G}(\omega)$  with elements  $G_{\mathbf{R},\mathbf{R}'}(\omega)$  is diagonalized by the lattice Fourier transformation

$$(U^\dagger \mathbf{G}(\omega) U)_{\mathbf{k}\mathbf{k}'} = G(\mathbf{k}, \omega) \delta_{\mathbf{k},\mathbf{k}'}. \quad (18)$$

From the retarded Green function  $\mathbf{G}^{(\text{ret})}(\omega) \equiv \lim_{\eta \searrow 0} \mathbf{G}(\omega + i\eta) \equiv \mathbf{G}(\omega + i0^+)$  with  $\omega \in \mathbb{R}$  we obtain the spectral density

$$A(\mathbf{k}, \omega) = -\frac{1}{\pi} \text{Im} G(\mathbf{k}, \omega + i0^+). \quad (19)$$

This is a central observable which is related, for  $\omega < 0$ , to the  $\mathbf{k}$ -resolved (angle-resolved) photoemission spectrum (PES), and, for  $\omega > 0$ , to the inverse photoemission spectrum (inverse photoemission, IPE). PES and IPE probe the occupied and the unoccupied part of the electronic

structure in the vicinity of the Fermi energy ( $\omega = 0$ ), respectively. With the help of the Dirac identity,  $\lim_{\eta \searrow 0} 1/(x + i\eta) = \mathcal{P}(1/x) - i\pi\delta(x)$ , we also have the expression

$$A_{\mathbf{R},\mathbf{R}'}(\omega) = \left\langle 0 \left| c_{\mathbf{R}',\sigma}^\dagger \delta(\omega - E_0 + H) c_{\mathbf{R},\sigma} \right| 0 \right\rangle + \left\langle 0 \left| c_{\mathbf{R},\sigma} \delta(\omega + E_0 - H) c_{\mathbf{R}',\sigma}^\dagger \right| 0 \right\rangle \quad (20)$$

for real  $\omega$ , and

$$G_{\mathbf{R},\mathbf{R}'}(\omega) = \int_{-\infty}^{\infty} d\omega' \frac{A_{\mathbf{R},\mathbf{R}'}(\omega')}{\omega - \omega'}. \quad (21)$$

The simplest case is that of a noninteracting tight-binding model with Hamiltonian

$$H_0 = \sum_{\mathbf{R}\mathbf{R}'\sigma} t_{\mathbf{R}\mathbf{R}'} c_{\mathbf{R}\sigma}^\dagger c_{\mathbf{R}'\sigma}. \quad (22)$$

Expressing the  $\delta$ -function in Eq. (20) as  $\delta(\omega) = (2\pi)^{-1} \int dt e^{-i\omega t}$ , using the Baker-Campbell-Hausdorff formula,  $e^B A e^{-B} = e^{-L_B} A$  for operators  $A, B$  and  $L_B A \equiv [A, B]$ , and the elementary commutator  $[c_{\mathbf{R}\sigma}, H_0] = \sum_{\mathbf{R}'} t_{\mathbf{R},\mathbf{R}'} c_{\mathbf{R}'\sigma}$ , we find

$$\mathbf{A}(\omega) = \delta(\omega - \mathbf{t}), \quad A(\mathbf{k}, \omega) = \delta(\omega - \epsilon(\mathbf{k})), \quad (23)$$

where  $\epsilon(\mathbf{k})$  are the eigenvalues of the hopping matrix  $\mathbf{t}$ , i.e., the tight-binding dispersion. Here, we discuss the case of electrons on a two-dimensional square lattice with hopping between nearest neighbors only, i.e.,  $t_{\mathbf{R},\mathbf{R}'} = -t$  if  $\mathbf{R}, \mathbf{R}'$  are nearest-neighbor sites.  $t = 1$  fixes the energy scale. The dispersion is obtained by lattice Fourier transformation,  $\epsilon(\mathbf{k}) \delta_{\mathbf{k}\mathbf{k}'} = (\mathbf{U}^\dagger \mathbf{t} \mathbf{U})_{\mathbf{k}\mathbf{k}'}$ , with

$$\epsilon(\mathbf{k}) = -2t(\cos k_x + \cos k_y). \quad (24)$$

With this we obtain the noninteracting spectral density as displayed in Fig. 3 (left).  $A(\mathbf{k}, \omega)$  has exactly one  $\delta$ -singularity for each  $\mathbf{k}$  in the reciprocal unit cell, e.g., in the first Brillouin zone. There is a well-defined Fermi surface, given by all  $\mathbf{k}$ -points in the BZ with vanishing excitation energy:  $\omega = \epsilon(\mathbf{k}) = 0$ . The band is half-filled. Different band fillings are obtained by introducing a chemical potential  $\mu \neq 0$  via the substitution  $H_0 \mapsto H_0 - \mu N$ , where  $N$  is the particle-number operator.

The *interacting* spectral density Fig. 3 (right) looks quite different. The example shows  $A(\mathbf{k}, \omega)$  for the same tight-binding model but with an additional on-site Coulomb interaction

$$H_1 = \frac{U}{2} \sum_{\mathbf{R}\sigma} n_{\mathbf{R}\sigma} n_{\mathbf{R}-\sigma} \quad (25)$$

of strength  $U$ , where  $n_{\mathbf{R}\sigma} \equiv c_{\mathbf{R}\sigma}^\dagger c_{\mathbf{R}\sigma}$  is the occupation-number operator.  $H = H_0 + H_1$  is the famous Hubbard model [18–20] which frequently serves as a prototype for method developments. The computation of the spectral density in the interacting cases is, of course, by no means trivial. The example shown here displays quantum Monte-Carlo data for the Hubbard model on  $L = L_x \times L_y = 64$  sites from a study performed about 20 years ago [21]. Since then we have seen various improvements of the QMC method but the infamous sign problem, which prevents an efficient simulation of the model off half-filling, for example, is still unsolved in

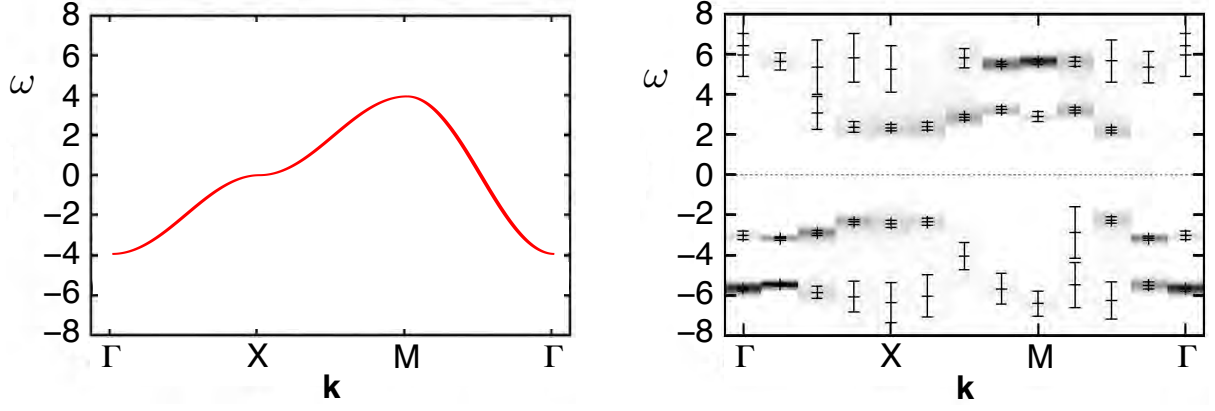


**Fig. 3:** Spectral function  $A(\mathbf{k}, \omega)$  for the two-dimensional Hubbard model at half-filling along high-symmetry paths in the first Brillouin zone.  $\Gamma = (0, 0)$ ,  $X = (\pi, 0)$ ,  $M = (\pi, \pi)$ . The nearest-neighbor hopping is set to  $t = 1$ . Left: Result for  $U = 0$ . Here,  $A(\mathbf{k}, \omega) = \delta(\omega - \epsilon(\mathbf{k}))$ , where  $\epsilon(\mathbf{k})$  is the tight-binding dispersion. Right: Quantum Monte-Carlo result for  $U = 8$ . Figure adapted from Refs. [21, 22].

general. At half-filling, however, the lattice QMC approach is very powerful. This is obvious when comparing to exact diagonalization (ED) techniques, for example, which suffer from the exponentially growing Hilbert-space with increasing system size. The enormous size of the Hilbert space dimension for  $L = 64$  is way beyond what can be accessed by ED.

## 5 Local and nonlocal correlations

The results displayed in Fig. 3 have been computed for the Hubbard model at  $U = 8$ , i.e.,  $U = W$ , where  $W$  is the width of the noninteracting band, and  $\mu = U/2$ , which enforces half-filling, and a high inverse temperature  $\beta = 10$ . The example is very instructive as it embodies a couple of famous many-body effects: First of all, it is obvious that the single-electron excitations are gapped in the interacting case; there is no finite spectral weight in the vicinity of  $\omega = 0$  and thus no Fermi surface. This is a nice demonstration of Mott-insulating behavior, i.e., the system is an interaction-driven insulator. The standard explanation is that, for strong  $U$ , each site of the lattice is almost perfectly occupied by exactly one electron as the gain in kinetic energy  $\sim t$  due to delocalization of the electrons in the ground state is much smaller than the energy penalty  $\sim U$  that would have to be paid when double occupancies were created. An excitation of the ground state carrying charge must therefore bridge a large gap of the order of  $U$ . This explains the insulating character of the system.

Second, while there are well-defined and dispersing single-electron excitations visible, these are not  $\delta$ -function-like but smeared out in energy to some degree. The intrinsic broadening of the excitations is in fact due to their decay as mediated by the interaction. This lifetime effect is clearly beyond the simple bandstructure picture. Quite generally, there are typically large ranges in the  $(\mathbf{k}, \omega)$ -plane, where the spectral weight is finite but where there are no well-defined peaks. This “incoherent background” must be seen as the result of complicated decay products. The initial excitation of the system affects a single electron only. The remaining final state  $c_{R\sigma}^{(\dagger)}|0\rangle$ ,

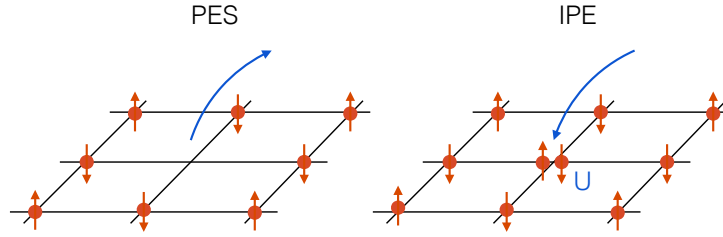


**Fig. 4:** Schematic representation of the high-energy single-electron excitations of the half-filled Hubbard model for strong  $U$ . The lower Hubbard band results from  $\omega < 0$  (photoemission, PES) excitations leaving a hole in the final state which propagates through the lattice. The upper Hubbard band results from  $\omega > 0$  (inverse photoemission, IPE) excitations leaving a propagating double occupancy in the final state.

however, is not an eigenstate. It may decay in a high-order process, involving high powers of  $H_0$  and  $H_1$ , into states with many low-energy excitations of many electrons. The phase space for such complex decay processes is not very much restricted by energy and momentum conservation, it is huge, and thus one would expect a broad and featureless continuum.

Third, there are still some well-defined structures with high spectral weight. For example, there are *two* “bands” with high spectral weight, one around  $\Gamma$  at negative frequencies  $\omega \approx -6$  (PES) and another one around the  $M$  points at positive frequencies  $\omega \approx +6$  (IPE), rather than a single band as in the  $U = 0$  limit. These are the so-called lower (LHB) and upper Hubbard bands (UHB), see Fig. 4. They are related to each other via the general constraint  $A(\mathbf{k}, \omega) = A(\mathbf{k} + \mathbf{Q}, -\omega)$  with  $\mathbf{Q} = (\pi, \pi)$ , which results from particle-hole symmetry present at half-filling and a bipartite lattice with nearest-neighbor hopping. Note that the bandstructure paradigm cannot explain those “bands”: Irrespective of the form of  $H_0$ , there is exactly one ( $\delta$ -like) peak per  $\mathbf{k}$ -point on the  $\omega$  axis. One therefore speaks about correlation-induced *satellites*. Physically, the lower Hubbard band results from the propagation of the hole in the final state of the electron-removal (photoemission) process. In the  $U \rightarrow \infty$  limit we expect that the final-state hole propagates almost freely through the lattice, such that a dispersive structure with spectral width of  $W_{\text{LHB}} = 8$  is generated. An analogous explanation holds for the upper Hubbard band seen in IPE. Here, the electron-addition (inverse photoemission) process produces an itinerant doubly occupied site in the final state resulting in a dispersive excitation with  $W_{\text{UHB}} = 8$  for strong  $U$ . The excitation energies can be read off from Eq. (20) (however, one has to include the  $\mu$ -shift in addition): The lower Hubbard band is centered around  $\omega = E_0 - E_n - \mu \approx -\mu = -U/2$  while the upper Hubbard band lies at  $\omega = E_n - E_0 - \mu \approx U - \mu = +U/2$ , such that their energy difference, the Hubbard gap, is given by  $\Delta_{\text{UHB-LHB}} \approx U$  for  $U \rightarrow \infty$ . Apart from their dispersion, the existence of the Hubbard bands is due to a local effect, namely due to the local charge correlation at the site where the (inverse) photoemission process takes place. Hubbard bands are said to be an effect of *local correlations*.

Besides the Hubbard bands at high excitation energies, there are rather well-defined low-energy structures in the spectrum at  $\omega \approx \pm 3$ . These result from *nonlocal correlations*, in particular from nonlocal antiferromagnetic correlations, as is explained by the superexchange mechanism, see Fig. 5: Recall that for strong  $U$ , the occupancy of each site is almost unity in the ground

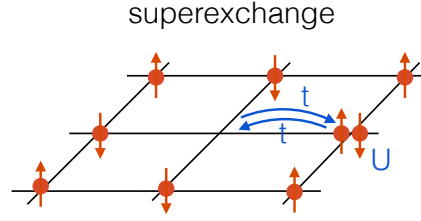


**Fig. 5:** Superexchange mechanism in the Hubbard model at half-filling and for strong  $U$ . See text for explanation.

state of the system. If the occupancy was perfectly unity, the ground state would have a macroscopic  $2^L$ -fold degeneracy as each localized electron corresponds to a local spin-1/2. The true ground state, however, has a small but important admixture of configurations with somewhat delocalized electrons. These result from the fact that the ground-state energy can be lowered by a second-order hopping process gaining delocalization energy, while a double occupancy is merely created virtually. Due to the Pauli principle, however, such superexchange processes are only possible, if neighboring spins align antiferromagnetically. Hence, the ground state is a nondegenerate singlet in which neighboring local spins

$$\mathbf{s}_R \equiv \frac{1}{2} \sum_{\sigma\sigma'} c_{R\sigma}^\dagger \boldsymbol{\tau}_{\sigma\sigma'} c_{R\sigma'} \quad (26)$$

( $\boldsymbol{\tau} = (\sigma_x, \sigma_y, \sigma_z)$  is the vector of Pauli matrices) are antiferromagnetically correlated. In fact, using strong-coupling perturbation theory at second order in  $t/U$ , one can map the low-energy sector of the Hubbard model onto the spin-1/2 Heisenberg model with antiferromagnetic exchange interaction  $J = 4t^2/U$  [23]. Hence, the *low-energy* excitations of the Hubbard model are nonlocal spin excitations with a band width of about  $2J$  (with  $2J = 1$  at  $U = 8$ ). These spin excitations couple to the single-electron excitations, they “dress” the moving hole (PES) or the moving doublon (IPE), i.e., the hole / doublon constantly emits and reabsorbs spin excitations during its motion through the antiferromagnetic spin structure. This gives rise to a renormalization of the Hubbard “bands” but also to novel structures in  $A(\mathbf{k}, \omega)$  at low frequencies (here, at intermediate  $U$ , at  $\omega \approx \pm 3$ ) which must be seen as fingerprints of nonlocal antiferromagnetic correlations.

Much higher resolution would be necessary to get still deeper insight into the physics of the model. Resolution is limited, however, by various factors: (i) The finite lattice size leads to an artificial discretization of  $\mathbf{k}$ -space. With  $L = 64$ , as in the present example, the spacing between  $\mathbf{k}$ -points along  $\Gamma$ - $X$ , i.e., along the  $k_x$ -line in the BZ ( $-\pi < k_x < \pi$ ) is  $\Delta k_x = 2\pi/8$ ; there are 4  $\mathbf{k}$ -points only between  $\Gamma$  and  $X$ . (ii) The QMC calculations must be run at finite temperatures. Here, the inverse temperature is  $\beta = 10$  which already has some unwanted impact, such as thermal broadening and thermally induced decay of correlations. (iii) For technical reasons, QMC is implemented on the imaginary time ( $\tau$ ) axis. Data obtained for  $A(\mathbf{k}, \tau)$  must be extrapolated, using the maximum-entropy method, for instance, to the real-frequency axis. This produces an additional unwanted broadening of spectral structures.

## 6 Cluster perturbation theory

Roughly, DMFT treats local correlations correctly but is not able to account for the effects of nonlocal correlations. The importance of the latter is a strong motivation to construct cluster extensions of the DMFT. To develop the main ideas and to get first insights, we will start with a much simpler approach, namely with the cluster perturbation theory (CPT) [24, 25].

Consider again the simple noninteracting tight-binding model  $H_0$ , as given by Eq. (22). The left diagram in Fig. 6 represents  $H_0$  for the two-dimensional case and for hopping between nearest neighbors only. Next, we consider a model which is obtained from  $H_0$  by grouping the  $L$  sites of the lattice into  $L/L_c$  identical clusters consisting of  $L_c$  sites each and by neglecting the hopping between the clusters, see Fig. 6 (middle). The corresponding Hamiltonian is

$$H'_0 = \sum_{\mathbf{R}_1 \mathbf{R}_2 \sigma} t'_{\mathbf{R}_1, \mathbf{R}_2} c_{\mathbf{R}_1 \sigma}^\dagger c_{\mathbf{R}_2 \sigma}. \quad (27)$$

This system is called the *reference system* opposed to the *original system* with Hamiltonian  $H_0$ . If  $\mathbf{t}$  with elements  $t_{\mathbf{R}_1, \mathbf{R}_2}$  is the hopping matrix of the original system, and  $\mathbf{t}'$  the hopping matrix of the reference system, then

$$\mathbf{V} = \mathbf{t} - \mathbf{t}' \quad (28)$$

is the neglected inter-cluster hopping, see Fig. 6, right. Obviously, the translation symmetry group of  $H'_0$  is described by a superlattice.

The Green function of the model  $H_0$  is

$$\mathbf{G}_0(\omega) = \frac{1}{\omega + \mu - \mathbf{t}}. \quad (29)$$

Here, we have explicitly introduced the chemical potential  $\mu$  (which is not important here but will be used later). Furthermore, we again employ a matrix notation and write  $\omega$  rather than  $\omega \mathbf{1}$  for short etc. Note that  $(\dots)^{-1}$  and  $1/(\dots)$  mean matrix inversion.

The reference system's Green function is

$$\mathbf{G}'_0(\omega) = \frac{1}{\omega + \mu - \mathbf{t}'} \quad (30)$$

In this case the matrix inverse is in a way simpler to compute since the hopping matrix  $\mathbf{t}'$  has a block structure as it does not connect sites in different clusters. Therefore, the following question comes up: Having the Green function of the reference system at hand, how can we get the Green function of the original model  $H_0$ ? With some algebra, one easily derives the equation

$$\mathbf{G}_0(\omega) = \mathbf{G}'_0(\omega) + \mathbf{G}'_0(\omega) \mathbf{V} \mathbf{G}_0(\omega), \quad (31)$$

which is solved by

$$\mathbf{G}_0(\omega) = \frac{1}{\mathbf{G}'_0(\omega)^{-1} - \mathbf{V}}. \quad (32)$$

We see that using Green functions it is formally rather easy to couple a system of isolated clusters. For the noninteracting system this is not of much importance. In particular, in Eq. (32) the block structure is lost when adding  $-\mathbf{V}$  to  $\mathbf{G}'_0(\omega)^{-1}$ .

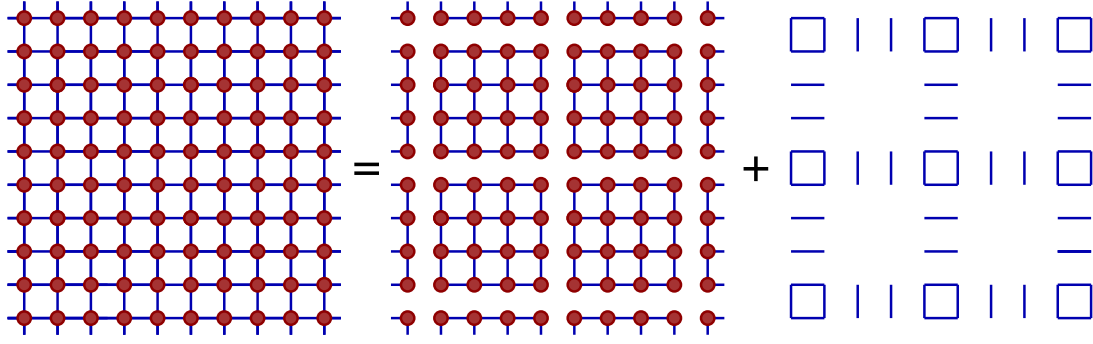


**Fig. 6:** Left: Graphical representation of a tight-binding model with hopping between nearest neighbors on a square lattice. Hopping matrix  $t$ . Middle: The same model but with vanishing hopping between identical clusters consisting of  $L_c = 16$  sites each. Hopping matrix  $t'$ . Right: The neglected inter-cluster hopping  $V$ . Taken from Ref. [26].

However, we are actually interested in interacting systems. Let us, therefore, take the Hubbard model as our original system  $H = H_0 + H_1$  with the interaction term given by Eq. (25). The reference model shall again be defined by switching off the inter-cluster hopping  $V$ . Its Hamiltonian is  $H' = H_0(t') + H_1$ . Note that since  $H_1$  consists of completely local terms, the reference system consists of a set of interacting but decoupled clusters. Therefore, it is comparatively easy to solve the problem exactly (by numerical means if necessary), while for the original lattice model this is a hard problem. Of course, there is no simple relation between the Green functions of the original and of the reference system like Eq. (31). Nevertheless, it is very tempting to assume that  $G(\omega)$  satisfies

$$G(\omega) = G'(\omega) + G'(\omega) V G(\omega), \quad (33)$$

where both  $G$  and  $G'$  are interacting Green functions. This equation constitutes the cluster perturbation theory [24, 25]. The CPT provides an approximate expression for  $G$  which is easy to compute (numerically) if  $L_c$  is not too large.

There is an independent and equivalent way to motivate the CPT: It starts from the Dyson equation for the reference system

$$G'(\omega) = G'_0(\omega) + G'_0(\omega) \Sigma'(\omega) G'(\omega), \quad (34)$$

which may be solved for the self-energy, i.e.,  $\Sigma'(\omega) = G'_0(\omega)^{-1} - G'(\omega)^{-1}$ . Assuming that  $\Sigma'(\omega)$  is a good approximation for the self-energy of the original system,

$$\Sigma(\omega) \approx \Sigma'(\omega), \quad (35)$$

and inserting into the Dyson equation of the original system,

$$G(\omega) = G_0(\omega) + G_0(\omega) \Sigma(\omega) G(\omega), \quad (36)$$

immediately yields the CPT equation (33) when using Eqs. (29) and (30).

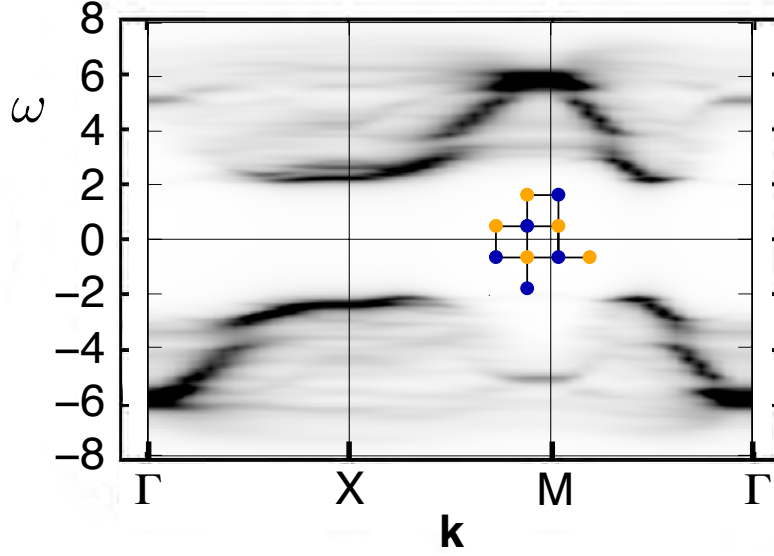


**Fig. 7:** The same as in Fig. 3 for  $U = 8$  but results are obtained with the CPT using  $L_c = 10$ -site clusters. See inset for cluster geometry. Figure adapted from Ref. [22].

The idea to approximate the self-energy by the self-energy of the reference system is motivated by the fact that the self-energy of the Hubbard model or, more generally, of models with local interactions, is a quantity that is “more local” than the Green function. In the limit of a high-dimensional hypercubic lattice with nearest-neighbor hopping  $t_{RR'} = \text{const}/D^{1/2}$ , for example, the nearest-neighbor elements of the self-energy scale as  $\Sigma_{RR'\sigma}(\omega) \sim 1/D^{3/2}$  while  $G_{RR'\sigma}(\omega) \sim 1/D^{1/2}$  [4]. While the CPT is a systematic approximation, which is controlled by the size of the clusters in the reference system and which trivially becomes exact in the infinite-cluster limit  $L_c \rightarrow \infty$ , it must be seen as a comparatively crude approximation for typical cluster sizes used in practice, see Ref. [27] and references therein, for instance. For cluster size  $L_c = 1$  it reduces to the simple Hubbard-I approximation. Still, the CPT can provide us with a rather good first idea about the Green function and the spectral density. This is demonstrated with Fig. 7 which shows the spectral density of the Hubbard model, as in Fig. 3, but obtained by CPT for clusters with  $L_c = 10$  sites. The cluster geometry is shown in the inset. One can easily see that this can be used for a tiling of the two-dimensional square lattice. As a rule of thumb, compact but asymmetric cluster shapes are preferable. Indeed, the CPT result quite nicely reproduces the results of the much more elaborate QMC approach.

## 7 Periodization schemes

There is an obvious problem, which is actually shared by any cluster approach that is formulated in real space. Namely, as the reference system is given by a set of decoupled clusters, the approximate self-energy does not preserve the translational symmetries of the original lattice. The CPT Green function  $G_{\mathbf{R},\mathbf{R}'}(\omega) = G_{\tilde{\mathbf{R}}\tilde{\mathbf{R}}',rr'}(\omega)$  is merely invariant under superlattice translations  $\tilde{\mathbf{R}} \rightarrow \tilde{\mathbf{R}} + \Delta\tilde{\mathbf{R}}$ . (Note that we use a notation with the spin-projection index  $\sigma$  suppressed). This means  $G_{\tilde{\mathbf{R}}\tilde{\mathbf{R}}',rr'}(\omega) = G_{\tilde{\mathbf{R}}+\Delta\tilde{\mathbf{R}},\tilde{\mathbf{R}}'+\Delta\tilde{\mathbf{R}},r,r'}(\omega)$ . Hence, Fourier transformation



$V$ , see Eq. (12), diagonalizes  $G$  with respect to the superlattice indices

$$\frac{L_c}{L} \sum_{\tilde{\mathbf{R}}\tilde{\mathbf{R}}'} V_{\tilde{\mathbf{k}},\tilde{\mathbf{R}}}^\dagger G_{\tilde{\mathbf{R}}\tilde{\mathbf{R}}',rr'}(\omega) V_{\tilde{\mathbf{R}}',\tilde{\mathbf{k}}} = G_{rr'}(\tilde{\mathbf{k}},\omega) \delta_{\tilde{\mathbf{k}}\tilde{\mathbf{k}}'} \quad (37)$$

with

$$G_{rr'}(\tilde{\mathbf{k}},\omega) = \left( \frac{1}{\omega + \mu - \mathbf{t}(\tilde{\mathbf{k}}) - \Sigma(\omega)} \right)_{rr'}. \quad (38)$$

Here, the  $V$ -Fourier transform  $\mathbf{t}(\tilde{\mathbf{k}})$  of the hopping matrix  $t_{\tilde{\mathbf{R}}\tilde{\mathbf{R}}',rr'}$  is an  $L_c \times L_c$  matrix with elements  $t_{rr'}(\tilde{\mathbf{k}})$  for each wave vector  $\tilde{\mathbf{k}}$  in the reciprocal supercell. The self-energy is “cluster-local”, i.e., it is diagonal in the superlattice indices  $\tilde{\mathbf{R}}, \tilde{\mathbf{R}}'$ , and thus, after  $V$ -Fourier transformation, is independent of  $\tilde{\mathbf{k}}$ . The “cluster-local” elements of  $G$  with  $\tilde{\mathbf{R}} = \tilde{\mathbf{R}}'$  are obtained by

$$G_{rr'}^{(\text{loc})}(\omega) = \frac{L_c}{L} \sum_{\tilde{\mathbf{k}} \in \text{RSC}} \left( \frac{1}{\omega + \mu - \mathbf{t}(\tilde{\mathbf{k}}) - \Sigma(\omega)} \right)_{rr'}. \quad (39)$$

From the fully local elements  $G_{rr}^{(\text{loc})}(\omega)$  we then get the local interacting density of states (LDOS) at a site  $\mathbf{R} = (\tilde{\mathbf{R}}, \mathbf{r})$  as

$$A_{\mathbf{R}}(\omega) = -\frac{1}{\pi} \text{Im} G_{rr}(\omega + i0^+). \quad (40)$$

One would expect that the LDOS exhibits the same (translational) symmetries as the Hamiltonian of the original system and of the original lattice:  $A_{\mathbf{R}}(\omega) = A(\omega)$ . Within the CPT, however, there is an artificial dependence of the LDOS on  $\mathbf{r}$ .

A modified cluster-perturbation theory, constructed in the same way as the standard CPT but considering periodic boundary conditions for each of the individual clusters, has been suggested by Zacher *et al.* [28]. It has been recognized [29], however, that this gives less convincing results in practice. The modified CPT makes the Green function invariant under translations within each cluster. However, since  $U \neq VW$ , there is also no improvement on the formal level.

One could also try to transform the original model and the reference system as well to reciprocal space. This straightforward idea means to express  $H$  and  $H'$  in terms of annihilators  $c_{\mathbf{k}}$  rather than  $c_{\mathbf{R}}$  and analogously for the creators and to employ the CPT decoupling thereafter. Clearly,  $H'$  will exhibit the full translational symmetry. However, the idea will not work for models with local interactions, such as the Hubbard model. A local interaction in real space transforms into a delocalized one in  $\mathbf{k}$ -space where the interaction parameters  $U_{\mathbf{k}\mathbf{k}'\mathbf{k}''\mathbf{k}'''}$  basically couple any  $\mathbf{k}$  point to any other.

With respect to the local spectral density (40), a pragmatic way out would be to average over the cluster sites

$$A(\omega) \equiv \frac{1}{L_c} \sum_{\mathbf{r}} A_{(\tilde{\mathbf{R}},\mathbf{r})}(\omega) = \frac{1}{L} \sum_{\mathbf{R}} A_{\mathbf{R}}(\omega). \quad (41)$$

One thus distinguishes between the CPT spectral density on the one hand and the translationally invariant (“physical”) spectral density on the other. Generally, a periodization operator  $\hat{T}$  can be defined which, for example, enforces a translationally invariant Green function:  $\mathbf{G}(\omega) \mapsto \hat{T}[\mathbf{G}](\omega)$ . A possible construction of  $\hat{T}$  is to start with a  $U$ -Fourier transform of the CPT Green function from  $\mathbf{R}$ -space to  $\mathbf{k}$ -space. As the Green function does not fully respect the translation symmetries, this transformation does not fully diagonalize the Green function, and we get  $G_{\mathbf{k}\mathbf{k}'}(\omega)$  with nonzero elements for  $\mathbf{k} \neq \mathbf{k}'$ . Periodization is then achieved by replacing  $G_{\mathbf{k}\mathbf{k}'}(\omega) \mapsto G_{\mathbf{k}\mathbf{k}}(\omega) \delta_{\mathbf{k},\mathbf{k}'} \equiv \hat{T}[\mathbf{G}]_{\mathbf{k}\mathbf{k}'}(\omega)$ . This provides us with a translationally invariant (physical) Green function  $\hat{T}[\mathbf{G}](\omega)$ . In real space, this periodization reads

$$\hat{T}[\mathbf{G}]_{\mathbf{R}\mathbf{R}'} = \frac{1}{L} \sum_{\mathbf{R}''\mathbf{R}'''} \delta_{\mathbf{R}-\mathbf{R}',\mathbf{R}''-\mathbf{R}'''} G_{\mathbf{R}''\mathbf{R}'''} . \quad (42)$$

For  $\mathbf{R} = \mathbf{R}'$ , in particular, we have

$$\hat{T}[\mathbf{G}]_{\mathbf{R}\mathbf{R}}(\omega) = \frac{1}{L} \sum_{\mathbf{R}''\mathbf{R}'''} \delta_{\mathbf{R}''\mathbf{R}'''} G_{\mathbf{R}''\mathbf{R}'''}(\omega) = \frac{1}{L} \sum_{\mathbf{R}} G_{\mathbf{R}\mathbf{R}}(\omega) = \frac{1}{L_c} \sum_{\mathbf{r}} G_{\mathbf{r}\mathbf{r}}(\omega), \quad (43)$$

consistent with Eq. (41). This periodization is actually a standard procedure and has also been used to produce the results displayed in Fig. 7. In addition a smoothening of the spectrum has been employed by replacing the positive infinitesimal  $0^+$  with a small but finite value  $\eta > 0$  in Eq. (19). This is necessary since the Green function of the reference system and thus the CPT self-energy consists of a finite number of poles only such that, even after periodization Eq. (41), the LDOS is composed of a finite number of  $\delta$ -peaks only.

A different periodization scheme is given by periodizing the CPT self-energy,

$$\Sigma(\omega) \mapsto \hat{T}[\Sigma](\omega) . \quad (44)$$

Concretely, with  $\Sigma_{(\tilde{\mathbf{R}},\mathbf{r}),(\tilde{\mathbf{R}}',\mathbf{r}')(\omega)} = \Sigma_{\mathbf{r},\mathbf{r}'}(\omega) \delta_{\tilde{\mathbf{R}},\tilde{\mathbf{R}}'}$ , we have

$$\hat{T}[\Sigma]_{(\tilde{\mathbf{R}},\mathbf{r}),(\tilde{\mathbf{R}}',\mathbf{r}')(\omega)} = \frac{1}{L_c} \sum_{\mathbf{r}'',\mathbf{r}'''} \delta_{\tilde{\mathbf{R}}+\mathbf{r}-\tilde{\mathbf{R}}'-\mathbf{r}'',\mathbf{r}''-\mathbf{r}'''} \Sigma_{\mathbf{r}'',\mathbf{r}'''}(\omega) . \quad (45)$$

This produces a self-energy which fully respects the translational symmetries and thus, via Eq. (36), a fully translationally invariant Green function. Both periodization schemes share the same *ad hoc* character. The periodization of the self-energy appears a bit more artificial, as the necessary *ad hoc* approximation is performed at an earlier stage of the theory rather than at the very end.

Note that any periodization scheme can also be used to restore point-group symmetries of the original lattices which are usually violated by the plain CPT as well. Fig. 8 gives some examples for various cluster sizes. In most cases, and already for  $L_c = 2$ , the reference system has a lower point-group symmetry. The periodization operator, Eq. (42), can be seen as an average over all possible translations. In basically the same way, by properly generalizing the operator  $\hat{T}$ , one can restore not only the translational but also the discrete rotational and reflection symmetries.

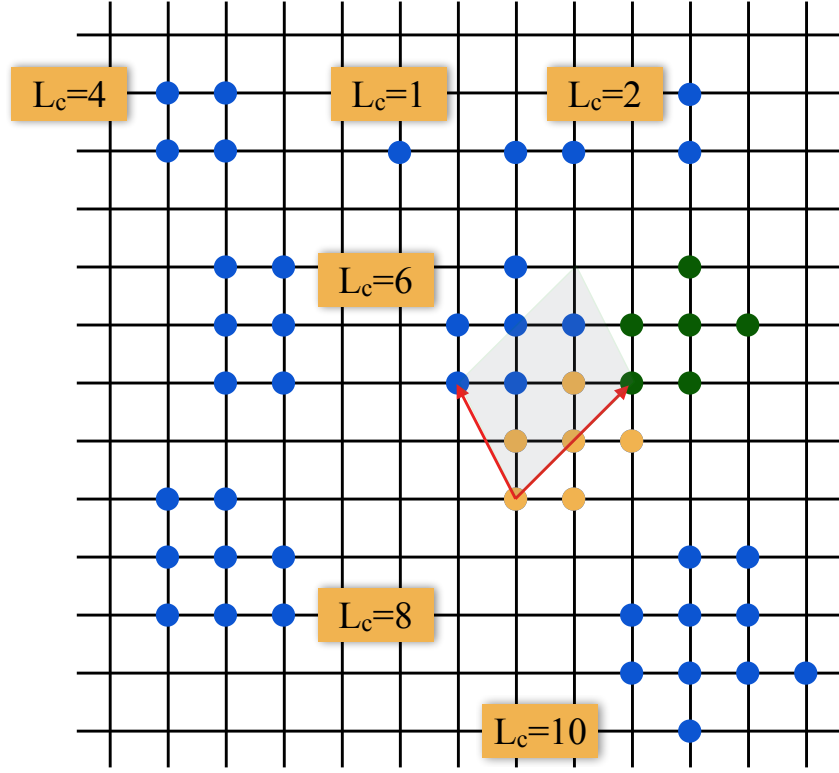


**Fig. 8:** Different tilings of the square lattice into clusters with  $L_c$  sites each. See text for discussion.

A completely different idea to generate a CPT-based approximation respecting the discrete symmetries is the “periodic CPT” which has been suggested by Tran Minh-Tien [30] and which is inspired by the dynamical cluster approximation (DCA) discussed below. Here, one modifies the hopping matrix of the *original system*,  $t \mapsto \bar{t}$ , rather than the hopping of reference system  $t'$ . The latter is still taken as a system consisting of identical isolated clusters but with periodic boundary conditions for each individual cluster. For a one-dimensional system, Fig. 9 illustrates the hopping matrix of the original system (a) and of the reference system (b). The symmetries of the latter are given by (i) the intra-cluster translations  $\mathbf{r}$  and by (ii) the superlattice translations  $\tilde{\mathbf{R}}$ . Now, the construction of  $\bar{t}$  is such that it exhibits the same translational symmetries. Consider a cluster translation  $(\tilde{\mathbf{R}}, \mathbf{r}) \mapsto (\tilde{\mathbf{R}}, \mathbf{r} + \Delta\mathbf{r})$  with  $\Delta\mathbf{r}$  connecting nearest neighbors in a cluster (with periodic boundary conditions on the cluster). The corresponding transformation of the hopping amplitudes of the reference system is a symmetry:  $t'_{\tilde{\mathbf{R}}, \mathbf{r}, \tilde{\mathbf{R}}', \mathbf{r}'} \mapsto t'_{\tilde{\mathbf{R}}, \mathbf{r} + \Delta\mathbf{r}, \tilde{\mathbf{R}}', \mathbf{r}' + \Delta\mathbf{r}} = t'_{\tilde{\mathbf{R}}, \mathbf{r}, \tilde{\mathbf{R}}', \mathbf{r}'}$ . To make it a symmetry of the hopping of the original system as well, some hopping amplitudes must be added. Panel (c) of the figure gives an example for a specific nearest-neighbor cluster translation which is equivalent with a cyclic permutation of the sites within each cluster. The upper part shows the hopping amplitudes present in  $t$ , while the lower one shows those that are generated by the translation. The hopping amplitudes generated by all cluster translations are included in the new hopping matrix  $\bar{t}$ , see panel (d).

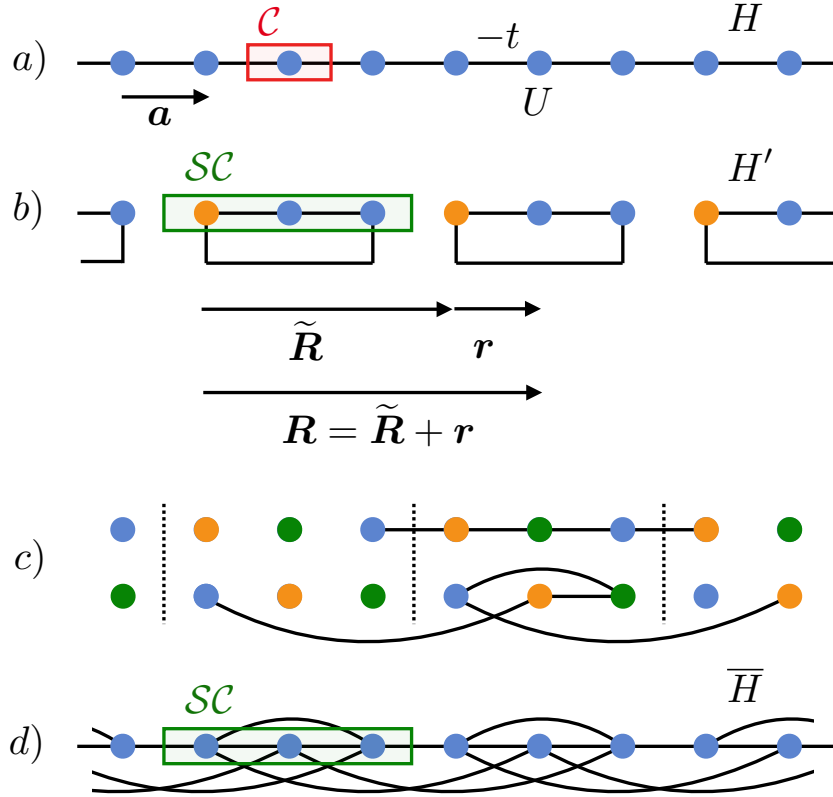


**Fig. 9:** Construction of the modified original system  $\bar{H}$  for a one-dimensional lattice. a) Original system  $H$ , black lines: nearest-neighbor hopping  $-t$ , on-site Hubbard interaction  $U$ , unit cell  $\mathcal{C}$ . b) Reference system  $H'$ : superlattice (basis) vector  $\tilde{\mathbf{R}}$ , cluster vector  $\mathbf{r}$ , supercell  $SC$  with  $L_c = 3$  (cf. Fig. 2). c) A cyclic permutation of the sites within each cluster is a symmetry of  $H'$ . Black lines in the upper panel: nearest-neighbor hopping parameters related to a given cluster. Lower panel: resulting hopping parameters after the transformation. d) Hopping parameters of the Hamiltonian  $\bar{H}$ , which is invariant (i) under all intra-cluster translations and (ii) under all superlattice translations.

Note that for  $L_c \rightarrow \infty$  the inclusion of the additional hopping amplitudes becomes irrelevant. Hence, the replacement  $t \mapsto \bar{t}$  is controlled by  $L_c$ , i.e., it becomes exact, up to irrelevant boundary terms, in the infinite-cluster limit. The explicit construction of  $\bar{t}$  is the following

$$\bar{t} = (\mathbf{V}\mathbf{W})U^\dagger t U(\mathbf{V}\mathbf{W})^\dagger. \quad (46)$$

Let us stress once more, that  $\mathbf{V}\mathbf{W} \neq U$  for clusters of finite size  $L_c$ . The first transformation  $U^\dagger t U$  diagonalizes the hopping matrix  $t$ , and the diagonal elements are given by  $\varepsilon(\mathbf{k}) = \varepsilon(\tilde{\mathbf{G}} + \tilde{\mathbf{k}})$  with a uniquely defined reciprocal superlattice vector  $\tilde{\mathbf{G}}$  and a uniquely defined wave vector  $\tilde{\mathbf{k}} \in \mathcal{R}SC$ . Double back transformation using  $\mathbf{V}$  and  $\mathbf{W}$  then yields:

$$\bar{t}_{\tilde{\mathbf{R}}\mathbf{r};\tilde{\mathbf{R}}'\mathbf{r}'} = \frac{1}{L_c} \sum_{\tilde{\mathbf{G}}} e^{i\tilde{\mathbf{G}}(\mathbf{r}-\mathbf{r}')} \frac{L_c}{L} \sum_{\tilde{\mathbf{k}}} e^{i\tilde{\mathbf{k}}(\tilde{\mathbf{R}}-\tilde{\mathbf{R}}')} \varepsilon(\tilde{\mathbf{k}} + \tilde{\mathbf{G}}). \quad (47)$$

Obviously,  $\bar{t}$  is invariant under both, superlattice translations as well as cluster translations.

Applying CPT to the original system Fig. 9(d) using the reference system Fig. 9(b) yields

$$\mathbf{G}(\omega) = \frac{1}{\omega + \mu - \bar{\mathbf{t}} + \boldsymbol{\Sigma}(\omega)} . \quad (48)$$

As the self-energy is taken from the reference system, it is diagonal with respect to superlattice translations  $\tilde{\mathbf{R}}$  and is  $\tilde{\mathbf{R}}$ -independent. Since the original as well as the reference system share the same symmetries both,  $\boldsymbol{\Sigma}(\omega)$  and  $\bar{\mathbf{t}}$  are diagonalized by  $\mathbf{V}\mathbf{W}$

$$G(\tilde{\mathbf{k}} + \tilde{\mathbf{G}}, \omega) = \frac{1}{\omega + \mu - \varepsilon(\tilde{\mathbf{k}} + \tilde{\mathbf{G}}) + \Sigma(\tilde{\mathbf{G}}, \omega)} . \quad (49)$$

Note that we have replaced the diagonal elements  $\bar{\varepsilon}(\tilde{\mathbf{k}}, \tilde{\mathbf{G}})$  of  $(\mathbf{V}\mathbf{W})^\dagger \bar{\mathbf{t}} (\mathbf{V}\mathbf{W})$  by the diagonal elements  $\varepsilon(\tilde{\mathbf{k}} + \tilde{\mathbf{G}})$  of  $\mathbf{U}^\dagger \mathbf{t} \mathbf{U}$ , which becomes correct for  $L_c \rightarrow \infty$  as discussed above. Likewise, again using the unique decomposition  $\mathbf{k} = \tilde{\mathbf{k}} + \tilde{\mathbf{G}}$ , we interpret  $G(\tilde{\mathbf{k}} + \tilde{\mathbf{G}}, \omega) \equiv G(\tilde{\mathbf{k}}, \tilde{\mathbf{G}}, \omega)$  as  $G(\mathbf{k}, \omega)$ , i.e., as the diagonal elements of  $\mathbf{U}^\dagger \mathbf{G}(\omega) \mathbf{U}$ . In this way we have achieved our goal, and we get a CPT Green function respecting the full translational symmetries of the original lattice. Obviously, the periodized CPT (P-CPT) employs an implicit periodization scheme, which is approximate for any finite  $L_c$  but becomes exact, as the CPT approximation itself, in the  $L_c \rightarrow \infty$  limit. We note that for finite  $L_c$ , the  $\mathbf{k}$ -dependence of the self-energy is discontinuous:  $\Sigma(\tilde{\mathbf{k}} + \tilde{\mathbf{G}}) = \Sigma(\tilde{\mathbf{G}})$  is  $\tilde{\mathbf{k}}$ -independent, i.e., within each of the  $L_c$  “patches”  $\mathcal{RSC}$  of the full reciprocal unit cell  $\mathcal{RC}$  of the original lattice, the self-energy is constant, while it jumps when crossing the boundaries between the patches. This unphysical feature of the P-CPT must be tolerated.

## 8 Self-consistent cluster-embedding approaches

A big disadvantage of the CPT and related cluster approximations is the lacking self-consistency. Let us recall that a generic mean-field theory not only takes a local perspective and focusses on a single site or on a small cluster cut out of an infinite lattice but also aims at a proper embedding of the site or the cluster in a mean field. The purpose of this mean field is to approximately account for the neglected environment of the cluster. The mean-field feeds back to the cluster problem but beyond that the quality of the mean-field theory improves considerably when the cluster observables feed back to the mean field as well, i.e., when cluster observables and mean field are determined self-consistently.

Table 2 gives an overview of various cluster approximations without (first column) and with self-consistent cluster embedding. Taking the self-energy of a single Hubbard site ( $L_c = 1$ ),

$$\Sigma_{\mathbf{R}\mathbf{R}'}(\omega) = \delta_{\mathbf{R}\mathbf{R}'} U \langle n_{\mathbf{R}-\sigma} \rangle + \delta_{\mathbf{R}\mathbf{R}'} \frac{U^2 \langle n_{\mathbf{R}-\sigma} \rangle (1 - \langle n_{\mathbf{R}-\sigma} \rangle)}{\omega + \mu - U(1 - \langle n_{\mathbf{R}-\sigma} \rangle)} , \quad (50)$$

as an approximation to compute the Green function for the Hubbard model is the essence of the Hubbard-I approximation. (Let us note that, in a strict sense, the Hubbard-I approximation does include some self-consistency and thus does not perfectly fit to the classification, see Ref. [18]).

impurity / cluster approaches		with self-consistent embedding	
Hubbard-I approach	[18]	DMFT	[1, 4]
CPT	[24, 25]	cellular DMFT (C-DMFT)	[9, 8]
simplified PC-DMFT		periodized C-DMFT	[31]
periodic CPT	[30]	DCA	[7]

**Table 2:** *Different cluster approximations. See text for discussion.*

The DMFT is a single-site mean-field theory as well ( $L_c = 1$ ) but with a self-consistent embedding of the site. It is important to realize that this is a dramatic improvement. Even though the DMFT self-energy is local,  $\Sigma_{RR'\sigma}(\omega) = \delta_{RR'} \Sigma_R(\omega)$ , it has a realistic  $\omega$  dependence with the typical branch cuts on the real axis rather than the simplistic single-pole structure of the Hubbard-I self-energy. The self-consistent DMFT embedding scheme is constructed such that one even recovers the exact solution of the Hubbard model in the limit, where the self-energy is local in fact [32], namely in the limit of infinite spatial dimensions [1].

Let us briefly recall the main idea for the Hubbard model as the original lattice model. To construct the single-site DMFT, we assume that the self-energy be local. In addition, a homogeneous (and nonmagnetic) phase is anticipated such that  $\Sigma_{RR'\sigma}(\omega) = \delta_{RR'} \Sigma(\omega)$ . We note in passing that this condition can be relaxed; this leads to real-space DMFT [33]. The most general reference system with a local self-energy and arbitrary  $\omega$ -dependence is given by a single interacting (“impurity”) site with  $U \neq 0$  hybridizing with a continuum of noninteracting bath degrees of freedom, i.e., by the single-impurity Anderson model

$$H' = \sum_{\sigma} \varepsilon_{\text{imp}} c_{\sigma}^{\dagger} c_{\sigma} + \frac{U}{2} \sum_{\sigma} n_{\text{imp},\sigma} n_{\text{imp},-\sigma} + \sum_{k\sigma} \varepsilon_k a_{k\sigma}^{\dagger} a_{k\sigma} + \sum_{k\sigma} \left( V_k c_{\sigma}^{\dagger} a_{k\sigma} + \text{H.c.} \right). \quad (51)$$

The local Green function on the impurity site is

$$G^{(\text{imp})}(\omega) = \frac{1}{\omega + \mu - \varepsilon_{\text{imp}} - \Delta(\omega) - \Sigma'(\omega)}. \quad (52)$$

The bath parameters, namely the hybridization strengths  $V_k$  and the on-site energies  $\varepsilon_k$ , enter the formalism via the hybridization function only:

$$\Delta(\omega) = \sum_k \frac{V_k^2}{\omega + \mu - \varepsilon_k}. \quad (53)$$

We will use the self-energy of the reference system as an approximation for the lattice model,  $\Sigma(\omega) = \Sigma'(\omega)$ . Obviously, a condition is needed to fix the hybridization function and therewith the parameters of the reference system. This self-consistency condition is obtained from the observation that the skeleton-diagram expansion leads to a functional relation between the self-energy and the Green function,  $\Sigma = \widehat{\Sigma}[G]$ , that is independent from the relation provided by the Dyson equation, see Fig. 10. On the single-site mean-field level or, equivalently, in the limit of infinite spatial dimensions, this functional is local, i.e.,  $\Sigma(\omega) = \widehat{\Sigma}[G^{(\text{loc})}](\omega)$  where

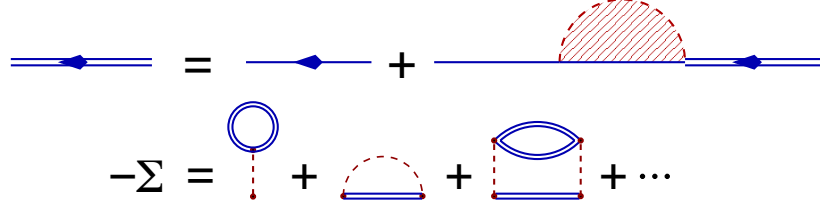


**Fig. 10:** Diagrammatic representation of the Dyson equation,  $G(\omega) = G_0(\omega) + G_0(\omega) \Sigma(\omega) G(\omega)$  (top). Representation of the skeleton-diagram expansion of the self-energy,  $\Sigma(\omega) = \hat{\Sigma}[G](\omega)$  (bottom).

$G^{(\text{loc})}(\omega) = G_{RR}(\omega)$  is the local (on-site) element of the Green function. Hence, the functional relation  $\hat{\Sigma}[\cdot]$  is exactly the same as that of the reference system:  $\Sigma'(\omega) = \hat{\Sigma}[G^{(\text{imp})}](\omega)$ . With  $\Sigma(\omega) = \Sigma'(\omega)$  this implies that

$$G^{(\text{imp})}(\omega) = G^{(\text{loc})}(\omega), \quad (54)$$

which is the famous self-consistency condition of DMFT.

The step from single-site DMFT to cellular DMFT is conceptually simple and corresponds to the step from the Hubbard-I approach to the CPT (see Tab. 2). One merely has to treat a finite Hubbard cluster with  $L_c > 1$  sites as a “super site” and adopt the same strategy. The actual work to be done consists in the numerical computation of the self-energy  $\Sigma'_{rr'}(\omega)$  of the Anderson “cluster” model

$$H' = \sum_{rr'\sigma} t_{rr'} c_{r\sigma}^\dagger c_{r'\sigma} + \frac{U}{2} \sum_{r\sigma} n_{r\sigma} n_{r-\sigma} + \sum_{k\sigma} \varepsilon_{rk} a_{rk\sigma}^\dagger a_{rk\sigma} + \sum_{rk\sigma} \left( V_{rk} c_{r\sigma}^\dagger a_{rk\sigma} + \text{H.c.} \right), \quad (55)$$

which is a small Hubbard model of  $L_c$  correlated sites, where each correlated site  $r$  hybridizes with an infinite number ( $k = 1, \dots, \infty$ ) of bath sites. The  $L_c \times L_c$  self-energy matrix is taken to approximate the “cluster local” self-energy of the Hubbard model,  $\Sigma_{\tilde{R}\tilde{R},rr'}(\omega) = \Sigma'_{rr'}(\omega)$ . With this at hand, one can compute the “cluster-local” elements of the Green function of the original model using the Dyson equation, cf. Eq. (39),

$$G_{rr'}^{(\text{loc})}(\omega) = \frac{L_c}{L} \sum_{\tilde{k} \in \mathcal{RSC}} \left( \frac{1}{\omega + \mu - t(\tilde{k}) - \Sigma(\omega)} \right)_{rr'} \quad (56)$$

and therewith the cluster Green function of the reference system via the C-DMFT self-consistency equation  $G_{rr'}^{(\text{cluster})}(\omega) = G_{rr'}^{(\text{loc})}(\omega)$ . Using the cluster analog of Eq. (52), where  $G^{(\text{imp})}(\omega)$  is replaced by the  $L_c \times L_c$  matrix  $G^{(\text{cluster})}(\omega)$ ,  $\Sigma'(\omega)$  by the matrix  $\Sigma'(\omega)$ ,  $\varepsilon_{\text{imp}}$  by the  $L_c \times L_c$  intra-cluster hopping matrix  $t' = t$ , and  $\Delta(\omega)$  by the diagonal matrix  $\Delta(\omega)$ , the diagonal elements of the latter are found as

$$\Delta_r(\omega) = \sum_{k\sigma} \frac{V_{rk}^2}{\omega + \mu - \varepsilon_{rk}} = \omega + \mu - t_{rr} - \Sigma_{rr}(\omega) - (G^{(\text{cluster})})_{rr}^{-1}(\omega). \quad (57)$$

The parameters of the reference system (55) are obtained as the poles and the weights of  $\Delta_r(\omega)$ , such that an updated cluster self-energy can be computed. This self-consistency cycle must be iterated until convergence is achieved.

The C-DMFT does not respect the translational symmetries of the underlying lattice. One way to restore the correct symmetry is the so-called periodized C-DMFT (PC-DMFT) [31], see third row in Tab. 2. Here, one employs the periodization operator  $\hat{T}$  to get a translationally invariant self-energy. The local Green function can thus be computed by  $U$ -Fourier transform and summation of  $\mathbf{k}$ . This yields the following PC-DMFT self-consistency equation:

$$G_{\mathbf{r}\mathbf{r}'}^{(\text{cluster})}(\omega) = G_{\mathbf{r}\mathbf{r}'}^{(\text{loc})}(\omega) = \frac{1}{L} \sum_{\mathbf{k}} \frac{e^{i\mathbf{k}(\mathbf{r}-\mathbf{r}')}}{\omega + \mu - \varepsilon(\mathbf{k}) - \hat{T}[\Sigma](\mathbf{k}, \omega)}. \quad (58)$$

The main difference as compared to the C-DMFT, Eq. (56), is that the periodized self-energy is used at each step in the self-consistency cycle.

For the dynamical cluster approximation (DCA, fourth row in Tab. 2), one must replace the original hopping  $\mathbf{t}$  by  $\bar{\mathbf{t}}$  only [31]. Both,  $\mathbf{t}$  and  $\bar{\mathbf{t}}$ , are invariant under superlattice translations. So we can compare  $t_{\mathbf{r}\mathbf{r}'}(\tilde{\mathbf{k}}) = (\mathbf{V}^\dagger \mathbf{t} \mathbf{V})_{\mathbf{r}\mathbf{r}'}(\tilde{\mathbf{k}})$  with  $\bar{t}_{\mathbf{r}\mathbf{r}'}(\tilde{\mathbf{k}}) = (\mathbf{V}^\dagger \bar{\mathbf{t}} \mathbf{V})_{\mathbf{r}\mathbf{r}'}(\tilde{\mathbf{k}})$ . One easily finds that these are equal up to a phase factor

$$\begin{aligned} \bar{t}_{\mathbf{r}\mathbf{r}'}(\tilde{\mathbf{k}}) &= \frac{1}{L_c} \sum_{\tilde{\mathbf{G}}} e^{i\tilde{\mathbf{G}}(\mathbf{r}-\mathbf{r}')} \varepsilon(\tilde{\mathbf{k}} + \tilde{\mathbf{G}}) \\ &= \frac{L_c}{L} \sum_{\tilde{\mathbf{R}}\tilde{\mathbf{R}'}} e^{-i\tilde{\mathbf{k}}(\tilde{\mathbf{R}}+\mathbf{r}-\tilde{\mathbf{R}}'-\mathbf{r}')} t_{\tilde{\mathbf{R}}+\mathbf{r}, \tilde{\mathbf{R}}'+\mathbf{r}'} \\ &= e^{-i\tilde{\mathbf{k}}(\mathbf{r}-\mathbf{r}')} t_{\mathbf{r}\mathbf{r}'}(\tilde{\mathbf{k}}). \end{aligned} \quad (59)$$

This is very easily implemented numerically. The DCA self-consistency condition reads

$$G_{\mathbf{r}\mathbf{r}'}^{(\text{cluster})}(\omega) = G_{\mathbf{r}\mathbf{r}'}^{(\text{loc})}(\omega) = \frac{L_c}{L} \sum_{\tilde{\mathbf{k}} \in \mathcal{RSC}} \left( \frac{1}{\omega + \mu - \bar{\mathbf{t}}(\tilde{\mathbf{k}}) - \Sigma(\omega)} \right)_{\mathbf{r}\mathbf{r}'}. \quad (60)$$

The decisive difference as compared to the C-DMFT is that  $\bar{\mathbf{t}}$  is also invariant under cyclic cluster translations, as it is the case for  $\mathbf{t}'$ . Hence, all matrices are simultaneously diagonalized by the cluster Fourier transformation  $\mathbf{W}$ , and we get a scalar self-consistency equation

$$G^{(\text{cluster})}(\tilde{\mathbf{G}}, \omega) = \frac{L_c}{L} \sum_{\tilde{\mathbf{k}}} \frac{1}{\omega + \mu - \varepsilon(\tilde{\mathbf{k}} + \tilde{\mathbf{G}}) - \Sigma(\tilde{\mathbf{G}}, \omega)}. \quad (61)$$

Which of the three cluster approaches, the C-DMFT, the PC-DMFT, and the DCA is the best one? This is a question that comes up immediately. An answer could be expected from a meta theory unifying all cluster approaches in a common theoretical framework. The self-energy-functional theory (SFT) [34, 10, 6] is in fact able to re-derive various approximations as stationary points of a general functional  $\Omega_{t,U}[\Sigma]$  for a given original lattice model with parameters  $\mathbf{t}$  and  $U$ . A particular approximation is defined by the choice of a reference system, with possibly different one-particle parameters  $\mathbf{t}'$  but the same interaction  $U$ . The reference system could be a system of decoupled clusters, also including noninteracting bath degrees of freedom, and is fixed by the structure of the  $\mathbf{t}'$  matrix. The self-energy of the reference system,  $\Sigma_{t',U}(\omega)$  is considered as a trial self-energy which must be optimized via the stationarity condition



$$\partial \Omega_{t,U}[\Sigma_{t',U}]/\partial t' = 0, \quad (62)$$

i.e., the self-energy is optimized by varying the one-particle parameters of the reference system. Taking the single-impurity Anderson model, Eq. (51), as a reference system, Eq. (62) recovers the DMFT self-consistency condition. For an Anderson cluster model, Eq. (55), the C-DMFT self-consistency condition is found. The DCA is obtained with the same reference system (with periodic boundaries) but applied to a different original model with  $t$  replaced by  $\bar{t}$ . Thereby, a set of external parameters of the self-energy functional is changed,  $\Omega_{t,U}[\Sigma] \rightarrow \Omega_{\bar{t},U}[\Sigma]$ , such that an unbiased comparison of the resulting optimal free energies is not possible. In case of the PC-DMFT, the parameters  $t$  and  $U$  remain unchanged, and the PC-DMFT self-consistency equation is also re-derived with the same reference system. Unfortunately, the form of the self-energy functional must be changed for this purpose,  $\Omega_{t,U}[\Sigma] \rightarrow \Omega_{t,U}[\hat{T}[\Sigma]]$ , and this means that a fair comparison is again not possible. One should note that the modification of the parameters of the original system (DCA) or the modification of the functional form (PC-DMFT) keep the systematic nature of the approach, i.e., they become irrelevant in the infinite-cluster limit and must therefore be considered as formally well justified. The SFT does provide the expected hierarchy among different approaches within each row of Tab. 2. E.g. the C-DMFT must be seen as superior compared to the CPT. In between, we find the variational cluster approach (VCA) which is defined by the same reference system as used for the CPT but with variational optimization of the intra-cluster hopping and the one-particle energies. There is also an interesting new approximation suggesting itself: Starting with the modified hopping  $\bar{t}$  and the reference system in Fig. 9b, generates a simplified DCA without bath degrees of freedom. This stands between the periodic CPT and the full DCA, see last row of Tab. 2.

Another criterion to decide between the different cluster approaches, could be their convergence behavior for  $L_c \rightarrow \infty$ . Consider first a *local* observable, such as the double occupancy in the Hubbard model or the local density of states, at a central site in an isolated cluster with  $L_c$  sites. Since nonlocal elements of Green functions typically decay exponentially with increasing distance, if the system is not at a critical point, one would expect an exponentially fast convergence of the observable with  $L_c \rightarrow \infty$ . This is the case for the C-DMFT, as the bath only couples to the surface sites of the cluster (assuming hopping between nearest neighbors only). The latter is easily seen by expanding both sides of the C-DMFT self-consistency equation,  $G_{rr'}^{(\text{cluster})}(\omega) = G_{rr'}^{(\text{loc})}(\omega)$ , and Eq. (57) in powers of  $1/\omega$  keeping terms of the order  $1/\omega^3$ , which eventually implies  $V_{rk} \neq 0$  for surface sites  $r$  only. Extended observables, e.g., the  $k$ -dependent Green function or the free energy, converge to the exact results with corrections  $\sim 1/L_1$ , where  $L_c = L_1^D$  for a  $D$ -dimensional hypercubic cluster. This is obvious since only  $2DL_1^{D-1}$  surface sites contribute to the average hybridization function compared to the total number of cluster sites  $L_1^D$ . For the DCA, on the other hand, where all sites in the cluster are coupled to the bath, convergence is faster with corrections  $\sim 1/L_c^2$ . A detailed discussion can be found in Ref. [5]. One should keep in mind, however, that with the cluster sizes that can be treated in practical calculations one is typically far from the regime where this scaling behavior can be seen.

A further important issue to be discussed is the description of *spontaneous* breaking of translational symmetry, e.g., in antiferromagnetic phases, charge-density-wave states, stripe order etc. Within the C-DMFT, if the cluster is large enough to contain the new unit cell, such phases can be found easily as there is no assumption made on the translational symmetry of the cluster self-energy. The DCA, on the other hand, does require translation symmetry on the cluster when using the self-consistency equation (61) formulated in reciprocal space. Symmetry breaking must then be anticipated and, considering e.g. antiferromagnetic order, one must introduce a reduced Brillouin zone and a constraint for the self-energy relating  $\mathbf{k}$  and  $\mathbf{k} + \mathbf{Q}_{\text{AF}}$ , where  $\mathbf{Q}_{\text{AF}}$  determines the type of antiferromagnetic ordering. The real-space formulation, Eq. (60) is much more elegant, as translation symmetry in the cluster can be broken spontaneously and arbitrarily, such that there is no need to anticipate a specific ordering pattern. In any case and for both, C-DMFT and DCA, it is clear, however, that a selected cluster size and cluster shape will necessarily bias to some degree the spatial modulation of the order parameter one is looking for. Calculations with different cluster geometries and sizes are therefore necessary. This must be seen as a big intrinsic disadvantage of the cluster approach. Finally, the description of the broken translation symmetries in the PC-DMFT is much more complicated and is discussed in Ref. [31], for example.

## 9 Discussion of selected results

One of the main topics of DMFT is the Mott metal-insulator transition in the Hubbard model [4]. For  $U = 0$  the system is a noninteracting metallic Fermi gas while for strong  $U$  the zero-temperature phase is a Mott insulator due to the high penalty for hopping processes producing doubly occupied sites. As a function of  $U$ , the single-site DMFT predicts a continuous metal-insulator transition at  $T = 0$ , see the  $T = 0$  end of the dashed line in Fig. 11 (left) [35]. The yellow area marks a coexistence regime, where the metallic and the insulating solution of the DMFT coexist. At finite temperatures, the free energy decides which one is stable, and the transition becomes discontinuous with a jump of, e.g., the double occupancy at the critical interaction  $U_c(T)$ . The dashed line of first order transitions ends in a second-order critical end point at  $U_{\text{MIT}}$ . At still higher temperatures there is a smooth crossover only, separating a bad-metal from a bad-insulator regime. The phase diagram, calculated for the Hubbard model on the square lattice, has the same structure as the corresponding phase diagram for the  $D = \infty$  hypercubic lattice. This unphysical essential independence of the results on the lattice dimension is characteristic for a mean-field approach. There is another serious problem. Namely, there is a macroscopically high entropy of the  $T = 0$  Mott-insulating ground state due to the  $2^L$ -fold degeneracy with respect to the orientation of the local magnetic moments. Within the DMFT, this degeneracy can only be lifted by long-range magnetic order, and in fact in the true DMFT ground state the system is an antiferromagnetic insulator for strong  $U$ . As has been discussed above (see Fig. 5), this is due to the superexchange mechanism favoring antiferromagnetic alignment of neighboring moments. This Heisenberg-insulator state, however, is suppressed in the DMFT calculation by enforcing spin symmetric solutions. The motivation is

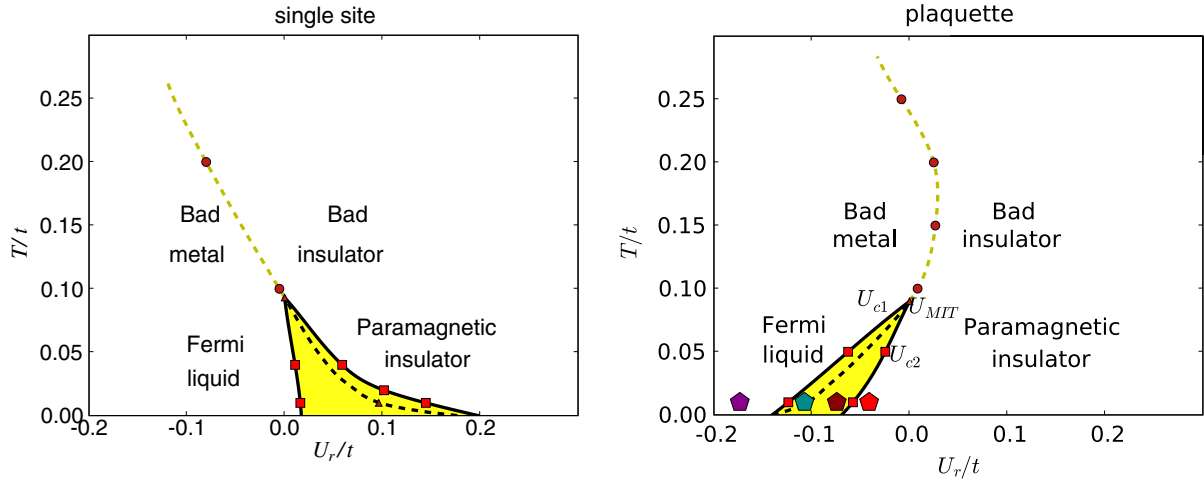


**Fig. 11:** Phase diagram of the paramagnetic Hubbard model at half-filling on the square lattice. Left: single-site DMFT. Right: C-DMFT,  $L_c = 4$ .  $U_r \equiv (U - U_{\text{MIT}})/U_{\text{MIT}}$  with  $U_{\text{MIT}} = 9.35t$  (DMFT),  $U_{\text{MIT}} = 6.05t$  (C-DMFT). Reprinted figure with permission from [35]. Copyright (2008) by the American Physical Society.

to uncover in this way the Mott transition in the paramagnetic state at temperatures below the Néel temperature  $T_N(U)$ . In the paramagnetic state and at finite temperatures, the large entropy stabilizes the Mott insulator as compared to the metallic Fermi-liquid state.

The C-DMFT can cure this defect since it incorporates the feedback of short-range antiferromagnetic correlations, i.e., the spin degeneracy can be lifted by forming a nonlocal spin-singlet state on neighboring sites *within* the reference system and thus corrects the cluster self-energy. Fig. 11 (right) shows the phase diagram as obtained with a  $L_c = 4$ -site (plaquette) calculation. It turns out that salient features of the DMFT phase diagram are preserved. In particular, there is again a coexistence of a metallic and an insulating phase in a certain  $U$ - $T$  range of the phase diagram, and a first-order transition line separating the metallic Fermi liquid at weaker  $U$  from the Mott insulator at stronger  $U$ . On the other hand, there are a couple of differences: First of all, the critical interaction is substantially reduced (see caption of Fig. 11). Second, the line of first-order transitions remains first order down to  $T = 0$ , i.e., the  $T = 0$  Mott transition is discontinuous rather than continuous as predicted by DMFT, see Ref. [36]. Most important, however, as the insulating phase at low temperatures now has a very small entropy, a decreasing temperature favors the insulator over the metal. At high temperatures, one expects and finds the same trend of the crossover lines since here correlations are broken up thermally. At low  $T$ , however, the first-order transition line bends back, and  $U_c(T)$  decreases with decreasing  $T$ .

The importance of short-range antiferromagnetic correlations is also highlighted by the local spectral function  $A(\omega)$  calculated within the DCA for  $L_c = 4$  shown in Fig. 12 [37]. Note that  $A(\omega)$  (black solid line) is slightly asymmetric. This is a slight artifact of the maximum-entropy method that must be employed to obtain real-frequency data from the Green function given on the Matsubara frequencies on the imaginary- $\omega$  axis, on which the numerical evaluation of the theory must be implemented when using a quantum Monte-Carlo cluster solver. Still there is a clear four-peak structure visible in  $A(\omega)$ . This exactly in line with the lattice QMC results shown in Fig. 3. Hence, one would expect that the low-excitation-energy peaks signal

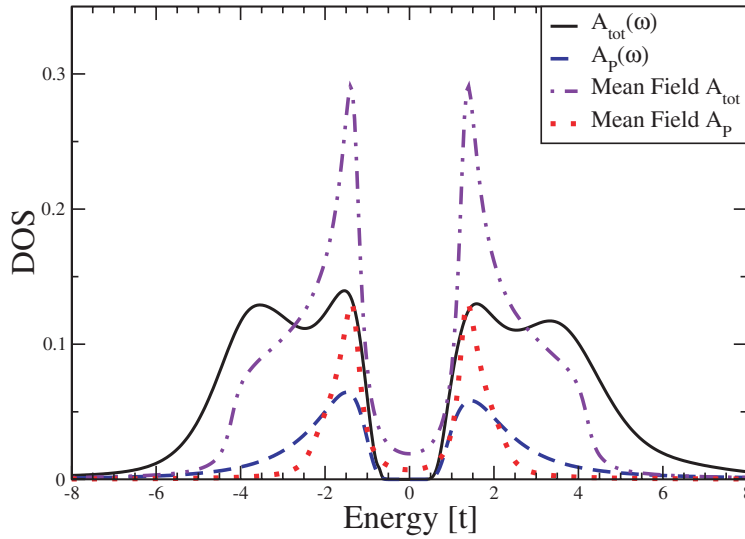


**Fig. 12:** Local density of states  $A(\omega)$  for the half-filled Hubbard model at  $U = 6t$  as obtained by the DCA with  $L_c = 4$ . Figure adapted from Ref. [37].

nonlocal antiferromagnetic correlations. This is corroborated by comparing with the spectral density obtained by a static (Hartree-Fock) mean-field calculation for the symmetry-broken antiferromagnetic state with the same gap (see dash-dotted line). The similarity to the DCA results in the low-frequency range emphasizes the importance of nonlocal correlations again. More than this, it also suggests that the gap is not necessarily a Mott-Hubbard gap but rather a “Slater” gap. In the static mean-field Slater theory, long-range antiferromagnetic order implies a doubling of the unit cell with a gap opening at the boundary of the reduced Brillouin zone.

The Mermin-Wagner theorem [17] actually excludes a spontaneous breaking of the  $SU(2)$  spin-rotational symmetry at any finite temperature in two spatial dimensions. Hence, antiferromagnetic order obtained in the static mean-field theory but also in the C-DMFT and DCA at low but finite temperatures (if solutions are not enforced to be spin-symmetric) must be seen as artifacts. However, this does not imply that the Slater mechanism for the gap opening is irrelevant. Namely, for small clusters, the antiferromagnetic correlation length well exceeds the linear cluster extension at low  $T$ . It has, indeed, been suggested that the metal-insulator transition is in fact of the Slater type in  $D = 2$  [37]. However, another important observation is that the transition is orbital (or  $\mathbf{k}$ ) selective [35, 36]. In the  $L_c = 4$  calculation, two of the orbitals  $(\pi, 0)$  and  $(0, \pi)$  exhibit a Mott-like transition where the spectral gap is opened because the self-energy  $\Sigma_{(\pi,0)}(\omega)$  develops a pole at  $\omega = 0$  while the remaining orbitals  $(0, 0)$  and  $(\pi, \pi)$  undergo a Slater-type transition. In a single-site mean-field theory, on the other hand, such momentum-space differentiation is impossible.

More recent studies [38] using lattice QMC as well as the  $D\Gamma A$ , a diagrammatic extension of DMFT [39], demonstrate that at low temperatures strong nonlocal antiferromagnetic correlations are responsible for opening a gap even at arbitrarily weak  $U$ . The system evolves from a Slater-like to a Heisenberg-like antiferromagnet at low but finite  $T$  but without explicitly breaking the  $SU(2)$  symmetry. This implies that actually no metal-insulator transition can be identified for  $D = 2$  and that the system is a paramagnetic insulator for all  $U$ .

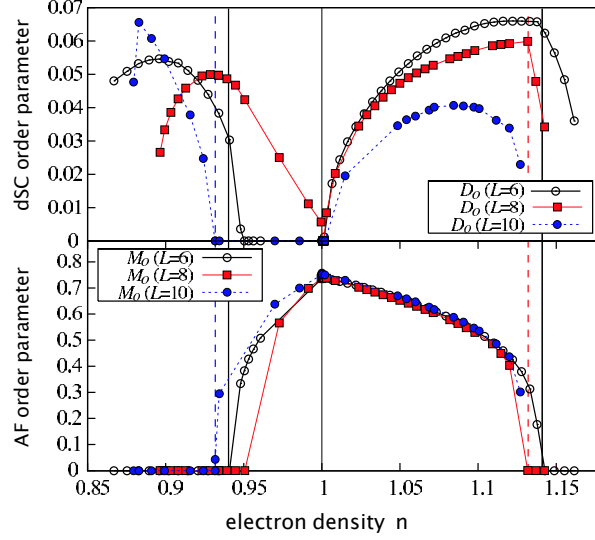


**Fig. 13:** Superconducting (top) and antiferromagnetic order parameter (bottom) as a function of the electron density  $n$  in the  $D = 2$  Hubbard model at  $T = 0$  and  $U = 8t$ . VCA results for different clusters:  $2 \times 3$ -,  $2 \times 4$ - and  $10$ -site clusters. Reprinted figure with permission from [40]. Copyright (2005) by the American Physical Society.

Let us finally discuss an application of a cluster approach to the  $D = 2$  Hubbard model which focusses on unconventional  $d$ -wave superconductivity. At zero temperature, spontaneous symmetry breaking is no longer excluded by the Mermin-Wagner theorem. A single-site mean-field theory, however, cannot treat symmetry-broken phases that are characterized by *nonlocal* order parameters. Fig. 13 displays results obtained by means of the VCA [40] for the Hubbard model on the  $D = 2$  square lattice with nearest-neighbor ( $t = 1$ ), next-nearest-neighbor diagonal ( $t' = -0.3$ ) and third-neighbor hopping ( $t'' = 0.2t$ ) at  $U = 8t$  and  $T = 0$ . Within the VCA, there is no bath continuum to be optimized but two symmetry-breaking Weiss fields which couple to the reference system  $H'$  of disconnected clusters. In particular,

$$H'_M = \sum_i (-1)^i (n_{i\uparrow} - n_{i\downarrow}) \quad (63)$$

probes antiferromagnetic order and

$$H'_D = \sum_{ij} \Delta_{ij} (c_{i\uparrow} c_{j\downarrow} + \text{H.c.}) \quad (64)$$

$d$ -wave superconductivity with  $\Delta_{ij} = D$  if sites  $i, j$  are nearest neighbors along the  $x$  axis and  $\Delta_{ij} = -D$  if sites  $i, j$  are nearest neighbors along the  $y$  axis. The corresponding AF and SC order parameters,  $M_{\text{AF}}$  and  $D_{\text{SC}}$  can be obtained from the normal and from the anomalous elements of the one-particle Green function in the Nambu formalism (see Ref. [40] for details) and are plotted in Fig. 13 as function of the filling  $n$ . The figure demonstrates that antiferromagnetism persists up to about  $\delta \equiv |1 - n| = 15\%$  doping on the electron-doped side ( $n > 1$ ) and about 6% on the hole-doped side. Superconductivity coexists with antiferromagnetism, but a pure SC phase is found as well, particularly at higher hole-doping levels. Unfortunately, there are strong finite-size and cluster-geometry effects such that, even if these results are physically very appealing and plausible, improved and more systematic cluster calculations are necessary to prove that the  $D = 2$  Hubbard model has a  $d$ -wave superconducting ground state.

## 10 Conclusions and open problems

Dynamical mean-field theory is in many cases too strong an approximation for the description of physical phenomena in low-dimensional lattice models. Conceptually, cluster extensions of the DMFT are highly important as they are able to bridge the gap between the single-site mean-field approach and the exact solution. In practice, however, it very much depends on the capabilities of the “cluster solver” if the cluster size  $L_c$  that can still be treated numerically is sufficiently large. In almost all interesting cases, i.e., for not too high temperatures etc., the accessible cluster sizes are unfortunately too small to allow for a systematic and reliable finite-size scaling, and thus we have to await further progress in the development of solver techniques (see Ref. [41], for example).

Still the cluster concept represents a big step forward. Its predictions can be checked systematically by comparing results for different cluster sizes, it provides complementary information to plain finite-size simulations, and it does account for important physics that is not captured by the single-site DMFT. In particular, by self-consistent mapping of the lattice problem onto a cluster with  $L_c > 1$ , it is possible to include the feedback of nonlocal two-particle correlations on the one-particle quantities, such as the formation of nonlocal opposed to local spin singlets. Nonlocal correlations on the length scale given by the linear extension of the cluster are treated accurately, while longer-range correlations are captured on the static mean-field level only.

The application of a cluster approach is thus advisable whenever the physics is crucially affected by nonlocal but short-range correlations. This is the case for the Mott transition in two dimensions, for example [35,36,38]. To describe phases with spontaneously broken symmetries that are characterized by a nonlocal order parameter, such as unconventional  $d$ -wave superconductivity, a cluster approach is even necessary.

The cluster extension of the DMFT is not unique. Among the various different approaches, the cellular DMFT and the dynamical cluster approximation are the most popular. Both are clearly superior as compared to the more simple cluster-perturbation theory. The variational cluster approximation stands in between and is attractive if an exact-diagonalization-based cluster solver shall be employed. If an absent or mild the fermionic sign problem permits the use of a quantum Monte-Carlo solver, the C-DMFT or DCA represent the methods of choice since the treatment of the noninteracting bath degrees of freedom comes “for free” and even tend to attenuate the sign problem. The periodized cellular approach is closely related but appears a bit inconvenient when systems with broken translation symmetries shall be studied. As a rule of thumb, the C-DMFT is preferable if local quantities are addressed while observables extending over the cluster size converge faster with increasing  $L_c$  within the DCA.

One should also be aware about a couple of remaining problems. Common to all cluster techniques is the problem that translation symmetries are broken artificially, as is most obvious in the CPT and the C-DMFT. Additional periodization schemes must be employed which, however, have some *ad hoc* character and do not remove a possible intrinsic bias of the approximation when studying phase diagrams involving spontaneously broken translation symmetries. The DCA involves a periodization scheme at a deeper level but is also not free of related artifacts

such as the discontinuous  $k$ -dependence of the self-energy. A problem related to artificially broken translation symmetries is given by lattice models with strongly reduced or even absent translation symmetries, such as impurities in a correlated lattice, nanostructures at solid surfaces, etc. Opposed to the real-space DMFT for inhomogeneous systems, there is no straightforward inhomogeneous cluster approach. Another problem, already present on the single-site mean-field level, is the proper treatment of models with nonlocal or even long-ranged interactions. Here, the cluster concept would allow for an explicit consideration of short-range nonlocal interactions on the scale of the cluster while an additional static mean-field decoupling was required for interaction terms across the cluster boundaries. There are, however, other and probably superior ways to tackle this problem, such as extended DMFT [42] or the dual-boson method [43].

Diagrammatic routes to treat nonlocal correlations beyond dynamical mean-field theory [39] represent a very promising alternative to cluster approaches. Here, the idea is compute corrections to the DMFT self-energy through additional Feynman diagrams and to start from a local approximation for the two-particle vertex instead of the bare Coulomb interaction as a building block. One of the big advantages is that nonlocal correlations can be accounted for without breaking translational symmetries. Compared to cluster extensions of DMFT, however, diagrammatic routes appear less systematic in approaching the full solution of correlated lattice fermion models.

## References

- [1] W. Metzner and D. Vollhardt, Phys. Rev. Lett. **62**, 324 (1989)
- [2] A. Georges and G. Kotliar, Phys. Rev. B **45**, 6479 (1992)
- [3] M. Jarrell, Phys. Rev. Lett. **69**, 168 (1992)
- [4] A. Georges, G. Kotliar, W. Krauth, and M.J. Rozenberg, Rev. Mod. Phys. **68**, 13 (1996)
- [5] T. Maier, M. Jarrell, T. Pruschke, and M.H. Hettler, Rev. Mod. Phys. **77**, 1027 (2005)
- [6] M. Potthoff, in A. Avella and F. Mancini (eds.): *Strongly Correlated Systems: Theoretical Methods*, Springer Series in Solid-State Sciences, Vol. 171, p. 303 (Springer, Berlin, 2012)
- [7] M.H. Hettler, A.N. Tahvildar-Zadeh, M. Jarrell, T. Pruschke, and H.R. Krishnamurthy, Phys. Rev. B **58**, R7475 (1998)
- [8] A.I. Lichtenstein and M.I. Katsnelson, Phys. Rev. B **62**, R9283 (2000)
- [9] G. Kotliar, S.Y. Savrasov, G. Pálsson, and G. Biroli, Phys. Rev. Lett. **87**, 186401 (2001)
- [10] M. Potthoff, M. Aichhorn, and C. Dahnken, Phys. Rev. Lett. **91**, 206402 (2003)
- [11] A.C. Hewson: *The Kondo Problem to Heavy Fermions* (Cambridge Univ. Press, 1993)
- [12] T. Moriya: *Spin Fluctuations in Itinerant Electron Magnetism*, Springer Series in Solid-State Sciences, Vol. 56 (Springer, Berlin, 1985)
- [13] H. Capellmann (Ed.): *Metallic Magnetism, Springer Topics in Current Physics*, Vol. 42 (Springer, Berlin, 1987)
- [14] N.M. Plakida: *High-Temperature Superconductivity* (Springer, Berlin, 1993)
- [15] J.R. Waldram: *Superconductivity of Metals and Cuprates* (IOP Publishing, London, 1996)
- [16] F. Gebhard: *The Mott Metal-Insulator Transition* (Springer, Berlin, 1997)
- [17] N.D. Mermin and H. Wagner, Phys. Rev. Lett. **17**, 1133 (1966)
- [18] J. Hubbard, Proc. R. Soc. London A **276**, 238 (1963)
- [19] M.C. Gutzwiller, Phys. Rev. Lett. **10**, 159 (1963)
- [20] J. Kanamori, Prog. Theor. Phys. (Kyoto) **30**, 275 (1963)
- [21] C. Gröber, R. Eder, and W. Hanke, Phys. Rev. B **62**, 4336 (2000)
- [22] C. Dahnken, M. Aichhorn, W. Hanke, E. Arrigoni, and M. Potthoff, Phys. Rev. B **70**, 245110 (2004)



- [23] F.H.L. Essler, H. Frahm, F. Göhmann, A. Klümper, and V. Korepin:  
*The One-Dimensional Hubbard Model* (Cambridge University Press, 2005)
- [24] C. Gros and R. Valenti, *Phys. Rev. B* **48**, 418 (1993)
- [25] D. Sénéchal, D. Pérez, and M. Pioro-Ladrière, *Phys. Rev. Lett.* **84**, 522 (2000)
- [26] M. Potthoff: *Making use of self-energy functionals: The variational cluster approximation*, in E. Pavarini, E. Koch, D. Vollhardt, and A. Lichtenstein (eds.):  
*DMFT at 25: Infinite Dimensions*, Modeling and Simulation, Vol. 4 (FZ Jülich, 2014)
- [27] D. Sénéchal, in A. Avella and F. Mancini (eds.): *Strongly Correlated Systems: Theoretical Methods*, Springer Series in Solid-State Sciences, Vol. 171, p. 237 (Springer, Berlin, 2012)
- [28] M.G. Zacher, R. Eder, E. Arrigoni, and W. Hanke, *Phys. Rev. Lett.* **85**, 2585 (2000)
- [29] D. Sénéchal, D. Pérez, and D. Plouffe, *Phys. Rev. B* **66**, 075129 (2002)
- [30] T. Minh-Tien, *Phys. Rev. B* **74**, 155121 (2006)
- [31] G. Biroli, O. Parcollet, and G. Kotliar, *Phys. Rev. B* **69**, 205108 (2004)
- [32] E. Müller-Hartmann, *Z. Phys. B* **76**, 211 (1989)
- [33] M. Potthoff and W. Nolting, *Phys. Rev. B* **59**, 2549 (1999)
- [34] M. Potthoff, *Euro. Phys. J. B* **32**, 429 (2003)
- [35] H. Park, K. Haule, and G. Kotliar, *Phys. Rev. Lett.* **101**, 186403 (2008)
- [36] M. Balzer, B. Kyung, D. Sénéchal, A.-M.S. Tremblay, and M. Potthoff,  
*Europhys. Lett.* **85**, 17002 (2009)
- [37] E. Gull, P. Werner, X. Wang, M. Troyer, and A.J. Millis, *Europhys. Lett.* **84**, 37009 (2008)
- [38] T. Schäfer, F. Geles, D. Rost, G. Rohringer, E. Arrigoni, K. Held, N. Blümer, M. Aichhorn,  
and A. Toschi, *Phys. Rev. B* **91**, 125109 (2015)
- [39] G. Rohringer, H. Hafermann, A. Toschi, A.A. Katanin, A.E. Antipov, M.I. Katsnelson,  
A.I. Lichtenstein, A.N. Rubtsov, and K. Held, *Rev. Mod. Phys.* **90**, 025003 (2018)
- [40] D. Sénéchal, P.-L. Lavertu, M.-A. Marois, and A.-M.S. Tremblay,  
*Phys. Rev. Lett.* **94**, 156404 (2005)
- [41] E. Gull, A. Millis, A. Lichtenstein, A. Rubtsov, M. Troyer, and P. Werner,  
*Rev. Mod. Phys.* **83**, 349 (2011)
- [42] R. Chitra and G. Kotliar, *Phys. Rev. Lett.* **84**, 3678 (2000)
- [43] A.N. Rubtsov, M.I. Katsnelson, and A.I. Lichtenstein, *Ann. Phys. (N.Y.)* **327**, 1320 (2012)



# 6 Charge Self-Consistency in Correlated Electronic Structure Calculations

Frank Lechermann

I. Institut für Theoretische Physik

Universität Hamburg

Jungiusstraße 9, 20355 Hamburg

## Contents

<b>1</b>	<b>Introduction</b>	<b>2</b>
<b>2</b>	<b>Self-consistency in numerical approaches to many-electron systems</b>	<b>3</b>
2.1	Hartree-Fock method . . . . .	3
2.2	Density-functional theory (DFT) in Kohn-Sham representation . . . . .	6
2.3	Dynamical mean-field theory (DMFT) . . . . .	8
2.4	Mixing . . . . .	10
<b>3</b>	<b>Realistic many-body account of correlated materials</b>	<b>11</b>
3.1	Combining DFT and DMFT: functionals . . . . .	11
3.2	Combining DFT and DMFT: in practice . . . . .	13
3.3	Relevance of charge self-consistency . . . . .	17
<b>4</b>	<b>An illustrative materials example: Metal-insulator transition in <math>V_2O_3</math></b>	<b>18</b>
4.1	Phase diagram and basic materials characteristics . . . . .	18
4.2	Electronic correlations within DFT+DMFT . . . . .	20
4.3	Charge self-consistency vs. one-shot . . . . .	22
<b>5</b>	<b>Concluding remarks</b>	<b>24</b>

# 1 Introduction

The last twenty years have witnessed extraordinary progress in the theoretical description and modeling of so-called strongly correlated materials. In these realistic condensed matter systems, the screening of the Coulomb interaction between electrons is too weak to rely on effective single-particle approaches. The electron-electron interaction becomes a natural competitor of the basic hopping processes, thus intriguing electronic many-body instabilities characterized by different degrees of itinerancy and localization occur.

The combination of density-functional theory (DFT) with dynamical mean-field theory (DMFT) emerged as a major approach to tackle the challenges of strongly correlated systems on a realistic level. Metal-insulator transitions, local-moment formation, spin and charge fluctuations, finite-temperature effects on correlated electron states, or the interplay of correlations with spin-orbit coupling are only a few hallmark topics that have been studied successfully with the so-called DFT+DMFT scheme. As a hybrid method, interfacing band theory and quantum chemistry for demanding condensed-matter problems, the basic formalism is delicate. In this chapter, the goal is to shed light on the specific aspect of “self-consistency” in numerical accounts of the correlated electronic structure of materials. Though there are various techniques where this issue applies, in order to keep the discussion straight and within reasonable length, the main body of this treatise will focus on the matter within DFT+DMFT, which is nowadays the key method for *strongly* correlated materials.

Briefly, in basic mathematical terms, *self-consistency* is figured as the both-way matching of an implicit defining function, e.g., a potential  $v(\mathbf{r})$ , with a depending function, e.g., a wave function  $\psi(\mathbf{r})$ , that are related by a set of (partial) differential equations derived from a variational treatment of the (free) energy of the system. Since such a set of equations is usually not solvable by analytical means, a numerical solution may be reached iteratively. Starting from some reasonable initial guess, consecutive constructions of  $\psi_v$  and  $v_\psi$  will eventually result in a *self-consistent solution* for  $\{v(\mathbf{r}), \psi(\mathbf{r})\}$  subject to the governing set of equations. Note that there are also still other kinds of (self-)consistencies in iterative mathematical equations, such as, e.g., for the Verhulst equation. In the DFT+DMFT context, and depending on how this approach is put into practice, we will encounter different situations of self-consistency of the given kind. Among those, *charge self-consistency* plays a singular role, as it closes the calculational iteration loop (in the sense sketched above) of the complete scheme on the outermost level.

In the present scope, charge self-consistency is attributed to a necessary incoherent theoretical description of an electronic system. In the simplest manner, one imagines the whole system being divided into two subsystems which are treated by a different degree of sophistication. Then, charge self-consistency holds if three features are installed:

1. Exchange of charge between the two subsystems is possible.
2. Even without explicit charge flow inbetween, the electronic structure within one subsystem (i.e., its field) affects the electronic structure in the other subsystem (and vice versa).
3. The combined theoretical scheme as a whole is self-consistent in the sense that the complete electronic structure is at a stationary point of the thermodynamics.

Although investigations without charge self-consistency may often provide already valuable insight into the physics of correlated materials, it turns out that in several important cases this form of self-consistency does not only matter by quantitative means. Qualitative differences, e.g., whether a given compound is Mott insulating or not, do occur.

The text is organized as follows. In section 2 the basic forms of self-consistency in the original Hartree-Fock method as well as in pure DFT and pure DMFT will be reviewed to set the stage. Section 3 then deals with a description of the DFT+DMFT approach, both on a formal and on a practical level. Emphasis will be put on the latter, especially on the relevance of the charge self-consistent aspect. To illustrate the presented theoretical concepts at work, a concrete materials examples is discussed in the final section 4.

## 2 Self-consistency in numerical approaches to many-electron systems

In order to get acquainted with the basic ideas and mechanisms of self-consistency problems in advanced quantum mechanics, let us first start with a condensed reminder of the canonical schemes of computational many-body theory for electronic systems. As for the complete rest of the paper, we will remain within the Born-Oppenheimer approximation of separating electronic and ionic degrees of freedom, focussing on the former one. Furthermore, we remain in the nonrelativistic regime, hence exclude, e.g., spin-orbit effects to keep the discussion elementary. Three different key observables will be discussed, namely the many-body wave function  $\Psi(\{\mathbf{r}\sigma\})$  in the context of Hartree-Fock, the electronic charge density  $\rho(\mathbf{r})$  in the context of DFT and the one-particle Green function  $G(\mathbf{k}, \omega)$  in the context of DMFT.

### 2.1 Hartree-Fock method

The Hartree-Fock (HF) method (see e.g. Ref. [1] for a review) is rooted in quantum chemistry, providing basic access to the electronic system of atoms and molecules with  $N$  electrons. It serves as the starting point for more involved approaches such as, e.g., Møller-Plesset theory or the configuration-interaction scheme.

Key idea is the ansatz for the many-body wave function  $\Psi(\{\mathbf{r}_i\sigma_i\}) =: \Psi(\{\mathbf{x}_i\})$  as a single Slater determinant, i.e.

$$\Psi_{\text{HF}}(\{\mathbf{x}_i\}) =: \hat{S}_- \prod_i^N \varphi_i(\mathbf{r}) \chi_i(\sigma) = \hat{S}_- \prod_i^N \phi_i(\mathbf{x}) \quad , \quad \text{with} \quad \varphi_i(\mathbf{r}) = \sum_{\nu}^M A_{i\nu} B_{\nu}(\mathbf{r}) . \quad (1)$$

Here,  $\hat{S}_-$  is the antisymmetrization operator,  $\varphi$  the real-space function,  $\chi$  the spin function and  $i = 1, N$ . The functions  $\varphi_i$  are expanded into  $M$  basis functions  $B_{\nu}$ , usually of atomic kind, with expansion coefficients  $A_{i\nu}$ . In the end, the  $A_{i\nu}$  are the parameters that will be optimized for the solution. It is very important to realize that the ansatz (1) marks the *simplest possible* wave function for an electronic system, describing independent electrons only subject to the

Pauli exclusion principle. The Hamiltonian of the electronic system with momenta  $p_i$  and the potential  $V_i$  of the nuclei is straightforwardly written as

$$\hat{H} = \sum_i^N \left( \frac{\hat{p}_i^2}{2m} + \hat{V}_i \right) + \frac{1}{2} \sum_{ij} \hat{v}_{ij} =: \sum_i^N \hat{h}_i + \frac{1}{2} \sum_{ij} \hat{v}_{ij} . \quad (2)$$

The two-particle operator  $\hat{v}_{ij}$  represents the Coulomb interaction between the electrons. To obtain a working scheme for the optimization of our trial wave function with regard to the given problem, we make use of the Ritz variational principle

$$\delta \left( \frac{\langle \Psi_{\text{HF}} | \hat{H} | \Psi_{\text{HF}} \rangle}{\langle \Psi_{\text{HF}} | \Psi_{\text{HF}} \rangle} \right) \stackrel{!}{=} 0 , \quad (3)$$

with the relevant expectation value reading

$$\langle \Psi_{\text{HF}} | \hat{H} | \Psi_{\text{HF}} \rangle = \sum_i \langle \phi_i | \hat{h} | \phi_i \rangle + \frac{1}{2} \sum_{ij} \left( \underbrace{\langle \phi_j \phi_i | \hat{v} | \phi_j \phi_i \rangle}_{\text{Coulomb (Hartree) term}} - \underbrace{\langle \phi_j \phi_i | \hat{v} | \phi_i \phi_j \rangle}_{\text{exchange (Fock) term}} \right), \quad (4)$$

and the corresponding real-space matrix elements

$$\langle \phi_i | \hat{h} | \phi_i \rangle = \int d\mathbf{r} \varphi_i^*(\mathbf{r}) h(\mathbf{r}) \varphi_i(\mathbf{r}), \quad (5)$$

$$\langle \phi_i \phi_j | \hat{v} | \phi_k \phi_l \rangle = \delta_{\sigma_i \sigma_k} \delta_{\sigma_j \sigma_l} \int d\mathbf{r} d\mathbf{r}' \varphi_i^*(\mathbf{r}) \varphi_j^*(\mathbf{r}') v(\mathbf{r}, \mathbf{r}') \varphi_k(\mathbf{r}) \varphi_l(\mathbf{r}'). \quad (6)$$

Note that the general Coulomb matrix element is spin dependent, though the interaction surely is not. The reason is the enforcement of the Pauli principle in electron-electron scattering process. The Ritz principle is most effectively put into practice via minimizing the functional form

$$\mathcal{F}[\Psi_{\text{HF}}] = \langle \Psi_{\text{HF}} | \hat{H} | \Psi_{\text{HF}} \rangle - \sum_i \varepsilon_i \langle \phi_i | \phi_i \rangle, \quad \text{with} \quad \delta \mathcal{F} \stackrel{!}{=} 0, \quad (7)$$

whereby the  $\varepsilon_i$  serve as lagrange multipliers. The variation implies here a functional differentiation with  $\phi_i \rightarrow \phi_i + \delta \phi_i$ . This leads to the single-particle or *Hartree-Fock equations* governed by the so-called Fock operator  $\hat{F}$ , i.e.

$$\hat{F} |\phi_i\rangle = \varepsilon_i |\phi_i\rangle \quad \forall i \quad (8)$$

and are written in real-space representation as ( $\hbar = 1$ )

$$\left( -\frac{1}{2m} \Delta + V(\mathbf{r}) + e^2 \sum_{j \neq i} \int d\mathbf{r}' \frac{|\varphi_j(\mathbf{r})|^2}{|\mathbf{r} - \mathbf{r}'|} \right) \phi_i(\mathbf{r}) - e^2 \sum_{j \neq i} \delta_{\sigma_i \sigma_j} \int d\mathbf{r}' \frac{\varphi_j^*(\mathbf{r}) \varphi_i^*(\mathbf{r}')}{|\mathbf{r} - \mathbf{r}'|} \phi_j(\mathbf{x}) = \varepsilon_i \phi_i(\mathbf{x}) \quad (9)$$

$$\Rightarrow \left( -\frac{1}{2m} \Delta + V(\mathbf{r}) + v_{\text{H}}(\mathbf{r}) \right) \varphi_i(\mathbf{r}) + \int d\mathbf{r}' v_{\text{X}}(\mathbf{r}, \mathbf{r}') \varphi_i(\mathbf{r}) = \varepsilon_i \varphi_i(\mathbf{r}). \quad (10)$$

The local Hartree potential  $v_{\text{H}}(\mathbf{r})$  describes the Coulomb repulsion between electrons, as familiar from classical electrostatics. The nonlocal exchange potential  $v_{\text{X}}(\mathbf{r}, \mathbf{r}')$  adds unique quantum

physics due to the Pauli principle: electrons with equal spin effectively feel a repelling potential to avoid each other not to join a common quantum state. Note already here that, in a quantum-chemistry definition, there is still a third mechanism, also of pure quantum kind, that influences the concerted arrangement among the electrons. It is called *correlation*, not directly related to spin, and goes beyond the Hartree-Fock picture, since it is encrypted in more complicated many-electron wave functions than the most simple one of single Slater-determinant kind. It is thus very important for the understanding of the Hartree-Fock equations to appreciate the ansatz (1) that lead to eq. (10).

For us here, the principle solution of the Schrödinger-like eq. (10) is the main concern. It becomes clear from (9) that contrary to the standard nuclear potential  $V(\mathbf{r})$ , the Hartree and exchange potential are not given from the beginning. They explicitly dependent on the wave functions  $\varphi_i$  we are actually looking for. Therefore, the implicit character of the Hartree-Fock equations forms a natural *self-consistency* problem. In the literature, these equations are thus also often termed *self-consistent field (SCF)* equations. Literally, the solution is defined by an iterative cycle as follows:

1. Start with an educated guess for the single-particle functions  $\varphi_i(\mathbf{r}) = \varphi_i^{(1)}(\mathbf{r})$  by invoking suitable linear combinations of the basis functions. For instance, an adequate kind of  $sp^n$  hybridization function might be meaningful for a carbon-based molecule.
2. Construct a first associated Hartree potential  $v_H^{(1)}(\mathbf{r}) = v_H^{\{\varphi_i^{(1)}\}}(\mathbf{r})$  and exchange potential  $v_X^{(1)}(\mathbf{r}) = v_X^{\{\varphi_i^{(1)}\}}(\mathbf{r}, \mathbf{r}')$  and solve the Hartree-Fock equations for a new set of eigenfunctions  $\varphi_i^{(2)}(\mathbf{r})$ .
3. Go back to step 2 and repeat  $p$  times until you reach convergence in the potentials, i.e.,  $|v_H^{(p)} - v_H^{(p-1)}| < \eta$  and  $|v_X^{(p)} - v_X^{(p-1)}| < \eta$  holds for small  $\eta$ .

We will remark in section 2.4 on further relevant technical aspects of performing this self-consistency cycle. If this cycle converges, it is obvious for us physicists that the resulting functions  $\varphi_i^{(p)}$  along with their eigenvalues  $\varepsilon_i^{(p)}$  represent a faithful solution to the problem. A *principle* convergence is ensured by the variational character of how we casted the problem. But note that in general, such self-consistency problems can underlie the issues of local vs. global minimum, existence of saddle-points, etc.. In this text however, we will not delve into these mathematical aspects of the solution space.

We have now encountered a first concrete self-consistency problem for many-electron systems. This Hartree-Fock method obviously may also be termed a *charge self-consistent method*, as the electronic charge density  $\rho(\mathbf{r})$  is implicitly also iterated in the cycle given above and can be expressed via a sum over the occupied orbitals

$$\rho(\mathbf{r}) = \sum_i^{\text{occ}} |\varphi_i(\mathbf{r})|^2. \quad (11)$$

Thus the charge distribution always matches the associated electron states and also the total charge is conserved. By this statement, we have assumed that *all* electrons of the system enter

in eq. (10). If instead, one decides to, e.g., “freeze” some core electrons in their atomic state and to only Hartree-Fock converge chosen valence electrons, then complete charge self-consistency would in principle not be achieved. Neither valence nor core charge density would be in accordance with the distribution at the global stability point of the system. Further relaxation of the core states could still modify the charge density of the whole system.

We leave the further analysis of the Hartree-Fock solution as well as the description of the plethora of different method flavors to the numerous textbooks on this matter, and continue by an theory advancement that builds up directly on the electronic charge density  $\rho(\mathbf{r})$ .

## 2.2 Density-functional theory (DFT) in Kohn-Sham representation

Besides the obvious flaw of Hartree-Fock in missing the effect of *correlation*, there are further serious drawbacks. The scheme is ill-defined for crystalline systems and the nonlocal exchange potential is computationally delicate and expensive. Instead of working directly with a many-body wave function  $\Psi(\{\mathbf{x}_i\})$ , it appears also more attractive to deal with a physically more tangible object.

Density-functional theory (DFT) puts the electronic charge density  $\rho(\mathbf{r})$  in the focus and has become the workhorse of quantum-mechanical calculations for materials since more than thirty years (see e.g. Refs. [2, 3] for reviews). It builds upon the theorems by Hohenberg and Kohn, stating, in short, first that  $\rho(\mathbf{r})$  bears *in principle* the same physically-relevant information as the much more complex  $\Psi(\{\mathbf{x}_i\})$ . Second, the functional  $E[\rho]$  of the system’s total energy has a minimum for the correct ground state charge density  $\rho_0(\mathbf{r})$ , thus ensuring a variational principle. Equipped with the already gathered knowledge, we may cast such a functional straightforwardly (by adjusting to the community-established nomenclature) in the form

$$E[\rho] = T[\rho] + \int d\mathbf{r} \rho(\mathbf{r}) v_{\text{ext}}(\mathbf{r}) + E_{\text{H}}[\rho] + E_{\text{QMB}}[\rho]. \quad (12)$$

The kinetic-energy contribution is denoted  $T[\rho]$ ,  $v_{\text{ext}}(\mathbf{r})$  is nothing but the former nuclear potential  $V(\mathbf{r})$  and  $E_{\text{H}}[\rho]$  describes the Hartree energy. All the remaining (and notorious) explicit quantum many-body terms, namely the effect of Pauli principle and correlation, enter the functional  $E_{\text{QMB}}[\rho]$ . The expression (12) is also important because of its hierarchical structure: in direct comparison, all but the term  $E_{\text{QMB}}$  are reasonably large.

To proceed towards a practical formalism, one invokes in the so-called *Kohn-Sham (KS) representation* of DFT a virtual non-interacting electron system [4]. Such a system is surely exactly represented by a single Slater determinant. As a key step, we demand that the electronic charge density, and then obviously also the total energy, of the real system and the virtual system coincide. This means that in our virtual system, there must be a rather tricky effective potential  $v_{\text{KS}}(r)$  at work that enforces this demand. It is hence natural to continue as follows

$$E[\rho] \stackrel{!}{=} E_{\text{virt. sys.}}[\rho] := T_{\text{S}}[\rho] + \int d\mathbf{r} \rho(\mathbf{r}) v_{\text{KS}}(\mathbf{r}) \quad (13)$$

$$= T_{\text{S}}[\rho] + \int d\mathbf{r} \rho(\mathbf{r}) v_{\text{ext}}(\mathbf{r}) + \frac{e^2}{2} \int d\mathbf{r} d\mathbf{r}' \frac{\rho(\mathbf{r})\rho(\mathbf{r}')}{|\mathbf{r} - \mathbf{r}'|} + E_{\text{xc}}[\rho]. \quad (14)$$



Equation (14) again establishes an educated guess based on what we learned from embarking on Hartree-Fock theory. The total energy has to consist of four terms: a kinetic energy  $T_S$  now of non-interacting electrons, an electron-nuclear interaction, a classical Hartree term, and last but not least a term that includes the quantum many-body terms, here named  $E_{xc}$ . Note that the latter *exchange-correlation functional* does not only include the effect of Pauli exchange and correlation, but also the difference  $T - T_S$  from implicit quantum many-body effects in the kinetic energy.

Why should the form (14) be preferred over the expression (12)? Because (14) is amenable to straightforward numerical treatment. Since deep down there may be only single-particle wave functions that build up the expression (14), we can immediately formulate the according variational principle

$$\delta \left( E[n] - \sum_i \varepsilon_i \langle \varphi_i | \varphi_i \rangle \right) \stackrel{!}{=} 0, \quad (15)$$

leading to the so-called *Kohn-Sham equations*

$$\left( -\frac{1}{2m} \Delta + v_{KS}(\mathbf{r}) \right) \varphi_i(\mathbf{r}) = \varepsilon_i \varphi(\mathbf{r}) \quad (16)$$

of effective-single-particle kind. Accordingly, the effective, or KS, potential reads

$$v_{KS}(\mathbf{r}) = v_{\text{ext}}(\mathbf{r}) + v_H(\mathbf{r}) + v_{xc}(\mathbf{r}), \text{ with } v_{xc}(\mathbf{r}) = \frac{\delta E_{xc}}{\delta \rho}. \quad (17)$$

In practice, the total energy is usually computed via expressing the kinetic-energy term through the eigenvalue sum, resulting in

$$E_{\text{DFT}} = \sum_i \varepsilon_i - \frac{e^2}{2} \int d\mathbf{r} d\mathbf{r}' \frac{\rho(\mathbf{r})\rho(\mathbf{r}')}{|\mathbf{r} - \mathbf{r}'|} - \int d\mathbf{r} \rho(\mathbf{r}) v_{xc}(\mathbf{r}) + E_{xc}[\rho]. \quad (18)$$

It is clear that the exchange-correlation part asks for approximations. Originally, reference to a numerically-exact quantum Monte-Carlo treatment of the homogeneous electron gas is made and the exchange-correlation energy (in fact, the correlation part, since the exchange part is analytically known) extracted via an analytical fit  $\epsilon_{xc}(\rho)$ . The resulting ansatz

$$E_{xc}[\rho] = \int d\mathbf{r} \rho(\mathbf{r}) \epsilon_{xc}(\rho(\mathbf{r})) \quad (19)$$

defines the so-called *local-density approximation (LDA)*. Further approximations for  $E_{xc}[\rho]$ , such as the generalized gradient approximation (GGA) which includes gradient terms of the charge density, exist. Finally, the electronic charge density is again expressed by the sum over the occupied effective single-particle states, i.e., of form (11). The careful reader may have noted that we did not include the spin degree of freedom by explicit means in our argumentation. This is due to the fact that in exact DFT, this degree of freedom is not of evident relevance, as an exact exchange-correlation functional incorporates the effect of spin. In practical and eventually approximate Kohn-Sham representation, eq. (16) gains a spin index describing spin-up and spin-down charge densities and the canonical xc-approximation is the local spin-density approximation (LSDA).

It is obvious from eqns. (16) and (17) that the practical Kohn-Sham scheme is again based on a self-consistency cycle similar to that described for the Hartree-Fock method. Here, the local Kohn-Sham potential  $v_{\text{KS}}(\mathbf{r})$  has to be iterated until convergence. Charge self-consistency is naturally ensured in KS calculations, although in principle, also here a possibly different treatment of, e.g., core and valence electrons would abandon an exact charge self-consistent state. Such differences indeed occur in various KS-based electronic structure codes of, e.g., selected augmented-wave or pseudopotential kind. However, the differences in the total charge density (especially in the relevant spatial regions) are very small and the resulting physics of interest is not affected. Thus for the rest of these notes, KS-based DFT is understood as a charge self-consistent framework.

Especially for solid-state system, Kohn-Sham calculations greatly improve on Hartree-Fock studies, since the reasonable treatment of the exchange and correlation within LDA enables the important description of screening of the Coulomb potential. For further aspects of density-functional theory and the Kohn-Sham representation we refer to the various excellent reviews. In the following, to simplify the writing, it is understood that “DFT” refers to the KS-representation of density-functional theory.

### 2.3 Dynamical mean-field theory (DMFT)

In terms of electronic correlations, we advanced from no consideration at all in Hartree-Fock to a reasonably-well treatment for many materials within DFT. Still, for some materials classes, e.g., transition-metal oxides, the DFT description of the correlated behavior of electrons remains insufficient. Most notably, in these systems the delicate competition among electrons between itinerancy and the tendency to localize in real space asks for a better modeling. The dynamical mean-field theory (DMFT) [5,6] is a hallmark condensed-matter framework that faces this task best for such *strongly correlated materials*. It utilizes the one-particle Green function as key to provide seminal access to the spectral properties and the total energy of an interacting electron system on a lattice, and was originally constructed in a model-Hamiltonian context.

Contrary to Hartree-Fock and original DFT, the DMFT approach is designed to work at finite temperature  $T$ . Hence we introduce fermionic Matsubara frequencies  $\omega_n := (2n+1)\pi T$  to write the correct Green function for the Hamiltonian  $H(\mathbf{k})$  at wave vector  $\mathbf{k}$  in reciprocal space as

$$G(\mathbf{k}, i\omega_n) = (i\omega_n + \mu - H(\mathbf{k}) - \Sigma(\mathbf{k}, i\omega_n))^{-1}, \quad (20)$$

whereby  $\mu$  is the chemical potential and  $\Sigma(\mathbf{k}, i\omega_n)$  the so-called *self-energy* of the system. Expression (20) looks quite different from the electronic-state descriptions we encountered so far. But the Green function formalism is just a different *representation* of the physics, especially tailored to systems with sizable correlations in the solid state. For instance, we could also easily express the Hartree-Fock or DFT pictures therein, namely via the according self-energies

$$\Sigma_{\text{HF}}(\mathbf{k}, i\omega_n) = \sum_{\mathbf{q}} (v_{\mathbf{kqkq}} - v_{\mathbf{qkkq}}) (e^{\beta(\varepsilon_{\mathbf{q}} - \mu)} + 1)^{-1}, \quad (21)$$

$$\Sigma_{\text{DFT}}(\mathbf{k}, i\omega_n) = \sum_{\mathbf{q}} (v_{\text{H}} + v_{\text{xc}})_{\mathbf{kqkq}} (e^{\beta(\varepsilon_{\mathbf{q}} - \mu)} + 1)^{-1}, \quad (22)$$

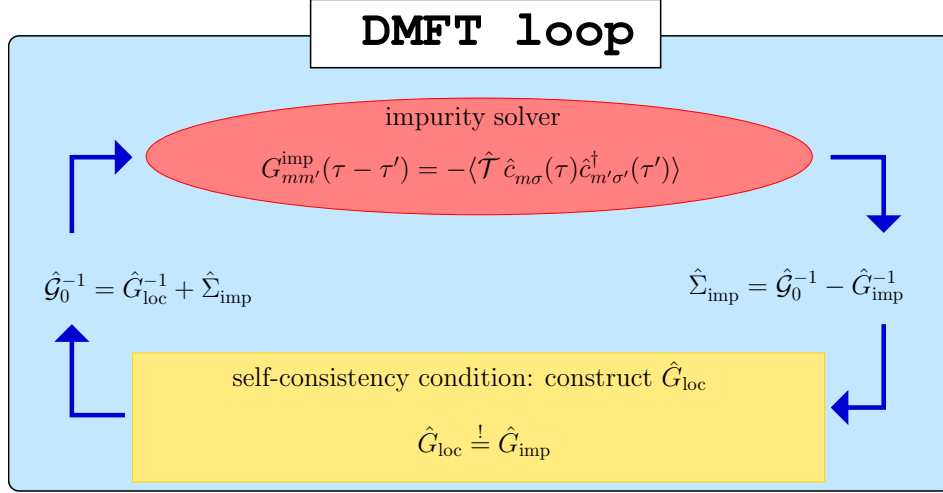


**Fig. 1:** Self-consistency loop of DMFT. The heavy task is performed by the impurity solver, computing the impurity Green function, e.g., in imaginary time  $\tau$  using quantum Monte Carlo.

with  $\beta = 1/T$  and where the matrix elements are reminiscent to their real-space analog (6). Note that both approaches display no true frequency dependence, the second factor in each expression, respectively, merely represents the simplest form of temperature dependence via the effect of the Fermi function. But importantly, frequency (or energy) dependence is a very relevant issue for describing interacting electrons: it regulates the impact of correlations on *different* energy scales due to the electrons' Janus-faced character hesitating between itinerancy and localization.

Eventually, DMFT is a theory that is designed to take care of that. Originally, it assumes a strong, i.e., only weakly-screened, *local* Coulomb interaction  $U$  effective on each lattice site. Then, in order to keep the full frequency dependence, but in the same time keeping the formalism operable, one drops the  $k$  dependence in the self-energy, i.e.

$$G^{\text{DMFT}}(\mathbf{k}, i\omega_n) := (i\omega_n + \mu - H(\mathbf{k}) - \Sigma_{\text{imp}}(i\omega_n))^{-1}. \quad (23)$$

The self-energy  $\Sigma_{\text{imp}}(i\omega_n)$  is then linked to a quantum-impurity problem of the general form

$$\Sigma_{\text{imp}}(i\omega_n) = \mathcal{G}_0(i\omega_n)^{-1} - G_{\text{imp}}(i\omega_n)^{-1}, \quad (24)$$

where the so-called *Weiss field*  $\mathcal{G}_0(i\omega_n)$  is a unique function of the local Hamiltonian (expressed within a localized basis). To close the equations, the DMFT self-consistency condition reads

$$G_{\text{loc}}^{\text{DMFT}}(i\omega_n) = \sum_{\mathbf{k}} [i\omega_n + \mu - H(\mathbf{k}) - \Sigma_{\text{imp}}(i\omega_n)]^{-1} \stackrel{!}{=} G_{\text{imp}}(i\omega_n). \quad (25)$$

The resulting iterative loop that is thereby implied to converge the DMFT self-energy is depicted in Fig. 1. Drawing a conceptual parallel between DFT and DMFT, while the former theory maps the interacting-electron problem onto the problem of non-interacting electrons in a highly-complicated potential, DMFT maps it to the problem of an interacting site within a self-consistent bath.

The challenging part is given by solving the quantum-impurity problem, to be done, e.g., with quantum Monte Carlo, Exact Diagonalization, etc.. Note that many-body wise, local-interaction diagrams are included to all orders in this non-perturbative theory. The vital energy dependence of the Weiss field ensures the qualitatively correct description of low-energy quasiparticle (QP) features as well as high-energy incoherent (Hubbard) excitations. Extensions to overcome the restriction to a  $k$ -independent self-energy, e.g., via cluster schemes, are available. But those will not be further pursued in the present text.

As for the previous approaches, charge self-consistency holds also for the DMFT method. But the issue of “self-consistency” has a more intriguing character than in Hartree-Fock and DFT. First, identical to these approaches, it serves to actually render the framework computationally feasible via the loop in Fig 1. But second, we deal with the structure of an explicit mean-field theory. This means that we replace the true surrounding of an interacting site by a *field*. This replacement itself is not an approximation, since “someone” could endow us with the exact field, just as “someone” could provide us the exact exchange-correlation functional in DFT. However here, we define this field by our self-consistent mean-field construction, hence marking the approximation.

## 2.4 Mixing

Before we move on to discuss the combined approach of DFT and DMFT in the next section, a few technical comments in view of solving the encountered self-consistency cycles are in order. In practice, the sketched flowcharts of iterating potentials (or self-energies) by directly replacing input- and output functions in a  $p$ -step process are in most cases extremely unstable. One needs to damp the whole iteration, usually via “mixing in” the potentials from previous steps, i.e.,

$$v^{(p+1)} = v^{(p+1)}(v^{(p)}, v^{(p-1)}, \dots) . \quad (26)$$

*Linear mixing* is the simplest form of this and reads

$$v_{\text{inp}}^{(p+1)} = (1 - \alpha) v_{\text{inp}}^{(p)} + \alpha v_{\text{out}}^{(p)} , \quad 0 < \alpha < 1 , \quad (27)$$

with  $v_{\text{inp(out)}}^{(p)}$  as the input(output) of step  $p$ . This means, not the straightforward output potential  $v_{\text{out}}^{(p)}$  is used for the input potential in step  $p+1$ , but a weighted mixture of the old input potential  $v_{\text{inp}}^{(p)}$  and  $v_{\text{out}}^{(p)}$ . With a small enough mixing parameter  $\alpha$ , convergence is nearly always ensured, yet then at the price of a slow and inefficient performance. More sophisticated variations of this kind of mixing, such as, e.g., *Anderson mixing*, may accelerate the convergence.

The mixing problem can also be approached more rigorously by formulating the search for a self-consistent solution as a root-finding problem of a tailored functional:

$$\mathcal{F}[v_{\text{inp}}] = v_{\text{out}}[v_{\text{inp}}] - v_{\text{inp}} \stackrel{!}{=} 0 . \quad (28)$$

As it is known from schooldays for ordinary functions  $f(x)$ , the Newton-Raphson method which involves the first derivative  $f'(x)$  deals with such a task. Similarly, for our problem

the first derivative of  $\mathcal{F}$  is needed which corresponds in physical terms to the dielectric function  $\epsilon(\mathbf{r}, \mathbf{r}')$  or in mathematical terms to the Jacobian matrix  $\mathbf{J}$ . However, computing this first derivative may be cumbersome and often also the resulting mixing based on that generalized Newton-Raphson scheme turns out too hard. It proves more successful to invoke another scheme for an iterative approximation of the Jacobian matrix (or variations thereof). Those so-called *quasi-Newton schemes* with the *Broyden method* as its most familiar representative improve in every iteration step the approximation to  $\mathbf{J}$  and are rather powerful in solving the mixing problem (28) especially for high-dimensional energy landscapes.

A good mixing scheme is very important to converge (or accelerate the convergence of) non-trivial self-consistency loops. In some cases, as, e.g., for many DMFT self-energies with statistical errors due to quantum Monte-Carlo, linear mixing may be sufficient. But especially for variational (saddle-point) problems, the mixing method often eventually decides if the whole framework converges and yields exploitable results. So even if “mixing” is not a highlighted physics theory like DFT or DMFT, it is very worthy and pays off to invest some time in dealing with it.

### 3 Realistic many-body account of correlated materials

Correlated materials are insufficiently described by DFT with conventional exchange-correlation functionals. There are static improvements, e.g., via methods like self-interaction correction, DFT+U, or hybrid functionals. While such schemes may mimic some physics of Mott-insulating systems, they usually show substantial deficiencies for the most-challenging problem of strongly correlated metals with a large deal of quantum fluctuations. The DMFT approach on the other hand is too heavy to be implemented in a complete realistic setting, since only a number of  $M < 10$  local orbitals can so far be handled in accurate quantum-impurity solvers. Therefore, the hybrid approach of DFT and DMFT early on appeared as a natural combination to tackle electronic correlations on a realistic level beyond model-Hamiltonian descriptions. And indeed, nowadays the DFT+DMFT framework belongs to the hallmark electronic structure approaches, and is unrivaled within the field of strongly correlated materials.

#### 3.1 Combining DFT and DMFT: functionals

Our introduction to DFT+DMFT starts on a formal level, to convince the reader that though this approach has a hybrid character, it is by no means a wild heuristic patchwork method leading to all kind of unphysical results. On the contrary, it is a physical and mathematically well-defined formalism built upon on a rock-solid functional description (for details see e.g. Refs. [7, 8]).

The idea is to identify a so-called *correlated subspace*  $\mathcal{C}$  in a complete DFT-pictured electronic system, e.g., a  $3d$  orbital manifold on a selected lattice site, where a DMFT treatment is necessary. First, we try to collect all relevant functions that govern such a combined scheme. From the DFT side, the electronic charge density  $\rho$  and the Kohn-Sham potential  $v_{\text{KS}}$  come to our mind. From the DMFT side in the correlated subspace, it is expected that the Green function

$G_C$  as well as the self-energy  $\Sigma_C$  matter. The potential  $v_{KS}$  and the self-energy  $\Sigma_C$  serve as sources from a field-theoretical perspective. Note that  $\rho$  and  $G_C$  are independent, since there is no way to reconstruct the full real-space charge density from a given Green function in  $\mathcal{C}$ . By hand, we need to account for a double-counting (DC) correction, since electron-electron interaction in  $\mathcal{C}$  is treated in both, DMFT and DFT, and enters the definition of  $\Sigma_C$ .

The free energy of the whole system may then be represented by the general *Baym-Kadanoff functional* form

$$\Omega[\mathbf{G}] = \text{Tr} \ln \mathbf{G} - \text{tr} \left( (\mathbf{G}_0^{-1} - \mathbf{G}^{-1}) \mathbf{G} \right) + \Phi[\mathbf{G}], \quad (29)$$

with  $\mathbf{G}$  as the full system Green function,  $\mathbf{G}_0$  as the non-interacting Green function. The expression  $\Phi[\mathbf{G}]$  marks the *Luttinger-Ward functional*, which describes the universal part of interacting electron systems. The Baym-Kadanoff representation of a DFT+DMFT system accordingly reads, avoiding explicit matrix notation,

$$\begin{aligned} \Omega_{\text{DFT+DMFT}}[\rho, G_C; v_{KS}, \Sigma_C] = & - \text{Tr} \ln \left( i\omega_n + \mu + \frac{1}{2m} \Delta - v_{KS}(\mathbf{r}) - P^\dagger \Sigma_C(i\omega_n) P \right) \\ & - \int d\mathbf{r} (v_{KS}(\mathbf{r}) - v_{\text{ext}}(\mathbf{r})) \rho(\mathbf{r}) - \text{Tr} (G_C(i\omega_n) \Sigma_C(i\omega_n)) \\ & + E_H[\rho(\mathbf{r})] + E_{xc}[\rho(\mathbf{r})] + \Phi_C[G_C(i\omega_n)]. \end{aligned} \quad (30)$$

The objects  $P, P^\dagger$  are projection operators that here “unfold” the self-energy  $\Sigma_C$  from the correlated subspace to the full Hilbert space of the system. The given functional can readily be varied with respect to our source terms, resulting in the known expressions for the charge density and the Green function  $G_C$

$$\frac{\delta \Omega}{\delta v_{KS}} = 0 \quad \Rightarrow \quad \rho(\mathbf{r}) = \frac{1}{\beta} \sum_n \langle \mathbf{r} | \hat{G} | \mathbf{r} \rangle, \quad (31)$$

$$\frac{\delta \Omega}{\delta \Sigma_C} = 0 \quad \Rightarrow \quad G_C(i\omega_n) = P G(i\omega_n) P^\dagger, \quad (32)$$

with

$$\hat{G} = \left( i\omega_n + \mu - \hat{H}_{KS} - \hat{P}^\dagger \hat{\Sigma}_C \hat{P} \right)^{-1}. \quad (33)$$

Equations (31) and (32) are very important for several reasons: They make clear, that although  $\rho$  and  $G_C$  are independent, there is surely a coupling via the full Green function. Charge self-consistency is implied when converging the general charge density, carrying the effects from DFT as well as DMFT. Furthermore, the “downfolding” from the full Hilbert space to the correlated subspace again via the projection operators  $P, P^\dagger$  is described. It becomes also obvious that our original set of governing functions is overcomplete, as at a stationary point the potential  $v_{KS}$  and the self-energy  $\Sigma_C$  are direct functions of  $\rho$  and  $G_C$ . To explore this, one may formally write  $\tilde{\Omega}_{\text{DFT+DMFT}}[\rho, G_C; v_{KS}, \Sigma_C] = \Omega_{\text{DFT+DMFT}}[\rho, G_C; v_{KS}[\rho, G_C], \Sigma_C[\rho, G_C]]$  and perform

$$\frac{\delta \tilde{\Omega}}{\delta \rho} = 0 \quad \Rightarrow \quad v_{KS}(\mathbf{r}) = v_{\text{ext}}(\mathbf{r}) + v_H(\mathbf{r}) + v_{xc}(\mathbf{r}), \quad (34)$$

$$\frac{\delta \tilde{\Omega}}{\delta G_C} = 0 \quad \Rightarrow \quad \Sigma_C(i\omega_n) = \frac{\delta \Phi_C}{\delta G_C} := \Sigma_{\text{imp}}(i\omega_n) - \Sigma_{\text{DC}}, \quad (35)$$

whereby we introduced the DC correction  $\Sigma_{\text{DC}}$ . Thus formally, the original relations for the Kohn-Sham potential and the DMFT self-energy are retained. The set of equations (31-35) define the working scheme of the DFT+DMFT approach.

Let us finally find an expression for the total energy. By defining the Kohn-Sham Green function

$$G_{\text{KS}}(\mathbf{k}, i\omega_n) := (i\omega_n + \mu - \varepsilon_{\mathbf{k}}^{\text{KS}})^{-1} \quad (36)$$

one can rewrite the free-energy functional as

$$\Omega_{\text{DFT+DMFT}} = \Omega_{\text{DFT}} + \text{Tr} \ln G_{\text{KS}}^{-1} - \text{Tr} \ln G^{-1} - \text{Tr}(G_{\mathcal{C}} \Sigma_{\mathcal{C}}) + \Phi_{\mathcal{C}}, \quad (37)$$

where  $\Omega_{\text{DFT}}$  is the free-energy analog to expression (14). For  $T \rightarrow 0$ , this leads to

$$E_{\text{DFT+DMFT}} = E_{\text{DFT}} - \sum_{\mathbf{k}\nu} \varepsilon_{\mathbf{k}\nu}^{\text{KS}} + \text{Tr}(GH_{\text{KS}}) + \text{Tr}(G_{\mathcal{C}} \Sigma_{\text{imp}}) - E_{\text{DC}}. \quad (38)$$

In this total-energy formula, the term  $E_{\text{DFT}}$  corresponds to (18) and  $\varepsilon_{\mathbf{k}\nu}^{\text{KS}}$  are the Kohn-Sham eigenvalues with band index  $\nu$  and  $E_{\text{DC}}$  is the double-counting correction to the energy. Note that the band sum  $\sum_{\mathbf{k}\nu} \varepsilon_{\mathbf{k}\nu}^{\text{KS}} = \text{Tr}(G_{\text{KS}} H_{\text{KS}})$  is already included in  $E_{\text{DFT}}$  and has to be subtracted, as it is replaced by the interaction-dressed  $\text{Tr}(GH_{\text{KS}})$ . Importantly, in the latter term the trace is performed with respect to the full interacting Green function  $G$ .

This concludes the formal discussion of the DFT+DMFT scheme and we will turn in the next section to the more practical aspects of an implementation of it.

### 3.2 Combining DFT and DMFT: in practice

First concrete implementations of the DFT+DMFT approach appeared at the end of the 1990s [9, 10]. Those original schemes performed in a so-called “one-shot” or “post-processing” manner. After a converged DFT calculation, the density of states (and later the full Kohn-Sham Hamiltonian  $H_{\text{KS}}$ ) of the correlated subspace  $\mathcal{C}$  entered an otherwise disjunct DMFT calculation. Hence within the one-shot approach, there was no feedback of the DMFT self-energy on the general electronic structure and charge self-consistency is not reached.

State-of-the-art implementations of the full scheme are charge self-consistent (e.g. [11–14]). A pictorial sketch of the framework, in line with the demonstrations in the last subsection, is given in Fig. 2. Both original self-consistency cycles of DFT and DMFT are interweaved to establish a novel self-consistent solution for the realistic correlated electronic structure. It becomes obvious, that especially the link between both traditional schemes, i.e., the down- and unfolding to/from the correlated subspace, is key to the method. As  $\mathcal{C}$  is by definition a local region in real space, a (partly) local-orbital representation is thus an essential building block of the DFT+DMFT framework [15]. Linear-muffin-tin-orbitals [16], Wannier(like) functions, e.g., of maximally-localized kind [17], or projected-local orbitals [18, 19] may provide a convenient representation thereof.

In the following, the implementation based on projected-local orbitals will be discussed (see Ref. [18] for more details). Let us start by defining  $m = 1, \dots, M$  orthonormal orbitals  $\{\chi_m^{\mathbf{R}}\}$  on the

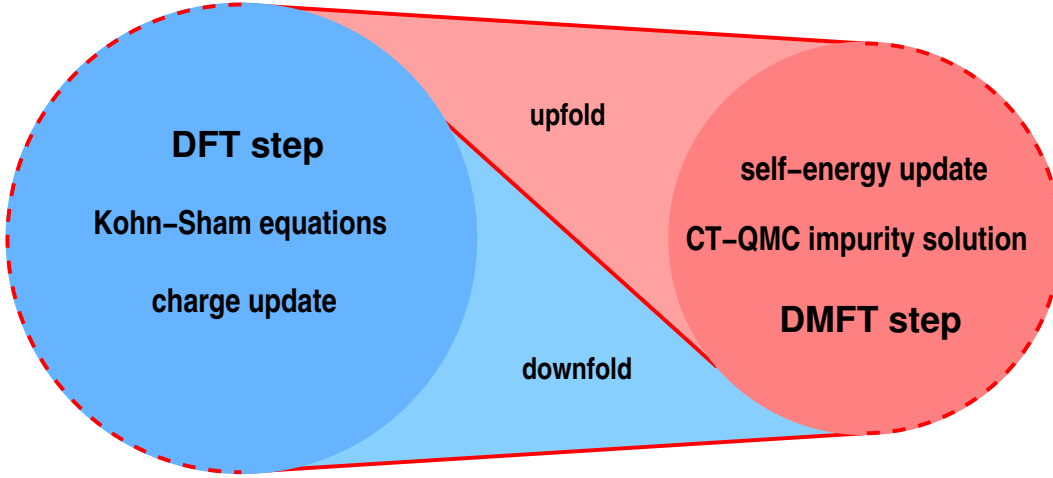


**Fig. 2:** State-of-the-art charge self-consistent DFT+DMFT loop. The calculation usually starts from a self-consistent Kohn-Sham solution. The correlated subspace is defined and the initial Weiss field  $\mathcal{G}_0$  constructed. Afterwards, a single (or more) DMFT step(s) is(are) performed. The impurity solution may, e.g., be achieved with the continuous-time quantum Monte-Carlo (CT-QMC) method. The obtained self-energies are upfolded and an updated charge density  $\rho(\mathbf{r})$  is computed. A new charge density implies a new Kohn-Sham potential, and a single new Kohn-Sham step is performed, from which a new Weiss field is generated, etc..

lattice site  $\mathbf{R}$  in  $\mathcal{C}$ . By the use of the complete set of KS states  $\{\psi_{\mathbf{k}\nu}\}$  at point  $k$  in reciprocal space, the Bloch transform of these local orbitals may be expressed via

$$|\chi_{\mathbf{k}m}^{\mathbf{R}}\rangle := \sum_{\mathbf{T}} e^{i\mathbf{k}\cdot(\mathbf{T}+\mathbf{R})} |\chi_m^{\mathbf{R}}\rangle = \sum_{\nu} |\psi_{\mathbf{k}\nu}\rangle \langle \psi_{\mathbf{k}\nu} | \chi_{\mathbf{k}m}^{\mathbf{R}} \rangle = \sum_{\nu} \langle \psi_{\mathbf{k}\nu} | \chi_{\mathbf{k}m}^{\mathbf{R}} \rangle |\psi_{\mathbf{k}\nu}\rangle, \quad (39)$$

whereby  $\mathbf{T}$  denotes a Bravais lattice vector and the sum over  $\nu$  covers the whole set of bands. Thus the Bloch transform represents a *Wannier function*. To render the approach more flexible, it proves useful to extend the concept of the correlated subspace also to energy space and to permit a restriction in the noted band sum to an energy window  $\mathcal{W}$ , i.e.

$$|\tilde{\chi}_{\mathbf{k}m}^{\mathbf{R}}\rangle = \sum_{\nu \in \mathcal{W}} \langle \psi_{\mathbf{k}\nu} | \chi_{\mathbf{k}m}^{\mathbf{R}} \rangle |\psi_{\mathbf{k}\nu}\rangle. \quad (40)$$

The resulting Bloch transform is then not anymore a true Wannier function. Yet one may promote it to one by proper orthonormalization

$$|w_{\mathbf{k}m}^{\mathbf{R}}\rangle = \sum_{\mathbf{R}'m'} (O(\mathbf{k})^{-1/2})_{mm'}^{\mathbf{R}\mathbf{R}'} |\tilde{\chi}_{\mathbf{k}m'}^{\mathbf{R}'}\rangle, \quad (41)$$

using the overlap matrix  $O_{mm'}^{\mathbf{R}\mathbf{R}'}(\mathbf{k}) := \langle \tilde{\chi}_{\mathbf{k}m}^{\mathbf{R}} | \tilde{\chi}_{\mathbf{k}m'}^{\mathbf{R}'} \rangle$ . To enable flexible transformations between the system's complete Bloch space (spanned by  $\{\psi_{\mathbf{k}\nu}\}$ ) and the correlated subspace (spanned by  $\{w_{\mathbf{k}m}^{\mathbf{R}}\}$ ) it proves useful to define the projection functions

$$P_{m\nu}^{\mathbf{R}}(\mathbf{k}) := \sum_{\mathbf{R}'m'} (O(\mathbf{k})^{-1/2})_{mm'}^{\mathbf{R}\mathbf{R}'} \langle \chi_{\mathbf{k}m}^{\mathbf{R}} | \psi_{\mathbf{k}\nu} \rangle. \quad (42)$$



For instance, the transformation from Bloch to Wannier space readily reads

$$|w_{\mathbf{k}m}^{\mathbf{R}}\rangle = \sum_{\nu \in \mathcal{W}} P_{\nu m}^{\mathbf{R}*}(\mathbf{k}) |\psi_{\mathbf{k}\nu}\rangle . \quad (43)$$

Assuming the full Green function operator of the system in the form (33), the Bloch Green function is given by

$$G_{\nu\nu'}^{\text{Bloch}}(\mathbf{k}, i\omega_n) = \langle \psi_{\mathbf{k}\nu} | \hat{G} | \psi_{\mathbf{k}\nu'} \rangle . \quad (44)$$

The downfolding equation from Bloch space to correlated subspace for the Green function and the upfolding equation from  $\mathcal{C}$  to Bloch space for the self-energy are then straightforwardly written as

$$G_{mm'}^{\mathbf{R}}(i\omega_n) = \sum_{\mathbf{k}, (\nu\nu') \in \mathcal{W}} P_{m\nu}^{\mathbf{R}}(\mathbf{k}) G_{\nu\nu'}^{\text{Bloch}}(\mathbf{k}, i\omega_n) P_{\nu'm'}^{\mathbf{R}*}(\mathbf{k}) , \quad (45)$$

$$\Sigma_{\nu\nu'}^{\text{Bloch}}(\mathbf{k}, i\omega_n) = \sum_{\mathbf{R}, mm'} P_{\nu m}^{\mathbf{R}*}(\mathbf{k}) \Sigma_{mm'}^{\mathbf{R}}(i\omega_n) P_{m'\nu'}^{\mathbf{R}}(\mathbf{k}) . \quad (46)$$

The local self-energy is given by the DMFT impurity solution corrected by the double-counting term through

$$\Sigma^{\mathbf{R}}(i\omega_n) = \Sigma_{\text{imp}}^{\mathbf{R}}(i\omega_n) - \Sigma_{\text{DC}}^{\mathbf{R}} . \quad (47)$$

Once the upfolding of the self-energy to the whole space is achieved, the complete charge density  $\rho(\mathbf{r})$  may be updated. At this point, a practical comment on the charge treatment in the different stages of the self-consistency cycle is in order. In principle, the sum rule for the total charge holds for the full DFT+DMFT charge density and the associated chemical potential  $\mu$ . However, it is surely advisable to have the correct total charge of the system already within the DFT part of the calculation. Otherwise the numerics may be cumbersome due to an ill-defined Coulomb balance between electrons and nuclei. Therefore we redefine the Kohn-Sham Green function (36) as

$$G_{\text{KS}}(\mathbf{k}, i\omega_n) := (i\omega_n + \mu_{\text{KS}} - \varepsilon_{\mathbf{k}}^{\text{KS}})^{-1} , \quad (48)$$

with the chemical potential  $\mu_{\text{KS}}$  chosen such as to enforce the correct total electronic charge  $N = \int d\mathbf{r} \rho(\mathbf{r})$  in the DFT part. The full charge density is then split into two parts, namely

$$\rho(\mathbf{r}) = \rho_{\text{KS}}(\mathbf{r}) + \Delta\rho(\mathbf{r}) = \frac{1}{\beta} \sum_n \left( \langle \mathbf{r} | \hat{G}_{\text{KS}} | \mathbf{r} \rangle + \langle \mathbf{r} | \hat{G} - \hat{G}_{\text{KS}} | \mathbf{r} \rangle \right) , \quad (49)$$

with  $\hat{G}_{\text{KS}}$  in analogy to (36). Since due to our choice of  $\rho_{\text{KS}}$  already carrying the total charge, the correction term  $\Delta\rho$  amounts to a redistribution of the charge density such that  $\int d\mathbf{r} \Delta\rho(\mathbf{r}) = 0$  holds. The correction kernel beyond DFT can also be rewritten as

$$\langle \mathbf{r} | \hat{G} - \hat{G}_{\text{KS}} | \mathbf{r} \rangle = \langle \mathbf{r} | \hat{G}_{\text{KS}} (\hat{G}_{\text{KS}}^{-1} - \hat{G}^{-1}) \hat{G} | \mathbf{r} \rangle = \langle \mathbf{r} | \hat{G}_{\text{KS}} (\hat{\Sigma}^{\text{Bloch}} - (\mu - \mu_{\text{KS}}) \hat{1}) \hat{G} | \mathbf{r} \rangle . \quad (50)$$

If we then define

$$\Delta N_{\nu\nu'}(\mathbf{k}) := \frac{1}{\beta} \sum_{n, \nu''\nu''' \in \mathcal{W}} G_{\nu\nu''}^{\text{KS}}(\mathbf{k}, i\omega_n) \left( \Sigma_{\nu''\nu'''}^{\text{Bloch}}(\mathbf{k}, i\omega_n) - (\mu - \mu_{\text{KS}}) \delta_{\nu''\nu'''} \right) G_{\nu'''\nu'}(\mathbf{k}, i\omega_n) , \quad (51)$$

the charge-correction term  $\Delta\rho$  reads

$$\Delta\rho(\mathbf{r}) = \sum_{\mathbf{k}, \nu\nu' \in \mathcal{W}} \langle \mathbf{r} | \psi_{\mathbf{k}\nu} \rangle \Delta N_{\nu\nu'}(\mathbf{k}) \langle \psi_{\mathbf{k}\nu'} | \mathbf{r} \rangle. \quad (52)$$

As the DFT contribution  $\rho_{\text{KS}}$  is by definition diagonal in the band indices, the complete correlated charge density after a DFT+DMFT step reads

$$\rho(\mathbf{r}) = \sum_{\mathbf{k}, \nu\nu'} \langle \mathbf{r} | \psi_{\mathbf{k}\nu} \rangle \left( f(\tilde{\varepsilon}_{\mathbf{k}\nu}^{\text{KS}}) \delta_{\nu\nu'} + \Delta N_{\nu\nu'}(\mathbf{k}) \right) \langle \psi_{\mathbf{k}\nu'} | \mathbf{r} \rangle, \quad (53)$$

where  $f$  is the Fermi-Dirac function and  $\tilde{\varepsilon}_{\mathbf{k}\nu}^{\text{KS}} = \varepsilon_{\mathbf{k}\nu}^{\text{KS}} - \mu_{\text{KS}}$ . Thus, because of the inadequacy of a pure band picture of strongly correlated materials additional off-diagonal terms in the band index contribute in the many-body system with additional real-space excitations. This updated charge density then defines a new Kohn-Sham effective potential  $v_{\text{KS}}$  and the charge self-consistency loop is closed.

Let us at the end of this section briefly comment on additional aspects of the DFT+DMFT formalism. So far, we did not say anything at all about the interacting Hamiltonian that governs the correlated subspace and which explicitly enters the DMFT iterations. Basically, one utilizes an  $m$ -orbital generalized Hubbard Hamiltonian, e.g., of Slater-Kanamori type

$$\begin{aligned} \hat{H}_{\text{int}}^c = & \sum_{\langle \mathbf{R}\mathbf{R}' \rangle mm' \sigma} t_{\mathbf{R}\mathbf{R}'}^{mm'} \hat{c}_{\mathbf{R}m\sigma}^\dagger \hat{c}_{\mathbf{R}'m'\sigma} + U \sum_{i\mathbf{R}m} \hat{n}_{\mathbf{R}m\uparrow} \hat{n}_{\mathbf{R}m\downarrow} \\ & + \frac{1}{2} \sum_{\mathbf{R}, m \neq m', \sigma} \left( (U - 2J_{\text{H}}) \hat{n}_{\mathbf{R}m\sigma} \hat{n}_{\mathbf{R}m'\bar{\sigma}} + (U - 3J_{\text{H}}) \hat{n}_{\mathbf{R}m\sigma} \hat{n}_{\mathbf{R}m'\sigma} \right) \\ & + \frac{1}{2} \sum_{\mathbf{R}m \neq m', \sigma} J_{\text{H}} \left( \hat{c}_{\mathbf{R}m\sigma}^\dagger \hat{c}_{\mathbf{R}m'\bar{\sigma}}^\dagger \hat{c}_{\mathbf{R}m\bar{\sigma}} \hat{c}_{\mathbf{R}m'\sigma} + \hat{c}_{\mathbf{R}m\sigma}^\dagger \hat{c}_{\mathbf{R}m\bar{\sigma}}^\dagger \hat{c}_{\mathbf{R}m'\bar{\sigma}} \hat{c}_{\mathbf{R}m'\sigma} \right). \end{aligned} \quad (54)$$

Here,  $t$  refers to the Kohn-Sham hopping matrix,  $U$  marks the Hubbard interaction,  $J_{\text{H}}$  the Hund's exchange and  $\hat{n} = \hat{c}^\dagger \hat{c}$ . For a discussion of this and related Hamiltonians we refer to [20]. The DMFT impurity solution subject to such Hamiltonian forms may nowadays, e.g., be obtained from the continuous-time quantum Monte-Carlo (CT-QMC) method (see e.g. Ref. [21] for a review). The interaction parameters are either chosen from a reasonable guess (often by connecting also to experimental data) or are computed from first-principles schemes such as the constrained random-phase approximation (cRPA).

The issue of double-counting is a well-known feature of DFT+DMFT and various forms are available for the correction term  $\Sigma_{\text{DC}}$ . Since conventional DFT exchange-correlation functionals are not representable within standard many-body diagrams, a straightforward analytical solution of the DC problem is not available. Usually, the double counting is assumed orbital independent (i.e. spherical) and a commonly used formula is based on the so-called fully-localized or atomic limit [22]

$$\Sigma_{\mathbf{R}m\sigma}^{\text{DC}} = U \left( \langle \hat{n}_{\mathbf{R}} \rangle - \frac{1}{2} \right) - J_{\text{H}} \left( \langle \hat{n}_{\mathbf{R}\sigma} \rangle - \frac{1}{2} \right). \quad (55)$$

Albeit the general topic is heavily debated, nonetheless, many results on the qualitative and even (semi)-quantitative physics of strongly correlated materials are not that sensitive to the details of double counting. Otherwise the DFT+DMFT approach would not be that successful. A solution to the DC problem may be achieved by abandoning the concrete KS-DFT environment and replace it by a true (weakly-correlated) many-body setting. The numerically very heavy GW+DMFT scheme [23] provides such a description.

Finally, note that in various multi-atom unit cells, the correlated subspace is often not only associated with a single lattice site, as already anticipated in our sums over the sites  $\mathbf{R}$  (e.g. in eq. (46)). For symmetry-equivalent sites, it suffices to compute the self-energy for a representative site and transfer it to the remaining sites via proper symmetry relations. In the case of various sites which are inequivalent by symmetry, e.g., the Fe sites with octahedral or tetrahedral environment in magnetite  $\text{Fe}_3\text{O}_4$ , a different impurity problem is defined for each symmetry-inequivalent site  $\mathbf{R}$  through [24]

$$\mathcal{G}_0^{\mathbf{R}}(i\omega_n)^{-1} = G^{\mathbf{R}}(i\omega_n)^{-1} + \Sigma_{\text{imp}}^{\mathbf{R}}(i\omega_n), \quad (56)$$

and the coupling is realized via the DFT+DMFT self-consistency condition invoking the computation of the complete lattice Green function.

### 3.3 Relevance of charge self-consistency

There is surely an intuitive believe that charge self-consistency is a good thing to have in an electronic structure calculation. But let us try to identify concrete features from a DFT+DMFT perspective that renders it superior to the simpler one-shot framework. Before doing so, one should mention that charge self-consistent DFT+DMFT calculations are numerically heavier than the latter. Not only because of the additional solution of a DFT problem at each iteration step, though especially for large supercell computations this further effort is still not negligible. What matters more is the usually slower convergence when demanding charge self-consistency, since the correlation-induced charge redistributions need additional numerical steps to settle.

Concerning the advantageous features, several points are noteworthy. First, the orbital occupations within the correlated subspace are due to change because of the relaxing surrounding electron structure. Second, importantly, the remaining electronic structure *outside* the correlated subspace  $\mathcal{C}$  (i.e. ligand states, etc.) may also “react” to the local-Coulomb effect within  $\mathcal{C}$ . The interweaving of both of these effects is very important for, e.g., orbital polarizations, local magnetic moments, magnetic exchange, and, not to forget, the total energy  $E_{\text{DFT+DMFT}}$ . Thus, for instance, even if the local orbital occupations within  $\mathcal{C}$  do not change much with charge self-consistency, the effect on a possible magnetic ordering may still be crucial.

It is obvious that the degree of correlation-induced charge redistributions also depends on the symmetry of the system. In highly-symmetric compounds, such as the cubic perovskite and “DMFT pet”  $\text{SrVO}_3$ , the impact of charge self-consistency is expected to be minor. But for lower-symmetry problems, often associated with various symmetry-inequivalent sites (such as oxide heterostructures), the effects can be crucial. Furthermore, for materials close to a Mott

transition, the systems are very susceptible to perturbations in the electronic structure, and charge self-consistency can have obvious qualitative effects, even if the crystal symmetry is seemingly high. We will discuss in section 4 the metal-insulator transition in  $V_2O_3$  as a prominent example.

Two general features are often observed in charge self-consistent DFT+DMFT. In cases where one-shot calculations lead to strong orbital polarization, e.g., within a crystal-field split  $3d(t_{2g})$  manifold, charge self-consistency weakens this tendency. This is understandable from the fact that a strong orbital polarization affects the ligand neighborhood in order to relax the electronic structure. This relevant “reaction” of the neighboring electrons has usually the effect of screening the original strong orbital polarization, i.e., reducing it from its one-shot magnitude. Second, it is furthermore observed that charge self-consistency tends to wash out differences between varying double-counting schemes [25].

## 4 An illustrative materials example: Metal-insulator transition in $V_2O_3$

After all the formal theory, the last section shall be used to discuss a concrete application of charge self-consistent DFT+DMFT to a challenging materials problem. We will realize that the theoretical description of the famous  $V_2O_3$  problem, benefits strongly from charge self-consistency.

### 4.1 Phase diagram and basic materials characteristics

Since about fifty years, vanadium sesquioxide  $V_2O_3$  poses a demanding problem in the understanding of correlated materials [26–28]. In the field of realistic interacting solid-state systems, the compound has without doubt the second most prominent phase diagram [26, 27], after the one of high- $T_c$  cuprates. Its canonical finite-temperature form (see Fig. 3a) includes three key phases, namely a paramagnetic-metallic (PM) one, a paramagnetic-insulating (PI) one, and an antiferromagnetic-insulating (AFI) phase at finite  $T$ . At ambient  $T$  and pressure, the stoichiometric compound is stable in the PM phase with a corundum crystal structure, i.e., the system is metallic at room temperature. The corundum structure (cf. Fig. 3b) has trigonal symmetry with V dimers along the  $c$ -axis and a V-based honeycomb lattice in the  $ab$ -plane. Upon lowering the temperature, a metal-insulator transition (MIT) towards the AFI phase, with notably a monoclinic crystal structure, occurs at  $T_N \sim 155$  K.

Formally, in  $V_2O_3$ , vanadium is in the oxidation state 3+, i.e., a valence configuration  $3d^2$ . Within the  $VO_6$  octahedra, the  $V(3d)$  manifold is first split into higher-energy  $e_g$  and lower-energy  $t_{2g}$  states due to the octahedral crystal field. Because of the tilted orientation of those octahedra, the additional trigonal crystal field splits threefold  $V-t_{2g}$  into  $a_{1g}$  and two degenerate  $e_g^\pi$  states. There are numerous DFT investigations of this compound [29–33]. On the corresponding level, a low-energy  $V-t_{2g}$  bandwidth of  $W \sim 2.6$  eV (see Fig. 4), harboring the two electrons in the occupied part, results around the Fermi level  $\varepsilon_F$ . The  $a_{1g}$  orbital points along the

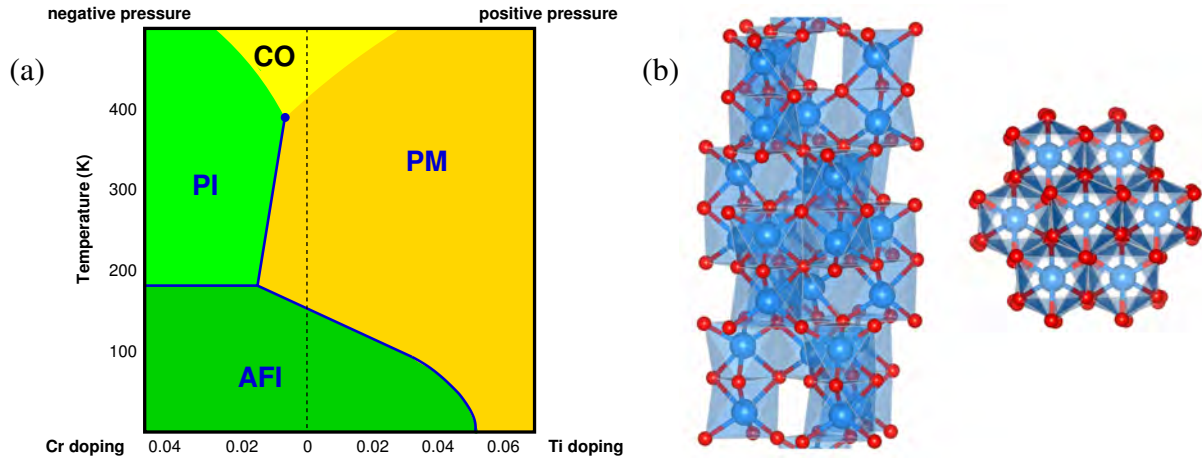


**Fig. 3:** Basic information on  $V_2O_3$ . (a) Temperature vs. pressure/doping phase diagram with the following phases: paramagnetic metal (PM), paramagnetic insulator (PI) and antiferromagnetic insulator (AFI). The 'CO' area marks the PI-PM crossover region. (b) Corundum structure with V (blue) and O (red), left: view with  $c$ -axis vertical; and right: view along  $c$ -axis.

$c$ -axis and along the V-V dimers, which therefore display a pronounced bonding/anti-bonding splitting. The  $e_g^\pi$  orbitals point inbetween the oxygens and are expected to describe more localized behavior than  $a_{1g}$ . An orbital polarization  $n(e_g^\pi)/n(a_{1g}) = 1.44/0.56 = 2.57$  in favor of  $e_g^\pi$  is obtained in DFT. Note that in the low- $T$  monoclinic AFI phase, the V-V dimer distance grows and does not shrink as in the akin  $VO_2$  compound. Thus a straightforward Peierls-like mechanism due to dimerization is not at the origin of the metal-insulator transition. But the in-plane degeneracy in the V-V distances within the honeycomb lattice is broken in the monoclinic phase. Thus after cubic and trigonal components in the crystal field, there is yet a further monoclinic one appearing, eventually splitting the  $e_g^\pi$  degeneracy. As seen in Fig. 3a, doping with Cr (or application of negative pressure) at ambient temperature results in another metal-insulator transition from the PM to the PI phase for about 1.5% of Cr dopants. This MIT is particularly interesting, since apparently no global symmetry is broken, i.e., the corundum symmetry and paramagnetism remain vital. Hence, seemingly, the  $V_2O_3$  phase diagram displays all characteristics of a “model phase diagram” for a strongly correlated system on a lattice: strong electronic correlations create local magnetic moments that order at low temperature via a MIT in an antiferromagnetic phase; upon application of negative pressure the lattice expands and a different MIT occurs due to a reduction of the hopping, while application of positive pressure or Ti doping stabilizes the metal due to a strengthening of the hopping. So far, so nice. But this simplistic model picture of  $V_2O_3$  has attained serious cracks over the many years of investigation, suggesting that especially the doping with Cr or Ti results in much more intriguing physics than originally envisioned. This lecture is not the place to go into full detail of this, but let us remark on only one relevant aspect (for more on this matter see, e.g., Ref. [34]). Though Cr(Ti) doping has the same phenomenological effect as negative(positive) pressure, i.e., driving localization(itinerancy), they do not coincide in terms of the microscopic mechanism. Namely, while Cr doping indeed expands the lattice [35], Ti doping does not contract the lattice, but actually also expands it (albeit not as strongly as Cr doping) [36].

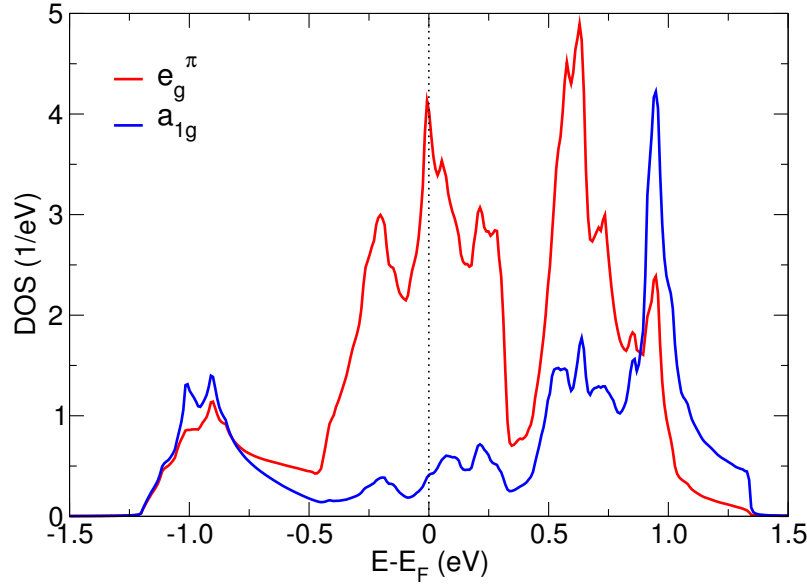


**Fig. 4:** Local  $V-t_{2g}$  density of states (DOS) for  $V_2O_3$ .

## 4.2 Electronic correlations within DFT+DMFT

When going beyond DFT for this strongly correlated material, the transition-metal  $t_{2g}$  electrons are usually chosen to form the correlated subspace of  $V_2O_3$ . An interacting Hamiltonian of Slater-Kanamori form (54), is conveniently governing this subspace. From a Hubbard  $U \sim 5$  eV, the ratio  $U/W \sim 2$  puts the  $V_2O_3$  system well into the strongly correlated regime. As the corundum structure builds up on two formula units in its primitive cell, there are four symmetry-equivalent V ions to take care of in multi-site DFT+DMFT. Also on the latter level, there exist already many studies for this hallmark material [37–39, 14, 40–43].

In the following, we want to restrict the discussion to the paramagnetic regime. We set the local Coulomb interactions to  $U = 5$  eV and  $J_H = 0.7$  eV and perform the calculations for  $T = 387$  K ( $\beta = 30$  eV $^{-1}$ ) and  $T = 193$  K ( $\beta = 60$  eV $^{-1}$ ). The focus is on two structural cases, namely the stoichiometric corundum unit-cell and the effective 2.8% Cr-doped corundum unit-cell, both based on the crystal data of Dernier [35]. Note importantly, that the cell with effective Cr doping differs only via the lattice parameters and the Wyckoff positions of V and O compared to the stoichiometric cell. In other words, the effect of 2.8% Cr dopants is taken into account only on the average by an effective refinement of the vanadium and oxygen positions. The explicit effects of the different valence of Cr compared to V as well as *local* structural relaxations due to Cr impurities are neglected. This approximation of the effect of Cr doping renders the computations in the doped case simple, but it is also a rough one. Nonetheless, this approximate treatment of Cr doping has nearly exclusively been used in former theoretical assessments of Cr-doped  $V_2O_3$ .

Figure 5 displays the  $k$ -integrated spectral functions  $A(\omega)$  at stoichiometry and with effective Cr doping. From the total spectral functions, three observations are readily made. First, vanadium sesquioxide is indeed a strongly correlated material, since it shows a substantially renormalized quasiparticle peak and lower/upper Hubbard bands due to the spectral-weight

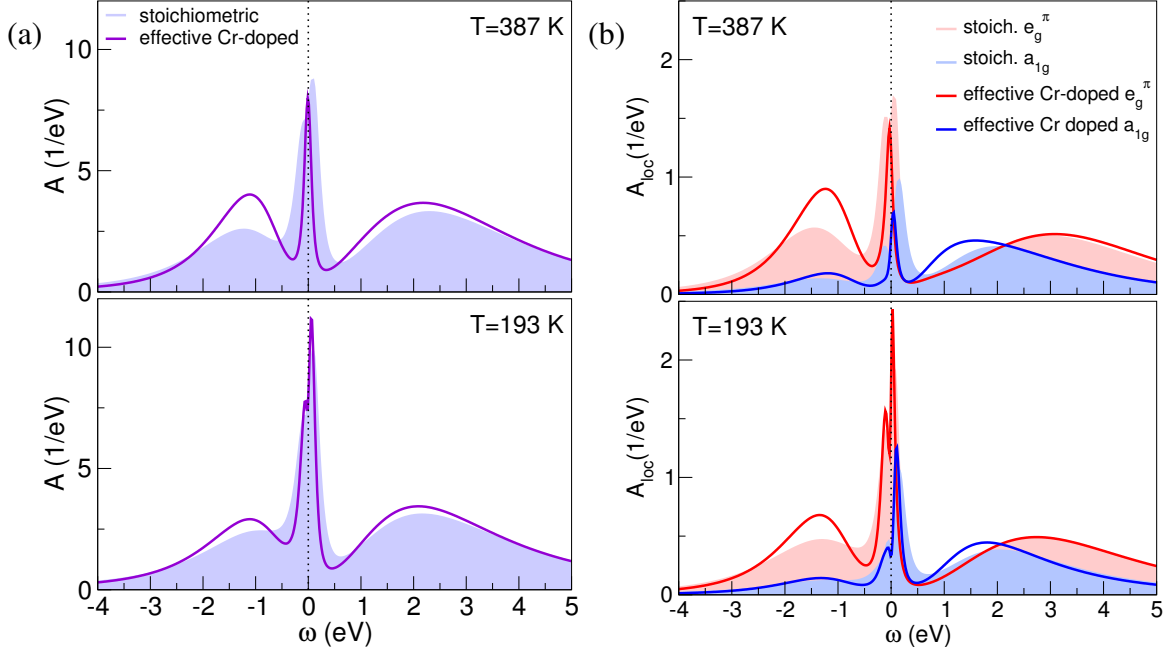


**Fig. 5:** DFT+DMFT  $k$ -integrated spectral functions  $A(\omega)$  for stoichiometric and effective Cr-doped (see text)  $\text{V}_2\text{O}_3$  at  $T = 387$  K (top) and  $T = 193$  K (bottom), respectively. (a) total  $A(\omega)$  and (b) local  $V-t_{2g}$   $A(\omega)$ .

transfer to incoherent local excitations at higher energy. Second, in line with the experimental phase diagram, with effective Cr doping the system is indeed more strongly correlated than at stoichiometry. Third, the spectral-weight transfer from low energy to high energy is stronger at *higher* temperatures. This means, that there is a rather small coherence scale of the QPs, leading to an increasing effective localization of the corresponding electrons for  $T$  larger than that scale. On the local level, the orbital polarization between  $e_g^\pi$  and  $a_{1g}$  is increased with correlations, actually from the DFT value  $n(e_g^\pi)/n(a_{1g}) = 1.44/0.56$  to the DFT+DMFT values  $n(e_g^\pi)/n(a_{1g}) = 1.58/0.42$  at stoichiometry and  $n(e_g^\pi)/n(a_{1g}) = 1.60/0.40$  for effective Cr doping. The increase of orbital polarization is explained by a trigonal-crystal-field enhancement due to electronic correlations [38, 39].

For completeness, Fig. 6 exhibits the  $k$ -resolved spectral function of stoichiometric  $\text{V}_2\text{O}_3$  along high-symmetry lines in the first Brillouin zone. Note that because of the strong correlations, the dispersion of the QPs is now “squeezed” in an energy window  $[-0.3, 0.3]$  eV, whereas on the DFT level we remember an effective bandwidth of  $W \sim 2.6$  eV. The spectral weight in this low-energy region is already substantially broadened, only along  $k_z$ , i.e., the line  $Z-\Gamma$ , displays a rather coherent QP part. The spectrum is in good agreement with recent angle-resolved photoemission (ARPES) experiments by Vecchio *et al.* [44], though the electron pocket at  $\Gamma$  is even deeper in energy within the experimental data.

Let us finally compare the electronic charge density  $\rho(\mathbf{r})$  from DFT and from charge self-consistent DFT+DMFT. Figure 7a shows the bonding charge density  $\rho_{\text{bond}} = \rho - \rho_{\text{atomic}}$  within the  $ab$ -plane of  $\text{V}_2\text{O}_3$ . The function  $\rho_{\text{bond}}$  is often more instructive than the pure  $\rho$ , since the latter is a large-valued function that mainly marks the ionic positions on the lattice with

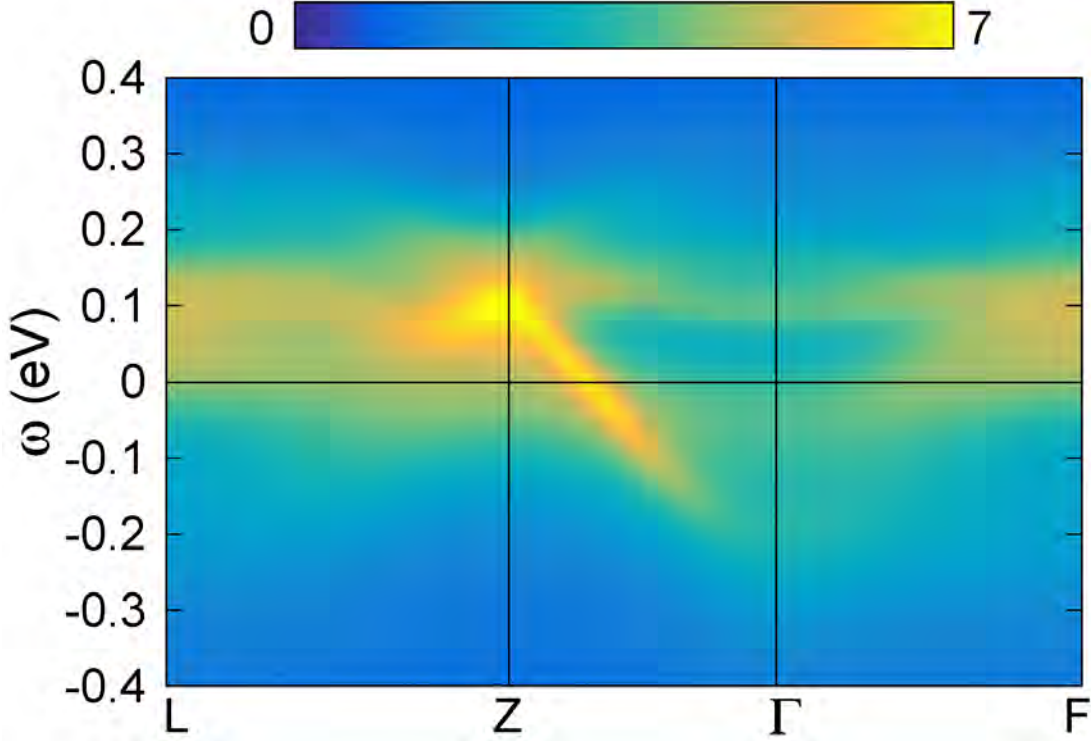


**Fig. 6:** DFT+DMFT  $k$ -resolved spectral function  $A(\mathbf{k}, \omega)$  for stoichiometric  $V_2O_3$  at  $T = 193$  K along high-symmetry lines in the first Brillouin zone.

its maxima. On the other hand,  $\rho_{\text{bond}}$  as a difference function has more contrast and reveals the charge redistributions due to the crystal environment. Here, one can see the charge transfer from V to O, especially originating from  $V-e_g$ . This is reasonable since  $V-e_g$  is strongly hybridized with  $O(2p)$ , which mainly responsible for the crystal bonding. The difference plot of  $\rho_{\text{diff}} = \rho_{\text{DFT+DMFT}} - \rho_{\text{DFT}}$  between DFT+DMFT and DFT in Fig. 7b verifies the already mentioned observation of enhanced  $V-e_g^\pi$  filling with correlations.

### 4.3 Charge self-consistency vs. one-shot

All the shown data corresponds to charge self-consistent DFT+DMFT. The relevance of charge self-consistency becomes already clear from our last finding of increased  $V-e_g^\pi$  filling with correlations. This increased filling affects the surrounding electronic structure and therefore has to be included on a complete self-consistent level.

However in  $V_2O_3$ , there are even much more dramatic consequences of charge self-consistency, which partly only become clear if one performs the same calculations at the simple one-shot level. If one does so, two major differences are observed. First, the orbital polarization already at stoichiometry is *much larger* [38, 39] than with charge self-consistency [14, 41–43, 34], nearly close to fully polarized  $V-e_g^\pi$ . Hence the trend of trigonal-crystal-field enhancement due to correlations is artificially too strong because of the missing feedback of the rest of the system. This is verified by the recent ARPES measurements [44] at stoichiometry, which show a sizable  $a_{1g}$  occupation close to the finding with charge self-consistency. Second, and maybe even more relevant, the effective Cr-doped structure is already insulating in one-shot



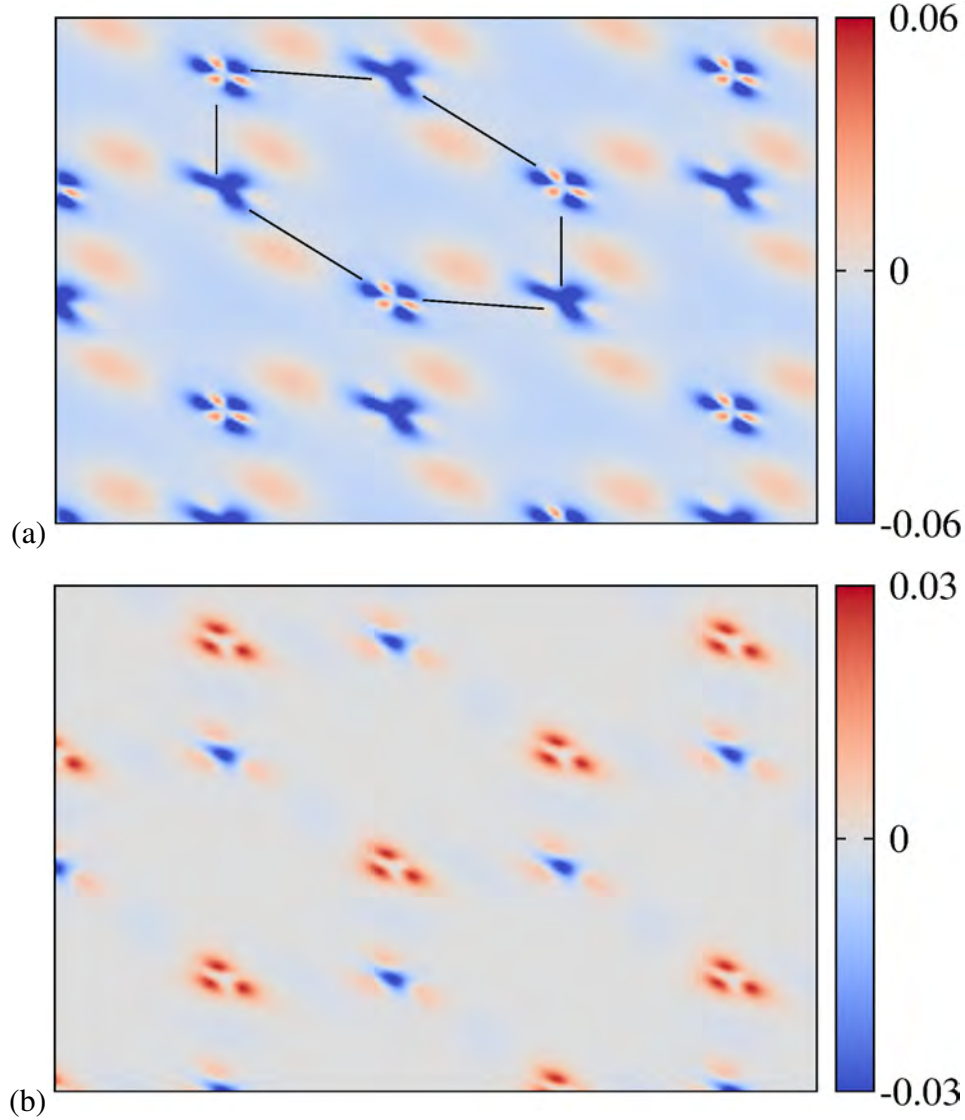


**Fig. 7:** Inclined view on the charge density within the  $ab$ -plane of  $V_2O_3$ . (a) DFT+DMFT bonding charge density  $\rho_{\text{bond}} = \rho - \rho_{\text{atomic}}$ . Black lines are guides to the eye for the V-based honeycomb structure. Note that this is an effective honeycomb lattice, which is not exactly flat due to two different height positions of V along  $c$ . (b) Charge-density difference  $\rho_{\text{diff}} = \rho_{\text{DFT+DMFT}} - \rho_{\text{DFT}}$  between DFT+DMFT and DFT. Note the enlarged occupation of the signatures of the  $V-e_g^\pi$  orbitals within DFT+DMFT (deep red parts).

DFT+DMFT (e.g. Ref. [39]). Now one could say that is a good thing, because it matches with the phase diagram for that amount of doping. But one has to remember the strong simplifications that are used to arrive at that result: neglect of charge self-consistency as well as neglect of the explicit defect chemistry due to the Cr dopants. Thus, this “positive” result truly emerges from the (neglect-)error cancellation, and does not explain the true driving force behind the PM-PI transition.

In fact recent work [34] shows, that an honest treatment of *both* electronic correlations *and* explicit defect chemistry due to doping is relevant to understand the phase diagram of  $V_2O_3$ .

## 5 Concluding remarks

In this short lecture, we introduced the self-consistency cycles of different electronic structure approaches with an emphasis on charge self-consistency in DFT+DMFT. The interplay between the basic-formal schemes as well as rather technical-numerical aspects is of natural importance in this field. Furthermore, although the described methodologies and their concrete computer-code implementations are often very elaborate, one should never use them in a “black-box” manner. It remains very important as a physicist or materials scientist to interpret and weigh the obtained data, if possible by thoughtful consideration of experimental knowledge. Hence, true scientific results only appear after the numerical data is processed by a critical mind.

## References

- [1] N.W. Ashcroft and N.D. Mermin: *Solid State Physics* (Saunders College Publishing, 1976)
- [2] R.O. Jones and O. Gunnarsson, *Rev. Mod. Phys.* **61**, 689 (1989)
- [3] W. Kohn, *Rev. Mod. Phys.* **71**, 1253 (1999)
- [4] W. Kohn and L.J. Sham, *Phys. Rev.* **140**, A1133 (1965)
- [5] W. Metzner and D. Vollhardt, *Phys. Rev. Lett.* **62**, 324 (1989)
- [6] A. Georges and G. Kotliar, *Phys. Rev. B* **45**, 6479 (1992)
- [7] S.Y. Savrasov and G. Kotliar, *Phys. Rev. B* **69**, 245101 (2004)
- [8] A. Georges: *in Lectures on the Physics of Highly Correlated Electron Systems VIII* (AIP Conference Proceedings 715, 2004), Ch. 3
- [9] V.I. Anisimov, A.I. Poteryaev, M.A. Korotin, A.O. Anokhin, and G. Kotliar, *J. Phys.: Condens. Matter* **9**, 7359 (1997)
- [10] A.I. Lichtenstein and M. Katsnelson, *Phys. Rev. B* **57**, 6884 (1998)
- [11] S.Y. Savrasov, G. Kotliar, and E. Abrahams, *Nature* **410**, 793 (2001)
- [12] J. Minár, L. Chioncel, A. Perlov, H. Ebert, M.I. Katsnelson, and A.I. Lichtenstein, *Phys. Rev. B* **72**, 045125 (2005)
- [13] L.V. Pourovskii, B. Amadon, S. Biermann, and A. Georges, *Phys. Rev. B* **76**, 235101 (2007)
- [14] D. Grieger, C. Piefke, O.E. Peil, and F. Lechermann, *Phys. Rev. B* **86**, 155121 (2012)
- [15] F. Lechermann, A. Georges, A. Poteryaev, S. Biermann, M. Posternak, A. Yamasaki, and O.K. Andersen, *Phys. Rev. B* **74**, 125120 (2006)
- [16] O.K. Andersen, *Phys. Rev. B* **12**, 3060 (1975)
- [17] N. Marzari, A.A. Mostofi, J.R. Yates, I. Souza, and D. Vanderbilt, *Rev. Mod. Phys.* **84**, 1419 (2012)
- [18] B. Amadon, F. Lechermann, A. Georges, F. Jollet, T.O. Wehling, and A.I. Lichtenstein, *Phys. Rev. B* **77**, 205112 (2008)
- [19] V.I. Anisimov, D.E. Kondakov, A.V. Kozhevnikov, I.A. Nekrasov, Z.V. Pchelkina, J.W. Allen, S.-K. Mo, H.-D. Kim, P. Metcalf, S. Suga, A. Sekiyama, G. Keller, I. Leonov, X. Ren, and D. Vollhardt, *Phys. Rev. B* **71**, 125119 (2005)

- [20] F. Lechermann: *Model Hamiltonians and Basic Techniques*, in E. Pavarini, E. Koch, D. Vollhardt, and A. Lichtenstein (eds.): *The LDA+DMFT approach to strongly correlated materials* Modeling and Simulation, Vol. 1 (Forschungszentrum Jülich, 2011), Ch. 3
- [21] E. Gull, A.J. Millis, A.I. Lichtenstein, A.N. Rubtsov, M. Troyer, and P. Werner, *Rev. Mod. Phys.* **83**, 349 (2011)
- [22] V.I. Anisimov, I.V. Solovyev, M.A. Korotin, M.T. Czyżyk, and G.A. Sawatzky, *Phys. Rev. B* **48**, 16929 (1993)
- [23] S. Biermann, F. Aryasetiawan, and A. Georges, *Phys. Rev. Lett.* **90**, 086402 (2003)
- [24] M. Potthoff and W. Nolting, *Phys. Rev. B* **59**, 2549 (1999)
- [25] M. Aichhorn, L. Pourovskii, and A. Georges, *Phys. Rev. B* **84**, 054529 (2011)
- [26] D.B. McWhan, T.M. Rice, and J.B. Remeika, *Phys. Rev. Lett.* **23**, 1384 (1969)
- [27] D.B. McWhan, J.B. Remeika, T.M. Rice, W.F. Brinkman, J.P. Maita, and A. Menth, *Phys. Rev. Lett.* **27**, 941 (1971)
- [28] C. Castellani, C.R. Natoli, and J. Ranninger, *Phys. Rev. B* **18**, 4945 (1978)
- [29] L.F. Mattheiss, *J. Phys.: Condens. Matter* **6**, 6477 (1994)
- [30] S.Y. Ezhov, V.I. Anisimov, D.I. Khomskii, and G.A. Sawatzky, *Phys. Rev. Lett.* **83**, 4136 (1999)
- [31] I.S. Elfimov, T. Saha-Dasgupta, and M.A. Korotin, *Phys. Rev. B* **68**, 113105 (2003)
- [32] V. Eyert, U. Schwingenschlögl, and U. Eckern, *Europhys. Lett.* **70**, 782 (2005)
- [33] Y. Guo, S.J. Clark, and J. Robertson, *J. Chem. Phys.* **140** (2014)
- [34] F. Lechermann, N. Bernstein, I.I. Mazin, and R. Valentí, arXiv:1801.08906 (2018)
- [35] P.D. Dernier, *J. Phys. Chem. Solids* **31**, 2569 (1970)
- [36] S. Chen, J.E. Hahn, C.E. Rice, and W.R. Robinson, *J. of Solid State Chem.* **44**, 192 (1982)
- [37] K. Held, G. Keller, V. Eyert, D. Vollhardt, and V.I. Anisimov, *Phys. Rev. Lett.* **86**, 5345 (2001)
- [38] G. Keller, K. Held, V. Eyert, D. Vollhardt, and V.I. Anisimov, *Phys. Rev. B* **70**, 205116 (2004)
- [39] A.I. Poteryaev, J.M. Tomczak, S. Biermann, A. Georges, A.I. Lichtenstein, A.N. Rubtsov, T. Saha-Dasgupta, and O.K. Andersen, *Phys. Rev. B* **76**, 085127 (2007)

- [40] M. Sandri, M. Capone, and M. Fabrizio, Phys. Rev. B **87**, 205108 (2013)
- [41] D. Grieger and F. Lechermann, Phys. Rev. B **90**, 115115 (2014)
- [42] X. Deng, A. Sternbach, K. Haule, D. Basov, and G. Kotliar, Phys. Rev. Lett. **113**, 246404 (2014)
- [43] I. Leonov, V.I. Anisimov, and D. Vollhardt, Phys. Rev. B **91**, 195115 (2015)
- [44] I. Lo Vecchio, J.D. Denlinger, O. Krupin, B.J. Kim, P.A. Metcalf, S. Lupi, J.W. Allen, and A. Lanzara, Phys. Rev. Lett. **117**, 166401 (2016)



# 7 LDA+DMFT: Multi-Orbital Hubbard Models

Eva Pavarini

Institute for Advanced Simulation

Forschungszentrum Jülich

## Contents

<b>1</b>	<b>Introduction</b>	<b>2</b>
<b>2</b>	<b>LDA+DMFT</b>	<b>5</b>
2.1	DMFT for the Hubbard dimer . . . . .	5
2.2	DMFT for the one-band Hubbard model . . . . .	12
2.3	DMFT for multi-orbital models . . . . .	15
2.4	Minimal material-specific models from LDA . . . . .	17
<b>3</b>	<b>Multi-orbital Hubbard models</b>	<b>21</b>
3.1	Atomic limit, multiplets and cubic crystal field . . . . .	23
3.2	Low-symmetry crystal field, orbital order and orbital degeneracy . . . . .	25
3.3	Spin-orbit interaction . . . . .	29
3.4	Non-spherical Coulomb terms and double-counting correction . . . . .	33
<b>4</b>	<b>Conclusion</b>	<b>36</b>
<b>A</b>	<b>The Anderson molecule</b>	<b>37</b>

# 1 Introduction

Most electronic properties of solids and molecules can be described – in the non-relativistic limit and in the Born-Oppenheimer approximation – by the electronic many-body Hamiltonian

$$\hat{H}_e^{\text{NR}} = -\frac{1}{2} \sum_i \nabla_i^2 - \sum_i \frac{Z}{r_i} + \sum_{i>j} \frac{1}{|\mathbf{r}_i - \mathbf{r}_j|}. \quad (1)$$

In practice, finding the exact eigenvalues and eigenvector of this Hamiltonian for a given system is impossible, unless the number of electrons is very small. This might sound as a gloomy conclusion for condensed-matter physics. The positive side is that, however, the exact solution of the many-body Hamiltonian (1) is, most likely, not even useful for understanding the properties of matter. One can grasp the reason by looking to a many-body problem for which an exact solution was found, the classical gravitational  $N$ -body system. Even without the complication of quantum mechanics, describing the behavior of many *interacting* classical bodies is a formidable task. This complexity is remarkable, since in the absence of interactions everything seems beautifully simple. Let us remind ourselves why. If a system is made of a single body with mass  $m_1$ , and its initial position,  $\mathbf{r}_1(0)$ , and velocity,  $\dot{\mathbf{r}}_1(0)$ , are known, we can predict its position at any time in the future by solving the trivial equation

$$m_1 \ddot{\mathbf{r}}_1 = 0.$$

If our system contains two such bodies, we can just do the same, the only possible complication being collisions; as a matter of fact, if we exclude collisions, the first body does not influence at all the second. The system of independent equations that we have to solve is just

$$m_1 \ddot{\mathbf{r}}_1 = 0 \quad \wedge \quad m_2 \ddot{\mathbf{r}}_2 = 0.$$

In the large- $N$  limit, assuming that all bodies have the same mass  $m_i = m$  and collisions are elastic, the system behaves as an ideal gas, whose macroscopic properties are described by the famous ideal-gas law  $PV = Nk_B T$ . As soon as we switch on the gravitational interaction, however, everything is suddenly awfully complicated. The two-body problem is already difficult by itself. The system of equations is now

$$\begin{cases} m_1 \ddot{\mathbf{r}}_1 = +\mathbf{F}_{12} \\ m_2 \ddot{\mathbf{r}}_2 = -\mathbf{F}_{12} \end{cases}$$

where

$$\mathbf{F}_{12} = -\frac{Gm_1 m_2 \hat{\mathbf{r}}}{r^2}, \quad \mathbf{r} = \mathbf{r}_1 - \mathbf{r}_2$$

is the force that the second body exerts on the first. This system can be solved exactly after changing variables to the center-of-mass and relative coordinates. Its solution yields a surprising emerging behavior, i.e., closed elliptical orbits. Let us add now one body more

$$\begin{cases} m_1 \ddot{\mathbf{r}}_1 = +\mathbf{F}_{12} + \mathbf{F}_{13} \\ m_2 \ddot{\mathbf{r}}_2 = -\mathbf{F}_{12} + \mathbf{F}_{23} \\ m_3 \ddot{\mathbf{r}}_3 = -\mathbf{F}_{13} - \mathbf{F}_{23}. \end{cases} \quad (2)$$



The three-body problem (2) was a mystery for a long time. It can even present *chaotic effects*; when chaos reigns, the behavior of the system in the future is very sensitive to small changes in the initial conditions. The problem was solved by Karl F. Sundman at the beginning of last century, who found – few cases excluded – a convergent series solution in powers of  $t^{1/3}$  [1]. The extension to the general  $N$ -body problem arrived in 1991 thanks to Qiudong Wang, at the time a young researcher. This story is nicely told in a review article by Florin Diacu [2], who concludes

*Did this mean the end of the  $N$ -body problem? Was this old question – unsuccessfully attacked by the greatest mathematicians of the last three centuries – merely solved by a student in a moment of rare inspiration? [...] Paradoxically [...] not; in fact we know nothing more than before having that solution.*

The explanation is that

*[...] these series solutions [...] have very slow convergence. One would have to sum up millions of terms to determine the motions of the particles for insignificantly short intervals of time. The round-off errors make these series unusable in numerical works. From the theoretical point of view, these solution add nothing to what was previously known about the  $N$ -body problem.*

Indeed, we are not even interested in knowing where all particles are at each moment. We do not want to reproduce the complete history of the formation of the solar system, atom by atom. We rather look for answers to questions such as “Is the solar system stable? If not, in what time frame will chaotic behavior manifest itself?”. We can now foresee that a similar conclusion would likely apply to the quantum case, had we at hand the exact solution of this, even more complex,  $N$ -body problem. Such a solution would contain too much information. We would need the lifetime of the universe or longer for extracting the answer to one of our questions, e.g., “why are some systems metals and other insulators?” or “what is the origin of superconductivity?”. We would *perfectly reproduce experimental phenomena*, without being able to tell anything about their origin.<sup>1</sup> We have thus to abandon the idea that all problems can be solved by a single magic algorithm which returns the exact solution, unless we can, in addition, build an oracle machine powerful enough to eliminate all the irrelevant data and identify the essential elements, providing answers to the real questions. We cannot exclude that one day artificial intelligence will be able to do that for us [3]. In the mean time, the strategy is to build minimal materials-specific models which capture the essence of the phenomenon we want to understand, and solve them as accurately as possible. Unfortunately, even for those models, in most cases only approximate solutions are available. Thus the simplifications made and the approximations adopted have to be put to the test. In this imperfect world, in which neither the model nor the solution method are exact, and in which there is no guarantee that the choices we made are indeed good enough, we have to try to explain reality. Finding realistic

<sup>1</sup>Indeed, agreement with experiments is highly overrated. A useful theory should explain, not merely reproduce, experimental measurements.

but minimal models (and, at the same time approximate methods of solution that work) is, of course, not at all trivial, and often involves refinements and corrections. This approach, despite its non-systematic, trial-and-error nature, proved itself very successful and allowed physicists to understand superconductivity, the Kondo effect, the metal-insulator transition, and much more. The first step to make progress is to rewrite the Hamiltonian in second quantization, the formalism that allows us to deal with many-body states and operators in a compact and elegant way. It is worth to remind ourselves that setting up the Hamiltonian in second quantization requires to identify and choose a complete *one-electron basis*. The selection of the basis is important, because certain choices allow us to build *better* models than others. Here *better* indicates a more advantageous compromise between two competing needs, (i) that the model is as realistic as possible and (ii) that its associated Fock space is as small as possible. The role of the basis becomes perhaps more clear with a simple example. The low-energy bound states of the hydrogen atom can be described, of course, in a basis of plane waves; the number of plane waves required is extremely high, however. In the many-body case, the basis might make the difference between being able to solve the relevant model or not. In this lecture we will adopt as basis Wannier functions,  $\psi_{im\sigma}(\mathbf{r})$ . First we will write the Hamiltonian using the complete set, and later we will see how to construct minimal models. Using a complete set of Wannier functions, the Hamiltonian (1) can be expressed as  $\hat{H}_e = \hat{H}_0 + \hat{H}_U$ . The one-electron term,  $\hat{H}_0$ , describes the kinetic energy and the attraction between electrons and nuclei, and is given by

$$\hat{H}_0 = - \sum_{\sigma} \sum_{ii'} \sum_{mm'} t_{m,m'}^{i,i'} c_{im\sigma}^{\dagger} c_{i'm'\sigma}.$$

Here  $c_{im\sigma}^{\dagger}$  ( $c_{im\sigma}$ ) creates (destroys) an electron with spin  $\sigma$  in orbital  $m$  at site  $i$ . The on-site ( $i = i'$ ) terms yield the crystal-field matrix  $\varepsilon_{m,m'} = t_{m,m'}^{i,i}$ , while the  $i \neq i'$  contributions are the hopping integrals. The parameters are given by

$$t_{m,m'}^{i,i'} = - \int d\mathbf{r} \overline{\psi_{im\sigma}(\mathbf{r})} \left( -\frac{1}{2} \nabla^2 + v_R(\mathbf{r}) \right) \psi_{i'm'\sigma}(\mathbf{r}), \quad (3)$$

where  $v_R(\mathbf{r})$  is the electron-nuclei interaction. The electron-electron repulsion  $\hat{H}_U$  is

$$\hat{H}_U = \frac{1}{2} \sum_{ii'jj'} \sum_{\sigma\sigma'} \sum_{mm'pp'} U_{mp\ m'p'}^{ij\ i'j'} c_{im\sigma}^{\dagger} c_{jp\sigma'}^{\dagger} c_{j'p'\sigma'} c_{i'm'\sigma},$$

where the (*bare*) Coulomb integrals can be expressed as

$$U_{mp\ m'p'}^{ij\ i'j'} = \int d\mathbf{r}_1 \int d\mathbf{r}_2 \overline{\psi_{im\sigma}(\mathbf{r}_1)} \overline{\psi_{jp\sigma'}(\mathbf{r}_2)} \frac{1}{|\mathbf{r}_1 - \mathbf{r}_2|} \psi_{j'p'\sigma'}(\mathbf{r}_2) \psi_{i'm'\sigma}(\mathbf{r}_1).$$

The simplest version of  $\hat{H}_e$  is the so-called Hubbard model, in which we consider only one orbital ( $m=m'=p=p'$ ) and we assume that the Coulomb term is local ( $i=i'=j=j'$ ). This yields

$$\hat{H} = - \sum_{\sigma} \sum_{ii'} t^{i,i'} c_{i\sigma}^{\dagger} c_{i'\sigma} + U \sum_i \hat{n}_{i\uparrow} \hat{n}_{i\downarrow} = \sum_{\mathbf{k}\sigma} \varepsilon_{\mathbf{k}} c_{\mathbf{k}\sigma}^{\dagger} c_{\mathbf{k}\sigma} + U \sum_i \hat{n}_{i\uparrow} \hat{n}_{i\downarrow}. \quad (4)$$

Even this apparently simple model cannot be solved exactly in the general case. This is because it contains already all the essence of the electronic many-body problem.

## 2 LDA+DMFT

The Hubbard model (4) and its multi-orbital generalizations are the minimal models for describing the Mott metal-insulator transition. The most successful method of solution capturing the nature of the Mott transition is DMFT, dynamical mean-field theory [4–7]. It is based on the local self-energy approximation, i.e., the assumption that  $\Sigma^\sigma(\mathbf{k}, \omega) \sim \Sigma_l^\sigma(\omega)$ . DMFT is exact for  $U = 0$  (band limit), for  $t^{i,i'} = 0$  (atomic limit), and in the limit of infinite coordination number [4, 5]. In the present section we will illustrate the basic ideas of this approach. First we will use a toy model that can be solved analytically, the Hubbard dimer. For this model the coordination number is equal to one, and thus, as one might expect, a local self-energy is a bad approximation. The example is nevertheless very useful to explain the essence of the method. Next we will extend to the one-band Hubbard model, and finally we will generalize to realistic multi-orbital many-body Hamiltonians.

### 2.1 DMFT for the Hubbard dimer

The two-site Hubbard model is given by

$$\hat{H} = \varepsilon_d \sum_{i\sigma} \hat{n}_{i\sigma} - t \sum_{\sigma} \left( c_{1\sigma}^\dagger c_{2\sigma} + c_{2\sigma}^\dagger c_{1\sigma} \right) + U \sum_i \hat{n}_{i\uparrow} \hat{n}_{i\downarrow},$$

with  $i = 1, 2$ . The ground-state for  $N = 2$  electrons (half filling) is the singlet<sup>2</sup>

$$|G\rangle_H = |2, 00\rangle_- = \frac{a_2}{\sqrt{2}} \left[ c_{1\uparrow}^\dagger c_{2\downarrow}^\dagger - c_{1\downarrow}^\dagger c_{2\uparrow}^\dagger \right] |0\rangle + \frac{a_1}{\sqrt{2}} \left[ c_{1\uparrow}^\dagger c_{1\downarrow}^\dagger + c_{2\uparrow}^\dagger c_{2\downarrow}^\dagger \right] |0\rangle \quad (5)$$

with

$$a_1^2 = \frac{1}{\Delta(t, U)} \frac{\Delta(t, U) - U}{2}, \quad a_2^2 = \frac{4t^2}{\Delta(t, U)} \frac{2}{\Delta(t, U) - U},$$

and

$$\Delta(t, U) = \sqrt{U^2 + 16t^2}.$$

The energy of this state is

$$E_0(2) = 2\varepsilon_d + \frac{1}{2}(U - \Delta(t, U)).$$

In the  $T \rightarrow 0$  limit, the exact local Matsubara Green function for spin  $\sigma$  takes then the form

$$G_{i,i}^\sigma(i\nu_n) = \frac{1}{4} \left[ \frac{1+w}{i\nu_n - (E_0(2) - \varepsilon_d + t - \mu)} + \frac{1-w}{i\nu_n - (E_0(2) - \varepsilon_d - t - \mu)} \right. \\ \left. + \frac{1-w}{i\nu_n - (-E_0(2) + U + 3\varepsilon_d + t - \mu)} + \frac{1+w}{i\nu_n - (-E_0(2) + U + 3\varepsilon_d - t - \mu)} \right],$$

---

<sup>2</sup>You can find all eigenstates and eigenvalues of this model for arbitrary filling in my chapter in Ref. [8].

where  $\nu_n = \pi(2n + 1)/\beta$  are fermionic Matsubara frequencies,  $\mu = \varepsilon_d + U/2$  is the chemical potential, and the weight is  $w = 2a_1a_2$ . The local Green function can be rewritten as the average of the Green function for the bonding ( $k = 0$ ) and the anti-bonding state ( $k = \pi$ ), i.e.,

$$G_{i,i}^\sigma(i\nu_n) = \frac{1}{2} \left( \underbrace{\frac{1}{i\nu_n + \mu - \varepsilon_d + t - \Sigma^\sigma(0, i\nu_n)}}_{G^\sigma(0, i\nu_n)} + \underbrace{\frac{1}{i\nu_n + \mu - \varepsilon_d - t - \Sigma^\sigma(\pi, i\nu_n)}}_{G^\sigma(\pi, i\nu_n)} \right).$$

The self-energy is given by

$$\Sigma^\sigma(k, i\nu_n) = \frac{U}{2} + \frac{U^2}{4} \frac{1}{i\nu_n - e^{ik} 3t}.$$

The self-energies  $\Sigma^\sigma(0, i\nu_n)$  and  $\Sigma^\sigma(\pi, i\nu_n)$  differ due to the phase  $e^{ik} = \pm 1$  in their denominators. The local self-energy is, by definition, the average of the two

$$\Sigma_l^\sigma(i\nu_n) = \frac{1}{2} \left( \Sigma^\sigma(\pi, i\nu_n) + \Sigma^\sigma(0, i\nu_n) \right) = \frac{U}{2} + \frac{U^2}{4} \frac{i\nu_n}{(i\nu_n)^2 - (3t)^2}.$$

The difference

$$\Delta\Sigma_l^\sigma(i\nu_n) = \frac{1}{2} \left( \Sigma^\sigma(\pi, i\nu_n) - \Sigma^\sigma(0, i\nu_n) \right),$$

thus measures the importance of non-local effects; it would be zero if the self-energy was independent of  $k$ . Next we define the hybridization function

$$F^\sigma(i\nu_n) = \frac{(t + \Delta\Sigma_l^\sigma(i\nu_n))^2}{i\nu_n + \mu - \varepsilon_d - \Sigma_l^\sigma(i\nu_n)}$$

which for  $U = 0$  becomes

$$F_0^\sigma(i\nu_n) = \frac{t^2}{i\nu_n}.$$

By using these definitions, we can rewrite the local Green function as

$$G_{i,i}^\sigma(i\nu_n) = \frac{1}{i\nu_n + \mu - \varepsilon_d - F^\sigma(i\nu_n) - \Sigma_l^\sigma(i\nu_n)}.$$

It is important to point out that the local Green function and the local self-energy satisfy the following *local Dyson equation*

$$\Sigma_l^\sigma(i\nu_n) = \frac{1}{\mathfrak{G}_{i,i}^\sigma(i\nu_n)} - \frac{1}{G_{i,i}^\sigma(i\nu_n)},$$

where  $\mathfrak{G}_{i,i}^\sigma(i\nu_n)$  is given by

$$\mathfrak{G}_{i,i}^\sigma(i\nu_n) = \frac{1}{i\nu_n + \mu - \varepsilon_d - F^\sigma(i\nu_n)}.$$

Thus, one could think of mapping the Hubbard dimer into an auxiliary quantum-impurity model, chosen such that, within certain approximations, the impurity Green function is close to the local Green function of the original problem. Is this possible? Let us adopt as auxiliary model the Anderson molecule

$$\hat{H}^A = \varepsilon_s \sum_{\sigma} \hat{n}_{s\sigma} - t \sum_{\sigma} \left( c_{d\sigma}^{\dagger} c_{s\sigma} + c_{s\sigma}^{\dagger} c_{d\sigma} \right) + \varepsilon_d \sum_{\sigma} \hat{n}_{d\sigma} + U \hat{n}_{d\uparrow} \hat{n}_{d\downarrow}. \quad (6)$$

The first constraint would be that Hamiltonian (6) has a ground state with the same occupations of the 2-site Hubbard model, i.e., at half filling,  $n_d = n_s = 1$ . The condition is satisfied if  $\varepsilon_s = \mu$ . This can be understood by comparing the Hamiltonian matrices of the two models in the Hilbert space with  $N = 2$  electrons. Let us order the two-electron states of the Hubbard dimer as

$$\begin{aligned} |1\rangle &= |2, 1, 1\rangle &= c_{1\uparrow}^{\dagger} c_{2\uparrow}^{\dagger} |0\rangle, \\ |2\rangle &= |2, 1, -1\rangle &= c_{1\downarrow}^{\dagger} c_{2\downarrow}^{\dagger} |0\rangle, \\ |3\rangle &= |2, 1, 0\rangle &= \frac{1}{\sqrt{2}} [c_{1\uparrow}^{\dagger} c_{2\downarrow}^{\dagger} + c_{1\downarrow}^{\dagger} c_{2\uparrow}^{\dagger}] |0\rangle, \\ |4\rangle &= |2, 0, 0\rangle &= \frac{1}{\sqrt{2}} [c_{1\uparrow}^{\dagger} c_{2\downarrow}^{\dagger} - c_{1\downarrow}^{\dagger} c_{2\uparrow}^{\dagger}] |0\rangle, \\ |5\rangle &= |2, 0, 0\rangle_1 &= c_{1\uparrow}^{\dagger} c_{1\downarrow}^{\dagger} |0\rangle, \\ |6\rangle &= |2, 0, 0\rangle_2 &= c_{2\uparrow}^{\dagger} c_{2\downarrow}^{\dagger} |0\rangle. \end{aligned}$$

In this basis the Hamiltonian has the matrix form

$$\hat{H}_2 = \begin{pmatrix} 2\varepsilon_d & 0 & 0 & 0 & 0 & 0 \\ 0 & 2\varepsilon_d & 0 & 0 & 0 & 0 \\ 0 & 0 & 2\varepsilon_d & 0 & 0 & 0 \\ 0 & 0 & 0 & 2\varepsilon_d & -\sqrt{2}t & -\sqrt{2}t \\ 0 & 0 & 0 & -\sqrt{2}t & 2\varepsilon_d + U & 0 \\ 0 & 0 & 0 & -\sqrt{2}t & 0 & 2\varepsilon_d + U \end{pmatrix}.$$

The ground state, the singlet given in Eq. (5), can be obtained by diagonalizing the lower  $3 \times 3$  block. For the Anderson molecule, ordering the basis in the same way ( $1 \rightarrow d, 2 \rightarrow s$ ), this Hamiltonian becomes

$$\hat{H}_2^A = \begin{pmatrix} \varepsilon_d + \varepsilon_s & 0 & 0 & 0 & 0 & 0 \\ 0 & \varepsilon_d + \varepsilon_s & 0 & 0 & 0 & 0 \\ 0 & 0 & \varepsilon_d + \varepsilon_s & 0 & 0 & 0 \\ 0 & 0 & 0 & \varepsilon_d + \varepsilon_s & -\sqrt{2}t & -\sqrt{2}t \\ 0 & 0 & 0 & -\sqrt{2}t & 2\varepsilon_d + U & 0 \\ 0 & 0 & 0 & -\sqrt{2}t & 0 & 2\varepsilon_s \end{pmatrix}.$$

By comparison, we may see that if  $\varepsilon_s = \varepsilon_d + U/2$ , the ground-state of  $\hat{H}_2^A$  has the form of the ground-state for the Hubbard dimer, i.e.,

$$|G\rangle_A = \frac{\alpha_2}{\sqrt{2}} [c_{d\uparrow}^\dagger c_{s\downarrow}^\dagger - c_{d\downarrow}^\dagger c_{s\uparrow}^\dagger] |0\rangle + \frac{\alpha_1}{\sqrt{2}} [c_{d\uparrow}^\dagger c_{d\downarrow}^\dagger + c_{s\uparrow}^\dagger c_{s\downarrow}^\dagger] |0\rangle.$$

The values of  $\alpha_1$  and  $\alpha_2$ , as well as the complete list of eigenvalues and eigenvectors of the Anderson molecule for  $\varepsilon_s = \varepsilon_d + U/2$  and arbitrary electron number  $N$ , can be found in the Appendix. The impurity Green function takes then the form

$$G_{d,d}^\sigma(i\nu_n) = \frac{1}{4} \left[ \frac{1+w'}{i\nu_n - (E_0(2) - E_-(1) - \mu)} + \frac{1-w'}{i\nu_n - (E_0(2) - E_+(1) - \mu)} \right. \\ \left. + \frac{1+w'}{i\nu_n - (E_-(3) - E_0(2) - \mu)} + \frac{1-w'}{i\nu_n - (E_+(3) - E_0(2) - \mu)} \right],$$

where

$$E_0(2) - E_\pm(1) - \mu = -\frac{1}{4} \left( 2\Delta(t, U/2) \pm \Delta(t, U) \right), \\ E_\pm(3) - E_0(2) - \mu = +\frac{1}{4} \left( 2\Delta(t, U/2) \pm \Delta(t, U) \right),$$

$$w' = \frac{1}{2} \frac{32t^2 - U^2}{\Delta(t, U) \Delta(t, U/2)}.$$

After some rearrangement we obtain a much simpler expression

$$G_{d,d}^\sigma(i\nu_n) = \frac{1}{i\nu_n + \mu - \varepsilon_d - \mathcal{F}_0^\sigma(i\nu_n) - \Sigma_A^\sigma(i\nu_n)}.$$

The impurity self-energy equals the local self-energy of the Hubbard dimer

$$\Sigma_A^\sigma(i\nu_n) = \frac{U}{2} + \frac{U^2}{4} \frac{i\nu_n}{(i\nu_n)^2 - (3t)^2}.$$

The hybridization function is given by

$$\mathcal{F}_0^\sigma(i\nu_n) = \frac{t^2}{i\nu_n}.$$

For  $U = 0$ ,  $G_{d,d}^\sigma(i\nu_n)$  equals the non-interacting impurity Green function

$$G_{d,d}^{0\sigma}(i\nu_n) = \frac{1}{i\nu_n + \mu - \varepsilon_d - \mathcal{F}_0^\sigma(i\nu_n)}.$$

The impurity Green function thus satisfies the *impurity Dyson equation*

$$\Sigma_A^\sigma(i\nu_n) = \frac{1}{G_{d,d}^{0\sigma}(i\nu_n)} - \frac{1}{G_{d,d}^\sigma(i\nu_n)}.$$

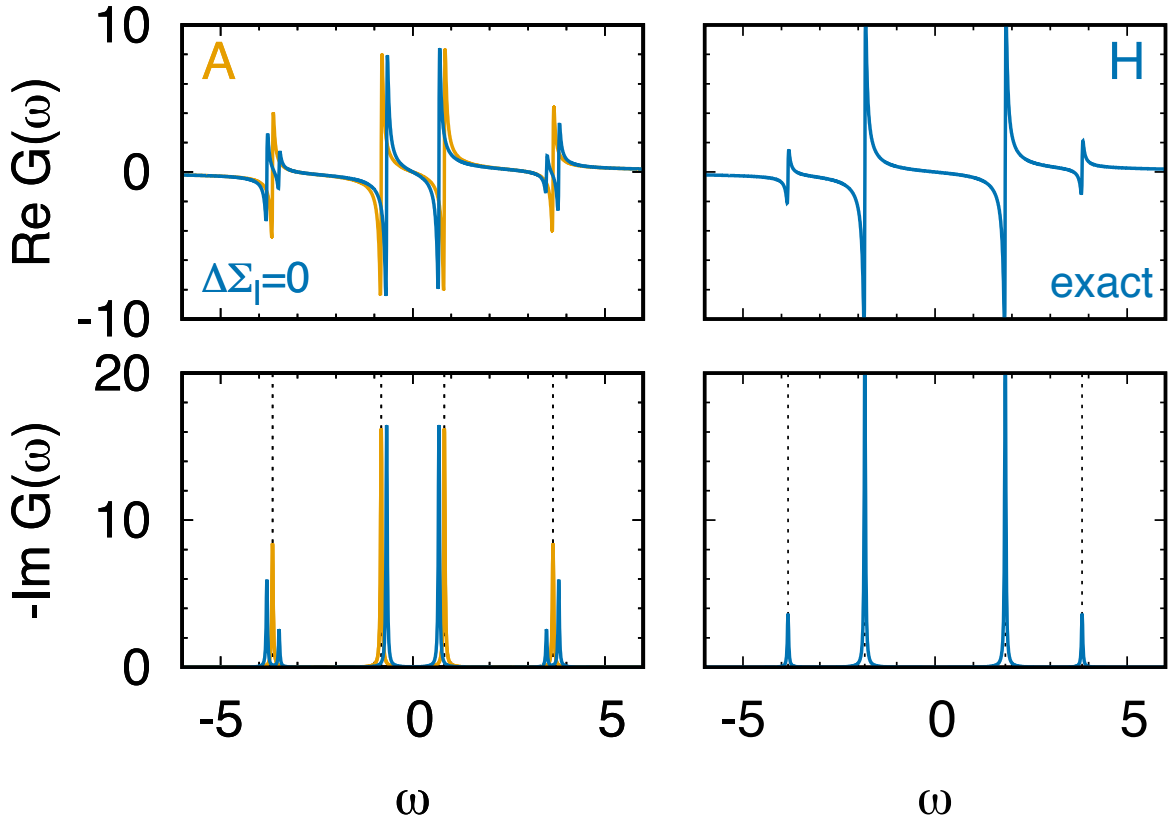


**Fig. 1:** Green functions of the Hubbard dimer ( $t = 1, U = 4$ ) and the Anderson molecule ( $\varepsilon_s = \varepsilon_d + U/2$ ) in the zero temperature limit. Left panels, blue: Hubbard dimer with local self-energy only, i.e., with  $\Delta\Sigma_l^\sigma(\omega) = 0$ . Left panels, orange: Anderson molecule. Right panels: Exact Green function of the Hubbard dimer. Dashed lines: poles of the Green function of the Anderson molecule (left) or Hubbard dimer (right).

In Fig. 1 we show the impurity Green function of the Anderson molecule (orange, left panels) and the local Green function of the 2-site Hubbard model, in the local self-energy approximation (blue, left panels) and exact (blue, right panels). Comparing left and right panels we can see that setting  $\Delta\Sigma_l^\sigma(\omega) = 0$  yields large errors. The left panels demonstrate, however, that the spectral function of the Anderson molecule is quite similar to the one of the Hubbard dimer with  $\Delta\Sigma_l^\sigma(\omega) = 0$ . The small remaining deviations come from replacing, in the impurity Dyson equation, the non-interacting impurity Green function with  $\mathfrak{G}_{i,i}^\sigma(i\nu_n)$  in the local self-energy approximation, i.e., with the *bath* Green function

$$\mathcal{G}_{i,i}^\sigma(i\nu_n) = \frac{1}{i\nu_n + \mu - \varepsilon_d - \mathcal{F}_l^\sigma(i\nu_n)},$$

where

$$\mathcal{F}_l^\sigma(i\nu_n) = \frac{t^2}{i\nu_n + \mu - \varepsilon_d - \Sigma_A^\sigma(i\nu_n)}.$$

We are now in the position of explaining how DMFT works for the Hamiltonian of the Hubbard dimer, choosing the Anderson molecule Hamiltonian (6) as the auxiliary quantum-impurity model. The procedure can be split in the following steps

1. Build the initial quantum impurity model with  $G_{d,d}^{0\sigma}(i\nu_n) = G_{i,i}^{0\sigma}(i\nu_n)$ . The initial bath is thus defined by energy  $\varepsilon_s = \varepsilon_d$  and hopping  $t$ .
2. Calculate the local Green function  $G_{d,d}^\sigma(i\nu_n)$  for the auxiliary model.
3. Use the local Dyson equation to calculate the impurity self-energy

$$\Sigma_A^\sigma(i\nu_n) = \frac{1}{G_{d,d}^{0\sigma}(i\nu_n)} - \frac{1}{G_{d,d}^\sigma(i\nu_n)}.$$

4. Calculate the local Green function of the Hubbard dimer setting the self-energy equal to the one of the quantum-impurity model

$$G_{i,i}^\sigma(i\nu_n) \sim \frac{1}{2} \left[ \frac{1}{i\nu_n + \mu - \varepsilon_d + t - \Sigma_A^\sigma(i\nu_n)} + \frac{1}{i\nu_n + \mu - \varepsilon_d - t - \Sigma_A^\sigma(i\nu_n)} \right].$$

5. Calculate a new bath Green function  $\mathcal{G}_{i,i}^\sigma(i\nu_n)$  from the local Dyson equation

$$\mathcal{G}_{i,i}^\sigma(i\nu_n) = \frac{1}{\Sigma_A^\sigma(i\nu_n) + 1/G_{i,i}^\sigma(i\nu_n)}.$$

6. Build a new  $G_{d,d}^{0\sigma}(i\nu_n)$  from  $\mathcal{G}_{i,i}^\sigma(i\nu_n)$ .
7. Restart from the second step.
8. Iterate till self-consistency, i.e., here till  $n_d^\sigma = n_i^\sigma$  and  $\Sigma_A^\sigma(i\nu_n)$  does not change any more.

The Anderson molecule satisfies the self-consistency requirements for  $\varepsilon_s = \mu$ . The remaining difference between  $G_{d,d}^\sigma(i\nu_n)$ , the impurity Green function, and  $G_{i,i}^\sigma(i\nu_n)$ , the local Green function of the Hubbard dimer in the local self-energy approximation, arises from the difference in the associated hybridization functions

$$\Delta\mathcal{F}_l(i\nu_n) = \mathcal{F}_l^\sigma(i\nu_n) - \mathcal{F}_0^\sigma(i\nu_n) = t^2 p^2 \left( -\frac{2}{i\nu_n} + \frac{1}{i\nu_n - \varepsilon_a} + \frac{1}{i\nu_n + \varepsilon_a} \right)$$

where  $p^2 = U^2/8\varepsilon_a^2$  and  $\varepsilon_a = \sqrt{9t^2 + U^2}/4$ . If we use the Anderson molecule as quantum-impurity model we neglect  $\Delta\mathcal{F}_l(i\nu_n)$ ; the error made is small, as shown in the left panels of Fig. 1. To further improve we would have to modify the auxiliary model adding more bath sites. Remaining with the Anderson molecule, let us compare in more detail its spectral function with the exact spectral function of the Hubbard dimer. Fig. 2 shows that the evolution as a function of  $U$  is different for the two Hamiltonians. Anticipating the discussion of next session, if we compare to the spectral function of the actual lattice Hubbard model, we could say that the Anderson molecule partially captures the behavior of the central “quasi-particle” or “Kondo”



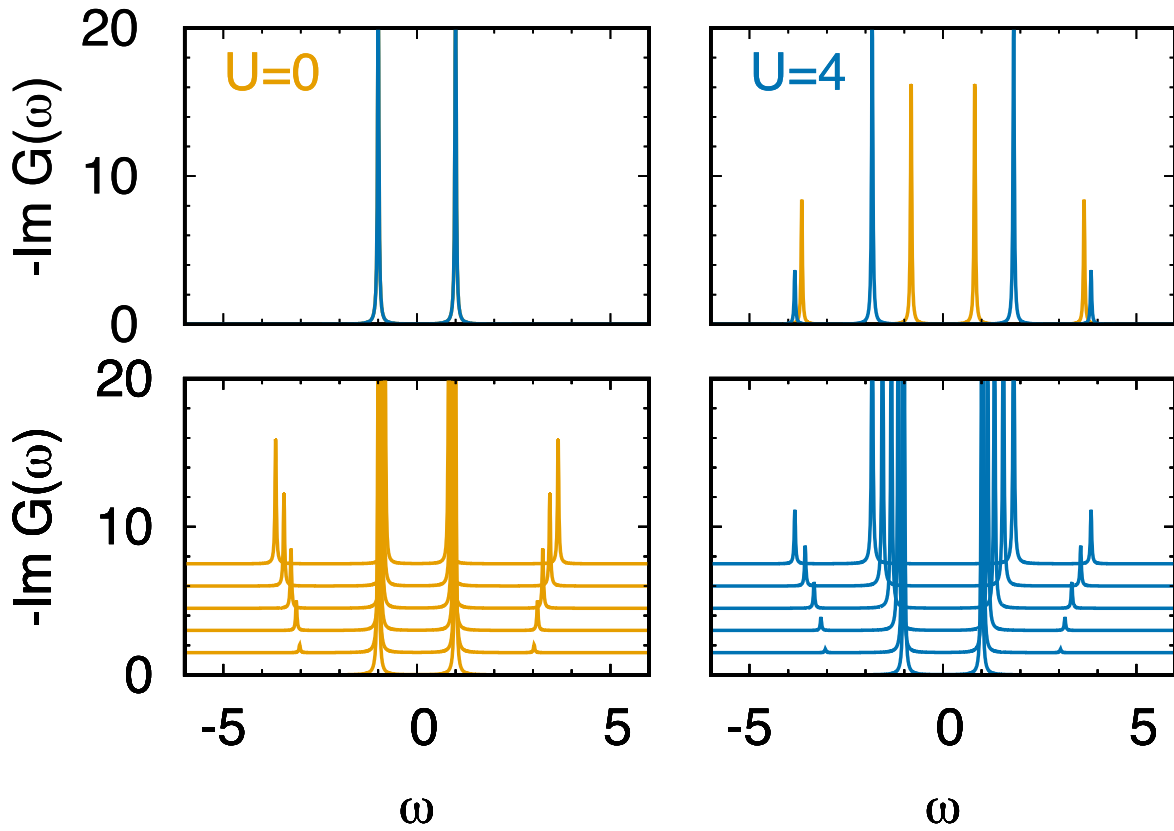


**Fig. 2:** Imaginary part of the Green function of the Anderson molecule (orange) and Hubbard dimer (blue) in the zero temperature limit. For the Hubbard dimer the exact Green functions are used, as in the right panels of Fig. 1. Parameters:  $t = 1$ ,  $\varepsilon_s = \mu$ . Top:  $U = 0$  (left) and  $U = 4t$  (right). Bottom: evolution with increasing  $U$  from 0 to  $4t$  in equal steps.

peak with increasing  $U$ , although the Kondo effect itself is unrealistically described; as a matter of fact, the Kondo energy gain (the “Kondo temperature”) is perturbative ( $\propto t^2/U$ ) in the case of the Anderson molecule, while it is exponentially small for a Kondo impurity in a metallic bath. On the other hand, the Hubbard dimer captures well the Hubbard bands and the gap in the large- $U$  limit. The example of the Anderson molecule also points to the possible shortcomings of calculations for the lattice Hubbard model (4), in which the DMFT quantum-impurity model is solved via exact diagonalization, however using a single bath site or very few; this might perhaps be sufficient in the limit of large gap,<sup>3</sup> but is bound to eventually fail approaching the metallic regime. Indeed, this failure is one of the reasons why the solution of the Kondo problem required the development of – at the time new – non-perturbative techniques such as the numerical renormalization group.

<sup>3</sup>For a discussion of bath parametrization in exact diagonalization and the actual convergence with the number of bath sites for the lattice Hubbard model see Ref. [9].

## 2.2 DMFT for the one-band Hubbard model

The Hubbard Hamiltonian (4) is in principle the simplest model for the description of the Mott metal-insulator transition. In the tight-binding approximation it becomes

$$\hat{H} = \varepsilon_d \sum_{\sigma i} \hat{n}_{i\sigma} - t \sum_{\sigma \langle ii' \rangle} c_{i\sigma}^\dagger c_{i'\sigma} + U \sum_i \hat{n}_{i\uparrow} \hat{n}_{i\downarrow}, \quad (7)$$

where  $\langle ii' \rangle$  is a sum over first neighbors. For  $U = 0$ , at half-filling, this Hamiltonian describes a metallic band. For  $t = 0$  it describes an insulating collection of disconnected atoms. Somewhere in between, at a critical value of  $t/U$ , a metal to insulator transition must occur. In this section we will discuss the DMFT solution of (7) and the picture of the metal-insulator transition emerging from it. The first step consists in mapping the original many-body Hamiltonian into an effective quantum-impurity model, such as the Anderson Hamiltonian

$$\hat{H}^A = \underbrace{\sum_{\mathbf{k}\sigma} \varepsilon_{\mathbf{k}}^s \hat{n}_{\mathbf{k}\sigma}}_{\hat{H}_{\text{bath}}} + \underbrace{\sum_{\mathbf{k}\sigma} \left( V_{\mathbf{k}}^s c_{\mathbf{k}\sigma}^\dagger c_{d\sigma} + \text{h.c.} \right)}_{\hat{H}_{\text{hyb}}} + \underbrace{\varepsilon_d \sum_{\sigma} \hat{n}_{d\sigma} + U \hat{n}_{d\uparrow} \hat{n}_{d\downarrow}}_{\hat{H}_{\text{imp}}}.$$

In this model the on-site Coulomb repulsion  $U$  appears only in the impurity Hamiltonian,  $\hat{H}_{\text{imp}}$ , while the terms  $\hat{H}_{\text{bath}}$  and  $\hat{H}_{\text{hyb}}$ , describe, respectively, the bath and the bath-impurity hybridization. In the next step, the quantum-impurity model is solved. Differently from the case of the Anderson molecule, this cannot be done analytically. It requires non-perturbative numerical methods, such as exact diagonalization, the numerical renormalization group or quantum Monte Carlo (QMC). Here we describe the DMFT self-consistency loop for a QMC quantum-impurity solver. Solving the quantum-impurity model yields the impurity Green function  $G_{d,d}^\sigma(i\nu_n)$ . From the impurity Dyson equation we can calculate the impurity self-energy

$$\Sigma_A^\sigma(i\nu_n) = (G_{d,d}^{0\sigma}(i\nu_n))^{-1} - (G_{d,d}^\sigma(i\nu_n))^{-1}.$$

Next, we adopt the local approximation, i.e., we assume that the self-energy of the Hubbard model equals the impurity self-energy. Then, the local Green function is given by

$$G_{i_c,i_c}^\sigma(i\nu_n) = \frac{1}{N_{\mathbf{k}}} \sum_{\mathbf{k}} \frac{1}{i\nu_n + \mu - \varepsilon_{\mathbf{k}} - \Sigma_A^\sigma(i\nu_n)},$$

where  $N_{\mathbf{k}}$  is the number of  $\mathbf{k}$  points. The local Dyson equation is used once more, this time to calculate the bath Green function  $\mathcal{G}^\sigma(i\nu_n)$ , which in turn defines a new quantum-impurity model. This procedure is repeated until self-consistency is reached, and

$$G_{i_c,i_c}^\sigma(i\nu_n) = G_{d,d}^\sigma(i\nu_n).$$

It is important to underline that self-consistency is key to the success of DMFT in describing the metal-to-insulator transition. This can, perhaps, be best understood looking at a simpler self-consistent method, the static mean-field or Hartree-Fock approach.<sup>4</sup> In the static mean-field

<sup>4</sup>Keeping in mind that many self-consistent solutions obtained with the Hartree-Fock method are spurious.

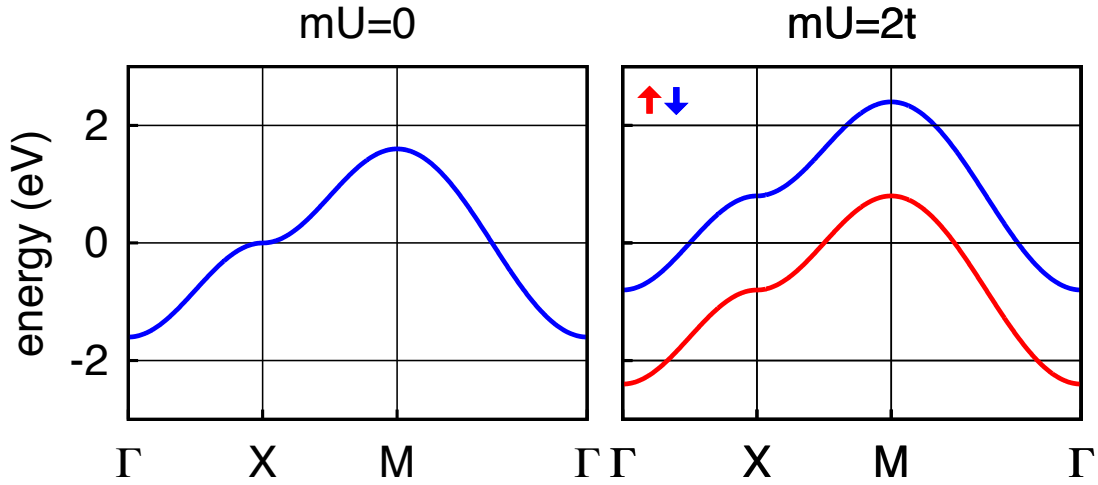


**Fig. 3:** The metal-insulator transition in ferromagnetic Hartree-Fock. The calculation is for a square lattice tight-binding model with dispersion  $\varepsilon_{\mathbf{k}} = -2t(\cos k_x + \cos k_y)$ .

approximation we replace the Coulomb interaction of the Hubbard model (7) with a one-body operator

$$U\hat{n}_{i\uparrow}\hat{n}_{i\downarrow} \longrightarrow U(\bar{n}_{i\uparrow}\hat{n}_{i\downarrow} + \hat{n}_{i\uparrow}\bar{n}_{i\downarrow} - \bar{n}_{i\uparrow}\bar{n}_{i\downarrow}),$$

where  $\bar{n}_{i\sigma}$  is the expectation value of  $\hat{n}_{i\sigma}$ ; for simplicity, here we additionally assume that  $\bar{n}_{i\sigma} = \bar{n}_{\sigma}$ . The approximation is then identical to replacing the Hamiltonian with

$$\hat{H}_{\text{MF}} = \sum_{\mathbf{k}\sigma} \left[ \varepsilon_{\mathbf{k}} + U \left( \frac{1}{2} - \sigma m \right) \right] \hat{n}_{\mathbf{k}\sigma}, \quad (8)$$

where  $\sigma = +1$  for spin up and  $\sigma = -1$  for spin down; thus  $h_{\text{eff}} = 2Um$  plays the role of an effective field (Weiss field). The self-consistency criterion is simply

$$\bar{n}_{\sigma} = \langle \hat{n}_{\sigma} \rangle_{\text{MF}},$$

where the expectation value  $\langle \hat{n}_{\sigma} \rangle_{\text{HF}}$  is calculated using the Hamiltonian  $\hat{H}_{\text{HF}}$ , which in turn depends on  $\bar{n}_{\sigma}$  via  $m$ . This gives the self-consistency equation

$$m = \frac{1}{2} \frac{1}{N_{\mathbf{k}}} \sum_{\mathbf{k}\sigma} \frac{\sigma e^{-\beta[\varepsilon_{\mathbf{k}} + U(\frac{1}{2} - \sigma m) - \mu]}}{1 + e^{-\beta[\varepsilon_{\mathbf{k}} + U(\frac{1}{2} - \sigma m) - \mu]}}.$$

If we set  $m = 0$  the equation is satisfied; for such a trivial solution the static mean-field correction in Eq. (8) merely redefines the chemical potential and has therefore no effect. For sufficiently large  $U$ , however, a non-trivial solution ( $m \neq 0$ ) can be found. If  $m \neq 0$  the spin up and spin down bands split, and eventually a gap can open. This is shown in Fig. (3). The static mean-field correction in Eq. (8) equals the contribution of the Hartree diagram to the self-energy,  $\Sigma_{\text{H}}^{\sigma}(i\nu_n) = U\bar{n}_{-\sigma}$ . In many-body perturbation theory, however,  $\bar{n}_{\sigma} = 1/2$ , i.e.,  $m = 0$ . In the self-consistent static mean-field approximation, instead,  $m$  can differ from zero, and a

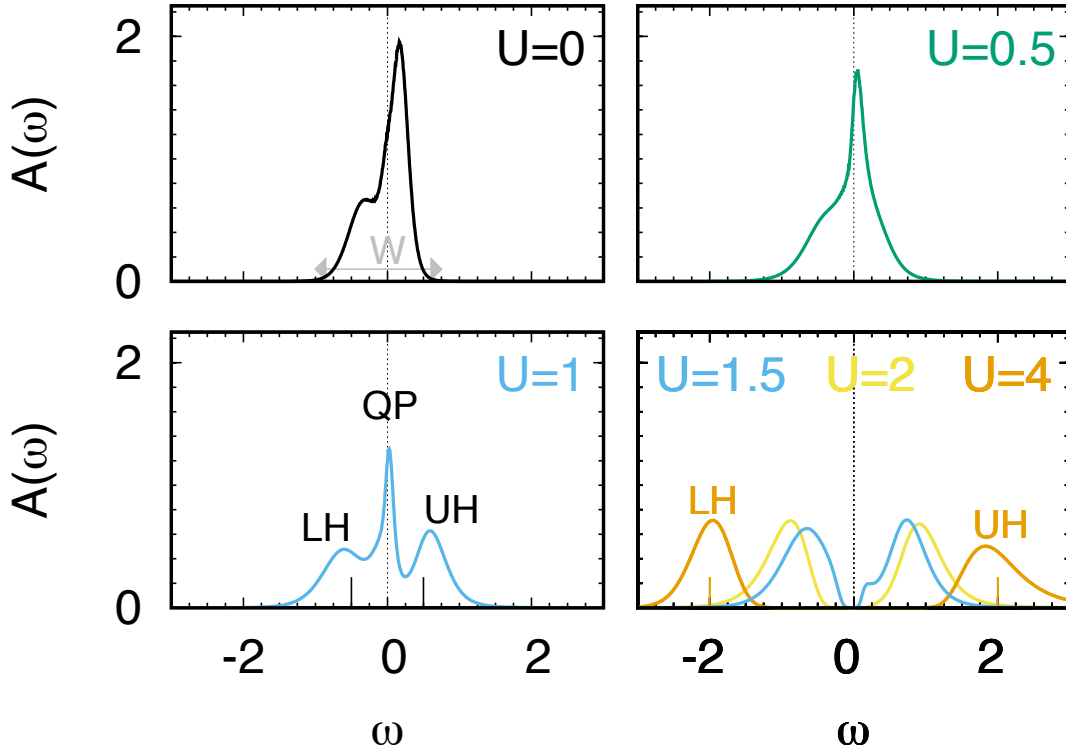


**Fig. 4:** *VOMoO<sub>4</sub>: LDA+DMFT spectral function at finite temperature for  $0 \leq U \leq 4$ . Energies are in eV and spectral functions in states/spin/eV. The calculations have been done using a continuous-time hybridization-expansion QMC solver [10]. A detailed LDA+DMFT study of the electronic and magnetic properties VOMoO<sub>4</sub> can be found in Ref. [11].*

phenomenon not described by the mere Hartree diagram can be captured, ferromagnetism in a correlated metal. In DMFT the role of the Weiss field is played by the bath Green function  $\mathcal{G}_{i,i}^{\sigma}(i\nu_n)$ . The emerging picture of the Mott transition is described in Fig. 4 for a representative single-band material. In the  $U = 0$  limit, the spectral function  $A_0(\omega)$  is metallic at half filling (top left panel). For finite  $U$ , if we set  $\Sigma_A^{\sigma}(\omega) = 0$  as initial guess, the DMFT self-consistency loop starts with  $A(\omega) = A_0(\omega)$ . For small  $U/t$ , the *converged* spectral function  $A(\omega)$  is still similar to  $A_0(\omega)$ . This can be seen comparing the  $U = 0.5$  and  $U = 0$  panels in Fig. 4. Further increasing  $U/t$ , sizable spectral weight is transferred from the zero-energy quasi-particle peak to the lower (LH) and upper (UH) Hubbard bands, centered at  $\omega \sim \pm U/2$ . This can be observed in the  $U = 1$  panel of Fig. 4. The system is still metallic, but with strongly renormalized masses and short lifetimes, reflected in the narrow quasi-particle (QP) peak. Finally, for  $U$  larger than a critical value ( $U \geq 1.5$  in the figure) a gap opens and the system is a Mott insulator. When this happens the self-energy diverges at low frequency, where

$$\Sigma_A^{\sigma}(\omega + i0^+) \sim \frac{U}{2} + \frac{A}{\omega + i0^+}.$$

In the large  $U/t$  limit the gap increases linearly with the Coulomb repulsion, i.e.,  $E_g(1) \sim U - W$ , where  $W$  is the bandwidth.

## 2.3 DMFT for multi-orbital models

The multi-orbital Hubbard-like Hamiltonian has the form

$$\begin{aligned}\hat{H} &= \hat{H}_0 + \hat{H}_U \\ \hat{H}_0 &= - \sum_{ii'} \sum_{\sigma} \sum_{mm'} t_{m\sigma, m'\sigma'}^{i, i'} c_{im\sigma}^\dagger c_{i'm'\sigma'} \\ \hat{H}_U &= \frac{1}{2} \sum_i \sum_{\sigma\sigma'} \sum_{mm'} \sum_{pp'} U_{mpm'p'} c_{im\sigma}^\dagger c_{ip\sigma'}^\dagger c_{ip'\sigma'} c_{im'\sigma},\end{aligned}$$

where  $m, m'$  and  $p, p'$  are different orbitals and the Coulomb tensor is local. The DMFT approach can be extended to solve models of this form, mapping them to multi-orbital quantum-impurity models. The main changes with respect to the formalism introduced in the previous section are then the following

$$\begin{aligned}\varepsilon_{\mathbf{k}} &\rightarrow (H_{\mathbf{k}})_{m\sigma, m'\sigma'} & (i\nu_n + \mu) &\rightarrow (i\nu_n + \mu) \hat{1}_{m\sigma, m'\sigma'} \\ t_{m\sigma, m'\sigma'}^{i, i'} &\rightarrow t_{m\sigma, m'\sigma'}^{i, i'} & \varepsilon_d &\rightarrow \varepsilon_{m\sigma, m'\sigma'}^{i, i'} = -t_{m\sigma, m'\sigma'}^{i, i}\end{aligned}$$

where  $\hat{1}$  is the unity matrix. As a consequence, the local Green function, the bath Green function, the hybridization function and the self-energy also become matrices in spin-orbital space

$$\mathcal{G}^\sigma(i\nu_n) \rightarrow \mathcal{G}_{m, m'}^{\sigma, \sigma'}(i\nu_n) \quad G^\sigma(i\nu_n) \rightarrow G_{m, m'}^{\sigma, \sigma'}(i\nu_n) \quad \Sigma^\sigma(i\nu_n) \rightarrow \Sigma_{m, m'}^{\sigma, \sigma'}(i\nu_n).$$

The corresponding generalization of the self-consistency loop is shown schematically in Fig. 5. Although the extension of DMFT to Hubbard models with many orbitals might appear straightforward, in practice it is not. The bottleneck is the solution of the generalized multi-orbital quantum-impurity problem. The most flexible solvers available so far are all based on QMC. Despite being flexible, QMC-based approaches have limitations. These can be classified in two types. First, with increasing the number of degrees of freedom, calculations become very quickly computationally too expensive – how quickly depends on the specific QMC algorithm used and the actual implementation. Thus, going beyond a rather small number of orbitals and reaching the zero-temperature limit is unfeasible in practice. The second type of limitation is more severe. Increasing the number of degrees of freedom leads, eventually, to the infamous sign problem; when this happens, QMC calculations cannot be performed at all. In order to deal with limitations of the first type, it is crucial to restrict QMC calculations to the essential degrees of freedom; furthermore, we should exploit symmetries, develop fast algorithms and use the power of massively parallel supercomputers to reduce the actual computational time. For the second type of problems not a lot can be done; nevertheless, it has been shown that a severe sign problem might appear earlier with some basis choices than with others [10]. Although eventually we cannot escape it, this suggests that the model set up can be used as a tool to expand the moderate sign-problem zone. For what concerns symmetries, in the paramagnetic case and in absence of spin-orbit interaction or external fields, an obvious symmetry to exploit

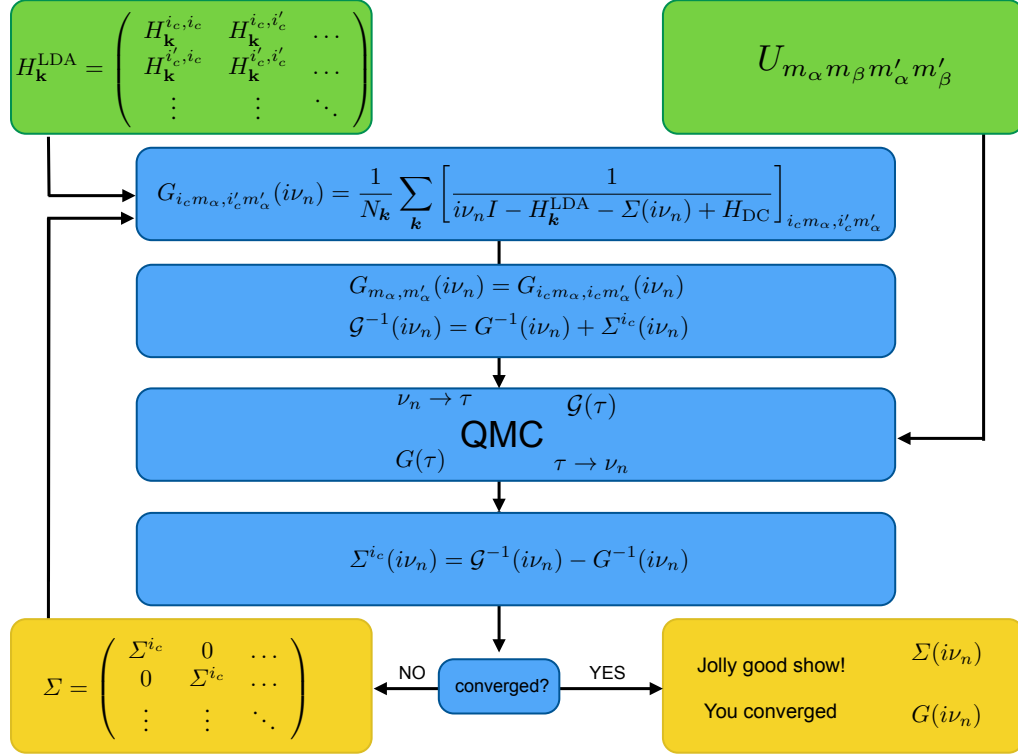


**Fig. 5:** LDA+DMFT self-consistency loop. The one-electron Hamiltonian is built in the basis of Bloch states obtained from localized Wannier functions, for example in the local-density approximation (LDA); this gives  $H_{\mathbf{k}}^{\text{LDA}}$ . The set  $\{i_c\}$  labels the equivalent correlated sites inside the unit cell. The local Green-function matrix is at first calculated using an initial guess for the self-energy matrix. The bath Green-function matrix is then obtained via the Dyson equation and used to construct an effective quantum-impurity model. The latter is solved via a quantum-impurity solver, here quantum Monte Carlo (QMC). This yields the impurity Green-function matrix. Through the Dyson equation the self-energy is then obtained, and the procedure is repeated until self-consistency is reached.

is the  $SO(3)$  rotational invariance of spins, from which follows

$$A_{m, m'}^{\sigma, \sigma'}(i\nu_n) = \delta_{\sigma, \sigma'} A_{m, m'}(i\nu_n),$$

where  $A = \mathcal{G}, G, \Sigma$ . In addition, if we use a basis of real functions, the local Green-function matrices are real and symmetric in imaginary time  $\tau$ , hence

$$A_{m, m'}^{\sigma, \sigma'}(\tau) = \delta_{\sigma, \sigma'} A_{m, m'}(\tau) = \delta_{\sigma, \sigma'} A_{m', m}(\tau).$$

Finally, often the unit cell contains several equivalent correlated sites, indicated as  $\{i_c\}$  in Fig. 5. In order to avoid expensive cluster calculations, we can use space-group symmetries to construct the matrices  $\mathcal{G}, G, \Sigma$  at a given site  $i'_c$  from the corresponding matrices at an equivalent site, e.g.,  $i_c = 1$ . Space-group symmetries also tell us if some matrix elements are zero. For example, for a model with only  $t_{2g}$  (or only  $e_g$ ) states, in cubic symmetry, in the paramagnetic case and in absence of spin-orbit interaction or external fields, we have

$$A_{m, m'}^{\sigma, \sigma'}(\tau) = \delta_{\sigma, \sigma'} A_{m, m}(\tau) \delta_{m, m'}.$$

## 2.4 Minimal material-specific models from LDA

How do we build realistic Hubbard-like models for correlated materials? The state-of-the art approach relies on constructing, for a given system, *material-specific* Wannier functions. The latter can be obtained via electronic structure calculations based on density-functional theory (DFT) [12, 13]. If we construct a complete basis of Wannier functions, the complete many-body Hamiltonian takes the form that we have seen in the introduction,  $\hat{H} = \hat{H}_0 + \hat{H}_U$ , with

$$\begin{aligned}\hat{H}_0 &= \hat{H}^{\text{LDA}} = - \sum_{\sigma} \sum_{ii'} \sum_{mm'} t_{m,m'}^{i,i'} c_{im\sigma}^{\dagger} c_{i'm'\sigma}, \\ \hat{H}_U &= \frac{1}{2} \sum_{ii'jj'} \sum_{\sigma\sigma'} \sum_{mm'pp'} U_{mp\ m'p'}^{ijj'j'} c_{im\sigma}^{\dagger} c_{jp\sigma'}^{\dagger} c_{j'p'\sigma'} c_{i'm'\sigma}.\end{aligned}$$

The potential entering in the hopping integrals, Eq. (3), is given by the self-consistent DFT reference potential

$$v_{\text{R}}(\mathbf{r}) = v_{\text{en}}(\mathbf{r}) + v_{\text{H}}(\mathbf{r}) + v_{\text{xc}}(\mathbf{r}) = - \sum_{\alpha} \frac{Z_{\alpha}}{|\mathbf{r} - \mathbf{R}_{\alpha}|} + \int d\mathbf{r}' \frac{1}{|\mathbf{r} - \mathbf{r}'|} + v_{\text{xc}}(\mathbf{r}).$$

The formula above shows that  $v_{\text{R}}(\mathbf{r})$  includes Coulomb effects, via the long-range Hartree term  $v_{\text{H}}(\mathbf{r})$  and the exchange-correlation contribution  $v_{\text{xc}}(\mathbf{r})$ ; for the latter we use, e.g., the LDA approximation. Thus in our Hamiltonian some Coulomb effects are included both in  $\hat{H}_0$ , via  $v_{\text{R}}(\mathbf{r})$ , and in  $\hat{H}_U$ . In order to avoid double counting, we have then to subtract from  $\hat{H}_U$  the effects already included in  $\hat{H}_0$ . Thus we have to replace

$$\hat{H}_U \rightarrow \Delta\hat{H}_U = \hat{H}_U - \hat{H}_{\text{DC}},$$

where  $\hat{H}_{\text{DC}}$  is the so-called double-counting correction. Unfortunately we do not know which correlation effects are indeed included in  $\hat{H}_0$  via the LDA reference potential, and therefore the exact expression of  $\hat{H}_{\text{DC}}$  is also unknown. The remarkable successes of the LDA suggest, however, that in many materials the LDA is overall a good approximation, and therefore, in those systems at least, the term  $\Delta\hat{H}_U$  can be completely neglected. What about strongly-correlated materials? Even in correlated systems, most likely the LDA works rather well for the delocalized electrons or in describing the average or the long-range Coulomb effects. Thus one can think of separating the electrons into *uncorrelated* and *correlated*; only for the latter we do take the correction  $\Delta\hat{H}_U$  into account explicitly, assuming furthermore that  $\Delta\hat{H}_U$  is local or almost local [12]. Typically, correlated electrons are those that partially retain their atomic character, e.g., those that originate from localized  $d$  and  $f$  shells; for convenience, here we assume that in a given system they stem from a single atomic shell  $l$  (e.g.,  $d$  for transition-metal oxides or  $f$  for heavy-fermion systems) and label their states with the atomic quantum numbers  $l$  and  $m = -l, \dots, l$  of that shell. Thus

$$U_{mp\ m'p'}^{ijj'j'} \sim \begin{cases} U_{mp\ m'p'}^l & ijj'j' = iiii \quad \wedge \quad mp, m'p' \in l \\ 0 & ijj'j' \neq iiii \quad \vee \quad mp, m'p' \notin l. \end{cases}$$

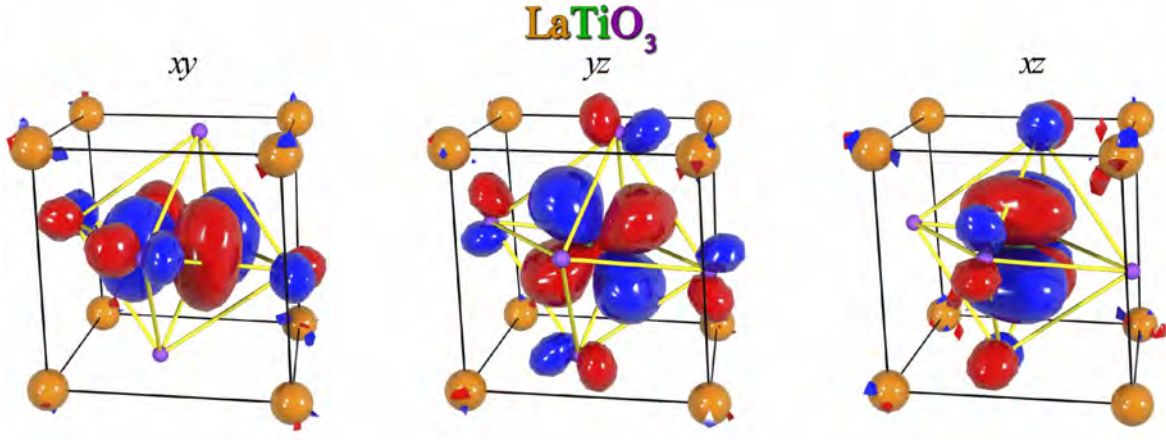


**Fig. 6:** NMTO Wannier-like orbitals for  $t_{2g}$  states in  $\text{LaTiO}_3$  obtained via massive downfolding to the  $t_{2g}$  bands. The  $t_{2g}$ -like orbitals have O  $p$  tails at the neighboring O sites reflecting the distortions of the lattice. The figure has been taken from Ref. [14].

Within this approximation  $\Delta\hat{H}_U$  is replaced by  $\Delta\hat{H}_U^l = \hat{H}_U^l - \hat{H}_{\text{DC}}^l$ , where  $\hat{H}_{\text{DC}}^l$  is, e.g., given by the static mean-field contribution of  $\hat{H}_U^l$ . There is a drawback in this procedure, however. By splitting electrons into correlated and uncorrelated we implicitly assume that the main effect of the latter is the renormalization or *screening* of parameters for the former, in particular of the Coulomb interaction. The computation of screening effects remains, unfortunately, a challenge. The calculation of exact screening would require the (impossible) solution of the original many-body problem, taking all degrees of freedom into account. Commonly-used approximate schemes are the constrained LDA approximation (cLDA) and the constrained random-phase approximation (RPA) [12, 13]. Both methods give reasonable estimates of screened Coulomb parameters for DMFT calculations. Typically cRPA calculations include more screening channels and are performed for less localized bases than cLDA calculations; thus cRPA parameters turn out to be often smaller than cLDA ones. To some extent, the difference can be taken as an estimate of the error bar. After we have selected the electrons for which we think it is necessary to include explicitly the Hubbard correction, in order to build the final Hamiltonian for DMFT calculations, it is often convenient to integrate out or *downfold*, in part or completely, the weakly correlated states. There are different degrees of downfolding. The two opposite extreme limits are (i) *no downfolding*, i.e., keep explicitly in the Hamiltonian all weakly-correlated states (ii) *massive downfolding*, i.e., downfold all weakly correlated states. If we perform massive downfolding, e.g., downfold to the  $d$  (or  $e_g$  or  $t_{2g}$ ) bands at the Fermi level, the Hamiltonian relevant for DMFT takes a simpler form. The LDA part is limited to the selected orbitals or bands, which, in the ideal case, are decoupled from the rest

$$\hat{H}^{\text{LDA}} = - \sum_{\sigma} \sum_{ii'} \sum_{m_{\alpha} m'_{\alpha}} t_{m_{\alpha} m'_{\alpha}}^{i, i'} c_{i m_{\alpha} \sigma}^{\dagger} c_{i' m'_{\alpha} \sigma}.$$



The local *screened* Coulomb interaction for this set of orbitals is the on-site tensor

$$\hat{H}_U^l = \frac{1}{2} \sum_i \sum_{\sigma\sigma'} \sum_{m_\alpha m'_\alpha} \sum_{m_\beta m'_\beta} U_{m_\alpha m_\beta m'_\alpha m'_\beta} c_{im_\alpha\sigma}^\dagger c_{im_\beta\sigma'}^\dagger c_{im'_\beta\sigma'} c_{im'_\alpha\sigma}.$$

It is important to point out that the level of downfolding does not modify the hardness of the quantum-impurity problem. If, for example, in studying a transition-metal oxide, we plan to treat only  $3d$  bands as correlated, it does not matter if we perform calculations with a Hamiltonian containing also, e.g., O  $p$  states, or we rather downfold all states but the  $3d$  and work with a set of Wannier basis spanning the  $3d$ -like bands only. The number of correlated orbitals in the quantum-impurity problem is the same.<sup>5</sup> One advantage of massive downfolding is that the double-counting correction typically becomes a shift of the chemical potential, and it is therefore not necessary to calculate it explicitly. A second important advantage is that the interpretation of the final results is simpler. Instead, a disadvantage is that the basis functions are less localized, and therefore the approximation of the Coulomb interaction to a local operator might be less justified, and in some cases it might be necessary to include non-local Coulomb terms. The effect of downfolding on the localization of Wannier functions is illustrated for example in Fig. 6. Considered all advantages and disadvantages, what is then the best way of performing DMFT calculations? There is no universal answer to this question; it depends on the problem we are trying to solve and the system we are studying. Independently on the degree of downfolding we chose, it is important to point out that a clear advantage of Wannier functions in general is that they carry information about the lattice, bonding, chemistry and distortions. This can be seen once more in Fig. 6, where orbitals are tilted and deformed by the actual structure and chemistry of the compound. Indeed, one might naively think of using an “universal” basis, for example atomic functions, the same for all systems. Apart the complications arising from the lack of orthogonality, such a basis has no built-in material-specific information, except lattice positions. It is therefore a worse starting point to describe the electronic structure, even in the absence of correlations; larger basis sets are required to reach the same accuracy. From the point of view of LDA+DMFT, an advantage of an universal basis would be that it is free from double-counting corrections; on the other hand, however, exactly because we do not use the LDA potential to calculate the hopping integrals, we also cannot count on the successes of LDA in the description of average and long-range Coulomb effects. For these reasons *ab-initio* Wannier functions remain so far the basis of choice. They can be built via the Nth-Order Muffin-Tin Orbital (NMTO) method [14], the maximal-localization scheme [15] or projectors. Fig. 6 shows examples of NMTO-based Wannier functions.

No matter what construction procedure is used, a common characteristic of *ab-initio* Wannier functions is that they are site-centered and localized.<sup>6</sup> Thus a question naturally arises: How important is it to use localized functions as one-electron basis? In the extreme limit in which the basis functions are independent of the lattice position (i.e., they are totally delocalized), the

<sup>5</sup>The choice might influence how severe the QMC sign problem is, however.

<sup>6</sup>Differences in localizations between the various construction procedures are actually small for the purpose of many-body calculations, provided that the same bands are spanned in the same way.

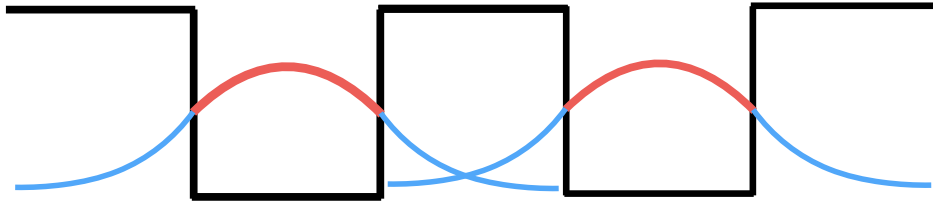


**Fig. 7:** *The problem of two quantum wells. The figure shows (schematically) for each well the wavefunction of a bound state. If we consider only the part of the wavefunction inside its own well (red in the figure), the differential overlap (and hence the hopping integral) between functions centered on different wells would be zero.*

Coulomb interaction parameters would be the same for every couple of lattice sites, no matter how distant. Thus a Hubbard-like model would be hard to justify. In the other extreme case, we could, hypothetically, adopt a basis so localized that  $\psi_{im\sigma}(\mathbf{r})\overline{\psi_{i'm'\sigma'}(\mathbf{r})} \sim \delta_{i,i'}\delta(\mathbf{r} - \mathbf{T}_i)$ . Even for such a basis, the unscreened Coulomb interaction is not local. It is given by

$$U_{mp\ m'p'}^{ij\ i'j'} \propto \frac{\delta_{i,i'}\delta_{j,j'}}{|\mathbf{T}_i - \mathbf{T}_j|},$$

hence it decays slowly with distance, although the (divergent) on-site term dominates. More generally, we can conclude that by increasing the localization of the basis we enhance the importance of the on-site Coulomb repulsion with respect to long-range terms; this better justifies Hubbard-like models. The example illustrates also how far we can go. A major problem with the basis discussed above is that it would be impossible to properly describe bonding, since the hopping integrals would be zero. Although such a basis is, of course, never used to build many-body models, there is a tempting approximation that has similar flaws. If one uses DFT-based electronic-structure techniques that tile the space in interstitial and non-overlapping atomic spheres (e.g., the LAPW method), it is tempting to use as basis for correlated electrons the atomic functions defined inside the atomic spheres. These functions are, by construction, much more localized than Wannier orbitals (even if no downfolding is performed in the Wannier construction). However, they do not form a complete basis set in the space of square-integrable functions. This is obvious because such a basis does not even span the LDA bands; to reproduce the bands we need, in addition, functions defined in the interstitial region. This is illustrated in Fig. 7 for a simple example of two quantum well potentials.<sup>7</sup> We therefore cannot use it to write the many-body Hamiltonian in the usual form  $\hat{H}_0 + \hat{H}_U$ . In conclusion, a basis which, as *ab-initio* Wannier functions, is complete and indeed spans the bands, is better justified, although we somewhat lose in localization.

<sup>7</sup> Another, but less severe, problem of atomic sphere truncations is that the results will depend on the sphere size, in particular when atomic spheres are small.

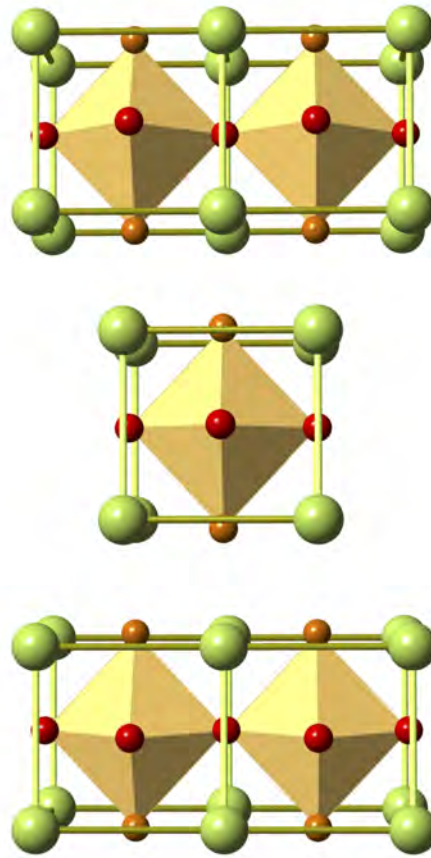


**Fig. 8:** The crystal structure of the tetragonal layered perovskite  $\text{Sr}_2\text{RuO}_4$ . The figure has been adapted from Ref. [16].

### 3 Multi-orbital Hubbard models

In this section we will discuss some of the specific effects emerging in multi-orbital Hubbard models, pointing out the differences with respect to the case of the one-band Hubbard model. As examples we will use perovskites with partially filled  $t_{2g}$  shells. A representative system of this kind is  $\text{Sr}_2\text{RuO}_4$ , whose layered crystal structure is shown in Fig. 8. The LDA bands of  $\text{Sr}_2\text{RuO}_4$  around the Fermi level ( $4d\ t_{2g}^4$  configuration) are shown in Fig. 9. The figure shows the  $4d\ t_{2g}$  bands crossing the Fermi level, in red the  $xz, yz$  bands and in blue the  $xy$  band. Due to the layered structure, the  $xz$  and  $yz$  bands are quasi one-dimensional and the  $xy$  band is quasi two-dimensional. Thus, they give rise, in first approximation, to a Fermi surface made of four crossing lines (from the  $xz, yz$  bands) and a circle (from the  $xy$  band). This is shown schematically in the left panel of Fig. 9. Experimentally,  $\text{Sr}_2\text{RuO}_4$  is a correlated metal down to 1.5 K; below this temperature it becomes an anomalous superconductor. The two other examples considered in this lecture are orbitally ordered Mott insulators. The first is

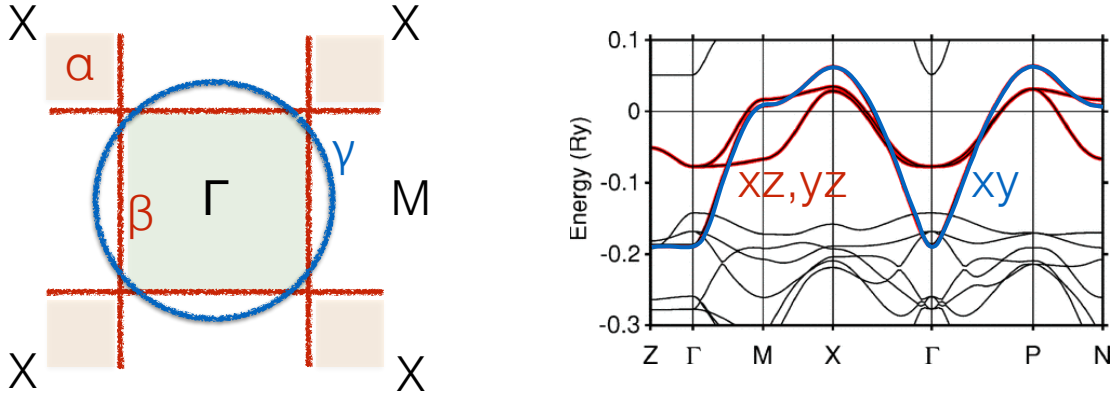


**Fig. 9:** Schematic representation of the Fermi surface of the tetragonal  $t_{2g}^4$  system  $\text{Sr}_2\text{RuO}_4$  (left) and the associated LDA band structure (right). The figure is rearranged from Ref. [16]. The band structure was calculated using the Nth-Order Muffin-Tin Orbital (NMTO) method.

$\text{Ca}_2\text{RuO}_4$ , isoelectronic and very similar to  $\text{Sr}_2\text{RuO}_4$ , except that its crystal symmetry is lower than tetragonal. The second is the 3-dimensional orthorhombic perovskite  $\text{YTiO}_3$ , with the electronic configuration  $3d^1 t_{2g}^1$ . For all these materials, if we massively downfold all bands but the  $t_{2g}$ , the associated 3-band Hubbard model becomes

$$\begin{aligned} \hat{H} = & \sum_{i\sigma} \sum_{mm'} \varepsilon_{m,m'} c_{im\sigma}^\dagger c_{im'\sigma} - \sum_{\sigma} \sum_{i \neq i'} \sum_{mm'} t_{m,m'}^{i,i'} c_{im\sigma}^\dagger c_{i'm'\sigma} \\ & + U \sum_{i,m} \hat{n}_{im\uparrow} \hat{n}_{im\downarrow} + \frac{1}{2} \sum_{\substack{i\sigma\sigma' \\ m \neq m'}} (U - 2J - J\delta_{\sigma,\sigma'}) \hat{n}_{im\sigma} \hat{n}_{im'\sigma'} \\ & - J \sum_{i,m \neq m'} \left( c_{im\uparrow}^\dagger c_{im\downarrow}^\dagger c_{im'\uparrow} c_{im'\downarrow} + c_{im\uparrow}^\dagger c_{im\downarrow} c_{im'\downarrow}^\dagger c_{im'\uparrow} \right), \end{aligned}$$

where  $m, m' = xy, yz, xz$ , and where  $U$  and  $J$  are the direct and exchange screened Coulomb integrals for  $t_{2g}$  electrons. The Coulomb interaction  $\hat{H}_U$  is here assumed to have full  $O(3)$  rotational symmetry, as in the atomic limit.<sup>8</sup> The first two terms of  $\hat{H}_U$  are the so-called density-density terms, and the last two are the pair-hopping and spin-flip interaction. In the Hamiltonian above we dropped the double-counting correction  $\hat{H}_{\text{DC}}$ , which in this case is a mere shift of the chemical potential, as we will see later. The energies  $\varepsilon_{m,m'}$  are the crystal-field matrix, and thus, in principle, in the atomic limit  $\varepsilon_{m,m'} = \varepsilon_d \delta_{m,m'}$ . In the following sections we will however consider as atomic limit the case in which only the hopping integrals  $t_{m,m'}^{i,i'}$  are zero.

<sup>8</sup>For the derivation of the Coulomb interaction  $\hat{H}_U$  for  $t_{2g}$  electrons starting from the complete Coulomb tensor of the free atom, see my chapter in Ref. [12].

### 3.1 Atomic limit, multiplets and cubic crystal field

Let us start considering the atomic limit. For the one-band Hubbard model, in the atomic limit, the local spectral function at half filling ( $d^1$  electronic configuration) is given by

$$G_{ii}^{\sigma}(i\nu_n) = \frac{1}{2} \left[ \frac{1}{i\nu_n - \underbrace{(\varepsilon_d - \mu)}_{E(N) - E(N-1) - \mu}} + \frac{1}{i\nu_n - \underbrace{(\varepsilon_d + U - \mu)}_{E(N+1) - E(N) - \mu}} \right]$$

with  $\mu = \varepsilon_d + U/2$ . The gap is  $E_g(1) = U$  and the spectral function displays a lower and an upper Hubbard peaks, located at energy  $\pm U/2$ . In the presence of many orbitals, the Hubbard peaks acquire a complicated structure. This is due to the fact that the eigenstates of the Coulomb matrix for a given number of electrons form multiplets with different energies. For the  $d^n$  configuration there are three independent Coulomb parameters on which the energy of a multiplet depends: the direct term  $U$ , the Hund's rule exchange coupling for  $t_{2g}$  electrons,  $J=J_1$ , and the Hund's rule exchange coupling for  $e_g$  electrons,  $J_2$ . For a free atom (symmetry  $O(3)$ ), the ground multiplet is determined by the three Hund's rules. The first of these rules says that the ground state has the maximum possible total spin  $S$ . Thus, for configuration  $d^4$ , the ground multiplet has  $S=2$ . Let us call  $-\Delta_H$  the Hund's rule energy gain, i.e., the energy difference between the ground and the first excited spin multiplet;  $\Delta_H$  is a function of  $J_1$  and  $J_2$  and is zero for  $J_1 = J_2 = 0$ . In cubic symmetry, the crystal field splits  $e_g$  and  $t_{2g}$  states, and  $\varepsilon_C = \varepsilon_{e_g} - \varepsilon_{t_{2g}} > 0$ ; if  $\varepsilon_C$  is very large, the first Hund's rule can be violated. In  $\text{LaMnO}_3$ , where the energy loss due to  $\varepsilon_C$  is smaller than  $\Delta_H$ , the ground multiplet has configuration  $t_{2g}^3 e_g^1$  and indeed  $S=2$  (high spin), in line with the first Hund's rule. In  $\text{Sr}_2\text{RuO}_4$  and  $\text{Ca}_2\text{RuO}_4$ , however, the cubic crystal field prevails, and the ground configuration is  $t_{2g}^4 e_g^0$ , with  $S=1$  (intermediate spin). Thus, if the crystal field  $\varepsilon_C$  is large and  $n \leq 6$ , the  $e_g$  orbitals will stay empty, hence, we can restrict the discussion to the  $t_{2g}$  orbitals and the  $t_{2g}^n e_g^0$  configuration. The energy of the corresponding multiplets are given in Tab. 1, assuming  $\varepsilon_{m,m'} = \varepsilon_{t_{2g}} \delta_{m,m'}$ , and setting for convenience  $\varepsilon_{t_{2g}} = 0$ . In the  $t_{2g}^1$  configuration, the atomic Matsubara Green function is

$$G_m^{\sigma}(i\nu_n) = \frac{1}{6} \left[ \frac{1}{i\nu_n + (\varepsilon_{t_{2g}} - \mu)} + \frac{3}{i\nu_n - (\varepsilon_{t_{2g}} + U - 3J - \mu)} + \frac{5/3}{i\nu_n - (\varepsilon_{t_{2g}} + U - J - \mu)} + \frac{1/3}{i\nu_n - (\varepsilon_{t_{2g}} + U + 2J - \mu)} \right], \quad (9)$$

and it is the same for all orbitals. The associated spectral function has one peak corresponding to  $E(1) - E(0) - \mu$ . This happens because there is only one state with zero electrons, the vacuum. Instead, there are three peaks corresponding to energy  $E(2) - E(1) - \mu$ ; they are associated with different multiplets of the  $t_{2g}^2$  configuration (Fig. 10). The atomic gap takes the value  $E_g(1) = U - 3J$ , i.e., it is smaller than in the case  $J = 0$  and it is smaller than in the one-orbital case. This expression of the atomic gap is also valid for other configurations,  $t_{2g}^2$ ,  $t_{2g}^4$ , and  $t_{2g}^5$ . Instead, at half filling ( $t_{2g}^3$ ), the atomic gap is  $E_g(3) = U + 2J$ , i.e., it is enhanced and not reduced by  $J$ . This can be easily verified by using Tab. 1.

$ N; S, m_S\rangle$	$E(N, S)$
$ 0\rangle$	
$ 1; \frac{1}{2}, \frac{\sigma}{2}\rangle = c_{m\sigma}^\dagger  0\rangle$	
$ 2; 0, 0\rangle_a = \frac{1}{\sqrt{3}} [c_{xz\uparrow}^\dagger c_{xz\downarrow}^\dagger + c_{yz\uparrow}^\dagger c_{yz\downarrow}^\dagger + c_{xy\uparrow}^\dagger c_{xy\downarrow}^\dagger]  0\rangle$	$U + 2J$
$ 2; 0, 0\rangle_b = \frac{1}{\sqrt{6}} [c_{xz\uparrow}^\dagger c_{xz\downarrow}^\dagger + c_{yz\uparrow}^\dagger c_{yz\downarrow}^\dagger - 2c_{xy\uparrow}^\dagger c_{xy\downarrow}^\dagger]  0\rangle$	$U - J$
$ 2; 0, 0\rangle_c = \frac{1}{\sqrt{2}} [c_{xz\uparrow}^\dagger c_{xz\downarrow}^\dagger - c_{yz\uparrow}^\dagger c_{yz\downarrow}^\dagger]  0\rangle$	$U - J$
$ 2; 1, \sigma, m''\rangle = c_{m\sigma}^\dagger c_{m'\sigma}^\dagger  0\rangle$	$U - 3J$
$ 2; 1, 0, m''\rangle = \frac{1}{\sqrt{2}} [c_{m\uparrow}^\dagger c_{m'\downarrow}^\dagger + c_{m\downarrow}^\dagger c_{m'\uparrow}^\dagger]  0\rangle$	$U - 3J$
$ 2; 0, 0, m''\rangle = \frac{1}{\sqrt{2}} [c_{m\uparrow}^\dagger c_{m'\downarrow}^\dagger - c_{m\downarrow}^\dagger c_{m'\uparrow}^\dagger]  0\rangle$	$U - J$
$ 3; \frac{3}{2}, \frac{3\sigma}{2}\rangle = c_{xz\sigma}^\dagger c_{yz\sigma}^\dagger c_{xy\sigma}^\dagger  0\rangle$	$3U - 9J$
$ 3; \frac{3}{2}, \frac{\sigma}{2}\rangle = \frac{1}{\sqrt{3}} [c_{xz\sigma}^\dagger c_{yz\sigma}^\dagger c_{xy-\sigma}^\dagger + c_{xz\sigma}^\dagger c_{yz-\sigma}^\dagger c_{xy\sigma}^\dagger + c_{xz-\sigma}^\dagger c_{yz\sigma}^\dagger c_{xy\sigma}^\dagger]  0\rangle$	$3U - 9J$
$ 3; \frac{1}{2}, \frac{\sigma}{2}\rangle_a = \frac{1}{\sqrt{6}} [-2c_{xz\sigma}^\dagger c_{yz\sigma}^\dagger c_{xy-\sigma}^\dagger + c_{xz\sigma}^\dagger c_{yz-\sigma}^\dagger c_{xy\sigma}^\dagger + c_{xz-\sigma}^\dagger c_{yz\sigma}^\dagger c_{xy\sigma}^\dagger]  0\rangle$	$3U - 6J$
$ 3; \frac{1}{2}, \frac{\sigma}{2}\rangle_b = \frac{1}{\sqrt{2}} [c_{xz\sigma}^\dagger c_{yz-\sigma}^\dagger - c_{xz-\sigma}^\dagger c_{yz\sigma}^\dagger] c_{xy\sigma}^\dagger  0\rangle$	$3U - 6J$
$ 3; \frac{1}{2}, \frac{\sigma}{2}, m\rangle_a = \frac{1}{\sqrt{2}} [c_{m'\uparrow}^\dagger c_{m'\downarrow}^\dagger + c_{m''\uparrow}^\dagger c_{m''\downarrow}^\dagger] c_{m\sigma}^\dagger  0\rangle$	$3U - 4J$
$ 3; \frac{1}{2}, \frac{\sigma}{2}, m\rangle_b = \frac{1}{\sqrt{2}} [c_{m'\uparrow}^\dagger c_{m'\downarrow}^\dagger - c_{m''\uparrow}^\dagger c_{m''\downarrow}^\dagger] c_{m\sigma}^\dagger  0\rangle$	$3U - 6J$
$ 4; 1, \sigma, m''\rangle = c_{m\sigma}^\dagger c_{m'\sigma}^\dagger c_{m''\uparrow}^\dagger c_{m''\downarrow}^\dagger  0\rangle$	$6U - 13J$
$ 4; 1, 0, m''\rangle = \frac{1}{\sqrt{2}} [c_{m\uparrow}^\dagger c_{m'\downarrow}^\dagger + c_{m\downarrow}^\dagger c_{m'\uparrow}^\dagger] c_{m''\uparrow}^\dagger c_{m''\downarrow}^\dagger  0\rangle$	$6U - 13J$
$ 4; 0, 0, m''\rangle = \frac{1}{\sqrt{2}} [c_{m\uparrow}^\dagger c_{m'\downarrow}^\dagger - c_{m\downarrow}^\dagger c_{m'\uparrow}^\dagger] c_{m''\uparrow}^\dagger c_{m''\downarrow}^\dagger  0\rangle$	$6U - 11J$
$ 4; 0, 0\rangle_a = \frac{1}{\sqrt{3}} [c_{xz\uparrow}^\dagger c_{xz\downarrow}^\dagger c_{yz\uparrow}^\dagger c_{yz\downarrow}^\dagger + c_{yz\uparrow}^\dagger c_{yz\downarrow}^\dagger c_{xy\uparrow}^\dagger c_{xy\downarrow}^\dagger + c_{xy\uparrow}^\dagger c_{xy\downarrow}^\dagger c_{xz\uparrow}^\dagger c_{xz\downarrow}^\dagger]  0\rangle$	$6U - 8J$
$ 4; 0, 0\rangle_b = \frac{1}{\sqrt{6}} [c_{xz\uparrow}^\dagger c_{xz\downarrow}^\dagger c_{yz\uparrow}^\dagger c_{yz\downarrow}^\dagger + c_{yz\uparrow}^\dagger c_{yz\downarrow}^\dagger c_{xy\uparrow}^\dagger c_{xy\downarrow}^\dagger - 2c_{xy\uparrow}^\dagger c_{xy\downarrow}^\dagger c_{xz\uparrow}^\dagger c_{xz\downarrow}^\dagger]  0\rangle$	$6U - 11J$
$ 4; 0, 0\rangle_c = \frac{1}{\sqrt{2}} [c_{xz\uparrow}^\dagger c_{xz\downarrow}^\dagger c_{yz\uparrow}^\dagger c_{yz\downarrow}^\dagger - c_{yz\uparrow}^\dagger c_{yz\downarrow}^\dagger c_{xy\uparrow}^\dagger c_{xy\downarrow}^\dagger]  0\rangle$	$6U - 11J$
$ 5; \frac{1}{2}, \frac{\sigma}{2}\rangle = c_{m\sigma}^\dagger c_{m'\uparrow}^\dagger c_{m'\downarrow}^\dagger c_{m''\uparrow}^\dagger c_{m''\downarrow}^\dagger  0\rangle$	$10U - 20J$
$ 6\rangle = c_{xz\uparrow}^\dagger c_{xz\downarrow}^\dagger c_{yz\uparrow}^\dagger c_{yz\downarrow}^\dagger c_{xy\uparrow}^\dagger c_{xy\downarrow}^\dagger  0\rangle$	$15U - 30J$

**Table 1:** The atomic  $t_{2g}$  states ( $m = xy, xz, yz$ ) in the basis which diagonalize the Coulomb interaction. The label  $\sigma$  in the first column takes the value  $\pm 1$ , while in the states it has the meaning  $\uparrow$  or  $\downarrow$ . The labels  $m, m'$  and  $m''$  indicate different orbitals.



**Fig. 10:** Atomic spectrum for the  $t_{2g}^2$  configuration. Left: exact. Right: density-density approximation (spin-flip and pair-hopping terms set to zero). In the density-density approximation the total spin is not a good quantum number: The lower-energy block of states collects the  $M_s = \pm 1$  states of the  $S = 1$  triplet, and the middle block mixes  $S = 0$  and  $S = 1$  states. The average Coulomb interaction is  $U - 2J$ , both in the exact and the approximate case. The spectrum is identical for the  $t_{2g}^4$  configuration, provided that all energies are shifted by  $5U - 10J$ .

### 3.2 Low-symmetry crystal field, orbital order and orbital degeneracy

When the symmetry is lower than cubic, the  $t_{2g}$  levels can split. For example, if the symmetry is tetragonal, the  $t_{2g}$  states split into a doublet,  $xz, yz$ , and a singlet,  $xy$ ; the tetragonal energy splitting is  $\varepsilon_{\text{CF}} = \varepsilon_{xy} - \varepsilon_{xz/yz}$ . In metallic  $\text{Sr}_2\text{RuO}_4$  the splitting  $\varepsilon_{\text{CF}}$  is relatively small ( $\sim 120$  eV), and the LDA+DMFT occupations of the different orbitals remain similar. In the insulating S-Pbca phase of  $\text{Ca}_2\text{RuO}_4$ ,  $\varepsilon_{\text{CF}}$  is larger,  $\sim 300$  meV, and the LDA+DMFT occupations are close to those of the  $xy^2xz^1yz^1$  configuration ( $xy$  orbital-order). The Mott insulator  $\text{YTiO}_3$  has even lower symmetry; because of the  $t_{2g}^1$  configuration, only the lowest energy  $t_{2g}$  crystal-field level is actually occupied. Let us consider an oversimplified model for  $\text{YTiO}_3$ , i.e., a tetragonal system which, in the atomic limit, has configuration  $xy^1xz^0yz^0$  at  $T = 0$ . How does the atomic Green-function matrix change with respect to the cubic case, Eq. (9)? The tetragonal symmetry implies that the imaginary time Green function has the matrix form

$$G_{im,im'}^{\sigma}(\tau) = \begin{pmatrix} G_{xy}^{i\sigma}(\tau) & 0 & 0 \\ 0 & G_{xz}^{i\sigma}(\tau) & 0 \\ 0 & 0 & G_{yz}^{i\sigma}(\tau) \end{pmatrix}, \quad \text{with} \quad G_{xz}^{i\sigma}(\tau) = G_{yz}^{i\sigma}(\tau).$$

For  $k_B T \ll \varepsilon_{\text{CF}} \ll U$ , the  $xy$  Matsubara Green function is given by

$$G_{xy}^{i\sigma}(i\nu_n) \sim \frac{1}{6} \left( \frac{3}{i\nu_n + (\varepsilon_{xy} - \mu)} + \frac{2}{i\nu_n - (\varepsilon_{xy} + U - J - \mu)} + \frac{1}{i\nu_n - (\varepsilon_{xy} + U + 2J - \mu)} \right).$$

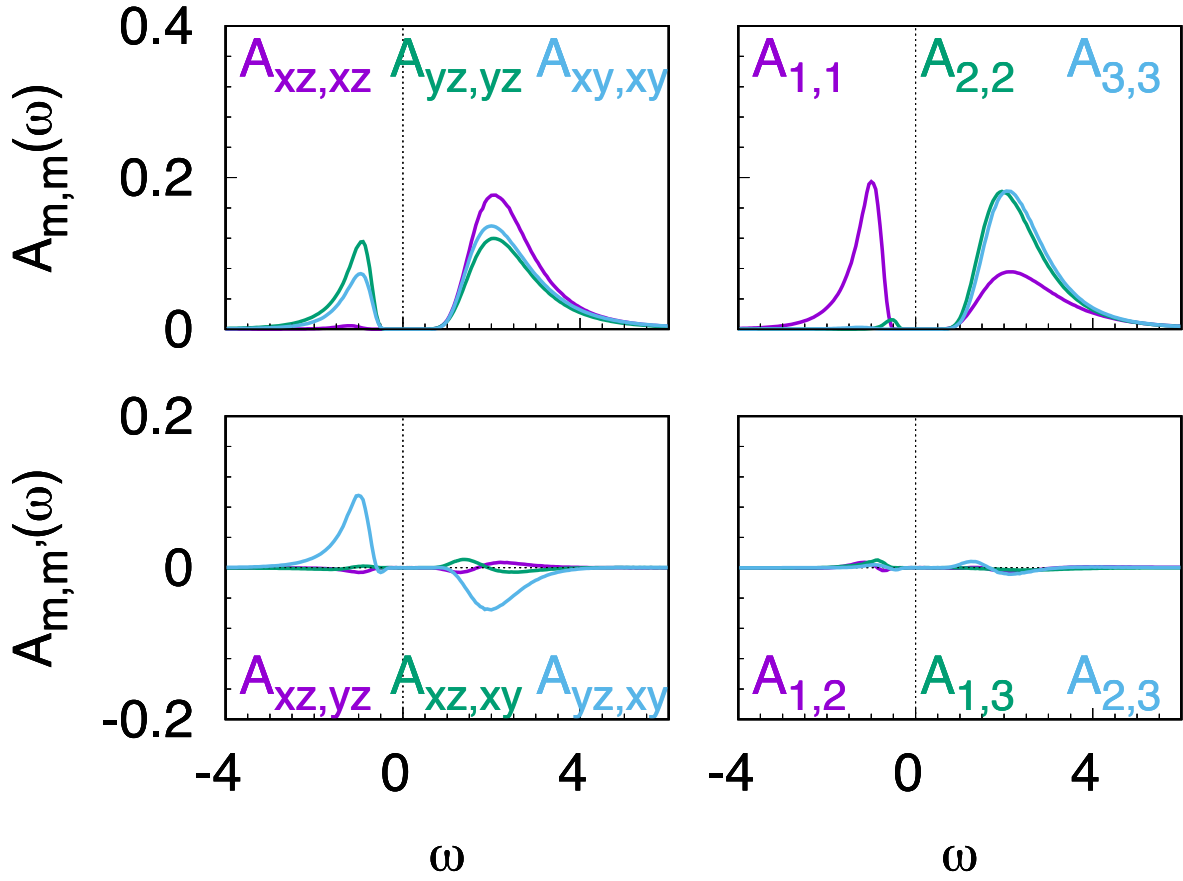


**Fig. 11:** The LDA+DMFT spectral function matrix of the orbitally-ordered  $t_{2g}^1$  system  $\text{YTiO}_3$ , in the  $(xz, yz, xy)$  basis (left panels) and in the crystal-field basis (right panels) [14, 17].

Here we neglected the small mixing of the three high-energy  $S = 0$  multiplets of the  $t_{2g}^2$  configuration ( $\varepsilon_{\text{CF}} \ll U$ ). The  $xz$  and  $yz$  Matsubara Green functions take instead the form

$$G_{xz/yz}^{i\sigma}(i\nu_n) \sim \frac{1}{4} \left( \frac{3}{i\nu_n - (\varepsilon_{xz/yz} + U - 3J - \mu)} + \frac{1}{i\nu_n - (\varepsilon_{xz/yz} + U - J - \mu)} \right).$$

The atomic-limit gap is then

$$E_g(1) \sim U - 3J + \varepsilon_{\text{CF}}.$$

From the expressions above we can see that the gap is inter-orbital and  $\varepsilon_{\text{CF}}$  increases it by a small amount. If the symmetry is lower than tetragonal, as in the case of  $\text{YTiO}_3$ , the Green function, the spectral-function and the self-energy become full  $3 \times 3$  matrices. Still, in the atomic limit, a crystal-field splitting favors the occupation of the lowest energy  $t_{2g}$  crystal-field orbital. This remains true beyond the atomic limit:  $\text{YTiO}_3$  is, indeed, an orbitally ordered Mott insulator with a gap of about 1 eV. This can be seen in the DMFT spectral-function matrix in Fig. 11.

The crystal-field splitting not only increases the gap but also reduces orbital degeneracy, favoring the onset of an orbitally ordered Mott-insulating state. The importance of orbital degeneracy



for the Mott gap was explained for the first time by E. Koch, O. Gunnarsson and R.M. Martin [18, 19]. The argument presented in their works is the following. Let us assume that a system is described by the multi-orbital Hubbard model for  $t_{2g}$  electrons with, however,  $J = 0$ . Let us assume that, in addition, its ground state is antiferromagnetic, as it typically is. The states relevant for the gap are those generated by adding or removing one electron from the ground state. In the large- $U$  limit their energy is approximately given by

$$\begin{aligned} E(N+1) &\sim nU + E(N) - \sqrt{k_+} W/2 \\ E(N-1) &\sim (n-1)U + E(N) - \sqrt{k_-} W/2, \end{aligned}$$

where  $n$  is the number of electrons per site and  $W$  is the band-width. The gap is then

$$E_g(N) \sim U - \frac{\sqrt{k_-} + \sqrt{k_+}}{2} W. \quad (10)$$

With respect to the atomic limit a term proportional to the bandwidth reduces the gap. To understand its origin we can go back to the case of the Hubbard dimer. For the dimer, the ground state is the singlet  $|G\rangle_H$ , given in Eq. (5). In the large- $U$  limit

$$|G\rangle_H = |N\rangle \sim \frac{1}{\sqrt{2}} [c_{1\uparrow}^\dagger c_{2\downarrow}^\dagger - c_{1\downarrow}^\dagger c_{2\uparrow}^\dagger] |0\rangle.$$

By creating or removing an electron at site 1, we generate the states

$$\begin{aligned} c_{1\uparrow}|N\rangle &\sim +\frac{1}{\sqrt{2}} c_{2\downarrow}^\dagger |0\rangle = +\frac{1}{\sqrt{2}} |N-1\rangle_2 \\ c_{1\uparrow}^\dagger |N\rangle &\sim -\frac{1}{\sqrt{2}} c_{1\uparrow}^\dagger c_{1\downarrow}^\dagger c_{2\uparrow}^\dagger |0\rangle = -\frac{1}{\sqrt{2}} |N+1\rangle_2 \end{aligned}$$

By applying the non-interacting Hamiltonian,  $\hat{H}_0$ , we then have

$$\begin{aligned} \hat{H}_0 |N-1\rangle_2 &= -t c_{1\downarrow}^\dagger |0\rangle = -t |N-1\rangle_1 \\ \hat{H}_0 |N+1\rangle_2 &= +t c_{2\uparrow}^\dagger c_{2\downarrow}^\dagger c_{1\uparrow}^\dagger |0\rangle = +t |N+1\rangle_1 \end{aligned}$$

In the atomic limit, the states  $(|N-1\rangle_1, |N-1\rangle_2)$  and the states  $(|N+1\rangle_1, |N+1\rangle_2)$  are degenerate. For  $t \neq 0$ , in the spaces defined by each one of these couple of degenerate states, the Hamiltonian is

$$\hat{H}_{N\pm} = \begin{pmatrix} E(N_\pm) & \pm t \\ \pm t & E(N_\pm) \end{pmatrix}$$

with  $N_\pm = N \pm 1$ . Thus the actual ground state is the bonding combination, and the associated bonding-energy gain is the square root of the second moment

$$M_\pm^{(2)} = {}_1\langle N_\pm | \hat{H}_0^2 | N_\pm \rangle_1 = t^2 = k_\pm (W/2)^2$$

where  $W = 2t$  (energy difference between antibonding and bonding state), and  $k_+ = k_- = 1$ . The ground-state correction of atomic energies in first order degenerate perturbation theory is

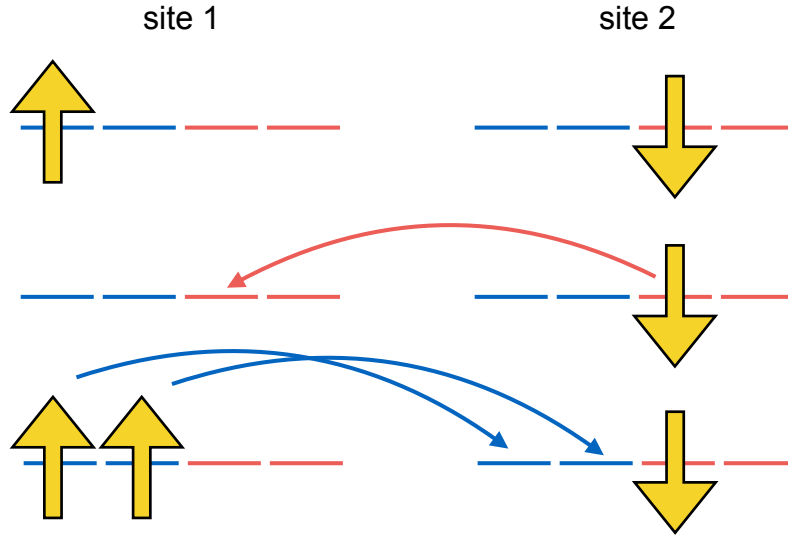


**Fig. 12:** Possible hopping paths for an extra hole and an extra electron in the case of orbital degeneracy  $d = 2$  and one electron per site. For simplicity only hopping between the same orbitals on neighboring sites is allowed. This figure was adapted from Fig. 4 of Ref. [19].

thus  $\Delta E(N_{\pm}) = -\sqrt{M_{\pm}^{(2)}}$ . Indeed, as one can verify from the exact Green function given in section 2.1, in the large- $U$  limit, the gap of the Hubbard dimer at half filling is  $E_g(1) \sim U - 2t$ . We can now generalize to the multi-orbital case. The second moment of the Hamiltonian is then  $M_{\pm}^{(2)} = \langle N_{\pm}^i | \hat{H}_0^2 | N_{\pm}^i \rangle = \sum_j |\langle N_{\pm}^i | \hat{H}_0 | N_{\pm}^j \rangle|^2$ , where  $|N_{\pm}^i\rangle$  is the state generated by adding or removing from the ground state an electron at site  $i$ , and  $|N_{\pm}^j\rangle$  are all the degenerate states generated from  $|N_{\pm}^i\rangle$  by hopping. For the single orbital dimer, as we have seen, there is only one  $|N_{\pm}^j\rangle$  state. If the number of degenerate orbitals  $d$  increases, however, so do the hopping possibilities;  $k_+$  and  $k_-$  equal the number of available hopping paths, which depends of course on the actual model. Let us assume that  $n = 1$  and  $t_{m,m'}^{i,i'} = t_{m,m'}^{i,i'} \delta_{m,m'}$ , i.e., only intra-orbital hopping between nearest neighbors is possible. If the model has two degenerate orbitals,  $k_- = 1$ . There are, however, two hopping possibilities for the extra electron, hence  $k_+ = 2$ . This is schematically illustrated in Fig. 12. As a result, in the orbitally-degenerate case there is a gap reduction with respect to the one-orbital case. This reduction, given in Eq. (10), can be viewed as a *hopping enhancement*. At half filling the enhancement factor is proportional to  $\sqrt{d}$  [18,19]. The relevance of orbital degeneracy for the Mott gap and thus for the Mott transition became apparent in many cases. For example, orbital degeneracy can be reduced by a relatively small crystal-field splitting, as it was shown in Ref. [17] for the series of  $3d^1$  perovskites. This happens because the crystal-field splitting makes some of the states higher in energy, so that they do not contribute to the second moment. Orbital degeneracy is also reduced by the Hund's rule coupling  $J$ , which makes some of the multiplets higher in energy, with similar effects. This effect plays a key role for Hund's metals [20].

### 3.3 Spin-orbit interaction

The main relativistic effect in solids is the spin-orbit interaction, whose strength grows increasing the atomic number  $Z$ . In correlated materials, the spin-orbit interaction competes with the Coulomb parameters, the crystal field, and the hopping integrals in determining magnetic and electronic properties. In the atomic limit, for the  $d$  shells the spin-orbit interaction is

$$\hat{H}_{\text{SO}} = \sum_{\mu} \lambda_{\mu} \sum_{mm'} \sum_{\sigma\sigma'} \epsilon_{m\sigma, m'\sigma'}^{\mu} c_{m\sigma}^{\dagger} c_{m'\sigma'}, \quad \epsilon_{m\sigma, m'\sigma'}^{\mu} = \langle m\sigma | l_{\mu} s_{\mu} | m'\sigma' \rangle,$$

where  $\mu = x, y, z$ , and  $\lambda_{\mu}$  are the spin-orbit couplings, with  $\lambda_{\mu} = \lambda$  in  $O(3)$  symmetry, and

$$\lambda \sim g \mu_B^2 \left\langle \frac{1}{r} \frac{d}{dr} v_R(r) \right\rangle.$$

Let us assume that, according to the first and second of Hund's rules,  $S$  is the total spin and  $L$  the total angular momentum of the ground multiplet; these  $LS$  states are  $(2L+1)(2S+1)$ -fold degenerate. If the spin-orbit coupling  $\lambda$  is small compared to the Hund's rule couplings  $J_1$  and  $J_2$ , the spin-orbit interaction can be treated as a perturbation splitting the  $LS$  manifold in eigenstates of the total angular momentum  $j$ . The third Hund's rule states that, if the outermost shell is less than half filled, the ground multiplet is the one with  $j = L - S$ ; if, instead, it is more than half filled, it is the one with  $j = L + S$ . For the  $d^1$  configuration,  $L = 2$  and  $S = 1/2$ , so that the quartet  $j = 3/2$  is the ground multiplet. In materials, the second and third of Hund's rules, and sometimes, as we have discussed, even the first, can be violated. This happens also in Mott insulators, where the atomic character is preserved to a large extent. A source of Hund's rules breakdown is the crystal field. The strength of the spin-orbit interaction  $\lambda$  has therefore to be compared not only to  $J_1$  and  $J_2$  but also to the relevant crystal-field couplings. In that respect, it is important to notice that  $\hat{H}_{\text{SO}}$  couples  $e_g$  and  $t_{2g}$  states. If, however, the cubic crystal field  $\varepsilon_C$  is large compared to  $\lambda$ , as typically is the case for  $4d$  systems, and the electronic configuration without spin-orbit interaction is  $t_{2g}^n e_g^0$ , we can safely downfold the  $e_g$  states. For cubic  $t_{2g}$  systems of this kind, the spin-orbit Hamiltonian can then be rewritten as

$$\begin{aligned} \hat{H}_{\text{SO}} &= \frac{i\lambda}{2} \left( \sum_{\sigma} \sigma c_{yz\sigma}^{\dagger} c_{xz\sigma} + c_{xz\uparrow}^{\dagger} c_{xy\downarrow} + i c_{yz\uparrow}^{\dagger} c_{xy\downarrow} + c_{xz\downarrow}^{\dagger} c_{xy\uparrow} - i c_{yz\downarrow}^{\dagger} c_{xy\uparrow} \right) + \text{h.c.} \\ &= -\frac{\lambda}{2} \left[ \sum_{\sigma m} m \sigma c_{m\sigma}^{\dagger} c_{m\sigma} + \sqrt{2} \left( c_{-1\uparrow}^{\dagger} c_{0\downarrow} + c_{0\uparrow}^{\dagger} c_{+1\downarrow} + c_{+1\downarrow}^{\dagger} c_{0\uparrow} + c_{0\downarrow}^{\dagger} c_{-1\uparrow} \right) \right], \end{aligned} \quad (11)$$

where

$$c_{+1,\sigma}^{\dagger} = -\frac{c_{xz,\sigma}^{\dagger} + i c_{yz,\sigma}^{\dagger}}{\sqrt{2}}, \quad c_{-1,\sigma}^{\dagger} = \frac{c_{xz,\sigma}^{\dagger} - i c_{yz,\sigma}^{\dagger}}{\sqrt{2}}, \quad c_{0,\downarrow}^{\dagger} = -i c_{xy,\sigma}^{\dagger}.$$

In the last line of Eq. (11) we have brought the spin-orbit interaction in the form it takes for  $p$  electrons (effective angular momentum  $l = 1$ ), apart, however, a minus sign in front. For the  $t_{2g}^1$  configuration the effective total angular momentum  $j$  can thus have the values  $3/2$  and  $1/2$ . The

local Green function matrix reflects the presence of spin-orbit interaction via extra off-diagonal terms. For a  $t_{2g}$  system with cubic symmetry its most general form is [21, 23]

$$G_{im,im'}^{\sigma,\sigma'}(\tau) = \left( \begin{array}{ccc|ccc} G_{xy}^{i\uparrow\uparrow}(\tau) & 0 & 0 & 0 & G_y^{i\uparrow\downarrow}(\tau) & -iG_x^{i\uparrow\downarrow}(\tau) \\ 0 & G_{yz}^{i\uparrow\uparrow}(\tau) & iG_z^{i\uparrow\uparrow}(\tau) & -G_y^{i\uparrow\downarrow}(\tau) & 0 & 0 \\ 0 & -iG_z^{i\uparrow\uparrow}(\tau) & G_{xz}^{i\uparrow\uparrow}(\tau) & iG_x^{i\uparrow\downarrow}(\tau) & 0 & 0 \\ \hline 0 & -G_y^{i\downarrow\uparrow}(\tau) & -iG_x^{i\downarrow\uparrow}(\tau) & G_{xy}^{i\downarrow\downarrow}(\tau) & 0 & 0 \\ G_y^{i\downarrow\uparrow}(\tau) & 0 & 0 & 0 & G_{yz}^{i\downarrow\downarrow}(\tau) & -iG_z^{i\downarrow\downarrow}(\tau) \\ iG_x^{i\downarrow\uparrow}(\tau) & 0 & 0 & 0 & iG_z^{i\downarrow\uparrow}(\tau) & G_{xz}^{i\downarrow\downarrow}(\tau) \end{array} \right)$$

where all  $G_m^{i\sigma\sigma'}(\tau)$  are real functions, and  $G_m^{i\sigma\sigma'}(\tau) = G_m^{i\sigma'\sigma}(\tau)$ , while  $G_x^{i\sigma\sigma'}(\tau) = G_y^{i\sigma\sigma'}(\tau) = G_z^{i\sigma\sigma'}(\tau)$ , and  $G_{xz}^{i\sigma\sigma}(\tau) = G_{yz}^{i\sigma\sigma}(\tau) = G_{xy}^{i\sigma\sigma}(\tau)$ . The local Green function above is diagonal in the basis of the eigenstates of the total angular momentum of the  $t_{2g}^1$  configuration. Among those, the  $j = 3/2$  quartet is generated by the creation operators

$$c_{-\frac{3}{2}}^\dagger = c_{-1,\downarrow}^\dagger \quad c_{-\frac{1}{2}}^\dagger = \frac{c_{-1,\uparrow}^\dagger + \sqrt{2}c_{0,\downarrow}^\dagger}{\sqrt{3}} \quad c_{+\frac{1}{2}}^\dagger = \frac{c_{+1,\downarrow}^\dagger + \sqrt{2}c_{0,\uparrow}^\dagger}{\sqrt{3}}, \quad c_{+\frac{3}{2}}^\dagger = c_{+1,\uparrow}^\dagger.$$

Instead, the  $j = 1/2$  doublet is generated by the creation operators

$$d_{-\frac{1}{2}}^\dagger = \frac{\sqrt{2}c_{-1,\uparrow}^\dagger - c_{0,\downarrow}^\dagger}{\sqrt{3}} \quad d_{+\frac{1}{2}}^\dagger = \frac{\sqrt{2}c_{+1,\downarrow}^\dagger - c_{0,\uparrow}^\dagger}{\sqrt{3}}.$$

By inverting these relations, we can express the  $t_{2g}$  creation and destruction operators as

$$\begin{aligned} c_{xz,\downarrow}^\dagger &= \frac{1}{\sqrt{6}} \left[ -\sqrt{3}c_{-\frac{3}{2}}^\dagger + c_{\frac{1}{2}}^\dagger + \sqrt{2}d_{\frac{1}{2}}^\dagger \right] & c_{xz,\uparrow}^\dagger &= \frac{-1}{\sqrt{6}} \left[ -\sqrt{3}c_{\frac{3}{2}}^\dagger + c_{-\frac{1}{2}}^\dagger + \sqrt{2}d_{-\frac{1}{2}}^\dagger \right] \\ c_{yz,\downarrow}^\dagger &= \frac{i}{\sqrt{6}} \left[ +\sqrt{3}c_{-\frac{3}{2}}^\dagger + c_{\frac{1}{2}}^\dagger + \sqrt{2}d_{\frac{1}{2}}^\dagger \right] & c_{yz,\uparrow}^\dagger &= \frac{i}{\sqrt{6}} \left[ +\sqrt{3}c_{\frac{3}{2}}^\dagger + c_{-\frac{1}{2}}^\dagger + \sqrt{2}d_{-\frac{1}{2}}^\dagger \right] \\ c_{xy,\downarrow}^\dagger &= \frac{i}{\sqrt{3}} \left[ +\sqrt{2}c_{-\frac{1}{2}}^\dagger - d_{-\frac{1}{2}}^\dagger \right] & c_{xy,\uparrow}^\dagger &= \frac{i}{\sqrt{3}} \left[ +\sqrt{2}c_{\frac{1}{2}}^\dagger - d_{\frac{1}{2}}^\dagger \right], \end{aligned}$$

and rewrite the Green function matrix in the new basis. It takes the simple form

$$G_{im_j,im_{j'}}^{j,j'}(\tau) = G_{\frac{3}{2}}^{i\uparrow\uparrow}(\tau)\hat{I}_{\frac{3}{2}} + G_{\frac{1}{2}}^{i\uparrow\uparrow}(\tau)\hat{I}_{\frac{1}{2}},$$

where  $\hat{I}_j$  is the identity matrix of dimension  $2j + 1$ . The spin-orbit Hamiltonian has the same diagonal form

$$\hat{H}_{\text{SO}} = -\frac{\lambda}{2} \sum_{m=-\frac{3}{2}}^{+\frac{3}{2}} \hat{n}_{\frac{3}{2},m} + \lambda \sum_{m=-\frac{1}{2}}^{+\frac{1}{2}} \hat{n}_{\frac{1}{2},m}.$$

One could thus conclude that the total angular momentum basis is the ideal one in the presence of spin-orbit interaction. We have, however, to pay attention to the fact that the crystal-field Hamiltonian is not diagonal in the angular momentum basis. Furthermore, if we change basis in the way just described, we have to transform accordingly  $\hat{H}_U$ , the Coulomb part of the Hamiltonian. We can see some of the effects of this transformation by considering a tetragonal system for which  $\varepsilon_{\text{CF}}$ , the tetragonal crystal-field splitting, is very large. In such a case the  $xy$  orbital is basically decoupled and we can assume  $\hat{H}_{\text{SO}} \sim \hat{H}_{\text{SO}}^z = \frac{i\lambda_z}{2} \sum_{\sigma} \sigma c_{yz\sigma}^{\dagger} c_{xz\sigma}$ . The interaction  $\hat{H}_{\text{SO}}^z$  is diagonal in the basis of spherical harmonics. The corresponding creation operators are

$$c_{-\frac{3}{2}}^{\dagger} = c_{-1,\downarrow}^{\dagger} \quad c_{-\frac{1}{2}}^{\dagger} = c_{-1,\uparrow}^{\dagger} \quad c_{+\frac{3}{2}}^{\dagger} = c_{+1,\uparrow}^{\dagger} \quad c_{+\frac{1}{2}}^{\dagger} = c_{+1,\downarrow}^{\dagger}.$$

In the spherical harmonics basis the Coulomb interaction for  $xz/yz$  orbitals takes the form

$$\begin{aligned} \hat{H}_U = & (U - J) (\hat{n}_{\frac{3}{2}} \hat{n}_{\frac{1}{2}} + \hat{n}_{-\frac{3}{2}} \hat{n}_{-\frac{1}{2}} + \hat{n}_{\frac{3}{2}} \hat{n}_{-\frac{3}{2}} + \hat{n}_{\frac{1}{2}} \hat{n}_{-\frac{1}{2}}) \\ & + (U - 3J) (\hat{n}_{\frac{3}{2}} \hat{n}_{-\frac{1}{2}} + \hat{n}_{-\frac{3}{2}} \hat{n}_{\frac{1}{2}}) - 2J (c_{\frac{3}{2}}^{\dagger} c_{\frac{1}{2}} c_{-\frac{3}{2}}^{\dagger} c_{-\frac{1}{2}} + c_{-\frac{1}{2}}^{\dagger} c_{-\frac{3}{2}} c_{\frac{1}{2}}^{\dagger} c_{\frac{3}{2}}). \end{aligned}$$

Thus, we can see that in the new basis the pair-hopping terms are zero and the density-density terms have a different prefactor than in the original  $xz, yz$  basis.<sup>9</sup>

What about LDA+DMFT calculations with spin-orbit interaction? Although  $\hat{H}_{\text{SO}}$  looks like an innocent one-body term, it turns out that, for real materials, calculations including this term are more difficult. This has two reasons: (i) they involve larger Green function matrices, e.g.,  $6 \times 6$  as in the case just discussed, hence they are more demanding computationally and (ii) they are often hampered by a much stronger sign problem. Thus, specific basis choices and approximations are used. A possible approach consists in working in the basis that diagonalizes the non-interacting local Green function or the non-interacting local Hamiltonian; such a basis typically reduces the sign problem, as was first shown in Ref. [10] for the case without spin-orbit interaction. For a system with tetragonal symmetry, the states that diagonalize the local Green function belong either to the  $\Gamma_6$  or to the  $\Gamma_7$  irreducible representations, both 2-dimensional. There are two (coupled)  $\Gamma_7$  representations, defining the space  $\Gamma_7' \oplus \Gamma_7''$ . The analytic expression of these states can be found in Refs. [16, 21, 23]. The transformation to the  $\Gamma_6 \oplus \Gamma_7' \oplus \Gamma_7''$  basis is, of course, in principle, a mere basis change. Approximations are made, however, if all off-diagonal elements of the Green function are set to zero or the Coulomb tensor is truncated, as often done, e.g., to further tame the sign problem.

In the presence of crystal-field splitting, if the spin-orbit interaction does not dominate, it is often preferable to perform the calculations in the  $t_{2g}$  basis. To this end, it is key to make QMC codes very efficient in order to reduce as much as possible statistical errors and increase the average sign. Exact LDA+SO+DMFT calculations in the  $t_{2g}$  basis have been successfully performed for  $\text{Sr}_2\text{RuO}_4$ , using an interaction-expansion continuous-time quantum Monte Carlo solver, and an orbital-dependent phase which makes the Green function matrix real [21, 23].

<sup>9</sup>For the transformation of the full Coulomb tensor from cubic to spherical harmonics, see, e.g., my chapter in Ref. [12]. It goes without saying that the total Green function (hence the gap) and the energy of the multiplets do not change if we change basis, although the components of the Green functions are basis dependent.

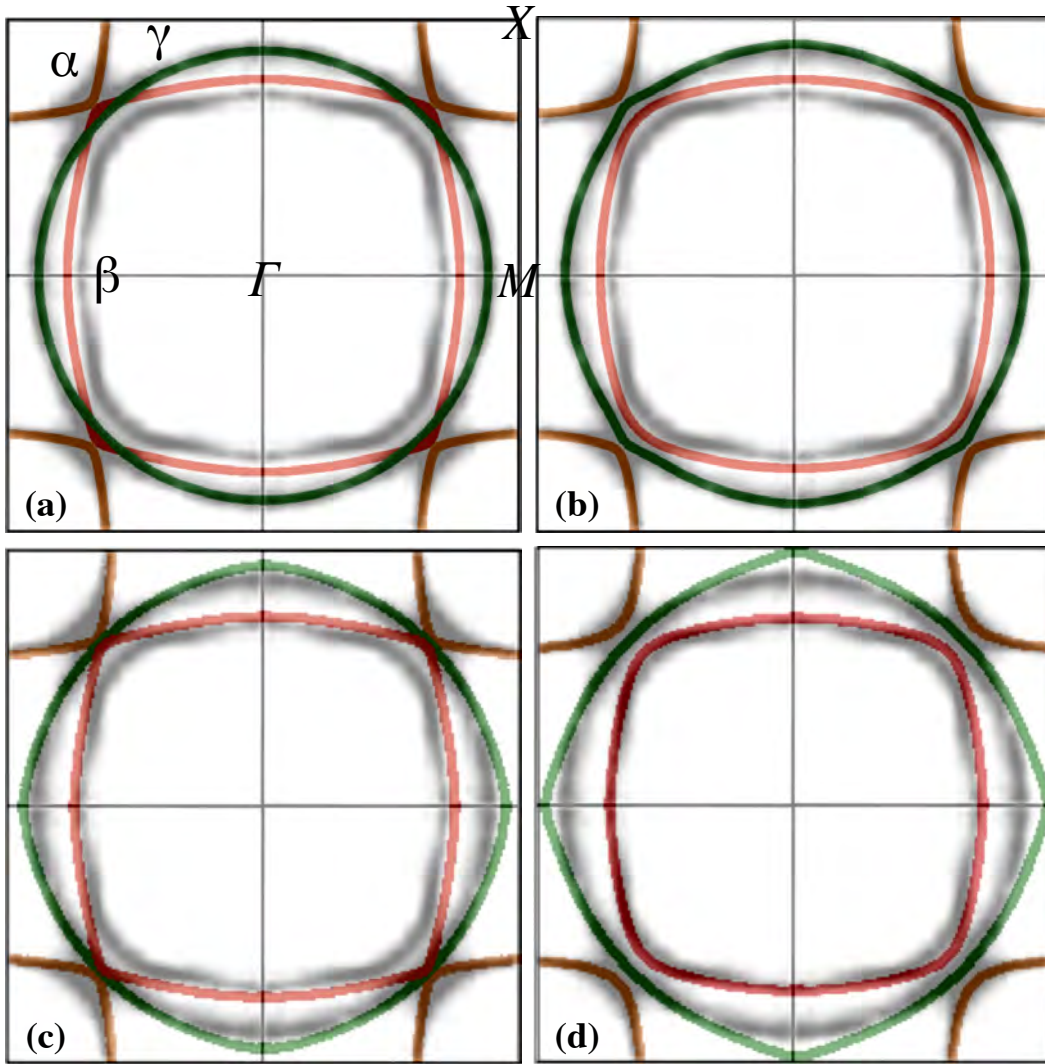


**Fig. 13:** Fermi surface of  $\text{Sr}_2\text{RuO}_4$  calculated with LDA (a), LDA+SO (b), LDA+DMFT (c) and LDA+SO+DMFT (d) [21]. The grey maps are experimental results from Ref. [22].

This approach allowed us to study, for example, the effects of the spin-orbit interaction on the Fermi surface without approximations. The results are shown in Fig. 13 in comparison with experimental data; we will discuss them in the next section. In Fig. 14 we show instead another example of LDA+SO+DMFT calculations, the orbital-resolved spectral function matrix of  $\text{Ca}_2\text{RuO}_4$ . The figure compares the spectral function matrices for the metallic L-Pbca phase and the insulating S-Pbca phase, both with and without spin-orbit interaction. In the case of the S-Pbca phase, the spectral function matrix shows that the system is orbitally ordered, with the configuration  $\sim xy^2xz^1yz^1$  corresponding to  $xy$  orbital order. The small gap is inter-orbital, and more specifically  $xy \rightarrow xz, yz$ .

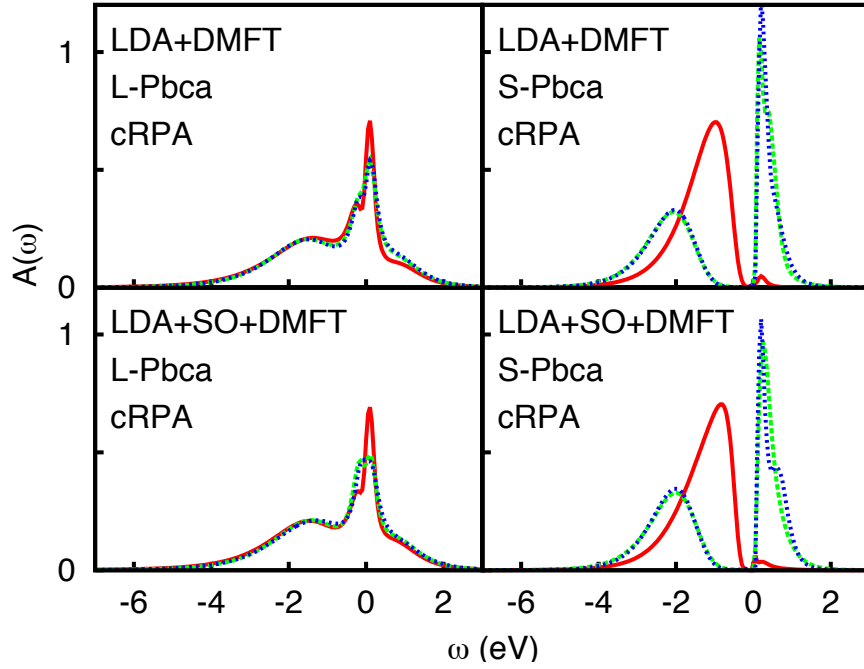


**Fig. 14:** Spectral function matrix for the  $t_{2g}^4$  system  $\text{Ca}_2\text{RuO}_4$ . Left: high-temperature  $L\text{-Pbca}$  metallic phase. Right: Low-temperature insulating  $S\text{-Pbca}$  phase.

### 3.4 Non-spherical Coulomb terms and double-counting correction

Up to now we have considered the Coulomb tensor spherical (symmetry  $O(3)$ ). This is exact for a free atom. The screened Coulomb tensor has, however, in general, the symmetry of the lattice. Taking into account non-spherical Coulomb terms is, in general hard, both because they make QMC calculations more difficult and can worsen the sign problem, and because in their presence the double-counting correction has to be explicitly accounted for, even when massive downfolding is used. For these reasons they are typically neglected. Recently it was shown that they can play a very important role for the Fermi surface, however [21]. Let us therefore discuss how the double-counting correction can be treated in the presence of such terms, following the approach of Ref. [21]. One of the classical approximations for the double-counting correction is the so called “around mean-field” approximation. The idea is that LDA describes well the average Coulomb term, in the absence of orbital polarization. This is equivalent to using as double-counting correction the Hartree term of the Coulomb interaction tensor, i.e., the operator

$$\begin{aligned}
 \hat{H}_U^{\text{DC}} = & U \sum_m (\hat{n}_{m\uparrow}\bar{n}_{m\downarrow} + \bar{n}_{m\uparrow}\hat{n}_{m\downarrow}) + (U - 2J) \sum_{m \neq m'} (\hat{n}_{m\uparrow}\bar{n}_{m'\downarrow} + \bar{n}_{m\uparrow}\hat{n}_{m'\downarrow}) \\
 & + (U - 3J) \sum_{\sigma} \sum_{m > m'} (\hat{n}_{m\sigma}\bar{n}_{m'\sigma} + \bar{n}_{m\sigma}\hat{n}_{m'\sigma}) - \mu \hat{N}_d \\
 & - U \sum_m \bar{n}_{m\uparrow}\bar{n}_{m\downarrow} + (U - 2J) \sum_{m \neq m'} \bar{n}_{m\uparrow}\bar{n}_{m'\downarrow} + (U - 3J) \sum_{\sigma} \sum_{m > m'} \bar{n}_{m\sigma}\bar{n}_{m'\sigma}
 \end{aligned}$$

where  $\bar{n}_{m\sigma} = n/d$ , if  $n$  is the number of the correlated electrons per site and  $d$  the orbital degeneracy. Within this approximation we have, after collecting all terms,

$$\begin{aligned}\hat{H}_U^{\text{DC}} &= (\delta\mu - \mu)\hat{N}_d - \frac{n^2}{d} [U(2d-1) - 5(d-1)] \\ \delta\mu &= \frac{n}{d} [U(2d-1) - 5J(d-1)].\end{aligned}$$

If we perform massive downfolding to the correlated bands, as previously mentioned, this is merely a shift of the chemical potential and can therefore be neglected. Let us now consider the case in which the Coulomb interaction has an additional term that does not change the average  $U$  but has tetragonal symmetry

$$\Delta\hat{H}_U = \frac{\Delta U}{3} (2\hat{n}_{xy\uparrow}\hat{n}_{xy\downarrow} - \hat{n}_{xz\uparrow}\hat{n}_{xz\downarrow} - \hat{n}_{yz\uparrow}\hat{n}_{yz\downarrow})$$

We can now use the around mean-field approximation for this term as well. We find

$$\begin{aligned}\Delta\hat{H}_U^{\text{DC}} &= \frac{n}{6} \frac{\Delta U}{3} \sum_{\sigma} (2\hat{n}_{xy\sigma} - \hat{n}_{xz\sigma} - \hat{n}_{yz\sigma}) = \frac{n}{6} \Delta U \sum_{\sigma} \hat{n}_{xy\sigma} - \delta\mu' \hat{N} \\ \delta\mu' &= \frac{n}{6} \frac{\Delta U}{3}.\end{aligned}$$

This term, in addition to a shift of the chemical potential, yields an effective change of the crystal-field splitting  $\varepsilon_{\text{CF}}$ , and has therefore to be accounted for explicitly.

How does  $\Delta U$  changes the Fermi surface of  $\text{Sr}_2\text{RuO}_4$ ? The Fermi surface is determined by the poles of the Green function at zero frequency. These depend on the non-interacting Hamiltonian and the self-energy matrix at zero frequency. In the Fermi-liquid regime, and within the DMFT local approximation, the effect of the self-energy is merely to modify the on-site part of the Hamiltonian, i.e., the crystal-field splitting and the spin-orbit couplings

$$\varepsilon_{\text{CF}} \rightarrow \varepsilon_{\text{CF}} + \Delta\varepsilon_{\text{CF}}(0),$$

$$\lambda_{\mu} \rightarrow \lambda_{\mu} + \Delta\lambda_{\mu}(0).$$

Both  $\Delta\varepsilon_{\text{CF}}(0)$  and  $\Delta\lambda_{\mu}(0)$  are positive for  $\text{Sr}_2\text{RuO}_4$ , and lead to an almost doubling of the LDA parameters. The positive  $\Delta\varepsilon_{\text{CF}}(0)$  shrinks the  $\beta$  sheet ( $xz/yz$  bands) and enlarges the  $\gamma$  ( $xy$  band) sheet. This can be understood from the schematic Fermi surface and the LDA band structure in Fig. 9. Enhancing the crystal-field splitting corresponds to slightly moving the  $xy$  band downwards and the  $xz/yz$  bands upwards with respect to the Fermi level. The enhancement of the spin-orbit couplings has a large Hartree-Fock component [23], since the spin-orbit interaction yields a small but finite off-diagonal occupation matrix. For a  $O(3)$ -symmetric Coulomb tensor, the Hartree-Fock enhancement of the spin-orbit coupling is thus

$$\begin{aligned}\frac{\Delta\lambda_z}{2} &= i(U-3J) n_{xz,yz}^{\uparrow\uparrow} \\ \frac{\Delta\lambda_y}{2} &= -(U-3J) n_{xy,yz}^{\uparrow\downarrow}, \\ \frac{\Delta\lambda_x}{2} &= -i(U-3J) n_{xy,xz}^{\uparrow\downarrow},\end{aligned}$$



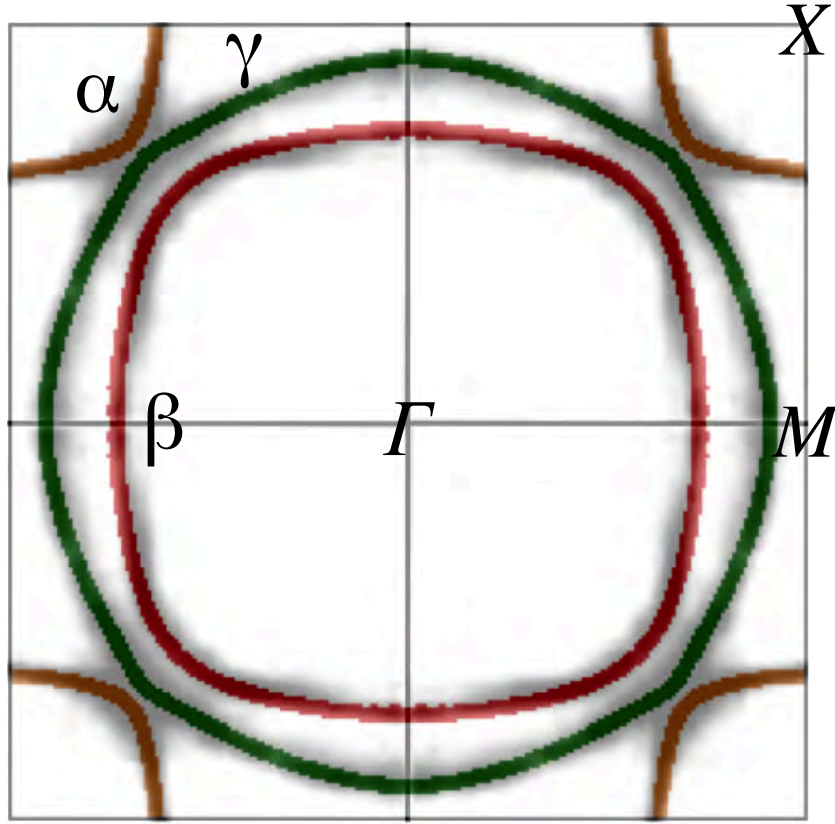


**Fig. 15:** The LDA+SO+DMFT Fermi surface of  $\text{Sr}_2\text{RuO}_4$  calculated including the effects of the non-spherical Coulomb term  $\Delta U$ .

where  $n_{m,m'}^{\sigma\sigma'}$  are the off-diagonal elements of the density matrix. The Coulomb-enhanced spin-orbit coupling improves the agreement with the experimental Fermi surface at the degeneracy points (e.g., along the  $\Gamma$ - $X$  direction). The agreement with ARPES data, however, further deteriorates for the  $\gamma$  sheet. This can be seen in Fig. 13, in which the LDA and LDA+DMFT Fermi surface are shown on top of ARPES data from Ref. [22].

Including correlation effects has thus two opposite effects: on the one hand, the agreement with experiments improves with respect to LDA for the  $\beta$  sheet; on the other hand, it deteriorates for the  $\gamma$  sheet. This can be seen comparing either panels (a) and (c) or panels (b) and (d) in Fig. 13. Introducing tetragonal terms, and in particular the term  $\Delta U$ , however, reduces the crystal-field enhancement to

$$\varepsilon_{\text{CF}} \rightarrow \varepsilon_{\text{CF}} + \Delta\varepsilon'_{\text{CF}}(0),$$

where  $\Delta\varepsilon'_{\text{CF}}(0)$  becomes almost zero for cRPA-based estimates of  $\Delta U$ . This leads to an almost perfect Fermi surface, as shown in Fig. 15. Non-spherical Coulomb terms turn out to be more important for properties that reflect the point symmetry of the lattice, like the Fermi surface, than for properties that average over orbitals, like total spectral function [23].

## 4 Conclusion

The many-body problem is the grand challenge of solid-state physics. The result of many electrons interacting together is a plethora of co-operative emergent properties. Among these are heavy quasiparticles and the Coulomb-driven metal-insulator transition. The LDA+DMFT approach has opened the possibility of describing and understanding these phenomena in real materials. This approach is based on the DMFT local approximation for the self-energy. DMFT is exact in several limits: the non-interacting limit, the atomic limit, and the limit of infinite coordination number. In typical strongly-correlated materials it turns out to be an excellent approximation. Approaches that go beyond the local approximation range from cluster extensions to various diagrammatic methods, among which the dual-particle based techniques. A key aspect of DMFT remains model building. Essential to that is the basis choice. The basis should be as localized as possible but should also carry as much information as possible about the actual system. Crucial is to choose a basis which indeed spans the whole space of correlated electrons, even if this reduces localization. Wannier functions built from LDA/GGA calculations satisfy all these requirements. It is also important to take into account the symmetry of the system, and consider the effect of small distortions – unless including them makes calculations impossible. We have seen in many cases that small details do matter. A small crystal-field can favor the onset of the metal-insulator transition [17]. Small non-spherical Coulomb terms can sizably deform the Fermi surface of a multi-band correlated metal [21]. Improving the models and developing new methods to solve complex realistic models is therefore key for future progress. While numerical codes become always more sophisticated, many-body physics is primarily driven by experimental discoveries, novel phenomena whose interpretation remain often a mystery for decades. Indeed, one can identify only very few cases in which theory has predicted unknown emergent phenomena. A famous example is anti-ferromagnetism, which was predicted using static mean-field theory. Remarkably, it turned out later that the original theoretical description was wrong. In the future there will be new classes of supercomputers and algorithms which will allow us to run always more realistic simulations. Although prediction will remain difficult, our ability of reconstructing experimental results will steadily increase. As physicists, however, our role is to understand and explain phenomena, not merely reproduce them. Even a calculation that reproduce exactly experiments does not add new knowledge, if it does not help us in explaining the origin of the observed phenomenon. This would be like having the exact solution of the classical  $N$ -body problem discussed in the introduction, from which we are not able to learn anything. Our major task remains thus to identify, with the help of computers and algorithms, the mechanisms behind phenomena, building a coherent picture.

## Appendices

### A The Anderson molecule

The Hamiltonian of the Anderson molecule is given by

$$\hat{H} = \varepsilon_s \sum_{\sigma} \hat{n}_{2\sigma} - t \sum_{\sigma} (c_{1\sigma}^{\dagger} c_{2\sigma} + c_{2\sigma}^{\dagger} c_{1\sigma}) + \varepsilon_d \sum_{\sigma} \hat{n}_{1\sigma} + U \hat{n}_{1\uparrow} \hat{n}_{1\downarrow}.$$

It commutes with the number of electron operator  $\hat{N}$ , with the total spin  $\hat{S}$  and with  $\hat{S}_z$ . Thus we can express the many-body states in the atomic limit as

$ N, S, S_z\rangle$		$N$	$S$	$E(N, S)$
$ 0, 0, 0\rangle$	$=  0\rangle$	0	0	0
$ 1, 1/2, \sigma\rangle_1$	$= c_{1\sigma}^{\dagger}  0\rangle$	1	1/2	$\varepsilon_d$
$ 1, 1/2, \sigma\rangle_2$	$= c_{2\sigma}^{\dagger}  0\rangle$	1	1/2	$\varepsilon_s$
$ 2, 1, 0\rangle$	$= \frac{1}{\sqrt{2}} [c_{1\uparrow}^{\dagger} c_{2\downarrow}^{\dagger} + c_{1\downarrow}^{\dagger} c_{2\uparrow}^{\dagger}]  0\rangle$	2	1	$\varepsilon_d + \varepsilon_s$
$ 2, 1, 1\rangle$	$= c_{2\uparrow}^{\dagger} c_{1\uparrow}^{\dagger}  0\rangle$	2	1	$\varepsilon_d + \varepsilon_s$
$ 2, 1, -1\rangle$	$= c_{2\downarrow}^{\dagger} c_{1\downarrow}^{\dagger}  0\rangle$	2	1	$\varepsilon_d + \varepsilon_s$
$ 2, 0, 0\rangle_0$	$= \frac{1}{\sqrt{2}} [c_{1\uparrow}^{\dagger} c_{2\downarrow}^{\dagger} - c_{1\downarrow}^{\dagger} c_{2\uparrow}^{\dagger}]  0\rangle$	2	0	$\varepsilon_d + \varepsilon_s$
$ 2, 0, 0\rangle_1$	$= c_{1\uparrow}^{\dagger} c_{1\downarrow}^{\dagger}  0\rangle$	2	0	$2\varepsilon_d + U$
$ 2, 0, 0\rangle_2$	$= c_{2\uparrow}^{\dagger} c_{2\downarrow}^{\dagger}  0\rangle$	2	0	$2\varepsilon_s$
$ 3, 1/2, \sigma\rangle_1$	$= c_{1\sigma}^{\dagger} c_{2\uparrow}^{\dagger} c_{2\downarrow}^{\dagger}  0\rangle$	3	1/2	$\varepsilon_d + 2\varepsilon_s$
$ 3, 1/2, \sigma\rangle_2$	$= c_{2\sigma}^{\dagger} c_{1\uparrow}^{\dagger} c_{1\downarrow}^{\dagger}  0\rangle$	3	1/2	$2\varepsilon_d + \varepsilon_s + U$
$ 4, 0, 0\rangle$	$= c_{1\uparrow}^{\dagger} c_{1\downarrow}^{\dagger} c_{2\uparrow}^{\dagger} c_{2\downarrow}^{\dagger}  0\rangle$	4	0	$2\varepsilon_d + 2\varepsilon_s + U$

For  $N = 1$  electrons the Hamiltonian can be written in the matrix form

$$\hat{H}_1 = \begin{pmatrix} \varepsilon_d & -t & 0 & 0 \\ -t & \varepsilon_s & 0 & 0 \\ 0 & 0 & \varepsilon_d & -t \\ 0 & 0 & -t & \varepsilon_s \end{pmatrix}.$$

The eigenstates are thus

$ 1, S, S_z\rangle_{\alpha}$	$E_{\alpha}(1, S)$	$d_{\alpha}(1, S)$
$ 1, 1/2, \sigma\rangle_+ = \alpha_1  1, 1/2, \sigma\rangle_1 - \alpha_2  1, 1/2, \sigma\rangle_2$	$\frac{1}{2} [\varepsilon_d + \varepsilon_s + \sqrt{(\varepsilon_d - \varepsilon_s)^2 + 4t^2}]$	2
$ 1, 1/2, \sigma\rangle_- = \alpha_2  1, 1/2, \sigma\rangle_1 + \alpha_1  1, 1/2, \sigma\rangle_2$	$\frac{1}{2} [\varepsilon_d + \varepsilon_s - \sqrt{(\varepsilon_d - \varepsilon_s)^2 + 4t^2}]$	2

where  $d_\alpha(N)$  is the spin degeneracy of the  $\alpha$  manifold. For  $\varepsilon_s = \varepsilon_d + U/2$  the eigenvalues are

$$E_\pm(1, S) = \varepsilon_d + \frac{1}{4}[U \pm \Delta(U, t)],$$

where

$$\Delta(t, U) = \sqrt{U^2 + 16t^2}.$$

The parameters  $\alpha_1$  and  $\alpha_2$  of the corresponding eigenvectors are

$$\alpha_1^2 = \frac{1}{\Delta(t, U)} \frac{\Delta(t, U) - U}{2} \quad \alpha_2^2 = \frac{4t^2}{\Delta(t, U)} \frac{2}{\Delta(t, U) - U}$$

For  $N=2$  electrons, the hopping integrals only couple the  $S=0$  states. The Hamiltonian is

$$\hat{H}_2 = \begin{pmatrix} \varepsilon_d + \varepsilon_s & 0 & 0 & 0 & 0 & 0 \\ 0 & \varepsilon_d + \varepsilon_s & 0 & 0 & 0 & 0 \\ 0 & 0 & \varepsilon_d + \varepsilon_s & 0 & 0 & 0 \\ 0 & 0 & 0 & \varepsilon_d + \varepsilon_s & -\sqrt{2}t & -\sqrt{2}t \\ 0 & 0 & 0 & -\sqrt{2}t & 2\varepsilon_d + U & 0 \\ 0 & 0 & 0 & -\sqrt{2}t & 0 & 2\varepsilon_s \end{pmatrix}$$

For  $\varepsilon_s = \varepsilon_d + U/2$  the eigenvalues and the corresponding eigenvectors are

$ 2, S, S_z\rangle_\alpha$	$E_\alpha(2, S)$	$d_\alpha(2, S)$
$ 2, 0, 0\rangle_+ = a_1 2, 0, 0\rangle_0 - \frac{a_2}{\sqrt{2}}[ 2, 0, 0\rangle_1 +  2, 0, 0\rangle_2]$	$2\varepsilon_d + \frac{U}{2} + \frac{1}{4}[U + 2\Delta(t, \frac{U}{2})]$	1
$ 2, 0, 0\rangle_o = \frac{1}{\sqrt{2}}[ 2, 0, 0\rangle_1 -  2, 0, 0\rangle_2]$	$2\varepsilon_d + U$	1
$ 2, 1, m\rangle_o =  2, 1, m\rangle$	$2\varepsilon_d + \frac{U}{2}$	3
$ 2, 0, 0\rangle_- = a_2 2, 0, 0\rangle_0 + \frac{a_1}{\sqrt{2}}[ 2, 0, 0\rangle_1 +  2, 0, 0\rangle_2]$	$2\varepsilon_d + \frac{U}{2} + \frac{1}{4}[U - 2\Delta(t, \frac{U}{2})]$	1

where

$$a_1^2 = \frac{1}{\Delta(t, \frac{U}{2})} \frac{\Delta(t, \frac{U}{2}) - \frac{U}{2}}{2} \quad a_2^2 = \frac{4t^2}{\Delta(t, \frac{U}{2})} \frac{2}{(\Delta(t, \frac{U}{2}) - \frac{U}{2})}$$

These states have the same form as in the case of the Hubbard dimer, but the ground state energy and the values of  $a_1$  and  $a_2$  are different. Finally, for  $N = 3$  electrons, the eigenstates are

$ 3, S, S_z\rangle_\alpha$	$E_\alpha(3, S)$	$d_\alpha(3, S)$
$ 3, 1/2, \sigma\rangle_+ = \alpha_2 1, 1/2, \sigma\rangle_1 + \alpha_1 1, 1/2, \sigma\rangle_2$	$3\varepsilon_d + U + \frac{1}{4}[U + \Delta(t, U)]$	2
$ 3, 1/2, \sigma\rangle_- = \alpha_1 1, 1/2, \sigma\rangle_1 - \alpha_2 1, 1/2, \sigma\rangle_2$	$3\varepsilon_d + U + \frac{1}{4}[U - \Delta(t, U)]$	2

## References

- [1] K.F. Sundman, *Acta Mathematica* **36**, 105 (1912)
- [2] F. Diacu, *The Mathematical Intelligencer* **18**, 66 (1996)
- [3] Y.N. Harari, *Homo Deus: A Brief History of Tomorrow*, Harvill Secker, Penguin Random House UK (2016)
- [4] W. Metzner and D. Vollhardt, *Phys. Rev. Lett.* **62**, 324 (1989)
- [5] E. Müller-Hartmann, *Z. Phys. B* **74**, 507 (1989);  
*Z. Phys. B* **76**, 211 (1989); *Int. J. Mod. Phys. B* **3**, 2169 (1989)
- [6] A. Georges and G. Kotliar, *Phys. Rev. B* **45**, 6479 (1992)
- [7] M. Jarrell, *Phys. Rev. Lett.* **69**, 168 (1992)
- [8] E. Pavarini, E. Koch, R. Scalettar, R. Martin (Eds):  
*The Physics of Correlated Insulators, Metals, and Superconductors*,  
Reihe Modeling and Simulation, Vol. 7 (Forschungszentrum Jülich, 2017)  
<http://www.cond-mat.de/events/correl17>
- [9] E. Koch, G. Sangiovanni, and O. Gunnarsson, *Phys. Rev. B* **78**, 115102 (2008)
- [10] A. Flesch, E. Gorelov, E. Koch, E. Pavarini, *Phys. Rev. B* **87**, 195141 (2013)
- [11] A. Kiani and E. Pavarini, *Phys. Rev. B* **94**, 075112 (2016)
- [12] E. Pavarini, E. Koch, A. Lichtenstein, D. Vollhardt (Eds.):  
*The LDA+DMFT approach to strongly-correlated materials*,  
Reihe Modeling and Simulation, Vol. 1 (Forschungszentrum Jülich, 2011)  
<http://www.cond-mat.de/events/correl11>
- [13] E. Pavarini, E. Koch, A. Lichtenstein, D. Vollhardt (Eds.):  
*DMFT at 25: Infinite Dimensions*,  
Reihe Modeling and Simulation, Vol. 4 (Forschungszentrum Jülich, 2014)  
<http://www.cond-mat.de/events/correl14>
- [14] E. Pavarini, A. Yamasaki, J. Nuss, and O.K. Andersen,  
*New. J. Phys* **7**, 188 (2005)
- [15] N. Marzari, A.A. Mostofi, J.R. Yates, I. Souza, and D. Vanderbilt,  
*Rev. Mod. Phys.* **84**, 1419 (2012)
- [16] G. Zhang and E. Pavarini, *Phys. Status Solidi RRL*, 1800211 (2018)

- 
- [17] E. Pavarini, S. Biermann, A. Poteryaev, A.I. Lichtenstein, A. Georges, and O.K. Andersen, Phys. Rev. Lett. **92**, 176403 (2004)
  - [18] O. Gunnarsson, E. Koch, and R.M. Martin, Phys. Rev. B **56**, 1146 (1996)
  - [19] E. Koch, O. Gunnarsson, and R.M. Martin, Phys. Rev. B **60**, 15714 (1999)
  - [20] See L. de' Medici, *Hund's Metals Explained*, in Ref. [8]
  - [21] G. Zhang, E. Gorelov, E. Sarvestani, and E. Pavarini, Phys. Rev. Lett. **116**, 106402 (2016)
  - [22] A. Damascelli, D.H. Lu, K.M. Shen, N.P. Armitage, F. Ronning, D.L. Feng, C. Kim, Z.-X. Shen, T. Kimura, Y. Tokura, Z.Q. Mao, and Y. Maeno, Phys. Rev. Lett. **85**, 5194 (2000)
  - [23] E. Sarvestani, G. Zhang, E. Gorelov, and E. Pavarini, Phys. Rev. B **97**, 085141 (2018)

# **8 Determining Orbital Wavefunctions using Core-Level Non-Resonant Inelastic X-Ray Scattering**

Liu Hao Tjeng

Max-Planck Institute for Chemical Physics of Solids

Nöthnitzer Str. 40, 01187 Dresden

## **Contents**

<b>1</b>	<b>Introduction</b>	<b>2</b>
<b>2</b>	<b>Non-resonant inelastic scattering (NIXS)</b>	<b>3</b>
<b>3</b>	<b>The local ground state wavefunction of <math>\text{CeB}_6</math></b>	<b>6</b>
<b>4</b>	<b>The local ground state wavefunction of intermediate valent <math>\text{SmB}_6</math></b>	<b>11</b>
<b>5</b>	<b>Discussion and concluding remarks</b>	<b>16</b>

# 1 Introduction

The spectacular physical properties often observed in materials containing transition-metal and rare-earth elements challenge our comprehension of solid-state physics. Their properties include superconductivity, unusually large magneto-resistance, metal-insulator transitions, heavy-fermion behavior, multi-ferroicity, and phenomena involving topologically protected states. We would like to understand how the electrons in these materials interact with each other so that they generate those unusual quantum phenomena. From a theoretical point of view it is clear that the equations we have to solve are so complicated that we will not be able to obtain exact solutions. In addition, to make things worse but also more fascinating, tiny changes in temperature, pressure, or the material's composition may cause large changes of their properties. Hence, it appears that there are many solutions available that are very close in energy.

With exact solutions out of reach, the objective is then to find smart approximations by which we can capture the essential physics to describe the *correlated* motion of the electrons in such materials. Experiments are necessary to determine which aspects of the electronic and lattice degrees of freedom are the important ones. Although conceptually clean and beautiful, theoretical simplifications in terms of, for instance, a Heisenberg model or a single band Hubbard model turn out to be inadequate. It now becomes more and more clear that the interplay between the relevant charge, orbital, and spin degrees of freedom of the transition metal and rare earth ions involved determines the intricate balance between band formation and electron correlation effects. This is shown very vividly, for example, for the metal-insulator-transitions taking place in  $V_2O_3$ ,  $Ca_{2-x}Sr_xRuO_4$ ,  $VO_2$ , and  $Ti_2O_3$  [1–8]. It may very well be that we need to develop and use different approximations for different materials or properties.

While a variety of experimental techniques are available to determine the relevant spin and charge quantum numbers, the detection of the active orbital wave functions remains a rather delicate endeavor. The standard experimental technique for  $4f$  systems is inelastic neutron scattering [9–13], but the analysis of magnetic intensities is often hampered by broadened lines, phonons in the same energy window as the magnetic excitations, or strong absorption of one of the sample's constituents (e.g. Rh, In, B, or Sm). For transition metal ions, the energy scale of the local excitations is usually much too large for neutrons. Another experimental method is x-ray absorption spectroscopy on single crystals, where the polarization dependence of the dipole-allowed core-level excitations, e.g.,  $2p \rightarrow 3d$  or  $3d \rightarrow 4f$  transitions, encodes the desired information concerning the orbital wave function [1, 2, 6, 8, 14–18].

However, this method which is based on dipolar electronic transitions has the limitation that symmetries with higher than twofold rotational symmetry cannot be detected (unless it is accompanied by a sufficiently large energy difference), e.g., for cubic systems.

We will present here the opportunities provided by a new x-ray technique, namely core-level non-resonant inelastic x-ray scattering (NIXS). This photon-in photon-out technique with hard x-rays has become feasible thanks to the high brilliance of modern synchrotrons and advanced instrumentation. The available large momentum transfers allow studying excitations that are dipole forbidden. These so-called *beyond dipole* or *multipolar* excitations contain extra infor-



mation, thus enabling us to obtain very detailed insight into the ground-state symmetry of the ion of interest. The interpretation of the spectra is straightforward and quantitative, facilitated also by the fact that the multipolar excitations are more excitonic than the dipole ones. Experimentally, NIXS comes also with the advantage that it is a bulk sensitive technique thanks to the large penetration depth of the hard x-rays used, meaning that there is no need to use ultra-high vacuum or special surface preparation procedures as commonly employed in more surface sensitive probes like soft-x-ray absorption or photoelectron spectroscopies. With the hard x-ray beams typically having a spot size of 50  $\mu\text{m}$  or smaller, NIXS allows also the measurement of much smaller samples than typically required for neutron experiments. In addition, NIXS is suitable for high pressure experiments, pressure being an important tuning parameter when studying phase diagrams.

We will discuss our case for the example of  $\text{SmB}_6$ , a material currently under intense investigation because of the expectation that it may be the first strongly correlated system that has non-trivial topological properties. The manuscript is organized as follows: We first describe the basic principles of the spectroscopic method NIXS. We then apply the method to  $\text{CeB}_6$ , which is a well studied material having the same crystal structure as  $\text{SmB}_6$ . Our objective here is to demonstrate that NIXS is indeed able to determine unambiguously and correctly the local ground state wave function in a cubic system. Finally, we present the NIXS results on  $\text{SmB}_6$ , which carries also the complication of having an intermediate valence state. We will show the consequences of our findings, not only for the experimental search for the properties of the topological surface states but, above all, for the theoretical modeling of this complex strongly correlated system.

## 2 Non-resonant inelastic scattering (NIXS)

The theoretical description of inelastic x-ray scattering can be found in a number of publications, see e.g. [19–27]. The double differential cross-section is the product of the Thomson photon cross section  $\left(\frac{d\sigma}{d\Omega}\right)_{\text{Tho}}$  and the dynamical structure factor  $S(\vec{q}, \omega)$

$$\frac{d^2\sigma}{d\Omega d\omega} = \left(\frac{d\sigma}{d\Omega}\right)_{\text{Tho}} S(\vec{q}, \omega). \quad (1)$$

The dynamical structure factor is a function of the scattering vector  $\vec{q} = \vec{k}_i - \vec{k}_f$  and the energy loss  $\omega = \omega_i - \omega_f$

$$S(\vec{q}, \omega) = \sum_f |\langle f | e^{i\vec{q} \cdot \vec{r}} | i \rangle|^2 \delta(\hbar\omega_i - \hbar\omega_f - \hbar\omega). \quad (2)$$

Here  $i$  and  $f$  are the initial and final states. The transition operator  $e^{i\vec{q} \cdot \vec{r}}$  can be expanded in semi-normalized (Racah's normalization) spherical harmonics  $C_{km}^{\hat{q}}$  and  $C_{km}^{\hat{r}}$ . This results in a sum over spherical Bessel functions  $j_k(\vec{q} \cdot \vec{r})$  and the wave functions can be factorized into a radial and angular part so that  $S(\vec{q}, \omega)$  can be written as

$$S(\vec{q}, \omega) = \sum_f \left| \sum_k i^k (2k+1) \langle R_f | j_k(\vec{q} \cdot \vec{r}) | R_i \rangle \sum_{m=-k}^k \langle \phi_f | C_{km}^{\hat{q}} C_{km}^{\hat{r}} | \phi_i \rangle \right|^2 \times \delta(\hbar\omega_i - \hbar\omega_f - \hbar\omega). \quad (3)$$

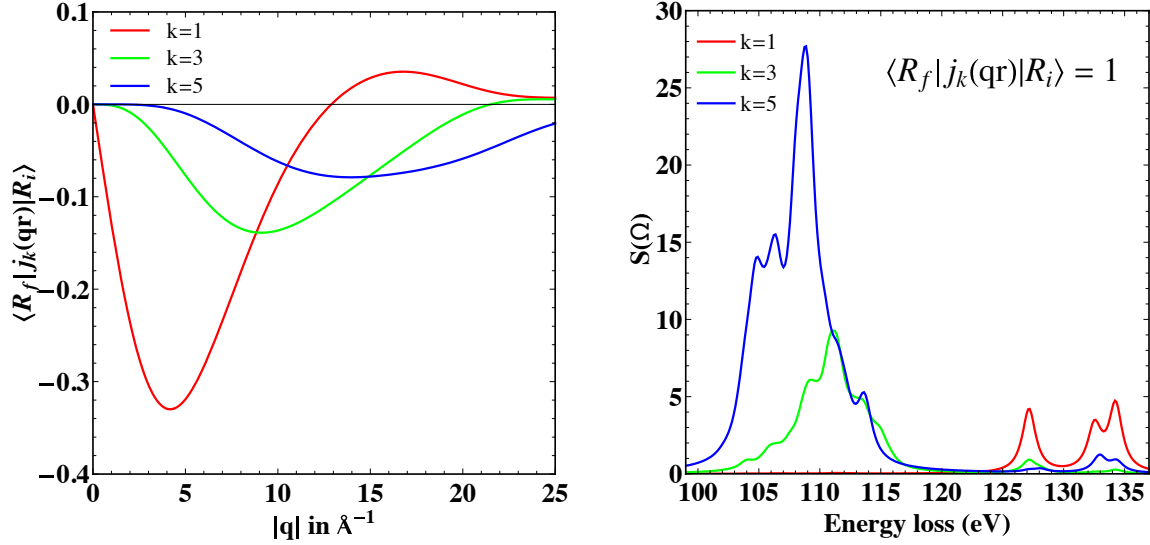


**Fig. 1:** Left:  $k^{\text{th}}$  order term of the radial part of  $S(\vec{q}, \omega)$  for a Ce  $4f^1$  ion as a function of momentum transfer. Right:  $k^{\text{th}}$  order contribution of the angular part of the scattering function expressed in terms of  $S(\omega)$  versus energy transfer for  $\langle R_f | j_k(\vec{q} \cdot \vec{r}) | R_i \rangle = 1$ , see Eq. (3).

Let us consider the  $4d \rightarrow 4f$  ( $N_{4,5}$ ) core-level transitions for rare-earth ions. Due to the triangle condition and parity selection rules, only terms with  $k=1$  (dipole), 3 (octupole), and 5 (triakontadipole) contribute. The radial part  $\langle R_f | j_k(\vec{q} \cdot \vec{r}) | R_i \rangle$  of the wave functions have been calculated for a Ce  $4f^1$  ion within the Hartree-Fock approximation using Cowan's code [28] and the  $k^{\text{th}}$  contributions are shown as function of momentum transfer  $|\vec{q}|$  in the left panel of Fig. 1. For moderate magnitudes of  $|\vec{q}|$  the radial part is dominated by dipole scattering, but already at  $5 \text{ \AA}^{-1}$  octupole scattering is non-negligible, and at even higher momentum transfers the scattering is dominated by the higher multipoles. This behavior is commonly called  $q$ -dependent multipole selection rules. The right panel of Fig. 1 shows the  $k^{\text{th}}$  order of the angular part as function of energy loss. Higher multipoles have different selection rules so that extra intensity at different energy losses becomes visible in the angular part, when at large  $|\vec{q}|$  octupole and triakontadipole transitions take place.

Having described the  $|\vec{q}|$  dependence of the NIXS intensities, we now focus on the vector  $\hat{q}$  dependence which is at the heart of our study. We first of all show the sensitivity of NIXS at the  $N_{4,5}$  edge to anisotropies in the wave function in general, by comparing simulated spectra for different directions of  $\hat{q}$ . These anisotropies arise, for example, when the initial and final states in Eq. (3) are eigenstates of a Hamiltonian that contains in addition to the atomic Coulomb and spin-orbit interactions also crystal-field terms.

We note that the interference terms which vanish if the angular intensity is integrated over all directions  $\hat{q}$  [25, 26] are included in our calculations. Figure 2 shows the simulation of  $S(\vec{q}, \omega)$  for large momentum transfers for the three pure  $J_z$  states of a  $J = 5/2$  ion like  $\text{Ce}^{3+}$  with one  $f$  electron ( $f^1$  configuration). Some realistic broadening due to life time and instrumental resolution has been considered (see below). Here [001] is the quantization axis. The pure states have rotational symmetry perpendicular to the quantization axis so that we compare so-called in-plane scattering ( $\hat{q} \parallel [100]$ ) with scattering out-of-plane, i.e., for  $\hat{q} \parallel [001]$  and some direction

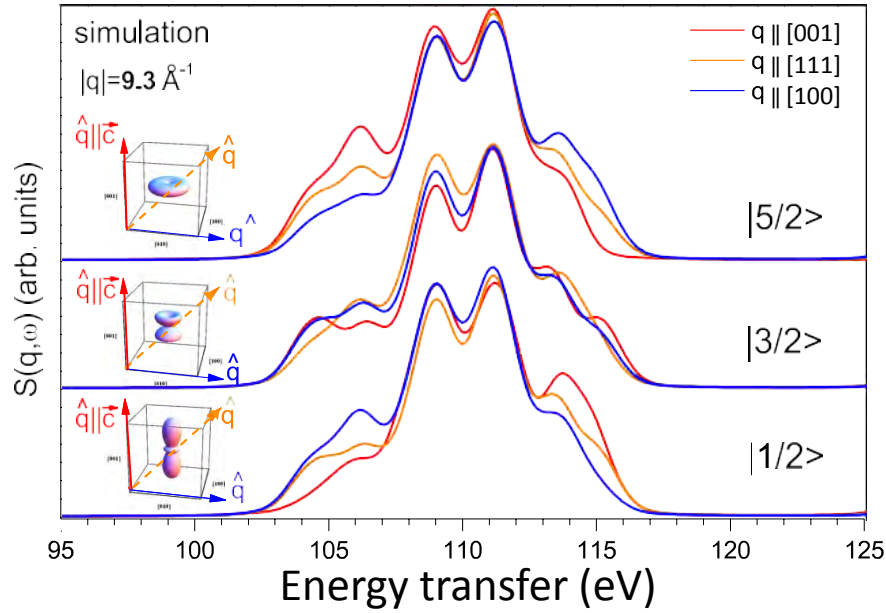


**Fig. 2:** Simulations for a  $Ce\ 4f^1$  ion: Comparison of the in-plane and out-of-plane scattering function  $S(\vec{q}, \omega)$  of pure  $J_z$  states, in-plane  $\hat{q} \parallel [100]$  (blue), out-of-plane  $\hat{q} \parallel [001]$  (red), and in between  $\hat{q} \parallel [111]$  (orange). The calculations are for  $|\vec{q}| = 9.3\ \text{\AA}^{-1}$  and are convoluted with a Lorentzian with  $FWHM=0.3\ \text{eV}$  and a Gaussian with  $FWHM=1.32\ \text{eV}$ . Adapted from Ref. [27]

in between ( $\hat{q} \parallel [111]$ ). There is a clear directional dependence, so that the different  $J_z$  states are distinguishable. This is at first sight similar or analogous to the in-plane/out-of-plane polarization dependence in soft x-ray absorption at the cerium  $M_{4,5}$  edge ( $3d \rightarrow 4f$ ) [18, 29]. However, on a closer look one can observe that the spectrum for ( $\hat{q} \parallel [111]$ ) can not be expressed as a linear combination of the  $\hat{q} \parallel [100]$  and  $\hat{q} \parallel [001]$  spectra. This shows that the directional dependence in NIXS contains more information than the polarization dependence in XAS.

A nice demonstration that NIXS provides more information than XAS is given by the study by Willers *et al.* [27]. Let us consider a  $Ce\ 4f^1$  ion in a tetragonal crystal field. The sixfold degenerate Hund's rule ground state of  $Ce^{3+}$  ( $J = 5/2$ ) is split into three Kramer's doublets and the eigenfunctions can be represented in the basis of  $|J_z\rangle$  when the fourfold symmetric tetragonal [001] axis is chosen as quantization axis. There are two  $\Gamma_7$  doublets  $\Gamma_7^1 = \alpha|\pm 5/2\rangle + \sqrt{1 - \alpha^2}|\mp 3/2\rangle$  and  $\Gamma_7^2 = \sqrt{1 - \alpha^2}|\pm 5/2\rangle - \alpha|\mp 3/2\rangle$ , and one  $\Gamma_6$  which is a pure  $|\pm 1/2\rangle$  doublet. The  $\Gamma_6$  as a pure  $|\pm 1/2\rangle$  has full rotational symmetry around [001] but the mixed  $\Gamma_7$  states do not. Both  $\Gamma_7$  states have a fourfold symmetry around [001] and for a given spatial distribution of the two  $\Gamma_7$  states there are two solutions which differ in their orientations within the (001) plane by  $45^\circ$ . Which orientation applies to the ground state depends on the sign of  $\alpha$ . For  $\alpha > 0$  the wings of a  $\Gamma_7$  ground state point along [100] and for  $\alpha < 0$  along [110]. The situation for  $\alpha = -0.68 < 0$  is depicted in Fig. 3, together with the corresponding NIXS spectra calculated for  $\hat{q} \parallel [100]$  and  $\hat{q} \parallel [110]$ . It clearly shows that the two spectra are distinguishable and a NIXS experiment (see Ref. [27]) has proven the feasibility. In XAS the situation is very different. The signal in XAS is purely dipole and can therefore not give any insight into the orientation of these fourfold rotational invariant orbitals; the spectra look identical for any polarization perpendicular to the  $c$ -axis.

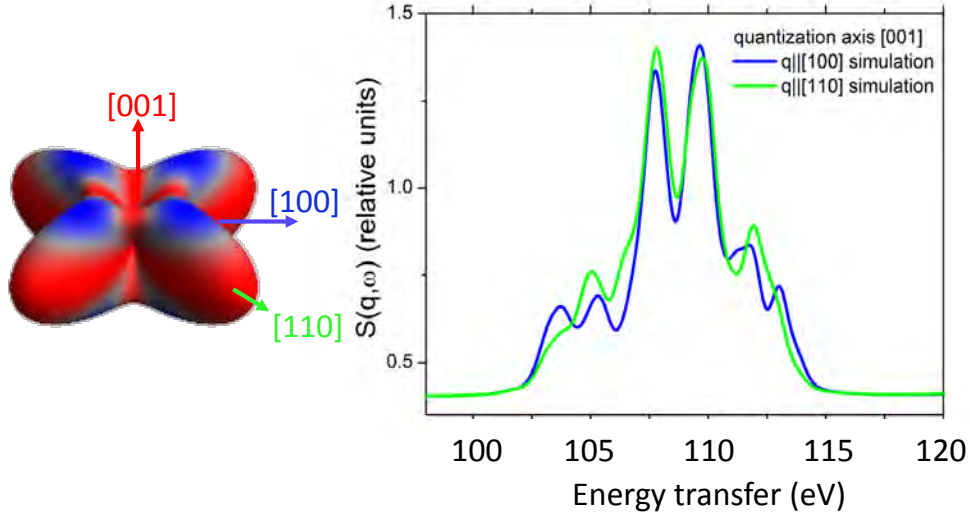


**Fig. 3:** *Simulation (top): The scattering function  $S(\vec{q}, \omega)$  for two in-plane directions  $\hat{q}||[100]$  (blue) and  $\hat{q}||[110]$  (green) assuming a  $\Gamma_7^1 = \alpha|\pm 5/2\rangle + \sqrt{1-\alpha^2}|\pm 3/2\rangle$  ground state for a Ce  $4f^1$  ion in a tetragonal crystal field with  $\alpha < 0$ . The calculations are convoluted with a Lorentzian with FWHM=0.3 eV and a Gaussian with FWHM=0.7 eV.*

We note that for a  $45^\circ$  rotation around the  $c$ -axis [001], i.e., for a positive value of  $\alpha$ , the NIXS spectra are inverted. We found that these in-plane NIXS spectra are fairly insensitive to the precise value of  $\alpha$  as long as  $\alpha$  is neither zero nor one. In the latter case the orbital would have full rotational symmetry around [001] and consequently  $S(\vec{q}, \omega)$  would look the same for both in-plane directions.

To conclude this section, NIXS is a spectroscopic method that can determine the active local orbital wave function with great detail due to the fact that higher than dipole transitions are utilized if the measurement is carried out with high momentum transfers.

### 3 The local ground state wavefunction of $\text{CeB}_6$

The material class of rare earth hexaborides has attracted considerable attention over the years. It comprises of a variety of different fascinating ground states (see Ref. [30] and references therein) which include exotic magnetically ordered phases, heavy fermion behavior, as well as Kondo insulating ground states.  $\text{CeB}_6$  is an important member of this material class and has been intensively studied for its rich magnetic phase diagram [31]. It crystallizes in the cubic CsCl structure. Fig. 4 displays how the crystal-electric field splits the sixfold degenerate  $j = 5/2$  multiplet state of the Ce  $4f^1$  into a  $\Gamma_8$  quartet and  $\Gamma_7$  doublet.

Upon cooling  $\text{CeB}_6$  enters a hidden-order phase at 3.2 K followed by an antiferromagnetic phase below 2.4 K. The application of an external field induces a dipole component with the wave vector of the quadrupolar ordering [33]. Theory suggests that the multipolar moments of the localized  $4f$  electrons interact with each other via the itinerant  $5d$  conduction electrons, breaking up the fourfold ground-state degeneracy of the Ce  $4f$  wave function in the cubic crystal field stabilizing an antiferro-quadrupolar (AFQ) order [34, 35], a conjecture that by now

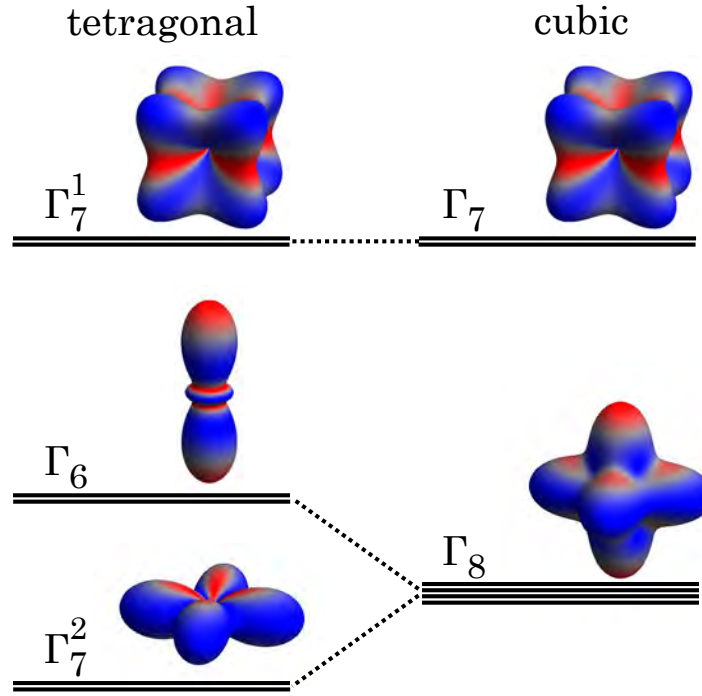


**Fig. 4:** Electron density plots for an  $f$ -electron in  $\text{Ce}^{3+}$ , left for tetragonal and right for cubic point symmetry. For tetragonal symmetry the crystal-field states expressed in  $J_z$  representation are  $\Gamma_6 = |\pm 1/2\rangle$ ,  $\Gamma_7^1 = \alpha|\pm 5/2\rangle - \sqrt{1-\alpha^2}|\mp 3/2\rangle$  and  $\Gamma_7^2 = \sqrt{1-\alpha^2}|\pm 5/2\rangle + \alpha|\mp 3/2\rangle$  with  $\alpha^2 \leq 1$ ; for cubic symmetry  $\alpha = \sqrt{1/6}$  so that  $\Gamma_7^1 = \sqrt{1/6}|\pm 5/2\rangle - \sqrt{5/6}|\mp 3/2\rangle$  and  $\Gamma_8 = (|\pm 1/2\rangle; \sqrt{5/6}|\pm 5/2\rangle + \sqrt{1/6}|\mp 3/2\rangle)$ . Figure adapted from Ref. [32]

has received credibility from studies using resonant x-ray diffraction [36, 37], inelastic neutron scattering [38–40], and electron spectroscopy [41, 42].

The quartet ground state had been originally deduced from an unusual low temperature shift of the crystal-field excitation at 46 meV in Raman and inelastic neutron scattering data [43, 44]. The energy shift was interpreted as a splitting of the quartet ground state in the low temperature phase in accordance with electron paramagnetic resonance (EPR) measurements [45]. A quartet ground state is also consistent with findings of the magnetic anisotropy [46], magnetic neutron form factor measurements [47], as well as x-ray diffraction (XRD) measurements of the electron density distribution at low temperatures and 300 K [48] with the claim that a level inversion may occur at higher temperatures [49].

Our objective now is to apply NIXS on this cubic system in the paramagnetic phase using the  $\text{Ce } N_{4,5} (4d \rightarrow 4f)$  excitation and to verify that the local ground state wave function is indeed the quartet  $\Gamma_8$ .

The NIXS measurements were performed at the beamline P01 of PETRA-III. The incident energy was selected with a Si(311) double monochromator. The P01 NIXS end-station has a vertical geometry with twelve Si(660) 1 m radius spherically bent crystal analyzers that are arranged in  $3 \times 4$  array (see Fig. 5). The fixed final energy was 9690 eV. The analyzers were positioned at scattering angles of  $2\theta \approx 150^\circ$ ,  $155^\circ$ , and  $160^\circ$  which corresponds at elastic scattering

## Inelastic X-ray Scattering geometry

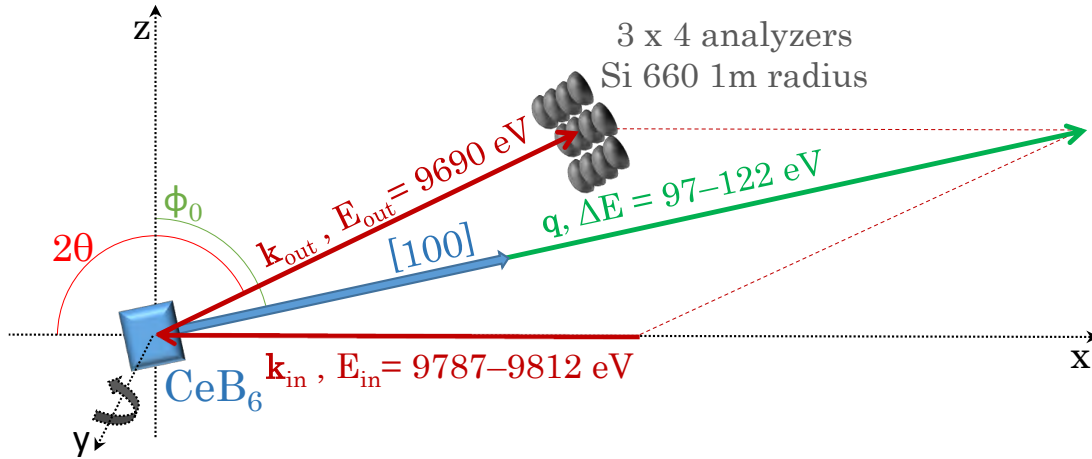


**Fig. 5:** Scattering geometry of the NIXS experiment for a typical  $N_{4,5}$  edge scan with  $\hat{q} \parallel [100]$ . Figure adapted from Ref. [32].

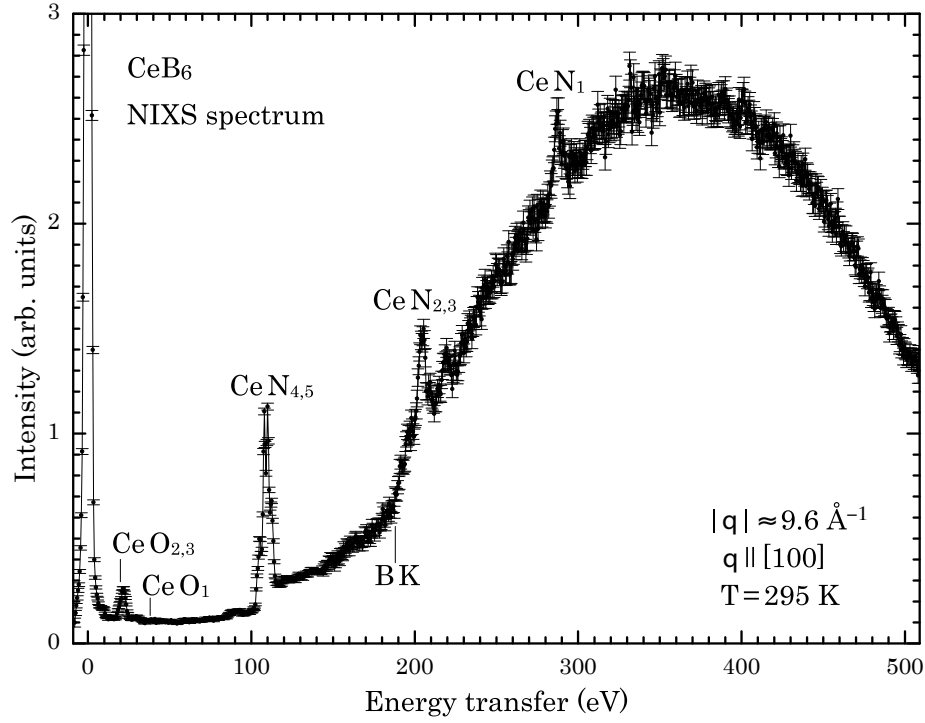
to an averaged momentum transfer of  $|\vec{q}| = (9.6 \pm 0.1) \text{ \AA}^{-1}$ . The scattered beam was detected by a position sensitive detector. The instrumental energy resolution was  $\approx 0.7 \text{ eV}$ . A sketch of the scattering geometry, showing the incoming and outgoing photons as well as the transferred momentum  $|\vec{q}|$ , is given in Fig. 5 for a scan with  $\hat{q} \parallel [100]$  in specular geometry. In order to realize another crystallographic direction, e.g.,  $\hat{q} \parallel [110]$ , the sample can be turned with respect to the scattering triangle, or a different sample with another polished surface may be mounted in specular geometry.

Figure 6 shows the NIXS spectrum across the Ce  $N_{4,5}$  ( $4d \rightarrow 4f$ ),  $N_{2,3}$  ( $4p \rightarrow 4f$ ), and  $N_1$  ( $4s \rightarrow 4f$ ) edges. The clear presence of the  $N_{2,3}$  and  $N_1$  edges demonstrates unambiguously that higher than dipole transition operators are active here. The accompanying Compton contribution has its maximum at about 350 eV energy transfer. It is important to note that the Ce white lines are clearly discerned from the Compton scattering, and that especially the Ce  $N_{4,5}$  white lines stand out with an excellent signal to background ratio, i.e.,  $N_{4,5}$  NIXS is an extremely powerful spectroscopic method.

The bottom set of curves in the top panel of Fig. 7 shows the Ce  $N_{4,5}$  NIXS spectra of CeB<sub>6</sub> (dots) taken at 17 K, for the three momentum directions  $\hat{q} \parallel [100]$  (black dots),  $\parallel [110]$  (green dots), and  $\parallel [111]$  (red dots). The temperature of 17 K is low enough to assure that only the local ground state is populated since the excited crystal-field state is at 46 meV [43, 44]. A constant background has been subtracted to account for the (weak) Compton signal (about 12% of the signal peak) (see Fig. 6).

There is a clear directional dependence that shows up strongest in the energy interval of 103 to 106 eV. Especially the  $\hat{q} \parallel [100]$  direction differs from the  $\hat{q} \parallel [110]$  and  $[111]$ . We can obtain a more detailed view of the directional dependence by constructing the difference spectra  $I_{\hat{q} \parallel [100]} - I_{\hat{q} \parallel [110]}$  that is displayed as dichroism in the bottom panel of Fig. 7 (black dots).

The Ce  $N_{4,5}$  NIXS data are simulated by calculating the  $4d^{10}4f^1 \rightarrow 4d^94f^2$  transition using the



**Fig. 6:** Experimental NIXS spectra of  $\text{CeB}_6$ : a wide scan covering the  $\text{Ce O}_5$ ,  $N_{4,5}$ ,  $N_{2,3}$ , and  $N_1$  edges, the  $BK$  edge as well as the Compton signal. The direction of momentum transfer is  $\hat{q} \parallel [100]$ . Figure adapted from Ref. [32].

full multiplet code *Quanty* [50] which includes Coulomb as well as spin-orbit interactions. A Gaussian and a Lorentzian broadening of  $\text{FWHM} = 0.7 \text{ eV}$  and  $0.4 \text{ eV}$ , respectively, are used to account for the instrumental resolution and life time effects. The atomic Hartree-Fock values were adjusted via the peak positions, resulting in reductions of 30 % and 22 % for the  $4f$ - $4f$  and  $4d$ - $4f$  Coulomb interactions, respectively. The reduction accounts for configuration-interaction effects not included in the Hartree-Fock scheme [16]. A momentum transfer of  $|\vec{q}| = 9.2 \text{ \AA}^{-1}$  has been used for the simulations (and not the experimental value of  $9.6 \pm 0.1 \text{ \AA}^{-1}$ ) so that the experimental peak ratio of the two main features around 108 and 110 eV is reproduced best. This fine tuning optimizes the multipole contributions to the scattering functions to mimic a minor adjustment of the calculated radial wave functions of the  $\text{Ce}^{3+}$  atomic wave function (see e.g. Ref. [27]).

We now compare the measured spectra and the dichroism therein with the simulations for the two possible scenarios, namely one with the  $\Gamma_7$  doublet as ground state and the other with the  $\Gamma_8$  quartet. The results are plotted in Fig. 7(a). The  $\Gamma_8$  quartet scenario reproduces in great detail the experimental spectra for all three  $\hat{q}$  directions. In contrast, the simulation based on the  $\Gamma_7$  doublet exhibits large discrepancies with respect to the experiment: the intensities of several features in the spectra are not correct. To make the difference between the two scenarios even more contrasting, we compare the experimental and calculated dichroic spectra, i.e.  $I_{\hat{q} \parallel [100]} - I_{\hat{q} \parallel [110]}$ , as displayed in bottom panel (b). There is an excellent match for the  $\Gamma_8$  quartet ground state scenario but a large mismatch for the  $\Gamma_7$  doublet. From these comparisons we can unambiguously conclude that the  $\Gamma_8$  quartet forms the ground state in  $\text{CeB}_6$ .



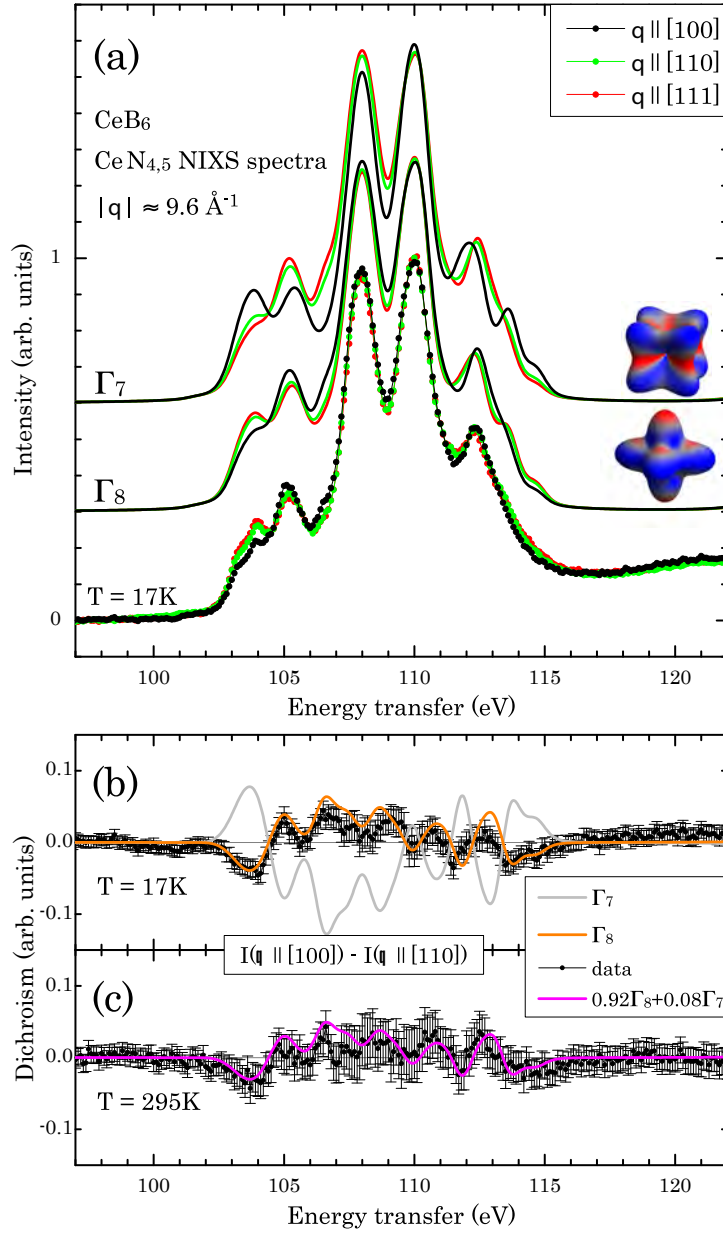


**Fig. 7:** Top panel (a): calculated and experimental NIXS spectra of the Ce  $N_{4,5}$ -edge of  $CeB_6$  for the three transferred momentum directions  $\hat{q} \parallel [100]$ ,  $[110]$ , and  $[111]$ . Bottom panel: difference spectra  $I(\hat{q} \parallel [100]) - I(\hat{q} \parallel [110])$  (black dots) (b) at low  $T$  and (c) at room temperature and respective simulations (see text). Figure adapted from Ref. [32].

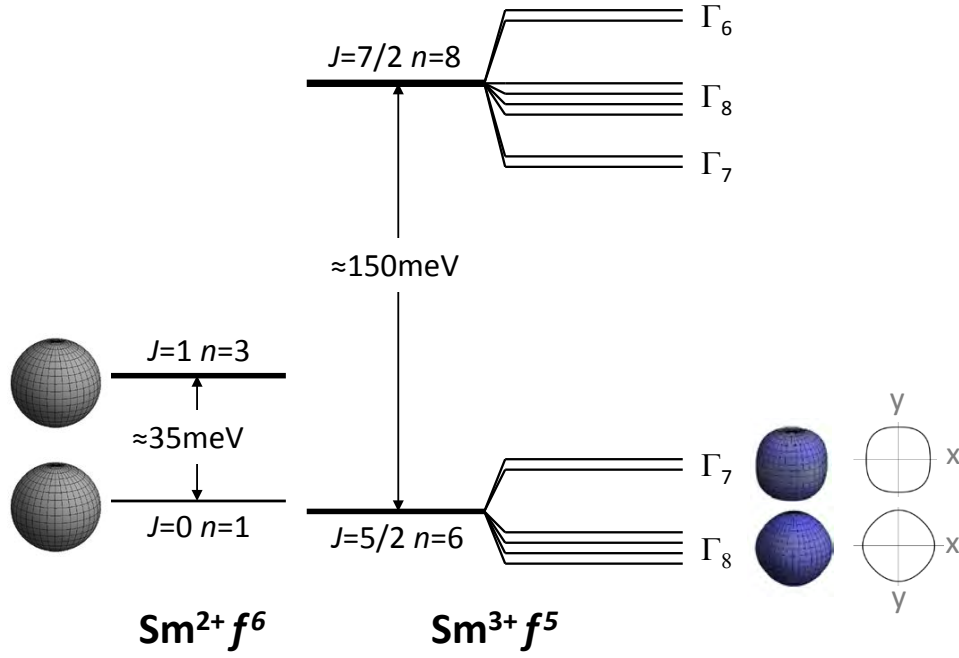
We have also taken spectra at  $T = 295\text{ K}$ . The spectra look very similar to the low temperature data but the dichroism is reduced by about 20%, see bottom panel (c) of Fig. 7. This reduction in the dichroism is fully consistent with a partial population of the excited  $\Gamma_7$  state at 46 meV. A simulation in which the Boltzmann weighted contributions of the  $\Gamma_8$  and  $\Gamma_7$  states are taken into account is represented by the magenta line in panel (c) of Fig. 7. The excellent agreement provides yet another evidence for the thorough understanding we have obtained using NIXS on the Ce  $4f$  symmetry and crystal-electric field effects in  $CeB_6$ .



## 4 The local ground state wavefunction of intermediate valent $\text{SmB}_6$

Having established that core-level NIXS is a powerful and reliable spectroscopic method to determine the local ground state wavefunction for  $\text{CeB}_6$ , we are now ready to tackle the puzzle of  $\text{SmB}_6$ . The intermediate valent and Kondo insulator  $\text{SmB}_6$  [51–55] has attracted considerable attention recently due to the prediction that this system should be a topological insulator [56–61]. If true,  $\text{SmB}_6$  would be the material to qualify as the first strongly correlated topological insulator. Indeed, the robust metallicity which is attributed to a topologically protected surface state could be a promising explanation for the long-standing mysterious low-temperature residual conductivity of  $\text{SmB}_6$  [53, 54, 62]. Many experimental techniques like angle-resolved photoelectron spectroscopy (ARPES) [63–71], scanning tunneling spectroscopy [72–76], resistivity and surface conductance measurements [77–84] have been applied to unveil its topological properties. A review is given by Ref. [85, 86].

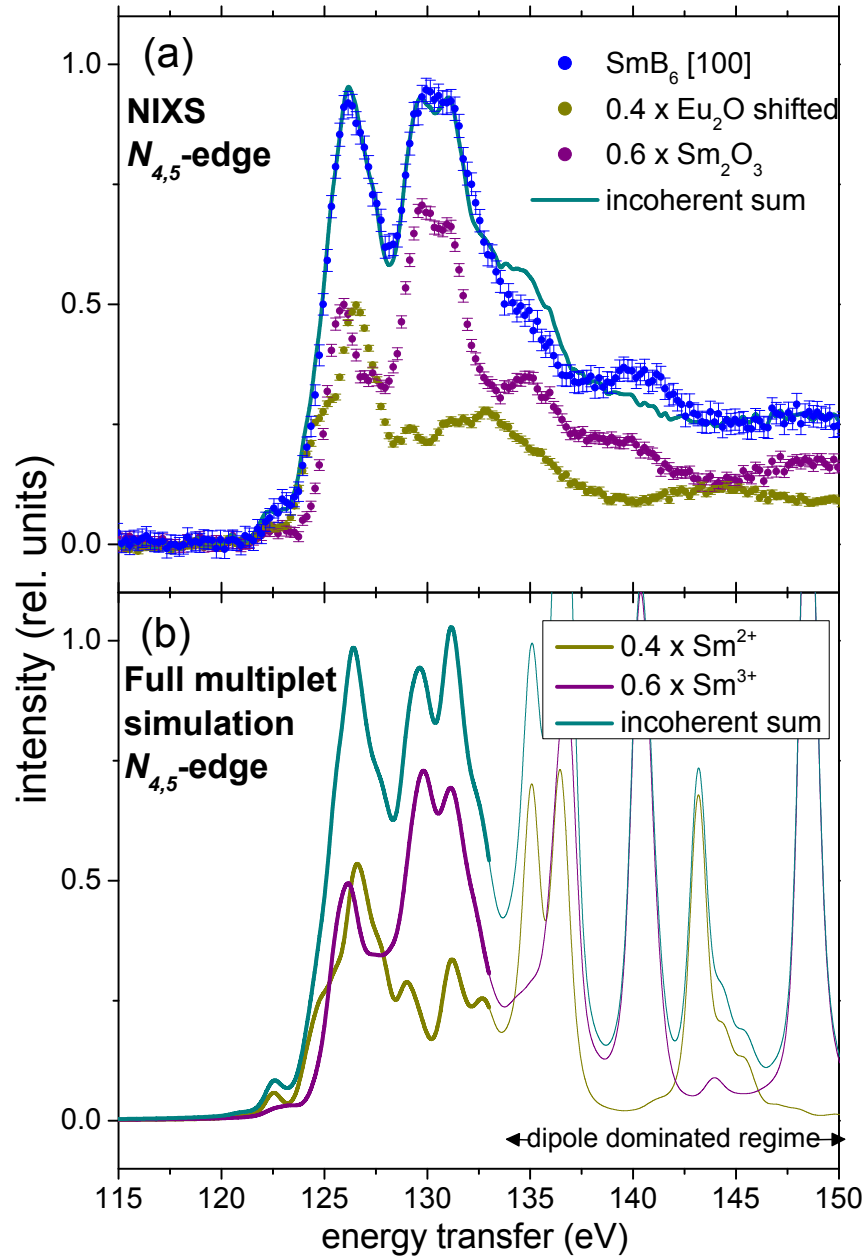
In  $\text{SmB}_6$ , the strong hybridization of the low lying  $4f$  states with conduction band  $d$  states gives rise to a hybridization gap of the order of 20 meV [63–68] and also leads to a partial occupation of the  $4f$  shell or a mixture of the  $\text{Sm } f^6$  ( $2+$ ) and  $f^5$  ( $3+$ ) configurations. For the valence at low temperatures, values of around 2.6 have been determined experimentally [87–93]. Hence the local electronic structure is described by the Hund’s rule ground states of the  $\text{Sm } f^6$  ( $2+$ ) and  $f^5$  ( $3+$ ) configurations with total orbital momenta of  $J = 0$  and  $5/2$ , respectively. The  $J = 5/2$  multiplet is further split into a  $\Gamma_7$  doublet and a  $\Gamma_8$  quartet due to the cubic crystal-electric field (CEF). Fig. 8 shows the ground- and first excited state of the two Sm configurations plus their electron charge density distributions. The charge densities of the  $J = 0$  and 1 states are spherical since neither the  $J = 0$  or 1 are split in a cubic potential [95]. This is contrasted by the charge densities of the CEF-split  $J = 5/2$  multiplet (and  $J = 7/2$ , not shown) that are anisotropic. The CEF scheme of  $\text{SmB}_6$  is however, not established. The classical tool, inelastic neutron scattering, has not been able to identify the CEF states, possibly due to the superposition of both  $\text{Sm } f^5$  and  $f^6$  configurations in this mixed valent compound and the strong neutron absorption despite double isotope samples [10, 11, 96]. A sharp excitation at 14 meV close to the hybridization gap was reported. It was assigned to a spin exciton and not to a CEF excitation since its intensity does not follow the  $4f$  magnetic form factor. Further magnetic intensities at about 35 meV, 115 meV, and 85 meV have been assigned to the inter-multiplet transitions of the  $\text{Sm}^{2+}$  configuration and of the CEF split  $\text{Sm}^{3+}$  configuration (see Fig. 8), and to some magnetoelastic coupling, respectively. In-gap transitions at about 15 meV in Raman spectra could be interpreted as CEF excitations but Raman does not yield the information about which state forms the ground state [97, 98]. A semi-empirical extrapolation method can predict CEF parameters across the rare earth series for highly diluted systems [99]. Applying such an extrapolation to the measured CEF schemes of  $\text{REB}_6$  with  $\text{RE} = \text{Ce}, \text{Pr}, \text{and Nd}$  [43, 100] yields for  $\text{SmB}_6$  a CEF splitting of the order of 15 meV with the  $\Gamma_8$  quartet as the ground state. However, the Kondo insulator  $\text{SmB}_6$  is not a highly diluted system and it is definitely not an ionic system but highly intermediate valent instead, questioning the validity of such an extrapolation.



**Fig. 8:**  $\text{Sm}^{2+}$  and  $\text{Sm}^{3+}$  total energy level diagram. The  $\text{Sm}^{2+}$  configuration is split into a  $J=0$  and  $J=1$ , and the  $\text{Sm}^{3+}$  into a  $J=5/2$  and  $J=7/2$  multiplet. The label  $n$  indicates the degeneracy. The  $\text{Sm}^{3+}$  multiplets are further split ( $\Gamma_i$ ) by the cubic crystal-electric field. The insets show the corresponding charge densities for six and five electrons and their 2D projections, respectively. Figure adapted from Ref. [94].

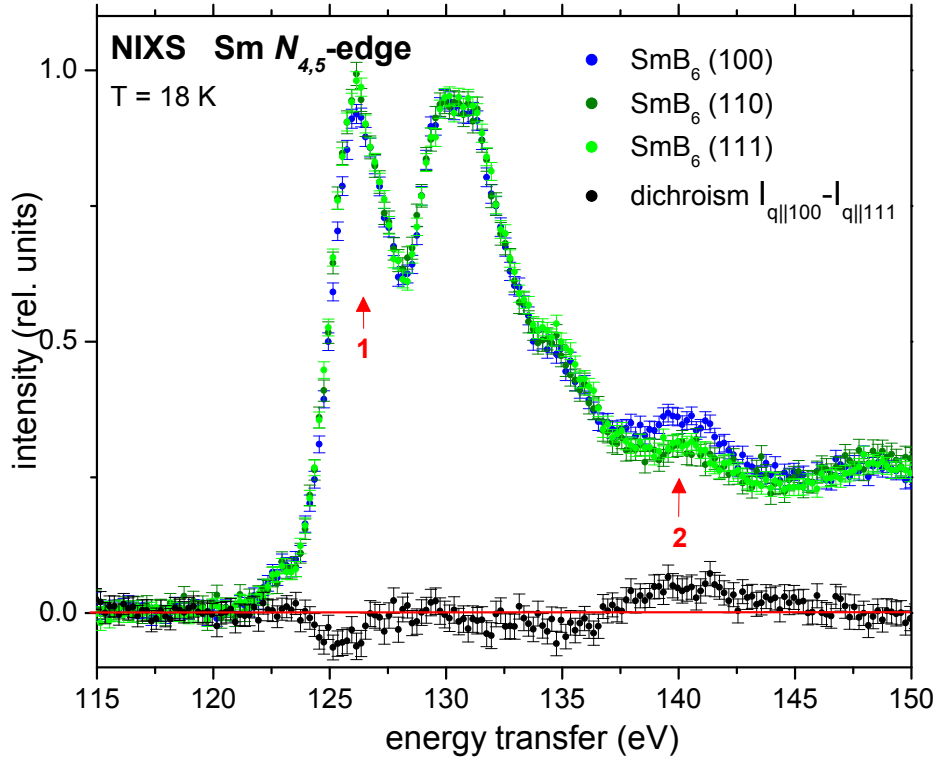
We have carried out  $N_{4,5}$  NIXS experiments on  $\text{SmB}_6$  and also on  $\text{Sm}_2\text{O}_3$ , and  $\text{Eu}_2\text{O}_3$  which we used as  $4f^5$  and  $4f^6$  reference systems, respectively. Fig. 9 shows the spectra:  $\text{SmB}_6$  (blue dots),  $\text{Sm}_2\text{O}_3$  (purple dots) and  $\text{Eu}_2\text{O}_3$  (dark yellow dots) after subtraction of a linear background and scaling to the Compton background. We have artificially shifted the  $\text{Eu}_2\text{O}_3$  spectrum by 6.8 eV to lower energies in order to account for the higher atomic number. We also have multiplied the  $\text{Sm}_2\text{O}_3$  spectrum by a factor 0.6 and the  $\text{Eu}_2\text{O}_3$  one by 0.4. We have done this in order to investigate whether the  $\text{SmB}_6$  spectrum can be interpreted using those of  $\text{Sm}_2\text{O}_3$  and  $\text{Eu}_2\text{O}_3$ . We thus compare the weighted sum of  $\text{Sm}_2\text{O}_3$  and  $\text{Eu}_2\text{O}_3$  (see dark cyan line) with the  $\text{SmB}_6$  spectrum, and we can observe that the weighted sum spectrum provides a satisfactory reproduction. This means that our NIXS data indicates that the Sm valence is about 2.6, in good agreement with other studies using a variety of different experimental methods [87–93].

Fig. 9 (b) shows the  $N_{4,5}$  full multiplet simulation for the  $\text{Sm}^{3+}$  (purple line) and  $\text{Sm}^{2+}$  (dark yellow line). The weighted sum (60% and 40%) of the simulated curves (dark cyan) describes the  $\text{SmB}_6$  spectrum very well in the energy region between 120 and 135 eV. This is the region where the high multipole scattering dominates. In the region above  $\approx 135$  eV, where the spectrum is given mostly by the dipole transitions the simulation produces spectral features that are too sharp with respect to the experiment because the interference with the continuum states is not included in the calculations. The high multipole excitations are more realistically reproduced since they are lower in energy and therefore further away from the continuum states and consequently more excitonic [101].



**Fig. 9:** (a) Experimental  $\text{SmB}_6$  data for  $\hat{q} \parallel [100]$  (blue dots) together with the weighted sum (dark cyan line) of the experimental  $\text{Sm}_2\text{O}_3$  ( $f^5$ ) (purple dots) and energy-shifted experimental  $\text{Eu}_2\text{O}_3$  ( $f^6$ ) (dark yellow dots). (b) Full multiplet simulation of  $\text{Sm}^{3+}$  (purple line) and  $\text{Sm}^{2+}$  spectra (dark yellow line) and their weighted sum (dark cyan). Figure adapted from Ref. [94].

Figure 10 shows the directional dependence of the  $\text{Sm } N_{4,5}$  of  $\text{SmB}_6$ . Although the effect is small, there are clear differences between the spectra in the energy regions marked with red arrows. At about 126 eV energy transfer the scattering of the  $\hat{q} \parallel [110]$  (light green dots) and  $\hat{q} \parallel [111]$  (dark green dots) directions are both stronger than for the  $\hat{q} \parallel [100]$  (blue dots), and at about 140 eV it is opposite. To show these directional differences in a more transparent manner, we also present in Fig. 10 the difference spectrum between the  $\hat{q} \parallel [100]$  and  $\hat{q} \parallel [111]$  (black dots): this so-called dichroic spectrum has unambiguously a negative peak at 126 eV whereas it displays positive intensity in a broader region around 140 eV.



**Fig. 10:**  $\text{SmB}_6$  NIXS data at 18 K for  $\hat{q} \parallel [100]$  (blue dots),  $\hat{q} \parallel [110]$  (dark green dots), and  $\hat{q} \parallel [111]$  (light green dots). The difference spectrum between the  $\hat{q} \parallel [100]$  and  $\hat{q} \parallel [111]$  directions is also displayed (black dots). Figure adapted from Ref. [94].

To interpret the observed directional dependence, it is important to know how each CEF state or multiplet component contributes to the dichroic signal. Therefore,  $S(\vec{q}, \omega)$  has been calculated taking into account a cubic CEF for the  $\text{Sm}^{3+} f^5$  ground state multiplet with  $J = 5/2$  assuming a  $\Gamma_8$  quartet or a  $\Gamma_7$  doublet ground state, and for the  $\text{Sm}^{2+} f^6$  multiplets with  $J = 0$  or  $J = 1$  (see Fig. 8). The calculations were performed for the two directions  $\hat{q} \parallel [100]$  and  $\hat{q} \parallel [111]$  and in Fig. 11 (a) the resulting dichroic signals are plotted. Here only the multipole scattering contributes to the dichroism, the dipole does not because the Sm site symmetry is cubic.

The first important finding is that the  $\text{Sm}^{2+}$  configuration does not show any dichroism at all (see dark red and green lines at zero dichroism) as we would expect for states with spherical charge densities, see Fig. 8. Hence, the observed directional dependence of the signal is solely due to the initial state of the  $\text{Sm}^{3+}$  Hund's rule ground state. The second important finding is that the  $\Gamma_8$  and  $\Gamma_7$  CEF states exhibit different and opposite dichroism (see orange and light blue lines), consistent with their opposite anisotropy in the charge densities, see Fig. 8. The opposite dichroism at 125 and 140 eV reduces the experimental challenge to a simple yes/no experiment and makes the determination of the CEF ground state of  $\text{Sm}^{3+}$  in  $\text{SmB}_6$  straightforward.

Figure 11 (b) shows the experimental dichroic spectrum (black dots) together with the calculated ones. The two possible CEF states of the  $J = 5/2$  configuration have now been scaled down to 60% to quantitatively account for the  $\text{Sm}^{3+}$  component in intermediate valent  $\text{SmB}_6$ . We can clearly observe that in the regions of pronounced dichroism (see red arrows) the sign of

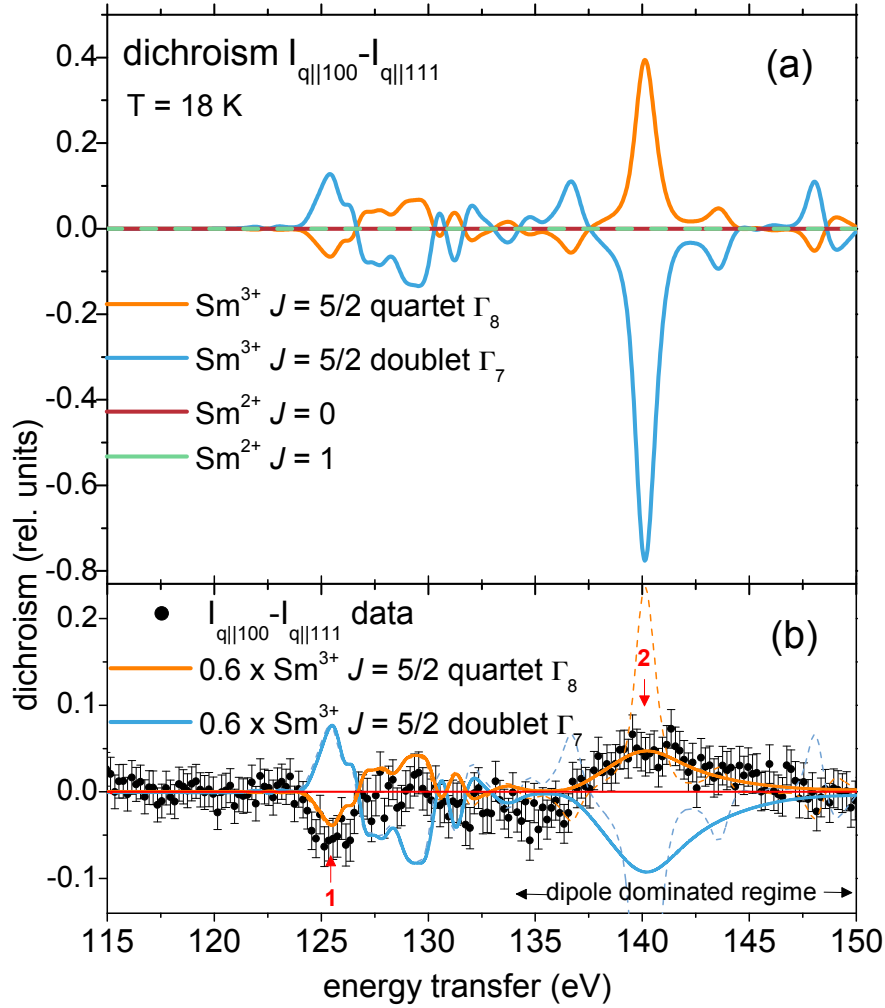


**Fig. 11:** (a) simulation of the  $\hat{q} \parallel [100]$  vs.  $\hat{q} \parallel [111]$  dichroic spectrum for the  $J=0$  (brown) and  $J=1$  (green) multiplet states of the  $\text{Sm}^{2+}$  configuration as well as for the  $\Gamma_8$  quartet (orange) and  $\Gamma_7$  doublet (light blue) of the  $J=5/2$   $\text{Sm}^{3+}$  configuration; (b) experimental dichroic spectrum (black dots) and simulated dichroic spectra for the  $\Gamma_8$  quartet (orange) and  $\Gamma_7$  doublet (light blue) scaled with the factor of 0.6 to account for the  $\text{Sm}^{3+}$  component of the ground state; dashed lines with energy independent broadening, solid lines with extra broadening in the dipole region (see text). Figure adapted from Ref. [94].

the experimental dichroic signal is correctly explained by the  $\Gamma_8$  quartet (orange line) but not at all by the  $\Gamma_7$  doublet state (light blue line). In addition, the  $\Gamma_8$  reproduces the experimental dichroism quantitatively in the high multipole region (see red arrow 1). The dichroism also fits quantitatively in the dipole region (see red arrow 2) when an extra broadening is applied ( $\text{FWHM} \geq 4$  eV beyond  $\approx 135$  eV energy transfer) to mimic the interference with continuum states. Note that sum rules still apply, i.e., the interference with the continuum states does not change the polarization, it only affects the broadening. The dashed lines correspond to the dipole calculation without the extra broadening. These results unambiguously establish that the CEF ground state of the  $\text{Sm } f^5$  component in  $\text{SmB}_6$  is the  $\Gamma_8$  quartet.

## 5 Discussion and concluding remarks

The finding that the  $\Gamma_8$  quartet forms the ground state of the Sm  $f^5$  component in SmB<sub>6</sub> has several consequences:

First of all, the theoretical predictions for the spin texture of the sought-after topological surface states depend very much whether the ground state of the  $f^5$   $J = 5/2$  configuration is the  $\Gamma_8$  quartet or the  $\Gamma_7$  doublet CEF state [102–104]. In fact, the winding of the spin textures is opposite for the two scenarios. Our finding of the  $\Gamma_8$  quartet supports very much the results of spin resolved APRES [69]. Xu *et al.* find spin polarized surface states, fulfilling time reversal as well as crystal symmetry, that have spins locked to the crystal momenta  $k$  such that at opposite momenta the surface states have opposite spins. The anticlockwise spin texture is in agreement with spin expectation values calculated by Baruselli and Vojta for a  $\Gamma_8$  ground state [102, 104]. Second, details of the character of the Sm  $4f$  bands matter for the formation of the hybridization gap [56–61]. Using *ab-initio* band structure calculations [105, 106, 59, 107] as a starting point, the intermediate valence of the Sm is associated with the fact that the Sm  $4f_{5/2}$  bands are fully below the Fermi level for all  $k$ -points of the Brillouin zone except in the vicinity of the  $X$ -point. There the strongly dispersing Sm  $5d$  band is positioned below the Fermi level; otherwise, i.e., at other  $k$  points, the Sm  $5d$  is unoccupied. The symmetry of the Sm  $5d$  band that is below the Fermi level at the  $X$ -point carries the label  $X_7^+$ . The Sm  $4f_{5/2}$  states splits into three bands at the  $X$ -point, and have the symmetry labels  $X_7^-$ ,  $X_7^-$ , and  $X_6^-$ . One of the  $X_7^-$  bands is made of the local  $\Gamma_7$  wave function, while the other  $X_7^-$  band and the  $X_6^-$  band originate from the local  $\Gamma_8$  wave function. See for example Kang *et al.* [107].

In order to have an insulating state, the highest and thus unoccupied  $4f_{5/2}$  band must be a  $X_7^-$  as to ensure a non-crossing situation between the  $X_7^-$  band of the  $4f_{5/2}$  and the  $X_7^+$  band of the  $5d$  in the region around the  $X$ -point due to hybridization. If the highest and unoccupied  $4f_{5/2}$  band were a  $X_6^-$ , then there were no hybridization with the  $X_7^+$  band of the  $5d$  in the region around the  $X$ -point, with the result that the two bands cross and no gap is opened. This means that a local  $\Gamma_7$  ground state would guarantee the formation of a gap, while a  $\Gamma_8$  may or may not open a gap. Further material specific details then determine whether the highest band is  $X_7^-$  or  $X_6^-$ . So our finding of the  $\Gamma_8$  as the local ground state wave function does not explain why SmB<sub>6</sub> is insulating. Reversely, knowing that SmB<sub>6</sub> is an insulator, our results then fix the energy order of the bands at the  $X$ -point: the highest (and unoccupied) is the  $X_7^-$  from the  $\Gamma_8$ , followed by the  $X_6^-$  from  $\Gamma_8$ , and the lowest is the  $X_7^-$  from the  $\Gamma_7$ .

Third, our finding of a  $\Gamma_8$  local ground-state symmetry contradicts in fact the outcome of several density functional band structure calculations [105, 106, 59, 107]. In band theory, the search for the ground state symmetry in SmB<sub>6</sub> translates into the question in which band the hole in the  $J = 5/2$  manifold resides. Kang *et al.* reported for the  $X$ -point an unoccupied  $4f$   $X_7^-$  state of  $\Gamma_7$  origin [107]. Also their  $k$ -integrated  $4f$   $J = 5/2$  partial density of states (pDOS) shows the hole residing in the  $\Gamma_7$  band, in line with the fact that the center of gravity of the  $\Gamma_7$  pDOS is higher in energy than that of the  $\Gamma_8$ . We would like to note that many theoretical studies have quoted these band structure calculations for having produced a local  $\Gamma_8$  ground state! This is

incorrect. Perhaps the mistake has been made by looking at the  $\Gamma$ -point: there the  $\Gamma_7^-$  band is indeed lower than the  $\Gamma_8^-$  band which is closer to the Fermi level giving rise to the wrong expectation that the *local*  $\Gamma_8$  is the state with the hole. However, we would like to point out that looking at just one particular point in the Brillouin zone is not sufficient for extracting the local crystal field scheme. It can only be deduced from the integration over the entire Brillouin zone. In fact, realizing that crystal-field effects are determined mainly by hybridization, the  $\Gamma$ -point is perhaps the worst possible location in  $k$ -space to look at since there the  $4f$  and the  $5d$  are non-bonding due to opposite parity, a virtue that is the very starting point for proposing  $\text{SmB}_6$  to be topologically non-trivial.

Fourth, we would like to note that the experimentally observed dichroism in our NIXS spectra can be explained by a pure  $\Gamma_8$  state, weighted with 0.6 to account for the contribution of the  $4f^5$  configuration in the ground state of  $\text{SmB}_6$ , see Fig. 11. This is surprising in view of the intermediate valent state of the compound, and in view that bands are important for the much discussed low energy properties. A conclusion that could be drawn from this is that the  $4f$  bands may be extremely narrow, much narrower than the crystal-field splitting between the  $\Gamma_8$  and  $\Gamma_7$  states. The fact that the spectral responses of  $4f$  ions are dominated by multiplet structures suggests that the hopping integral for the transfer of a electron from a  $4f^6$  to a neighboring  $4f^5$  site will be hampered by the fact that the ground state of a  $4f^6$  ion is a  $J = 0$  state and that of a  $4f^5$  ion a  $J = 5/2$ . It is not impossible to convert a  $4f^6$   $J = 0$  to a  $4f^5$   $J = 5/2$  and simultaneously a  $4f^5$   $J = 5/2$  to a  $4f^6$   $J = 0$  by transferring only an  $s = 1/2$  particle without energy cost, but the probability for such a large change in quantum numbers is tiny and is given by the *fractional parentage* as described in the recent lecture notes of Sawatzky [108].

To summarize, we have utilized the high multipole contributions in the core-level non-resonant inelastic x-ray scattering process to determine the symmetry of the Sm crystal-field ground state  $4f$  wave function in  $\text{SmB}_6$ . We have found a clear directional dependence of the spectra that allows for the unambiguous identification of the  $\Gamma_8$  quartet state of the Sm  $f^5$   $J=5/2$  configuration as the state which governs the topological properties of  $\text{SmB}_6$ . Follow-up calculations should be performed within a reduced basis of only  $\Gamma_8$  states for the construction of a low-energy many-body Hamiltonian.

## Acknowledgments

I would like to acknowledge Andrea Severing, Martin Sundermann, Maurits Haverkort, and Peter Thalmeier for their invaluable input.

## References

- [1] J.-H. Park, L.H. Tjeng, A. Tanaka, J.W. Allen, C.T. Chen, P. Metcalf, J.M. Honig, F.M.F. de Groot, and G.A. Sawatzky, *Phys. Rev. B* **61**, 11506 (2000)
- [2] T. Mizokawa, L.H. Tjeng, H.-J. Lin, C.T. Chen, S. Schuppler, S. Nakatsuji, H. Fukazawa, and Y. Maeno, *Phys. Rev. B* **69**, 132410 (2004)
- [3] A. Tanaka, *J. Phys. Soc. Jpn.* **73**, 152 (2004)
- [4] A.I. Poteryaev, A.I. Lichtenstein, and G. Kotliar, *Phys. Rev. Lett.* **93**, 086401 (2004)
- [5] S. Biermann, A. Poteryaev, A.I. Lichtenstein, and A. Georges, *Phys. Rev. Lett.* **94**, 026404 (2005)
- [6] M.W. Haverkort, Z. Hu, A. Tanaka, W. Reichelt, S.V. Streltsov, M.A. Korotin, V.I. Anisimov, H.H. Hsieh, H.-J. Lin, C.T. Chen, D.I. Khomskii, and L.H. Tjeng, *Phys. Rev. Lett.* **95**, 196404 (2005)
- [7] T.C. Koethe, Z. Hu, M.W. Haverkort, C. Schüßler-Langeheine, F. Venturini, N.B. Brookes, O. Tjernberg, W. Reichelt, H.H. Hsieh, H.-J. Lin, C.T. Chen, and L.H. Tjeng, *Phys. Rev. Lett.* **97**, 116402 (2006)
- [8] C.F. Chang, T.C. Koethe, Z. Hu, J. Weinen, S. Agrestini, L. Zhao, J. Gegner, H. Ott, G. Panaccione, H. Wu, M.W. Haverkort, H. Roth, A.C. Komarek, F. Offi, G. Monaco, Y.-F. Liao, K.-D. Tsuei, H.-J. Lin, C.T. Chen, A. Tanaka, and L.H. Tjeng, *Phys. Rev. X* **8**, 021004 (2018)
- [9] A. Severing, E. Holland-Moritz, B.D. Rainford, S.R. Culverhouse, and B. Frick, *Phys. Rev. B* **39**, 2557 (1989)
- [10] P.A. Alekseev, V.N. Lazukov, R. Osborn, B.D. Rainford, I.P. Sadikov, E.S. Konovalova, and Y.B. Paderno, *Europhys. Lett.* **23**, 347 (1993)
- [11] P.A. Alekseev, J.M. Mignot, J. Rossat-Mignod, V.N. Lazukov, I.P. Sadikov, E.S. Konovalova, and Y.B. Paderno, *J. Phys.: Condens. Matter* **7**, 289 (1995)
- [12] D.T. Adroja, K. McEwen, J.-G. Park, A.D. Hillier, N. Takeda, P. Riseborough, and T. Takabatake, *J. Optoelectron. Adv. M.* **10**, 1719 (2008)
- [13] D.T. Adroja, A.D. Hillier, Y. Muro, T. Takabatake, A.M. Strydom, A. Bhattacharyya, A. Daoud-Aladin, and J.W. Taylor, *Phys. Scr.* **88**, 068505 (2013)
- [14] C.T. Chen, L.H. Tjeng, J. Kwo, H.L. Kao, P. Rudolf, F. Sette, and R.M. Fleming, *Phys. Rev. Lett.* **68**, 2543 (1992)
- [15] F. de Groot, *J. Electron. Spectrosc. Relat. Phenom.* **67**, 529 (1994)
- [16] A. Tanaka and T. Jo, *J. Phys. Soc. Jpn.* **63**, 2788 (1994)



- [17] S.I. Csiszar, M.W. Haverkort, Z. Hu, A. Tanaka, H.H. Hsieh, H.-J. Lin, C.T. Chen, T. Hibma, and L.H. Tjeng, *Phys. Rev. Lett.* **95**, 187205 (2005)
- [18] P. Hansmann, A. Severing, Z. Hu, M.W. Haverkort, C.F. Chang, S. Klein, A. Tanaka, H.H. Hsieh, H.-J. Lin, C.T. Chen, B. Fåk, P. Lejay, and L.H. Tjeng, *Phys. Rev. Lett.* **100**, 066405 (2008)
- [19] W. Schülke: *Electron Dynamics by Inelastic X-Ray Scattering* (Oxford University Press, 2007)
- [20] J.A. Soininen, A.L. Ankudinov, and J.J. Rehr, *Phys. Rev. B* **72**, 045136 (2005)
- [21] M.W. Haverkort, A. Tanaka, L.H. Tjeng, and G.A. Sawatzky, *Phys. Rev. Lett.* **99**, 257401 (2007)
- [22] R.A. Gordon, G.T. Seidler, T.T. Fister, M.W. Haverkort, G.A. Sawatzky, A. Tanaka, and T.K. Sham, *Europhys. Lett.* **81**, 26004 (2008)
- [23] R. Caciuffo, G. van der Laan, L. Simonelli, T. Vitova, C. Mazzoli, M.A. Denecke, and G.H. Lander, *Phys. Rev. B* **81**, 195104 (2010)
- [24] J.A. Bradley, G.T. Seidler, G. Cooper, M. Vos, A.P. Hitchcock, A.P. Sorini, C. Schlimmer, and K.P. Nagle, *Phys. Rev. Lett.* **105**, 053202 (2010)
- [25] J.A. Bradley, K.T. Moore, G. van der Laan, J.P. Bradley, and R.A. Gordon, *Phys. Rev. B* **84**, 205105 (2011)
- [26] G. van der Laan, *Phys. Rev. Lett.* **108**, 077401 (2012)
- [27] T. Willers, F. Strigari, N. Hiraoka, Y.Q. Cai, M.W. Haverkort, K.-D. Tsuei, Y.F. Liao, S. Seiro, C. Geibel, F. Steglich, L.H. Tjeng, and A. Severing, *Phys. Rev. Lett.* **109**, 046401 (2012)
- [28] R. Cowan: *The theory of atomic structure and spectra* (University of California, Berkley, 1981)
- [29] T. Willers, B. Fåk, N. Hollmann, P.O. Körner, Z. Hu, A. Tanaka, D. Schmitz, M. Enderle, G. Lapertot, L.H. Tjeng, and A. Severing, *Phys. Rev. B* **80**, 115106 (2009)
- [30] L. Sun and Q. Wu, *Rep. Prog. Phys.* **79**, 084503 (2016)
- [31] J. Effantin, J. Rossat-Mignod, P. Burlet, H. Bartholin, S. Kunii, and T. Kasuya, *J. Magn. Magn. Mater.* **47-48**, 145 (1985)
- [32] M. Sundermann, K. Chen, H. Yavaş, H. Lee, Z. Fisk, M.W. Haverkort, L.H. Tjeng, and A. Severing, *Europhys. Lett.* **117**, 17003 (2017)
- [33] W. Erkelens, L. Regnault, P. Burlet, J. Rossat-Mignod, S. Kunii, and T. Kasuya, *J. Magn. Magn. Mater.* **63-64**, 61 (1987)
- [34] R. Shiina, H. Shiba, and P. Thalmeier, *J. Phys. Soc. Jpn.* **66**, 1741 (1997)

- [35] A. Akbari and P. Thalmeier, *Phys. Rev. Lett.* **108**, 146403 (2012)
- [36] S.W. Lovesey, *J. Phys.: Condens. Matter* **14**, 4415 (2002)
- [37] T. Matsumura, T. Yonemura, K. Kunimori, M. Sera, and F. Iga, *Phys. Rev. Lett.* **103**, 017203 (2009)
- [38] G. Friemel, Y. Li, A. Dukhnenko, N. Shitsevalova, N. Sluchanko, A. Ivanov, V. Filipov, B. Keimer, and D. Inosov, *Nat. Commun.* **3**, 830 (2012)
- [39] P.Y. Portnichenko, S.V. Demishev, A.V. Semeno, H. Ohta, A.S. Cameron, M.A. Surmach, H. Jang, G. Friemel, A.V. Dukhnenko, N.Y. Shitsevalova, V.B. Filipov, A. Schneidewind, J. Ollivier, A. Podlesnyak, and D.S. Inosov, *Phys. Rev. B* **94**, 035114 (2016)
- [40] A.S. Cameron, G. Friemel, and D.S. Inosov, *Rep. Prog. Phys.* **79**, 066502 (2016)
- [41] M. Neupane, N. Alidoust, I. Belopolski, G. Bian, S.-Y. Xu, D.-J. Kim, P.P. Shibayev, D.S. Sanchez, H. Zheng, T.-R. Chang, H.-T. Jeng, P.S. Riseborough, H. Lin, A. Bansil, T. Durakiewicz, Z. Fisk, and M.Z. Hasan, *Phys. Rev. B* **92**, 104420 (2015)
- [42] A. Koitzsch, N. Heming, M. Knupfer, P.Y. Büchner, B. Portnichenko, A.V. Dukhnenko, N.Y. Shitsevalova, V.B. Filipov, L.L. Lev, V.N. Strocov, J. Ollivier, and D.S. Inosov, *Nat. Commun.* **7**, 10876 (2016)
- [43] E. Zirngiebl, B. Hillebrands, S. Blumenröder, G. Güntherodt, M. Loewenhaupt, J.M. Carpenter, K. Winzer, and Z. Fisk, *Phys. Rev. B* **30**, 4052 (1984)
- [44] M. Loewenhaupt, J. Carpenter, and C.-K. Loong, *J. Magn. Magn. Mater.* **52**, 245 (1985)
- [45] C. Terzioglu, D.A. Browne, R.G. Goodrich, A. Hassan, and Z. Fisk, *Phys. Rev. B* **63**, 235110 (2001)
- [46] N. Sato, S. Kunii, I. Oguro, T. Komatsubara, and T. Kasuya, *J. Phys. Soc. Jpn.* **53**, 3967 (1984)
- [47] F. Givord, J.-X. Boucherle, P. Burlet, B. Gillon, and S. Kunii, *J. Phys.: Condens. Matter* **15**, 3095 (2003)
- [48] K. Tanaka and Y. Onuki, *Acta Cryst. B* **58**, 423 (2002)
- [49] R. Makita, K. Tanaka, Y. Onuki, and H. Tatewaki, *Acta Cryst. B* **63**, 683 (2007)
- [50] M.W. Haverkort, *J. Phys.: Conf. Ser.* **712**, 012001 (2016)
- [51] A. Menth, E. Buehler, and T.H. Geballe, *Phys. Rev. Lett.* **22**, 295 (1969)
- [52] R.L. Cohen, M. Eibschütz, and K.W. West, *Phys. Rev. Lett.* **24**, 383 (1970)
- [53] J.W. Allen, B. Batlogg, and P. Wachter, *Phys. Rev. B* **20**, 4807 (1979)
- [54] B. Gorshunov, N. Sluchanko, A. Volkov, M. Dressel, G. Knebel, A. Loidl, and S. Kunii, *Phys. Rev. B* **59**, 1808 (1999)

- [55] P.S. Riseborough, *Adv. Phys.* **49**, 257 (2000)
- [56] M. Dzero, K. Sun, V. Galitski, and P. Coleman, *Phys. Rev. Lett.* **104**, 106408 (2010)
- [57] T. Takimoto, *J. Phys. Soc. Jpn.* **80**, 123710 (2011)
- [58] M. Dzero, K. Sun, P. Coleman, and V. Galitski, *Phys. Rev. B* **85**, 045130 (2012)
- [59] F. Lu, J. Zhao, H. Weng, Z. Fang, and X. Dai, *Phys. Rev. Lett.* **110**, 096401 (2013)
- [60] M. Dzero and V. Galitski, *J. Exp. Theo. Phys.* **117**, 499 (2013)
- [61] V. Alexandrov, M. Dzero, and P. Coleman, *Phys. Rev. Lett.* **111**, 226403 (2013)
- [62] K. Flachbart, K. Gloos, E. Konovalova, Y. Paderno, M. Reiffers, P. Samuely, and P. Švec, *Phys. Rev. B* **64**, 085104 (2001)
- [63] N. Xu, X. Shi, P.K. Biswas, C.E. Matt, R.S. Dhaka, Y. Huang, N.C. Plumb, M. Radović, J.H. Dil, E. Pomjakushina, K. Conder, A. Amato, Z. Salman, D.M. Paul, J. Mesot, H. Ding, and M. Shi, *Phys. Rev. B* **88**, 121102 (2013)
- [64] Z.-H. Zhu, A. Nicolaou, G. Levy, N.P. Butch, P. Syers, X.F. Wang, J. Paglione, G.A. Sawatzky, I.S. Elfimov, and A. Damascelli, *Phys. Rev. Lett.* **111**, 216402 (2013)
- [65] M. Neupane, N. Alidoust, S.-Y. Xu, T. Kondo, Y. Ishida, D.J. Kim, C. Liu, I. Belopolski, Y.J. Jo, T.-R. Chang, H.-T. Jeng, T. Durakiewicz, L. Balicas, H. Lin, A. Bansil, S. Shin, Z. Fisk, and M. Hasan, *Nat. Commun.* **4**, 2991 (2013)
- [66] J. Jiang, S. Li, T. Zhang, Z. Sun, F. Chen, Z. Ye, M. Xu, Q. Ge, S. Tan, X. Niu, M. Xia, B. Xie, Y. Li, X. Chen, H. Wen, and D. Feng, *Nat. Commun.* **4**, 3010 (2013)
- [67] J. Denlinger, J.W. Allen, J.-S. Kang, K. Sund, J.-W. Kim, J.H. Shim, B.I. Min, D.-J. Kim, and Z. Fisk, *arXiv:1312.6637* (2013)
- [68] J.D. Denlinger, J.W. Allen, J.-S. Kang, K. Sun, B.-I. Min, D.-J. Kim, and Z. Fisk, *JPS Conf. Proc.* **3**, 017038 (2014)
- [69] N. Xu, P.K. Biswas, J.H. Dil, R.S. Dhaka, G. Landolt, S. Muff, C.E. Matt, X. Shi, N.C. Plumb, M. Radovic, E. Pomjakushina, K. Conder, A. Amato, S.V. Borisenko, R. Yu, H.-M. Weng, Z. Fang, X. Dai, J. Mesot, H. Ding, and M. Shi, *Nat. Commun.* **5**, 4566 (2014)
- [70] N. Xu, C.E. Matt, E. Pomjakushina, X. Shi, R.S. Dhaka, N.C. Plumb, M. Radović, P.K. Biswas, D. Evtushinsky, V. Zabolotnyy, J.H. Dil, K. Conder, J. Mesot, H. Ding, and M. Shi, *Phys. Rev. B* **90**, 085148 (2014)
- [71] P. Hlawenka, K. Siemensmeyer, E. Weschke, A. Varykhalov, J. Sánchez-Barriga, N.Y. Shitsevalova, A.V. Dukhnenko, V.B. Filipov, S. Gabáni, S. Flachbart, O. Rader, and E.D.L. Rienks, *Nat. Commun.* **9**, 517 (2018)

- [72] M.M. Yee, Y. He, A. Soumyanarayanan, D.J. Kim, Z. Fisk, and J.E. Hoffman, arXiv:1308.1085 (2013)
- [73] S. Rössler, T.-H. Jang, D.-J. Kim, T.L.H., Z. Fisk, and S. Steglich, F. Wirth, Proc. Natl. Acad. Science. U.S.A. **111**, 4798 (2014)
- [74] W. Ruan, C. Ye, M. Guo, F. Chen, X. Chen, G.-M. Zhang, and Y. Wang, Phys. Rev. Lett. **112**, 136401 (2014)
- [75] S. Rössler, L. Jiao, D.J. Kim, S. Seiro, K. Rasim, F. Steglich, L.H. Tjeng, Z. Fisk, and S. Wirth, Phil. Mag. **96**, 3262 (2016)
- [76] L. Jiao, S. Rössler, D.J. Kim, L.H. Tjeng, Z. Fisk, F. Steglich, and S. Wirth, Nat. Commun. **7**, 13762 (2016)
- [77] M. Ciomaga Hatnean, M.R. Lees, D.McK. Paul, and G.A. Balakrishnan, Sci. Rep. **3** 3403 (2013)
- [78] X. Zhang, N.P. Butch, P. Syers, S. Ziemak, R.L. Greene, and J. Paglione, Phys. Rev. X **3**, 011011 (2013)
- [79] D.J. Kim, S. Thomas, T. Grant, J. Botimer, Z. Fisk, and J. Xia, Sci. Rep. **3**, 3150 (2013)
- [80] S. Wolgast, C. Kurdak, K. Sun, J.W. Allen, D.-J. Kim, and Z. Fisk, Phys. Rev. B **88**, 180405 (2013)
- [81] D.J. Kim, J. Xia, and Z. Fisk, Nat. Mater. **13**, 466 (2014)
- [82] S. Wolgast, Y.S. Eo, T. Öztürk, G. Li, Z. Xiang, C. Tinsman, T. Asaba, B. Lawson, F. Yu, J.W. Allen, K. Sun, L. Li, C. Kurdak, D.-J. Kim, and Z. Fisk, Phys. Rev. B **92**, 115110 (2015)
- [83] S. Thomas, D.J. Kim, S.B. Chung, T. Grant, Z. Fisk, and J. Xia, Phys. Rev. B **94**, 205114 (2016)
- [84] Y. Nakajima, P. Syers, X. Wang, R. Wang, and J. Paglione, Nat. Phys. **12**, 213 (2016)
- [85] M. Dzero, J. Xia, V. Galitski, and P. Coleman, Annu. Rev. Condens. Matter Phys. **7**, 249 (2016)
- [86] J.W. Allen, Phil. Mag. **96**, 3227 (2016)
- [87] J.W. Allen, L.I. Johansson, I. Lindau, and S.B. Hagstrom, Phys. Rev. B **21**, 1335 (1980)
- [88] J.M. Tarascon, Y. Ishikawa, B. Chevalier, J. Etourneau, P. Hagenmuller, and K. Kasaya, J. Physique **41**, 1141 (1980)
- [89] M. Mizumaki, S. Tsutsui, and F. Iga, J. Phys.: Conf. Ser. **176**, 012034 (2009)

- [90] H. Hayashi, N. Kanai, N. Kawamura, M. Mizumaki, K. Imura, N.K. Sato, H.S. Suzuki, and F. Iga, *J. Anal. At. Spectrom.* **28**, 373 (2013)
- [91] P. Lutz, M. Thees, T.R. Peixoto, B.Y. Kang, B.K. Cho, C.H. Min, and F. Reinert, *Phil. Mag.* **96**, 3307 (2016)
- [92] N.P. Butch, J. Paglione, P. Chow, Y. Xiao, C.A. Marianetti, C.H. Booth, and J.R. Jeffries, *Phys. Rev. Lett.* **116**, 156401 (2016)
- [93] Y. Utsumi, D. Kasinathan, K.-T. Ko, S. Agrestini, M.W. Haverkort, S. Wirth, Y.-H. Wu, K.-D. Tsuei, D.-J. Kim, Z. Fisk, A. Tanaka, P. Thalmeier, and L.H. Tjeng, *Phys. Rev. B* **96**, 155130 (2017)
- [94] M. Sundermann, H. Yavaş, K. Chen, D.J. Kim, Z. Fisk, D. Kasinathan, M.W. Haverkort, P. Thalmeier, A. Severing, and L.H. Tjeng, *Phys. Rev. Lett.* **120**, 016402 (2018)
- [95] K. Lea, M. Leask, and W. Wolf, *J. Phys. Chem. Sol.* **23**, 1381 (1962)
- [96] W.T. Fuhrman, J. Leiner, P. Nikolić, G.E. Granroth, M.B. Stone, M.D. Lumsden, L. DeBeer-Schmitt, P.A. Alekseev, J.-M. Mignot, S.M. Koohpayeh, P. Cottingham, W.A. Phelan, L. Schoop, T.M. McQueen, and C. Broholm, *Phys. Rev. Lett.* **114**, 036401 (2015)
- [97] P. Nyhus, S.L. Cooper, Z. Fisk, and J. Sarrao, *Phys. Rev. B* **52**, R14308 (1995)
- [98] P. Nyhus, S.L. Cooper, Z. Fisk, and J. Sarrao, *Phys. Rev. B* **55**, 12488 (1997)
- [99] B. Frick and M. Loewenhaupt, *Z. Phys. B* **63**, 213 (1986)
- [100] M. Loewenhaupt and M. Prager, *Z. Phys. B* **62**, 195 (1986)
- [101] S. Sen Gupta, J.A. Bradley, M.W. Haverkort, G.T. Seidler, A. Tanaka, and G.A. Sawatzky, *Phys. Rev. B* **84**, 075134 (2011)
- [102] P.P. Baruselli and M. Vojta, *Phys. Rev. Lett.* **115**, 156404 (2015)
- [103] M. Legner, A. Rüegg, and M. Sgrist, *Phys. Rev. Lett.* **115**, 156405 (2015)
- [104] P.P. Baruselli and M. Vojta, *Phys. Rev. B* **93**, 195117 (2016)
- [105] A. Yanase and H. Harima, *Prog. Theor. Phys. Suppl.* **108**, 19 (1992)
- [106] V.N. Antonov, B.N. Harmon, and A.N. Yaresko, *Phys. Rev. B* **66**, 165209 (2002)
- [107] C.-J. Kang, J. Kim, K. Kim, J. Kang, J.D. Denlinger, and B.I. Min, *J. Phys. Soc. Jpn.* **84**, 024722 (2015)
- [108] G. Sawatzky, in E. Pavarini, E. Koch, J. van den Brink and G. Sawatzky (eds.): *Quantum Materials: Experiments and Theory*, Modeling and Simulation Vol. 6 (Forschungszentrum Jülich, 2016)



# 9 DMRG for Multiband Impurity Solvers

Hans Gerd Evertz

Institute for Theoretical and Computational Physics

Graz University of Technology, Austria

## Contents

<b>1</b>	<b>Introduction</b>	<b>2</b>
1.1	Impurity solvers in DMFT . . . . .	2
1.2	Calculation of impurity Green function in time evolution approaches . . . . .	4
<b>2</b>	<b>Matrix product state techniques</b>	<b>5</b>
2.1	Matrix product states (MPS) . . . . .	5
2.2	Different MPS representations of a state . . . . .	11
2.3	Time evolution . . . . .	15
2.4	Matrix product operators (MPO) and DMRG . . . . .	18
2.5	Previous MPS impurity solvers . . . . .	20
<b>3</b>	<b>Fork tensor product state (FTPS) method</b>	<b>21</b>
3.1	Geometry and tensors . . . . .	21
3.2	Star representation of the bath orbitals . . . . .	22
3.3	Kanamori Hamiltonian and FTPOs . . . . .	22
3.4	Ground state and time evolution . . . . .	23
<b>4</b>	<b>Results</b>	<b>25</b>
4.1	SrVO <sub>3</sub> : 3 orbitals . . . . .	26
4.2	SrMnO <sub>3</sub> : 5 orbitals . . . . .	27
<b>5</b>	<b>Conclusions</b>	<b>29</b>

# 1 Introduction

The computationally most difficult task in Dynamical Mean Field Theory (DMFT) [1–4] is the calculation of the self energy  $\Sigma(\omega)$  or, equivalently, the spectral function  $A(\omega)$ . For typical physically relevant systems with three or five orbital impurities, this becomes demanding, and the energy resolution of standard techniques has been limited. In this chapter, a new method is described, dubbed *Fork Tensor Product States* (FTPS) [5, 6], which is as efficient as the best established methods for multiple orbitals, but has much better energy resolution at large energies, by way of using real-time evolution of an excited state. It is based on so-called Matrix Product State (MPS) techniques [7], which are related to the Density Matrix Renormalization Group (DMRG) [8].

The new method and the results described in this chapter are largely the work of my former student Daniel Bauernfeind, described in detail in his Ph.D. thesis [9]. I would like to thank him very much for a great collaboration.

## 1.1 Impurity solvers in DMFT

For the description of a material in DMFT, one first calculates the band structure by some variant of Density-Functional Theory (DFT) and projects the spectrum onto a few low lying effective orbitals, from which an effective Hamiltonian is constructed. Some aspects of this procedure will be discussed later in the results section. DMFT then treats the effective Hamiltonian locally, for example on a single site, which will be discussed here. The effect of all other sites is subsumed by the interaction with an effective bath, resulting in an effective Anderson Impurity Model (AIM) like

$$H_{\text{AIM}} = H_{\text{loc}} + \sum_k V_k \left( c_k^\dagger c_0 + h.c. \right) + \sum_k \varepsilon_k n_k. \quad (1)$$

Here,  $H_{\text{loc}}$  is the local interacting Hamiltonian,  $k$  is, e.g., a momentum space index numbering the noninteracting bath sites with local energy  $\varepsilon_k$  and occupation number  $n_k = c_k^\dagger c_k$ , and  $V_k$  is the hopping strength from the impurity (indicated by index zero) to the bath site.

For this model, the impurity spectral function  $A(\omega)$  has to be calculated. It is then used together with the lattice structure of the material examined to determine new bath parameters  $V_k$ ,  $\varepsilon_k$  in an iteration of the DMFT loop, until self-consistency is reached.

The bath represents a continuous spectrum of energies of the material around the impurity. Therefore the number  $N_B$  of sites in the bath and the corresponding spacing of the energies  $\varepsilon_k$  (as well as the choice of their values) limits the energy resolution which can be achieved. Often, the AIM is transformed into an equivalent representation as a *Wilson chain* [10, 11], i.e., a tight binding chain of length  $N_B$  with the impurity site coupled at one end.

Let us very briefly touch on some of the current impurity solvers and their strengths and weaknesses.



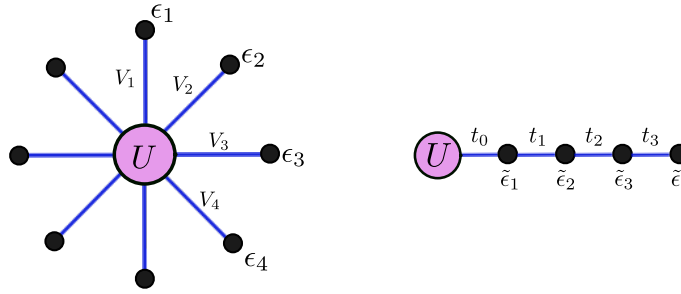


**Fig. 1:** Anderson impurity model in two different representations. The circle marked by  $U$  represents the interacting site. Left: star geometry, a direct representation of Eq. (1). Right: Wilson chain, obtained after a unitary transformation.

### Continuous time quantum Monte Carlo

The state of the art work horse for DMFT calculations is probably Continuous Time Quantum Monte Carlo (CTQMC) [12, 13], usually in its CT-HYB variant. Here, the impurity problem is expressed in a Lagrangian formulation in continuous *imaginary time*, with a chain of length  $\beta = 1/T$ , the inverse of the temperature. The Green function  $G(\tau)$  is measured, with statistical errors, in imaginary time, and needs to be transformed by a so-called analytic continuation to real time / real frequency, usually done with some variant of the Maximum Entropy method. This transformation is badly conditioned, especially for non-exact data. One of the consequences is that the energy resolution of the resulting spectrum becomes rather bad at large energies. We will see some examples in the section on results. The computational effort for CTQMC usually grows *exponentially* with the number of orbitals. An additional difficulty of CTQMC is a potential Monte-Carlo *sign problem* which then drastically limits the attainable inverse temperatures and numbers of orbitals.

### Exact diagonalization / Configuration interaction

When there are not too many bath sites, the impurity spectral function  $A(\omega)$  can be calculated with Exact Diagonalization (ED) [14–16], but will then consist of a limited number of delta-peaks. This can be improved, for example by using different bath discretizations within the same calculation or by optimizing the discretization in Configuration Interaction (CI) schemes [17, 18]. For a single orbital, spectra with good resolution have been achieved. However, for more orbitals, the energy resolution has been very limited by, for example, only 3 bath sites for 3 orbitals in Ref. [17].

### Numerical Renormalization Group

The Numerical Renormalization Group (NRG) [10, 11] provides one of the standard approaches to impurity solvers. It works on the real frequency axis, successively integrating out degrees of freedom on high energy scales in a logarithmic fashion in a Wilson chain. It can provide very good energy resolution at low energies, even for several orbitals [19–21], but by construction is rather coarse at large energies. The number of orbitals enters exponentially into the computational effort. NRG amounts to a calculation with matrix product states (see below).

## Dynamical DMRG

The so-called *Dynamical DMRG* (DDMRG) [22–25] and *Correction Vector* (CV) [26] approaches are variants of DMRG in which  $A(\omega)$  can be calculated very precisely, although with some broadening, directly at a chosen frequency. However, a separate calculation is necessary for every frequency, so that multiple orbitals become infeasible.

## Time evolution with matrix product states

Matrix product state methods also provide precise techniques to calculate the time evolution of pure states after a local excitation at the impurity site. Most methods have been developed in a closely related variant using Chebyshev polynomials [27–30] for up to 2 orbitals [30]. Direct real time evolution has been employed for one and two orbitals by Ganahl *et al.* [31], with very good energy resolution. However, the computational effort may grow exponentially with the number of orbitals and has in the past been far too large for more than two orbitals. More orbitals have only been reached in imaginary time [32], with associated energy resolution difficulties. In the present chapter we will see how to overcome these problems.

## 1.2 Calculation of impurity Green function in time evolution approaches

Impurity solvers using time evolution techniques employ the following general steps (leaving out spin and orbital indices for simplicity):

- Given the bath parameters, calculate the ground state  $|\psi_0\rangle$  of the corresponding Anderson impurity model, with energy  $E_0$ .
- Apply an annihilation operator to obtain the excited state  $|\psi_1\rangle = c_0|\psi_0\rangle$ .
- Time evolve, i.e., calculate  $e^{iHt} |\psi_1\rangle$ .
- Calculate the overlap with  $|\psi_1\rangle$ , namely  $G^<(t) = \langle\psi_1| e^{iHt} |\psi_1\rangle e^{-iE_0t}$ , which provides one part of the Green function.
- The resulting function  $G(t)$  can, if desired, be post-processed with so-called *linear prediction* [27, 7, 31] (essentially a fit with  $\mathcal{O}(100)$  Lorentzians) in order to further improve the energy resolution.
- Fourier transform to obtain  $A(\omega)$ .

More details can be found in Refs. [31, 5, 6, 9]. The Fork Tensor Product State (FTPS) approach to be described in the present chapter is based on the Matrix Product State (MPS) formalism, which we will therefore first discuss in some detail. For FTPS we will then introduce a special efficient tensor geometry. Both MPS (and DMRG) as well as FTPS require an essentially linear bath geometry. Yet we shall see that, quite surprisingly, it will be much more efficient to directly enumerate the sites  $k$  of the bath degrees of freedom (the so-called star geometry) along an artificial chain, instead of employing Wilson chains for the bath. At the end of the chapter we will discuss results and performance of the new method.

## 2 Matrix product state techniques

### 2.1 Matrix product states (MPS)

Matrix product states constitute the formalism behind DMRG. In order to understand the FTPS method, we need to go into some detail on the MPS approach. For a much more complete exposition, including all the references to the original literature, I refer to the great review by U. Schollwöck [7]. For a quick reading of this section, the graphical representation Fig. 2 and its explanation contain some of the most important aspects.

The state space of many-particle models grows exponentially with the number of particles involved. Such models can therefore be treated exactly only for very small systems. The MPS approach permits very precise and efficient approximations even for very large systems. It has allowed for, e.g., DMRG calculations of the ground state energy of Heisenberg models on several hundred sites to 10-digit precision, and can also be used to time-evolve a state. Note that a convenient library of tensor routines is available for such calculations [33].

#### 2.1.1 Example: Heisenberg spin chain

In order to keep notation reasonably simple for the discussion of MPS, in this section we shall treat the one-dimensional spin-1/2 Heisenberg model with open boundary conditions

$$\hat{H} = \sum_{i=1}^{L-1} \hat{H}_i \quad \text{with} \quad \hat{H}_i = \frac{J_{xy}}{2} (S_i^+ S_{i+1}^- + S_i^- S_{i+1}^+) + J_z S_i^z S_{i+1}^z, \quad (2)$$

where  $S_j^\pm = S_j^x \pm iS_j^y$ , thus  $S_j^+ |\downarrow\rangle_j = |\uparrow\rangle_j$  and  $S_j^- |\uparrow\rangle_i = |\downarrow\rangle_j$ . The representation of  $S_j^\alpha$  in the  $z$ -basis at site  $j$  is  $\sigma^\alpha/2$  (we leave out  $\hbar$ ).

A chain of  $L$  sites has  $2^L$  basis states, which are  $|s_1, s_2, \dots, s_L\rangle$  with  $s_j \in \{\uparrow, \downarrow\}$  in the  $z$ -basis. In case of isotropic couplings  $J_{xy} = J_z =: J$  we get  $\hat{H} = J \sum_j \vec{S}_j \cdot \vec{S}_{j+1}$ . This model is also a good approximation of the strongly repulsive Hubbard model ( $U \gg t$ ) at half filling.

Note that on a one-dimensional chain, the Heisenberg model is equivalent to a model of tight-binding spinless fermions

$$\hat{H} = \sum_{j=1}^{L-1} t \left( c_j^\dagger c_{j+1} + h.c. \right) + V \hat{n}_j \hat{n}_{j+1} - \frac{V}{2} (\hat{n}_j + \hat{n}_{j+1}) + \frac{1}{4}$$

by the Jordan-Wigner transformation. With fermions, the only new aspect for MPS is the minus sign that appears upon interchanging two fermions. It can be dealt with by a suitable operator which we will discuss in the chapter on FTPS.

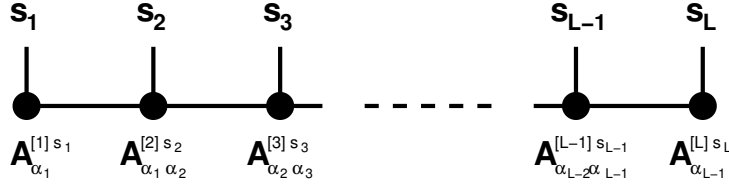


**Fig. 2:** Graphical representation of an MPS. Black circles represent matrices  $A$ . Lines connected to the circles represent indices, which are summed over when the lines of two circles are connected. The horizontal set of circles and lines therefore represents the product of matrices in Eq. (4). The vertical lines denote the remaining physical indices  $s_i$ .

### 2.1.2 Matrix product state ansatz

A general state of the Heisenberg chain is

$$|\psi\rangle = \sum_{s_1, s_2, \dots, s_L} c_{s_1, s_2, \dots, s_L} |s_1, s_2, \dots, s_L\rangle \quad (3)$$

with  $2^L$  complex numbers as coefficients. We will now write the coefficients in a different way, as a product of matrices, with one matrix for every lattice-site. This can always be done exactly (see later) when the matrices are chosen big enough, namely up to  $2^{L/2} \times 2^{L/2}$ . We will later see that much smaller matrices ( $\mathcal{O}(100) \times \mathcal{O}(100)$ ) can already provide an extremely good approximation to physically relevant states. The ansatz is

$$|\psi\rangle = \sum_{s_1, s_2, \dots, s_L} \sum_{\alpha_1, \alpha_2, \dots, \alpha_{L-1}} A_{\alpha_1}^{[1] s_1} A_{\alpha_1, \alpha_2}^{[2] s_2} A_{\alpha_2, \alpha_3}^{[3] s_3} \dots A_{\alpha_{L-2}, \alpha_{L-1}}^{[L-1] s_{L-1}} A_{\alpha_{L-1}}^{[L] s_L} |s_1, s_2, \dots, s_L\rangle. \quad (4)$$

The  $A$  can be taken to be square matrices (except for the first and last  $A$ , which are vectors), and  $\alpha_j = 1 \dots \chi$  are the matrix indices. The upper index  $[j]$  numbers the lattice sites. The matrices  $A$  usually differ from site to site. At each site  $j$ , there are two matrices,  $A^{[j]\uparrow}$ , and  $A^{[j]\downarrow}$ , corresponding to the values  $s_j = \uparrow$  and  $s_j = \downarrow$  in the basis vector  $|s_1, s_2, \dots, s_L\rangle$ . For a given state, the matrices  $A$  are not unique: one can replace any pair of matrices  $A^{[j]} A^{[j+1]}$  by  $(A^{[j]} X) (X^{-1} A^{[j+1]})$ , with any invertible matrix  $X$ . It is very helpful to denote this ansatz for the coefficients in a graphical way, as shown in Fig. 2. Let us look at some simple examples.

• *Single basis state (product state)* A state like  $|\downarrow\downarrow\uparrow\downarrow\uparrow\downarrow\rangle$  is called “product state” since it can be written as a product  $|\downarrow\rangle_1 |\downarrow\rangle_2 |\uparrow\rangle_3 |\downarrow\rangle_4 |\uparrow\rangle_5 |\downarrow\rangle_6$  and it does not contain any linear combination.

$ \psi\rangle$	$=$	$ $	$\downarrow$	$\downarrow$	$\uparrow$	$\downarrow$	$\uparrow$	$\downarrow$	$\rangle$
$j$	$=$		1	2	3	4	5	6	
$A_j^\uparrow$	$=$		0	0	1	0	1	0	
$A_j^\downarrow$	$=$		1	1	0	1	0	1	

The “matrices”  $A$  are just single numbers here.

• *Singlet,  $L=2$  sites*

$$|\psi\rangle = \frac{1}{\sqrt{2}} \left( \begin{array}{c} | \quad \uparrow \quad \downarrow \quad \rangle \\ - \quad | \quad \downarrow \quad \uparrow \quad \rangle \end{array} \right)$$

$$A_j^\uparrow = (1, 0), \quad - \begin{pmatrix} 0 \\ 1 \end{pmatrix} / \sqrt{2}$$

$$A_j^\downarrow = (0, 1), \quad \begin{pmatrix} 1 \\ 0 \end{pmatrix} / \sqrt{2}$$

• *Nonlocal singlet*

$$|\psi\rangle = \frac{1}{\sqrt{2}} \left( \begin{array}{c} | \quad \downarrow \quad \downarrow \quad \uparrow \quad \downarrow \quad \downarrow \quad \downarrow \quad \downarrow \quad \rangle \\ - \quad | \quad \downarrow \quad \downarrow \quad \downarrow \quad \downarrow \quad \downarrow \quad \uparrow \quad \downarrow \quad \downarrow \quad \rangle \end{array} \right)$$

$$A_j^\uparrow = 0, \quad 0, \quad (1, 0), \quad \begin{pmatrix} 0 & 0 \\ 0 & 0 \end{pmatrix}, \quad \begin{pmatrix} 0 & 0 \\ 0 & 0 \end{pmatrix}, \quad - \begin{pmatrix} 0 \\ 1 \end{pmatrix} / \sqrt{2}, \quad 0, \quad 0$$

$$A_j^\downarrow = 1, \quad 1, \quad (0, 1), \quad \begin{pmatrix} 1 & 0 \\ 0 & 1 \end{pmatrix}, \quad \begin{pmatrix} 1 & 0 \\ 0 & 1 \end{pmatrix}, \quad \begin{pmatrix} 1 \\ 0 \end{pmatrix} / \sqrt{2}, \quad 1, \quad 1$$

### 2.1.3 Singular value decomposition (SVD)

The SVD is an extremely important and versatile tool from linear algebra and the central technical ingredient of MPS techniques. It is different from the familiar eigenvalue decomposition (see below), and it exists for every real or complex matrix. It is widely used for, e.g., image processing, signal processing, optimizations, etc. *Every* real or complex  $n \times m$  matrix  $M$  can be decomposed like

$$M = U D V^\dagger \quad (5)$$

with a diagonal matrix  $D$  that contains only *positive real numbers* (or zero), which are called the *singular values* of  $M$ . It is of dimension  $N = \min(n, m)$ . Furthermore,

$$U^\dagger U = \mathbb{1}, \quad V^\dagger V = \mathbb{1}, \quad D = \begin{pmatrix} \lambda_1 & & & & \\ & \ddots & & & \\ & & \lambda_r & & \\ & & & 0 & \\ & & & & \ddots \\ & & & & & 0 \end{pmatrix}. \quad (6)$$

We will always order  $\lambda_1 \geq \lambda_2 \geq \dots \geq \lambda_r > \lambda_{r+1} = 0 = \dots = \lambda_N = 0$ . The number  $r$  of non-zero entries  $\lambda$  is called the rank of the matrix  $M$ , which need not be square. When, e.g.,

$m \leq n$ , the SVD looks like  $\boxed{M} = \boxed{U} \boxed{D} \boxed{V^\dagger}$  and  $V^\dagger$  cannot be unitary. This version of the SVD, with (in general) non-square matrices  $U$  and  $V^\dagger$ , is called a “thin SVD”. The values  $\lambda_i$  are uniquely determined. The matrices  $U$  and  $V^\dagger$  are not unique: within each subspace (dimension  $\geq 1$ ) of equal singular values, one can multiply  $U$  with a unitary matrix and  $V^\dagger$  with the inverse, without changing  $M$ . When  $M$  is real, then  $U$  and  $V^\dagger$  can also be chosen real. When  $M$  is real and quadratic, then  $U$  and  $V^\dagger$  are rotations (basis transformations), and  $D$  scales the directions in the intermediate basis. The eigenvalue decomposition of matrices  $M^\dagger M$  and  $MM^\dagger$  both have eigenvalues  $\lambda_j^2$ . When  $M$  is quadratic and all eigenvalues are  $\geq 0$ , then the eigenvalue decomposition  $M = UDU^\dagger$  is the same as the SVD.

The computational cost of a SVD is  $\min(mn^2, m^2n)$ . Many applications of the SVD involve **truncation**: one replaces small singular values by zero. This provides an *approximation* to  $M$ , which is usually very good and often of *far* smaller dimension, providing for much lower computational cost.

### Representation of the SVD with square matrices

When  $M$  is not quadratic, then either  $U$  or  $V^\dagger$  is not quadratic in the SVD  $M = UDV^\dagger$ . Alternatively, one can write the SVD with *unitary* quadratic matrices  $\tilde{U}$  and  $\tilde{V}$ :

$$M = UDV^\dagger = \tilde{U}\tilde{D}\tilde{V}^\dagger \quad (7)$$

This can be interpreted as a basis transformation by  $\tilde{V}^\dagger$ , a weighting of directions by  $\tilde{D}$ , and another basis transformation by  $\tilde{U}$ . When  $M$  is  $m \times n$  dimensional, then  $\tilde{U}$  is  $m \times m$ ,  $\tilde{D}$  is  $m \times n$ , and  $\tilde{V}^\dagger$  is  $n \times n$ .

• Case  $m \leq n$ :

$$\boxed{M} = \boxed{U} \boxed{D \text{---} 0 \text{ } 0 \text{ } 0} \boxed{\begin{array}{c} V^\dagger \\ \hline \text{(rest)} \end{array}}$$

In this case,  $\tilde{U} = U$ . The lower rows of  $\tilde{V}^\dagger$  contain extra eigenvectors, beyond those in  $V^\dagger$ . They do not contribute to  $M$  because of the zeroes in  $\tilde{D}$ . Since the eigenvectors in  $\tilde{V}^\dagger$  are orthogonal, the application of  $M$  to such a vector gives zero, i.e., they belong to the *null space* of  $M$ . (The directions  $j$  beyond the rank  $r$ , with vanishing singular value  $\lambda_{j>r} = 0$  also belong to the null space). When considering the action of  $M$  on the full vector space, this null space can be ignored (see below).

• Case  $m \geq n$ :

$$\boxed{M} = \boxed{\begin{array}{c|c} U & \text{(rest)} \end{array}} \boxed{\begin{array}{c} D \\ \hline 0 \end{array}} \boxed{V^\dagger}$$

Now  $\tilde{V} = V$ .

## Pseudoinverse

We first discuss the case of a square matrix  $M$ . Formally, the inverse is

$$M^{-1} = (\tilde{U} \tilde{D} \tilde{V}^\dagger)^{-1} = \tilde{V} \tilde{D}^{-1} \tilde{U}^\dagger, \quad (8)$$

since  $\tilde{U}$  and  $\tilde{V}$  are unitary. But the matrix  $M$  can contain singular values  $\lambda_{j>r} = 0$ . In these directions  $j$ ,  $M$  does not act, and the inverse  $\tilde{D}^{-1}$  would contain infinity.

It is much better to *exclude this null space* completely also from the inverse, i.e., to set  $\tilde{D}^{-1}$  to zero there. This is called the *pseudoinverse*

$$\lambda_j \mapsto \frac{1}{\lambda_j}, \quad \text{but } 0 \mapsto 0. \quad (9)$$

In practice, one maps singular values to zero when they are below some threshold (e.g.  $10^{-10}$ ). Using the pseudoinverse,  $M^{-1}M$  becomes

$$M^{-1}M = \tilde{V} \tilde{D}^{-1} \tilde{U}^\dagger \tilde{U} \tilde{D} \tilde{V}^\dagger = \begin{pmatrix} 1 & & & & \\ & \ddots & & & \\ & & 1 & & \\ & & & 0 & \\ & & & & \ddots \\ & & & & & 0 \end{pmatrix} = \dots = M M^{-1} \quad (10)$$

in which only (up to) the first  $r$  components correspond to the unity matrix, while the rest vanishes. The same considerations apply when  $M$  is not square,  $n > m$  or  $m > n$ . Then  $M^{-1}M$  is an  $n \times n$  matrix. and  $MM^{-1}$  is  $m \times m$ . They are both of the form Eq. (10).

### 2.1.4 Schmidt decomposition, reduced density matrix, and entanglement

Consider any quantum-mechanical system and two arbitrarily chosen subsystems  $A$  and  $B$ , for instance the left and right side of a one dimensional chain with some arbitrary split. Let  $|j\rangle_A$  be the orthonormal basis states of subsystem A, and  $|k\rangle_B$  those of subsystem B. Then a general pure state of the total system is

$$|\Psi\rangle = \sum_{j,k} c_{jk} |j\rangle_A |k\rangle_B, \quad (11)$$

where  $c_{jk}$  are coefficients. We now regard  $c_{jk}$  as a matrix and look at its singular value decomposition

$$c_{jk} = \tilde{U} \tilde{D} \tilde{V}^\dagger, \quad \text{with } \tilde{U} \text{ and } \tilde{V} \text{ unitary.} \quad (12)$$

Written in matrix components, this becomes  $c_{jk} = \sum_{\alpha=1}^{\chi} \lambda_{\alpha} \tilde{U}_{j\alpha} (\tilde{V}^\dagger)_{\alpha k}$ , where  $\chi$  is the rank of the matrix  $c_{jk}$ , the so called Schmidt-rank. Since  $\tilde{U}$  and  $\tilde{V}$  are unitary, it is possible to perform two basis transformations:  $|A\rangle_{\alpha} := \sum_j \tilde{U}_{j\alpha} |j\rangle_A$  and  $|B\rangle_{\alpha} := \sum_k (\tilde{V}^\dagger)_{\alpha k} |k\rangle_B$  and express the state  $|\Psi\rangle$  in the new basis

$$|\Psi\rangle = \sum_{\alpha=1}^{\chi} \lambda_{\alpha} |A\rangle_{\alpha} |B\rangle_{\alpha}, \quad \text{with } \chi \leq \min(\dim(A), \dim(B)). \quad (13)$$

This Schmidt-decomposition of a general state  $|\Psi\rangle$  always exists. The normalization  $\langle\Psi|\Psi\rangle = 1$  implies

$$\sum_{\alpha} \lambda_{\alpha}^2 = 1. \quad (14)$$

### Reduced density matrix of a pure state

The density matrix of a *pure* state is  $\hat{\rho} = |\Psi\rangle\langle\Psi|$ , which can be written

$$\hat{\rho} = \sum_{\alpha=1}^{\chi} \sum_{\beta=1}^{\chi} \lambda_{\alpha} \lambda_{\beta} |A\rangle_{\alpha} \langle B|_{\beta} \langle A|_{\beta} \langle B|_{\alpha}.$$

The *reduced density matrix* for the subsystem  $A$  is

$$\hat{\rho}_A = \text{tr}_B \hat{\rho} = \sum_{\gamma} \langle B| \hat{\rho} |B\rangle_{\gamma} = \sum_{\gamma=1}^{\chi} \lambda_{\gamma}^2 |A\rangle_{\gamma} \langle A|, \quad (15)$$

since the bases  $|A\rangle$  and  $|B\rangle$  are orthonormal. This is a sum over eigenvalues  $\lambda_{\gamma}^2$  times a corresponding projection operator  $|A\rangle_{\gamma} \langle A|$ . When the Schmidt rank  $\chi$  is larger than one, the state is entangled and the reduced density matrix represents a mixed state, as we will see next.

### Von Neumann entanglement entropy

Similar in definition to the entropy of a statistical system  $S = -\text{tr}(\hat{\rho} \ln \hat{\rho})$ , the von Neumann entanglement entropy between two subsystems  $A$  and  $B$  is defined as the entropy of the reduced density matrix:

$$S_A := -\text{tr}_A(\hat{\rho}_A \ln \hat{\rho}_A) \quad (16)$$

When the Schmidt decomposition of  $|\psi\rangle$  and thus the reduced density matrix Eq. (15) is known, the von Neumann entropy is simply

$$S_A = -\sum_{\gamma=1}^{\chi} \lambda_{\gamma}^2 \ln \lambda_{\gamma}^2 = S_B. \quad (17)$$

$S_A$  takes its maximum possible value of  $\ln \chi$  when all  $\lambda_{\gamma}$  are of equal value. Note that the entanglement entropy between two subsystems is invariant under unitary transformations *within* a subsystem, but usually *not* under a transformation which mixes both subsystems, like e.g., a spatial Fourier transform.

### Examples for a two site system

For a *product state*,  $|\Psi\rangle = |\uparrow_A \uparrow_B\rangle = |\uparrow\rangle_A |\uparrow\rangle_B$  is already the Schmidt decomposition. The reduced density matrix is  $\hat{\rho}_A = |\uparrow\rangle_A \langle\uparrow|$ , which is a pure state, and the entanglement entropy between the two sites is  $S_A = S_B = -1^2 \ln 1^2 = 0$ .

For a *singlet*,  $|\Psi\rangle = \frac{1}{\sqrt{2}}(|\uparrow\rangle_A |\downarrow\rangle_B - |\uparrow\rangle_B |\downarrow\rangle_A)$  is also already the Schmidt decomposition, the reduced density matrix is  $\hat{\rho}_A = \sum_{\alpha=1}^2 \lambda_{\alpha}^2 |A\rangle_{\alpha} \langle A| = \frac{1}{2}(|\uparrow\rangle_A \langle\uparrow| + |\downarrow\rangle_A \langle\downarrow|)$ , which in matrix notation is one half the unit matrix, and the entanglement entropy is  $S_A = -2 \cdot \frac{1}{2} \ln \frac{1}{2} = \ln 2$ .



## 2.2 Different MPS representations of a state

### 2.2.1 Exact representation

The coefficients of any pure state  $|\Psi\rangle = \sum_{s_1 \dots s_L} c_{s_1 \dots s_L} |s_1 \dots s_L\rangle$  can be written as a “matrix product state” by going through the system site by site and performing Schmidt decompositions, i.e., basis transformations, at each site.

**First site.** We treat the coefficients  $c_{s_1, (s_2 \dots s_L)}$  as a matrix with row index  $s_1$  and column index  $(s_2 \dots s_L)$  and apply an SVD

$$c_{s_1, (s_2 \dots s_L)} = \sum_{\alpha_1=1}^2 \underbrace{U_{s_1 \alpha_1}^{[1]}}_{2 \times 2 \text{ matrix}} \lambda_{\alpha_1}^{[1]} V_{\alpha_1 (s_2 \dots s_L)}^\dagger$$

The upper index [1] denotes the first lattice site. Since the index  $s_1$  has only two values,  $s_1 = \uparrow$  and  $s_1 = \downarrow$ , the matrix  $U^{[1]}$  is  $(2 \times 2)$  dimensional. We split it into two  $(1 \times 2)$ -matrices  $A^{[1]\uparrow}$  and  $A^{[1]\downarrow}$  for the two spin components  $\uparrow$  and  $\downarrow$ .

$$\begin{array}{ccc} \boxed{U_{s_1 \alpha_1}^{[1]}} & = & \boxed{\begin{array}{c} s_1^\uparrow \\ \hline s_1^\downarrow \end{array}} & =: & \boxed{\begin{array}{c} A_{\alpha_1}^\uparrow \\ \hline A_{\alpha_1}^\downarrow \end{array}} \\ \alpha_1 = 1, 2 & & \alpha_1 = 1, 2 & & \alpha_1 = 1, 2 \end{array}$$

$U$  is a unitary matrix. It contains a basis transformation from the basis  $s_1 = \uparrow, s_1 = \downarrow$  to a new basis with indices  $\alpha_1 = 1, 2$ . Similarly,  $V^\dagger$  defines a *basis transformation* on the vectors  $|s_2, s_3, \dots, s_L\rangle$ , i.e., we get the Schmidt decomposition

$$|\Psi\rangle = \sum_{\alpha_1=1}^2 \lambda_{\alpha_1}^{[1]} |\Phi_{\alpha_1}^L\rangle |\Phi_{\alpha_1}^R\rangle, \quad (18)$$

where  $L(R)$  denote the left(right) subsystem.

**Second site.** We now regard  $\lambda_{\alpha_1} V_{\alpha_1 (s_2 \dots s_L)}^\dagger$  (including the diagonal matrix  $\lambda$ ) as a matrix element with row index  $(\alpha_1 s_2)$  and column index  $(s_3 \dots s_L)$  and decompose it with an SVD

$$\lambda_{\alpha_1} V_{\alpha_1 (s_2 \dots s_L)}^\dagger = \sum_{\alpha_2=1}^4 \underbrace{U_{(\alpha_1 s_2) \alpha_2}^{[2]}}_{4 \times 4 \text{ matrix}} \lambda_{\alpha_2}^{[2]} V_{\alpha_2 (s_3 \dots s_L)}^\dagger$$

The summation index  $\alpha_2$  now goes up to 4, because of the possible combinations of  $\alpha_1 = \{1, 2\}$  and  $s_2 = \{\uparrow, \downarrow\}$ .<sup>1</sup> The  $4 \times 4$  matrix  $U^{[2]}$  is again unitary and a basis transformation from  $\{\alpha_1 s_2\}$  to  $\{\alpha_2\}$  which we split up into two  $2 \times 4$  matrices  $A^{[2]\uparrow}$  and  $A^{[2]\downarrow}$  for the two spin indices  $s_2$

$$\begin{array}{ccc} \boxed{U_{\alpha_1 s_2 \alpha_2}^{[2]}} & =: & \boxed{\begin{array}{c} A_{\alpha_2}^\uparrow \\ \hline A_{\alpha_2}^\downarrow \end{array}} \\ \alpha_2 = 1 \dots 4 & & \alpha_2 = 1 \dots 4 \end{array}$$

<sup>1</sup>The actual range of  $\alpha$  can be smaller, when the coefficients of  $|\Psi\rangle$  are such that the SVD has a lower rank, e.g., for a product state (rank 1).

**After iteration up to site  $j$ .** we get the following representation of the state  $|\Psi\rangle$

$$|\Psi\rangle = \sum_{s_1 \dots s_L} \sum_{\alpha_1}^2 \sum_{\alpha_2}^4 \sum_{\alpha_3}^8 \dots U_{s_1 \alpha_1}^{[1]} U_{(\alpha_1 s_2) \alpha_2}^{[2]} \dots U_{(\alpha_{j-1} s_j) \alpha_j}^{[j]} \lambda_{\alpha_j}^{[j]} V_{\alpha_j (s_{j+1} \dots s_L)}^\dagger |s_1 \dots s_L\rangle. \quad (19)$$

This is also a Schmidt decomposition of  $|\Psi\rangle$ , between sites  $j$  and  $j+1$ . By splitting up each  $U$ -matrix into two distinct matrices for  $\uparrow$  and  $\downarrow$  spin indices, we can also write

$$U_{s_1 \alpha_1}^{[1]} U_{(\alpha_1 s_2) \alpha_2}^{[2]} U_{(\alpha_2 s_3) \alpha_3}^{[3]} \dots = A_{\alpha_1}^{[1] s_1} A_{\alpha_1 \alpha_2}^{[2] s_2} A_{\alpha_2 \alpha_3}^{[3] s_3} \dots$$

**Exact MPS representation of  $|\Psi\rangle$ .** Continuing until the last lattice site, we find that indeed an arbitrary state  $|\Psi\rangle$  can be represented exactly by a matrix product state

$$|\Psi\rangle = \sum_{s_1 \dots s_L} \sum_{\{\alpha_i\}} A_{\alpha_1}^{[1] s_1} A_{\alpha_1 \alpha_2}^{[2] s_2} A_{\alpha_2 \alpha_3}^{[3] s_3} \dots A_{\alpha_{L-2} \alpha_{L-1}}^{[L-1] s_{L-1}} A_{\alpha_{L-1}}^{[L] s_L} |s_1 \dots s_L\rangle \quad (20)$$

represented graphically in Fig. 2. The range of the intermediate indices  $\alpha_i$  is equal to the rank of the corresponding SVD. Note that between sites  $L-1$  and  $L$ , this rank is at most 2, and between sites  $L-2$  and  $L-1$ , it is at most 4. Thus, an *exponentially large maximum rank of up to  $2^{L/2}$*  is reached in the middle of the chain for a general state.

### 2.2.2 Left-Normalization

Each of the matrices  $U^{[i]}$  comes from an SVD and therefore satisfies  $U^{[j]\dagger} U^{[j]} = \mathbb{1}$ , which also provides for normalized basis transformations. In terms of the matrices  $A^{[j]}$  this becomes

$$\sum_{s_j} A^{[j] s_j \dagger} A^{[j] s_j} = \mathbb{1} \quad (21)$$

Written in matrix components, this equation reads

$$\sum_{s_j, \alpha_{j-1}} A_{\alpha_{j-1} \alpha'}^{*[j] s_j} A_{\alpha_{j-1} \alpha}^{[j] s_j} = \delta_{\alpha \alpha'} \quad \text{or graphically} \quad \alpha_{j-1} \left[ \begin{array}{c} \text{A}^{[j]\dagger} \\ \hline \text{A}^{[j]} \end{array} \right]_{\alpha_j} = \delta_{\alpha \alpha'} \quad (22)$$

In the graphical representation, closed lines imply a summation. The normalization of the whole MPS,  $\langle \Psi | \Psi \rangle = 1$ , can now be deduced in a simple way, by applying the graphical form of Eq. (22) site by site. The state Eq. (4) and Fig. 2, written with A-matrices, is called *left-normalized*.

### 2.2.3 Canonical form of an MPS

Each Schmidt decomposition in the derivation of the MPS also gave us the singular values  $\lambda_\alpha$ , i.e., information about the reduced density matrix at that step. We now write this information explicitly in the MPS. We take the singular values  $\lambda_\alpha$  out of the A-matrices; this defines new matrices  $\Gamma$

$$A_{\alpha_{j-1} \alpha_j}^{[j] s_j} =: \lambda_{\alpha_{j-1}}^{[j-1]} \Gamma_{\alpha_{j-1} \alpha_j}^{[j] s_j} \quad (23)$$

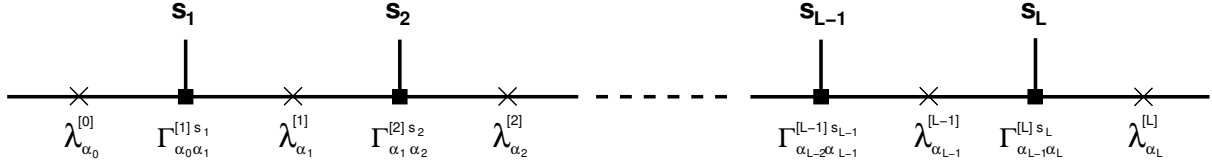


**Fig. 3:** Graphical representation for the canonical form of MPS matrices.

When the A-matrices are given, one can obtain the  $\Gamma$  matrices by multiplying A with the *pseudoinverse* of  $\lambda$ . Graphically, the “MPS state” (actually the coefficient  $c_{s_1 s_2 \dots s_L}$ ) is shown in Fig. 3, where we denote  $\lambda$ -matrices by crosses, and  $\Gamma$ -matrices by squares. The  $\lambda^{[j]}$  are located between sites  $j$  and  $j+1$ . They are the singular values of the Schmidt decomposition at that bond,  $c_{s_1 s_2 \dots s_L} = U \lambda V^\dagger$ . In a product state, all  $\Gamma^{[i]}$  are numbers 0 or 1, and all  $\lambda^{[i]} = 1$ . Since the first “matrix”  $A_{\alpha_0 \alpha_1}^{[1] s_1}$  is just a vector, the first index  $\alpha_0$  on  $\Gamma_{\alpha_0 \alpha_1}^{[1] s_1}$  is superfluous. We still write  $\Gamma_{\alpha_0 \alpha_1}^{[1] s_1}$  as a matrix, for easier notation later on, by letting the index  $\alpha_0$  only have one value  $\alpha_0 = 1$  and  $\lambda_{\alpha_0}^{[0]} \equiv 1$ . Similarly,  $\alpha_L$  has only the one value  $\alpha_L \equiv 1$  and  $\Gamma_{\alpha_{L-1} \alpha_L}^{[L] s_L}$  is actually a vector. At the right hand side we have introduced a final  $\lambda_{\alpha_L}^{[L]} \equiv 1$ . The normalization Eq. (22) now becomes an equation for  $\Gamma$  and  $\lambda$ , shown below on the left hand side

$$\sum_{s_j} (\Gamma^{[j] s_j})^\dagger (\lambda^{[j-1]})^2 \Gamma^{[j] s_j} = \mathbb{1} \qquad \sum_{s_j} \Gamma^{[j] s_j} (\lambda^{[j]})^2 (\Gamma^{[j] s_j})^\dagger = \mathbb{1} \quad (24)$$

A similar normalization can also be shown to hold when summing over the second matrix index of  $\Gamma^{[j]}$  by an iterative construction of the MPS from the right. This normalization is displayed on the right side of the equation above.

#### 2.2.4 B-matrices, right-normalization, and mixed normalization

Instead of combining  $A^{[j]} = \lambda^{[j-1]} \Gamma^{[j]}$  as in Eq. (23), one can group the matrices of the canonical representation via  $B^{[j]} = \Gamma^{[j]} \lambda^{[j]}$ , so that instead of Eq. (4) we get an equivalent product of B-matrices for the coefficients of  $|\psi\rangle$ . The B-matrices are *right-normalized*, as spelled out on the right side of Eq. (24).

In DMRG, the coefficients of states are usually expressed in the so-called *mixed-canonical* form  $AA \dots A \lambda B \dots BB$  which follows directly from the canonical form in Fig. 3. The diagonal matrix  $\lambda$  contains the singular values of a Schmidt decomposition at the corresponding bond.

An unnormalized state can be brought into one of the canonical forms essentially by repeating an analogue of the steps outlined in section 2.2.1: successive SVDs from one end to the other.

## Truncation

In order to achieve an efficient representation of a state, with relatively small matrices, we can approximate the state by discarding small singular values  $\lambda_\alpha$ . This needs to be done in the canonical or mixed canonical representation, in which the  $\lambda_\alpha$  do contain the Schmidt singular values. When all  $\lambda_{\alpha > \alpha_0}^{[j]}$  are discarded, the matrices  $\Gamma^{[j]}$  and  $\Gamma^{[j+1]}$  can be *truncated* correspondingly beyond matrix index  $\alpha_0$ . One can either discard values below a certain threshold  $\varepsilon$  (e.g.  $10^{-10}$ ), which results in a varying matrix dimension, or one can set a maximum matrix dimension  $\chi_{\max}$  beyond which all singular values are discarded.

The quality of the approximation is related to how much of the reduced density matrix  $\rho = \text{diag}(\lambda_1^2, \lambda_2^2, \dots)$  is discarded. This can be quantified by the so-called **truncated weight**

$$t_w = 1 - \sum_{\alpha=1}^{\chi_{\max}} \lambda_\alpha^2, \quad (25)$$

which should stay below some small threshold like  $\ll 10^{-8}$  for precise calculations. In order to keep the state normalized, we have to re-normalize the remaining  $\lambda_\alpha$

$$\lambda_\alpha \rightarrow \lambda_\alpha / \sqrt{1 - t_w}, \quad \text{so that} \quad \sum_\alpha \lambda_\alpha^2 = 1. \quad (26)$$

The normalizations of the A-matrices and the  $\Gamma$ -matrices are unaffected by the truncation, except that the matrix  $\mathbb{1}$  in Eq. (21) is also truncated.

## How large do the matrices need to be?

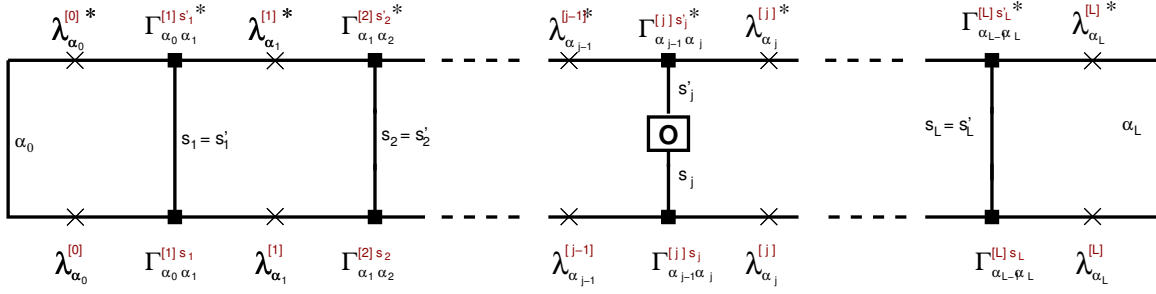
The discarded weight  $t_w$  is small when the singular values  $\lambda_\alpha$  decay quickly. This is the case when the entanglement entropy Eq. (17),  $S_A = -\sum_{\gamma=1}^{\chi} \lambda_\gamma^2 \ln \lambda_\gamma^2$  is small. We saw earlier that the maximum entanglement entropy of a reduced density matrix of size  $\chi$  is  $\ln \chi$ . Thus one can estimate that one may need matrices of up to order  $\chi_{\max} \sim e^{S_A}$  for a good representation of a state. In 1D, the border of two subsystem  $A$  and  $B$  is just a point. All entanglement between  $A$  and  $B$  must go through this point. One can show that for the ground state of gapped Hamiltonians with local couplings one needs only about  $\chi_{\max} \sim \xi$  where  $\xi$  is the maximum of the spatial correlation length and the size of the system. This is the reason why matrix product states work so well in one-dimensional physical systems. However, in general dimension  $D$ ,  $S_{\max} \sim L^{D-1}$ , the so-called area-law, which implies that the matrix dimension will need to grow exponentially in more than 1D.

## Expectation values of one-site operators

A big advantage of the MPS representation is that only a few local matrices are needed to calculate the effect of a local operator on the state (see below), or its expectation value. We will here look at the expectation value of a one-site operator  $\hat{O}^{[j]}$  that acts only on the spin at site  $j$ , for example  $\hat{S}_z^{[j]}$ , whose matrix representation is the third Pauli matrix. Its expectation value is

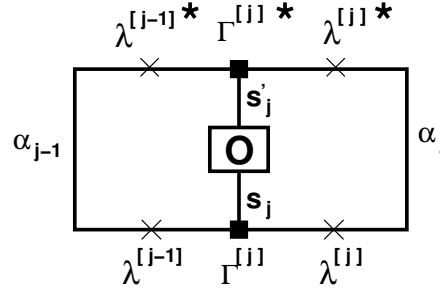
$$\langle \Psi | \hat{O}^{[j]} | \Psi \rangle = \sum_{\{s\}, \{s'\}} \langle s'_1 \dots s'_L | \dots \lambda^{*[j]} \Gamma^{*[j]s'_j} \lambda^{*[j-1]} \dots \textcolor{red}{O}_{s_j s'_j}^{[j]} \dots \lambda^{[j-1]} \Gamma^{[j]s_j} \lambda^{[j]} \dots | s_1 \dots s_L \rangle \quad (27)$$

In graphical representation, this becomes



At the interior vertical lines, the spins  $s'_i$  from the bra vector  $\langle\psi|$  and  $s_i$  from the ket vector  $|\psi\rangle$  meet. Since  $\langle s'_i | s_i \rangle = \delta_{s_i s'_i}$ , they have to be equal, except at the location  $j$  of the operator  $\hat{O}^{[j]}$ . Note that all lambda values are actually real, since they are singular values.

This expression can now be simplified by using the normalization Eqs. (24), which iteratively cause all matrices from both ends of the chain up to site  $j$  to just contribute Kronecker deltas. The remaining contribution is, in graphical representation



With  $M_{\alpha_{j-1}\alpha_j}^{s_j} := \lambda_{\alpha}^{[j-1]} \Gamma_{\alpha_{j-1}\alpha_j}^{[j] s_j} \lambda_{\alpha_j}^{[j]}$  this becomes

$$\langle\psi|\hat{O}^{[j]}|\psi\rangle = \sum_{s,s'} \langle s' | \hat{O} | s \rangle \text{tr}(M^{s'})^\dagger M^s. \quad (28)$$

## 2.3 Time evolution

The time evolution of a state in the Schrödinger picture for a time-independent Hamiltonian is given by  $|\Psi(t)\rangle = e^{-i\hat{H}t}|\Psi(0)\rangle$ . We will discuss the case of Hamiltonians with local or nearest neighbor interactions, like in (2).

### 2.3.1 Trotter Suzuki decomposition

The difficulty now is that the Hamiltonians of adjacent sites do not commute,  $[\hat{H}_i, \hat{H}_{i+1}] \neq 0$  and as a consequence the exponential  $e^{-i\hat{H}t}$  cannot be expressed as a product of local operators  $e^{-i\hat{H}t} \neq \prod_j e^{-i\hat{H}_j t}$ . But the Hamiltonians of next nearest neighbor sites do commute:  $[\hat{H}_i, \hat{H}_{i+2}] = 0$ . It is thus helpful to decompose  $\hat{H}$  into a sum of even and odd site Hamiltonians

$$\hat{H} = \hat{H}_{\text{even}} + \hat{H}_{\text{odd}} = \sum_{j,\text{odd}} \hat{H}_j + \sum_{j,\text{even}} \hat{H}_j \quad (29)$$

such that

$$e^{-i\hat{H}_{\text{even}} t} = \prod_{j,\text{even}} e^{-i\hat{H}_j t} \quad \text{and} \quad e^{-i\hat{H}_{\text{odd}} t} = \prod_{j,\text{odd}} e^{-i\hat{H}_j t}. \quad (30)$$

Within  $\hat{H}_{\text{even}}$ , all terms commute, and also within  $H_{\text{odd}}$ , but  $[\hat{H}_{\text{even}}, \hat{H}_{\text{odd}}] \neq 0$ . Next we subdivide the time  $t$  into small “time slices” of length  $\Delta t$

$$e^{-i\hat{H}t} = \left( e^{-i\hat{H}\Delta t} \right)^{\frac{t}{\Delta t}} = \left( e^{-i(\hat{H}_{\text{even}} + \hat{H}_{\text{odd}})\Delta t} \right)^{\frac{t}{\Delta t}}.$$

Now we use the Baker-Hausdorff formula to get

$$e^{-i\hat{H}t} = \left( e^{-i\hat{H}_{\text{even}}\Delta t} e^{-i\hat{H}_{\text{odd}}\Delta t} \left( 1 + \mathcal{O}\left((\Delta t)^2[\hat{H}_{\text{even}}, \hat{H}_{\text{odd}}]\right) \right) \right)^{\frac{t}{\Delta t}}.$$

Writing this product of  $t/\Delta t$  terms explicitly yields

$$e^{-i\hat{H}t} = \left( e^{-i\hat{H}_{\text{even}}\Delta t} e^{-i\hat{H}_{\text{odd}}\Delta t} e^{-i\hat{H}_{\text{even}}\Delta t} \dots e^{-i\hat{H}_{\text{even}}\Delta t} \right) \left( 1 + \mathcal{O}(\Delta t) \right). \quad (31)$$

We lost one order of  $\Delta t$  because of the  $(t/\Delta t)$  many factors. The Trotter-Suzuki decomposition leads to a series of operators  $e^{-i\hat{H}_j t}$  which only act on two adjacent sites at once. The time evolution of the system is traced back to application of these 2-site operators. This strategy was introduced in the context of quantum Monte Carlo by Suzuki. It is also used for several popular MPS time evolution methods.

The smaller the time step  $\Delta t$ , the smaller the error in the method. One can gain another order of  $\Delta t$  with almost no effort by the *2nd order Trotter Suzuki approximation*

$$e^{-i\hat{H}\Delta t} = e^{-i\hat{H}_{\text{even}}\Delta t/2} e^{-i\hat{H}_{\text{odd}}\Delta t} e^{-i\hat{H}_{\text{even}}\Delta t/2} + \mathcal{O}((\Delta t)^3). \quad (32)$$

For the time evolution of a state  $|\Psi\rangle$  this requires no more effort than the first order approximation, because  $e^{-i\hat{H}_{\text{even}}\Delta t/2} e^{-i\hat{H}_{\text{even}}\Delta t/2} = e^{-i\hat{H}_{\text{even}}\Delta t}$ . The only difference occurs when measurements are performed: for the 2nd order approximation, measurements have to be performed after *half*-time-steps  $e^{-i\hat{H}_{\text{even}}\Delta t/2}$ .

### 2.3.2 Application of 2-site operators

In order to calculate the time evolution, we need to apply the 2-site operators  $\hat{H}_i$  to  $|\Psi\rangle$ . For a general 2-site operator, we want to calculate

$$|\Psi'\rangle = \hat{O}^{[j,j+1]} |\Psi\rangle. \quad (33)$$

The structure of MPS as products of matrices located on individual sites is again very helpful. Since  $\hat{O}^{[j,j+1]}$  acts on sites  $j$  and  $j+1$ , only the  $\Gamma$ -matrices at these sites and the  $\lambda$ -matrix in *between* are affected, but not the outer  $\lambda$ -matrices containing the entanglement with the environment. Let  $\chi$  be the dimension of all these matrices. The calculations turn out to be easier when one also includes the two outer  $\lambda$ -matrices. We therefore look at the part of the MPS shown in Fig. 4. This object has spin indices  $s_j, s_{j+1}$  on which the operator will act, and free matrix indices  $\alpha$  and  $\gamma$ . It is the graphical representation of

$$\psi_{\alpha\gamma}^{s_j s_{j+1}} := \sum_{\beta} \lambda_{\alpha}^{[j-1]} \Gamma_{\alpha\beta}^{[j] s_j} \lambda_{\beta}^{[j]} \Gamma_{\beta\gamma}^{[j+1] s_{j+1}} \lambda_{\gamma}^{[j+1]}. \quad (34)$$

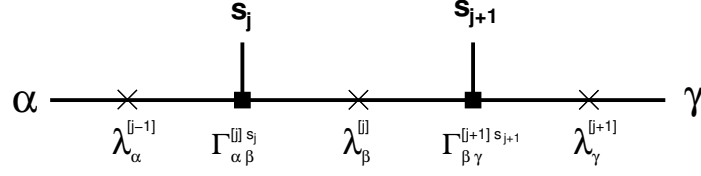


**Fig. 4:** The coefficients  $\psi_{\alpha\gamma}^{s_j s_{j+1}}$  of an MPS affected by two-site operators.

In the context of DMRG, it is called the wave-function. The application of  $\hat{O}$  on  $\psi$  yields

$$\tilde{\psi}_{\alpha\gamma}^{s'_j s'_{j+1}} := \sum_{s_j, s_{j+1}} \langle s'_j s'_{j+1} | \hat{O} | s_j s_{j+1} \rangle \psi_{\alpha\gamma}^{s_j s_{j+1}}. \quad (35)$$

We want to express  $|\Psi'\rangle$  as a normalized MPS, similar to  $|\Psi\rangle$ . We therefore need to write  $\tilde{\psi}$  in the same form as the original  $\psi$ , with new normalized matrices  $\tilde{\Gamma}_{\alpha\beta}^{[j] s'_j}$ ,  $\tilde{\lambda}_\beta$ , and  $\tilde{\Gamma}_{\beta\gamma}^{[j+1] s'_{j+1}}$ .

In order to get there, we first interpret  $\tilde{\psi}$  as a matrix with two indices, a row index  $(\alpha s'_j)$  and a column index  $(\gamma s'_{j+1})$

$$\bar{\psi}_{(\alpha s'_j), (\gamma s'_{j+1})} := \tilde{\psi}_{\alpha\gamma}^{s'_j s'_{j+1}}. \quad (36)$$

Next we perform an SVD on  $\bar{\psi}$

$$\bar{\psi}_{(\alpha s'_j), (\gamma s'_{j+1})} = \sum_{\beta=1}^{2\chi} U_{(\alpha s'_j)\beta} \tilde{\lambda}_\beta V_{\beta(\gamma s'_{j+1})}^\dagger. \quad (37)$$

Note that  $U$  is the unchanged  $\lambda^{[j-1]}$  times a new  $\Gamma^{[j]}$  and is equivalent to a new A-matrix, and  $V^\dagger$  is a new  $\Gamma^{[j+1]}$  times the unchanged  $\lambda^{[j+1]}$ , equivalent to a new B-matrix.

Because of the presence of  $s'_j$  and  $s'_{j+1}$  in the indices (with 2 values  $\uparrow, \downarrow$ ), this SVD has a Schmidt rank up to *twice the rank* of the original matrices  $\Gamma, \lambda$ . If we kept this increased rank, then the matrix dimensions would explode exponentially during the time evolution. We therefore need to truncate the matrix dimensions, for example back to the original  $\chi$ , by discarding the smallest singular values in  $\tilde{\lambda}$ . We then need to calculate the discarded weight  $t_w$  and re-normalize  $\tilde{\lambda}_\beta \rightarrow \tilde{\lambda}_\beta / \sqrt{1 - t_w}$ . The matrices  $U$  and  $V^\dagger$  are also truncated at the new size.

In the so-called **tebd** algorithm [34, 35], which works in the canonical representation, new  $\Gamma$ -matrices are then extracted, by splitting the *unchanged* outer matrices  $\lambda^{[j-1]}$  and  $\lambda^{[j]}$  off  $U$  and  $V^\dagger$ , by means of applying the pseudoinverse:

$$\tilde{\Gamma}_{\alpha\beta}^{[j] s'_j} = (\lambda_\alpha^{[j-1]})^{\text{inv}} U_{(\alpha s'_j)\beta} \quad , \quad \tilde{\Gamma}_{\beta\gamma}^{[j+1] s'_{j+1}} = V_{\beta(\gamma s'_{j+1})}^\dagger (\lambda_\gamma^{[j+1]})^{\text{inv}}. \quad (38)$$

As desired, this results in updated  $\chi \times \chi$  matrices  $\tilde{\Gamma}_{\alpha\beta}^{[j] s'_j}$ ,  $\tilde{\lambda}_\beta$ , and  $\tilde{\Gamma}_{\beta\gamma}^{[j+1] s'_{j+1}}$ . This method has the disadvantage of potential instabilities from the divisions. They can also be avoided [7].

A different valid time-evolution with similarly small Trotter error, which is not commonly used but will be employed in the FTPS method, does not step by two sites in even/odd fashion, but **steps only by one site**, using  $\tilde{\lambda}^{[j]} V^{[j+1]\dagger}$  from Eq. (37) multiplied from the right with  $\Gamma^{[j+2]} \lambda^{[j+2]}$  as the next  $\psi^{s_{j+1} s_{j+2}}$  to be updated.

A mathematical equivalent of tebd is the **t-DMRG** algorithm [36, 37], which works in the mixed-canonical representation, i.e., with only A and B matrices, and with the even/odd Trotter split. When moving from the left to the right, the U matrix from the SVD defines the matrix  $A^{[j]}$  of the updated state. In order to step another site to the right,  $\psi^{s_{j+1} s_{j+2}}$  introduced in the previous paragraph is subjected to another SVD:  $\psi = UDV^\dagger$ , which yields  $A^{[j+1]}$  from U, while D should be the unchanged  $\lambda^{[j+1]}$  and  $V^\dagger$  the unchanged  $\Gamma^{[j+2]} \lambda^{[j+2]}$ . Multiplying  $DV^\dagger$  from the right by the next B-matrix ( $=\Gamma^{[j+3]} \lambda^{[j+3]}$ ) provides the next wave function  $\psi$  in t-DMRG, at the disadvantage of an additional SVD operation.

Another possibility for time evolution is by way of repeated application of the complete Hamiltonian to the state, in the simplest case as  $(1 + H\Delta t)^{t/(\Delta t)}$ . The complete Hamiltonian can be applied as a so-called Matrix-Product Operator (**MPO**), to be discussed next.

### Swap gate

A swap gate switches the physical role of two neighboring sites in an MPS [38, 7]. It amounts to applying the two-site operator

$$S_{ij} = \delta_{s_i, s'_j} \delta_{s_j, s'_i} (-1)^{n_i n_j} \quad (39)$$

to a state with physical indices  $s_i, s_j$ . The sign factor provides for fermion anticommutation.

## 2.4 Matrix product operators (MPO) and DMRG

In the same way as the coefficients of a state can be expressed as a product of matrices in Eq. (4) this can also be done for the coefficients of a many-particle operator  $\hat{O}$  in terms of matrices  $W_{\alpha_{i-1}\alpha_i}^{[s_i, s'_i]}$

$$\hat{O} = \sum_{\{s_i\}, \{s'_i\}} W^{s_1, s'_1} W^{s_2, s'_2} \dots W^{s_L, s'_L} |s'_1, s'_2, \dots, s'_L\rangle \langle s_1, s_2, \dots, s_L|, \quad (40)$$

where the internal matrix indices  $\alpha_i$  have been omitted. The graphical representation of this MPO is shown in Fig. 5. Methods for obtaining the W-matrices can, e.g., be found in Ref. [7]. For a simple Anderson impurity model, they will be shown explicitly below.

### 2.4.1 DMRG ground state search

The DMRG method [8, 7] optimizes the energy of a state  $|\psi\rangle$  site by site (or in pairs of sites) in order to find the state with minimum energy. Here we just provide a brief idea of the method. It works in the mixed canonical representation. Each optimization of a local MPS matrix  $A^{[i]}$  can be formulated as a linear equation

$$H_i^{\text{eff}} A^{[i]} = \lambda A^{[i]}, \quad (41)$$

for which the matrix with the lowest eigenvalue  $\lambda$  needs to be found, for example with a Lanczos method. The effective Hamiltonian  $H^{\text{eff}}$  is most easily expressed in graphical form, as in Fig. 5.



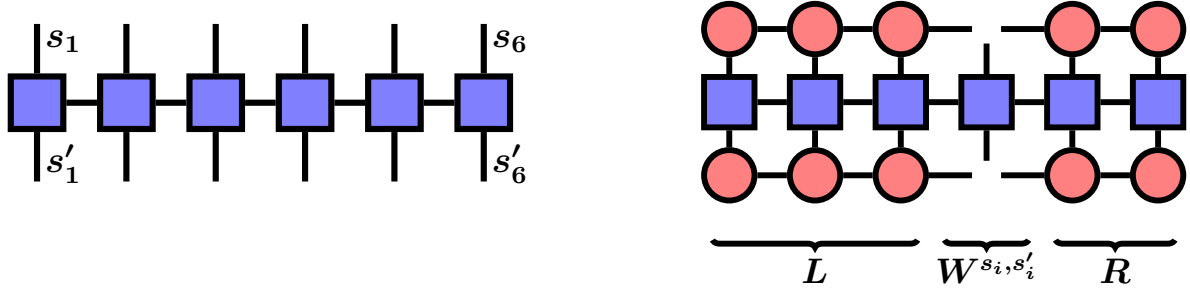


**Fig. 5:** Left: graphical representation of a matrix product operator. The disconnected lines symbolize again physical degrees of freedom  $s_i$ . The operator connects to an MPS with the lower indices, which implies a summation over  $\{s_i\}$ , producing a new MPS with indices  $\{s'_i\}$ . Right: Effective Hamiltonian for DMRG. It is applied to an MPS matrix  $A_{\alpha_{i-1}\alpha_i}^{[s_i]}$  on the bottom, producing an effective A-matrix on the top, which has to satisfy Eq. (41).

This local minimization works amazingly well, as mentioned earlier. Sometimes it can, however, get stuck in local minima. Because of the limited amount of entanglement available in an MPS, DMRG tends, for example, to converge to an ordered state, like, e.g., a Néel state in case of an antiferromagnet. Care must be taken to either avoid this or to correctly interpret the resulting state.

#### 2.4.2 MPO representation of an Anderson impurity model Hamiltonian

Let us now explicitly discuss an MPO which represents an Anderson impurity model Hamiltonian. More details can be found in Ref. [9]. To keep indices manageable, we will first discuss the standard AIM with a single orbital

$$H = \sum_{k\sigma} \varepsilon_k n_{k\sigma} + \sum_{k\sigma} V_k (c_{0\sigma}^\dagger c_{k\sigma} + h.c.) + \sum_{\sigma} \varepsilon_0 n_{0\sigma} + U n_{0\uparrow} n_{0\downarrow}. \quad (42)$$

We number sites like in Fig. 6. We will need MPOs of internal dimension 4 in order to code the four terms in  $H$ . For the leftmost site, the  $W$ -tensor of the MPO is a vector in internal MPO space. (This space is denoted by the horizontal indices in Fig. 5.) The physical indices are not written explicitly in the equations below; they are implied by the operators.

$$W_{1\uparrow} = (\varepsilon_1 n_{1\uparrow} \quad \mathbb{1} \quad V_1 c_{1\uparrow} \quad V_1 c_{1\uparrow}^\dagger) \quad (43)$$

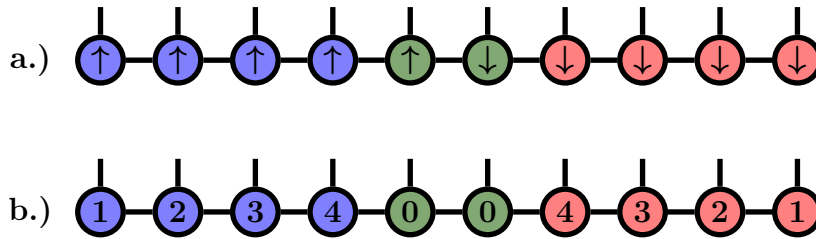


**Fig. 6:** Numbering of sites for a single orbital Anderson impurity model. Here the number of bath sites for each spin is  $N_B = 4$ .

Each following site of the left bath gets

$$W_{k\uparrow} = \begin{pmatrix} \mathbb{1} & 0 & 0 & 0 \\ \varepsilon_k n_{k\uparrow} & \mathbb{1} & V_k c_{k\uparrow} & V_k c_{k\uparrow}^\dagger \\ 0 & 0 & p & 0 \\ 0 & 0 & 0 & p \end{pmatrix} \quad (44)$$

as a  $W$ -tensor. The operator  $p = (-1)^n$  provides for a Jordan-Wigner transformation, i.e., it ensures fermionic commutation rules. Now

$$\prod_{k=1}^{N_b} W_{k\uparrow} = \left( \sum_{k=1}^{N_b} \varepsilon_k n_{k\uparrow} \quad \mathbb{1} \quad \sum_{k=1}^{N_b} V_k c_{k\uparrow} \quad \sum_{k=1}^{N_b} V_k c_{k\uparrow}^\dagger \right) \quad (45)$$

(with the  $p$  operators omitted in the last equation).

$W$ -tensors for the spin-down chain are equivalent, but with transposed matrices, and a column instead of a vector for the rightmost MPO. Finally, the  $W$ -tensors for the impurity sites are

$$W_{0\uparrow} = \begin{pmatrix} 0 & \mathbb{1} & 0 \\ \mathbb{1} & \varepsilon_0 n_{0\uparrow} & n_{0\uparrow} \\ 0 & c_{0\uparrow}^\dagger & 0 \\ 0 & c_{0\uparrow} & 0 \end{pmatrix}, \quad W_{0\downarrow} = \begin{pmatrix} \mathbb{1} & \varepsilon_0 n_{0\downarrow} & c_{0\downarrow}^\dagger & c_{0\downarrow} \\ 0 & \mathbb{1} & 0 & 0 \\ 0 & U n_{0\downarrow} & 0 & 0 \end{pmatrix}. \quad (46)$$

Multiplying all these matrices together produces the desired Hamiltonian Eq. (42).

## 2.5 Previous MPS impurity solvers

As spelled out in the introduction, we need to calculate the ground state of an Anderson Impurity Model (AIM), apply a creation or annihilation operator, and time evolve. In order to do this efficiently with MPS, where the computational effort for matrix dimension  $m$  grows like  $m^3$ , we need small matrices and few physical degrees of freedom per site. For a single spinful orbital, it turns out that it is best to split spin-up and spin-down into the chain geometry of Fig. 6 (top). Using real-time evolution, this allows for a very precise impurity solver, with large baths (easily  $\mathcal{O}(100)$  and more) and with excellent energy resolution in DMFT [31]. With two orbitals, a successful strategy has been to split the *orbitals* into two separate chains, which also provided a precise impurity solver [31]. An advantage of this geometry is that the spins of each orbital, which are likely to be entangled, are located together. However, now the local Hilbert space at each MPS site has doubled, from two states (occupied, unoccupied) to the four states of a spinful orbital. Unfortunately this *squares* the computational effort. With a geometry like in Fig. 6, the computational effort will grow like

$$\text{computational effort} \sim m^{3 \times n_{\text{orbital}}}. \quad (47)$$

More than two orbitals have turned out to be infeasible with this geometry, and the MPS approach to impurity solvers was stuck at this stage for a while.

### 3 Fork tensor product state (FTPS) method

#### 3.1 Geometry and tensors

The key ingredient of the new FTPS method is the geometry of Fig. 7. This is a special case of a so-called Tree Tensor Network. For a 2-orbital NRG calculation such a geometry was also employed in Ref. [39]. Each bath chain has a fixed spin and orbital, i.e., the local Hilbert space dimension in the bath is only two (occupied/unoccupied). In addition, the interacting impurity site is also split up into a chain of FTPS sites with dimension two (single orbital of fixed spin). An apparent disadvantage of the FTPS geometry seems to be that entanglement between bath sites of different spin or different orbitals has to be transported by the encoding matrices over a large distance, so that each bond may have to carry a lot of entanglement. This is however similar to the situation in Fig. 6 and turns out not to be a big problem on the bonds between the bath sites. The actual bottleneck in this approach is the entanglement on the vertical bonds in the figure, between the sites representing the impurity, which must contain the entanglement between the baths as well as additional large entanglement from the interaction between the impurity degrees of freedom. As we will see, the computational effort for precise calculations will still remain reasonable.

The FTPS sites for the impurity (like  $B_{\uparrow}$ ) now each contain a *tensor* with three instead of two bond indices, and one physical index, like  $I_{\alpha\beta\gamma}^s$ . Because of the geometric tree structure, a cut through any bond still bipartitions the system into two subsystems. Therefore one can still obtain a Schmidt decomposition. In the case of MPS, we needed to combine one bond index  $\alpha$  with a physical index  $s$  of an MPS "matrix"  $A_{\alpha\beta}^s$  in order to obtain a matrix  $A_{(\alpha s),\beta}$  to which an SVD can be applied. For FTPS, we need to combine the indices of the impurity tensors. To get an idea of the computational effort, suppose that the impurity bond dimensions are  $m$ , the bath bond dimension at the impurity is  $n$ , and the physical Hilbert space dimension is  $d(=2)$ . Then the size of the matrix is  $m n d \times m$  and the computational effort for the SVD will be  $\mathcal{O}(m^3 n d)$ . For all bipartitions, one can also obtain properly normalized states, and therefore apply all the usual MPS and DMRG algorithms. Note that off-diagonal hybridizations can in principle be incorporated into the method [5].

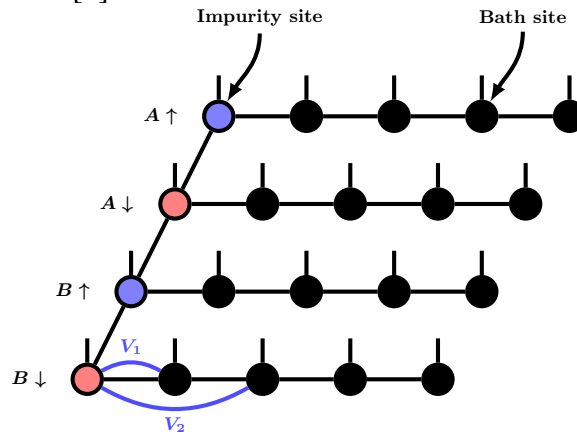


**Fig. 7:** Tensor geometry of the Anderson impurity model for the FTPS method, drawn for two orbitals A and B. Further orbitals can be incorporated with additional bath chains. From [5].

### 3.2 Star representation of the bath orbitals

A second ingredient of FTPS is a special encoding of the bath. Usually, the bath has been represented in MPS approaches as a tight binding Wilson chain, which can be obtained from Eq. (1) by a basis transformation. The Wilson chain appears natural for MPS since it is a one-dimensional physical system with only nearest neighbor hopping and local energies for occupied sites. It was shown by Wolf *et al.* [40], that, quite surprisingly, it can be better to use the original bath sites  $k$  of Eq. (1) sequentially as the sites of a bath chain. This so-called *star geometry* (see Fig. 1) is also used in FTPS. One can, for example, number the sites by increasing local energy  $\varepsilon_k$ . The advantage is that sites with low  $\varepsilon_k$  will be almost completely occupied, and sites with large  $\varepsilon_k$  almost completely unoccupied, so that they do not contribute much to the entanglement. Only sites with intermediate  $\varepsilon_k$  will have sizeable contributions from both occupied and unoccupied basis states and therefore contribute to the entanglement. Wolf *et al.* [40] showed that the maximum matrix dimension necessary in star geometry can be considerably lower than in the Wilson chain representation.

The disadvantage of the star geometry comes from artificially putting it on a chain of sites in order to apply the MPS formalism. Each bath site interacts with the impurity, by the hopping strength  $V_k$ , but not with its neighbors. We thus have many *non-local* couplings, from each bath site to the impurity, which are usually difficult and expensive for MPS approaches. Wolf *et al.* [40] treated the nonlocal hopping with a Krylov based [41] method.

We will instead use successive *swap* operations which effectively transport the impurity site (like  $B_\uparrow$ ) along its chain, and later back, so that interactions become local. Details will be described below. It turns out that this approach, together with a specific Trotter breakup, has a very small error in time evolution, which is more than an order of magnitude better than with the Wilson chain representation for similar computational effort.

### 3.3 Kanamori Hamiltonian and FTPOs

In the results section, we will treat the multi-orbital Kanamori Hamiltonian

$$\begin{aligned}
 H &= H_{\text{loc}} + H_{\text{bath}} \\
 H_{\text{loc}} &= \varepsilon_0 \sum_{m\sigma} n_{m0\sigma} + H_{\text{DD}} + H_{\text{SF}} + H_{\text{PH}} \\
 H_{\text{DD}} &= U \sum_m n_{m0\uparrow} n_{m0\downarrow} + (U - 2J) \sum_{m' > m, \sigma} n_{m0\sigma} n_{m'0\bar{\sigma}} + (U - 3J) \sum_{m' > m, \sigma} n_{m0\sigma} n_{m'0\sigma} \\
 H_{\text{SF}} &= J \sum_{m' > m} \left( c_{m0\uparrow}^\dagger c_{m0\downarrow} c_{m'0\uparrow}^\dagger c_{m'0\downarrow} + \text{h.c.} \right) \\
 H_{\text{PH}} &= -J \sum_{m' > m} \left( c_{m0\uparrow}^\dagger c_{m0\downarrow}^\dagger c_{m'0\uparrow} c_{m'0\downarrow} + \text{h.c.} \right) \\
 H_{\text{bath}} &= \sum_{ml\sigma} \varepsilon_l n_{ml\sigma} + V_l \left( c_{m0\sigma}^\dagger c_{ml\sigma} + \text{h.c.} \right),
 \end{aligned} \tag{48}$$

where  $m$  numbers the orbitals.

$H_{\text{DD}}$  contains density interactions and  $H_{\text{SF}}$  and  $H_{\text{PH}}$  incorporate spin-flip and pair-hopping terms. For our FTPS geometry, the MPOs ("Matrix Product Operators") now become FTPOs ("Fork Tensor Product Operators") with tensors in the same geometry as the FTPS in Fig. 7. For the bath, the  $W$ -tensors are very similar to the single orbital case. For the impurities, one needs tensors with two or three auxiliary indices for the connections in the fork structure, and two physical indices. Since the Kanamori Hamiltonian contains more terms than the simple AIM Hamiltonian in Eq. (42), the  $W$ -tensors become much larger, up to  $8 \times 13 \times 4$ , with 4 corresponding to the MPO dimension of the bath tensors, Eq. (45), for one bath chain. Details can be found in Ref. [9].

### 3.4 Ground state and time evolution

#### Ground state

Given the FTPO representation of the Kanamori Hamiltonian and the tree geometry which assures a bipartition of the system at every bond, the ground state can now be calculated by the DMRG method. For FTPS, this takes a considerable amount of computer time, and care needs to be taken that the true ground state is reached.

The most expensive parts of the calculation are SVDs. For the bath chains this is relatively inexpensive, since they have the structure of an MPS and the entanglement in the chains is relatively small in practice. The most expensive part is in the optimization of the impurity tensors and the accompanying SVDs. When the bonds between impurity tensors have dimension  $m$  and the bonds from the last bath tensor to the corresponding impurity tensor has dimension  $n$ , the cost for two-site DMRG will scale like  $\mathcal{O}(mnd)^3$ , where  $d = 2$  is the physical dimension.

#### Time evolution of the FTPS

The time evolution operator for a small time step can be decomposed by repeated application of the second order Suzuki Trotter approximation into [5]

$$e^{-i\Delta t H} \approx \prod_{m' > m} e^{-i\frac{\Delta t}{2}(H_{\text{SF},m,m'} + H_{\text{PH},m,m'})} e^{-i\frac{\Delta t}{2}H_{\text{DD}}} e^{-i\Delta t H_{\text{free}}} e^{-i\frac{\Delta t}{2}H_{\text{DD}}} \prod_{m' > m} e^{-i\frac{\Delta t}{2}(H_{\text{SF},m,m'} + H_{\text{PH},m,m'})}, \quad (49)$$

where  $H_{\text{free}} = H_{\text{bath}} + \varepsilon_0 \sum_{m\sigma} n_{m0\sigma}$ . Note that  $H_{\text{SF}}$  and  $H_{\text{PH}}$  commute with each other, but not with  $H_{\text{DD}}$ . The time evolution operators for  $H_{\text{DD}}$ ,  $H_{\text{SF}}$ , and  $H_{\text{PH}}$  can each be written as an FTPO, i.e., an operator acting on the impurity tensors in the FTPS:  $H_{\text{DD}}$  does not change particle numbers. Therefore fermion anticommutation plays no role and the FTPO for  $e^{-i\Delta t H_{\text{DD}}}$  can be constructed by exponentiating the  $4^{N_{\text{orb}}} \times 4^{N_{\text{orb}}}$  matrix of  $H_{\text{DD}}$  and then bringing it into FTPO-form (i.e. a product of local tensors) by repeated SVDs.

$H_{\text{SF}}$  and  $H_{\text{PH}}$  do move fermions between orbitals, so that the fermion sign needs to be treated. Both cases can be simplified in the same way because  $\hat{A}^3 = \hat{A}$  for  $J\hat{A} = H_{\text{SF}}$  and for  $-J\hat{A} = H_{\text{PH}}$ . Then

$$e^{-i\Delta t J\hat{A}} = \mathbb{1} + \hat{A}^2 \left( \cos(\Delta t J) - 1 \right) - i\hat{A} \sin(\Delta t J). \quad (50)$$

FTPOs for  $\hat{A}$  and  $\hat{A}^2$  with the correct fermion signs can be constructed directly. With respect to bond indices connecting impurity orbitals, they become sparsely populated matrices of sizes up to  $6 \times 10$  [9]. To perform time evolution with, e.g.,  $e^{-i\Delta t H_{\text{DD}}}$ , one applies the corresponding FTPO and subsequently brings the state back into normalized form. This leaves the time evolution with  $H_{\text{free}}$  to be performed. Since in Eq. (48) there are no terms connecting different baths, it decomposes directly into separate time evolutions for each bath chain.

### Time evolution of a bath chain in star representation

As mentioned above, we choose the star representation for the baths. In Ref. [40], the time evolution was done by a Krylov technique, which involves multiple applications of the MPO for  $H_{\text{free}}$  constructed in section 2.4. In the best case, up to two orders of magnitude were saved in CPU time vs. a Wilson chain calculation. In our FTPO method we use a different technique based on a Trotter expansion. A comparison between different techniques for the star geometry has not yet been performed.

Each chain  $(m, \sigma)$  is evolved independently. For ease of notation, we leave out the orbital and spin indices  $m$  and  $\sigma$  and now number the sites from left to right as 0 (impurity), 1, 2, 3,  $\dots$ ,  $N_B$  (cf. Eq. (51)). Defining  $V_0 = 0$  we can write  $H_{\text{free}} = \sum_{l=0}^{N_B} H_l$  with  $H_l = \varepsilon_l n_l + V_l (c_0^\dagger c_l + \text{h.c.})$  and use the second order Trotter expansion  $e^{-i\Delta t H_{\text{free}}} = e^{-i\frac{\Delta t}{2} H_0} e^{-i\Delta t \sum_{l=1}^{N_B} H_l} e^{-i\frac{\Delta t}{2} H_0} + \mathcal{O}(\Delta t^3)$ , which after iteration becomes

$$e^{-i\Delta t H_{\text{free}}} = \prod_{l=0}^{N_B} e^{-i\frac{\Delta t}{2} H_0} \prod_{l=N_B}^0 e^{-i\frac{\Delta t}{2} H_0} + \mathcal{O}(\Delta t^3). \quad (51)$$

At first glance this looks just like a first order Trotter expansion with two time steps of size  $\Delta t/2$ , but due to the reversed order in the second part, the expansion is in fact of second order. Eq. (51) still contains long-range hopping. We solve this problem by use of swap gates: First apply the nearest neighbor two-site operator  $e^{-i\frac{\Delta t}{2} H_0}$  which connects an impurity site and the first bath site and subsequently *swap* these two sites. These two operations can be combined into a single two-site gate, so that no additional SVD is necessary. Now the impurity is located between bath sites 1 and 2 and we can apply  $e^{-i\frac{\Delta t}{2} H_1}$  followed by another swap of the impurity to the right, and so on. The procedure is graphically depicted in Fig. 8. After reaching the last bath site on the right, the time evolutions continue to the left, following Eq. (51) until at the end the impurity site is back at its original location.

We find [42] that this time evolution in star geometry produces results which are more than an order of magnitude more precise than results with a Wilson chain geometry. Furthermore, indirectly due to the almost diagonal nature of Eq. (42), the error does almost *not* grow with bath size  $N_B$ , differently from what would have been expected naively from Eq. (51).

This completes the steps listed in section 1.2 for the impurity solver, i.e., for calculating the spectral function  $A(\omega)$ , which can then be fed into the DMFT iteration to obtain an improved bath spectral function, until the DMFT loop converges.

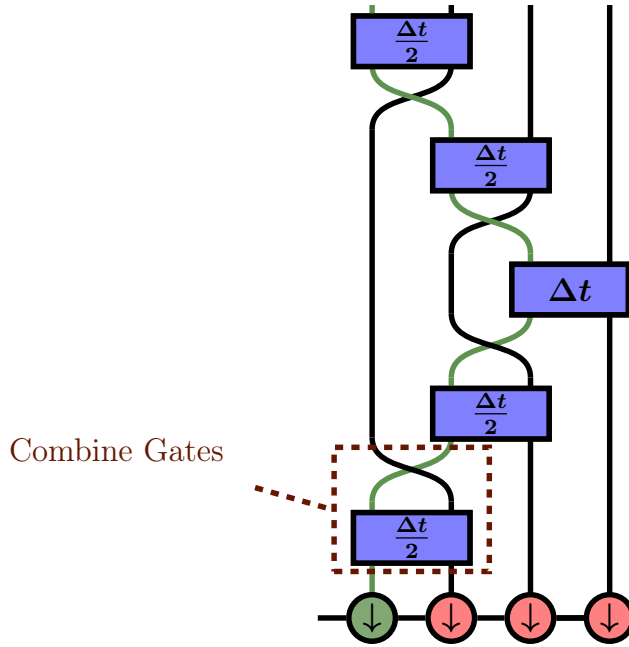


**Fig. 8:** Sequence of time evolution gates for the bath.

## 4 Results

In order to provide an impression of the possibilities and limitations of the real time FTPS solver, we will consider some examples. Further details can be found in Refs. [5,6]. Before we go to DMFT spectra, let us first look at the parameters involved in an FTPS calculation, and at related checks of correctness, robustness, and convergence.

*Correctness.* The solver and its implementation was checked by comparison to exact solutions of small interacting and large non-interacting systems, as well as by comparison to results of an earlier one- and two-orbital MPS solver [31], which itself had been thoroughly verified.

*Bath size.* FTPS work on a discretized bath representing the hybridization function  $\Delta(\omega)$ , with completely flexible discretization. It becomes more precise when the number  $N_B$  of sites in the bath chains is increased, which is quite inexpensive to do because the MPS calculations on the bath in star geometry are very efficient (in contrast to, e.g., Exact Diagonalization). Baths of  $\mathcal{O}(100)$  sites per orbital and spin can be treated and the results shown are converged in  $N_B$  up to some small variations [5,6].

*Matrix dimension and truncated weight.* The numerical approximation in MPS/FTPS methods is in the finite bond dimension achievable ( $\mathcal{O}(100) - \mathcal{O}(1000)$ ), associated with a truncated weight  $t_W$ , usually of the order of  $10^{-8}$ . Convergence of results was verified in Ref. [5].

*Time evolution.* Time evolution is done in finite steps, e.g.,  $\Delta t = 0.01$  eV, small enough so that the associated Trotter errors are not important. However, during time evolution, the entanglement increases, making larger matrices necessary, and eventually limiting the maximum time which can be reached reliably. Fortunately, the Green function  $G(t)$  only involves a local excitation from the ground state at the impurity, for which entanglement growth is quite slow. In the examples below, time evolution was done both forward and backward in time [43] and

typical total times reached were  $16 \text{ eV}^{-1}$ . The finite maximum time puts some limit on the energy resolution. This can be improved by so-called „linear prediction” [27, 7, 31] of the time series, which is badly named and actually amounts to a clever way of describing the spectrum with  $\mathcal{O}(100)$  or more Lorentzians. The reliability of this procedure for a DMFT solver, including very sharp spectral features, was investigated in detail in [31]. In the FTPS calculations for  $\text{SrVO}_3$ , the extrapolation is, for example, done to  $250 \text{ eV}^{-1}$ . In order to avoid effects of the remaining cut-off and potential inaccuracies, the Fourier transform from  $G(t)$  to  $A(\omega)$  in these calculations was performed with a broadening of  $\eta = 0.02 \text{ eV}$ . The full five-orbital calculations for  $\text{SrMnO}_3$  were more demanding. A maximum bath size of  $N_B = 49$  was used, during the DMFT loop a broadening of  $\eta = 0.2 \text{ eV}$ , and for the final spectrum a broadening of only  $\eta = 0.01 \text{ eV}$  in order to obtain optimal energy resolution.

#### 4.1 $\text{SrVO}_3$ : 3 orbitals

Fig. 9 shows DMFT spectra obtained with the FTPS solver [5] for the benchmark material  $\text{SrVO}_3$  modeled by the Kanamori Hamiltonian with 3 orbitals, in comparison to results obtained by CTQMC at similar computational effort. Both spectra show a compatible central peak, an excitation below, and an upper Hubbard peak around 3 eV. However, the FTPS spectrum resolves much more detailed structure, especially within the upper Hubbard band, and even peaks around 8 eV. Both are missing in the CTQMC results. In Ref. [5] it is shown that this is due to the analytic continuation (by a standard Maximum Entropy technique) from the imaginary times/frequencies of the CTQMC to the real frequencies of the Green function. Indeed, when one transforms the FTPS Green function to imaginary frequency, it is compatible with the CTQMC Green function, which however has fairly large statistical errors. When one adds such noise to the FTPS Green function in imaginary frequency and transforms back to real frequency, the result is almost identical to the CTQMC spectrum, without structure in the upper Hubbard band and beyond.

At the central peak, FTPS is less precise than CTQMC, because very small frequencies correspond to very large times, which are less precisely calculated in FTPS. Conversely, high energies (small times) are *easiest* to resolve with FTPS. The structure of the spectrum in the upper Hubbard band contains interesting physics. In Ref. [5] it is shown that the peaks correspond directly to the excitations of the atomic model, i.e., the Kanamori Hamiltonian without bath, but shifted and broadened by the interaction with the bath. The atomic energies and corresponding states are shown in Table 1. From the positions of the peaks, one can thus extract couplings for an effective atomic model which would have peaks at the same positions (with some slight variations). The bare  $U = 4 \text{ eV}$  becomes  $U_{\text{eff}} = 5.97 \text{ eV}$ ,  $\varepsilon_0 = -0.86 \text{ eV}$  goes to  $\varepsilon_{0,\text{eff}} = -2.00 \text{ eV}$  and the Hund’s coupling becomes  $J_{\text{eff}} = 0.59(6) \text{ eV}$ ,  $0.66(3) \text{ eV}$ , and  $0.72(2) \text{ eV}$  at bare couplings of  $0.5 \text{ eV}$ ,  $0.6 \text{ eV}$ , and  $0.7 \text{ eV}$ , respectively. The amplitude of the peaks relates to their degeneracy in the atomic description. However, the detailed shape of the peaks is entirely due to the interaction with the bath and is not covered by this effective atomic model.



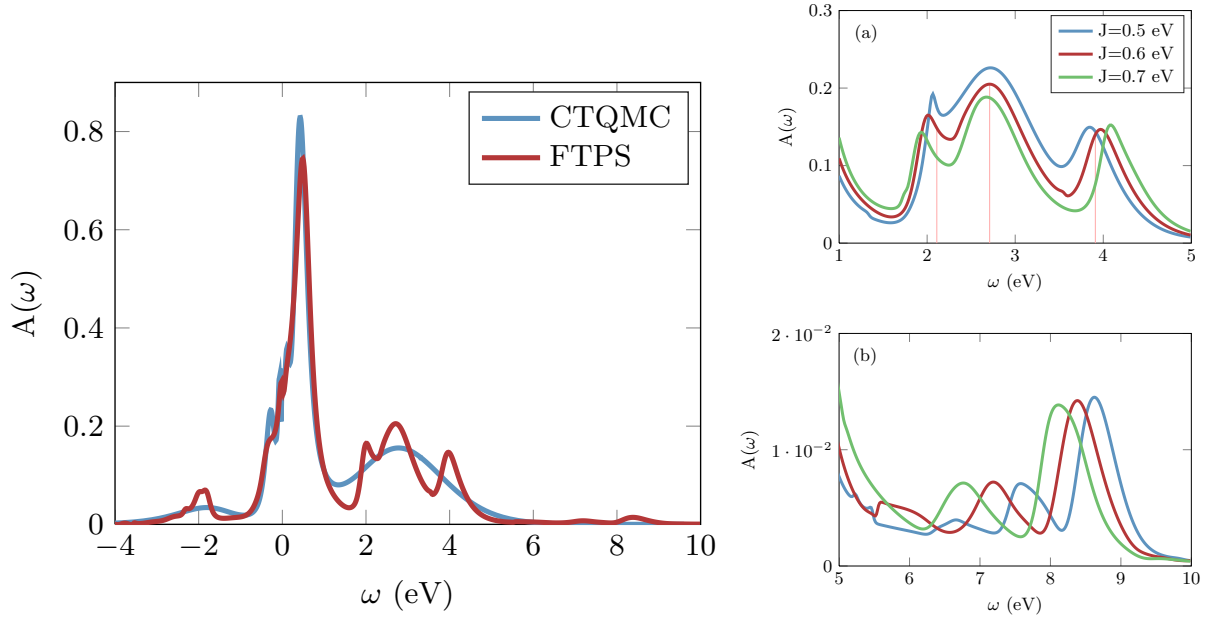


**Fig. 9:** DMFT spectra for  $\text{SrVO}_3$ , at  $U = 4 \text{ eV}$  and  $J = 0.6 \text{ eV}$ , for a case without spin-flip and pair-hopping terms. With full rotational symmetry, i.e., including those terms, similar results are obtained. From Ref. [5].

particle sector	atomic energy	degeneracy	state
0	$\varepsilon_0$	1	$ 0, 0, 0\rangle$
1	0	6	$ \uparrow, 0, 0\rangle \dots$
2	$U - 3J + \varepsilon_0$	6	$ \uparrow, \uparrow, 0\rangle \dots$
	$U - 2J + \varepsilon_0$	6	$ \uparrow, \downarrow, 0\rangle \dots$
	$U + \varepsilon_0$	3	$ \uparrow\downarrow, 0, 0\rangle \dots$
3	$3U - 9J + 2\varepsilon_0$	2	$ \uparrow, \uparrow, \uparrow\rangle \dots$
	$3U - 5J + 2\varepsilon_0$	6	$ \uparrow, \uparrow, \downarrow\rangle \dots$
	$3U - 7J + 2\varepsilon_0$	12	$ \uparrow\downarrow, \uparrow, 0\rangle \dots$

**Table 1:** States of the Kanamori Hamiltonian without spin-flip and pair-hopping terms.

Amazingly, even the next set of excitations, around 8 eV, is resolved very well by the FTPS calculation, even though the amplitudes are very small. Again the individual peaks correspond to atomic excitations, however with somewhat different effective couplings. This set of peaks is entirely missing in the CTQMC results, likely because analytic continuation becomes extremely difficult at high energies.

## 4.2 $\text{SrMnO}_3$ : 5 orbitals

Finally, we will briefly discuss results for a full five-orbital calculation with FTPS, for the material  $\text{SrMnO}_3$ . In Ref. [6], such calculations were used to examine the influence of different strategies for getting from a DFT spectrum to an effective Hamiltonian, specifically which orbitals and which range of energies of the DFT spectrum to include. It was shown that for  $\text{SrMnO}_3$ , it is important to use a wide energy range and to include the  $e_g$  orbitals. In the DFT spectrum (not shown), the  $e_g$  orbitals have are almost completely located above the Fermi en-

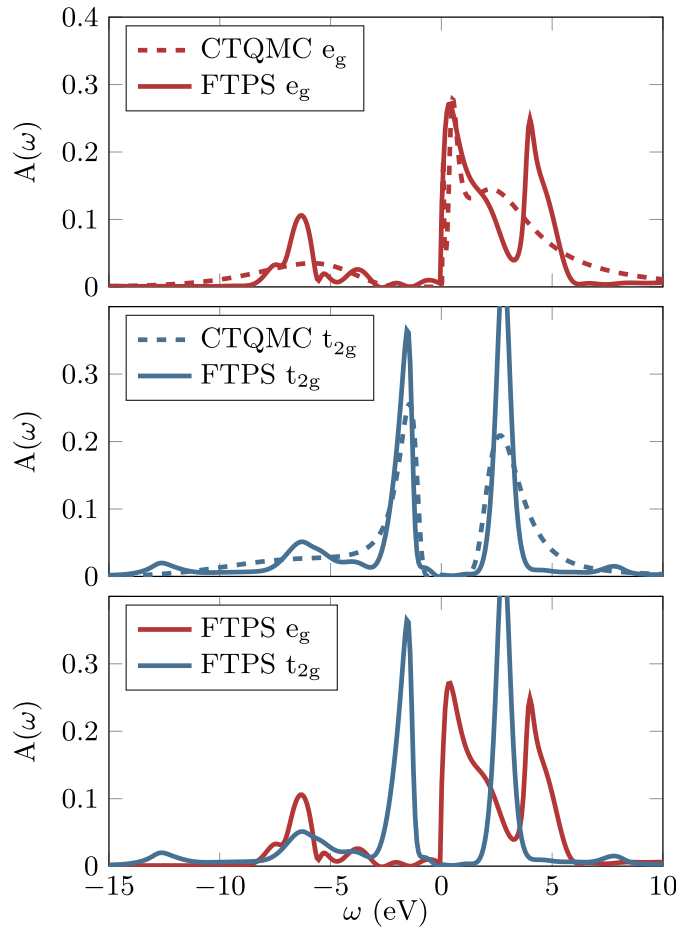


**Fig. 10:** DMFT spectra for  $\text{SrMnO}_3$  in a five orbital description, from FTPS calculations and from CTQMC. From [6].

ergy. Fig. 10 shows DMFT spectra for five-orbital calculations with a wide energy window. The FTPS spectra are compatible with the CTQMC but show considerably more detail. CTQMC is especially difficult for the  $e_g$  orbitals here because they are almost unoccupied, which makes the number of events for measuring the Green function in the Monte Carlo small.

From the combined spectrum in Fig. 10 (bottom) one sees that the size of the gap is in fact determined by the  $e_g$  contribution to the spectrum. Here one can also identify the  $e_g$  vs.  $t_{2g}$  nature of the successive peaks in the spectrum.

Fig. 11 compares the total FTPS DMFT spectrum to experimental results for the Mn-3d orbitals in  $\text{SrMnO}_3$  obtained by Kim *et al.* [44] with two different experimental techniques: photo emission spectroscopy (PES) below the Fermi energy and xray absorption spectroscopy (XAS) above. The normalization of the experimental results is arbitrary; they were therefore normalized to the same area as the corresponding parts of the FTPS spectrum in the figure. The absolute position of the XAS spectrum is not well known; for the figure it was shifted by 0.8 eV to lower energies.

The theoretical prediction from FTPS and the experimental result in Fig. 11 then agree rather well, both in the peak structure and in their bandwidths below and above the Fermi energy. Notably, the assignment of orbitals to peaks from the experimental conclusions agrees with those of the theoretical peaks and their atomic nature (similar to table 1 [6]).

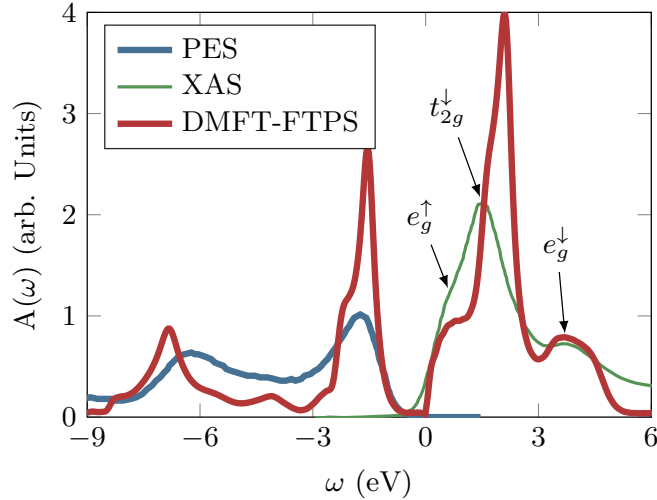


**Fig. 11:** Spectrum for  $\text{SrMnO}_3$  obtained by FTPS compared to experimental results [44], from [6]. The assignment of orbitals to peaks above the Fermi energy is from the experimental paper. Spin up refers to an excitation with majority spin, and spin down with minority spin.

Encouragingly for the new method, the new FTPS calculations took about the same computational time (about 700 CPU hours on 8 cores) per DMFT iteration as the CTQMC calculations for this full five-orbital calculation, while providing considerably better energy resolution.

## 5 Conclusions

The new FTPS impurity solver for DMFT is based on the Matrix Product State (MPS) formalism that is also the basis for DMRG, and on tensor extensions thereof. It works by calculating the ground state for an impurity model with a given hybridization function, generating an excitation, and then time evolving it directly in real time. It reaches very good energy resolution even and especially at high energies, impossible to achieve for example with CTQMC. The latter can have an advantage at very small frequencies.

The key new ingredient with respect to numerous earlier MPS based methods is the fork-like structure of Fig. 7, which separates the baths for different impurities and spin directions as much as possible and makes the method very efficient – as fast as CTQMC for three- and five-orbitals in calculations done so far. The FTPS method is very new. Its possibilities and limitations remain to be explored. Further improvements and generalizations are likely possible. The method will hopefully enable new investigations and physical insight in DMFT calculations.

## Acknowledgements

Most of all, I would like to thank my former Ph.D. student Daniel Bauernfeind, whose ideas and implementation have been the main contribution to FTPS, for his great work and collaboration. I thank my collaborators Manuel Zingl, Robert Triebl, Markus Aichhorn, and Florian Maislinger for the enjoyable and fruitful work together, Frank Verstrate and Ulli Schollwöck for numerous illuminating discussions on matrix product state techniques, and the Austrian Science Fund (FWF SFB Vicom F41, P04) for financial support.

## References

- [1] W. Metzner and D. Vollhardt, Phys. Rev. Lett. **62**, 324 (1989)
- [2] A. Georges, G. Kotliar, W. Krauth, and M.J. Rozenberg, Rev. Mod. Phys. **68**, 13 (1996)
- [3] A. Georges, A. Poteryaev, S. Biermann, M. Posternak, A. Yamasaki, and O.K. Andersen, Phys. Rev. **B 74**, 125120 (2006)
- [4] G. Kotliar, S.Y. Savrasov, K. Haule, V.S. Oudovenko, O. Parcollet, and C.A. Marianetti, Rev. Mod. Phys. **78**, 865 (2006)
- [5] D. Bauernfeind, M. Zingl, R. Triebl, M. Aichhorn, and H.G Evertz, Phys. Rev. **X 7**, 031013 (2017)
- [6] D. Bauernfeind, R. Triebl, M. Zingl, M. Aichhorn, and H.G. Evertz, Phys. Rev. **B 97**, 115156 (2018)
- [7] U. Schollwöck, Ann. Phys. **326**, 96 (2011)
- [8] S.R. White, Phys. Rev. Lett. **69**, 2863 (1992)
- [9] D. Bauernfeind, Ph.D. thesis, Graz 2018
- [10] K.G. Wilson, Rev. Mod. Phys. **47**, 773 (1975)
- [11] R. Bulla, T.A. Costi, and T. Pruschke, Rev. Mod. Phys. **80**, 395 (2008)
- [12] P. Werner, A. Comanac, L. de' Medici, M. Troyer, and A.J. Millis, Phys. Rev. Lett. **97**, 076405 (2006)
- [13] E. Gull, A.J. Millis, A.I. Lichtenstein, A.N. Rubtsov, M. Troyer, and P. Werner, Rev. Mod. Phys. **83**, 349 (2011)
- [14] M. Caffarel and W. Krauth, Phys. Rev. Lett. **72**, 1545 (1994)
- [15] M. Capone, L. de' Medici, and A. Georges, Phys. Rev. **B 76**, 245116 (2007)
- [16] J. Kolorenc, A.B. Shick, and A.I. Lichtenstein, Phys. Rev. **B 92**, 085125 (2015)
- [17] D. Zgid, E. Gull, and G.K.L. Chan, Phys. Rev. **B 86**, 165128 (2012)
- [18] Y. Lu, M. Höppner, O. Gunnarsson, and M.W. Haverkort, Phys. Rev. **B 90**, 085102 (2014)
- [19] K.M. Stadler, Z.P. Yin, J. von Delft, G. Kotliar, and A. Weichselbaum, Phys. Rev. Lett. **115**, 136401 (2015)
- [20] A. Horvat, R. Zitko, and J. Mravlje, Phys. Rev. **B 94**, 165140 (2016)
- [21] K.M. Stadler, A.K. Mitchell, J. von Delft, and A. Weichselbaum, Phys. Rev. **B 93**, 235101 (2016)

- [22] E. Jeckelmann, Phys. Rev. **B 66**, 045114 (2002)
- [23] S. Nishimoto and E. Jeckelmann, J. Phys.: Condens. Matter **16**, 613 (2004)
- [24] R. Peters, Phys. Rev. **B 84**, 075139 (2011)
- [25] M. Karski, C. Raas, and G.S. Uhrig, Phys. Rev. **B 72**, 113110 (2005),  
Phys. Rev. **B 77**, 075116 (2008)
- [26] T.D. Kühner and S.R. White, Phys. Rev. **B 60**, 335 (1999)
- [27] S.R. White and I. Affleck, Phys. Rev. **B 77**, 134437 (2008)
- [28] A. Holzner, A. Weichselbaum, I.P. McCulloch, U. Schollwöck, and J. von Delft,  
Phys. Rev. B **83**, 195115 (2011)
- [29] M. Ganahl, P. Thunström, F. Verstraete, K. Held, and H.G. Evertz,  
Phys. Rev. **B 90**, 045144 (2014)
- [30] F.A. Wolf, I.P. McCulloch, O. Parcollet, and U. Schollwöck,  
Phys. Rev. **B 90**, 115124 (2014)
- [31] M. Ganahl, M. Aichhorn, H.G. Evertz, P. Thunström, K. Held, and F. Verstraete,  
Phys. Rev. **B 92**, 155132 (2015)
- [32] F.A. Wolf, A. Go, I.P. McCulloch, A.J. Millis, and U. Schollwöck,  
Phys. Rev. **X 5**, 041032 (2015)
- [33] ITensor library, <http://itensor.org/>
- [34] G. Vidal, Phys. Rev. Lett. **91**, 147902 (2003)
- [35] G. Vidal, Phys. Rev. Lett. **93**, 040502 (2004)
- [36] S.R. White and A.E. Feiguin, Phys. Rev. Lett. **93**, 076401 (2004)
- [37] A.J. Daley, C. Kollath, U. Schollwöck, and G. Vidal,  
J. Stat. Mech.: Theory Exp., P04005 (2004)
- [38] E.M. Stoudenmire and S.R. White, New J. Phys. **12**, 055026 (2010)
- [39] A. Holzner, A. Weichselbaum, and J. von Delft, Phys. Rev. **B 81**, 125126 (2010)
- [40] F.A. Wolf, I.P. McCulloch, and U. Schollwöck, Phys. Rev. **B 90**, 235131 (2014)
- [41] P. Schmitteckert, Phys. Rev. **B 70**, 121302 (2004)
- [42] D. Bauernfeind and H.G. Evertz, in preparation
- [43] T. Barthel, New J. Phys. **15**, 073010 (2013)
- [44] D.H. Kim, H.J. Lee, B. Dabrowski, S. Kolesnik, J. Lee, B. Kim, B.I. Min, and J.-S. Kang,  
Phys. Rev. **B 81**, 073101 (2010)



# 10 Quantum Monte Carlo Methods for Fermion-Boson Problems

Fakher F. Assaad

Institut für Theoretische Physik und Astrophysik

Universität Würzburg

Am Hubland, D-97074 Würzburg

## Contents

<b>1</b>	<b>Introduction</b>	<b>2</b>
<b>2</b>	<b>Model systems</b>	<b>3</b>
2.1	The Su-Schrieffer-Heeger model . . . . .	4
2.2	Unconstrained lattice gauge theories . . . . .	4
2.3	Duality transformations and a Falikov-Kimball model . . . . .	6
2.4	Models of fermions coupled to Ising spins . . . . .	8
2.5	Symmetries . . . . .	9
<b>3</b>	<b>General formulation of the BSS algorithm</b>	<b>9</b>
3.1	Partition function: discrete variables . . . . .	10
3.2	From discrete to continuous fields . . . . .	11
3.3	Positivity of the determinant . . . . .	12
3.4	Calculation of observables . . . . .	13
3.5	Summary . . . . .	14
<b>4</b>	<b>Sampling strategies</b>	<b>14</b>
4.1	Single spin flips . . . . .	14
4.2	Langevin and molecular dynamics: calculation of forces . . . . .	15
4.3	Langevin dynamics . . . . .	15
4.4	Hybrid molecular dynamics . . . . .	16
<b>5</b>	<b>Conclusions</b>	<b>18</b>
<b>A</b>	<b>Determinant formula for fermions</b>	<b>19</b>
<b>B</b>	<b>Determinant formula for Majoranas</b>	<b>21</b>

# 1 Introduction

Fermion-boson systems play an important role in many domains of physics. An example in the solid state is the electron-phonon problem that leads to many collective phenomena such as superconductivity [1–3], charge density waves [4,5], and topological effects [6,7]. In high energy physics, especially lattice gauge theories, the bosonic modes account for the gauge fields that mediate interactions between fermion matter fields. Recently a number of so called designer Hamiltonians have been introduced to describe a variety of phases and quantum phase transitions [8–14]. As we will see, these models all fall in the class of electron-boson Hamiltonians and are designed to capture the essential physics at hand without encountering the infamous sign problem. In doing so, nematic and ferromagnetic quantum phase transitions in metals as well as topological states of matter can be studied unbiasedly and on *large* system sizes.

In a former issue of these lecture notes [15] we had already considered this problem, but for the special case of non-interacting bosons coupled to interacting fermions. We had adopted an action based formalism and integrated-out the bosonic degrees of freedom in favor of a fermion-only problem, albeit with retarded interactions. Such action-based problems are conveniently solved within the continuous-time interaction-expansion (CT-INT) algorithm [16,17] that is very powerful for a variety of models including the electron-phonon problem [18–20]. Integrating-out the phonons certainly facilitates things and local sampling strategies turn out to be efficient in many cases. However the approach has some drawbacks. i) The computational effort scales as the cube of the number of (interacting) fermion sites,  $N$ , times the cube of the inverse temperature  $\beta$ . Even if the pre-factor of this scaling law is small, it will ultimately be hard to reach very large system sizes. For example, for the one dimensional Holstein model, a very efficient directed loop algorithm for retarded interactions has been formulated that clearly out-performs the CT-INT approach [21]. ii) Integrating-out the bosons actually can generate a negative sign problem which would not occur in formulations where the bosons are explicitly taken into account. This happens in the two dimensional case [22]. iii) Finally, integrating-out the bosonic modes is only possible if they do not interact.

In this review we will discuss various formulations of the auxiliary-field QMC (AFQMC) approach for electron-boson systems. We will concentrate only on models where the so called negative sign problem is absent, such that the problem reduces to the sampling of a non-local probability distribution in a high dimensional space. There has recently been tremendous progress in defining the class of problems that can be solved without encountering the negative sign problem [23–26]. The models we will define here are certainly inspired from these new insights. In particular we will start with a *many body classic*, the Su-Schrieffer-Heeger (SSH) model [6] introduced to study soliton excitations in polyacetylene. Here we will consider the two dimensional case, and show that in limiting cases the model is equivalent to  $Z_2$  lattice gauge theories where the Gauss law is dynamically imposed at low temperatures. Models with  $Z_2$  symmetries, local or global, are more easily formulated by considering Ising bond variables coupled to fermions. This class of problems shows extremely rich phase diagrams [8–14] and it is of great interest to find efficient algorithms to simulate them.



Since, as mentioned above, the infamous negative sign problem is absent in the class of models we will consider, the reader could ask the pertinent question: what is then so hard? It is the sampling. For fermion-boson problems, the major issue that we will encounter are very long autocorrelation times [27] when adopting simple single spin-flip updates. Historically for the Ising model cluster updates circumvent critical slowing down [28]. The beauty of these algorithms is that, as one approaches the critical point, blocks of spins, the size of which tracks the correlation length, are flipped and accepted with unit probability. Cluster algorithms have been formulated for problems where the action is local. For fermion systems the action is highly non-local and defining cluster algorithms for fermions is an open question.

Faced with this challenge, one can progress in various ways. One approach is to use concepts of machine learning, more specifically so called self-learning algorithms [29, 30]. Here the idea is to define a simpler *auxiliary* model on the same configuration space as the original one endowed with a set of free parameters. Assume that one has a representative set of configurations and associated weights for the original model, then we can train (i.e. tune the free parameters) of the auxiliary model, so as to at best reproduce the data set of configurations and weights. If this step is successful, one will then use the auxiliary model to propose new configurations.

In this review we will adopt other strategies, presented in [31], to argue that so called hybrid molecular-dynamics sampling is the method of choice for a class of electron-boson problems. We will combine two approaches: the Blankenbecler-Scalapino-Sugar (BSS) formulation [32] of the AFQMC supplemented by a hybrid molecular-dynamics sampling of the fields [33, 34]. This review is organized as follows. In the next section we will first introduce a set of models, that are all free of the negative sign problem and that fall in the category of fermion-boson problems. They all have in common an  $O(2N)$  symmetry where  $N$  corresponds to the number of fermion flavors. In Sec. 3 we will derive in all details the equations required to formulate the AFQMC. Our approach will be based on the Grassmann algebra, aspects of which are reviewed in Appendix A. It is however beyond the scope of this monograph to discuss the detailed implementation of the algorithm. For this, we refer the reader to [35] and to [36] for a generic implementation of the AFQMC. In the last section, we will give some reasons why single spin-flip updates suffer from long autocorrelation times. To circumvent this problem we will discuss alternative forms of sampling strategies, in particular Langevin and hybrid molecular dynamics. We have tested favorably these ideas in Ref. [31]. Finally, we give our conclusions.

## 2 Model systems

In this section we review a number of models that show extremely rich phase diagrams with exotic phases and quantum phase transitions. They are all related to each other, and fall in the greater class of fermion-boson models. We will start with the canonical Su-Schrieffer-Heeger (SSH) model and show that in limiting cases it maps onto unconstrained  $Z_2$  lattice gauge theories. Using duality transformations we can map  $Z_2$  lattice gauge theories, in the absence of *visons*, to Falikov-Kimball models [37]. Finally, breaking the local  $Z_2$  symmetry to a global one, naturally leads to the problem of fermions coupled to an Ising model in a transverse field.

## 2.1 The Su-Schrieffer-Heeger model

In the one-dimensional case, the SSH model describes solitonic excitations in polyacetylene [6]. In this dimension, the model can be solved efficiently with the CT-INT approach [38, 15]. In higher dimensions the phase diagram of the model is essentially unknown and the CT-INT approach suffers from a negative sign problem. The model is given by

$$\hat{H} = \hat{H}_{\text{el}} + \hat{H}_{\text{ph}} + \hat{H}_{\text{ep}}. \quad (1)$$

Here

$$\hat{H}_{\text{el}} = -t \sum_{\langle i,j \rangle, \sigma} \left( \hat{c}_{i,\sigma}^\dagger \hat{c}_{j,\sigma} + \hat{c}_{j,\sigma} \hat{c}_{i,\sigma}^\dagger \right), \quad (2)$$

is the kinetic energy and  $\langle i, j \rangle$  denotes the nearest neighbors of a square lattice.  $\hat{c}_{i,\sigma}^\dagger$  creates an electron in a Wannier state centered around lattice site  $i$ , and with flavor index  $\sigma$ . We allow the flavor index to take any integer value. Remarkably, this will not introduce a negative sign problem. Harmonic oscillators on links account for the lattice vibrations,

$$\hat{H}_{\text{ph}} = \sum_{\langle i,j \rangle} \left( \frac{\hat{p}_{\langle i,j \rangle}^2}{2m} + \frac{m\omega^2}{2} \hat{x}_{\langle i,j \rangle}^2 \right), \quad (3)$$

with  $\hat{p}$ ,  $\hat{x}$  being the canonical conjugate momentum and position operators. The electron-phonon coupling leads to a modulation of the hopping matrix element:

$$\hat{H}_{\text{ep}} = g \sum_{\langle i,j \rangle, \sigma} \hat{x}_{\langle i,j \rangle} \left( \hat{c}_{i,\sigma}^\dagger \hat{c}_{j,\sigma} + \hat{c}_{j,\sigma}^\dagger \hat{c}_{i,\sigma} \right) \quad (4)$$

with coupling strength  $g$ . To simplify the notation we label bond indices as

$$b := \langle i, j \rangle, \quad (5)$$

and introduce the bond hopping as

$$\hat{K}_b := \sum_{\sigma} \left( \hat{c}_{i,\sigma}^\dagger \hat{c}_{j,\sigma} + \hat{c}_{j,\sigma}^\dagger \hat{c}_{i,\sigma} \right). \quad (6)$$

## 2.2 Unconstrained lattice gauge theories

Unconstrained lattice gauge theories can be derived from the above SSH model, provided that we set the hopping matrix element to zero. This step certainly violates the harmonic approximation central to the very definition of phonons. Nevertheless the model is well defined, and the flexibility inherent to systems of cold atoms trapped in optical lattices may offer possible realizations of such systems [39]. Introducing the boson operators,

$$\hat{b}_{\langle i,j \rangle}^\dagger = \frac{\omega m \hat{x}_{\langle i,j \rangle} - i \hat{p}_{\langle i,j \rangle}}{\sqrt{2\omega m}}, \quad (7)$$

we can rewrite the model as

$$\hat{H}_{Z_2} = g \sqrt{\frac{1}{2\omega m}} \sum_{\langle i,j \rangle} \left( \hat{b}_{\langle i,j \rangle}^\dagger + \hat{b}_{\langle i,j \rangle} \right) \hat{K}_{\langle i,j \rangle} + \omega \sum_b \hat{b}_{\langle i,j \rangle}^\dagger \hat{b}_{\langle i,j \rangle}. \quad (8)$$

Due to the lack of a direct hopping term, the above model acquires a local symmetry. In particular, the boson parity on the four links emanating from site  $i$  times the fermion parity on the site is a local conserved Ising variable. That is, for

$$\hat{Q}_i = (-1)^{\hat{n}_{\langle i,i+ax \rangle}^b + \hat{n}_{\langle i,i-ax \rangle}^b + \hat{n}_{\langle i,i+ay \rangle}^b + \hat{n}_{\langle i,i-ay \rangle}^b} (-1)^{\hat{n}_i^c} \quad (9)$$

we have

$$[\hat{Q}_i, \hat{H}_{Z_2}] = 0 \quad \text{with} \quad \hat{Q}_i^2 = 1 \quad \text{and} \quad [\hat{Q}_i, \hat{Q}_j] = 0. \quad (10)$$

In the above,  $\hat{n}_{\langle i,j \rangle}^b = \hat{b}_{\langle i,j \rangle}^\dagger \hat{b}_{\langle i,j \rangle}$  and  $\hat{n}_i^c = \sum_\sigma \hat{c}_{i,\sigma}^\dagger \hat{c}_{i,\sigma}$ .  $\hat{Q}_i$  defines a  $Z_2$  charge that is conserved locally in space but not in time.<sup>1</sup> To see this we note that

$$[\hat{Q}_i, \hat{b}_{\langle n,m \rangle}] = 2\hat{Q}_i \hat{b}_{\langle n,m \rangle} (\delta_{i,m} + \delta_{i,n}) \quad \text{and} \quad [\hat{Q}_i, \hat{c}_{j,\sigma}] = 2\hat{Q}_i \hat{c}_{j,\sigma} \delta_{i,j} \quad (11)$$

such that

$$\langle \hat{c}_i \hat{c}_j^\dagger \rangle = \delta_{i,j} \quad (12)$$

and a similar equation holds for the bosons. The above merely states that since the electron carries a  $Z_2$  charge that is locally conserved in space, the equal time propagator between different lattice sites has to vanish. The difference between the above Hamiltonian and lattice gauge theories is that the  $Z_2$  charge is not conserved along the imaginary time axis:  $\langle \hat{c}_i(\tau) \hat{c}_j^\dagger \rangle = \delta_{i,j}$  with  $\hat{c}_i(\tau) = e^{\tau \hat{H}} \hat{c}_i e^{-\tau \hat{H}}$ . Such so called unconstrained gauge theories, where the Gauss law is not imposed, have recently attracted considerable interest [10, 40, 41].

The above model has the same symmetries as a  $Z_2$  lattice gauge theory and the exact relationship can be obtained by restricting the boson Hilbert space to two states: the vacuum and the first excited state,  $\{|0\rangle, |1\rangle = \hat{b}^\dagger |0\rangle\}$ . This reduction of the Hilbert space amounts to replacing the soft core bosons by hard core ones,  $\hat{b}^\dagger \hat{b}^\dagger = 0$ , which is certainly a valid approximation in the antiadiabatic limit,  $\omega \rightarrow \infty$ . Next, we define Ising variables:  $|\pm\rangle = \frac{1}{\sqrt{2}} (|1\rangle \pm |0\rangle)$  such that for

$$\hat{X}_b = 2\hat{b}_b^\dagger \hat{b}_b - 1, \quad \hat{Z}_b = \hat{b}_b^\dagger + \hat{b}_b \quad (13)$$

$$\hat{X}_b |\pm\rangle = |\mp\rangle \quad \text{and} \quad \hat{Z}_b |\pm\rangle = \pm |\pm\rangle. \quad (14)$$

With this reading, the SSH model reduces, up to a constant, to

$$\hat{H}_{Z_2} = \sum_{\langle i,j \rangle} \hat{Z}_{\langle i,j \rangle} \hat{K}_{\langle i,j \rangle} - h \sum_{\langle i,j \rangle} \hat{X}_{\langle i,j \rangle} \quad (15)$$

Here we have set  $g/\sqrt{2\omega m} = 1$  such that  $h = -g^2/4m$ . Under the above mapping the conserved  $Z_2$  charge transforms to

$$\hat{Q}_i = \hat{X}_{\langle i,i+ax \rangle} \hat{X}_{\langle i,i-ax \rangle} \hat{X}_{\langle i,i+ay \rangle} \hat{X}_{\langle i,i-ay \rangle} (-1)^{\hat{n}_i^c}. \quad (16)$$

<sup>1</sup> This stems from the fact that the constraint, say  $\hat{Q}_i = 1$ , is not imposed on the Hilbert space.

The above model has captured a considerable amount of interest [10, 11, 14]. It is extremely simple and hosts deconfined and confined phases of matter as well as exotic quantum phase transitions (see Fig. 1).

### 2.3 Duality transformations and a Falikov-Kimball model

In interacting systems, interaction terms that do not break the macroscopic symmetries of the model will generically be dynamically generated. For example in the functional renormalization group [42] flow, one will be able to study the dynamically generated interactions in various channels. Let us follow this idea in the context of the above unconstrained lattice gauge theories. On a square lattice, the flux term

$$\hat{H}_F = F \sum_i \hat{Z}_{\langle i, i+a_x \rangle} \hat{Z}_{\langle i+a_x, i+a_x+a_y \rangle} \hat{Z}_{\langle i+a_x+a_y, i+a_y \rangle} \hat{Z}_{\langle i+a_y, i \rangle} \quad (17)$$

does not break any symmetries of the model and will hence be dynamically generated. In fact, for  $h = 0$  in Eq. (15), the Ising fields will order so as to accommodate a  $\pi$ -flux ( $\hat{Z}_{\langle i, i+a_x \rangle} \hat{Z}_{\langle i+a_x, i+a_x+a_y \rangle} \hat{Z}_{\langle i+a_x+a_y, i+a_y \rangle} \hat{Z}_{\langle i+a_y, i \rangle} = -1$ ) per plaquette [10, 43], so as to dynamically generate Dirac fermions. A Falikov-Kimball model [37] is related to Eq. (15) in the sector where the flux per plaquette vanishes

$$\hat{Z}_{\langle i, i+a_x \rangle} \hat{Z}_{\langle i+a_x, i+a_x+a_y \rangle} \hat{Z}_{\langle i+a_x+a_y, i+a_y \rangle} \hat{Z}_{\langle i+a_y, i \rangle} = 1. \quad (18)$$

This corresponds to the zero *vison*, i.e., plaquettes with  $\pi$ -flux, sector. Let us work in a basis where  $\hat{Z}$  is diagonal and consider a zero vison state. The transverse Ising field term creates a pair of visons on neighboring plaquettes and thereby violates the zero vison constraint. The first non-trivial term that complies with the constraint reads

$$\tilde{h} \sum_i \hat{X}_{\langle i, i+a_x \rangle} \hat{X}_{\langle i, i-a_x \rangle} \hat{X}_{\langle i, i+a_y \rangle} \hat{X}_{\langle i, i-a_y \rangle}. \quad (19)$$

The zero vison constraint can be satisfied with the Ansatz

$$\hat{Z}_{\langle i, j \rangle} = \hat{\tau}_i^z \hat{\tau}_j^z \quad \text{where} \quad \hat{\tau}^z = \begin{pmatrix} 1 & 0 \\ 0 & -1 \end{pmatrix}. \quad (20)$$

With this rewriting

$$\hat{X}_{\langle i, i+a_x \rangle} \hat{X}_{\langle i, i-a_x \rangle} \hat{X}_{\langle i, i+a_y \rangle} \hat{X}_{\langle i, i-a_y \rangle} = \hat{\tau}_i^x \quad \text{with} \quad \hat{\tau}^x = \begin{pmatrix} 0 & 1 \\ 1 & 0 \end{pmatrix}. \quad (21)$$

Hence in the zero vison sector, the unconstrained  $Z_2$  lattice gauge theory, is given by

$$\hat{H}_{FK} = \sum_{\langle i, j \rangle, \sigma} \left( \hat{\tau}_i^z c_{i, \sigma}^\dagger \hat{\tau}_j^z c_{j, \sigma} + h.c. \right) - \tilde{h} \sum_i \hat{\tau}_i^x \quad (22)$$

and the local conservation law reads

$$\hat{Q}_i = \hat{X}_{\langle i, i+a_x \rangle} \hat{X}_{\langle i, i-a_x \rangle} \hat{X}_{\langle i, i+a_y \rangle} \hat{X}_{\langle i, i-a_y \rangle} (-1)^{\hat{n}_i^c} \equiv \hat{\tau}_i^x (-1)^{\hat{n}_i^c}. \quad (23)$$

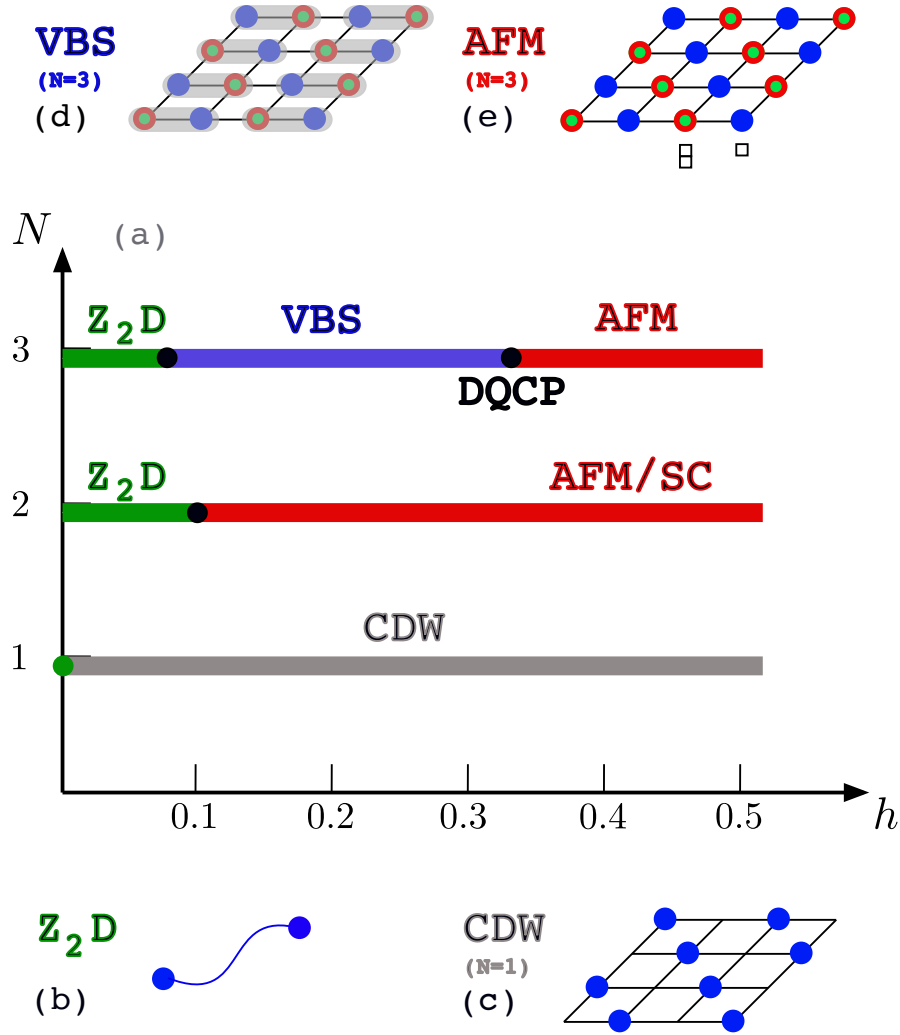


**Fig. 1:** Schematic zero temperature phase diagram of the model in Eq. (15) in the  $N$  vs.  $h$  plane (a) as well as cartoons (b)-(e) of a selected number of phases. The fermions carry a global  $U(1)$  electrical charge as well as a local  $Z_2$  one. (a): We observe a  $Z_2$  Dirac deconfined phase ( $Z_2D$ ), a Néel antiferromagnet phase ( $AFM$ ) (or a superconductor ( $SC$ ), depending on the pattern of particle-hole symmetry breaking), a charge density wave ( $CDW$ ) phase as well as a valence bond solid ( $VBS$ ). For  $N = 1$ , we do not find evidence for a  $Z_2D$  phase beyond  $h = 0$ , consistent with the arguments in the main text. The phase transitions from the  $Z_2D$  to  $AFM/SC$  ( $N = 2$ ) and  $VBS$  ( $N = 3$ ) are seemingly continuous. At  $N = 3$  we observe a deconfined quantum critical point ( $DQCP$ ) between the  $VBS$  and  $AFM$  phases. (b)-(e) Cartoons of the corresponding phases. Circles correspond to fermions and the color code to the flavor index. Circles with two colors represent a pair of fermions on a site with corresponding flavors. The low energy properties of the  $Z_2D$  phase resemble  $SU(N)$  fermions propagating freely in space-time and connected by a  $Z_2$  gauge string (b). The symmetry broken phases correspond to the confined phases of the model. At  $N = 3$  the  $AFM$  phase, (e), has the fundamental (conjugate) representation of  $SU(3)$  on sublattice A (B). The corresponding Young tableaux are included. The  $VBS$  phase, (d), corresponds to a pattern of inter-site  $SU(3)$  singlets. This Figure is reproduced from Ref. [10].

The explicit form of the Falikov-Kimball model can now be obtained by defining the fermion operator  $\hat{f}_{i,\sigma}^\dagger = \hat{\tau}_i^z \hat{c}_{i,\sigma}^\dagger$  and noting that  $\hat{\tau}_i^x = \hat{Q}_i (-1)^{\hat{n}_i^f}$ . Finally, since  $(-1)^{\hat{n}_i^f} = \prod_\sigma (2\hat{f}_{i,\sigma}^\dagger \hat{f}_{i,\sigma} - 1)$  we obtain

$$\hat{H}_{FK} = \sum_{\langle i,j \rangle, \sigma} \left( \hat{f}_{i,\sigma}^\dagger \hat{f}_{j,\sigma} + h.c. \right) - \tilde{h} \sum_i \hat{Q}_i \prod_\sigma \left( 2\hat{f}_{i,\sigma}^\dagger \hat{f}_{i,\sigma} - 1 \right). \quad (24)$$

Since  $Q_i$  is a  $Z_2$  local conserved quantity, it can be interpreted as the static density of spinless fermions in a  $SU(N)$  symmetric Falikov-Kimball model [37]. A detailed study of this model shows that it harbors fractionalized orthogonal metal phases at finite temperature [44], while at low temperatures the Ising variables order ( $\hat{Q}_i = 1$ ), such that the physics of the Hubbard model is recovered. Finally in the particle-hole symmetric case and in the limit of infinite dimensions, the model is equivalent to the Hubbard model [45, 44].

## 2.4 Models of fermions coupled to Ising spins

The common feature of this class of models is again to couple fermion degrees of freedom to Ising spins. However, and in contrast to the above, one will allow spontaneous  $Z_2$  symmetry breaking such that the ordering of the Ising spins can trigger a transition in the fermionic system. This route to engineer models that can be simulated without encountering the infamous negative sign problem has recently been very successful [8–14].

The models presented in the above section have an extensive set of conserved local quantities,  $\hat{Q}_i$ , and as a consequence the correlation functions  $\langle \hat{Z}_b \hat{Z}_{b'} \rangle$  vanishes for  $b \neq b'$ . In other words, there is a local  $Z_2$  symmetry, and local symmetries cannot be broken [46]. To avoid this, one has to add terms that reduce the local  $Z_2$  symmetry of the model from to a global one. Among many choices, one can add an Ising term of the form

$$J \sum_{\langle b,b' \rangle} \hat{Z}_b \hat{Z}_{b'} \quad (25)$$

between nearest neighbor bonds, as well as a direct hopping

$$-t \sum_b \hat{K}_b \quad (26)$$

such that the general model we will consider is given by

$$\hat{H} = \sum_b \left( -t + g \hat{Z}_b \right) \sum_{\sigma=1}^N \left( \hat{c}_{i,\sigma}^\dagger \hat{c}_{j,\sigma} + \hat{c}_{j,\sigma}^\dagger \hat{c}_{i,\sigma} \right) - h \sum_{\langle i,j \rangle} \hat{X}_{\langle i,j \rangle} + J \sum_{\langle b,b' \rangle} \hat{Z}_b \hat{Z}_{b'}. \quad (27)$$

The last two terms correspond to an Ising model in a transverse field. When formulating the path integral for this model, one will notice that it is identical to a  $D+1$  Ising model,<sup>2</sup> albeit with space-time anisotropic couplings. Since anisotropies in the couplings are irrelevant in the sense of the renormalization group, the critical phenomena of the model fall in the  $D+1$ -dimensional Ising universality class. Coupling to gapless fermions can be relevant and lead to

<sup>2</sup> D corresponds to the spacial dimension

novel critical points. This idea has been successfully used to study a variety of phenomena such as the dynamical generation of quantum spin Hall [47] and Kekule mass terms [13] in Dirac systems as well as Ising nematic [48] and ferromagnetic [12] transitions in metals. This very rich set of phenomena can be studied by merely appropriately choosing the lattice, the coupling between the Ising and fermion degrees of freedom, as well as the interaction between the Ising spins.

## 2.5 Symmetries

The symmetries of the model will be very important to avoid the negative sign problem. In the form of Eq. (27) the  $SU(N)$  spin symmetry is manifest. On bipartite lattices this symmetry is enhanced to a  $O(2N)$  one. To see this, we define the Majorana fermions

$$\hat{\gamma}_{i,\sigma,1} = \hat{c}_{i,\sigma} + \hat{c}_{i,\sigma}^\dagger, \quad \hat{\gamma}_{i,\sigma,2} = \frac{1}{i} \left( \hat{c}_{i,\sigma} - \hat{c}_{i,\sigma}^\dagger \right) \quad (28)$$

on sub-lattice A, and

$$\hat{\gamma}_{i,\sigma,1} = \frac{1}{i} \left( \hat{c}_{i,\sigma} - \hat{c}_{i,\sigma}^\dagger \right), \quad \hat{\gamma}_{i,\sigma,2} = - \left( \hat{c}_{i,\sigma} + \hat{c}_{i,\sigma}^\dagger \right) \quad (29)$$

on sub-lattice B. The above Majorana fermions satisfy the anti-commutation relations

$$\left\{ \hat{\gamma}_{i,\sigma,n}, \hat{\gamma}_{j,\sigma',n'} \right\} = 2\delta_{i,j} \delta_{\sigma,\sigma'} \delta_{n,n'}. \quad (30)$$

Provided that the hopping matrix elements occur only between the two sub-lattices, the Hamiltonian can be written as

$$\hat{H} = \sum_{\langle i,j \rangle} \left( -t + g \hat{Z}_{\langle i,j \rangle} \right) \sum_{\sigma=1}^N \sum_{n=1}^2 \frac{i}{2} \hat{\gamma}_{i,\sigma,n} \hat{\gamma}_{j,\sigma,n} - h \sum_{\langle i,j \rangle} \hat{X}_{\langle i,j \rangle} + \sum_{b,b'} J_{b,b'} \hat{Z}_b \hat{Z}'_{b'}. \quad (31)$$

Here the global  $O(2N)$  symmetry,  $\hat{\gamma}_i \rightarrow O \hat{\gamma}_i$  where  $O$  corresponds to an orthogonal  $O(2N)$  transformation and  $\hat{\gamma}_i^T = (\hat{\gamma}_{i,1,1} \cdots \hat{\gamma}_{i,N,1}, \hat{\gamma}_{i,1,2} \cdots \hat{\gamma}_{i,N,2})$ , is manifest. This symmetry plays an important role in the formulation of the negative sign free Monte Carlo algorithm.

## 3 General formulation of the BSS algorithm

In this section, we will show how to simulate the model of Eq. (27). It is beyond the scope of this article to offer a detailed account of the auxiliary-field QMC approach, and for a detailed review the interested reader is referred to Ref. [35]. We also note that an open-source implementation of this algorithm is available online at <https://alf.physik.uni-wuerzburg.de> [36]. This implementation allows to simulate the model defined in Eq. (27). Here we will concentrate on the general formulation and place emphasis on issues arising when considering boson-fermion problems. For the numerical stabilization of the algorithm as well as for an efficient implementation, the reader is referred to the aforementioned references.

### 3.1 Partition function: discrete variables

The Hilbert space of the Hamiltonian of Eq. (27) accounts for the Ising degree of freedom per bond and to  $N$ -flavored fermions per site. Thereby, the partition function reads

$$Z = \text{Tr} \left( e^{-\beta \hat{H}} \right) = \text{Tr} \left( \left( \prod_b e^{-\Delta\tau(-t+g\hat{Z}_b)\hat{K}_b} \right) e^{-\Delta\tau \sum_{b,b'} J_{b,b'} \hat{Z}_b \hat{Z}'_{b'}} e^{\Delta\tau h \sum_b \hat{X}_b} \right)^{L_\tau} + \mathcal{O}(\Delta\tau^2), \quad (32)$$

where the trace runs over the fermion Fock space and the bond Ising degrees of freedom. In the above  $\beta = L_\tau \Delta\tau$ , and we have used an asymmetric Trotter decomposition that introduces a systematic error of order  $\Delta\tau^2$ .<sup>3</sup> We carry out the trace over the Ising variables by introducing a complete set of Ising spins on each time slice

$$\hat{Z}_b |s_1, \dots, s_{N_b}\rangle = s_b |s_1, \dots, s_{N_b}\rangle, \quad \sum_{s_1, \dots, s_{N_b}} |s_1, \dots, s_{N_b}\rangle \langle s_1, \dots, s_{N_b}| = \hat{1}_I. \quad (33)$$

Here  $N_b$  counts the number of bonds and  $\hat{1}_I$  is the unit operator in the Ising space. Noting that

$$\left\langle \underline{s} \left| e^{\Delta\tau h \sum_b \hat{X}_b} \right| \underline{s}' \right\rangle = \gamma^{N_b} e^{K \sum_b s_b s'_b} \quad \text{with} \quad \tanh(K) = e^{-2\Delta\tau h}, \quad \gamma = \frac{e^{\Delta\tau K}}{2 \cosh(\Delta\tau h)} \quad (34)$$

and  $|\underline{s}\rangle = |s_1, \dots, s_{N_b}\rangle$  we obtain

$$Z = \gamma^{N_b L_\tau} \sum_{\underline{s}_1, \dots, \underline{s}_{L_\tau}} e^{-S_0(\{\underline{s}\})} \text{Tr}_F \left( \prod_{\tau, b} e^{-\Delta\tau(-t+g s_{b,\tau}) \hat{K}_b} \right). \quad (35)$$

Here  $\underline{s}$  has acquired an imaginary time index with boundary condition  $\underline{s}_0 = \underline{s}_{L_\tau}$  and

$$S_0(\{\underline{s}\}) = \sum_{\tau=1}^{L_\tau} \left( \sum_{b,b'} \Delta\tau J_{b,b'} s_{b,\tau} s_{b',\tau} - K \sum_b s_{b,\tau} s_{b,\tau-1} \right). \quad (36)$$

Using the determinant formulas derived in the appendix, we can integrate out the fermions, to obtain

$$Z = \gamma^{N_b L_\tau} \sum_{\underline{s}_1, \dots, \underline{s}_{L_\tau}} e^{-S_0(\{\underline{s}\})} \det \left( 1 + \prod_{\tau, b} e^{-\Delta\tau(-t+g s_{b,\tau}) K_b} \right)^N, \quad (37)$$

where the sparse matrices  $K_b$  are defined as  $\hat{K}_b = \sum_{\sigma, i, j} \hat{c}_{i,\sigma}^\dagger (K_b)_{i,j} \hat{c}_{j,\sigma}$ . Note that since the fermions symmetrically couple to the Ising fields  $s_{b,\tau}$  the trace is block diagonal in the flavor index  $\sigma = 1, \dots, N$ . Thereby we just have to compute the determinant for one flavor and elevate it to the power  $N$ . This explicitly reflects the  $\text{SU}(N)$  symmetry of our formulation.

<sup>3</sup>Strictly speaking the error should be of order  $\Delta\tau$ . However, one can show that for our specific model the coefficient of the linear in  $\Delta\tau$  error vanishes [49].



### 3.2 From discrete to continuous fields

In the above formulation, the configuration space for the Monte Carlo sampling will corresponds to a set of discrete Ising fields. As will be apparent, it may be more efficient to consider continuous fields, for which sampling strategies such as hybrid molecular or Langevin dynamics can be used. Instead of considering the discrete Ising spin we will introduce a Gaussian transformation that formulates the problem in terms of the average magnetization. These types of transformations explicitly show the equivalence between Ising and scalar fields. We use the short hand notation

$$S_0(\{\underline{s}\}) = \frac{1}{2} \underline{s}^T \mathbf{A} \underline{s}, \quad (38)$$

where  $\mathbf{A}$  is a  $N_b L_\tau \times N_b L_\tau$  matrix and  $\underline{s}^T = (\underline{s}_1^T, \dots, \underline{s}_{L_\tau}^T)$ , and will assume that  $\mathbf{A}$  is positive definite. Here there is no loss of generality since  $\underline{s}^T \underline{s} = N_b L_\tau$  such that we can add a constant to  $\mathbf{A}$  so as to guarantee that all the eigenvalues are positive. Next we use the Gaussian identity

$$\int_{\mathbb{R}^{N_b L_\tau}} \underbrace{d\phi_1 \dots d\phi_{N_b L_\tau}}_{\equiv D\phi} e^{-\frac{1}{2} \phi^T \mathbf{A}^{-1} \phi - \underline{s}^T \phi} = (2\pi)^{N_b L_\tau/2} \sqrt{\det \mathbf{A}} e^{\frac{1}{2} \underline{s}^T \mathbf{A} \underline{s}}. \quad (39)$$

With  $C = (2\pi)^{N_b L_\tau/2} \sqrt{\det \mathbf{A}}$ , the partition function reads

$$Z = C \int_{\mathbb{R}^{N_b L_\tau}} D\phi e^{-\frac{1}{2} \phi^T \mathbf{A}^{-1} \phi} \text{Tr}_F \left( \prod_{\tau, b} \left( \sum_{s=\pm 1} e^{-s\phi_{b,\tau}} e^{-\Delta\tau(-t+gs)\hat{K}_b} \right) \right), \quad (40)$$

and we can evaluate  $\sum_{s=\pm 1} e^{-s\phi_{b,\tau}} e^{-\Delta\tau(-t+gs)\hat{K}_b}$  using the fact that  $\Delta\tau$  is small

$$\begin{aligned} \sum_{s=\pm 1} e^{-s\phi_{b,\tau}} e^{-\Delta\tau(-t+gs)\hat{K}_b} &= \sum_{s=\pm 1} e^{-s\phi_{b,\tau}} \left( 1 - \Delta\tau(-t+gs)\hat{K}_b \right) + \mathcal{O}(\Delta\tau^2) \\ &= 2 \cosh(\phi_{b,\tau}) \left( 1 - \Delta\tau(-t+g \tanh(\phi_{b,\tau})\hat{K}_b) \right) + \mathcal{O}(\Delta\tau^2) \\ &= 2 \cosh(\phi_{b,\tau}) \exp \left( -\Delta\tau(-t+g \tanh(\phi_{b,\tau}))\hat{K}_b \right) + \mathcal{O}(\Delta\tau^2). \end{aligned} \quad (41)$$

Thereby, the partition function can now be written as

$$Z = 2^{N_b L_\tau} C \int_{\mathbb{R}^{N_b L_\tau}} D\phi e^{-\frac{1}{2} \phi^T \mathbf{A}^{-1} \phi + \sum_{b,\tau} \log \cosh(\phi_{b,\tau})} \text{Tr}_F \left( \prod_{\tau, b} e^{-\Delta\tau(-t+g \tanh(\phi_{b,\tau}))\hat{K}_b} \right), \quad (42)$$

where we have omitted the Trotter error. Using the determinant formula for fermions, we see that

$$Z = 2^{N_b L_\tau} C \int_{\mathbb{R}^{N_b L_\tau}} D\phi e^{-S(\phi)} \quad (43)$$

with

$$S(\phi) = \frac{1}{2} \phi^T \mathbf{A}^{-1} \phi - \sum_{b,\tau} \log \cosh(\phi_{b,\tau}) - N \log \det \mathbf{M}(\phi) \quad (44)$$

and

$$\mathbf{M}(\phi) = 1 + \left( \prod_{\tau, b} e^{-\Delta\tau(-t+g \tanh(\phi_{b,\tau}))\hat{K}_b} \right). \quad (45)$$

For future purposes, it will be useful to introduce the super-index

$$\underline{t} = (\tau, b) \quad (46)$$

that runs over the sequence of space-time bonds, and the propagators

$$\hat{U}_\phi(\underline{t}_2, \underline{t}_1) = \prod_{\underline{t}=\underline{t}_1+1}^{\underline{t}_2} e^{-\Delta\tau(-t+g \tanh(\phi_{\underline{t}}))\hat{K}_{b_{\underline{t}}}} \quad \text{for } \underline{t}_2 \geq \underline{t}_1. \quad (47)$$

Note that  $\hat{U}_\phi(\underline{t}, \underline{t}) = \hat{1}$ .

### 3.3 Positivity of the determinant

An exact enumeration of the Ising spins for large euclidean volumes  $N_b L_\tau$  is prohibitively expensive. A way out is to estimate the sum stochastically with importance sampling methods. This reading requires

$$P(\{\underline{s}\}) = \frac{e^{-S_0(\{\underline{s}\})} \det \left( 1 + \prod_{\tau, b} e^{-\Delta\tau(-t+gs_{b,\tau})K_b} \right)^N}{\sum_{\underline{s}_1, \dots, \underline{s}_{L_\tau}} e^{-S_0(\{\underline{s}\})} \det \left( 1 + \prod_{\tau, b} e^{-\Delta\tau(-t+gs_{b,\tau})K_b} \right)^N} \quad (48)$$

to be positive. Obviously, for even values of  $N$  and since  $K_b$  are real symmetric matrices, the weight will be positive for each configuration. What about odd values of  $N$ ? Using the Majorana basis introduced above, we have for a single flavor

$$\text{Tr}_F \prod_{\tau, b=\langle i, j \rangle} e^{-\Delta\tau(-t+gs_{b,\tau})(\hat{c}_i^\dagger \hat{c}_j + \hat{c}_j^\dagger \hat{c}_i)} = \left( \text{Tr}_M \prod_{\tau, b=\langle i, j \rangle} e^{-\Delta\tau(-t+gs_{b,\tau})\frac{i}{2}\hat{\gamma}_i \hat{\gamma}_j} \right)^2. \quad (49)$$

Here  $\text{Tr}_M$  corresponds to the trace over a single Majorana mode. We now want to show that  $\text{Tr}_M \prod_{\tau, b=\langle i, j \rangle} e^{-\Delta\tau(-t+gs_{b,\tau})\frac{i}{2}\hat{\gamma}_i \hat{\gamma}_j}$  is a real number

$$\overline{\text{Tr}_M \prod_{\tau, b=\langle i, j \rangle} e^{-\Delta\tau(-t+gs_{b,\tau})\frac{i}{2}\hat{\gamma}_i \hat{\gamma}_j}} = \text{Tr}_M \prod_{\tau, b=\langle i, j \rangle} e^{-\Delta\tau(-t+gs_{b,\tau})\frac{-i}{2}\hat{\gamma}_i \hat{\gamma}_j} = \text{Tr}_M \prod_{\tau, b=\langle i, j \rangle} e^{-\Delta\tau(-t+gs_{b,\tau})\frac{i}{2}\hat{\eta}_i \hat{\eta}_j} \quad (50)$$

with

$$\hat{\eta}_i = \begin{cases} \hat{\gamma}_i & \text{for } i \in A \\ -\hat{\gamma}_i & \text{for } i \in B \end{cases} \quad (51)$$

Since the above is a canonical transformation, the trace over the  $\hat{\eta}$ 's is equal to that of the  $\hat{\gamma}$ 's. Note that we have used the fact that the hopping links only the A and B sub-lattices. Thereby the  $O(2N)$  symmetry of the model allows us to show that for arbitrary number of colors  $P(\{\underline{s}\})$  is positive semidefinite. For more general symmetry based arguments that lead to the absence of a negative sign problem, the reader is referred to Refs [23, 25, 26, 50]. In Appendix B we summarize some useful determinant identities for Majorana fermions. Note that the positivity of the determinant is valid for both discrete or continuous fields.

### 3.4 Calculation of observables

The calculation of observables proceeds as follows. Let us consider observables  $\hat{O}$  that involve only fermionic degrees of freedom such that

$$\langle O \rangle = \frac{1}{\int D\phi e^{-S(\phi)}} \int D\phi e^{-S(\phi)} \frac{\text{Tr}_F \left( \hat{U}_\phi(L_\tau N_b, 0) \hat{O} \right)}{\text{Tr}_F \hat{U}_\phi(L_\tau N_b, 0)}. \quad (52)$$

We now consider observables of the form

$$\hat{O} = T \hat{c}_{i_1}(\underline{t}_1) \hat{c}_{i'_1}^\dagger(\underline{t}'_1) \cdots \hat{c}_{i_n}(\underline{t}_n) \hat{c}_{i'_n}^\dagger(\underline{t}'_n) \quad (53)$$

with

$$\hat{c}_i(\underline{t}) = \hat{U}_\phi^{-1}(\underline{t}, 0) \hat{c}_i \hat{U}_\phi(\underline{t}, 0). \quad (54)$$

In this section we omit the spin or flavor index.  $T$  corresponds to the time ordering in which the time indices,  $\underline{t}$ , are organized in ascending order. To achieve this ordering, one will permute operators and not forget to include the sign of the permutation in the result. For example,  $T \hat{c}_i(\underline{1}) \hat{c}_j^\dagger(\underline{3}) = -\hat{c}_j^\dagger(\underline{3}) \hat{c}_i(\underline{1})$ . Using the Grassmann algebra briefly introduced in Appendix A we can show that

$$\begin{aligned} \frac{\text{Tr}_F \left( \hat{U}_\phi(L_\tau N_b, 0) \hat{O} \right)}{\text{Tr}_F \hat{U}_\phi(L_\tau N_b, 0)} &= \frac{\int \prod_{i, \underline{t}} d\xi_i^\dagger(\underline{t}) d\xi_i(\underline{t}) e^{-\sum_{i, \underline{t}, i', \underline{t}'} \xi_i^\dagger(\underline{t}) G_{i, i'}^{-1}(\underline{t}, \underline{t}') \xi_{i'}(\underline{t}')} \xi_{i_1}(\underline{t}_1) \xi_{i'_1}^\dagger(\underline{t}'_1) \cdots \xi_{i_n}(\underline{t}_n) \xi_{i'_n}^\dagger(\underline{t}'_n)}{\int \prod_{i, \underline{t}} d\xi_i^\dagger(\underline{t}) d\xi_i(\underline{t}) e^{-\sum_{i, \underline{t}, i', \underline{t}'} \xi_i^\dagger(\underline{t}) G_{i, i'}^{-1}(\underline{t}, \underline{t}') \xi_{i'}(\underline{t}')}} \\ &= \det \begin{pmatrix} G_{i_1, i'_1}(\underline{t}_1, \underline{t}'_1) & \cdots & G_{i_1, i'_n}(\underline{t}_1, \underline{t}'_n) \\ \vdots & \ddots & \vdots \\ G_{i_n, i'_1}(\underline{t}_n, \underline{t}'_1) & \cdots & G_{i_n, i'_n}(\underline{t}_n, \underline{t}'_n) \end{pmatrix}. \end{aligned} \quad (55)$$

The last equation corresponds to Wick's theorem, the demonstration of which can be found in Ref. [51]. Hence the knowledge of the Green function  $G$  is sufficient to compute any correlation function. For  $\underline{t} \geq \underline{t}'$

$$G_{i, i'}(\underline{t}, \underline{t}') = \frac{\text{Tr}_F \left( \hat{U}_\phi(L_\tau N_b, \underline{t}) \hat{c}_i \hat{U}_\phi(\underline{t}, \underline{t}') \hat{c}_{i'}^\dagger \hat{U}_\phi(\underline{t}', 0) \right)}{\text{Tr}_F \hat{U}_\phi(L_\tau N_b, 0)}. \quad (56)$$

Noting that

$$\hat{U}_\phi^{-1}(\underline{t}, \underline{t}') \hat{c}_i \hat{U}_\phi(\underline{t}, \underline{t}') = \sum_j B_\phi(\underline{t}, \underline{t}')_{i, j} \hat{c}_j \quad (57)$$

with

$$B_\phi(\underline{t}_2, \underline{t}_1) = \prod_{\underline{t}=\underline{t}_1+1}^{\underline{t}_2} e^{-\Delta\tau(-t+g \tanh(\phi_{\underline{t}}))K_{b_{\underline{t}}}} \quad \text{for } \underline{t}_2 \geq \underline{t}_1, \quad (58)$$

the calculation of the imaginary time displaced Green function reduces to the calculation of the equal time one

$$\begin{aligned} G_{i,i'}(\underline{t}', \underline{t}') &= \frac{\text{Tr}_F \left( \hat{U}_\phi(L_\tau N_b, \underline{t}') \hat{c}_i \hat{c}_{i'}^\dagger \hat{U}_\phi(\underline{t}', 0) \right)}{\text{Tr}_F \hat{U}_\phi(L_\tau N_b, 0)} \\ &= \delta_{i,i'} - \frac{\partial}{\partial \eta} \log \text{Tr}_F \left( \hat{U}_\phi(L_\tau N_b, \underline{t}') e^{\eta c^\dagger O^{(i',i)} c} \hat{U}_\phi(\underline{t}', 0) \right) \Big|_{\eta=0} \end{aligned} \quad (59)$$

with  $c^\dagger O^{(i',i)} c = \hat{c}_{i'}^\dagger \hat{c}_i$ . Using the determinant formula and the fact that  $\det A = e^{\text{Tr} \log A}$  one obtains

$$G(\underline{t}', \underline{t}') = \left( 1 + B_\phi(\underline{t}', 0) B_\phi(L_\tau N_b, \underline{t}') \right)^{-1}. \quad (60)$$

The equal time Green function allows to compute any equal time correlation function and as we will see it will also determine the Monte Carlo dynamics. For a given operator  $\hat{O}$ , we denote by  $\langle\langle \hat{O} \rangle\rangle_\phi$  the result of the Wick decomposition for a given field configuration  $\phi$ .

### 3.5 Summary

All in all, we have now recast our problem into a form where importance sampling can be used. Our probability distribution

$$P(\phi) = \frac{e^{-S(\phi)}}{\int D\phi e^{-S(\phi)}} \quad (61)$$

is positive semi-definite and for each configuration of fields we are in the position of computing the expectation value of any operator  $\hat{O}$ . Our task is now to sample  $P(\phi)$  so as to compute quantities of the form

$$\langle \hat{O} \rangle = \int D\phi P(\phi) \langle\langle \hat{O} \rangle\rangle_\phi. \quad (62)$$

## 4 Sampling strategies

The semi-positiveness of the determinant allows us to avoid the negative sign problem, and to thereby potentially formulate a code that scales polynomially in the Euclidean system size. However, care has to be taken with sampling strategies. We will argue below that single spin flips algorithms are bound to fail for small values of  $h$  and that a possible remedy stems from using global updating schemes such as hybrid molecular or Langevin dynamics. Both these updating schemes can only be formulated for continuous fields.

### 4.1 Single spin flips

Just by analyzing the form of the action,  $S_0$ , one will readily see that single spin flips are bound to be inefficient in the small  $h$  limit. The first term,  $-K \sum_{b,\tau} s_{b,\tau} s_{b,\tau+1}$ , corresponds to a one-dimensional ferromagnetic Ising model at  $K = \text{arctanh}(e^{-2\Delta\tau h})$ . For this problem [52] the correlation length is set by  $\xi^{-1} = \log(\coth(K)) = 2\Delta\tau h$ . Thereby, kinks or domain walls of

the ferromagnetic order in the imaginary time direction will be separated by a length scale set by  $\xi$ . However single spin flips produce pairs of kinks separated by the imaginary time step  $\Delta\tau$  and will be very inefficient if  $\Delta\tau/\xi$  is *small*. Since  $\Delta\tau$  is dimension full we have to set a scale to appreciate this result. Let us consider the model of Eq. (27), and let us assume that  $g$  is the largest scale which we set to unity. We will then have to choose  $\Delta\tau \ll 1$  to validate the Trotter decomposition, such that  $\Delta\tau/\xi = \Delta\tau^2 h \ll 1$ , and the single spin flip update will be very inefficient. This argument is based on the discreteness of the imaginary time such that with continuous time methods it may be possible to circumvent sampling issues using Ising fields.

## 4.2 Langevin and molecular dynamics: calculation of forces

In Langevin and hybrid molecular dynamics the key point is to compute the forces

$$\frac{\partial S(\phi)}{\partial \phi} \quad (63)$$

and to assess if they are bounded or not. For our bosonic problems we can show explicitly that the determinant is positive semi-definite and we will make the bold assumption that it vanishes only at isolated points. Away from these isolated points, the forces will be bounded and we foresee that the Langevin and hybrid molecular dynamics walks through configuration space will be smooth. As argued in Ref. [31] this is not the case for the Hubbard model. In fact choosing a Hubbard-Stratonovich transformation that couples to the  $z$ -component of spin, splits the configuration space in distinct regions separated by logarithmic barriers where the forces diverge. For these types of landscapes formulating Langevin and hybrid molecular dynamics is very challenging. In Ref. [31] we have tested positively the above assumption for the special case of the SSH model.

Starting from the action of Eq. (44) the forces can be computed as

$$\frac{\partial S(\phi)}{\partial \phi_{\underline{t}}} = \frac{1}{2} (\mathbf{A}^{-1} \phi + \phi^T \mathbf{A}^{-1})_{\underline{t}} - \tanh \phi_{\underline{t}} + Ng \Delta\tau (1 - \tanh^2 \phi_{\underline{t}}) \text{Tr} \left( K_{\underline{t}} (1 - G(\underline{t}, \underline{t})) \right). \quad (64)$$

Here we see that the equal time Green function,  $G(\underline{t}, \underline{t})$ , is the only fermionic quantity required to compute the forces.

## 4.3 Langevin dynamics

Langevin dynamics corresponds to a stochastic differential equation for the fields  $\phi$ . They acquire a Langevin time  $t_l$  and satisfy the stochastic differential equation

$$\phi_{\underline{t}}(t_l + \delta t_l) = \phi_{\underline{t}}(t_l) - \frac{\partial}{\partial \phi_{\underline{t}}(t_l)} S(\phi) \delta t_l + \sqrt{2 \delta t_l} \eta_{\underline{t}}. \quad (65)$$

Here,  $\eta_{\underline{t}}$  are independent Gaussian stochastic variables satisfying

$$\langle \eta_{\underline{t}} \rangle_{\eta} = 0 \quad \text{and} \quad \langle \eta_{\underline{t}} \eta_{\underline{t}'} \rangle_{\eta} = \delta_{\underline{t}, \underline{t}'}. \quad (66)$$

We refer the reader to Ref. [53] for a more in depth introduction to stochastic differential equations. To see that the above indeed produced the desired probability distribution in the long Langevin time limit, we can transform the Langevin equation to the corresponding Fokker-Planck equation. Let  $P(\phi, t_l)$  be the distribution of fields at Langevin time  $t_l$ . Then

$$P(\phi, t_l + \delta t_l) = \int D\phi' P(\phi', t_l) \left\langle \delta \left( \phi - \left( \phi' - \frac{\partial S(\phi')}{\partial \phi'} \delta t_l + \sqrt{2\delta t_l} \boldsymbol{\eta} \right) \right) \right\rangle_{\eta} \quad (67)$$

where  $\delta$  corresponds to the  $L_\tau N_b$  dimensional Dirac  $\delta$ -function. Taylor expanding up to order  $\delta t_l$  and averaging over the stochastic variable yields

$$P(\phi, t_l + \delta t_l) = \int D\phi' P(\phi', t_l) \left( \delta(\phi' - \phi) - \frac{\partial S(\phi')}{\partial \phi'} \frac{\partial}{\partial \phi'} \delta(\phi' - \phi) \delta t_l + \frac{\partial}{\partial \phi'} \frac{\partial}{\partial \phi'} \delta(\phi' - \phi) \delta t_l \right) + \mathcal{O}(\delta t_l^2). \quad (68)$$

Integration by parts and taking the limit of infinitesimal time steps gives the Fokker-Planck equation

$$\frac{\partial}{\partial t_l} P(\phi, t_l) = \frac{\partial}{\partial \phi} \left( P(\phi, t_l) \frac{\partial S(\phi)}{\partial \phi} + \frac{\partial P(\phi, t_l)}{\partial \phi} \right). \quad (69)$$

The stationary,  $\frac{\partial}{\partial t_l} P(\phi, t_l) = 0$ , normalizable solution to the above equation corresponds to the desired probability distribution

$$P(\phi) = \frac{e^{-S(\phi)}}{\int D\phi e^{-S(\phi)}}. \quad (70)$$

As mentioned above, Langevin dynamics will work well provided that the forces show no singularities. The great advantage of such an updating scheme is that there is no rejection and that all fields are updated at each step. The following points that highlight potential issues with Langevin dynamics are in order:

- Langevin dynamics will be carried out at a finite Langevin time step and thereby we have introduced a further source of systematic error.
- The factor  $\sqrt{2\delta t_l}$  multiplying the stochastic variable makes the noise dominant on short time scales. On these times scales Langevin dynamics essentially corresponds to a random walk. This has the advantage that one can circumvent potential barriers, but may render the updating scheme less efficient than the hybrid molecular dynamics approach.

## 4.4 Hybrid molecular dynamics

Hybrid molecular dynamics circumvents the aforementioned drawbacks of Langevin dynamics. It does not introduce a systematic error and does not boil down to a random walk at small time steps. The approach is based on the Metropolis-Hastings importance sampling formula. (The reader is referred to the lecture notes in Ref. [15] by the same author, where aspects of the theory of Monte Carlo sampling are discussed in Appendix A.) Let  $C$  and  $C'$  be configurations in the *Monte Carlo* space. The probability of accepting a move from  $C$  to  $C'$  is given by

$$P(C \rightarrow C') = \max \left( \frac{T_0(C' \rightarrow C) P(C')}{T_0(C \rightarrow C') P(C)}, 1 \right), \quad (71)$$

where  $T_0(C' \rightarrow C)$  is the probability of *proposing* a move from  $C'$  to  $C$ . In the Monte Carlo approach, we will iterate the above procedure so as to generate a time series of configurations  $C_m$ . Provided that we are able to reach all configurations in the Monte Carlo space from any starting configuration,

$$\lim_{n \rightarrow \infty} \frac{1}{n} \sum_{m=1}^n \delta_{C_m, C} = P(C). \quad (72)$$

Ideally, one would like to propose global, ergodic moves that satisfy  $P(C \rightarrow C') = 1$  and thereby *hope* to have *small* autocorrelation times. This is a property of cluster algorithms such as the loop [35], SSE [54], or Wolff [28] algorithms.

We will start by expanding the configuration space to  $C = \{\mathbf{p}, \phi\}$  and define the Hamiltonian

$$H(\mathbf{p}, \phi) = \frac{\mathbf{p}^2}{2} + S(\phi). \quad (73)$$

$\mathbf{p}$  and  $\phi$  are canonical conjugate. Clearly,

$$\langle \hat{O} \rangle = \frac{\int D\phi e^{-S(\phi)} \langle \langle \hat{O} \rangle \rangle_\phi}{\int D\phi e^{-S(\phi)}} = \frac{\int D\phi D\mathbf{p} e^{-H(\mathbf{p}, \phi)} \langle \langle \hat{O} \rangle \rangle_\phi}{\int D\phi D\mathbf{p} e^{-H(\mathbf{p}, \phi)}} \quad (74)$$

and in the hybrid molecular dynamics scheme we sample

$$P(\mathbf{p}, \phi) = \frac{e^{-H(\mathbf{p}, \phi)}}{\int D\phi D\mathbf{p} e^{-H(\mathbf{p}, \phi)}}. \quad (75)$$

Hybrid molecular dynamics consists of two steps:

**Step 1:** Updating the momenta  $\mathbf{p}$

Here we choose

$$T_0(C' = \{\mathbf{p}', \phi\} \rightarrow C = \{\mathbf{p}, \phi\}) = \frac{e^{-\mathbf{p}^2}}{\int d\mathbf{p} e^{-\mathbf{p}^2}} \quad (76)$$

such that  $P(C \rightarrow C') = 1$ .

**Step 2:** Updating the positions  $\phi$

This step is numerically expensive and uses the Hamiltonian equations of motion

$$\dot{\mathbf{p}} = -\frac{\partial H}{\partial \phi} \quad \text{and} \quad \dot{\phi} = \frac{\partial H}{\partial \mathbf{p}} \quad (77)$$

that conserve energy,  $H$ , for time independent Hamiltonians. As for the Langevin dynamics, the fields acquire an additional time index,  $t_m$ , and  $\dot{\phi} = \frac{d\phi}{dt_m}$ . We can propagate the fields over a given molecular dynamics time interval,  $T_M$ , to obtain

$$\{\mathbf{p}, \phi\}(t_m + T_m) = U_{T_m}^H(\{\mathbf{p}, \phi\}(t_m)) \quad (78)$$

where  $U_{T_m}^H(\{\mathbf{p}, \phi\}(t_m))$  propagates the initial state  $\{\mathbf{p}, \phi\}(t_m)$  with Hamiltonian dynamics for a time interval  $T_m$ . The Hamiltonian equations of motion are time reversal symmetric and, according to Liouville's theorem, conserve volumes in phase space. Thereby,

$$\frac{T_0(\{\mathbf{p}, \phi\}(t_m + T_m) \rightarrow \{\mathbf{p}, \phi\}(t_m)) e^{-H(\{\mathbf{p}, \phi\}(t_m + T_m))}}{T_0(\{\mathbf{p}, \phi\}(t_m) \rightarrow \{\mathbf{p}, \phi\}(t_m + T_m)) e^{-H(\{\mathbf{p}, \phi\}(t_m))}} = 1 \quad (79)$$

and the acceptance will be of unity. Clearly this corresponds to the ideal case, and in practice the integration will be carried out with a finite time step such that the energy will not be conserved exactly and the acceptance will not be unity. Provided that we choose an integrator that is time reversal symmetric (see below) then the Monte Carlo acceptance-rejection step will cure this systematic error. The acceptance-rejection step of the molecular dynamics trajectory is the reason why this updating scheme is coined *hybrid* molecular dynamics. The algorithm then proceeds by iterating step 1 followed by step 2.

#### 4.4.1 The leap-frog integrator

In practice one will adopt an integrator that conserves time reversal symmetry such as the Leapfrog algorithm. Our Hamiltonian can be split into  $H_1 = \mathbf{p}^2/2$  and  $H_2 = S(\phi)$ . Propagating with  $H_1$  only allows for an exact solution since in this case  $\mathbf{p}$  is constant and  $\phi(t) = \phi(t = t_0) + (t - t_0)\mathbf{p}$ . Similarly for  $H_2$ ,  $\phi$  is constant and  $\mathbf{p}(t) = \mathbf{p}(t = t_0) - (t - t_0)\frac{\partial S(\phi)}{\partial \phi}$ . Hence both for  $H_1$  and  $H_2$  the propagation can be carried out exactly, such that time reversal symmetry and Liouville's theorem hold. In very much the same manner as for the symmetric Trotter decomposition, the leapfrog approach carries out a  $\delta t_m$  time interval propagation of the full Hamiltonian  $H = H_1 + H_2$  as

$$U_{\delta t_m}^H = U_{\delta t_m/2}^{H_1} \circ U_{\delta t_m}^{H_2} \circ U_{\delta t_m/2}^{H_1} + \mathcal{O}(\delta t_m^2). \quad (80)$$

Clearly time reversal is satisfied and because of this property the error contains only even powers of the time step. The energy  $H = H_1 + H_2$  will however not be conserved exactly such that, as mentioned above, the molecular dynamics trajectory will be accepted according to:

$$\max\left(\frac{T_0(\{\mathbf{p}, \phi\}(t_m + T_m) \rightarrow \{\mathbf{p}, \phi\}(t_m)) e^{-H(\{\mathbf{p}, \phi\}(t_m + T_m))}}{T_0(\{\mathbf{p}, \phi\}(t_m) \rightarrow \{\mathbf{p}, \phi\}(t_m + T_m)) e^{-H(\{\mathbf{p}, \phi\}(t_m))}}, 1\right) = \max\left(\frac{e^{-H(\{\mathbf{p}, \phi\}(t_m + T_m))}}{e^{-H(\{\mathbf{p}, \phi\}(t_m))}}, 1\right). \quad (81)$$

## 5 Conclusions

In these notes, we have discussed a set of very interesting boson-fermion models that are free of the negative sign problem, but that are numerically challenging due to sampling issues. The case was made that the underlying  $O(2N)$  symmetry of the Hamiltonians we considered render hybrid molecular dynamics an attractive sampling strategy. This statement was partially tested in Ref. [31]. More work is required to further test this conjecture that will hopefully allow us to unravel many salient aspects of a class of boson-fermion problems.

## Acknowledgments

I am very indebted to S. Beyer and F. Goth who wrote a hybrid molecular dynamics code to test aspects of the conjecture presented in these notes. Many thanks to J. Hofmann, M. Hohenadler, F. Parisen Toldin, M. Raczkowski, T. Sato, J. Schwab, M. Ulybyshev, Z. Wang, M. Weber for discussions on algorithmic issues and/or on boson-fermion problems.



## Appendices

### A Determinant formula for fermions

In this appendix, we derive a set of so called determinant formulas for fermions. They are the basis for various forms of fermion Monte Carlo approaches and an elegant derivation is based on fermion coherent states. The reader is referred to Ref. [51] for a detailed introduction to the Grassmann algebra. Here we will briefly summarize the important formulas and concepts. Grassmann numbers,  $\xi$ , anti-commute and are defined as

$$\hat{c}_x |\xi\rangle = \xi_x |\xi\rangle \quad (82)$$

with

$$\{\xi_x^\#, \xi_{x'}^{\#'}\} = \{\xi_x^\#, \hat{c}_{x'}^{\#'}\} = 0 \quad (83)$$

and

$$|\xi\rangle = \prod_x (1 - \xi_x \hat{c}_x^\dagger) |0\rangle. \quad (84)$$

In the above the subscript  $x$  denotes the quantum numbers of a single particle state and  $\# = \dagger, \cdot$ . Integration over Grassmann variables is defined as

$$\int d\xi_x \xi_x = 1, \quad \int d\xi_x = 0, \quad (85)$$

such that for example  $\int d\xi_x d\xi_x^\dagger \xi_x \xi_x^\dagger = -1$  due to the anticommuting properties of the algebra. The following identities for overlaps

$$\langle \xi | \xi' \rangle = e^{\sum_x \xi_x^\dagger \xi'_x}, \quad (86)$$

the resolution of unity in the Fock space

$$\hat{1} = \int \prod_x d\xi_x^\dagger d\xi_x e^{-\sum_x \xi_x^\dagger \xi_x} |\xi\rangle \langle \xi|, \quad (87)$$

and the trace over the Fock space

$$\text{Tr } \hat{A} = \int \prod_x d\xi_x^\dagger d\xi_x e^{-\sum_x \xi_x^\dagger \xi_x} \langle -\xi | \hat{A} | \xi \rangle \quad (88)$$

hold. Finally, we will need the determinant formula

$$\int \prod_x d\xi_x^\dagger d\xi_x e^{-\sum_{x,y} \xi_x^\dagger M_{x,y} \xi_y} = \det M. \quad (89)$$

As mentioned above, these formulas are *standard* and can be found in Ref. [51].

Our aim is compute

$$\text{Tr} \left( e^{\hat{c}^\dagger A_n \hat{c}} e^{\hat{c}^\dagger A_2 \hat{c}} \dots e^{\hat{c}^\dagger A_1 \hat{c}} \right), \quad (90)$$

where  $\hat{c}^\dagger = (\hat{c}_1^\dagger, \dots, \hat{c}_{N_s}^\dagger)$  with  $N_s$  the number of single particle states. The first step is to transform  $e^{\hat{c}^\dagger A \hat{c}}$  into a normal ordered expression. We will see that for a general  $A$

$$e^{\hat{c}^\dagger A \hat{c}} = :e^{\hat{c}^\dagger (e^A - 1) \hat{c}}: , \quad (91)$$

where  $: \hat{O} :$  denotes the normal ordering of the operator  $\hat{O}$ . To prove the above, we diagonalize  $A$ :  $\lambda = UAU^{-1}$ , with  $\lambda$  a diagonal matrix, and define  $\hat{\eta}^\dagger = \hat{c}^\dagger U$  and  $\hat{\gamma} = U^{-1} \hat{c}$ . These operators satisfy the anti-commutations rules

$$\{\hat{\eta}_x^\dagger, \hat{\gamma}_y\} = \delta_{x,y}, \quad \text{and} \quad \{\hat{\eta}_x^\dagger, \hat{\eta}_y^\dagger\} = \{\hat{\gamma}_x, \hat{\gamma}_y\} = 0 \quad (92)$$

such that

$$e^{\hat{c}^\dagger A \hat{c}} = \prod_x e^{\lambda_x \hat{\eta}_x^\dagger \hat{\gamma}_x} = \prod_x (1 + (e^{\lambda_x} - 1) \hat{\eta}_x^\dagger \hat{\gamma}_x) = \prod_x :e^{\hat{\eta}_x^\dagger (e^{\lambda_x} - 1) \hat{\gamma}_x}: = :e^{\sum_x \hat{\eta}_x^\dagger (e^{\lambda_x} - 1) \hat{\gamma}_x}: = :e^{\hat{c}^\dagger (e^A - 1) \hat{c}}: . \quad (93)$$

With the above, we can evaluate the matrix element

$$\langle \xi | e^{\hat{c}^\dagger A \hat{c}} | \xi' \rangle = e^{\xi^\dagger (e^A - 1) \xi'} \langle \xi | \xi' \rangle = e^{\xi^\dagger (e^A) \xi'} . \quad (94)$$

Using the Grassmann trace formula and inserting the resolution of unity between the operators, we obtain

$$\begin{aligned} \text{Tr} \left( e^{\hat{c}^\dagger A_n \hat{c}} \dots e^{\hat{c}^\dagger A_2 \hat{c}} e^{\hat{c}^\dagger A_1 \hat{c}} \right) &= \int \prod_{x, \tau=1}^n d\xi_x^\dagger(\tau) d\xi_x(\tau) e^{-\left( \sum_{x, \tau=1}^n \xi_x^\dagger(\tau) \xi_x(\tau) - \sum_{\tau=1}^n \xi^\dagger(\tau+1) e^{A_\tau} \xi(\tau) \right)} \\ &= \int \prod_{x, \tau=1}^n d\xi_x^\dagger(\tau) d\xi_x(\tau) e^{-\xi_x^\dagger(\tau) G_{(x, \tau), (x', \tau')}^{-1} \xi_{x'}(\tau')} . \end{aligned} \quad (95)$$

In the above, the Grassmann fields have acquired an extra dimension  $\tau$  and we have defined  $\xi_x^\dagger(n+1) = -\xi_x^\dagger(1)$ . Finally with the determinant formula we can integrate over the Grassmann variables and obtain

$$\text{Tr} \left( e^{\hat{c}^\dagger A_n \hat{c}} \dots e^{\hat{c}^\dagger A_2 \hat{c}} e^{\hat{c}^\dagger A_1 \hat{c}} \right) = \det \begin{pmatrix} 1 & 0 & \dots & 0 & e^{A_n} \\ -e^{A_2} & 1 & \dots & 0 & 0 \\ \vdots & & \ddots & \dots & 0 \\ 0 & \dots & \dots & -e^{A_{n-1}} & 1 \end{pmatrix} . \quad (96)$$

The size of this matrix is of  $nN_s \times nN_s$ , and is the starting point for many applications in the realm of the so called hybrid QMC approaches used in the high energy community. For many applications in the solid state, it is more convenient to reduce the size of the matrix down to  $N_s \times N_s$ . This can be achieved with Schur's determinant identity

$$\det \begin{pmatrix} A & B \\ C & D \end{pmatrix} = \det(D) \det(A - BD^{-1}C) \quad (97)$$

Setting  $D = 1$ , corresponding to the bottom right unity matrix,  $C = (0, \dots, -e^{-A_{n-1}})$  and  $B^T = (e^{A_n}, \dots, 0)$  gives

$$\det \begin{pmatrix} 1 & 0 & \dots & 0 & e^{A_n} \\ -e^{A_2} & 1 & \dots & 0 & 0 \\ \vdots & & \ddots & \dots & 0 \\ 0 & \dots & \dots & -e^{A_{n-1}} & 1 \end{pmatrix} = \det \begin{pmatrix} 1 & 0 & \dots & 0 & e^{A_n} e^{A_{n-1}} \\ -e^{A_2} & 1 & \dots & 0 & 0 \\ \vdots & & \ddots & \dots & 0 \\ 0 & \dots & \dots & -e^{A_{n-2}} & 1 \end{pmatrix}. \quad (98)$$

Iteration produces the final result

$$\text{Tr} \left( e^{\hat{c}^\dagger A_n \hat{c}} \dots e^{\hat{c}^\dagger A_2 \hat{c}} e^{\hat{c}^\dagger A_1 \hat{c}} \right) = \det (1 + e^{A_n} \dots e^{A_2} e^{A_1}). \quad (99)$$

## B Determinant formula for Majoranas

Here we will prove the following identity

$$\text{Tr}_M \left( e^{i\hat{\gamma}^T T_1 \hat{\gamma}} \dots e^{i\hat{\gamma}^T T_L \hat{\gamma}} \right) = \sqrt{\det(1 + e^{4iT_1} \dots e^{4iT_L})}, \quad (100)$$

where  $T_\tau$  are skew symmetric real matrices of even dimension ( $T_\tau^T = -T_\tau$ ), and  $\hat{\gamma}^T = (\hat{\gamma}_{1,1}, \hat{\gamma}_{1,2}, \dots, \hat{\gamma}_{n,1}, \hat{\gamma}_{n,2})$  are Majorana fermions.

First, we show that one can find an antisymmetric matrix  $h$  that satisfies

$$e^{i\hat{\gamma}^T T_1 \hat{\gamma}} \dots e^{i\hat{\gamma}^T T_L \hat{\gamma}} = e^{i\hat{\gamma}^T h \hat{\gamma}}. \quad (101)$$

The above follows from the fact that, using the anti-commutation rules of Majorana fermions,

$$\frac{d}{d\tau} \underbrace{e^{-i\tau \hat{\gamma}^T T \hat{\gamma}} \hat{\gamma}_i e^{i\tau \hat{\gamma}^T T \hat{\gamma}}}_{\equiv \hat{\gamma}_i(\tau)} = 4i \sum_j T_{i,j} \hat{\gamma}_j(\tau) \quad (102)$$

such that

$$\hat{\gamma}(\tau) = e^{4i\tau T} \hat{\gamma}. \quad (103)$$

Iteration gives

$$e^{-i\hat{\gamma}^T T_L \hat{\gamma}} \dots e^{-i\hat{\gamma}^T T_1 \hat{\gamma}} \hat{\gamma} e^{i\hat{\gamma}^T T_1 \hat{\gamma}} \dots e^{i\hat{\gamma}^T T_L \hat{\gamma}} = e^{4iT_1} \dots e^{4iT_L} \hat{\gamma} \equiv e^{-i\hat{\gamma}^T h \hat{\gamma}} \hat{\gamma}_i e^{i\hat{\gamma}^T h \hat{\gamma}}. \quad (104)$$

The last equality is the defining equation for  $h$  and leads to

$$e^{4iT_1} \dots e^{4iT_L} = e^{4ih}. \quad (105)$$

That  $h$  is skew symmetric stems from the fact that, by definition,  $e^{4ih} (e^{4ih})^T = 1$ . We will proceed by assuming that  $h$  is a real skew symmetric matrix.<sup>4</sup> Thereby one can find an orthogonal transformation  $O$  such that

$$O^T h O = \text{diag} \left( \begin{pmatrix} 0 & \lambda_1 \\ -\lambda_1 & 0 \end{pmatrix}, \dots, \begin{pmatrix} 0 & \lambda_n \\ -\lambda_n & 0 \end{pmatrix} \right) \equiv \lambda. \quad (106)$$

<sup>4</sup>A generalization to complex skew symmetric matrices is mentioned in Ref. [50]

Since  $O$  is orthogonal,  $\hat{\eta} \equiv O^T \hat{\gamma}$  are Majorana fermions and

$$\text{Tr}_M e^{i\hat{\gamma}^T h \hat{\gamma}} = \text{Tr}_M e^{i\hat{\gamma}^T O \lambda O^T \hat{\gamma}} = \text{Tr}_M \prod_{i=1}^n e^{2i\lambda_i \hat{\eta}_{i,1} \hat{\eta}_{i,2}} = \text{Tr}_M \prod_{i=1}^n (\cosh(2\lambda_i) + \sinh(2\lambda_i) \hat{\eta}_{i,1} \hat{\eta}_{i,2}). \quad (107)$$

We can now *re-fermionize* the Majorana operators

$$\hat{\eta}_{i,1} = \hat{c}_i + \hat{c}_i^\dagger, \quad \hat{\eta}_{i,2} = \frac{1}{i}(\hat{c}_i - \hat{c}_i^\dagger), \quad (108)$$

and carry out the trace for each fermion flavor, to obtain

$$\begin{aligned} \text{Tr}_M e^{i\hat{\gamma}^T h \hat{\gamma}} &= \text{Tr}_F \prod_{i=1}^n (\cosh(2\lambda_i) + \sinh(2\lambda_i) \frac{1}{i} (2\hat{c}_i^\dagger \hat{c}_i - 1)) \\ &= \prod_{i=1}^n 2 \cosh(2\lambda_i) = \left( \prod_i^n (e^{4\lambda_i} + e^{-4\lambda_i} + 2) \right)^{1/2} = \left( \det(1 + e^{4iO^T h O}) \right)^{1/2} \\ &= (\det(1 + e^{4ih}))^{1/2} = (\det(1 + e^{4iT_1} \dots e^{4iT_L}))^{1/2}. \end{aligned} \quad (109)$$

## References

- [1] J. Bardeen, L.N. Cooper, and J.R. Schrieffer, Phys. Rev. **108**, 1175 (1957)
- [2] A. Migdal, JETP **34**, 996 (1958)
- [3] G. Eliashberg, JETP **11**, 696 (1960)
- [4] P.A. Lee, T.M. Rice, J.W. Serene, L.J. Sham, and J.W. Wilkins, Comm. Condens. Matter Phys. **12**, 99 (1986)
- [5] M. Hohenadler and H. Fehske, ArXiv:1706.00470 (2017)
- [6] W.P. Su, J.R. Schrieffer, and A.J. Heeger, Phys. Rev. B **22**, 2099 (1980)
- [7] A.P. Schnyder, S. Ryu, A. Furusaki, and A.W.W. Ludwig, Phys. Rev. B **78**, 195125 (2008)
- [8] E. Berg, M.A. Metlitski, and S. Sachdev, Science **338**, 1606 (2012)
- [9] Y. Schattner, S. Lederer, S.A. Kivelson, and E. Berg, ArXiv e-prints (2015)
- [10] F.F. Assaad and T. Grover, Phys. Rev. X **6**, 041049 (2016)
- [11] S. Gazit, M. Randeria, and A. Vishwanath, Nat. Phys. **13**, 484 (2017)
- [12] X.Y. Xu, K. Sun, Y. Schattner, E. Berg, and Z.Y. Meng, Phys. Rev. X **7**, 031058 (2017)
- [13] T. Sato, M. Hohenadler, and F.F. Assaad, Phys. Rev. Lett. **119**, 197203 (2017)
- [14] S. Gazit, F.F. Assaad, S. Sachdev, A. Vishwanath, and C. Wang, ArXiv:1804.01095 (2018)
- [15] F.F. Assaad: *Continuous-Time QMC Solvers for Electronic Systems in Fermionic and Bosonic Baths*, in E. Pavarini, E. Koch, D. Vollhardt, A. Lichtenstein (eds.): *DMFT at 25: Infinite Dimensions*, Modeling and Simulation Vol. 4 (Forschungszentrum Jülich, 2014)
- [16] A.N. Rubtsov, V.V. Savkin, and A.I. Lichtenstein, Phys. Rev. B **72**, 035122 (2005)
- [17] F.F. Assaad and T.C. Lang, Phys. Rev. B **76**, 035116 (2007)
- [18] M. Hohenadler, F.F. Assaad, and H. Fehske, Phys. Rev. Lett. **109**, 116407 (2012)
- [19] M. Hohenadler, Phys. Rev. Lett. **117**, 206404 (2016)
- [20] M. Weber, F.F. Assaad, and M. Hohenadler, Phys. Rev. B **94**, 245138 (2016)
- [21] M. Weber, F.F. Assaad, and M. Hohenadler, Phys. Rev. Lett. **119**, 097401 (2017)
- [22] M. Weber and M. Hohenadler, ArXiv:1709.01096 (2017)

- [23] C. Wu and S.-C. Zhang, Phys. Rev. B **71**, 155115 (2005)
- [24] E.F. Huffman and S. Chandrasekharan, Phys. Rev. B **89**, 111101 (2014)
- [25] Z.-X. Li, Y.-F. Jiang, and H. Yao, Phys. Rev. Lett. **117**, 267002 (2016)
- [26] Z.C. Wei, C. Wu, Y. Li, S. Zhang, and T. Xiang, Phys. Rev. Lett. **116**, 250601 (2016)
- [27] M. Hohenadler and T.C. Lang, in H. Fehske, R. Schneider, and A. Weisse (eds.): *Computational Many-Particle Physics* (Springer-Verlag, Heidelberg, 2008), pp. 357–366
- [28] U. Wolff, Phys. Rev. Lett. **62**, 361 (1989)
- [29] C. Chen, X.Y. Xu, J. Liu, G. Batrouni, R. Scalettar, and Z.Y. Meng, ArXiv:1802.06177 (2018)
- [30] C. Zhang, B. Shahbaba, and H. Zhao, ArXiv:1506.05555 (2015)
- [31] S. Beyl, F. Goth, and F.F. Assaad, Phys. Rev. B **97**, 085144 (2018)
- [32] R. Blankenbecler, D.J. Scalapino, and R.L. Sugar, Phys. Rev. D **24**, 2278 (1981)
- [33] S. Duane and J.B. Kogut, Phys. Rev. Lett. **55**, 2774 (1985)
- [34] S. Duane, A.D. Kennedy, B.J. Pendleton, and D. Roweth, Phys. Lett. **B195**, 216 (1987)
- [35] F. Assaad and H. Evertz, in H. Fehske, R. Schneider, and A. Weiße (eds.): *Computational Many-Particle Physics* (Springer, Heidelberg, 2008), pp. 277–356
- [36] M. Bercx, F. Goth, J.S. Hofmann, and F.F. Assaad, SciPost Phys. **3**, 013 (2017)
- [37] L.M. Falicov and J.C. Kimball, Phys. Rev. Lett. **22**, 997 (1969)
- [38] M. Weber, F.F. Assaad, and M. Hohenadler, Phys. Rev. B **91**, 245147 (2015)
- [39] E. Zohar, J.I. Cirac, and B. Reznik, Rep. Prog. Phys. **79**, 014401 (2016)
- [40] C. Prosko, S.-P. Lee, and J. Maciejko, Phys. Rev. B **96**, 205104 (2017)
- [41] A. Smith, D.L. Kovrizhin, R. Moessner, and J. Knolle, ArXiv:1803.06575 (2018)
- [42] W. Metzner, M. Salmhofer, C. Honerkamp, V. Meden, and K. Schönhammer, Rev. Mod. Phys. **84**, 299 (2012)
- [43] E.H. Lieb, Phys. Rev. Lett. **73**, 2158 (1994)
- [44] M. Hohenadler and F.F. Assaad, ArXiv:1804.05858 (2018)
- [45] R. Žitko and M. Fabrizio, Phys. Rev. B **91**, 245130 (2015)

- [46] S. Elitzur, Phys. Rev. D **12**, 3978 (1975)
- [47] Y.-Y. He, X.Y. Xu, K. Sun, F.F. Assaad, Z.Y. Meng, and Z.-Y. Lu, Phys. Rev. B **97**, 081110 (2018)
- [48] Y. Schattner, S. Lederer, S.A. Kivelson, and E. Berg, Phys. Rev. X **6**, 031028 (2016)
- [49] R.M. Fye, Phys. Rev. B **33**, 6271 (1986)
- [50] Z.-C. Wei, ArXiv:1712.09412 (2017)
- [51] J.W. Negele and H. Orland: *Quantum Many body systems* (Addison-Wesley, 1988)
- [52] R.J. Baxter: *Exactly solved models in statistical mechanics* (Academic Press, London, 1989)
- [53] C.W. Gardiner: *Handbook of Stochastic Methods* (Springer, 1985)
- [54] A.W. Sandvik, Phys. Rev. B **59**, R14157 (1999)





# 11 Analytic Continuation of Quantum Monte Carlo Data

Erik Koch

Jülich Supercomputer Centre and  
Institute for Advanced Simulation  
Forschungszentrum Jülich

## Contents

<b>1</b>	<b>Setting the stage</b>	<b>3</b>
1.1	Analytic continuation . . . . .	3
1.2	Analytic properties of the integral equations . . . . .	6
1.3	Preparing the data . . . . .	8
<b>2</b>	<b>Optimization methods</b>	<b>9</b>
2.1	Least squares and singular values . . . . .	9
2.2	Non-negative least-squares . . . . .	12
2.3	Linear regularization . . . . .	13
2.4	Maximum entropy . . . . .	17
<b>3</b>	<b>Average spectrum method</b>	<b>20</b>
<b>4</b>	<b>Conclusions</b>	<b>24</b>
<b>A</b>	<b>Technical appendices</b>	<b>25</b>
A.1	Blocking method for correlated data . . . . .	25
A.2	Non-negative least-squares algorithm (NNLS) . . . . .	27
A.3	Shannon entropy . . . . .	29
A.4	Sampling from a truncated normal distribution . . . . .	32

The analytic continuation of Monte Carlo data may appear as an exercise in achieving the unachievable. To understand why, let us consider the example of a fermionic finite-temperature Matsubara Green function  $G(\tau)$ . For imaginary times  $\tau \in [0, \beta]$  it is related to the spectral function  $\rho(\omega)$  by the integral equation

$$G(\tau) = -\frac{1}{2\pi} \int_{-\infty}^{\infty} \frac{e^{-\omega\tau}}{1 + e^{-\beta\omega}} \rho(\omega) d\omega.$$

While calculating  $G(\tau)$  from  $\rho(\omega)$  is a straightforward integral, the inverse problem is hard. This is not because we have to solve a Fredholm equation of the first kind, the difficulty rather arises from the remarkable insensitivity of the imaginary-time data on changes in the spectral function. To illustrate this, we write the spectral function as a sum of delta-peaks  $w_i \delta(\omega - \varepsilon_i)$ , for which the imaginary-time Green function becomes a linear combination of exponentials

$$G(\tau) = -\frac{1}{2\pi} \sum_i w_i (1 - n_{\text{FD}}(\varepsilon_i)) e^{-\varepsilon_i \tau} = -\frac{1}{2\pi} \sum_i w_i n_{\text{FD}}(\varepsilon_i) e^{+\varepsilon_i(\beta - \tau)},$$

where we have introduced the Fermi-Dirac distribution  $n_{\text{FD}}(\varepsilon) = 1/(e^{+\beta\varepsilon} + 1)$ . While a peak at zero energy simply contributes a constant to  $G(\tau)$ , the contribution of peaks at large frequencies,  $|\varepsilon| \gg 0$ , is only noticeable close to  $\tau = 0$  or  $\beta$ , while inside the interval  $(0, \beta)$  it becomes exponentially small. To reconstruct the spectral function reliably over the entire  $\omega$ -range, we thus need to know  $G(\tau)$  very accurately very close to the boundaries of the interval  $(0, \beta)$ .

Numerical simulations can give, however, only a finite number of data points,  $G(\tau_j)$ . Apparently, this does not provide enough information to reconstruct a continuous spectral function: we expect that there are many different spectral functions  $\rho(\omega)$  that reproduce a given set of data points  $\{G(\tau_j)\}$ . Such a problem without a well-defined solution is called ill posed [1]. If we insist on obtaining a unique result, we need to add constraints, e.g., by including additional information about what kind of solution we consider reasonable. In addition, Monte Carlo data are noisy. When reconstructing the spectral function, we thus need to take the accuracy of the data into account and quantify how reliable the result is, given the noise in the input. Both types of information, the estimate of the reliability of the data and our expectations about a reasonable solution of the inverse problem, can be handled using Bayesian reasoning [2].

In the following we will introduce the analytic properties that allow the continuation of Green and correlation functions. We then describe how to quantify the statistical errors in the numerical data and to set up the inverse problem. In the main part we use this to give an overview of methods to solve the inverse problem. The most straightforward approach simply performs a least-squares fit to the data points. We explain why this approach is ill posed and how it fails spectacularly. We then discuss the idea of regularization by introducing assumptions about a reasonable solution. This makes the problem well posed, but dependent on prior information. The effect of the prior information included in the regularizer can be quantified using Bayesian techniques. We discuss how they are used to argue for the different flavors of the Maximum Entropy method. Finally we introduce the average spectrum method which tries to avoid introducing prior information by calculating  $\rho(\omega)$  as a functional integral over the space of all possible spectral functions.

# 1 Setting the stage

## 1.1 Analytic continuation

A system at finite temperature with time-independent Hamiltonian  $H$  is described as an ensemble of eigenstates,  $H|n\rangle = E_n|n\rangle$ , weighted by their Boltzmann factor. The expectation value of an operator  $A$  is thus given by

$$\langle A \rangle = \frac{\sum_n e^{-\beta E_n} \langle n|A|n \rangle}{\sum_n e^{-\beta E_n}} = \frac{1}{Z} \text{Tr} (e^{-\beta H} A). \quad (1)$$

For a canonical ensemble the trace is over the  $N$ -electron Hilbert space. For a grand-canonical ensemble we get the same expression when measuring energies relative to the chemical potential, i.e., choosing  $\mu = 0$ , and taking the trace over the entire Fock space.

Time correlation functions can be calculated using the Heisenberg picture

$$\langle A(t' + t)B(t') \rangle = \frac{1}{Z} \text{Tr} e^{-\beta H} e^{iH(t'+t)} A e^{-iH(t'+t)} e^{iHt'} B e^{-iHt'} = \langle A(t)B \rangle = \langle AB(-t) \rangle, \quad (2)$$

where the  $t'$ -independence follows from the cyclic property of the trace  $\text{Tr} ABC = \text{Tr} CAB$ . Monte Carlo techniques are ideal to evaluate the high-dimensional sums needed to calculate such traces [3]. But since the time-evolution leads to complex coefficients, Monte Carlo sampling will have to fight with a serious phase-problem. This can be avoided using a Wick rotation, i.e., working in imaginary time. For this we need to analytically continue (2). This is straightforward: simply replace  $t$  in the analytic expression by the complex variable  $\zeta = t - i\tau$  and determine for what values of  $\zeta$  the result is well defined. This is most easily done using the spectral representation, i.e., evaluating the trace in the basis of eigenfunctions

$$\langle A(t - i\tau)B \rangle = \frac{1}{Z} \text{Tr} e^{(it+\tau-\beta)H} A e^{-(it+\tau)H} B = \frac{1}{Z} \sum_{n,m} e^{(it+\tau-\beta)E_n} e^{-(it+\tau)E_m} \langle n|A|m \rangle \langle m|B|n \rangle. \quad (3)$$

For systems with a finite number of states the sum is always analytic, while for systems where the spectrum is not bounded from above, we need  $\beta \geq \tau \geq 0$  to maintain absolute convergence. Thus (2) can be analytically continued to a stripe below the real axis  $\{\zeta \in \mathbb{C} \mid -\beta \leq \text{Im} \zeta \leq 0\}$ . We can then use quantum Monte Carlo to sample the function  $C_{AB}(\tau) := \langle A(-i\tau)B \rangle$  for  $\tau \in [0, \beta]$ . The analytic continuation back to the real axis is a bit less obvious, since QMC only gives us the function values, i.e., the left hand side of (3) for  $t = 0$ , but not the explicit functional form on the right hand side, for which we would have to know all eigenenergies and matrix elements. We can, however, define a spectral function that neatly contains all the required information by taking the Fourier transform

$$\int_{-\infty}^{\infty} dt e^{i\omega t} \langle A(t)B \rangle = \frac{2\pi}{Z} \sum_{n,m} e^{-\beta E_n} \langle n|A|m \rangle \langle m|B|n \rangle \delta(\omega - (E_m - E_n)) =: \rho_{AB}(\omega) \quad (4)$$

in terms of which we can write (3) as

$$\langle A(t - i\tau)B \rangle = \frac{1}{2\pi} \int_{-\infty}^{\infty} d\omega e^{-(it+\tau)\omega} \rho_{AB}(\omega). \quad (5)$$

For the special case  $t = 0$  this gives us an integral equation directly relating  $\rho_{AB}(\omega)$  to  $C_{AB}(\tau)$

$$C_{AB}(\tau) = \frac{1}{2\pi} \int_{-\infty}^{\infty} d\omega e^{-\omega\tau} \rho_{AB}(\omega), \quad (6)$$

which is, however, not suited for practical calculations since the integral kernel,  $\exp(-\omega\tau)$ , diverges for  $\omega \rightarrow -\infty$ . We can get around this problem by modifying the kernel, dividing it by a function that makes it finite, and correspondingly multiplying the spectral function to leave the integral unchanged

$$C(\tau) = \frac{1}{2\pi} \int_{-\infty}^{\infty} d\omega \frac{e^{-\omega\tau}}{\mu(\omega)} \underbrace{\mu(\omega)\rho_{AB}(\omega)}_{=: \tilde{\rho}(\omega)}. \quad (7)$$

A suitable kernel modification would be  $\mu(\omega) = 1 \pm e^{-\beta\omega}$ , which makes the kernel finite for  $\omega \rightarrow -\infty$  as long as  $\tau \leq \beta$ , while keeping it finite for  $\omega \rightarrow +\infty$ . To analytically continue  $C_{AB}(\tau) = \langle A(-i\tau)B \rangle$  to the real axis we then solve the integral equation (with finite kernel)

$$C_{AB}(\tau) = \frac{1}{2\pi} \int_{-\infty}^{\infty} d\omega \frac{e^{-\omega\tau}}{1 \pm e^{-\beta\omega}} \tilde{\rho}_{AB}^{\pm}(\omega) \quad (8)$$

for  $\tilde{\rho}_{AB}^{\pm}(\omega)$  and use  $\rho_{AB}(\omega) = \tilde{\rho}_{AB}^{\pm}(\omega)/(1 \pm e^{-\beta\omega})$  in (5) to calculate the analytical continuation on the real axis. Note that  $1/(1 \pm e^{-\beta\omega}) \in [0, 1]$ . In fact, for the plus sign it is the Fermi-Dirac function  $n_{\text{FD}}(-\omega) = 1 - n_{\text{FD}}(\omega)$ , while for the minus it is  $-n_{\text{BE}}(-\omega) = n_{\text{BE}}(\omega) - 1$ .

It is reasonable to expect that  $\tilde{\rho}_{AB}^{\pm}(\omega)$  is a spectral function in its own right. Reordering the spectral representation (4), we can write it as

$$\begin{aligned} \tilde{\rho}_{AB}^{\pm}(\omega) &= \rho_{AB}(\omega) \pm \rho_{AB}(\omega) e^{-\beta\omega} \\ &= \rho_{AB}(\omega) \pm \frac{2\pi}{Z} \sum_{n,m} e^{-\beta E_n} \langle n|A|m \rangle \langle m|B|n \rangle \delta(\omega - (E_m - E_n)) e^{-\beta(E_m - E_n)} \\ &= \rho_{AB}(\omega) \pm \rho_{BA}(-\omega). \end{aligned} \quad (9)$$

Comparing with (3) and (4) we see that  $\tilde{\rho}_{AB}^{\pm}(\omega)$  is the spectral function of

$$iG_{AB}^{\pm}(t) := \langle A(t)B \rangle \pm \langle B(-t)A \rangle = \langle A(t)B \rangle \pm \langle BA(t) \rangle = \langle [A(t), B]_{\pm} \rangle, \quad (10)$$

which, for  $t > 0$ , is the retarded correlation function  $G_{AB}^{R\pm}(t) = \Theta(t) G_{AB}^{\pm}(t)$ , with  $\Theta$  the step function,  $\Theta(t > 0) = 1$  and  $\Theta(t < 0) = 0$ . As discussed above, the first term can be analytically continued to  $\{\zeta \in \mathbb{C} \mid -\beta \leq \text{Im} \zeta \leq 0\}$ , while the second term can be continued to the stripe of width  $\beta$  above the real axis. It is thus natural to define the Matsubara function

$$-G_{AB}^{M\pm}(\tau) := \langle \mathcal{T}_{\tau}^{\pm} A(-i\tau)B(0) \rangle \quad (11)$$

with the imaginary-time ordering  $\mathcal{T}_{\tau}^{\pm} A(-i\tau)B(0) = \Theta(\tau)A(-i\tau)B(0) \mp \Theta(-\tau)B(0)A(-i\tau)$  taking care of selecting the appropriate analytic term for the given  $\tau$ . This introduces a discontinuity at  $\tau = 0$

$$G_{AB}^{M\pm}(0^+) - G_{AB}^{M\pm}(0^-) = -\langle [A, B]_{\pm} \rangle. \quad (12)$$

From the cyclic property of the trace in (3), it follows that the Matsubara functions for positive and negative  $\tau$  are related (anti)symmetrically, i.e. for  $\tau \in (0, \beta)$

$$G_{AB}^{M\pm}(\beta - \tau) = -\langle A(-i(\beta - \tau))B \rangle = -\langle B(-i\tau)A \rangle = -\langle BA(i\tau) \rangle = \mp G_{AB}^{M\pm}(-\tau). \quad (13)$$

For  $\tau \in (0, \beta]$  we obviously have (remember the sign introduced in (11))  $G_{AB}^{M\pm}(\tau) = -C_{AB}(\tau)$ , so that from (8) we obtain

$$G_{AB}^{M\pm}(\tau) = -\frac{1}{2\pi} \int_{-\infty}^{\infty} d\omega \frac{e^{-\omega\tau}}{1 \pm e^{-\beta\omega}} \tilde{\rho}_{AB}^{\pm}(\omega) \quad \text{for } \tau \in [0, \beta]. \quad (14)$$

It is convenient to choose the sign in the kernel modification to obtain a simple relation for the sum rule, which directly follows from the spectral representation, using  $|n\rangle\langle n| = \mathbb{1}$

$$\frac{1}{2\pi} \int_{-\infty}^{\infty} d\omega \tilde{\rho}_{AB}^{\pm}(\omega) = \langle [A, B]_{\pm} \rangle. \quad (15)$$

For observables and bosonic operators we thus choose the commutator, while for fermionic Green functions it is more convenient to choose the anticommutator.

For the special case  $B = A^\dagger$  we find

$$\tilde{\rho}_{AA^\dagger}^{\pm}(\omega) = \frac{2\pi}{Z} \sum_{n,m} (e^{-\beta E_n} \pm e^{-\beta E_m}) |\langle n|A|m\rangle|^2 \delta(\omega - (E_m - E_n)), \quad (16)$$

which is obviously non-negative for the fermionic case, for the bosonic sign choice it is non-negative for  $\omega = (E_m - E_n) > 0$ , non-positive for  $\omega < 0$ , and vanishes at least linearly at  $\omega = 0$ . We can thus define a non-negative function  $\tilde{\rho}_{AB}^-(\omega)/\omega$  which is regular at  $\omega = 0$

$$\lim_{\omega \rightarrow 0} \frac{\tilde{\rho}_{AB}^-(\omega)}{\omega} = \frac{2\pi\beta}{Z} \sum_{n,m} e^{-\beta E_n} |\langle n|A|m\rangle|^2 \delta(E_n - E_m) \quad (17)$$

so that we can rewrite (14) with non-negative functions as

$$G_{AA^\dagger}^{M+}(\tau) = -\frac{1}{2\pi} \int_{-\infty}^{\infty} d\omega \frac{e^{-\omega\tau}}{1 + e^{-\beta\omega}} \tilde{\rho}_{AA^\dagger}^+(\omega) \quad (18)$$

$$G_{AA^\dagger}^{M-}(\tau) = -\frac{1}{2\pi} \int_{-\infty}^{\infty} d\omega \frac{\omega e^{-\omega\tau}}{1 - e^{-\beta\omega}} \frac{\tilde{\rho}_{AA^\dagger}^-(\omega)}{\omega}, \quad (19)$$

which, when  $A$  is an annihilator, applies to the diagonal elements of Green functions.

When  $A$  is an observable, we see from (9) that  $\tilde{\rho}_{AA}^-(\omega) = -\tilde{\rho}_{AA}^-(-\omega)$ , so that we can restrict the integral to  $\omega > 0$

$$G_{AA}^{M-}(\tau) = -\frac{1}{2\pi} \int_0^\infty d\omega \frac{\omega(e^{-\omega\tau} + e^{-\omega(\beta-\tau)})}{1 - e^{-\beta\omega}} \frac{\tilde{\rho}_{AA}^-(\omega)}{\omega} \quad \text{when } A \text{ hermitian.} \quad (20)$$

We could actually cancel the factor  $\omega$  in the integrand since  $\tilde{\rho}_{AA}^-(\omega \geq 0)$  is non-negative by itself, but when calculating susceptibilities it is common to keep it, since it shows the behavior for  $\omega \rightarrow 0$ , (17), more clearly.

## 1.2 Analytic properties of the integral equations

We can gain some insight into the integral equations (18) and (19) by realizing that they are intimately related to the Euler and Bernoulli polynomials [4]. Introducing the reduced variables  $x = \beta\omega$  and  $y = \tau/\beta \in [0, 1]$  and the functions  $f(x) = \tilde{\rho}^\pm(x/\beta)/\beta$  (scaled to conserve the sum rule) and  $g(y) = G^{M^\pm}(\beta y)$  we obtain, for the fermionic case

$$g(y) = -\frac{1}{2\pi} \int_{-\infty}^{\infty} dx \frac{e^{-xy}}{1 + e^{-x}} f(x), \quad (21)$$

from which we see that, for fixed kernel, the spectral function is spread out over an ever wider range as we go to lower temperatures. The scaled kernel of this equation is essentially the generating function of the Euler polynomials  $E_n(s)$  on  $s \in [0, 1]$ , which are defined by

$$\frac{2e^{st}}{e^t + 1} = \sum_{n=0}^{\infty} E_n(s) \frac{t^n}{n!}. \quad (22)$$

With  $s = \tau/\beta$  and  $t = -\beta\omega$  we find from (18)

$$G^{M^+}(\tau) = -\frac{1}{4\pi} \sum_{n=0}^{\infty} E_n(\tau/\beta) \frac{(-\beta)^n}{n!} \int_{-\infty}^{\infty} d\omega \omega^n \tilde{\rho}^+(\omega) \quad (23)$$

that the fermionic Matsubara function is a linear combination of Euler polynomials, where the expansion coefficients of  $E_n(\tau/\beta)$  is proportional to the  $n$ -th moment of the spectral function. Since the Euler polynomials are not orthogonal, to determine the moments of  $\tilde{\rho}$  from  $G^{M^+}(\tau)$ , we first have to find the dual functions  $E^n(s)$  with  $\int_0^1 ds E^n(s) E_m(s) = \delta_{n,m}$ . Integrating them with the generating function (22) we obtain

$$\int_0^1 ds E^n(s) e^{st} = \frac{t^n}{n!} \frac{e^t + 1}{2}, \quad (24)$$

which is solved by

$$E^n(s) = \frac{(-1)^n}{2 n!} \left( \delta^{(n)}(s-1) + \delta^{(n)}(s) \right), \quad (25)$$

where  $\delta^{(n)}(s-a)$  is the  $n$ -th derivative of the delta function at  $s = a$  (to make the evaluation for  $a = 0$  and  $1$  unique, we consider the limit from inside the interval of integration). Integration by parts then produces  $(-1)^n$  times the  $n$ -th derivative of the rest of the integrand at  $a$ . Using this in (23) and rewriting the Matsubara function at  $\beta$  as that at  $0^-$ , eq. (13), we find that the discontinuity in the  $n$ -th derivative of the Matsubara function is proportional to the  $n$ -th moment of the spectral function

$$\frac{d^n G^{M^+}(\beta)}{d\tau^n} + \frac{d^n G^{M^+}(0)}{d\tau^n} = \frac{d^n G^{M^+}(0^+)}{d\tau^n} - \frac{d^n G^{M^+}(0^-)}{d\tau^n} = -\frac{(-1)^n}{2\pi} \int_{-\infty}^{\infty} d\omega \omega^n \tilde{\rho}^+(\omega). \quad (26)$$

The higher moments contain the information about the spectral function at large frequencies. Extracting the derivatives from Monte Carlo data for  $G(\tau)$  is difficult. Instead, they can be sampled directly: For  $\tau > 0$  we have, (11),

$$-G^{M^+}(\tau) = \langle A(-i\tau)B \rangle = \frac{1}{Z} \text{Tr} e^{-\beta H} e^{\tau H} A e^{-\tau H} B. \quad (27)$$

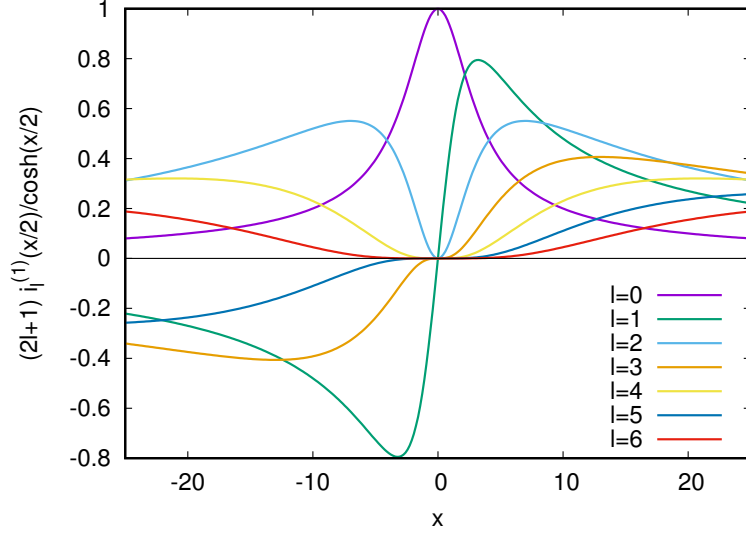


**Fig. 1:** Dependence of the scaled Legendre kernel  $(2l + 1)i_l^{(1)}(x/2)/\cosh(x/2)$  on the order  $l$ . For  $l = 0$ ,  $G_l$  contains information about the spectral function close to the Fermi level, while for increasing  $l$  it probes ever larger frequencies. As the Legendre polynomials themselves, the kernel is even/odd for even/odd  $l$ .

Taking the derivative with respect to  $\tau$  brings down the Hamiltonian to the left and the right of  $A$ , producing  $\langle [H, A(-i\tau)] B \rangle$ . Repeated derivatives produce repeated commutators defined by  $[H; A]_n = [H; [H; A]_{n-1}]$  and  $[H; A]_0 = A$  as in the Baker-Campbell-Hausdorff formula. The moments can then be determined directly by sampling the expectation values

$$\langle [[H; A]_n, B] \rangle = -\frac{(-1)^n}{2\pi} \int_{-\infty}^{\infty} d\omega \omega^n \tilde{\rho}^+(\omega). \quad (28)$$

Working with the Euler polynomials can become cumbersome due to their lack of orthogonality. This inconvenience can be overcome by expressing them in terms of orthogonal polynomials, e.g., shifted Legendre polynomials  $P_l(2y - 1)$ . When the Matsubara function is expanded as [5]

$$G^{M+}(\tau) = \sum_{l=0}^{\infty} \frac{\sqrt{2l+1}}{\beta} G_l P_l(2\tau/\beta - 1) \quad \text{with} \quad G_l = \sqrt{2l+1} \int_0^{\beta} d\tau P_l(2\tau/\beta - 1) G^{M+}(\tau)$$

the expansion coefficients are related to the spectral function via (18) by

$$G_l = (-1)^{l+1} \sqrt{2l+1} \frac{\beta}{4\pi} \int_{-\infty}^{\infty} d\omega \frac{i_l^{(1)}(\beta\omega/2)}{\cosh(\beta\omega/2)} \tilde{\rho}(\omega), \quad (29)$$

where  $i_l^{(1)}(x)$  are the modified spherical Bessel functions of first kind. As shown in Fig. 1, for increasing  $l$  the integral kernel probes spectral features at higher and higher frequencies. From the derivatives of the recursion relation  $(2l + 1)P_l(x) = P'_{l+1}(x) - P'_{l-1}(x)$  and (26) we find that the  $n$ -th moment of the spectral function is given by a sum over all even or odd Legendre coefficients, starting at  $l = n$

$$(-1)^{n+1} \frac{2}{n!} \sum_{k=0}^{\infty} \frac{\sqrt{4k+2n+1}}{\beta^{2k+n+1}} \frac{(2(k+n))!}{(2(k-n))!} G_{2k+n} = \frac{1}{2\pi} \int_{-\infty}^{\infty} d\omega \omega^n \tilde{\rho}^+(\omega). \quad (30)$$

For bosonic Matsubara functions we can obtain similar results using the Bernoulli polynomials  $B_n(s)$  whose generating function is directly related to the bosonic kernel.

### 1.3 Preparing the data

Certainly the most important aspect of preparing Monte Carlo data for analytic continuation is the decision what data to sample. As we have seen, the information about spectral features further away from the chemical potential is concentrated in the Matsubara function extremely close to  $\tau = 0$  and  $\beta$ . Reconstructing the spectral function from data given on a uniform  $\tau$ -grid, we can therefore only expect to get reasonable results close to the chemical potential. Using, on the other hand, the derivatives of the Matsubara function at  $\tau = 0$  and  $\beta$  gives us the moments of the spectral function, which, as we know, e.g., form the Lanczos method [6], accurately characterize the spectral function over the entire frequency range using just a few tens of the lowest moments.

The second concern is to properly characterize the statistical errors in the Monte Carlo data. Considering the integral equation

$$g(y) = \int K(y, x) f(x) dx, \quad (31)$$

the actual numerical data is not given as the function  $g(y)$  but as vectors of  $M$  discrete data points  $\mathbf{g} = (g_1, \dots, g_M)^\dagger$  representing  $g(y)$ . The mean over  $K$  independent samples is then

$$\bar{\mathbf{g}} = \frac{1}{K} \sum_{k=1}^K \mathbf{g}_k \quad (32)$$

with its statistical uncertainty being characterized by the  $M \times M$  covariance matrix

$$\mathbf{C} = \frac{1}{K(K-1)} \sum_{k=1}^K (\mathbf{g}_k - \bar{\mathbf{g}})(\mathbf{g}_k - \bar{\mathbf{g}})^\dagger. \quad (33)$$

By the central limit theorem the probability density of measuring  $\bar{\mathbf{g}}$  with covariance matrix  $\mathbf{C}$  instead of the exact result  $\mathbf{g}_{\text{exact}}$  is then

$$p(\bar{\mathbf{g}}, \mathbf{C} | \mathbf{g}_{\text{exact}}) = \frac{1}{(2\pi)^{M/2} \det \mathbf{C}} e^{-(\bar{\mathbf{g}} - \mathbf{g}_{\text{exact}})^\dagger \mathbf{C}^{-1} (\bar{\mathbf{g}} - \mathbf{g}_{\text{exact}})/2}. \quad (34)$$

This probability will play a central role in the reconstruction of the spectral function representing  $\mathbf{g}_{\text{exact}}$ . It is, therefore, crucial to have an accurate estimate of  $\mathbf{C}$ . Rewriting it as

$$\mathbf{C} = \frac{1}{K(K-1)} \sum_k (\mathbf{g}_k - \bar{\mathbf{g}})(\mathbf{g}_k - \bar{\mathbf{g}})^\dagger = \frac{1}{K(K-1)} \sum_k \mathbf{g}_k \mathbf{g}_k^\dagger - \frac{1}{K-1} \bar{\mathbf{g}} \bar{\mathbf{g}}^\dagger$$

and realizing that  $\mathbf{g} \mathbf{g}^\dagger$  is the (scaled) projector onto  $\mathbf{g}$ , we see that the covariance matrix is a linear combination of  $K$  projectors to one-dimensional subspaces. We therefore need  $K > M$  independent samples  $\mathbf{g}_k$  in (33) to have a chance of obtaining a non-singular covariance matrix. Thus, reducing the discretization error requires taking more samples. The easiest way for obtaining independent samples are independent Monte Carlo runs, e.g., on a parallel computer. If we do not have enough CPUs available, we need to construct independent samples from a sequential run. This can be done, e.g., using the blocking technique described in appendix, A.1.



For the numerical solution of the integral equation (31) we also have to discretize  $f(x)$  into a vector  $\mathbf{f} = (f_1, \dots, f_N)^\dagger$ , e.g., by representing it as a piecewise constant function of value  $f_n$  on interval  $n$ . The integral equation then becomes a simple linear equation  $\mathbf{g} = \mathbf{K} \mathbf{f}$ , where the kernel matrix is obtained, e.g., from the Riemann sum [7]

$$g(y_m) = \sum_n K(y_m, x_n) w_n f(x_n), \quad (35)$$

with  $w_n$  the width of interval  $n$  or, when the functions are expanded in an orthonormal set of functions  $|\psi_m\rangle$  like in the Legendre expansion of the Green function, it is given by

$$g_m = \sum_n \int dy \int dx \overline{\psi_m(y)} K(y, x) \varphi_n(x) f_n = \sum_n \langle \psi_m | K | \varphi_n \rangle f_n. \quad (36)$$

Assuming  $\mathbf{f}$  is the exact model, i.e., it gives the exact data,  $\mathbf{K} \mathbf{f} = \mathbf{g}_{\text{exact}}$ , it follows from (34)

$$p(\bar{\mathbf{g}}, \mathbf{C} | \mathbf{f}) \propto e^{-(\bar{\mathbf{g}} - \mathbf{K} \mathbf{f})^\dagger \mathbf{C}^{-1} (\bar{\mathbf{g}} - \mathbf{K} \mathbf{f})/2} \quad (37)$$

Factorizing the inverse covariance matrix,  $\mathbf{C}^{-1} = \mathbf{T}^\dagger \mathbf{T}$ , e.g., by Cholesky decomposition, we can absorb the explicit dependence on  $\mathbf{C}$  by introducing  $\tilde{\mathbf{g}} := \mathbf{T} \bar{\mathbf{g}}$  and  $\tilde{\mathbf{K}} := \mathbf{T} \mathbf{K}$

$$(\bar{\mathbf{g}} - \mathbf{K} \mathbf{f})^\dagger \mathbf{C}^{-1} (\bar{\mathbf{g}} - \mathbf{K} \mathbf{f}) = (\tilde{\mathbf{g}} - \tilde{\mathbf{T}} \mathbf{f})^\dagger (\tilde{\mathbf{g}} - \tilde{\mathbf{T}} \mathbf{f}) = \|\tilde{\mathbf{g}} - \tilde{\mathbf{T}} \mathbf{f}\|^2. \quad (38)$$

The covariance of the transformed data  $\tilde{\mathbf{g}}$  is then the unit matrix, i.e. the transformation produces uncorrelated data point  $\tilde{g}_n$  that all have the same (unit) errorbar.

## 2 Optimization methods

After discretization of model  $\mathbf{f}$  and data  $\mathbf{g}$  and transformation to  $\tilde{\mathbf{g}}$ , analytic continuation is reduced to solving the linear system

$$\tilde{\mathbf{g}} = \tilde{\mathbf{K}} \mathbf{f}. \quad (39)$$

Nothing could be easier than that! When the number of data points  $M$  we are given equals the number of points  $N$  at which we want to know the model, the solution is unique,  $\mathbf{f} = \tilde{\mathbf{K}}^{-1} \tilde{\mathbf{g}}$ , as long as the kernel is not singular. When  $M > N$  the model is overdetermined so that in general there will be no solution. Normally, however, we want to know the model at many more positions than we are given data points,  $M < N$  so that the solution is underdetermined. A natural choice is then the  $\mathbf{f}$  that gives the best fit to the data.

### 2.1 Least squares and singular values

When we ask for a best-fit, we first have to define what we mean by that. Least-squares methods define “best” in the least-squares sense: minimize  $\chi^2(\mathbf{f}) := \|\tilde{\mathbf{g}} - \tilde{\mathbf{T}} \mathbf{f}\|^2$ . We can justify this choice using Bayesian reasoning: As we have noted in (37), the probability of measuring  $\tilde{\mathbf{g}}$  when the true model is  $\mathbf{f}$  is given by  $p(\tilde{\mathbf{g}} | \mathbf{f}) = (2\pi)^{-M/2} \exp(-\chi^2(\mathbf{f})/2)$ . We can invert

this relation using Bayes' theorem [2],  $p(B|A)p(A) = p(A, B) = p(A|B)p(B)$ , stating that the probability of outcome  $A$  and  $B$  can be written as the probability of  $B$  given  $A$  times the probability of  $A$ , or, equivalently, as the probability of  $A$  given  $B$  times that of  $B$ . For the relation between model and data this implies

$$p(\mathbf{f}|\tilde{\mathbf{g}}) = \frac{p(\tilde{\mathbf{g}}|\mathbf{f})p(\mathbf{f})}{p(\tilde{\mathbf{g}})}. \quad (40)$$

The most probable model  $\mathbf{f}$  given  $\tilde{\mathbf{g}}$  thus maximizes  $p(\tilde{\mathbf{g}}|\mathbf{f})p(\mathbf{f})$ . In the absence of any further information about possible models it is reasonable to assume that  $p(\mathbf{f})$  is the same for all  $\mathbf{f}$ , i.e., to use an “uninformative prior”. A model that maximizes  $p(\mathbf{f}|\tilde{\mathbf{g}})$  is then one that maximizes  $\exp(-\chi^2(\mathbf{f})/2)$ . It is called a “maximum likelihood estimator” and gives a best fit in the least-squares sense. Since the rank of the kernel matrix,  $\text{rank } \mathbf{K} \leq \min(N, M)$ , for  $M < N$  the least-squares solution will not be unique: We can add any vector that is mapped by  $\mathbf{K}$  into zero, without changing the fit. The least-squares problem is thus ill-posed. The usual way of making the solution unique is to ask in addition that  $\mathbf{f}_{\text{LS}}$  has vanishing overlap with any vector that is mapped to zero, i.e.,  $\mathbf{f}_{\text{LS}}$  is orthogonal to the null space of  $\tilde{\mathbf{K}}$ .

A practical tool for the theoretical analysis of least-squares problems as well as for numerical calculations is the singular value decomposition (SVD) of the matrix  $\tilde{\mathbf{K}} = \mathbf{U}\mathbf{D}\mathbf{V}^\dagger$ , where  $\mathbf{U}$  is a unitary  $M \times M$  matrix whose column vectors  $|\mathbf{u}_m\rangle$  define an orthonormal basis in data space and  $\mathbf{V}$  likewise is a unitary  $N \times N$  matrix with columns  $|\mathbf{v}_n\rangle$  spanning the space of models, while  $\mathbf{D}$  is a diagonal  $M \times N$  matrix with diagonal elements  $d_1 \geq d_2 \geq \dots \geq d_{\min(N, M)} \geq 0$ . For the underdetermined case,  $M < N$ , the singular value decomposition can be pictured as

$$\boxed{\tilde{\mathbf{K}}} = \boxed{\mathbf{U}} \boxed{\mathbf{D}} \boxed{\mathbf{V}^\dagger}.$$

For the least-squares solution it is convenient to define the reduced singular value decomposition, where the null space of  $\tilde{\mathbf{K}}$  is dropped in  $\mathbf{V}$ , pictorially,

$$\boxed{\tilde{\mathbf{K}}} = \boxed{\mathbf{U}} \boxed{\hat{\mathbf{D}}} \boxed{\hat{\mathbf{V}}^\dagger}.$$

The singular value decomposition provides a spectral representation of the kernel

$$\tilde{\mathbf{K}} = \sum_{i=1}^{\min(M, N)} |\mathbf{u}_i\rangle d_i \langle \mathbf{v}_i| \quad (41)$$

which allows us to write the residue vector for  $M < N$  as

$$|\tilde{\mathbf{g}}\rangle - \tilde{\mathbf{K}}|\mathbf{f}\rangle = |\tilde{\mathbf{g}}\rangle - \sum_i |\mathbf{u}_i\rangle d_i \langle \mathbf{v}_i|\mathbf{f}\rangle = \sum_i |\mathbf{u}_i\rangle \left( \langle \mathbf{u}_i|\tilde{\mathbf{g}}\rangle - d_i \langle \mathbf{v}_i|\mathbf{f}\rangle \right) \quad (42)$$

so that the least-squares solution (for which the residue vanishes when  $d_M > 0$ ) is

$$|\mathbf{f}_{\text{LS}}\rangle = \sum_i \frac{\langle \mathbf{u}_i|\tilde{\mathbf{g}}\rangle}{d_i} |\mathbf{v}_i\rangle \quad \text{or, equivalently,} \quad \mathbf{f}_{\text{LS}} = \hat{\mathbf{V}}\hat{\mathbf{D}}^{-1}\mathbf{U}^\dagger\tilde{\mathbf{g}}. \quad (43)$$

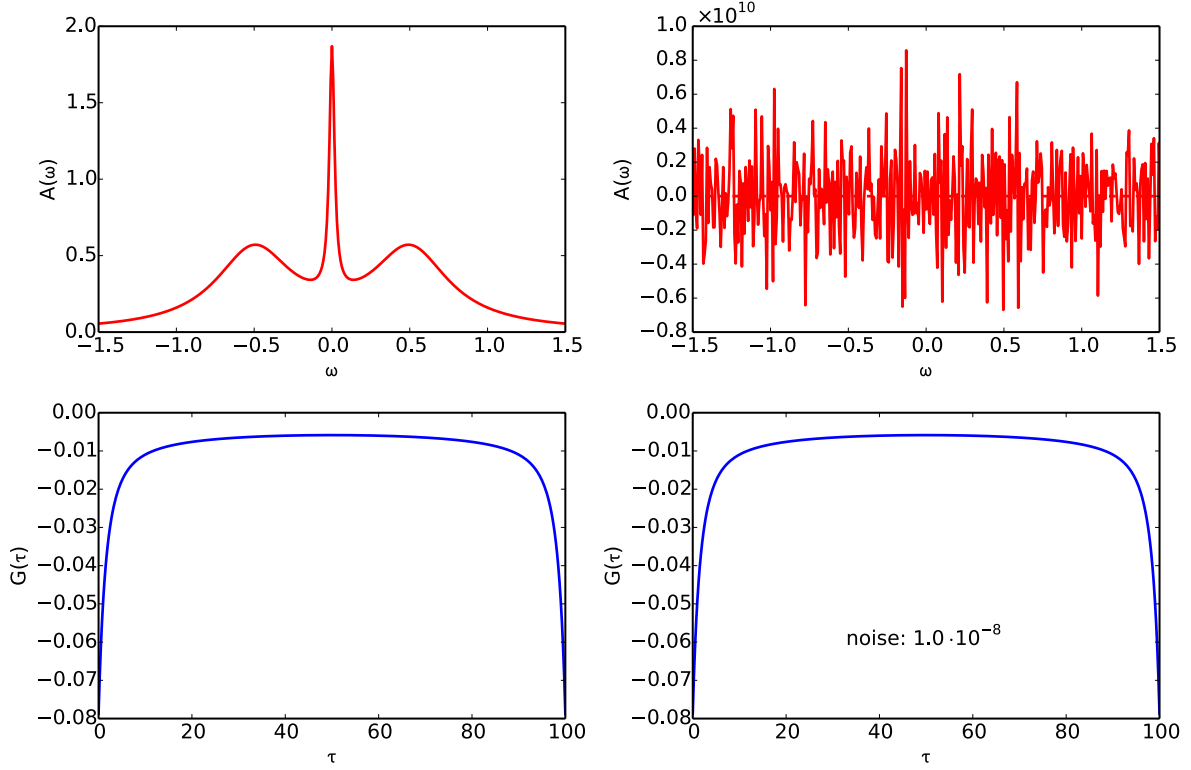


**Fig. 2:** Least-squares solution for the analytical continuation of a fermionic imaginary-time Green function. The exact data (bottom left) is constructed from a simple model spectral function consisting of three Lorentz peaks (top left). We add noise of amplitude  $10^{-8}$  to the data (bottom right). The least-squares solution given the noisy data is shown in the top right panel. It varies over ten orders of magnitude showing no resemblance at all to the original model.

As simple and elegantly the least-squares solution can be constructed, as useless it is for the analytic continuation problem. This is illustrated in Fig. 2, showing that  $\mathbf{f}_{\text{LS}}$ , despite giving a perfect fit to the data and, in particular, fulfilling the sum rule for  $\sum_n f_n$ , is completely dominated by numerical noise. What is the reason for this catastrophic failure? Making the noise in the data explicit,  $\tilde{\mathbf{g}} = \tilde{\mathbf{g}}_{\text{exact}} + \Delta\tilde{\mathbf{g}}$  we see that

$$|\mathbf{f}_{\text{LS}}\rangle = |\mathbf{f}_{\text{exact}}\rangle + \sum \frac{\langle \mathbf{u}_i | \Delta\tilde{\mathbf{g}} \rangle}{d_i} |\mathbf{v}_i\rangle. \quad (44)$$

When the kernel has close to vanishing singular values, the noise component is divided by a number close to numerical accuracy. This is, in fact, what we are seeing in Fig. 2: dividing noise of order  $10^{-8}$  by the numerical epsilon of double precision numbers (of order  $10^{-16}$ ), we would expect the least-squares solution to vary over about eight orders of magnitude. We can verify this picture more quantitatively by looking at the singular values of the kernel matrix, shown in Fig. 3. The exponential decay of the singular values seen in this example actually is the hallmark of an ill-conditioned problem. It is a consequence of the orthogonality of the modes  $|\mathbf{v}_i\rangle$ : With increasing  $i$  they develop more and more nodes. Integrating over these oscillating modes with the positive fermionic Green function kernel means that the integral will decrease with the number of nodes. Once the singular value reaches the machine precision, the singular modes become numerically degenerate. These modes contribute negligibly to the fit of the data, but cause the catastrophic numerical instability of the least-squares result.

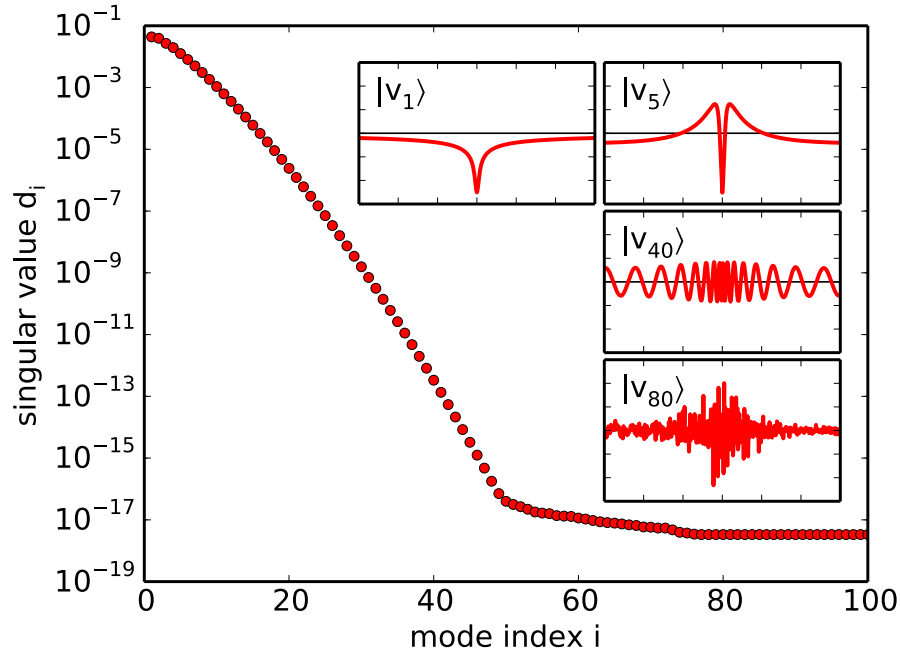


**Fig. 3:** Singular values of the kernel matrix used in Fig. 2 on a logarithmic scale. The singular values decay exponentially until leveling off at a value determined by the numerical accuracy of the calculation. The insets show some of the singular modes  $|v_i\rangle$ . With increasing mode index  $i$ , i.e., decreasing singular value, they have an increasing number of nodes. Once the singular value reaches the numerical accuracy, the singular modes become numerically degenerate so that the SVD routine returns arbitrary linear combinations as exemplified here for  $|v_{80}\rangle$ .

## 2.2 Non-negative least-squares

When motivating the least-squares approach using Bayesian reasoning, (40), one assumption was that we have no knowledge whatsoever about the possible models. When we are interested, e.g., in a diagonal spectral function, this is not quite true: We actually do know that  $\mathbf{f}$  cannot be negative, cf. (18). To incorporate this information, the prior probability  $p(\mathbf{f})$  should, in fact, vanish when  $\mathbf{f}$  has a component  $f_n < 0$ . In other words, we really should maximize the likelihood over non-negative models only:  $\max_{\mathbf{f} \geq 0} \exp(-\chi^2(\mathbf{f}))$ . This approach is called non-negative least squares fitting (NNLS). A practical algorithm is discussed in A.2. It will, in general, not give a perfect fit,  $\chi^2(\mathbf{f}_{\text{NNLS}}) > 0$ , but what is not fitted is the part of the data that is incompatible with a non-negative model, i.e., pure noise.

As shown in Fig. 4, using non-negative least squares gives a dramatic improvement over the least-squares solution. Just incorporating the information about the non-negativity of the model reduces the oscillations in the result by nine orders of magnitude, bringing it into a reasonable range. This is because the amplitude of oscillating modes is now strongly limited by non-negativity. In fact, the constraints give the modes with small singular value or in the null space an important role: All modes except the first have nodes, so they can often not be included in the solution with their optimal value (43) without violating the constraint. Since the contribution of the modes with tiny singular value to the fit is tiny, they are free to arrange such that the modes with larger  $d_i$  can move closer to their optimum. Thus in NNLS the behavior of all modes is coupled, making the fit much more robust. Moreover, the non-negativity constraint makes the

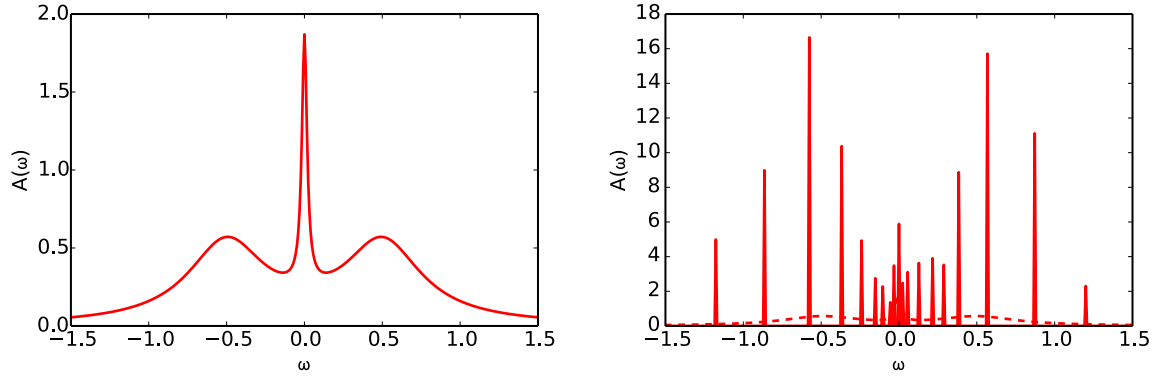


**Fig. 4:** *Non-negative least-squares solution of the same problem as in Fig. 2. Using our knowledge about the non-negativity of the spectral function gives a dramatic improvement, bringing the solution from a scale of the order of  $\pm 10^{10}$  to a positive function with peaks of the order of  $10^2$  so that the original model shown on the left can actually also be seen in the plot on the right (dashed line). While the NNLS solution does show some resemblance to the original function it is far too spiky, even in the present case of exceedingly small noise ( $\sim 10^{-8}$ ) in the data.*

problem well posed, i.e., giving a unique solution. Still, the spiky NNLS solutions indicate that we are still overfitting the noise in the data and this problem becomes stronger when considering data with noise levels larger than the  $\sim 10^{-8}$  used for the example.

While the least-squares approaches do take information about the covariance of the data into account, via the modification of the kernel from  $\mathbf{K}$  to  $\tilde{\mathbf{K}}$ , so that the data points that are given with higher accuracy have more weight, the result are completely independent of the absolute scale of  $\mathbf{C}$ : Multiplying it by a scalar  $\sigma^2$  simply rescales all singular values of  $\tilde{\mathbf{K}}$  by  $1/\sigma$ , which is compensated by the same rescaling of  $\tilde{\mathbf{g}}$ , leaving the solution unchanged. Thus the least-squares type solutions completely neglect the information about the overall noise in the data. This problem can be addressed when we include our intuition that the “true” solution should show some degree of smoothness. We then have to introduce a measure of smoothness, which puts an absolute scale in the fitting problem. This is the idea behind regularization approaches.

### 2.3 Linear regularization

To understand the failure of the least-squares methods better, we expand the noisy data and the fit in their respective singular modes  $|\mathbf{u}_m\rangle$  and  $|\mathbf{v}_n\rangle$ . For the example of Fig. 2 this is shown in Fig. 5. It shows that, initially, the expansion parameters of  $\mathbf{g}$  decrease somewhat faster with the mode index  $i$  than the singular values. Consequently the expansion of the least squares solution also decrease with  $i$ . But once the  $\langle \mathbf{u}_i | \mathbf{g} \rangle$  reach the level of the noise in the data, here  $\sigma = 10^{-8}$ , at  $i \approx 30$ , the expansion coefficients of the data remain constant while the singular values decrease further, leading to exponentially increasing contributions of the highly oscillating modes with large  $i$  that render the least-squares solution useless. The situation is quite similar for the non-negative least squares solution. The main difference is that the contributions of the modes with small or vanishing singular value are bounded  $|\langle \mathbf{v}_n | \mathbf{f}_{\text{NNLS}} \rangle| \lesssim 1$  by the non-negativity combined with the sum-rule for the model.

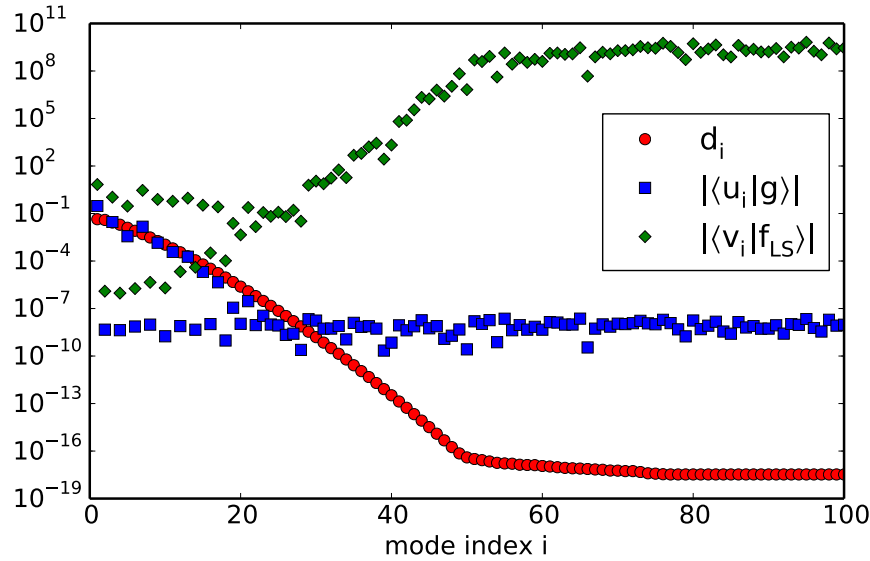


**Fig. 5:** Picard plot for the example of Fig. 2. Since the model is symmetric, the expansion coefficients for the odd modes should vanish. For noisy data, instead of vanishing, the coefficients of odd modes are at the noise level. The even coefficients initially decay somewhat faster than the singular values so that the corresponding coefficients of the least-squares solution decrease with  $i$ . Once the  $\langle \mathbf{u}_i | \mathbf{g} \rangle$  have decreased to the noise level, here  $10^{-8}$ , they remain at that level while the singular values decrease further. This leads to exponentially increasing contributions of the corresponding modes to the least-squares solution.

By maximizing the likelihood  $e^{-\chi^2(\mathbf{f})/2}$ , with or without non-negativity constraint, we apparently overfit the noise that becomes most visible in the modes for which the singular value is below their contribution to the (noisy) data. The assumption behind this is that the exact solution cannot be dominated by the highly oscillating modes with vanishing singular value, i.e., that  $\langle \mathbf{u}_i | \mathbf{g}_{\text{exact}} \rangle / d_i$ , for large  $i$  decreases with the mode index. This is called the Picard condition. When it is not fulfilled, the reconstruction of the exact model is hopeless, since the relevant information is contained in vanishingly small coefficients  $\langle \mathbf{u}_i | \mathbf{g}_{\text{exact}} \rangle$  that will be completely masked by the noise, cf. (44). When the exact model is not highly oscillating, the Picard condition holds and we have a chance of reconstructing the model from noisy data.

When the Picard condition is fulfilled we can get rid of a large part of the noise by suppressing the contribution of modes with singular value below the noise level in the data. This amounts to a least-squares fit with a truncated singular value decomposition, where the singular values beyond a limiting index are set to zero,  $d_{i > i_{\text{trunc}}} := 0$ .

A somewhat more refined method is to continuously switch off the small singular modes. This is called Tikhonov regularization. Introducing a regularization parameter  $\alpha$ , the Tikhonov solution is given by

$$\mathbf{f}_T(\alpha) = \sum_{i=1}^M \frac{d_i}{d_i^2 + \alpha^2} \langle \mathbf{u}_i | \tilde{\mathbf{g}} \rangle, \quad (45)$$

which in the limit  $\alpha \rightarrow 0$  becomes the least-squares solution (43), while for  $\alpha \rightarrow \infty$  the solution vanishes. For finite regularization parameter modes with large singular value  $d_i \gg \alpha$  are not affected, while the contribution of small singular values to  $\mathbf{f}_T(\alpha)$  vanishes. To employ

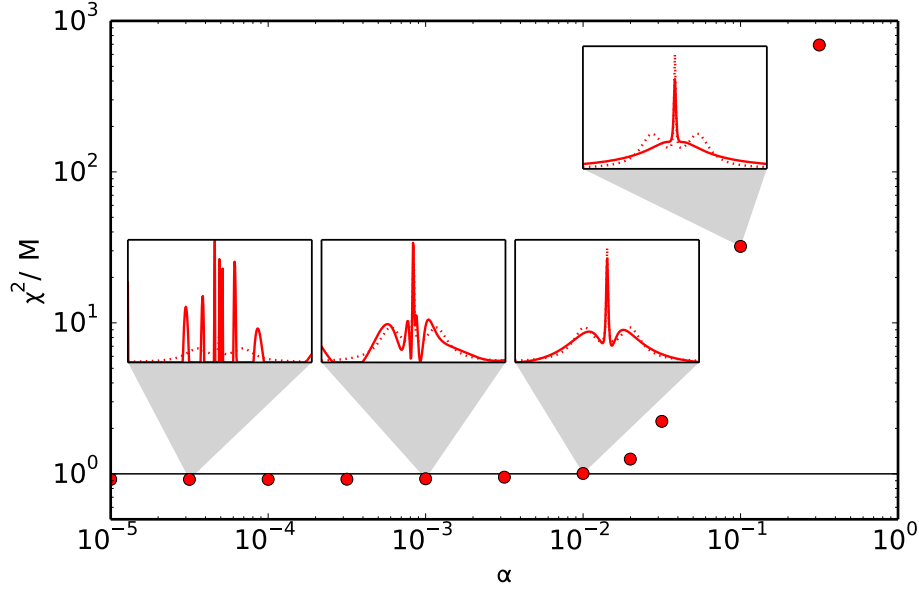


**Fig. 6:** Non-negative Tikhonov regularization for the example of Fig. 2, but with noise level increased from  $10^{-8}$  to  $10^{-4}$ . The insets show the solutions  $\mathbf{f}_T(\alpha)$  at selected values of  $\alpha$ . The dotted line shows the exact model for comparison. For small  $\alpha$  the method overfits the noise, leading to strongly oscillating solutions, while the quality of the fit changes little. For large  $\alpha$  the method underfits the data, leading to a rapid increase in  $\chi^2(\mathbf{f}_T(\alpha))$  and a loss of structure in the reconstructed models. The solid line indicates the expected noise in the data,  $\chi^2 = M$ , relevant for the discrepancy principle.

Tikhonov regularization for non-negative models we need to formulate it as an optimization problem. Expanding in singular modes and completing the square, it can be written as

$$\begin{aligned} \|\tilde{\mathbf{K}}\mathbf{f} - \tilde{\mathbf{g}}\|^2 + \alpha^2 \|\mathbf{f}\|^2 &= \sum_{i=1}^M (\langle \mathbf{u}_i | \tilde{\mathbf{g}} \rangle - d_i \langle \mathbf{v}_i | \mathbf{f} \rangle)^2 + \alpha^2 \sum_{n=1}^N \langle \mathbf{v}_n | \mathbf{f} \rangle^2 \\ &= \sum_{i=1}^M \left( \frac{\alpha^2 \langle \mathbf{u}_i | \tilde{\mathbf{g}} \rangle}{d_i^2 + \alpha^2} + \left( \frac{d_i \langle \mathbf{u}_i | \tilde{\mathbf{g}} \rangle}{\sqrt{d_i^2 + \alpha^2}} + \sqrt{d_i^2 + \alpha^2} \langle \mathbf{v}_i | \mathbf{f} \rangle \right)^2 \right) + \alpha^2 \sum_{n=M+1}^N \langle \mathbf{v}_n | \mathbf{f} \rangle^2 \end{aligned} \quad (46)$$

which attains its minimum  $\sum_i \alpha^2 \langle \mathbf{u}_i | \tilde{\mathbf{g}} \rangle / (d_i^2 + \alpha^2)$  for the unique solution (45). In Bayesian terms, (40), Tikhonov regularization chooses  $p(\mathbf{f}) \propto e^{-\alpha^2 \|\mathbf{f}\|^2 / 2}$  as prior probability.

Alternatively, we can express Tikhonov regularization as a least-squares problem with an expanded kernel and data as

$$\min_{\mathbf{f}} \left( \|\tilde{\mathbf{K}}\mathbf{f} - \tilde{\mathbf{g}}\|^2 + \alpha^2 \|\mathbf{f}\|^2 \right) = \min_{\mathbf{f}} \left\| \begin{pmatrix} \tilde{\mathbf{K}} \\ \alpha \mathbf{1}_N \end{pmatrix} \mathbf{f} - \begin{pmatrix} \tilde{\mathbf{g}} \\ 0_N \end{pmatrix} \right\|^2. \quad (47)$$

Performing the minimization over all models gives Tikhonov regularization, restricting the optimization to  $\mathbf{f} \geq 0$  defines the non-negative Tikhonov regularization method.

The crucial question is how to choose the regularization parameter  $\alpha$ . Fig. 6 shows the results of non-negative Tikhonov regularization for the example of Fig. 2 increasing, however, the noise level from  $10^{-8}$  to  $10^{-4}$  to make the problem not too easy. For small  $\alpha$  the solutions show

strong oscillations, while the mean-square misfit,  $\chi^2$ , increases only little with  $\alpha$ . For large  $\alpha$  the solution becomes featureless except for the peak at the Fermi level, which is already present in the leading singular mode, cf. Fig. 3, while  $\chi^2(\mathbf{f}_T(\alpha))$  rapidly gets worse. A compromise between overfitting of the noise in the data and smoothness of the model should be reached when  $\alpha$  is chosen such that the deviation from the optimum fit  $\chi^2(\mathbf{f}_T(\alpha)) = \|\tilde{\mathbf{g}} - \tilde{\mathbf{K}}\mathbf{f}_T(\alpha)\|^2$  equals the noise expected in  $M$  data points  $\tilde{g}_m$  with unit covariance:  $\chi^2 = M$ . This criterion for choosing the regularization parameter is called the discrepancy principle [8]. We can formulate it as a constrained optimization problem with  $\alpha^{-2}$  playing the role of the Lagrange parameter:

$$\min_{\mathbf{f}} \|\mathbf{f}\|^2 + \frac{1}{\alpha^2} \left( \|\tilde{\mathbf{g}} - \tilde{\mathbf{K}}\mathbf{f}\|^2 - M \right) \quad (48)$$

has the same variational equation as (46).

The regularization parameter  $\alpha$  is the crucial ingredient of any regularization approach. Its role is to strike a balance between fitting the noisy data and keeping the solution smooth in some sense. While it is clear that with increasingly accurate data the chosen  $\alpha$  should get smaller, there is no unique procedure for actually determining its value. The discrepancy principle is just one very reasonable way of choosing  $\alpha$  but there is a plethora of other approaches, see [8] for a first overview. Likewise, the choice of the regularizer is not unique. Instead of  $\|\mathbf{f}\|^2 = \langle \mathbf{f} | \mathbf{1} | \mathbf{f} \rangle$  we could choose any positive semidefinite  $N \times N$  matrix  $\mathbf{M}$  and use  $\langle \mathbf{f} | \mathbf{M} | \mathbf{f} \rangle \geq 0$  instead. An obvious choice follows when we remember that  $\mathbf{f}$  is the discretized version of the model function  $f(x)$ . As in (35), assuming a uniform  $x$ -grid, we can then write

$$\frac{1}{N} \|\mathbf{f}\|^2 = \frac{1}{N} \sum_{n=1}^N |f_n|^2 \approx \int dx |f(x)|^2. \quad (49)$$

Changing the integration variable from  $x$  to  $z$ , the integral and its Riemann sum in the new coordinates becomes

$$\int dx |f(x)|^2 = \int dz \frac{dx}{dz} |f(x(z))|^2 \approx \frac{1}{N} \sum_{n=1}^N \frac{dx(z_n)}{dz} |f(x(z_n))|^2 \quad (50)$$

so that Tikhonov regularization,  $\mathbf{M} = \mathbf{1}$ , on the old grid becomes regularization on the  $z$ -grid with a diagonal matrix  $\mathbf{M}$  that contains the Jacobian factors  $M_{nn} = \frac{dx(z_n)}{dz}$  on the diagonal. Alternative choices of  $\mathbf{M}$  impose smoothness by implementing finite-difference versions of the first or higher derivatives, choosing, e.g.,

$$\sum_{n=1}^{N-1} |f_n - f_{n+1}|^2 = \langle \mathbf{f} | \begin{pmatrix} 1 & -1 & 0 & 0 & \cdots & 0 & 0 & 0 & 0 \\ -1 & 2 & -1 & 0 & & 0 & 0 & 0 & 0 \\ 0 & -1 & 2 & -1 & & 0 & 0 & 0 & 0 \\ \vdots & & & & & & & & \vdots \\ 0 & 0 & 0 & 0 & & -1 & 2 & -1 & 0 \\ 0 & 0 & 0 & 0 & & 0 & -1 & 2 & -1 \\ 0 & 0 & 0 & 0 & \cdots & 0 & 0 & -1 & 1 \end{pmatrix} | \mathbf{f} \rangle. \quad (51)$$



A regularizer that penalizes the  $k$ -th derivative does not have full rank. For, e.g., the first derivative matrix in (51), all constant models give zero. In practice there is, however, no problem since the information about the low moments of the model are usually well contained in the modes with the largest singular values.

Going back to the Tikhonov regularizer, we might wonder why it actually has the effect of smoothing the solution. After all,  $\|\mathbf{f}\|^2 = \sum_n |f_n|^2$  is local, i.e., does not depend on the change in neighboring values. So if we permuted the coordinate values  $\{1, \dots, N\}$  in an arbitrary way, the value of  $\|\mathbf{f}\|^2$  would remain unchanged. The main reason why the identity regularizer  $\mathbf{M} = \mathbb{1}$  leads to smooth models is that it reduces the effect of modes with small singular value. As we have seen in Fig. 3 these modes are highly oscillatory, while the modes that are least affected are the ones with few nodes that are relatively smooth. Still, even the leading mode is not entirely featureless. While a simple first derivative regularizer like (51) would reduce the contribution of such a mode, that is usually strongly supported by the data, Tikhonov will leave it largely unaffected. In that sense, Tikhonov regularization respects the variations in the important modes. To emulate this with a derivative regularizer would require to laboriously tailor an  $\mathbf{M}$  suitable for every specific kernel  $\tilde{\mathbf{K}}$ .

There is also a second aspect. As we noted above,  $\mathbf{f}_T(\alpha \rightarrow \infty) = 0$ . When we impose a sum rule, however, we force the solution to be finite and find from

$$\min_{\mathbf{f}} \left( \sum_n f_n^2 + \lambda_0 \left( 1 - \sum_n f_n \right) \right) \quad (52)$$

that the Tikhonov regularizer prefers a flat solution,  $f_n = 1/N$ , or, in the case of a general diagonal matrix,  $f_n \propto 1/M_{nn}$ . These are the models resulting in the absence of data, i.e., for diverging variance resulting in vanishing  $\tilde{\mathbf{K}}$  and  $\tilde{\mathbf{g}}$ , except for the 0-th moment sum-rule. They are called the default model of the regularizer.

We are, of course, not limited to bilinear regularizers of the type  $\langle \mathbf{f} | \mathbf{M} | \mathbf{f} \rangle$ . An important non-linear regularizer is the entropy of the model. It is the basis of the maximum entropy approach.

## 2.4 Maximum entropy

Maximum entropy methods differ from Tikhonov-type regularization in the assumptions they make about the solutions. While Tikhonov is based on the Picard condition giving preference to the modes with large singular value, maximum entropy favors models that contain as little information as possible. This is measured by the information entropy, see A.3 for details. Using the generalized entropy (89)

$$H(\mathbf{f}; \boldsymbol{\rho}) = - \sum_n \left( f_n \ln \frac{f_n}{\rho_n} - f_n + \rho_n \right) \quad (53)$$

as regularizer that should be maximized, we have to solve the non-linear optimization problem

$$\min_{\mathbf{f}} \left( \chi^2(\mathbf{f}) - \alpha H(\mathbf{f}; \boldsymbol{\rho}) \right), \quad (54)$$

where we use  $\alpha$  instead of  $\alpha^2$  as in (46) to conform with the conventions used, e.g., in [9]. A convenient property of the non-linear entropy regularizer is that it automatically ensures the positivity of the solution since the gradient

$$-\frac{\partial H(\mathbf{f}; \boldsymbol{\rho})}{\partial f_n} = \ln \frac{f_n}{\rho_n} \quad (55)$$

diverges for  $f_n \rightarrow 0$  while the gradient of the fit function

$$\frac{\partial \frac{1}{2} \chi^2(\mathbf{f})}{\partial f_n} = \frac{\partial}{\partial f_n} \frac{1}{2} \sum_m \left( \tilde{g}_m - \sum_{n'} \tilde{K}_{mn'} f_{n'} \right)^2 = - \sum_m \tilde{K}_{nm}^\dagger \left( \tilde{g}_m - \sum_{n'} \tilde{K}_{mn'} f_{n'} \right) \quad (56)$$

is always finite, so that any solution of the variational equations  $f_n$  has the same sign as  $\rho_n$ . Since it is straightforward to also calculate the Hessians

$$\frac{\partial^2 \frac{1}{2} \chi^2(\mathbf{f})}{\partial f_{n'} \partial f_n} = \sum_m \tilde{K}_{nm}^\dagger \tilde{K}_{mn'} \quad \text{and} \quad -\frac{\partial^2 H(\mathbf{f}; \boldsymbol{\rho})}{\partial f_{n'} \partial f_n} = \frac{1}{f_n} \delta_{nn'} \quad (57)$$

it is straightforward to solve the non-linear minimization problem using, e.g., the Levenberg-Marquardt method. The only slight complication being that finite steps in the iteration might change the sign of some component  $f_n$ .

In the absence of data, minimizing (54), i.e., setting (55) to zero, we find  $\mathbf{f} = \boldsymbol{\rho}$ . Thus  $\boldsymbol{\rho}$  is the default model and, as in (88) or (50) it can be related to the choice of the grid. Even when we have decided on a default model, we still have to determine the value of the regularization parameter. Choosing it according to the discrepancy principle is called historic MaxEnt [9]. Other flavors of the maximum entropy method determine the regularization parameter using Bayesian methods. For this we write the entropy regularizer as a prior probability

$$p(\mathbf{f} | \boldsymbol{\rho}, \alpha) \propto e^{+\alpha H(\mathbf{f}; \boldsymbol{\rho})} \quad (58)$$

so that the minimization (54) becomes equal to maximizing the posterior probability, cf. (40),

$$p(\mathbf{f} | \tilde{\mathbf{g}}, \boldsymbol{\rho}, \alpha) = \frac{p(\tilde{\mathbf{g}} | \mathbf{f}, \boldsymbol{\rho}, \alpha) p(\mathbf{f} | \boldsymbol{\rho}, \alpha)}{p(\tilde{\mathbf{g}})} \propto e^{-\chi^2(\mathbf{f})/2 + \alpha H(\mathbf{f}; \boldsymbol{\rho})}, \quad (59)$$

where we have used that the QMC data  $\tilde{\mathbf{g}}$  is actually independent of our choice of regularization parameter and default model. The Bayesian approach to determining the regularization parameter uses the posterior probability of  $\alpha$

$$p(\alpha | \tilde{\mathbf{g}}, \boldsymbol{\rho}) = \int \prod_n \frac{df_n}{\sqrt{f_n}} p(\mathbf{f}, \alpha | \tilde{\mathbf{g}}, \boldsymbol{\rho}) = \int \prod_n 2d\sqrt{f_n} \frac{p(\mathbf{f} | \tilde{\mathbf{g}}, \boldsymbol{\rho}, \alpha) p(\alpha | \tilde{\mathbf{g}}, \boldsymbol{\rho})}{p(\tilde{\mathbf{g}}, \boldsymbol{\rho})} \quad (60)$$

obtained from marginalizing out  $\mathbf{f}$ , i.e., integrating over the space of models  $\mathbf{f}$ . The peculiar choice of the integration measure,  $2d\sqrt{f_n}$ , is discussed in [9]. It naturally appears in the expression for the entropy when using Stirling's approximation to one order higher than in the derivation given in A.3, which rather suggests that the factor  $1/\sqrt{f_n}$  should be considered part of the entropic prior and not the integration measure.

For historic MaxEnt it was not necessary to know the normalized probabilities (58) and (59). When, however, we want to compare the probabilities of different renormalization parameters, we need to determine the normalization of the distributions that depend on  $\alpha$  by, again, integrating over  $\mathbf{f}$

$$Z_{\chi^2}(\tilde{\mathbf{g}}) = \int_{-\infty}^{\infty} \prod_n df_n e^{-\chi^2(\mathbf{f})} = (2\pi)^{M/2} \quad (61)$$

$$Z_H(\boldsymbol{\rho}, \alpha) := \int \prod_n df_n \frac{e^{+\alpha H(\mathbf{f}, \boldsymbol{\rho})}}{\prod_{n'} \sqrt{f_{n'}}} \quad (62)$$

Since the likelihood is a Gaussian, the integral is straightforward, cf. (34). The normalization of the entropic prior is more difficult. In MaxEnt such functional integrals are approximated by Gaussian integrals obtained from expanding the exponent to second order about its maximum. As already discussed above, the entropy term is maximized when the model equals the default model. The second-order expansion (57) is thus given by the diagonal matrix  $-\delta_{nn'}/\rho_n$ , i.e., the entropy becomes just a Tikhonov regularizer with general diagonal matrix. Also expanding  $1/\sqrt{f_n} \approx (1 - (f_n - \rho_n)/2\rho_n)/\sqrt{\rho_n}$ , the normalization of the entropy prior thus is approximated by that of the simple Tikhonov prior without non-negativity constraint [9]

$$Z_H(\boldsymbol{\rho}, \alpha) \approx \prod_n \int_{-\infty}^{\infty} df_n \frac{e^{-\frac{\alpha(f_n - \rho_n)^2}{2\rho_n}}}{\sqrt{\rho_n}} \left(1 - \frac{f_n - \rho_n}{2\rho_n}\right) = \left(\frac{2\pi}{\alpha}\right)^{N/2}. \quad (63)$$

To calculate  $p(\alpha | \tilde{\mathbf{g}}, \boldsymbol{\rho})$ , (60), we still have to choose a prior probability  $p(\alpha | \tilde{\mathbf{g}}, \boldsymbol{\rho})$ . From the discrepancy principle it seems reasonable that it should be independent of the data normalized to have a unit covariance matrix. If we also assume that  $\alpha$  is independent of the default model, we only have to choose  $p(\alpha)$ . Assuming that the prior is scale invariant

$$p(\alpha) d\alpha \stackrel{!}{=} p(s\alpha) d(s\alpha) \quad (64)$$

one obtains the Jeffreys prior  $p(\alpha) \propto 1/\alpha$  [2], which might not be the most appropriate choice, since the scale of the regularization parameter is fixed by the noise in the data, which we know. Using all this for calculating the posterior probability of the renormalization parameter, there are two different flavors of how  $\alpha$  enters the analytical continuation: Historic MaxEnt chooses the  $\alpha$  that maximizes  $p(\alpha | \tilde{\mathbf{g}}, \boldsymbol{\rho})$  to determine  $\mathbf{f}_{\text{historic}} = \mathbf{f}(\alpha_{\text{max}})$ . Bryan's method no longer insists on picking a specific value of  $\alpha$ . The approach rather determines the model as the average over all regularization parameters, weighted with their posterior probability

$$\mathbf{f}_{\text{Bryan}} = \int_0^{\infty} d\alpha \mathbf{f}(\alpha) p(\alpha | \tilde{\mathbf{g}}, \boldsymbol{\rho}). \quad (65)$$

It might seem that the MaxEnt approaches could be improved by actually performing the integrals over model space exactly rather than using simple Gaussian approximations that even violate the non-negativity of the models, which is one of the precious priors that we are sure

of. But doing these integrals is fiendishly hard. A second drawback of MaxEnt, or rather of all regularization approaches, is the need to deal with a regularization parameter, introducing the need for making assumptions about its behavior, its prior probability and the like, for which there is no apparent solution. If only we could efficiently integrate over model space there might be a way of eliminating all these complication arising from the need to regularize. Instead of looking for a solution that maximizes some posterior probability, we could ask for the average over all possible models, weighted with their likelihood. This approach which is free of explicit regularization parameters is the average spectrum method.

### 3 Average spectrum method

The average spectrum methods is an appealing alternative to the optimization approaches. It was probably first proposed by White [10] and reinvented several times after. The basic idea is of striking elegance: The spectral function is obtained as the average over all physically admissible functions, weighted by how well they fit the data

$$f_{\text{ASM}}(x) := (2\pi)^{-M/2} \int_{f(x) \geq 0} \mathcal{D}f f(x) e^{-\chi^2[f]}. \quad (66)$$

Due to the ill-conditioning of the inverse problem there are very many functions that differ drastically but essentially fit the data equally well. Taking the average, we can thus expect that the spectral features not supported by the data will be smoothed out, providing a regularization without the need for explicit parameters. So far the practical application of this conceptually appealing approach has, however, been hampered by the immense computational cost of numerically implementing the functional integration.

It is worth emphasizing that the non-negativity constraint is essential. An unconstrained integration over the Gaussian in (66) actually produces a least-squares solution. Since the width of the likelihood increases with the inverse of the singular value this would, of course, be numerically very inefficient, and since the width diverges for the modes in the null space of the kernel, their contribution will never converge to a definite value, reflecting that the problem is underdetermined.

When we discretize the model function  $f(x)$  as discussed in Sec. 1.3, the functional integral becomes

$$\mathbf{f}_{\text{ASM}} \propto \prod_{n=1}^N \int_0^\infty df_n \mathbf{f} e^{-\chi^2(\mathbf{f})/2}, \quad (67)$$

where the  $N$ -dimensional integral can be evaluated by Monte Carlo techniques. The most straightforward approach is to perform a random walk in the space of non-negative vectors  $\mathbf{f}$ , updating a single component,  $f_n \rightarrow f'_n$ , at a time. Detailed balance is fulfilled when we sample the new component  $f'_n$  for the conditional distribution  $\propto e^{-\chi^2(\mathbf{f}; f'_n)/2}$  with

$$\chi^2(\mathbf{f}; f'_n) := \left\| \underbrace{\tilde{\mathbf{g}} - \tilde{\mathbf{K}} \mathbf{f} + \tilde{\mathbf{K}}_n f_n}_{=:\tilde{\mathbf{g}}_n} - \tilde{\mathbf{K}}_n f'_n \right\|^2 = \tilde{\mathbf{K}}_n^\dagger \tilde{\mathbf{K}}_n \left( f'_n - \tilde{\mathbf{K}}_n^\dagger \tilde{\mathbf{g}}_n / \tilde{\mathbf{K}}_n^\dagger \tilde{\mathbf{K}}_n \right)^2, \quad (68)$$

where  $\tilde{\mathbf{K}}_n$  is the  $n$ -th column of  $\tilde{\mathbf{K}}$ . We thus have to sample  $f'_n$  from a univariate Gaussian of width  $\sigma = 1/||\tilde{\mathbf{K}}_n||$  centered at  $\mu = \tilde{\mathbf{K}}_n^\dagger \tilde{\mathbf{g}}_n / ||\tilde{\mathbf{K}}_n||^2$  and truncated to the non-negative values  $f'_n \in [0, \infty)$ . This can be done very efficiently, e.g., as described in A.4.

Still, sampling components can be very slow because the width of the Gaussian (68) is, in general set by the inverse of the largest singular value, i.e., the random walk performs only exceedingly small steps. This is even more evident when sampling spectral functions, where we cannot change just a single  $f_n$  without violating the sum-rule (15). A way around is to introduce global moves along the principal axes of  $\chi^2$ , i.e., along the singular modes.

Transforming to the new bases  $\mathbf{h} := \mathbf{U}^\dagger \tilde{\mathbf{g}}$  in data and  $\mathbf{e} := \mathbf{V}^\dagger \mathbf{f}$  in model space diagonalizes

$$\chi^2(\mathbf{f}) = ||\mathbf{U}^\dagger \tilde{\mathbf{g}} - \mathbf{D}\mathbf{V}^\dagger \mathbf{f}||^2 = \sum_{i=1}^M (h_i - d_i e_i)^2 \quad (69)$$

so that in the new basis the integral (67) factorizes into Gaussian integrals

$$e_i^{\text{ASM}} \propto \int_{\mathbf{f} \geq 0} d e_i e_i e^{-(h_i - d_i e_i)^2 / 2}. \quad (70)$$

Without non-negativity constraint the integrals would be independent and result in a least-squares solution. With the constraint they are coupled via their range of integration. Updating modes  $e_i \rightarrow e'_i$  is restricted by the condition  $\mathbf{f}' = \mathbf{f} + (e'_i - e_i)\mathbf{V}_i \geq 0$ , where  $\mathbf{V}_i$  is the  $i$ -th column vector of  $\mathbf{V}$ . This is equivalent to  $e'_i \geq e_i - f_n/V_{ni}$  for  $V_{ni} > 0$  and correspondingly for  $V_{ni} < 0$  so that  $e'_i$  is constrained to

$$\max \left\{ \frac{f_n}{V_{ni}} \middle| V_{ni} < 0 \right\} \leq e_i - e'_i \leq \min \left\{ \frac{f_n}{V_{ni}} \middle| V_{ni} > 0 \right\}. \quad (71)$$

Sampling modes is usually much more efficient than sampling components: For modes with large singular value the Gaussian is narrow so that the random walk quickly jumps close to the optimal value  $h_i/d_i$  and then takes small steps around there. For modes with small or zero singular value the distribution is very broad so that the random walk can take large steps, allowing for an efficient sampling. Still, sampling may become inefficient when non-negativity restricts a mode to a very narrow interval. This will happen when  $\mathbf{f}$  has regions where it becomes very small, e.g., in the tail of the spectral function. Then the scale for the step size is not given by the singular value but rather by the width of the interval (71). Also this problem can be overcome by using a real space renormalization group technique, introducing blocks of varying size in which modes are sampled. This way the method can interpolate efficiently between sampling components, i.e., blocks of size 1, and sampling modes, i.e., blocks of size  $N$ . Details of the method and its performance are given in [11, 12].

Using this method, we find that the results of the average spectrum method actually depend on the choice of the discretization (67). This is not a problem of the particular method, but a general feature of the functional integral and would also affect, e.g., MaxEnt were it to do the normalization and marginalization integrals exactly, see e.g. Sec. 6.2 of [2]. We find that the choice of the coordinates for the discretization grid plays the role of a default model, while the number of grid points  $N$  acts as a regularization parameter.

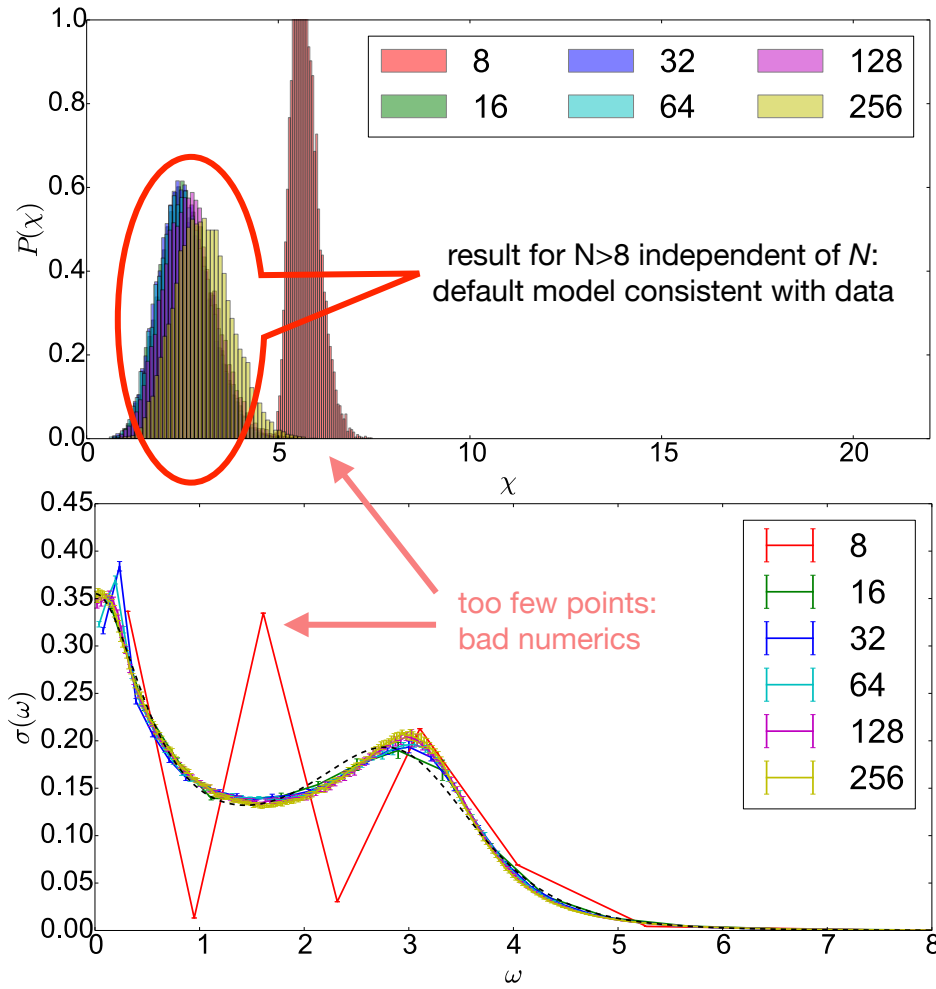


**Fig. 7:** Average spectrum method on a Gaussian grid determined from NNLS for an optical conductivity reconstructed from Matsubara data [11]. The resulting spectral shown below are rather insensitive to the choice of the regularization parameter, the number of grid points  $N$ , except for  $N = 8$  where the coarse grid leads to discretization errors when evaluating the Fredholm integral. The exact model is shown as the dashed line for comparison. The top panel shows the histograms of  $\chi$  taken during the Monte Carlo sampling of the functional integral. The small variations in the histograms indicate a robust choice of the grid.

The reason for this is that the notion of sampling uniformly, i.e., with a flat prior, is tied to the choice of a specific grid. This is most easily understood when we consider what happens when we double the number of grid points. On the original grid we sample  $f \in [0, \infty)$ . On the denser grid we represent  $f$  over the large interval by two values  $\hat{f}_1$  and  $\hat{f}_2$  over intervals of half the width, so that  $f = \hat{f}_1 + \hat{f}_2$ . If we sample the  $\hat{f}_i \in [0, \infty)$  with a flat prior,  $p(\hat{f}_i) = \text{const.}$ , this implies a probability distribution for  $f$

$$p(f) = \int_0^\infty d\hat{f}_1 p(\hat{f}_1) \int_0^\infty d\hat{f}_2 p(\hat{f}_2) \delta(\hat{f}_1 + \hat{f}_2 - f) \propto \int_0^f d\hat{f}_1 = f \quad (72)$$

which is not flat. Properly defining the flat prior as  $p(\hat{f}_i) = \lim_{\lambda \rightarrow \infty} e^{-\hat{f}_i/\lambda}/\lambda$ ,  $p(f)$  becomes a gamma distribution. More generally, we find that sampling with a flat distribution on a particular grid defines a measure for the functional integral (66) represented by a gamma process [11].

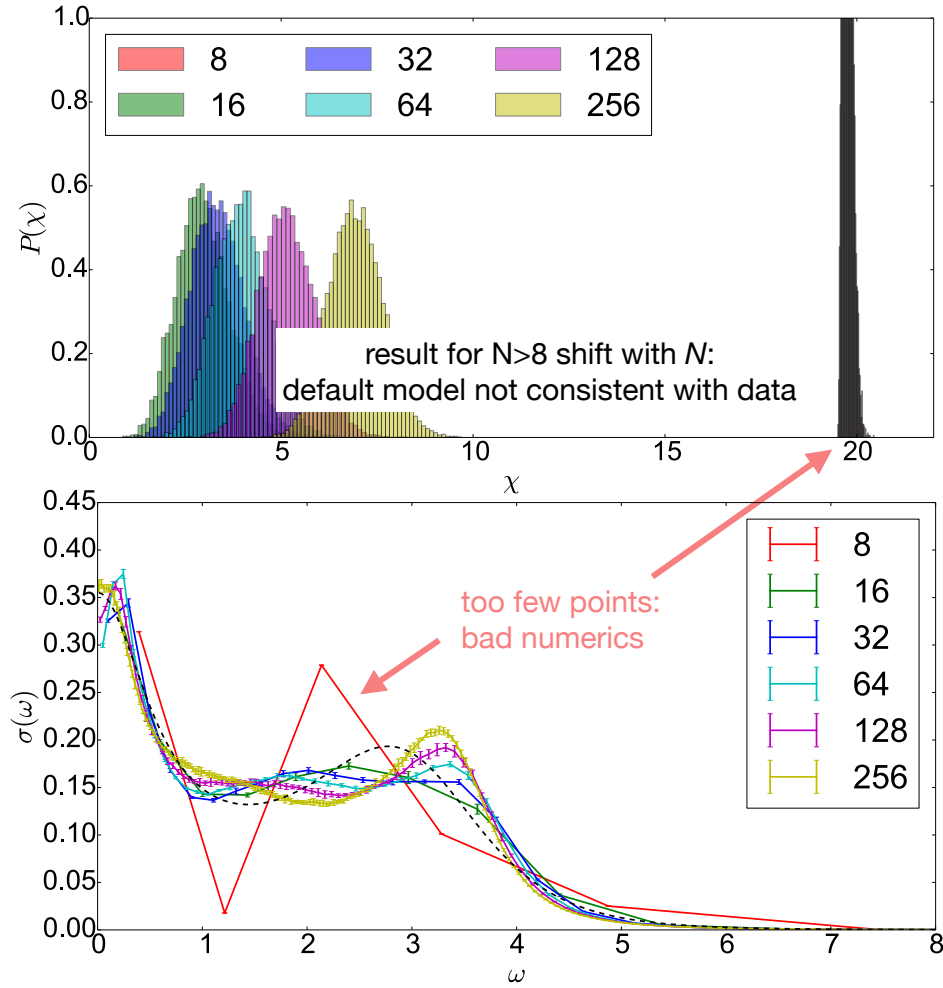


**Fig. 8:** Average spectrum method on a Lorentzian grid of the same width as the Gaussian in Fig. 7. The resulting spectral functions shown below are now quite sensitive to the choice of the regularization parameter, the number of grid points  $N$ . In the top panel we see from the histograms of  $\chi$  that the fit sizeably deteriorates with increasing  $N$ , indicating problems with the choice of the grid.

Still, we can give a practical recipe for determining the regularization parameters and checking the quality of the results. To find the grid type (default model), we use non-negative least-squares to determine the width of the spectrum. This implies a Gaussian grid of particular width. We then vary the number of grid points to check how the results change with increasing  $N$ . When  $N$  is too small, the result will be inaccurate because of discretization errors in evaluating the integral (31) entering  $\chi^2$ . When  $N$  becomes too large there is a rapidly increasing number of vectors  $\mathbf{f}$  that, despite having a small weight  $e^{-\chi^2(\mathbf{f})/2}$ , contribute to the average due to their sheer number. In between there will be a region, where the results are fairly independent of the actual choice of  $N$ . This is shown in Fig. 7. When the grid is not chosen well, as in Fig. 8, where the grid uses a Lorentzian density of the same width as the Gaussian in the previous figure, results vary strongly with  $N$ .

This approach gives already reliable and robust results. When we have to deal with particularly difficult cases, we can use Bayesian techniques to make the method even more robust by sampling over different grids, albeit at an increased computational cost [11].

## 4 Conclusions

As for so many problems, there is no magic solution to the problem of analytic continuation. Any method can only reconstruct what is in the data and must substitute missing information ideally by exact prior knowledge or, otherwise, by mere assumptions about the solution. The most important aspect of analytic continuation is thus encountered already before the solution of the inverse problem is even started. Depending on what features of the model we are interested in, we have to decide where to measure the data. If we want, e.g., to reconstruct the spectral function far from the Fermi level, it does not help to just have highly accurate values for the Green function when they are not close enough to  $\tau = 0$  or  $\beta$  to give information about the discontinuity in its derivatives.

Moreover, it is deceiving to just look at the single result returned by a regularization approach. There is not “the” solution, rather every method produces an expected solution with its uncertainty quantified by a non-intuitive  $N \times N$  covariance matrix. This is, however, rarely analyzed because it is hard to calculate and difficult to interpret. Still, there are approaches to estimate the error in observables derived by integrating over the spectrum. They are nicely discussed in [9] and should be used wherever possible.

We have presented the approaches to the analytic continuation problem in the order of increasing sophistication and accuracy – and numerical cost. The analysis of QMC data should ideally follow this progression until the desired information about the spectral function has been reliably obtained. A Picard plot will give a first impression of how much information is actually contained in the data and what can be expected from a straightforward linear regularization. Despite the uncontrolled approximations in the practical flavors of MaxEnt, the approach has developed into the standard approach for analytical continuation. The average spectrum method, that is now numerically competitive, provides an appealing alternative since it makes all assumptions via the choice of the discretization explicit, while being numerically exact.

The most important lesson is that results of analytic continuation must not be overinterpreted. When the results depend on the details of the method, they rather reflect the choices made by the approach than the data. Thus before interpreting details of the spectral function, we have to make sure that they are robust under (reasonable) variations in the regularization parameters. The discrepancy principle and the fit histogram are practical methods for doing this.



## A Technical appendices

### A.1 Blocking method for correlated data

Let us assume we have an ergodic Markov chain Monte Carlo method, e.g., using Metropolis sampling, that generates a set of  $K$  data points  $m_1, \dots, m_K$  drawn from a probability distribution  $p(m) dm$  and we are interested in the mean value  $\mu = \int dm p(m) m$ . The obvious estimate for  $\mu$  is the average  $\bar{m} = \sum_{k=1}^K m_k / K$ . It will, of course, be different for different Monte Carlo runs, but, by the central limit theorem, for large  $K$  the averages  $\bar{m}$  of different runs will tend to be distributed as a Gaussian centered at  $\mu$  with variance

$$\sigma^2(\bar{m}) = \langle \bar{m}^2 \rangle - \langle \bar{m} \rangle^2 = \frac{1}{K^2} \sum_{k,l=0}^K \left( \langle m_k m_l \rangle - \langle m_k \rangle \langle m_l \rangle \right), \quad (73)$$

where  $\langle \cdot \rangle$  is the average over all possible Monte Carlo runs producing  $K$  data points. How can we estimate  $\sigma^2(\bar{m})$  from the simulation data of a single run? Splitting the double sum

$$\sigma^2(\bar{m}) = \underbrace{\frac{1}{K} \frac{1}{K} \sum_{k=1}^K \left( \langle m_k^2 \rangle - \mu^2 \right)}_{= \langle m^2 \rangle - \mu^2 =: s_0} + \frac{1}{K^2} \sum_{k \neq l} \left( \langle m_k m_l \rangle - \mu^2 \right) \quad (74)$$

we see that for uncorrelated data,  $\langle m_k m_l \rangle = \langle m_k \rangle \langle m_l \rangle$  for  $k \neq l$ , the variance is given by  $s_0/K$ . But in general, samples obtained from Markov chain Monte Carlo will be positively correlated, so that  $\sigma^2(\bar{m}) \geq s_0/K$ . We can eliminate this correlation using an elegant renormalization group technique [13]. For this we consider the transformation of the original data set  $m_1, \dots, m_K$  of  $K$  samples (assuming  $K$  is even) into half as many data points, obtained by averaging

$$\hat{m}_{\hat{k}} := \frac{m_{2\hat{k}-1} + m_{2\hat{k}}}{2}. \quad (75)$$

Obviously, the average of the new data points  $\sum_{\hat{k}=1}^{K/2} \hat{m}_{\hat{k}} / (K/2)$  is still  $\bar{m}$  and thus must have the same distribution as the averages of the original data. Consequently,  $\sigma^2(\bar{m})$  must remain invariant under the blocking transformation (75). Looking at the uncorrelated part of the variance for the blocked data  $\hat{m}_{\hat{k}}$  and remembering that the ensemble average  $\langle m_k^2 \rangle$  is independent of  $k$ , we see that

$$\hat{s}_0 = \frac{1}{K/2} \sum_{\hat{k}=1}^{K/2} \left( \frac{\langle m_{2\hat{k}-1}^2 + 2m_{2\hat{k}-1}m_{2\hat{k}} + m_{2\hat{k}}^2 \rangle}{4} - \mu^2 \right) = \frac{s_0}{2} + \frac{1}{2K/2} \sum_{\hat{k}=1}^{K/2} (\langle m_{2\hat{k}-1}m_{2\hat{k}} \rangle - \mu^2) \quad (76)$$

contains part of the correlations not contained in  $s_0$ . Therefore  $\hat{s}_0/(K/2) \geq s_0/K$ . Under repeated blocking transformations the uncorrelated part of the variance will thus increase. When it reaches a plateau, i.e., a fixed-point under the blocking transformation, it becomes equal to  $\sigma^2(\bar{m})$  and the blocked data has become uncorrelated.

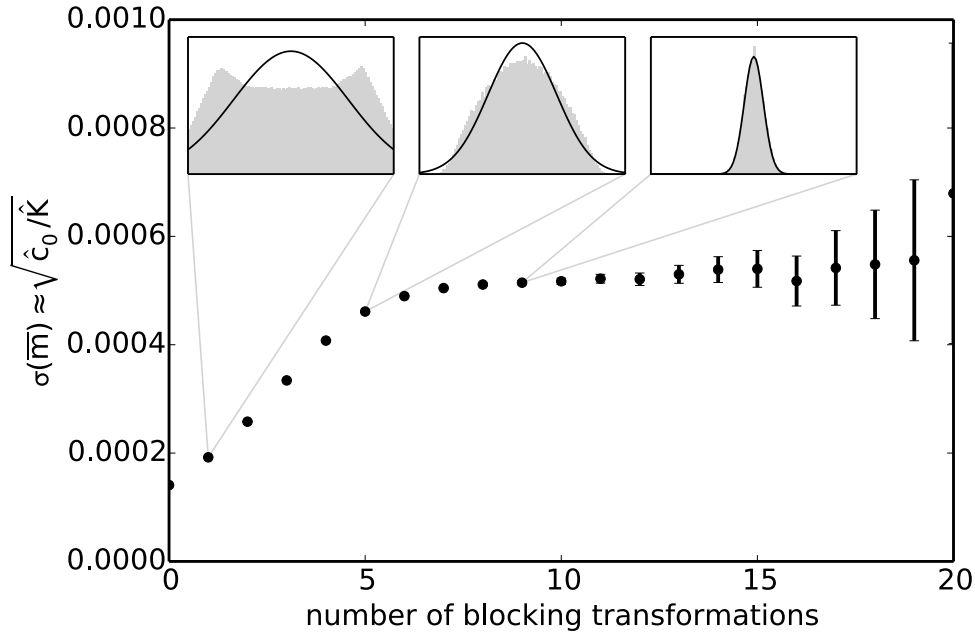


**Fig. 9:** Estimate of the standard deviation of the average of correlated data obtained with the blocking method. Initially the variance is severely underestimated but the estimate increases with each blocking step until a plateau is reached, at which point the blocked data has become uncorrelated. By that time the distribution of the  $\hat{m}_{\hat{K}}$  has become Gaussian of width  $\hat{c}_0$ , as shown in the insets. Eventually the number of blocked samples,  $\hat{K} = K/2^n$ , become so small that the estimates become unreliable.

We can try to estimate the ensemble average  $s_0$  from the data from one specific simulation run as  $\sum_{k=1}^K (m_k^2 - \bar{m}^2)/K$ . Taking the ensemble average and comparing to  $s_0$

$$\frac{1}{K} \sum_{k=1}^K (\langle m_k^2 \rangle - \langle \bar{m}^2 \rangle) = \frac{1}{K} \sum_{k=1}^K (\langle m_k^2 \rangle - \langle \bar{m} \rangle^2) - (\langle \bar{m}^2 \rangle - \langle \bar{m} \rangle^2) = s_0 \left(1 - \frac{1}{K}\right)$$

we find that the unbiased estimator actually is

$$s_0 \approx c_0 := \frac{1}{K-1} \sum_{k=1}^K (m_k^2 - \bar{m}^2) \quad \Rightarrow \quad \sigma^2(\bar{m}) \approx \frac{1}{K(K-1)} \sum_{k=1}^K (m_k^2 - \bar{m}^2). \quad (77)$$

In an actual implementation of the blocking method, we repeatedly block the data and calculate the corresponding estimator of the uncorrelated variance  $\hat{s}_0/\hat{K}$ . An example is shown in Fig. 9. As expected,  $\hat{c}_0/\hat{K}$  increases with each blocking step until it reaches a plateau. There the blocked data  $\hat{m}_{\hat{K}}$  are uncorrelated and, by the central limit theorem, approach Gaussian variables of variance  $\sigma^2(\hat{m}) = \hat{K}\sigma^2(\bar{m})$ . For such variables the variance of the variance  $\sigma^2(\bar{m})$  is given by  $\langle (\hat{c}_0/\hat{K})^2 \rangle - \langle \hat{c}_0/\hat{K} \rangle^2 = 2\sigma^4(\bar{m})/(\hat{K}-1)$ , which provides us with the errorbars. Since the number of blocked data points is halved in each step, eventually the blocked sample becomes very small and  $\hat{c}_0/\hat{K}$  starts to fluctuate, also indicated by rapidly increasing errorbars. We can then identify the plateau by checking when  $\hat{s}_0/\hat{K}$  does not change between blocking steps within its error bar.

## A.2 Non-negative least-squares algorithm (NNLS)

The model  $\mathbf{f}$  fitting a given data vector  $\mathbf{g}$  best in the least-squares sense minimizes the norm of the residual vector  $\chi^2(\mathbf{f}) = \|\mathbf{K}\mathbf{f} - \mathbf{g}\|^2$ . At the minimum  $\mathbf{f}_{\text{LS}}$  the gradient  $\mathbf{w}$  vanishes

$$w_n(\mathbf{f}_{\text{LS}}) := \frac{1}{2} \frac{\partial \chi^2(\mathbf{f})}{\partial f_n} \bigg|_{\text{LS}} = \text{Re} \left( \mathbf{K}^\dagger (\mathbf{K} \mathbf{f}_{\text{LS}} - \mathbf{g}) \right)_n = 0 \quad \forall n. \quad (78)$$

Since  $\chi^2$  is a non-negative quadratic form in  $\mathbf{f}$  stationary points must be minima

$$\chi^2(\mathbf{f}_{\text{LS}} + \boldsymbol{\delta}) = \chi^2(\mathbf{f}_{\text{LS}}) + 2\boldsymbol{\delta}^\top \mathbf{w}(\mathbf{f}_{\text{LS}}) + \|\mathbf{K}\boldsymbol{\delta}\|^2 \geq \chi^2(\mathbf{f}_{\text{LS}}). \quad (79)$$

The least-squares fit can be found from the singular value decomposition (SVD)  $\mathbf{K}^\dagger = \mathbf{V}\mathbf{D}\mathbf{U}^\dagger$

$$\mathbf{f}_{\text{LS}} = \mathbf{V}\mathbf{D}^{-1}\mathbf{U}^\dagger \mathbf{g}, \quad (80)$$

where the diagonal matrix  $\mathbf{D}$  has dimension  $K = \text{rank}(\mathbf{K})$  while the matrix  $\mathbf{U}$  is  $M \times K$  and  $\mathbf{V}$  is  $N \times K$ -dimensional. In terms of the SVD the gradient (78) is given by

$$\mathbf{w}(\mathbf{f}) = \text{Re} \mathbf{V}\mathbf{D}(\mathbf{D}\mathbf{V}^\top \mathbf{f} - \mathbf{U}^\dagger \mathbf{g}). \quad (81)$$

This way of calculating the gradient is numerically more stable than calculating it directly in terms of  $\mathbf{K}$ . It also immediately shows that the gradient vanishes for  $\mathbf{f}_{\text{LS}}$ .

Finding the best fit,  $\min \|\mathbf{K}\mathbf{f} - \mathbf{g}\|^2$ , under the constraint  $\mathbf{f} \geq 0$  (non-negative least-squares, NNLS) is more complicated. When all components of the unconstrained solution are non-negative,  $(\mathbf{f}_{\text{LS}})_n \geq 0$ , it is obviously also the solution of the constrained problem. When there are components  $(\mathbf{f}_{\text{LS}})_n < 0$  we might expect that the constrained fit assumes its minimum on the boundary,  $(\mathbf{f}_{\text{NNLS}})_n = 0$ , where the gradient is positive  $w_n > 0$ . These are the Karush-Kuhn-Tucker conditions [14]:

$$f_n > 0 \quad \text{and} \quad w_n = 0 \quad \text{or} \quad f_n = 0 \quad \text{and} \quad w_n \geq 0. \quad (82)$$

We distinguish the two cases by defining the two sets  $\mathcal{P} = \{n | f_n > 0\}$  and  $\mathcal{Z} = \{n | f_n = 0\}$  which partition the set of indices,  $\mathcal{P} \cup \mathcal{Z} = \{1, \dots, N\}$ .

When  $\mathbf{f}_{\text{KT}}$  fulfills the Karush-Kuhn-Tucker conditions, it minimizes  $\chi^2(\mathbf{f})$  on  $\mathbf{f} \geq 0$ . To see this we consider a vector  $\mathbf{f}_{\text{KT}} + \boldsymbol{\delta}$  with  $\delta_z \geq 0$  so that  $\mathbf{f}_{\text{KT}} + \boldsymbol{\delta} \geq 0$ . Then

$$\chi^2(\mathbf{f}_{\text{KT}} + \boldsymbol{\delta}) = \chi^2(\mathbf{f}_{\text{KT}}) + 2\boldsymbol{\delta}^\top \mathbf{w}(\mathbf{f}_{\text{KT}}) + \|\mathbf{K}\boldsymbol{\delta}\|^2 \geq \chi^2(\mathbf{f}_{\text{KT}}) \quad (83)$$

since  $\boldsymbol{\delta}^\top \mathbf{w} = \sum_n \delta_n w_n = \sum_{n \in \mathcal{P}} \delta_n w_n + \sum_{n \in \mathcal{Z}} \delta_n w_n \geq 0$ , where the first sum vanishes because of the gradient, while in the second sum both factors in each term are non-negative. Conversely, when  $\mathbf{f}_{\text{NNLS}}$  solves the non-negative least-squares problem it must fulfill the Karush-Kuhn-Tucker condition, otherwise an infinitesimal change (respecting non-negativity) of a component violating it could lower  $\chi^2$ . Thus, to solve the NNLS problem we just have to find a vector that fulfills the Karush-Kuhn-Tucker conditions. For this we can simply go through all possible partitionings of the indices  $\{1, \dots, N\} = \mathcal{P} \cup \mathcal{Z}$ . For a given partitioning we determine the

least-squares solution on the indices in  $\mathcal{P}$ , i.e., we minimize  $\|K P_{\mathcal{P}} \mathbf{f} - \mathbf{g}\|^2$ , where  $P_{\mathcal{P}}$  is the projector to the space spanned by the components in  $\mathcal{P}$ . This makes sure that the gradients for these components vanish,  $w_p = 0$ , while  $f_z = 0$ . If also  $f_p \geq 0$  for all  $p \in \mathcal{P}$  and  $w_z \geq 0$  for all  $z \in \mathcal{Z}$ , we have found the NNLS solution, otherwise we try the next partitioning. The only problem is that there are  $2^N$  partitionings of the  $N$  indices (each index can be either in  $\mathcal{P}$  or  $\mathcal{Z}$ ).

A practical algorithm [14] considers possible partitionings in a much more efficient way. We start from some partition for which  $\mathbf{f}_{\mathcal{P}} > 0$  and  $\mathbf{w}_{\mathcal{P}} = 0$ , e.g., an empty positive set,  $\mathcal{P} = \{\}$  and  $\mathbf{f}_{\{\}} = 0$ . Given a set  $\mathcal{P}$  and the corresponding  $\mathbf{f}_{\mathcal{P}}$  for which the Karush-Kuhn-Tucker condition is not yet fulfilled, we add the component  $i$  with the most negative gradient. Least-squares fitting on the expanded set  $\mathcal{P}' = \mathcal{P} \cup \{i\}$  will produce an improved fit  $\chi^2(\mathbf{f}_{\mathcal{P}'}) < \chi^2(\mathbf{f}_{\mathcal{P}})$ : because of the negative gradient, the new component will not stay at zero but rather take a positive value. In case  $\mathbf{f}_{\mathcal{P}'} \geq 0$ , we calculate the new gradient. If it is non-negative, we have found the Karush-Kuhn-Tucker solution, otherwise we repeat the procedure. Each iteration will produce a non-negative solution with improved fit, so that we will converge to the minimum of  $\chi^2(\mathbf{f})$  under the constraint  $\mathbf{f} \geq 0$ .

In general, however, the least squares solution  $\mathbf{f}_{\mathcal{P}'}$  will have negative components. In this case, we can find a mixing with the previous fit  $\mathbf{f}_{\alpha} = (1-\alpha)\mathbf{f}_{\mathcal{P}} + \alpha\mathbf{f}_{\mathcal{P}'}$  with  $\alpha \in (0, 1)$ , that brings the most negative component of  $\mathbf{f}_{\mathcal{P}'}$  to zero. Since  $\chi^2(\mathbf{f}_{\alpha}) \leq (1-\alpha)\chi^2(\mathbf{f}_{\mathcal{P}'}) + \alpha\chi^2(\mathbf{f}_{\mathcal{P}}) < \chi^2(\mathbf{f}_{\mathcal{P}})$  the fit will still be improved. We remove the components where  $\mathbf{f}_{\alpha}$  vanishes from  $\mathcal{P}'$  and perform a least-squares fit on the new set, repeating the procedure until we get a non-negative least squares solution. This must happen after a finite number of iterations, since in each step at least one element is removed from the positive set while the resulting  $\mathbf{f}_{\alpha} \geq 0$  keeps improving the fit  $\chi^2(\mathbf{f}_{\alpha}) < \chi^2(\mathbf{f}_{\mathcal{P}})$ . Thus we can continue the outer loop with  $\mathbf{f}_{\alpha}$ , calculating the new gradient and adding the component where it is most negative to the positive set.

Since each step produces a  $\mathbf{f} \geq 0$  with improved fit, the algorithm does not visit any partitioning twice and will thus always converge. At worst it may take  $2^N$  steps, but in practice the down-hill search produces a solution after trying less than hundred partitionings. Numerically, the most delicate part is the calculation of the gradient, which should be stabilized using a factorization of the kernel. Obviously, checking the Karush-Kuhn-Tucker condition for the gradient must take the numerical accuracy into account. Moreover, the implementation may not converge, when, after adding the component with the most negative gradient, the least-squares fit gives that component a negative value. This can only happen as a consequence of numerical errors. In this case we rather include the component with the second most negative gradient in  $\mathcal{P}$ .

Note that the non-negative least squares solution  $\mathbf{f}_{\text{NNLS}}$  is unique, unlike the least-squares solution (80), to which we can add any multiple of a vector with zero singular value without changing the fit. While the least-squares problem is thus ill-posed when there are vectors that do not contribute to the fit, these vectors play a crucial role in non-negative least squares fitting: They take values such that the modes that are important for the fit can approach their optimal value as closely as possible without violating the constraint. Thus NNLS is well posed.

```

1: function NNLS( $K, g$ )
2:    $\mathbf{f} \leftarrow 0$ 
3:    $\mathcal{Z} \leftarrow \{1, \dots, N\}$  ▷ below we use the abbreviation  $\mathcal{P} = \{1, \dots, N\} \setminus \mathcal{Z}$ 
4:   loop
5:      $\mathbf{w} \leftarrow K^\dagger(K\mathbf{f} - g)$  ▷ for robust calculation use, e.g., SVD
6:     if  $\mathbf{w}[\mathcal{Z}] \geq 0$  then return  $\mathbf{f}$ 
7:     end if
8:      $i \leftarrow \text{argmin}(\mathbf{w}[\mathcal{Z}])$  ▷ find component with most negative gradient
9:      $\mathcal{Z} \leftarrow \mathcal{Z} \setminus \{i\}$ 
10:    loop
11:       $\mathbf{f}' \leftarrow LS(K\mathbf{P}\mathbf{f}, g)$  ▷ LS solution on components  $\mathcal{P}$ 
12:      ▷  $\mathbf{f}_i > 0$ , if not: numerical error in gradient! Do not pick  $i$  again this round
13:      if  $\mathbf{f}'[\mathcal{P}] > 0$  then
14:         $\mathbf{f} \leftarrow \mathbf{f}'$ 
15:        break
16:      end if
17:       $\alpha \leftarrow \min \left\{ \frac{\mathbf{f}_i}{\mathbf{f}_i - \mathbf{f}'_i} \mid i \in \mathcal{P} \wedge \mathbf{f}'_i \geq 0 \right\}$ 
18:       $\mathbf{f} \leftarrow (1 - \alpha)\mathbf{f} + \alpha\mathbf{f}'$  ▷ now  $\mathbf{f} \geq 0$  and  $\mathbf{f}_i = 0$  for  $i = \text{argmin}$ 
19:       $\mathcal{P} \leftarrow \mathcal{P} \setminus \{i \mid \mathbf{f}_i = 0\}$ 
20:    end loop
21:  end loop
22: end function

```

**Fig. 10:** Function that returns the non-negative least-squares solution  $\mathbf{f} \geq 0$  of  $\mathbf{g} = K\mathbf{f}$ .

### A.3 Shannon entropy

When developing *The Mathematical Theory of Communication*, Claude Shannon introduced the bit as the amount of information needed to decide between two equally probable events [15]. Receiving an unlikely (surprising) message should convey more information than receiving a likely one, and the information contained in two independent messages should be the sum of the information carried by each individually. These axioms lead to  $-\log_2 p_i$  as the information contained in receiving a message of probability  $p_i$ . Summing over a set of  $M$  possible messages of probabilities  $p_i$  and weighting the information contained in them by their probability defines the average information or entropy of an information source

$$H(\{p_i\}) = - \sum p_i \log_2 p_i. \quad (84)$$

It gives a lower limit to the number of bits needed for encoding the  $N$  messages. The maximum number of bits,  $\log_2 N$ , is needed when we know least about which message to expect, i.e., when all probabilities are the same. In the opposite limit, when one of the messages is certain, we need not encode it at all. Thus the entropy of an information source measures our ignorance before receiving one of the possible messages.

Changing the base of the logarithm,  $\log_b(x) = \log_2(x)/\log_2(b)$ , for  $b > 1$  simply multiplies the entropy by a positive constant, i.e., changes the units in which we measure information. For convenience, we use the natural logarithm,  $\ln$ , working in natural units,  $1 \text{ nat} \approx 1.44 \text{ bits}$ .

An alternative derivation [2] of (84) starts by considering microstates representing the probabilities as  $p_i = n_i/M$  by placing  $N$  (distinguishable) objects into  $M$  bins. Since we can place any of the  $N$  objects into any of the  $M$  bins, there are  $M^N$  such states. The number of different ways of placing the objects into bins and obtaining the same set of  $\{n_i\}$ , i.e., the same macrostate, is also easily determined: We can pick any  $n_1$  of the  $N$  objects and put them into the first bin. Then we can pick any  $n_2$  of the remaining  $N - n_1$  objects and put them into the second bin. The probability of realizing a macrostate  $\{n_1, \dots, n_M\}$  is thus

$$\frac{1}{M^N} \binom{N}{n_1} \binom{N - n_1}{n_2} \binom{N - n_1 - n_2}{n_3} \dots \binom{n_M}{n_M} = \frac{1}{M^N} \frac{N!}{n_1! n_2! \dots n_M!}.$$

Taking the logarithm and using the Stirling approximation  $\ln n! \approx n \ln n - n$  we find

$$-N \ln M + N \ln N - N - \sum_{i=1}^M (n_i \ln n_i - n_i) = N \left( \ln \frac{1}{M} - \sum_i p_i \ln p_i \right),$$

which is proportional to the  $H(\{p_i\})$  minus the entropy of a flat distribution  $\{1/M\}$ .

Subtracting the entropy of the flat distribution becomes crucial when taking the limit of a continuous probability distribution: encoding an infinite number of messages will, in general, take an infinite number of bits. Subtracting  $-\log 1/M$  keeps the limit  $M \rightarrow \infty$  finite. To see this, we discretize a continuous distribution  $p(x)$  on an equidistant grid of  $M$  points,  $p_i = p(x_i)\Delta x$  with  $\Delta x = (x_{\max} - x_{\min})/M = (\int dx)/M$ , and take the limit of the Riemann sum

$$-\sum_{i=1}^M p_i \ln \left( \frac{p_i}{1/M} \right) = -\sum_{i=1}^M \Delta x p(x_i) \ln \left( \frac{p(x_i)\Delta x}{1/M} \right) \rightarrow -\int dx p(x) \ln \left( \frac{p(x)}{1/\int dx} \right).$$

This defines the entropy of a distribution  $p(x)$

$$H[p] = -\int dx p(x) \ln \left( \frac{p(x)}{1/\int dx} \right). \quad (85)$$

We can find the  $p(x)$  that maximizes this functional from the variational principle. Remembering that the functional derivatives are defined by the expansion

$$H[p + \delta p] = H[p] + \int dx \frac{\delta H[p]}{\delta p(x)} \delta p(x) + \frac{1}{2} \int dx dx' \frac{\delta^2 H[p]}{\delta p(x') \delta p(x)} \delta p(x') \delta p(x) + \mathcal{O}^3(\delta p)$$

we read off the first variation from

$$H[p + \delta p] = -\int dx (p + \delta p) \left( \underbrace{\ln(p + \delta p)}_{=\ln p + \ln(1 + \frac{\delta p}{p}) = \ln p + \frac{\delta p}{p} + \mathcal{O}^2} + \ln \int dx \right) = H[p] - \int dx \underbrace{\left( 1 + \ln \frac{p(x)}{1/\int dx} \right)}_{=-\frac{\delta H[p]}{\delta p(x)}} \delta p + \mathcal{O}^2,$$

where we have used  $\ln(1+x) = x - x^2/2 + \dots$ . In second order we find  $\delta^2 H[p]/\delta p(x') \delta p(x) = -2\delta(x - x')/p(x) \leq 0$  so that the stationary points are maxima. Imposing normalization of the 0-th moment via a Lagrange parameter, the variational equation becomes

$$0 = \frac{\delta}{\delta p(x)} H[p] + \lambda_0 (1 - \int dx p(x)) = -1 - \ln p(x) - \ln \int dx - \lambda_0$$

which is solved by the constant distribution, where  $\lambda_0 = -1$  is fixed by normalization

$$p(x) = \frac{1}{\int dx} e^{-(1+\lambda_0)} = \frac{1}{\int dx}. \quad (86)$$

Inserting into (85) we find  $H[1/\int dx] = 0$ , as is must by construction.

Likewise, we can ask which distribution maximizes the entropy, when we know in addition its first moment  $\mu = \int dx x p(x)$ . The variational equation then contains two Lagrange parameters

$$0 = \frac{\delta}{\delta p(x)} H[p] + \lambda_0 (1 - \int dx p(x)) + \lambda_1 (\mu - \int dx x p(x)) = -1 - \ln \frac{p(x)}{1/\int dx} - \lambda_0 - \lambda_1 x$$

and we obtain a Boltzmann distribution

$$p_\mu(x) = \frac{1}{\int dx} e^{-(1+\lambda_0+\lambda_1 x)}, \quad (87)$$

where  $\lambda_0$  and  $\lambda_1$  are fixed by solving the system  $\int dx p_\mu(x) = 1$  and  $\int dx x p_\mu(x) = \mu$ . Likewise, when we also know the variance of  $p(x)$ , maximizing the entropy results in a Gaussian.

Given the entropy functional, it is natural to ask what happens under a change of variable. Remembering that density functions transform as  $p(x) dx = p(z) dz$ , we find

$$H[p] = - \int \frac{dx}{dz} dz p(z) \frac{dz}{dx} \ln \left( \frac{p(z) \frac{dz}{dx}}{1/\int dx} \right) = - \int dz p(z) \ln \left( \frac{p(z)}{\rho(z)} \right),$$

where we introduced  $\rho(z) dz = dx/\int dx$ . It reflects how the intervals on  $x$  change under the under transformation to  $z$ . When we define  $\rho(x) = 1/\int dx$ , we see that the form of the entropy functional is invariant under coordinate transformations

$$H[p | \rho] = - \int dx p(x) \ln \frac{p(x)}{\rho(x)}. \quad (88)$$

This is the relative entropy or Kullback-Leibler divergence. From  $\ln x \leq x - 1$  it follows that  $H[p] \leq 0$ . By construction, the maximum is attained for  $p(x) = \rho(x)$ . The relative entropy describes the average information contained in the distribution  $p(x)$  when what we expected was the distribution  $\rho(x)$ . The prior  $\rho(x)$  plays the role of a density of states: from the functional derivative of the relative entropy  $\delta H[p]/\delta p(x) = -1 - \ln(p(x)/\rho(x))$  we see that the solutions of the variational equations for  $p(x)$  derived above become proportional to  $\rho(x)$ .

For convenience we might want to allow non-normalized densities of states  $\tilde{\rho}(x)$  and correspondingly drop the normalization constraint for  $\tilde{p}(x)$ . If we write [16]

$$\tilde{H}[\tilde{p} | \tilde{\rho}] = \int dx \left( \tilde{p}(x) - \tilde{\rho}(x) - \tilde{p}(x) \ln \frac{\tilde{p}(x)}{\tilde{\rho}(x)} \right) \quad (89)$$

we obtain from the variational equation  $\delta \tilde{H}/\delta \tilde{p} = 0$  (without normalization constraint) the solution  $\tilde{p}(x) = \tilde{\rho}(x)$  with  $\tilde{H}[\tilde{\rho} | \tilde{\rho}] = 0$  as for (88).

We note that a flat prior  $\rho(x) = \text{const.}$  is bound to the choice of variable: Given any  $\rho(z)$  we can always transform to  $x(z) \propto \int^z \rho(z') dz'$  to obtain  $\rho(x) = \rho(z) dz/dx = \text{const.}$ , where  $x$  must be restricted to a finite interval to be normalizable.

## A.4 Sampling from a truncated normal distribution

It is straightforward to generate a random variable  $x$  with a normal probability distribution

$$p_n(x) = \frac{1}{\sqrt{2\pi}} e^{-x^2/2} \quad (90)$$

using, e.g., the Box-Muller method [17]. When taking a constraint into account, we need, however, variables with a normal distribution restricted to some interval,  $x \in [a, b]$ .

$x \geq a$ : When  $x$  is restricted to be larger than some value  $a$ , a straightforward approach is to sample normally distributed values  $x$  until we find an  $x > a$ . The probability for finding such an  $x$  is, on average, just the integral over the Gaussian

$$\bar{P}_n(a) = \int_a^\infty dx p_n(x) = I(a). \quad (91)$$

This is easily written in terms of the complementary error function  $\text{erfc}(z) = 2/\sqrt{\pi} \int_z^\infty dt e^{-t^2}$ . For  $a > 0$

$$I(a \geq 0) = \frac{1}{2} \text{erfc}(a/\sqrt{2}), \quad (92)$$

while for  $a < 0$

$$I(a \leq 0) = 1 - I(-a). \quad (93)$$

The average acceptance probability (91) is shown in figure 11. For  $a$  to the left of the peak of the normal distribution it is very likely that a proposed random variable  $x$  is larger than  $a$  and thus is accepted. For  $a > 0$  this probability is, however, rapidly decreasing to zero, meaning that we would have to propose very many normally distributed variables  $x$  until we find one that is larger than  $a$ . This is very inefficient, so for  $a > 0$  we need a better approach. Following [18], we generate random variables  $x \geq a$  with an exponential probability distribution

$$p_{\text{exp}}(x) = \alpha e^{-\alpha(x-a)}. \quad (94)$$

These are easily obtained as  $x = a - \ln(u/\alpha)/\alpha$  from uniformly distributed random numbers  $u \in [0, 1)$ . To transform these exponentially distributed random numbers  $x \geq a$  into the desired normally distributed random numbers we use the rejection method [17], accepting  $x$  with probability proportional to the ratio  $p_n(x)/p_{\text{exp}}(x)$  of the desired and the proposed probability distribution functions. To obtain a probability, we introduce a prefactor to make sure that for no  $x \geq a$  the ratio exceed one. Completing the square in the exponential we find

$$p_{\text{acc}}(x; A) = \frac{1}{A} \frac{e^{-x^2/2}}{e^{-\alpha(x-a)}} = \frac{1}{A} \underbrace{e^{-(x-\alpha)^2/2}}_{\leq 1} e^{\alpha^2/2 - \alpha a} \stackrel{!}{\leq} 1. \quad (95)$$

For  $x \geq a$  the choice  $A = e^{\alpha^2/2 - \alpha a}$  maximizes the acceptance probability, which becomes

$$p_{\text{acc}}(x) = e^{-(x-\alpha)^2/2}. \quad (96)$$



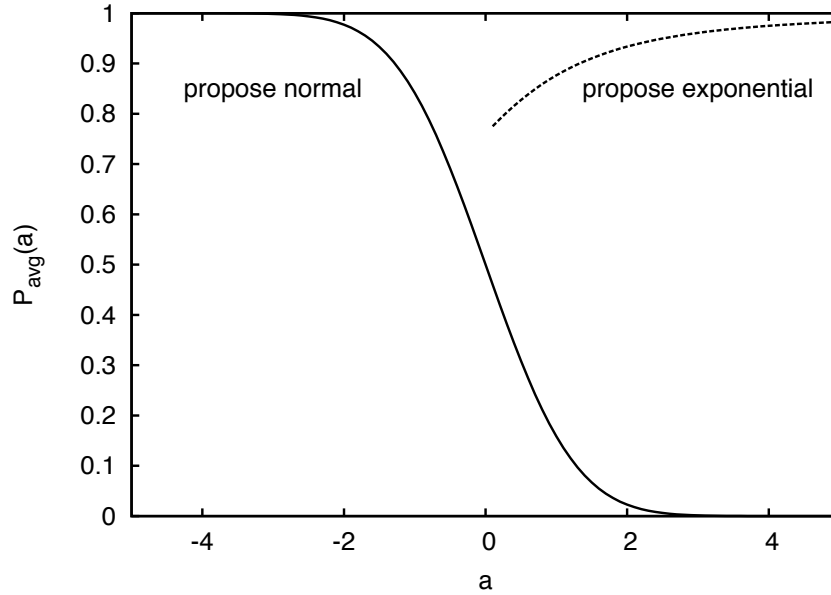


**Fig. 11:** Efficiency of the methods for sampling from a normally distributed variable  $x$  restricted to the interval  $[a, \infty)$ : For  $a < 0$  the average acceptance probability for an unrestricted normally distributed random variable ( $\bar{P}_n(a)$ , full line) is larger than  $1/2$ , while for  $a > 0$  it rapidly approaches zero. For positive  $a$  we therefore propose exponentially distributed random numbers ( $\bar{P}_{\text{exp}}(a \geq 0)$ , dotted line), for which the average acceptance probability is at least  $\sqrt{\pi/2e} \approx 0.76$ .

The corresponding average acceptance probability is then the integral of the product of the probability for proposing a value  $x$  times the probability for accepting it

$$\bar{P}_{\text{exp}}(a \geq 0) = \int_a^\infty dx p_{\text{exp}}(x) p_{\text{acc}}(x) = \sqrt{2\pi} \alpha e^{-\alpha^2/2 + \alpha a} I(a) \quad (97)$$

In this expression  $\alpha$  is still a free parameter, which we choose to maximize the average acceptance. Solving the variational equation we obtain

$$\alpha = \frac{a + \sqrt{a^2 + 4}}{2}. \quad (98)$$

We note that for  $a \geq 0$ ,  $\bar{P}_{\text{exp}}(a)$  has the same form as (91), differing, however, by a prefactor  $\gamma_{\text{exp}} = \sqrt{2\pi} \alpha e^{-\alpha^2/2 + \alpha a}$  which grows faster than the complementary error function decays. Therefore, as can be seen from Fig. 11, for  $a > 0$  this method is dramatically more efficient than sampling from an unbounded uniform distribution. Thus for  $a < 0$  we choose the method with  $\gamma_n = 1$ , while for  $a \geq 0$  we choose  $\gamma_{\text{exp}}$ , obtaining an average acceptance probability  $\bar{P}_\gamma(a) = \gamma(a) I(a)$ .

**$x \geq b$ :** When we need to sample a normal variable constrained from above we can use the same methods as above, sampling  $-x \geq -b$ , with average acceptance probability  $\bar{P}_\gamma(-b)$ .

**$a \leq x \leq b$ :** When the random variable is constrained to a finite interval, an obvious approach is to first sample an  $x \in [a, \infty)$  and to accept it if  $x \leq b$ . The average acceptance probability is then  $\bar{P}_\gamma(a)$  for proposing an  $x \in [a, \infty)$ , times  $\int_a^b dx p_n(x) / \int_a^\infty dx p_n(x)$  for accepting it, i.e.,

$$\bar{P}_\gamma(a, b) = \gamma(I(a) - I(b)). \quad (99)$$

For large intervals this will be an efficient approach, while for narrow intervals the acceptance will go to zero. In this case it becomes more efficient to propose  $x$  uniformly distributed on  $[a, b]$  and accept them with probability

$$p_{\text{acc}} = e^{-(x^2 - m^2)/2}, \quad (100)$$

where  $m$  is the coordinate at which the normal distribution assumes its maximum value on  $[a, b]$ , ensuring that  $p_{\text{acc}} \leq 1$ . When  $0 \in [a, b]$  then  $m = 0$ , otherwise  $m = \min(|a|, |b|)$ . The average acceptance probability for this approach is

$$\bar{P}_u(a, b) = \int_a^b dx \frac{1}{b-a} e^{-(x^2 - m^2)/2} = \frac{e^{m^2/2}}{b-a} \sqrt{2\pi} (I(a) - I(b)). \quad (101)$$

Again, (101) differs from (99) only by its prefactor  $\gamma_u$ , which increases as the width of the interval  $b - a$  becomes smaller.

For a given interval  $[a, b]$  we then choose the most efficient method:

- $a < 0 < b$ : Since  $a < 0$  we have to choose between normal sampling with  $\gamma_n = 1$  and uniform sampling with  $\gamma_u = \sqrt{2\pi}/(b-a)$ . For  $\gamma_n = \gamma_u$  both methods have the same average acceptance probability. Solving this gives us the critical width  $w_0 = \sqrt{2\pi}$ . For intervals  $b-a < w_0$  we thus use uniform sampling with  $\gamma_u$ , otherwise  $\gamma_n$ . The worst case is  $\bar{P}_{\gamma=1}(0, w_0) = I(0) - I(w_0) = \text{erf}(\sqrt{\pi})/2 \approx 0.49$ .
- $0 < a < b$ : Since  $a > 0$  we choose between exponential sampling with  $\gamma_{\text{exp}} = \sqrt{2\pi} \alpha e^{-\alpha^2/2 + \alpha a}$  and  $\gamma_u = \sqrt{2\pi} e^{a^2/2}/(b-a)$ . Solving  $\gamma_{\text{exp}} = \gamma_u$  gives the critical width  $w_{>}(a) = e^{(\alpha-a)^2/2}/\alpha$ . For intervals  $b-a < w_{>}(a)$  we use uniform sampling with  $\gamma_u$ , otherwise  $\gamma_{\text{exp}}$ . The worst case is  $\bar{P}_{\gamma}(0, w_{>}(0)) = \gamma_{\text{exp}}(I(0) - I(\sqrt{e})) = \sqrt{\pi/2} e \text{erf}(\sqrt{e/2}) \approx 0.68$ .
- $a < b < 0$ : We sample  $-x$  in the interval from  $-b$  to  $-a$  as described above.

Overall, we can thus sample from a truncated normal distribution with an average acceptance larger than  $\text{erf}(\sqrt{\pi})/2 \approx 0.49$ .

The generalization to sampling from a Gaussian distribution  $\exp(-(x-\mu)^2/2\sigma^2)/\sqrt{2\pi}\sigma$  of variance  $\sigma$  centered at  $\mu$  restricted to  $x \in [a, b]$  is then straightforward: use  $x = \sigma\tilde{x} + \mu$ , where  $\tilde{x}$  is sampled, as described above, from a normal distribution (90) on the interval  $[(a-\mu)/\sigma, (b-\mu)/\sigma]$ .

## References

- [1] J. Hadamard, Princeton Univ. Bull. **13**, 49–52 (1902): ...ces problèmes se présentait comme parfaitement bien posé, je veux dire comme *possible et déterminé*.
- [2] D.S. Sivia and J. Skilling: *Data Analysis: A Bayesian Tutorial* (Oxford Univ. Press, 2006)
- [3] A. Flesch, E. Gorelov, E. Koch, and E. Pavarini, Phys. Rev. B **87**, 195141 (2013)
- [4] A. Erdélyi (ed.): *Higher Transcendental Functions* (McGraw-Hill, New York, 1953)
- [5] L. Boehnke, H. Hafermann, M. Ferrero, F. Lechermann, and O. Parcollet, Phys. Rev. B **84**, 075145 (2011)
- [6] E. Koch: *The Lanczos Method* in E. Pavarini, E. Koch, D. Vollhardt, A. Lichtenstein (eds.): *The LDA+DMFT approach to strongly correlated materials* Modeling and Simulation Vol. 1 (Forschungszentrum Jülich, 2011)
- [7] J. Waldvogel inn: W. Gautschi, G. Mastroianni, T. Rassias (eds): *Approximation and Computation*, Springer Optimization and Its Applications, Vol. 42 (Springer, New York, 2010) p. 267
- [8] P.C. Hansen: *Discrete Inverse Problems* (SIAM, Philadelphia, 2010)
- [9] M. Jarrell: *The Maximum Entropy Method: Analytic Continuation of QMC Data* in E. Pavarini, E. Koch, F. Anders, and M. Jarrell (eds.): *Correlated Electrons: From Models to Materials* Modeling and Simulation Vol. 2 (Forschungszentrum Jülich, 2012)
- [10] S.R. White in D.P. Landau, K.K. Mon, and B.B. Schüttler: *Computer Simulation Studies in Condensed Matter Physics III* (Springer, 1991) p. 145–153
- [11] K. Ghanem: *Stochastic Analytic Continuation: A Bayesian Approach* PhD Thesis (RWTH Aachen, 2017)
- [12] K. Ghanem and E. Koch, arXiv
- [13] H. Flyvbjerg and H.G. Petersen, J. Chem. Phys. **91**, 461(1989)
- [14] C.L. Lawson and R.J. Hanson: *Solving Least Squares Problems* (SIAM, 1995)
- [15] C. Shannon, Bell Syst. Tech. J. **27**, 379 and 623 (1948)
- [16] J. Skilling, in J. Skilling (ed.): *Maximum Entropy and Bayesian Methods* (Kluwer, Dordrecht, 1989) p. 45–52
- [17] W.H. Press, S.A. Teukolsky, W.T. Vetterling, and B.P. Flannery: *Numerical Recipes* (Cambridge University Press, 2007)
- [18] C.P. Robert Statistics and Computing **5**, 121 (1995)



# 12 Introduction to Diagrammatic Approaches

Hartmut Hafermann

Mathematical and Algorithmic Sciences Lab,

Paris Research Center

Huawei Technologies France SASU

92100 Boulogne-Billancourt, France

## Contents

<b>1</b>	<b>Introduction</b>	<b>2</b>
1.1	Hubbard model . . . . .	3
1.2	Dynamical mean-field theory . . . . .	4
<b>2</b>	<b>Diagrammatic perturbation theory</b>	<b>6</b>
2.1	Coherent state path integrals . . . . .	7
2.2	Perturbation theory . . . . .	9
<b>3</b>	<b>Diagrammatic extensions of dynamical mean-field theory</b>	<b>12</b>
3.1	Dual fermions . . . . .	13
3.2	Perturbation theory for the dual propagator . . . . .	16
3.3	Self-energy diagrams . . . . .	17
3.4	Dual perturbation theory in momentum space . . . . .	22
<b>4</b>	<b>Numerical results</b>	<b>23</b>
4.1	Second-order approximation . . . . .	23
4.2	Ladder approximation . . . . .	24
<b>5</b>	<b>Summary and outlook</b>	<b>28</b>

# 1 Introduction

Correlated materials are at the heart of modern solid state physics. These strongly interacting many-body quantum systems can display such diverse phenomena as the Mott transition [1], non-Fermi-liquid and heavy-Fermion behavior [2], and high-temperature superconductivity [3]. At the same time they pose one of most difficult theoretical challenges. The reason is that they are in the middle of two extremes. In solids with broad energy bands electrons can largely avoid each other while moving through the crystal. The properties of such materials are successfully described in a picture of nearly-independent electrons moving freely in an effective potential generated by all other electrons as described by Bloch waves. In such a momentum-space description the interaction is a perturbation. The framework of density-functional theory (DFT) provides a very successful and often even quantitative description of the microscopic properties of such materials, including simple metals like aluminum, or semiconductors and band-insulating materials. It may even be used to design materials with desired properties.

When electrons cannot avoid each other, the process where an electron hops to a neighboring occupied orbital may be energetically so unfavorable that electrons will remain localized. Mott showed that this scenario can be understood in a real-space picture. These Mott insulators are erroneously predicted to be metallic by band theories, with a classic example being NiO.

Strongly correlated materials are in the middle of these two regimes and exhibit a delicate balance between the kinetic and potential energy. Their name emphasizes the fact that the motion of electrons in these materials is correlated in the true sense of the word: they do not move independently. Neither a real-space nor a momentum-space description appears appropriate – a situation which may be as hard to grasp as particle-wave duality.

Materials that fall under this category often have open  $d$ - or  $f$ -electron shells. Examples are the transition metals V, Fe, Co, Ni, Cu, and their oxides. For example,  $\text{CuO}_2$  planes determine the properties of the high-temperature superconductors. Small microscopic changes can have drastic macroscopic effects. These materials are typically very sensitive to externally controllable parameters, such as pressure and doping, and are therefore promising candidates for applications. The development of reliable theoretical tools to calculate their material specific properties therefore remains one of the primary concerns of modern theoretical condensed matter physics.

An exact solution of the many-particle problem is clearly out of reach and we have to resort to approximate methods. Naturally, certain limiting cases are the most accessible. In the opposite regimes of weak and strong interaction, diagrammatic perturbation theory allows us to make quantitative predictions. Importantly, it also provides us with the intuition for the underlying microscopic processes. We will discuss the foundations of diagrammatic perturbation theory below. In correlated materials, however, where the kinetic- is of the order of the potential energy, such a perturbative description necessarily breaks down. In this regime dynamical mean-field theory (DMFT) has provided important insights [4]. It becomes exact in both the localized and noninteracting itinerant regimes and in the limit of infinite dimensions or coordination number [5].

Correlated materials typically are not close to any of these limits. While DMFT describes the important strong local temporal correlations, as a mean-field theory it completely neglects spatial correlations. This shortcoming is well illustrated by the fact that DMFT correctly predicts the temperature dependence of the local moment in the transition metals iron and nickel, but overestimates their Curie temperatures. Phenomena in which the electrons are qualitatively affected by the presence of extended collective excitations cannot be described within DMFT. Because of the complexity of the problem, there is not a single method which gives 'the best' answer. Instead, we are aiming to study the problem using different approximate methods. These will have inherent limitations and exhibit limited parameter ranges of applicability. We may be even unaware of the precise nature of these limitations. It may therefore not be possible to distinguish true physics from artifacts of the method, so that we risk drawing the wrong conclusions. The approach of the theoretical physicist will therefore be to apply different methods to obtain complementary viewpoints and, step by step, draw a complete picture of the underlying physics.

In this lecture, we will concentrate on the so-called diagrammatic extensions of DMFT [6]. These form a relatively recent class of methods which come in different flavors. They nevertheless all build on the common idea to formulate a diagrammatic perturbation theory around DMFT as the starting point, with the main goal to describe the effect of spatial correlations.

In the following we first describe the Hubbard model, which is believed to capture essential properties of correlated materials, and briefly introduce the Green function as a probe for its properties. We then formulate the basic equations of dynamical mean-field theory and sketch the mathematical foundations of diagrammatic perturbation theory. After a brief introduction to diagrammatic extensions of DMFT we develop a diagrammatic perturbation theory for correlated systems by the example of dual fermions. We conclude this chapter with the discussion of some illustrative results and an outlook on further developments.

## 1.1 Hubbard model

The Hubbard model describes electrons hopping from site to site on a lattice as depicted in Fig. 1, with a probability that is determined by the hopping-integrals  $t$ . Whenever two electrons occupy the same site, their mutual repulsion incurs an energy penalty  $U$ . Because of its simplicity it is probably the most widely studied model in this context. For concreteness we consider the two-dimensional single-band model whose Hamiltonian is given by

$$H = -t \sum_{\langle ij \rangle \sigma} c_{i\sigma}^\dagger c_{j\sigma} + U \sum_i n_{i\uparrow} n_{i\downarrow}. \quad (1)$$

Here the indices label the sites on the lattice and the first sum in the kinetic term is over all pairs of sites or bonds.

In the absence of interaction, we can simply diagonalize the kinetic energy term in reciprocal space:  $\sum_{\mathbf{k}\sigma} \varepsilon_{\mathbf{k}} c_{\mathbf{k}\sigma}^\dagger c_{\mathbf{k}\sigma}$ . The second, potential energy term is apparently diagonal in the real-space occupation number basis. In the opposite regimes of large and small interaction, we can either view the kinetic or potential energy as a perturbation and formulate a diagrammatic



**Fig. 1:** *Left: Illustration of the Hubbard model showing lattice sites on which electrons interact with Hubbard interaction  $U$  (red) connected by bonds through the hopping integrals  $t$ . Right: DMFT picture of model showing a collection of decoupled sites exerted to an electronic bath, as indicated by the blue spheres.*

perturbation theory. We will however primarily be interested in the case where the interaction becomes comparable to the bandwidth  $U \sim W = 8t$ , where such a perturbative description necessarily breaks down.

A complete solution would provide us with the entire spectrum of the Hamiltonian, which would completely specify the equilibrium thermodynamics of the model and include information even on many-particle correlations. A much simpler object is the single-particle Green function. The Matsubara Green function

$$G_{\alpha_1\alpha_2}(\tau_1 - \tau_2) = -\frac{1}{Z} \text{Tr} \left( e^{-\beta(\hat{H} - \mu\hat{N})} T_\tau c_{\alpha_1}(\tau_1) c_{\alpha_2}^\dagger(\tau_2) \right), \quad (2)$$

where  $\beta$  denotes inverse temperature, completely specifies the thermal single-particle properties. It can be viewed as a probe of the system: A particle inserted into the system in a certain state  $\alpha_2 \equiv \{i\sigma\}$  at time  $\tau_2$  evolves until we remove it in state  $\alpha_1$  at a later time  $\tau_1$ . The Green function is the thermal average of this process and tells us how electrons propagate in the system. For this reason, it is sometimes called a propagator. The bosonic (fermionic) Matsubara Green function is a  $2\beta$ -(anti-)periodic function of imaginary time. As a result, its Fourier representation is a function of odd  $\nu_n = (2n+1)\pi/\beta$  (fermionic) or even  $\nu_n = 2m\pi/\beta$  (bosonic) discrete Matsubara frequencies. This simplifies calculations significantly. The retarded Green function is obtained from the Matsubara Green function through analytical continuation  $\omega_n \rightarrow \omega + i0^+$ , which allows to compute the density of states. The latter contains a wealth of information and, for example, tells us whether a system is metallic or insulating.

## 1.2 Dynamical mean-field theory

DMFT has been an important step towards the understanding of correlated electrons in solids. One of the challenges is to reconcile two vastly different energy scales to describe the redistribution of spectral weight through the interaction. DMFT for the first time allowed a simultaneous description of both the long-lived coherent quasiparticles and the short-lived incoherent high-energy excitations. The former give rise to the 'quasiparticle peak' and the latter lead to broad Hubbard bands in the electronic spectrum.



DMFT fully accounts for the local, time-dependent quantum fluctuations. We can understand this by viewing it as the quantum analog of classical mean-field theories, which provides an intuitive understanding of the approach. The construction of an approximation, in analogy to the classical case, results in a nontrivial mean-field theory. The mean-field can no longer be represented by a single number, but rather by a time or frequency-dependent field, hence the name 'dynamical'.

The electronic self-energy may be expressed as a functional of the Green function. The central approximation of DMFT is to assume that this functional is purely local and a functional of the local Green function only:  $\Sigma = \Sigma[G^{\text{loc}}]$ . Under this assumption, we may write the DMFT lattice Green function in the form

$$G_{\mathbf{k}\nu}^{\text{DMFT}} = \frac{1}{i\nu + \mu - \varepsilon_{\mathbf{k}} - \Sigma[G^{\text{loc}}]}. \quad (3)$$

The right-hand side is a functional of the local Green function  $G^{\text{loc}} = \frac{1}{N} \sum_{\mathbf{k}} G_{\mathbf{k}\nu}^{\text{DMFT}}$ . This is a complicated self-consistent problem. The unknown local Green function determines the self-energy, which in turn fixes the local Green function.

Even if we knew  $G^{\text{loc}}$ , we still had to sum *all* diagrams for the local self-energy. As shown by Georges and Kotliar [7], we can introduce a local effective quantum impurity model as a tool to accomplish this. Often an Anderson impurity model is used whose action reads

$$S_{\text{imp}}[c^*, c] = -\sum_{\nu\sigma} c_{\nu\sigma}^* (i\nu + \mu - \Delta_{\nu}) c_{\nu\sigma} + U \sum_{\omega} n_{\omega\uparrow} n_{-\omega\downarrow},$$

where  $\nu$  are fermionic and  $\omega$  are bosonic Matsubara frequencies. Here we have introduced the hybridization function  $\Delta_{\nu}$ , which plays the role of a frequency-dependent Weiss field. In this description the lattice no longer enters explicitly. Instead we can picture the situation as a given lattice site immersed in a structureless 'bath' of conduction electrons. We can imagine that such a description becomes more and more accurate when the coordination number grows large. Electrons can hop from the bath onto the impurity and back. Because of the mutual repulsion when two electrons occupy the same site, the dynamics will strongly depend on the time spent on the impurity. The Weiss field and Green function will therefore still have a non-trivial energy dependence. As we can see in the illustration in Fig. 1, however, different lattice sites are completely decoupled in the DMFT description. The motion of electrons in different parts of the lattice is no longer correlated. We say that DMFT neglects spatial correlations.

By solving the impurity model for a given hybridization we obtain the impurity self-energy and Green function, which are related by a form of Dyson's equation,

$$g_{\nu} = \frac{1}{i\nu + \mu - \Delta_{\nu} - \Sigma[g]}. \quad (4)$$

We could attempt to do this perturbatively. As for the lattice, this will, however, not work in the strongly correlated regime we are interested in. Since the problem is local, it is nevertheless simpler than that of the lattice. Fortunately, sophisticated and accurate methods exist to solve it efficiently and in particular to compute the impurity Green function  $g_{\nu} := -\langle c_{\nu\sigma} c_{\nu\sigma}^* \rangle_{\text{imp}}$ . Notable examples are continuous-time quantum Monte Carlo methods [8].

The hybridization function encodes the dynamics generated by all electrons on average and is a priori unknown. Instead of finding the local lattice Green function, the problem has been reduced to determining the hybridization self-consistently.

If we identify the impurity self-energy with that of the lattice, the hybridization will determine the right-hand side of (3). If we additionally identify the local lattice Green function with the impurity Green function, we obtain the following equation that implicitly determines the hybridization function

$$g_\nu = \frac{1}{N} \sum_{\mathbf{k}} \frac{1}{g_\nu^{-1} + \Delta_\nu - \varepsilon_{\mathbf{k}}} . \quad (5)$$

This equation is the only place where the structure of the lattice enters in DMFT, namely in the form of the dispersion  $\varepsilon_{\mathbf{k}}$ .

In practice, we obtain the self-consistent solution by repeatedly solving the impurity model. Starting from an initial guess for the hybridization, we can iteratively update it based on the solution of the impurity model according to

$$\Delta_\nu \leftarrow \Delta_\nu + \xi (g_\nu^{-1} - (G_\nu^{\text{loc}})^{-1}), \quad (6)$$

where  $G_\nu^{\text{loc}}$  is calculated from (3) using the impurity self-energy. A solution is found once the impurity Green function equals the local lattice Green function:  $g_\nu = G_\nu^{\text{loc}}$ .  $\xi \in ]0, 1[$  is a parameter to control the convergence speed. The loop typically converges in a few iterations.

## 2 Diagrammatic perturbation theory

Perturbation theory can be applied when the problem at hand is close, in some sense, to a solvable reference problem. This implies that it can be described in terms of a small perturbation of this reference. Often the reference problem is the non-interacting one and the perturbation series is a series expansion in powers of the interaction. Wick's theorem allows to express the result in terms of the interaction and products of the known non-interacting Green function. If the coupling,  $U$  in case of the Hubbard model, is small, the series will converge to the exact result within any desired accuracy after a finite number of terms. If this is not the case, one may attempt to obtain an approximation by summing an infinite partial series of dominant terms.

The expressions in the expansion become, however, increasingly difficult to handle with increasing order as we will see in a few examples below. In addition the number of terms grows factorially. It helps to visualize the expressions in terms of Feynman diagrams, where one assigns a symbol to the interaction and depicts non-interacting Green functions as lines. This yields a diagrammatic perturbation theory. The usefulness of diagrammatic perturbation theory hinges on the following simplifications.

The linked cluster theorem significantly simplifies the problem, because it allows one to concentrate on connected diagrams. Another simplification is obtained by gathering diagrams with the same structure which yield the same contribution. Finally, one can formulate a set of rules

which allows one to obtain the analytical expression corresponding to any diagram just from its structure, without the need to consider the term in the expansion where it came from.

The diagrammatic perturbation theory is often developed in terms of expectation values of time-ordered second-quantized operators. The theory can equally well be formulated in terms of path integrals. In case of fermions these are coherent state path integrals. Instead of operators we integrate over Grassmann variables to capture the fermion statistics. The expressions are formally very similar and it is often straightforward to translate from one description to the other. The dual fermion approach and the associated perturbation theory are formulated in terms of coherent state path integrals. We therefore briefly introduce them and formulate the perturbation theory in terms of them. An excellent introduction to coherent states and the coherent state path integral can be found in [9].

## 2.1 Coherent state path integrals

For concreteness, we consider systems of fermions. Starting point for the description of the thermodynamic properties of quantum many-particle systems is the grand canonical partition function  $Z = \text{Tr} e^{-\beta(\hat{H} - \mu\hat{N})}$ , where  $\hat{H}$  is the Hamiltonian in second quantized form,  $\hat{N}$  is the operator of the total particle number and the chemical potential  $\mu$  controls the number of particles of the grand canonical ensemble.

Let us first recall the properties of coherent states. Coherent states  $|\phi\rangle$  are eigenstates of the annihilation operator  $c_\alpha$  with eigenvalue  $\phi_\alpha$ :  $c_\alpha |\phi\rangle = \phi_\alpha |\phi\rangle$ . For fermions, the eigenvalues are Grassmann numbers. The most important property of the Grassmann algebra is that its generators anticommute:  $\phi_\alpha \phi_\beta + \phi_\beta \phi_\alpha = 0$ . This implies in particular that  $\phi_\alpha^2 = 0$ . It is straightforward to show that the state

$$|\phi\rangle = e^{-\sum_\alpha \phi_\alpha c_\alpha^\dagger} |0\rangle = \prod_\alpha (1 - \phi_\alpha c_\alpha^\dagger) |0\rangle \quad (7)$$

has the desired property. The adjoint of the coherent state is  $\langle 0 | \prod_\alpha (1 + \phi_\alpha^* c_\alpha)$ . The overlap of two coherent states follows straightforwardly:

$$\langle \phi | \phi' \rangle = \langle 0 | \prod_\alpha (1 + \phi_\alpha^* c_\alpha) \prod_{\alpha'} (1 - \phi_{\alpha'} c_{\alpha'}^\dagger) | 0 \rangle = \prod_\alpha (1 + \phi_\alpha^* \phi_\alpha) = e^{\sum_\alpha \phi_\alpha^* \phi_\alpha}. \quad (8)$$

The matrix element of a normal-ordered operator  $A[c_\alpha^\dagger, c_\alpha]$  therefore is given by

$$\langle \phi | A[c_\alpha^\dagger, c_\alpha] | \phi \rangle = \langle \phi | \phi \rangle A[\phi_\alpha^*, \phi_\alpha] = e^{\sum_\alpha \phi_\alpha^* \phi_\alpha} A[\phi_\alpha^*, \phi_\alpha]. \quad (9)$$

The following closure relation is essential for the formulation of the fermionic coherent state path integral:

$$\int \prod_\alpha d\phi_\alpha^* d\phi_\alpha e^{-\sum_\alpha \phi_\alpha^* \phi_\alpha} |\phi\rangle \langle \phi| = 1. \quad (10)$$

The coherent states form an over-complete set of states in a generalized Fock space, that is, the set of linear combinations of states in the Fermion Fock space with coefficients in the Grassmann algebra. Any physical Fermion state can be expanded in terms of them.

Given two states  $|\psi\rangle$  and  $|\phi\rangle$  in the Fock space, it follows from the anticommutation relations of Grassmann numbers that  $\langle\psi|\phi\rangle\langle\phi|\psi\rangle = \langle-\phi|\psi\rangle\langle\psi|\phi\rangle$ . For a complete set of states  $\{|n\rangle\}$  in the Fock space, the trace of a second quantized operator  $A$  can be written

$$\begin{aligned}\mathrm{Tr} A &= \sum_n \langle n| A |n\rangle = \int \prod_{\alpha} d\phi_{\alpha}^* d\phi_{\alpha} e^{-\sum_{\alpha} \phi_{\alpha}^* \phi_{\alpha}} \sum_n \langle n|\phi\rangle \langle\phi| A |n\rangle \\ &= \int \prod_{\alpha} d\phi_{\alpha}^* d\phi_{\alpha} e^{-\sum_{\alpha} \phi_{\alpha}^* \phi_{\alpha}} \langle-\phi| A \sum_n |n\rangle \langle n|\phi\rangle \\ &= \int \prod_{\alpha} d\phi_{\alpha}^* d\phi_{\alpha} e^{-\sum_{\alpha} \phi_{\alpha}^* \phi_{\alpha}} \langle-\phi| A |\phi\rangle.\end{aligned}\quad (11)$$

With these prerequisites, the grand canonical partition function can be expressed in the form

$$Z = \mathrm{Tr} e^{-\beta(\hat{H}-\mu\hat{N})} = \int \prod_{\alpha} d\phi_{\alpha}^* d\phi_{\alpha} e^{-\sum_{\alpha} \phi_{\alpha}^* \phi_{\alpha}} \langle-\phi| e^{-\beta(\hat{H}-\mu\hat{N})} |\phi\rangle, \quad (12)$$

where for fermions, the trace imposes antiperiodic boundary conditions.

We can obtain a coherent state path integral representation of the partition function by viewing the exponential as an imaginary-time evolution operator describing the evolution of the state from time zero to  $\beta$ . While its matrix elements cannot be evaluated directly, we can exploit the fact that the infinitesimal evolution operator can be obtained in normal-ordered form. To this end, we break the time interval  $[0, \beta]$  into  $M$  time steps of size  $\epsilon = \beta/M$ , such that  $e^{-\beta(\hat{H}-\mu\hat{N})} = (e^{-\epsilon(\hat{H}-\mu\hat{N})})^M$ .

The second quantized operator  $e^{-\epsilon(\hat{H}-\mu\hat{N})}$  is in approximate normal-ordered form, up to a correction of order  $\epsilon^2$ ,  $e^{-\epsilon(\hat{H}-\mu\hat{N})} = :e^{-\epsilon(\hat{H}-\mu\hat{N})}: + \mathcal{O}(\epsilon^2)$ . Using (9), to evaluate the matrix elements, we can write the partition function in the limit  $\epsilon \rightarrow 0$  in the form

$$\begin{aligned}Z &= \int \prod_{k=1}^M \prod_{\alpha} d\phi_{\alpha,k}^* d\phi_{\alpha,k} e^{-\sum_{k=1}^M \sum_{\alpha} \phi_{\alpha,k}^* \phi_{\alpha,k}} \prod_{k=1}^M \langle-\phi_{\alpha,k}| :e^{-\epsilon(\hat{H}-\mu\hat{N})}: + \mathcal{O}(\epsilon^2) |\phi_{\alpha,k-1}\rangle \\ &= \int \prod_{k=1}^M \prod_{\alpha} d\phi_{\alpha,k}^* d\phi_{\alpha,k} e^{-\sum_{k=1}^M \sum_{\alpha} (\phi_{\alpha,k}^* \phi_{\alpha,k} - \phi_{\alpha,k}^* \phi_{\alpha,k-1}) - \epsilon \sum_{k=1}^M \sum_{\alpha} (H[\phi_{\alpha,k}^*, \phi_{\alpha,k-1}] - \mu \phi_{\alpha,k}^* \phi_{\alpha,k-1})} \\ &= \int \prod_{k=1}^M \prod_{\alpha} d\phi_{\alpha,k}^* d\phi_{\alpha,k} e^{-S[\phi_{\alpha,k}^*, \phi_{\alpha,k-1}]},\end{aligned}\quad (13)$$

where  $\phi_{\alpha,0} = -\phi_{\alpha,M}$  because of antiperiodic boundary conditions and we have defined the action

$$S[\phi_{\alpha}^*, \phi_{\alpha}] = \epsilon \left( \sum_{k=1}^M \sum_{\alpha} \phi_{\alpha,k}^* \frac{\phi_{\alpha,k} - \phi_{\alpha,k-1}}{\epsilon} - \mu \phi_{\alpha,k}^* \phi_{\alpha,k-1} + H[\phi_{\alpha,k}^*, \phi_{\alpha,k-1}] \right). \quad (14)$$

In the limit  $\epsilon \rightarrow 0$ , it is convenient to introduce the notation

$$\phi_{\alpha,k}^* \frac{\phi_{\alpha,k} - \phi_{\alpha,k-1}}{\epsilon} \equiv \phi_{\alpha}^*(\tau) \frac{\partial}{\partial \tau} \phi_{\alpha}(\tau), \quad H[\phi_{\alpha,k}^*, \phi_{\alpha,k-1}] \equiv H[\phi_{\alpha}^*(\tau), \phi_{\alpha}(\tau)]. \quad (15)$$

Splitting the Hamiltonian into a one-body operator and an interaction,  $H = \sum_{\alpha} \varepsilon_{\alpha} \phi_{\alpha}^* \phi_{\alpha} + V[\phi_{\alpha}^*(\tau), \phi_{\alpha}(\tau)]$ , the path integral can symbolically be written in trajectory notation as

$$Z = \int_{\phi_{\alpha}(\beta) = -\phi_{\alpha}(0)} \mathcal{D}[\phi_{\alpha}^*(\tau), \phi_{\alpha}(\tau)] e^{-\int_0^{\beta} d\tau (\sum_{\alpha} \phi_{\alpha}^*(\tau) (\frac{\partial}{\partial \tau} + \varepsilon_{\alpha} - \mu) \phi_{\alpha}(\tau) + V[\phi_{\alpha}^*(\tau), \phi_{\alpha}(\tau)]} . \quad (16)$$

Formally, the problem has been reduced to quadrature. We have to integrate over all possible realizations of paths  $\phi_{\alpha}(\tau)$ ,  $\phi_{\alpha}^*(\tau)$ , weighted by the exponential of the action  $S[\phi_{\alpha}^*(\tau), \phi_{\alpha}(\tau)]$ . In general, it amounts to computing high-dimensional integrals, so that Monte Carlo methods are particularly suitable for this task [9, 8]. It must be kept in mind that even though the notation suggests it, it neither implies continuity nor differentiability of the paths and all quantities are defined in terms of the discrete expressions (13) and (14).

## 2.2 Perturbation theory

In the following, we will develop a perturbation theory based on the path integral formulation of the partition function and the Green function (2),

$$G_{\alpha_1 \alpha_2}(\tau_1 - \tau_2) = -\frac{1}{Z} \int \mathcal{D}[\phi_{\alpha}^*(\tau), \phi_{\alpha}(\tau)] e^{-S[\phi_{\alpha}^*(\tau), \phi_{\alpha}(\tau)]} \phi_{\alpha_1}(\tau_1) \phi_{\alpha_2}^*(\tau_2). \quad (17)$$

Given that the fermionic path integral always implies antiperiodic trajectories, we omit the indication here and in what follows. Furthermore we need not explicitly indicate the time-ordering, remembering that it is implicit in the construction of the path integral.

We can view Green function as a thermal average over the interacting system, as symbolized by the following notation:  $G_{\alpha_1 \alpha_2}(\tau_1 - \tau_2) = -\langle \phi_{\alpha_1}(\tau_1) \phi_{\alpha_1}^*(\tau_2) \rangle$ . We readily obtain a perturbation expansion of the single-particle Green function in powers of the interaction

$$\begin{aligned} G_{\alpha_1 \alpha_2}(\tau_1 - \tau_2) &= -\frac{Z_0}{Z} \left\langle e^{-\int_0^{\beta} d\tau V[\phi_{\alpha}^*(\tau), \phi_{\alpha}(\tau)]} \phi_{\alpha_1}(\tau_1) \phi_{\alpha_2}^*(\tau_2) \right\rangle_0 \\ &= -\frac{Z_0}{Z} \sum_{n=0}^{\infty} \frac{(-1)^n}{n!} \int_0^{\beta} d\tau'_1 \dots d\tau'_n \langle V[\phi_{\alpha}^*(\tau'_1), \phi_{\alpha}(\tau'_1)] \dots V[\phi_{\alpha}^*(\tau'_n), \phi_{\alpha}(\tau'_n)] \phi_{\alpha_1}(\tau_{\alpha_1}) \phi_{\alpha_2}^*(\tau_{\alpha_2}) \rangle_0. \end{aligned} \quad (18)$$

The partition function of the non-interacting system,  $Z_0$ , is obtained by setting the interacting  $V = 0$  in (16). It remains to evaluate the non-interacting average over a product of Grassmann fields arising in above expression. This is accomplished using Wick's theorem, which allows to express it in terms of a product of non-interacting Green functions. Wicks's theorem is usually formulated in terms of second-quantized operators. In its familiar form it states that the non-interacting expectation value of a time-ordered product of operators can be written as the sum over all complete contractions. A contraction of two time-dependent operators is defined as a symbolic pairing of these operators, which evaluates to their non-interacting expectation value. In a complete contraction of a set of an even number of fields, each operator is paired with exactly one other. Having defined thermal expectation values in terms of Grassmann fields, we can equally well write a contraction in terms of them

$$\underbrace{\phi_{\alpha_1}(\tau_1) \phi_{\alpha_2}^*(\tau_2)} := \langle \phi_{\alpha_1}(\tau_1) \phi_{\alpha_2}^*(\tau_2) \rangle_0 = -G_{\alpha_1 \alpha_2}^0(\tau_1 - \tau_2). \quad (19)$$

In terms of Grassmann numbers, Wick's theorem is based on the following Gaussian integral

$$\frac{\int \mathcal{D}[\phi^*, \phi] \phi_{i_1} \phi_{i_2} \dots \phi_{i_n} \phi_{j_n}^* \dots \phi_{j_2}^* \phi_{j_1}^* e^{-\sum_{ij} \phi_i^* M_{ij} \phi_j}}{\int \mathcal{D}[\phi^*, \phi] e^{-\sum_{ij} \phi_i^* M_{ij} \phi_j}} = \sum_{\sigma \in S_n} \text{sgn}(\sigma) M_{i_{\sigma(n)}, j_n}^{-1} \dots M_{i_{\sigma(1)}, j_1}^{-1}. \quad (20)$$

For simplicity we write  $M_{ij}^{-1}$  for the elements of the inverse of  $M$ . The left-hand side has the form of an expectation value over a product of fields. On the right-hand side we have a sum over the elements of the permutation group  $S_n$ , which is the Leibniz formula for the determinant of the inverse of  $M$ .

Before relating this expression to the familiar statement of Wick's theorem, we prove it by means of the following generating function

$$G(J^*, J) := \frac{\int \mathcal{D}[\phi^*, \phi] e^{-\sum_{ij} \phi_i^* M_{ij} \phi_j + \sum_i \phi_i^* J_i + J_i^* \phi_i}}{\int \mathcal{D}[\phi^*, \phi] e^{-\sum_{ij} \phi_i^* M_{ij} \phi_j}} = e^{J_i^* M_{ij}^{-1} J_j}. \quad (21)$$

The name generating function will become apparent below. Here the sources  $J^*, J$  are Grassmann numbers and  $M$  is a complex matrix with elements  $M_{ij}$ . We evaluate the following derivatives

$$\left. \frac{\delta^{2n} G}{\delta J_{i_1}^* \dots \delta J_{i_n}^* \delta J_{j_n} \dots \delta J_{j_1}} \right|_{J=J^*=0} = (-1)^n \frac{\int \mathcal{D}[\phi^*, \phi] \phi_{i_1} \dots \phi_{i_n} \phi_{j_n}^* \dots \phi_{j_1}^* e^{-\sum_{ij} \phi_i^* M_{ij} \phi_j}}{\int \mathcal{D}[\phi^*, \phi] e^{-\sum_{ij} \phi_i^* M_{ij} \phi_j}}. \quad (22)$$

Here we have used that the derivatives anticommute with Grassmann numbers. Applying the same derivatives to the right-hand side of (21) yields

$$\begin{aligned} & \left. \frac{\delta^{2n}}{\delta J_{i_1}^* \dots \delta J_{i_n}^* \delta J_{j_n} \dots \delta J_{j_1}} \left( e^{\sum_{ij} J_i^* M_{ij} J_j} \right) \right|_{J=J^*=0} \\ &= (-1)^n \frac{\delta^n}{\delta J_{i_1}^* \dots \delta J_{i_n}^*} \left( \sum_{k_n} J_{k_n}^* M_{k_n, j_n}^{-1} \right) \dots \left( \sum_{k_1} J_{k_1}^* M_{k_1, j_1}^{-1} \right) \left( e^{\sum_{ij} J_i^* M_{ij} J_j} \right) \Big|_{J=J^*=0} \\ &= (-1)^n \sum_{\sigma \in S_n} \text{sgn}(\sigma) M_{i_{\sigma(n)}, j_n}^{-1} \dots M_{i_{\sigma(1)}, j_1}^{-1}, \end{aligned} \quad (23)$$

which proves the identity (20). It remains to prove the identity for the generating function, Eq. (21). This is readily accomplished by imposing the linear shift transformation whose Jacobian is unity (summation over repeated indices implied),

$$\phi_i^* \rightarrow \phi_i^* + J_j^* M_{ji}^{-1}, \quad \phi_i \rightarrow \phi_i + M_{ij}^{-1} J_j, \quad (24)$$

upon which the exponential on the left-hand side of (21) transforms to

$$\exp(-\phi_i^* M_{ij} \phi_j + \phi_i^* J_i + J_i^* \phi_i) \rightarrow \exp(-\phi_i^* M_{ij} \phi_j + J_i^* M_{ij}^{-1} J_j). \quad (25)$$

The term containing the sources  $J, J^*$  can be taken out of the integral. The numerator is seen to cancel the denominator, hence proving the identity.

A first application of Wick's theorem is the evaluation of the noninteracting Green function. By inserting the discrete matrix  $M_{ij} = -(\partial_\tau + \varepsilon_\alpha - \mu)_{ij}^{-1}$  defined through (14) into Eq. (20) and replacing  $\phi_j$  by  $\phi_{\alpha,k}$  in the matrix elements of the path integral, we obtain

$$\begin{aligned} G_{\alpha_1\alpha_2}^0(\tau_1 - \tau_2) &= -\frac{\int \mathcal{D}[\phi_\alpha^*(\tau), \phi_\alpha(\tau)] e^{-\int_0^\beta d\tau \sum_\alpha \phi_\alpha^*(\tau)(\frac{\partial}{\partial\tau} + \varepsilon_\alpha - \mu)\phi_\alpha(\tau)} \phi_{\alpha_1}(\tau_1), \phi_{\alpha_2}^*(\tau_2)}{\int \mathcal{D}[\phi_\alpha^*(\tau), \phi_\alpha(\tau)] e^{-\int_0^\beta d\tau \sum_\alpha \phi_\alpha^*(\tau)(\frac{\partial}{\partial\tau} + \varepsilon_\alpha - \mu)\phi_\alpha(\tau)}} \\ &= -(\partial_\tau + \varepsilon_\alpha - \mu)_{\alpha_1\tau_1; \alpha_2\tau_2}^{-1} = G_{\alpha_1}^0(\tau_1 - \tau_2) \delta_{\alpha_1\alpha_2}. \end{aligned} \quad (26)$$

This shows that the non-interacting Green function equals the inverse of the matrix  $-(\frac{\partial}{\partial\tau} + \varepsilon_\alpha - \mu)$  and allows us to recast the action in the following form

$$S[\phi_\alpha^*(\tau), \phi_\alpha(\tau)] = \int_0^\beta d\tau \left( -\sum_\alpha \phi_\alpha^*(\tau) G_\alpha^{0-1}(\tau_{\alpha_1} - \tau_{\alpha_2}) \phi_\alpha(\tau) + V[\phi_\alpha^*(\tau), \phi_\alpha(\tau)] \right). \quad (27)$$

Similarly, with  $M_{ij} = -(\partial_\tau + \varepsilon_\alpha - \mu)_{ij}^{-1}$ , the left-hand side of Eq. (20) equals the non-interacting average of fields. The right-hand side evaluates to a sum over products of non-interacting Green functions, or, by means of Eq. (19), to the sum over all complete contractions. To see this, we note that the sign of the permutation apparently equals the sign of the permutation that brings the fields in each contraction next to each other in the desired order.

With Wick's theorem at hand, we can evaluate the non-interacting expectation values in each term of the perturbation expansion for the Green function. This allows us to obtain successively more accurate approximations. The result is expressed in terms of the coupling and the known non-interacting Green function. As will be shown below, we can depict these elements with symbols and draw a diagram for each of the resulting expressions to obtain a diagrammatic perturbation theory.

The right-hand side of Eq. (20) contains a sum over all permutations of indices, so that the number of terms grows factorially with order. The construction of perturbation expansions in practice would be hopeless without two major simplifications.

The first simplification is based on the observation that different contractions at a given order can lead to structurally identical diagrams, which give the same contribution to the overall result. Instead of enumerating all of them, their multiplicity can be accounted for in terms of combinatorial factors. Another major simplification is given by the linked-cluster theorem: Any diagram generated by the perturbation expansion (18) can be decomposed into two parts: one is a connected part with an incoming and an outgoing line which stems from the contractions involving  $\phi_{\alpha_1}(\tau_1)$  and  $\phi_{\alpha_2}(\tau_2)$ . The second part is a (not necessarily connected) part consisting of diagrams without external lines contributing to the vacuum amplitude. It is straightforward to verify that the perturbation expansion of the partition function,

$$\frac{Z}{Z_0} = \left\langle e^{-\int_0^\beta d\tau V[\phi_\alpha^*(\tau), \phi_\alpha(\tau)]} \right\rangle_0, \quad (28)$$

generates all the disconnected vacuum fluctuation graphs that appear in the expansion of the Green function. The linked-cluster theorem states that the logarithm of the above expectation

value, or  $\ln Z/Z_0$ , yields the sum over all connected graphs. An important consequence is that this contribution exactly cancels the factor  $(Z/Z_0)^{-1}$  in the expansion of Green function, Eq. (18). As a consequence, when evaluating the perturbation expansion of  $G$ , we only have to take into account the fully connected diagrams with external lines.

### 3 Diagrammatic extensions of dynamical mean-field theory

We have seen that diagrammatic perturbation theory is a powerful tool to construct approximations starting from a solvable reference system. The problem we are facing when dealing with strongly correlated systems is that neither the non-interacting, nor the localized limit are appropriate starting points. DMFT, on the other hand, already includes the presumably dominant strong local temporal correlations. It would hence be desirable to include the effects of the presumably weaker spatial correlations beyond DMFT perturbatively.

It turns out that there are different ways to systematically construct a perturbation expansion around DMFT. It is crucial, however, that the DMFT reference system is solvable. Here and in contrast to DMFT solvable means that not only the single-particle Green function, but at least the two-particle and in principle all many-particle Green functions are assumed to be known. Fortunately, reasonable approximations can be constructed from the knowledge of the single- and two-particle Green function only. The need to compute higher-order correlation functions of an impurity model explains why the first works of this kind appeared only around ten years ago. To a large extent these developments were driven by the advent of continuous-time quantum impurity solvers, which allow the efficient and accurate computation of higher-order correlation functions [8].

The first approaches along these lines were the dynamical vertex approximation (D $\Gamma$ A) [10, 11] and the dual fermion approach [12]. A number of different approaches followed [6]. While the construction and the justification of necessary approximation differs for the various approaches, the underlying principle is the same: the propagators and the interaction vertices of the diagrammatic perturbation theory are obtained from the numerical solution of the impurity model. Non-local processes are described in terms of renormalized propagation between sites and a local frequency-dependent interaction between particles. Care has to be taken in the choice of propagators and vertex functions to avoid double counting of contributions that are already contained in DMFT.

The advantage of such methods is that the diagrammatic expressions are relatively inexpensive to evaluate numerically, so that it becomes possible to treat truly long-ranged correlations. The results, however, will be approximate on any scale. On the other hand, the diagrammatic approach provides intuition about the underlying microscopic origin of the observed effects. We will discuss some examples in the result section below.



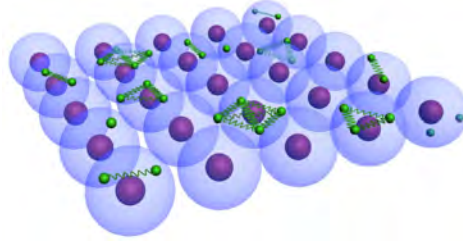


**Fig. 2:** Illustration of the dual fermion approach. Spatial correlations neglected in the DMFT description of Fig. 1 are mediated through dual fermions (green). The dual fermions interact locally via  $n$ -particle interactions.

### 3.1 Dual fermions

In the following we show how to construct a diagrammatic perturbation theory around DMFT, based on the idea of dual fermions. We then study the perturbation expansion in detail and formulate the rules of the diagrammatic perturbation theory.

As in conventional perturbation theory, we separate the problem into a solvable reference system and a perturbation. The underlying idea is to treat the strong local correlations on the level of the single-site impurity model and to embrace the presumably weaker coupling between the sites perturbatively. A diagrammatic extension of DMFT is obtained by setting the hybridization function equal to its DMFT value.

In the Grassmann path integral formalism, the Hubbard model is described by the action

$$S[c^*, c] = - \sum_{\nu\sigma} c_{\nu\sigma}^* (i\nu + \mu - \varepsilon_{\mathbf{k}}) c_{\nu\sigma} + U \sum_{\omega} n_{\omega\uparrow} n_{-\omega\downarrow},$$

We can formally add and subtract an arbitrary hybridization function at each lattice site. The lattice action can then be expressed in terms of the impurity action as follows

$$S_{\text{latt}}[c^*, c] = \sum_i S_{\text{imp}}[c_i^*, c_i] - \sum_{\mathbf{k}\nu\sigma} c_{\mathbf{k}\nu\sigma}^* (\Delta_{\nu} - \varepsilon_{\mathbf{k}}) c_{\mathbf{k}\nu\sigma}. \quad (29)$$

In this form, the lattice problem can be viewed as a collection of impurity models at each lattice site, each with their own electronic bath. The sites are spatially coupled by a hybridization- and dispersion-dependent term. In principle it is possible to develop a perturbation theory around the impurity model (and around DMFT for a correspondingly chosen hybridization function) directly from this starting point: We could change the basis to transform the second term to a sum over sites instead of momenta and expand the path integral  $Z = \int \mathcal{D}[c^*, c] \exp(-S_{\text{latt}})$  in that second term. The integration over the fields  $c^*, c$  could formally be performed and would give rise to averages of the form  $\langle c_{i_1}^* c_{j_1} \dots c_{i_n}^* c_{j_n} \rangle_{\text{imp}}$ . There is clearly no Wick theorem in this case, but we could nevertheless compute at least some of these impurity correlation functions numerically and evaluate the perturbation series. It turns out that the dual fermion approximation is a clever resummation of diagrams appearing in this approach [13].

To derive it, we first take a somewhat different route. Here we decouple the impurity models by introducing new fermionic fields  $f, f^*$ , the dual fermions. This is achieved by means of

a Hubbard-Stratonovich transformation. Formally this transformation is a Gaussian integral which we can obtain by generalizing (21) using the substitutions

$$\phi_i^* \rightarrow f_i^*, \quad \phi_j \rightarrow f_j, \quad J_i^* \rightarrow c_j^* b_{ji}, \quad J_j \rightarrow b_{ij} c_j, \quad (30)$$

which yields

$$\frac{\int \mathcal{D}[f^*, f] e^{-\sum_{ij} f_i^* M_{ij} f_j + \sum_{ij} f_i^* b_{ij} c_j + c_i^* b_{ij} f_j}}{\int \mathcal{D}[f^*, f] e^{-\sum_{ij} f_i^* M_{ij} f_j}} = e^{\sum_{ijkl} c_i^* b_{ij} M_{jk}^{-1} b_{kl} c_l}. \quad (31)$$

Letting  $M_{ij}^{-1} = \Delta_{ij} - \varepsilon_{ij}$  and setting the coupling between the physical and dual fermions to the local quantity  $b_{ij} = -g_{ij}^{-1}$ , we obtain the partition function in the form

$$Z = D_f \int \mathcal{D}[f^*, f] e^{-\sum_{\mathbf{k}\nu\sigma} f_{\mathbf{k}\nu\sigma}^* g_{\nu\sigma}^{-1} (\Delta_{\nu\sigma} - \varepsilon_{\mathbf{k}})^{-1} g_{\nu\sigma}^{-1} f_{\mathbf{k}\nu\sigma}} \int \mathcal{D}[c^*, c] e^{-\sum_i (S_{\text{imp}}[c_i^*, c_i] + S_{\text{cf}}[c_i^*, c_i; f_i^*, f_i])}. \quad (32)$$

Here  $D_f$  is a determinant which arises from the numerator in Eq. (31) and which will be irrelevant for the calculation of expectation values. The term  $S_{\text{cf}}$  is the local coupling between dual and physical fermions

$$S_{\text{cf}}[c^*, c; f^*, f] = \sum_{\nu\sigma} \left( f_{\nu\sigma}^* g_{\nu\sigma}^{-1} c_{\nu\sigma} + c_{\nu\sigma}^* g_{\nu\sigma}^{-1} f_{\nu\sigma} \right).$$

The goal is to arrive at a representation which depends solely on dual variables. We can formally perform the second integral by expanding the exponential in powers of  $S_{\text{cf}}$ . We can do this for each site  $i$  separately. For a translationally invariant system, the result will be site-independent

$$\int \mathcal{D}[c_i^*, c_i] e^{-S_{\text{imp}}[c_i^*, c_i]} e^{-S_{\text{cf}}[c_i^*, c_i; f_i^*, f_i]} = \sum_{\substack{n=0 \\ n \text{ even}}}^{\infty} \frac{(-1)^n}{n!} \left\langle \left( \sum_{\nu\sigma} (f_{\nu\sigma}^* g_{\nu\sigma}^{-1} c_{\nu\sigma} + c_{\nu\sigma}^* g_{\nu\sigma}^{-1} f_{\nu\sigma}) \right)^n \right\rangle_{\text{imp}}.$$

Only even orders contribute since the Gaussian integral over an odd number of  $c$  and  $c^*$  must vanish due to particle conservation. Let us exemplify this step for the first non-vanishing term. We have

$$\begin{aligned} & \frac{1}{2} \sum_{\nu\sigma} \sum_{\nu'\sigma'} \langle f_{\nu\sigma}^* g_{\nu\sigma}^{-1} c_{\nu\sigma} c_{\nu'\sigma'}^* g_{\nu'\sigma'}^{-1} f_{\nu'\sigma'} + c_{\nu\sigma}^* g_{\nu\sigma}^{-1} f_{\nu\sigma} f_{\nu'\sigma'}^* g_{\nu'\sigma'}^{-1} c_{\nu'\sigma'} \rangle_{\text{imp}} \\ &= \sum_{\nu\sigma} \sum_{\nu'\sigma'} g_{\nu\sigma}^{-1} g_{\nu'\sigma'}^{-1} \langle c_{\nu\sigma} c_{\nu'\sigma'}^* \rangle_{\text{imp}} f_{\nu\sigma}^* f_{\nu'\sigma'} = - \sum_{\nu\sigma} f_{\nu\sigma}^* g_{\nu\sigma}^{-1} f_{\nu\sigma}, \end{aligned} \quad (33)$$

where in the first line we have used the anticommutation relations to bring the two terms into the same form. In the second line we have used the definition of the Green function for the impurity,  $\langle c_{\nu\sigma} c_{\nu'\sigma'}^* \rangle_{\text{imp}} = -g_{\nu\sigma} \delta_{\nu\nu'} \delta_{\sigma\sigma'}$ , which is diagonal in spin and frequency.

We can apply the same procedure to the higher order terms. For example, the fourth-order term involves averages of the form

$$g_{\nu\nu'\omega}^{\sigma\sigma'\sigma'} := \langle c_{\nu\sigma} c_{\nu+\omega,\sigma}^* c_{\nu'+\omega,\sigma'}^* c_{\nu'\sigma'} \rangle_{\text{imp}}. \quad (34)$$

The result of this expansion can be cast into the following form

$$\ln \langle e^{-S_{\text{ct}}[c_i^*, c_i; f_i^*, f_i]} \rangle_{\text{imp}} = - \sum_{\nu\sigma} f_{\nu\sigma}^* g_{\nu\sigma}^{-1} f_{\nu\sigma} - \tilde{V}[f^*, f]. \quad (35)$$

As one might expect from the linked-cluster theorem, the left hand side generates the *connected* correlation functions of the impurity model coupled to dual variables. To leading order, the resulting dual interaction is given by

$$\tilde{V}[f^*, f] = -\frac{1}{4} \sum_{\nu\nu'\omega\sigma_i} \gamma_{\nu\nu'\omega}^{\sigma_1\sigma_2\sigma_3\sigma_4} f_{\nu\sigma_1}^* f_{\nu+\omega,\sigma_2} f_{\nu'+\omega,\sigma_3}^* f_{\nu'\sigma_4} + \dots, \quad (36)$$

where  $\gamma$  is the reducible two-particle vertex of the impurity model

$$\gamma_{\nu\nu'\omega}^{\sigma\sigma'\sigma'} := \frac{g_{\nu\nu'\omega}^{\sigma\sigma'\sigma'} - \beta g_{\nu\sigma} g_{\nu'\sigma'} \delta_\omega + \beta g_{\nu\sigma} g_{\nu+\omega\sigma} \delta_{\nu\nu'} \delta_{\sigma\sigma'}}{g_{\nu\sigma} g_{\nu+\omega,\sigma} g_{\nu'+\omega\sigma'} g_{\nu'\sigma'}}. \quad (37)$$

The higher-order terms contain the three-particle (six-leg) and higher-order vertices describing the interaction between a successively larger number of particles. In terms of the original Hubbard interaction, the vertices correspond to the sum of many high-order processes.

Combining Eqs. (32) and (35), we see that the action in dual variables is given by

$$\tilde{S}[f^*, f] = - \sum_{\mathbf{k}\nu\sigma} f_{\mathbf{k}\nu\sigma}^* \tilde{G}_{\mathbf{k}\nu\sigma}^{0-1} f_{\mathbf{k}\nu\sigma} + \tilde{V}[f^*, f] \quad (38)$$

and the dual Green function is identified from the bilinear terms in the same two equations as

$$\tilde{G}_{\mathbf{k}\nu\sigma}^0 = (g_{\nu\sigma}^{-1} + (\Delta_{\nu\sigma} - \varepsilon_{\mathbf{k}}))^{-1} - g_{\nu\sigma}. \quad (39)$$

We have reformulated the problem in terms of a Green function and an interaction which can be computed given the solution of the impurity model. The interaction, however, is rather complicated and frequency-dependent. So what have we gained? To see this, we first establish a connection to DMFT by noting that by means of (3), the bare dual Green function can be written in the form  $G_{\mathbf{k}\nu\sigma}^{\text{DMFT}} - g_{\nu\sigma}$ . While the hybridization function is arbitrary by construction, see Eq. (29), we can fix it through the self-consistency condition  $\sum_{\mathbf{k}} \tilde{G}_{\mathbf{k}\nu\sigma}^0 = 0$ . It apparently corresponds to the DMFT self-consistency condition discussed in Sec. 1.2.

At this point we have used the bare dual Green function and have not taken the dual interaction into account. DMFT corresponds to the case of non-interacting dual fermions. This is not surprising, since in the DMFT description sites are decoupled. It means that even the lowest-order corrections based on the action (38) will already introduce corrections beyond DMFT.

Once diagrams are taken into account, the hybridization function can be fixed using a similar condition on the interacting dual Green function,  $\sum_{\mathbf{k}} \tilde{G}_{\mathbf{k}\nu\sigma} = 0$ . This corresponds to the summation of an infinite partial series: all diagrams with a local propagator are eliminated from the expansion. This property is unique to the dual fermion approach and highlights the fact that the dual Green function is not a physical, but rather an auxiliary quantity. Since we have used an exact transformation to introduce the associated field, we can nevertheless establish exact relations between dual and physical quantities. In particular, the physical self-energy is given in terms of the dual self-energy  $\tilde{\Sigma}$  by

$$\Sigma_{\mathbf{k}\nu\sigma} = \Sigma_{\nu\sigma}^{\text{imp}} + \frac{\tilde{\Sigma}_{\mathbf{k}\nu\sigma}}{1 + \tilde{\Sigma}_{\mathbf{k}\nu\sigma} g_{\nu\sigma}}. \quad (40)$$

### 3.2 Perturbation theory for the dual propagator

We are now in the position to construct the diagrammatic perturbation theory for the dual propagator and the dual self-energy. To this end, we explicitly expand the path integral in powers of the dual interaction and apply Wick's theorem to evaluate the resulting expressions. We will show a couple of example diagrams to illustrate the procedure. We then describe the particularities of the dual perturbation theory, namely the determination of combinatorial prefactors of the diagrams and how to determine the sign of resulting expressions. Finally we arrive at the general Feynman rules for evaluating the expression of any diagram appearing in the diagrammatic perturbation theory.

To have a more condensed notation, we gather frequency-, spin and other possible indices into a single Greek index. To emphasize that the diagrams describe non-local corrections, we write the positions explicitly and use Latin indices for them. To further clearly mark external lines of a diagram, we use the combined index  $1 \equiv \{i_1, \alpha_1\}$ . Even though the three-particle vertex  $\gamma^{(6)}$  is often neglected in actual calculations, we consider it here to illustrate how the theory generalizes to higher-order vertices.

We start from the definition of the dual propagator

$$\tilde{G}_{12} := -\langle f_1 f_2^* \rangle = -\frac{1}{\tilde{Z}} \int \mathcal{D}[f^*, f] f_1 f_2^* e^{-\tilde{S}[f^*, f]}, \quad (41)$$

where the dual action is given by

$$\tilde{S}[f^*, f] = -\sum_{k, \alpha\beta} f_\alpha^* \tilde{G}_{\alpha\beta}^{0-1} f_\beta + \sum_i V_i[f_i^*, f_i]. \quad (42)$$

Formally these equations have the same form as those discussed in the introduction of the diagrammatic perturbation theory. This means in particular that we can make use of Wick's theorem and the linked cluster theorem. We can therefore concentrate on connected diagrams. Before considering the diagrams, let us first derive some explicit expressions. The perturbation series is generated by expanding the exponential appearing under the path integral in the interaction

$$e^{-\sum_i V_i[f_i^*, f_i]} = 1 - \sum_i V_i[f_i^*, f_i] + \frac{1}{2!} \sum_{i,j} V_i[f_i^*, f_i] V_j[f_j^*, f_j] - \frac{1}{3!} \sum_{i,j,k} V_i[f_i^*, f_i] V_j[f_j^*, f_j] V_k[f_k^*, f_k] + \dots \quad (43)$$

The zero-order term yields the bare dual Green function

$$\tilde{G}_{12}^0 = -\frac{1}{\tilde{Z}} \int \mathcal{D}[f^*, f] f_1 f_2^* e^{-\tilde{S}_0[f^*, f]}, \quad (44)$$

with  $\tilde{S}_0[f^*, f] = -\sum_{\alpha\beta} f_\alpha^* \tilde{G}_{\alpha\beta}^{0-1} f_\beta$ . The next order gives two local contributions for the Green function  $\tilde{G}_{12}$ , one from each of the vertices

$$\left(-\frac{1}{4}\right) \sum_i \gamma_{i\alpha\beta\gamma\delta}^{(4)} \int \mathcal{D}[f^*, f] f_1 f_2^* f_{i\alpha}^* f_{i\beta} f_{i\gamma}^* f_{i\delta} e^{-\tilde{S}_0[f^*, f]}, \quad (45)$$

$$\left(\frac{1}{36}\right) \sum_i \gamma_{i\alpha\beta\gamma\delta\epsilon\zeta}^{(6)} \int \mathcal{D}[f^*, f] f_1 f_2^* f_{i\alpha}^* f_{i\beta} f_{i\gamma}^* f_{i\delta} f_{i\epsilon}^* f_{i\zeta} e^{-\tilde{S}_0[f^*, f]}. \quad (46)$$

The second-order terms (only those involving  $\gamma^{(4)}$  and  $\gamma^{(6)}$ ) are

$$-\frac{1}{2!} \left(-\frac{1}{4}\right)^2 \sum_{i,j} \gamma_{i\alpha\beta\gamma\delta}^{(4)} \gamma_{j\kappa\lambda\mu\nu}^{(4)} \int \mathcal{D}[f^*, f] f_1 f_2^* f_{i\alpha}^* f_{i\beta}^* f_{i\gamma}^* f_{i\delta}^* f_{j\kappa}^* f_{j\lambda}^* f_{j\mu}^* f_{j\nu}^* e^{-\tilde{S}_0[f^*, f]} \quad (47)$$

$$-\frac{1}{2!} \left(-\frac{1}{4} \frac{1}{36}\right) \sum_{i,j} \gamma_{i\alpha\beta\gamma\delta}^{(4)} \gamma_{j\kappa\lambda\mu\nu\epsilon\zeta}^{(6)} \int \mathcal{D}[f^*, f] f_1 f_2^* f_{i\alpha}^* f_{i\beta}^* f_{i\gamma}^* f_{i\delta}^* f_{j\kappa}^* f_{j\lambda}^* f_{j\mu}^* f_{j\nu}^* f_{j\epsilon}^* f_{j\zeta}^* e^{-\tilde{S}_0[f^*, f]} \quad (48)$$

$$-\frac{1}{2!} \left(-\frac{1}{4} \frac{1}{36}\right) \sum_{i,j} \gamma_{i\kappa\lambda\mu\nu\epsilon\zeta}^{(6)} \gamma_{j\alpha\beta\gamma\delta}^{(4)} \int \mathcal{D}[f^*, f] f_1 f_2^* f_{i\kappa}^* f_{i\lambda}^* f_{i\mu}^* f_{i\nu}^* f_{i\epsilon}^* f_{i\zeta}^* f_{j\alpha}^* f_{j\beta}^* f_{j\gamma}^* f_{j\delta}^* e^{-\tilde{S}_0[f^*, f]} \quad (49)$$

$$-\frac{1}{2!} \left(\frac{1}{36}\right)^2 \sum_{i,j} \gamma_{i\alpha\beta\gamma\delta\epsilon\zeta}^{(6)} \gamma_{j\kappa\lambda\mu\nu\rho\eta}^{(6)} \int \mathcal{D}[f^*, f] f_1 f_2^* f_{i\alpha}^* f_{i\beta}^* f_{i\gamma}^* f_{i\delta}^* f_{i\epsilon}^* f_{i\zeta}^* f_{j\kappa}^* f_{j\lambda}^* f_{j\mu}^* f_{j\nu}^* f_{j\rho}^* f_{j\eta}^* e^{-\tilde{S}_0[f^*, f]} \quad (50)$$

Likewise, the third-order term involving only the two-particle vertex  $\gamma^{(4)}$  is the following:

$$+\frac{1}{3!} \left(-\frac{1}{4}\right)^3 \sum_{i,j,k} \gamma_{i\alpha\beta\gamma\delta}^{(4)} \gamma_{j\kappa\lambda\mu\nu}^{(4)} \gamma_{k\epsilon\zeta\rho\eta}^{(4)} \int \mathcal{D}[f^*, f] f_1 f_2^* f_{i\alpha}^* f_{i\beta}^* f_{i\gamma}^* f_{i\delta}^* f_{j\kappa}^* f_{j\lambda}^* f_{j\mu}^* f_{j\nu}^* f_{k\epsilon}^* f_{k\zeta}^* f_{k\rho}^* f_{k\eta}^* e^{-\tilde{S}_0[f^*, f]} \quad (51)$$

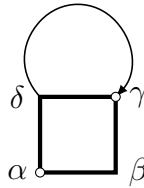
The terms quickly grow very complicated and it is hard to see the structure in these expressions. In the following we show how we can represent the relevant contributions in terms of diagrams.

### 3.3 Self-energy diagrams

In general we can use the Dyson equation to sum infinite partial series of diagrams. We therefore concentrate on one-particle irreducible self-energy diagrams in the following. We obtain these simply from diagrams for the Green function by omitting the contractions corresponding to the external lines (those connecting  $f_1$  and  $f_2^*$ ). With the exception of diagram a), which we include for illustration, we omit any diagram with a local closed loop on at least one of its vertices. Their contribution vanishes because the local part of the dual Green function is taken to be zero via the self-consistency condition. A contraction in the following is defined as  $f_{i\alpha} f_{j\beta}^* = -\tilde{G}_{ij\alpha\beta}$ .

We simply write  $\tilde{G}$  instead of  $\tilde{G}^0$  because the expressions are also valid when written in terms of the interacting Green functions.

• Diagram (a)



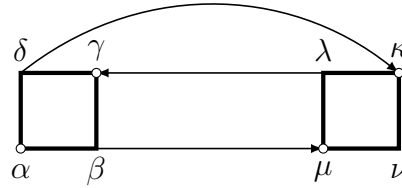
This diagram is derived from (45). The corresponding pairing or contraction is

$$+f_1 f_2^* f_{i\alpha}^* f_{i\beta}^* f_{i\gamma}^* f_{i\delta}^* = -f_1 f_{i\alpha}^* f_{i\delta}^* f_{i\gamma}^* f_{i\beta}^* f_2^* = (-1)^4 \tilde{G}_{1i\alpha} \tilde{G}_{i\beta 2} \tilde{G}_{ii\delta\gamma} . \quad (52)$$

The combinatorial prefactor of a diagram is the prefactor of the contribution times the number of pairings that lead to the same (topologically equivalent) diagram. Apparently we obtain

the same diagram if we exchange the 'incoming' points of the vertex (marked by open circles in the figure) or the outgoing ones. This yields 4 pairings which result in the same diagram, which cancels the prefactor  $1/4$  of the vertex. The corresponding correction to the self-energy is thus  $\Sigma_{ii\alpha\beta}^{(a)} = -\gamma_{i\alpha\beta\gamma\delta}^{(4)} \tilde{G}_{ii\delta\gamma}$ .

• Diagram (b)



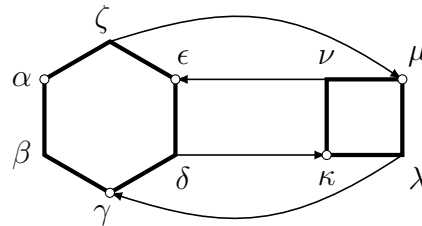
This diagram yields the first non-local correction. The relevant term in the perturbation expansion is (47). The particular pairing corresponding to this diagram is:

$$\begin{aligned} +f_1 f_2^* f_{i\alpha}^* f_{i\beta} f_{i\gamma}^* f_{i\delta} f_{j\kappa}^* f_{j\lambda} f_{j\mu}^* f_{j\nu} &= -f_1 f_{i\alpha}^* f_{i\beta} f_{j\mu}^* f_{j\lambda} f_{i\gamma}^* f_{i\delta} f_{j\kappa}^* f_{j\nu} f_2^* \\ &= (-1)^6 \tilde{G}_{1i\alpha} \tilde{G}_{ij\beta\mu} \tilde{G}_{ji\lambda\gamma} \tilde{G}_{ij\delta\kappa} \tilde{G}_{i\nu 2}. \end{aligned} \quad (53)$$

There are 16 different pairings that correspond to the same diagram. We can count them as follows: Draw two squares corresponding to the two vertices. There are four possibilities to connect an incoming line (two on each vertex). After attaching the incoming line to say,  $\alpha$ , there are two possibilities to attach the outgoing line, since it must be connected to the other vertex to yield the desired diagram. Connect this line to  $\nu$ . Now there are two more possibilities to draw a directed line connecting the two vertices: A line going from the left to the right vertex can only be connected to one point on the left vertex, but to two on the right one. After this line is connected, say from  $\gamma$  to  $\lambda$ , there is only one possibility to connect the remaining two lines. The number of equivalent pairings is thus  $4 \cdot 2 \cdot 2 = 16$ . The correction to the self-energy is hence given by

$$\Sigma_{ij\alpha\nu}^{(b)} = -\frac{1}{2} \gamma_{i\alpha\beta\gamma\delta}^{(4)} \gamma_{j\kappa\lambda\mu\nu}^{(4)} \tilde{G}_{ij\beta\mu} \tilde{G}_{ji\lambda\gamma} \tilde{G}_{ij\delta\kappa}. \quad (54)$$

• Diagram (c)



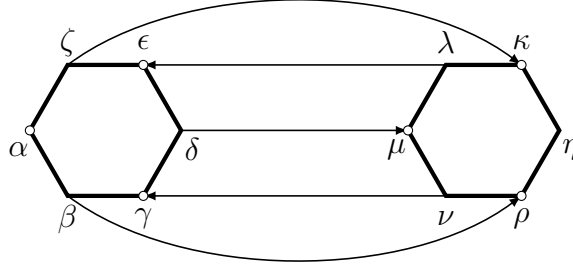
This diagram appears in the two terms (48) and (49), which differ in the order of vertices. The corresponding pairing is

$$\begin{aligned} f_1 f_2^* f_{i\alpha}^* f_{i\beta} f_{i\gamma}^* f_{i\delta} f_{i\epsilon}^* f_{i\zeta} f_{j\kappa}^* f_{j\lambda} f_{j\mu}^* f_{j\nu} &= +f_1 f_{i\alpha}^* f_{j\lambda} f_{i\gamma}^* f_{i\delta} f_{j\kappa}^* f_{j\nu} f_{i\epsilon}^* f_{i\zeta} f_{j\mu}^* f_{i\beta} f_2^* \\ &= (-1)^6 \tilde{G}_{1i\alpha} \tilde{G}_{ji\lambda\gamma} \tilde{G}_{ij\delta\kappa} \tilde{G}_{jiv\epsilon} \tilde{G}_{ij\zeta\mu} \tilde{G}_{i\beta 2}. \end{aligned} \quad (55)$$

Counting the number of equivalent pairings as before yields 36. The self-energy correction therefore reads

$$\Sigma_{ii\alpha\beta}^{(c)} = \left(\frac{1}{4}\right) \sum_j \gamma_{i\alpha\beta\gamma\delta\epsilon\zeta}^{(6)} \gamma_{j\kappa\lambda\mu\nu}^{(4)} \tilde{G}_{ji\lambda\gamma} \tilde{G}_{ij\delta\kappa} \tilde{G}_{jiv\epsilon} \tilde{G}_{ij\zeta\mu}. \quad (56)$$

• Diagram (d)



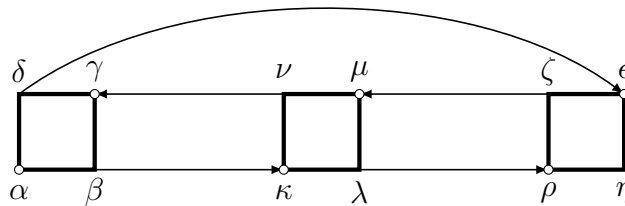
This diagram stems from (50). It corresponds to the pairing

$$\begin{aligned} f_1 f_{i\alpha}^* f_{i\beta} f_{i\gamma}^* f_{i\delta} f_{i\epsilon}^* f_{i\zeta} f_{j\kappa}^* f_{j\lambda} f_{j\mu}^* f_{j\nu} f_{j\rho}^* f_{j\eta} f_2 &= f_1 f_{i\alpha}^* f_{i\beta} f_{j\rho}^* f_{j\nu} f_{i\gamma}^* f_{i\delta} f_{j\mu}^* f_{j\lambda} f_{i\epsilon}^* f_{i\zeta} f_{j\kappa}^* f_{j\eta} f_2 \\ &= (-1)^7 \tilde{G}_{1i\alpha} \tilde{G}_{ij\beta\rho} \tilde{G}_{jiv\gamma} \tilde{G}_{ij\delta\mu} \tilde{G}_{ji\lambda\epsilon} \tilde{G}_{ij\zeta\kappa} \tilde{G}_{j\eta 2}. \end{aligned} \quad (57)$$

Here the number of equivalent pairings already becomes quite large: 216. The prefactor is hence given by  $(1/2)(1/36)^2 \times 216 = 1/12$ . The self-energy correction reads

$$\Sigma_{ij\alpha\eta}^{(d)} = \left(\frac{1}{12}\right) \gamma_{i\alpha\beta\gamma\delta\epsilon\zeta}^{(6)} \gamma_{j\kappa\lambda\mu\nu\rho\eta}^{(6)} \tilde{G}_{ij\beta\rho} \tilde{G}_{jiv\gamma} \tilde{G}_{ij\delta\mu} \tilde{G}_{ji\lambda\epsilon} \tilde{G}_{ij\zeta\kappa}. \quad (58)$$

• Diagram (e)



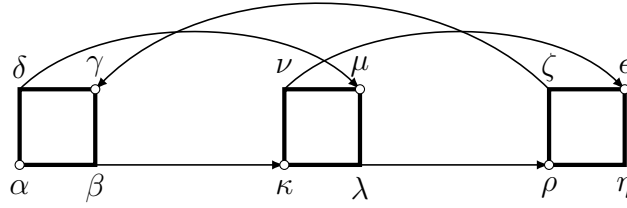
The diagram stems from (51). The corresponding pairing is

$$\begin{aligned} f_1 f_{i\alpha}^* f_{i\beta} f_{i\gamma}^* f_{i\delta} f_{j\kappa}^* f_{j\lambda} f_{j\mu}^* f_{j\nu} f_{k\epsilon}^* f_{k\zeta} f_{k\rho}^* f_{k\eta} f_2 &= -f_1 f_{i\alpha}^* f_{i\beta} f_{j\kappa}^* f_{j\nu} f_{i\gamma}^* f_{i\delta} f_{k\epsilon}^* f_{j\lambda} f_{k\rho}^* f_{k\zeta} f_{j\mu}^* f_{k\eta} f_2 \\ &= (-1)^8 \tilde{G}_{1i\alpha} \tilde{G}_{ij\beta\kappa} \tilde{G}_{jiv\gamma} \tilde{G}_{ik\delta\epsilon} \tilde{G}_{jk\lambda\rho} \tilde{G}_{kj\zeta\mu} \tilde{G}_{\eta 2} \end{aligned} \quad (59)$$

and the number of equivalent pairings is: 384. This gives the self-energy correction

$$\Sigma_{ik\alpha\eta}^{(e)} = (-1) \sum_j \gamma_{i\alpha\beta\gamma\delta}^{(4)} \gamma_{j\kappa\lambda\mu\nu}^{(4)} \gamma_{k\epsilon\zeta\rho\eta}^{(4)} \tilde{G}_{ij\beta\kappa} \tilde{G}_{jiv\gamma} \tilde{G}_{ik\delta\epsilon} \tilde{G}_{jk\lambda\rho} \tilde{G}_{kj\zeta\mu}. \quad (60)$$

• Diagram (f)



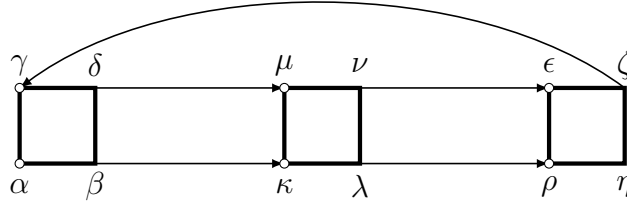
The diagram stems from the same term as diagram (e). The following pairing:

$$\begin{aligned}
 f_1 f_{i\alpha}^* f_{i\beta} f_{i\gamma}^* f_{i\delta} f_{j\kappa}^* f_{j\lambda} f_{j\mu}^* f_{j\nu} f_{k\epsilon}^* f_{k\zeta} f_{k\rho}^* f_{k\eta} f_2^* &= -f_1 f_{i\alpha}^* f_{i\beta} f_{j\kappa}^* f_{k\zeta} f_{i\gamma}^* f_{i\delta} f_{j\mu}^* f_{j\lambda} f_{k\rho}^* f_{j\nu}^* f_{k\epsilon} f_{k\eta} f_2^* \\
 &= (-1)^8 \tilde{G}_{1i\alpha} \tilde{G}_{ij\beta\kappa} \tilde{G}_{ki\zeta\gamma} \tilde{G}_{ij\delta\mu} \tilde{G}_{jk\lambda\rho} \tilde{G}_{jk\nu\epsilon} \tilde{G}_{k\eta 2},
 \end{aligned} \tag{61}$$

however, leads to a topologically inequivalent diagram, as seen in the figure. The number of equivalent pairings is also different from diagram (e) and equal to 96. The resulting self-energy correction reads

$$\Sigma_{ik\alpha\eta}^{(f)} = \left(-\frac{1}{4}\right) \sum_j \gamma_{i\alpha\beta\gamma\delta}^{(4)} \gamma_{j\kappa\lambda\mu\nu}^{(4)} \gamma_{k\epsilon\zeta\rho\eta}^{(4)} \tilde{G}_{ij\beta\kappa} \tilde{G}_{ki\zeta\gamma} \tilde{G}_{ij\delta\mu} \tilde{G}_{jk\lambda\rho} \tilde{G}_{jk\nu\epsilon}. \tag{62}$$

We can deform this diagram as shown below by drawing the vertex in a different way. We see that we have two parallel arrows connecting neighboring vertices. This diagram therefore describes renormalization of the self-energy by scattering of particle-particle pairs. Diagram (e) by contrast describes renormalization through particle-hole scattering.



### 3.3.1 Determination of combinatorial prefactors

As we have seen, the determination of the combinatorial prefactors by counting the number of equivalent pairings becomes cumbersome already for diagrams at moderate orders of the perturbation theory. It is therefore desirable to have general rules to obtain these prefactors simply by looking at the structure of a diagram. Fortunately we can derive such rules by the following analysis:

First consider diagrams which contain no equivalent lines. Equivalent lines are equally directed lines connecting to the same or same two vertices. This is the case for diagrams (a) and (e). The prefactor of such a diagram is unity at any order of the perturbation theory. In order to see this, recall that the prefactor of each vertex is  $1/[(n/2)!]^2$ , where  $n$  is the number of edges. This applies to higher-order vertices as well. It is exactly the number of possibilities to permute equivalent endpoints of each vertex among themselves. For example, the three-particle vertex

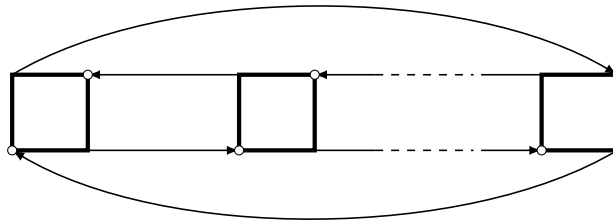


has 3 incoming endpoints, and there are  $3!$  permutations of them. We have the same number for the outgoing ones, which yields  $(3!)^2$  permutations.

An additional factor  $1/m!$  arises from the expansion of the exponential, where  $m$  is the perturbation order. Attaching a label to each vertex of one sort (e.g. two-particle vertices) to make them distinguishable, one sees that all  $m!$  permutations appear in a complete contraction. If vertices of different sorts are present in a diagram, the factor corresponding to the permutation of these vertices among themselves explicitly appears in the expansion, for example the  $2!$  terms (48) and (49) contributing to diagram (c). Hence a diagram corresponds to the sum of  $1/[(n/2)!]^2 m!$  contributions with the same value, so that the prefactor exactly cancels.

This only holds if all ways of attaching the lines or permuting the vertices yield a different, *distinguishable* diagram. If for example two vertices are connected by  $k$  equivalent lines, this reduces the number of distinguishable diagrams (pairings) by the number of permutations of these lines, since a permutation yields the identical, distinguishable diagram. Hence the prefactor is cancelled only up to a factor  $1/k!$  for each set of  $k$  equivalent lines connecting the same two vertices. For example, there are two equivalent lines going from left to right and three parallel lines from right to left in diagram (d). Hence the prefactor is  $1/2! \cdot 1/3! = 1/12$ . Diagram (f) has two sets of two equivalent lines, while diagram (e) does not. This yields a prefactor of  $(1/2!)^2 = 1/4$  for diagram (f) instead of unity for diagram (e).

For vacuum fluctuation diagrams, that is, those with no external lines and no unpaired endpoints, additional symmetry factors arise. An example is the generic  $n$ -th order ring diagram shown below. In this diagram,  $2n$  cyclic permutations of the sequences  $(1, 2, \dots, n)$  and  $(n, \dots, 2, 1)$  correspond to the same distinguishable diagram. Hence the symmetry factor of this diagram is  $1/(2n)$ . The symmetry factor is obviously unity for self-energy diagrams. The diagrammatic rules for the dual propagator are similar to those for Hugenholtz diagrams [14].



### 3.3.2 Determination of the sign

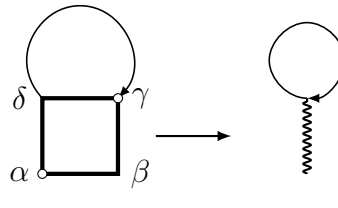
Finally we need rules to determine the sign of a given diagram. For the case where the dual potential is truncated after the two-particle interaction term, they can be obtained as follows:

A priori, i.e., regardless of the particular pairing, the contribution to a diagram for Green function or the self-energy has positive sign. A sign of  $(-1)^n$ , where  $n$  is the order or the number of vertices, arises from the expansion of the exponential. This sign cancels at any order due to the negative prefactor of  $-1/4$  of each vertex. In each contribution, the Grassmann numbers appear as  $-f f^* f^* f \dots f^* f$ , where the sign is due to the definition of Green function,  $\tilde{G} = -\langle f f^* \rangle$ . Reversing the order of pairs to form a complete contraction and recalling that a contraction of two Grassmann numbers is defined as  $\underbrace{f f^*}_{\text{contraction}} = -\tilde{G}$ , one sees that a diagram has positive sign. An

overall sign of  $(-1)^{n_L}$  of a diagram arises due to  $n_L$  closed fermion loops, as in standard perturbation theory. It is, however, not obvious how to count the loops for a given diagram in the present antisymmetrized technique, where the interaction is fully antisymmetric with respect to permutation of its endpoints. This can be resolved by comparing with the *unsymmetrized* technique, where the interaction has the form  $U_{\alpha\beta\gamma\delta} f_\alpha^* f_\beta^* f_\gamma f_\delta = U \delta_{\alpha\beta} \delta_{\gamma\delta} f_\alpha^* f_\beta^* f_\gamma f_\delta$ , which can be represented by a wiggly line as in


(63)

Since the order of Grassmann variables is the same for the interaction  $\gamma_{\alpha\beta\gamma\delta} f_\alpha^* f_\beta^* f_\gamma f_\delta$ , the sign of a diagram is obtained by replacing the square by a wiggly line as in


(64)

and counting the number of closed loops (a single loop in this example). The relative orientation of the line and the square must be kept fixed, e.g., both the line and the square in (64) have been rotated counterclockwise by  $\pi/2$  with respect to (63).

### 3.4 Dual perturbation theory in momentum space

With the above prerequisites, we are now in the position to formulate the dual perturbation theory in momentum space. The rules to evaluate the expression for a given diagram are:

- draw all topologically distinct connected diagrams involving any  $n$ -body interaction  $\gamma^{(2n)}$  depicted by regular polygons with  $2n$  edges or endpoints, whereof  $n$  are outgoing (incoming) endpoints, where a directed line originates (terminates)
- connect the vertices with directed lines, compliant with ingoing and outgoing endpoints
- with each line associate a dual Green function  $\tilde{G}_{\mathbf{k}\nu}$
- assign a frequency, momentum, orbital and spin label to each endpoint
- sum / integrate over all internal variables taking into account energy-, momentum-, and spin-conservation at each vertex
- for each tuple of  $n$  equivalent lines, associate a factor  $1/n!$
- multiply the expression by  $(T/N)^m S^{-1} \times s$ , where  $m$  counts independent frequency / momentum summations and  $S$  and  $s$  are the symmetry factor and sign described above.

## 4 Numerical results

In the following, we describe two important diagrammatic approximations to the dual self-energy and show results to illustrate their physical content.

### 4.1 Second-order approximation

We start with the second-order approximation given by diagram (b). We refer to it as  $DF^{(2)}$ . Applying the above rules of the perturbation theory, we obtain the following expression

$$\begin{aligned} \tilde{\Sigma}_{\mathbf{k}\nu\sigma} = & -\frac{1}{2} \frac{T^2}{N^2} \sum_{\mathbf{k}'\mathbf{q}} \sum_{\nu'\omega} \sum_{\sigma'} \gamma_{\nu\nu'\omega}^{\sigma\sigma'\sigma'} \tilde{G}_{\mathbf{k}+\mathbf{q}\nu+\omega\sigma} \tilde{G}_{\mathbf{k}'+\mathbf{q}\nu'+\omega\sigma'} \tilde{G}_{\mathbf{k}'\nu'\sigma'} \gamma_{\nu'\nu\omega}^{\sigma'\sigma'\sigma\sigma} \\ & -\frac{1}{2} \frac{T^2}{N^2} \sum_{\mathbf{k}'\mathbf{q}} \sum_{\nu'\omega} \gamma_{\nu\nu'\omega}^{\sigma\bar{\sigma}\bar{\sigma}\sigma} \tilde{G}_{\mathbf{k}+\mathbf{q}\nu+\omega\bar{\sigma}} \tilde{G}_{\mathbf{k}'+\mathbf{q}\nu'+\omega\bar{\sigma}} \tilde{G}_{\mathbf{k}'\nu'\sigma} \gamma_{\nu'\nu\omega}^{\sigma\bar{\sigma}\bar{\sigma}\sigma}. \end{aligned} \quad (65)$$

Here we have left out the first-order contribution. Similarly to DMFT, we repeatedly solve the impurity model. Contrary to DMFT the hybridization is updated to make the local part of the interacting (instead of non-interacting) dual Green function and the first-order diagram zero. The hybridization is therefore different from DMFT. In addition, we evaluate the self-energy in each iteration and renormalize the Green function self-consistently using Dyson's equation.

Fig. 3 shows results for the spectral function obtained in  $DF^{(2)}$  and DMFT just above the critical interaction at which the model becomes insulating, which is  $U_c = 9.35t$  in DMFT, while it is significantly reduced by spatial correlations to  $6.64t$  in  $DF^{(2)}$ . The  $DF^{(2)}$  value agrees much better with the cellular DMFT value of  $U_c = 6.05t$ , which takes nearest-neighbor correlations into account [15]. For better comparability the energy axis has been scaled by  $U_c$ . We observe a significantly richer structure in the  $DF^{(2)}$  spectral function. While most spectral weight follows the non-interacting dispersion (red line), we observe relatively broad 'shadow bands' marked by arrows roughly following the dispersion shifted by the antiferromagnetic nesting vector  $\mathbf{q} = (\pi, \pi)$  (blue line). These bands originate from short-range dynamical antiferromagnetic correlations included through the self-energy correction. While the solution is paramagnetic, spins on neighboring sites favor to align antiferromagnetically on short time scales.

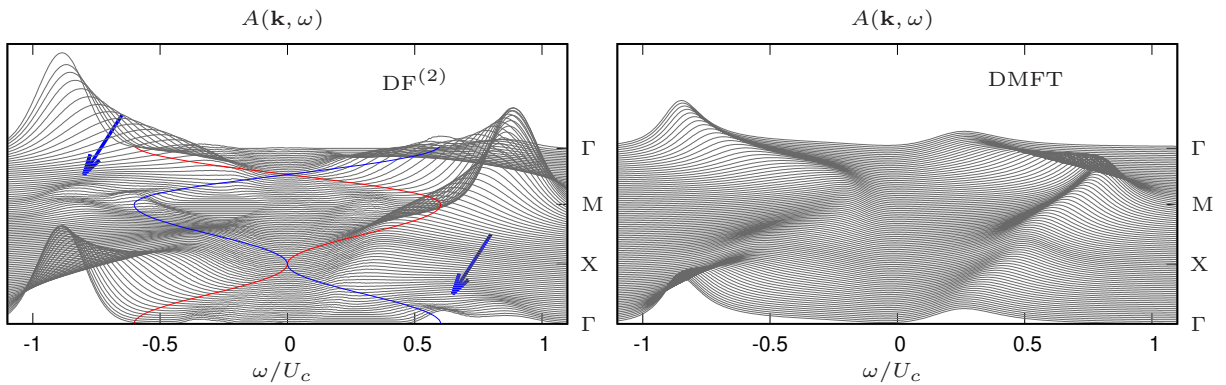


**Fig. 3:** Momentum resolved spectral function in  $DF^{(2)}$  and DMFT along high-symmetry lines in the Brillouin zone in the paramagnetic insulator. The  $DF^{(2)}$  spectral function exhibits shadow bands due to short-range antiferromagnetic correlations.

## 4.2 Ladder approximation

A more sophisticated approximation is the so-called ladder dual fermion approximation (LDFA)

$$\Sigma^{\text{LDFA}} = - \text{[diagram: square with a loop on top]} - \frac{1}{2} \text{[diagram: two squares connected by a horizontal line with an arrow pointing right]} - \text{[diagram: three squares connected by two horizontal lines with arrows pointing right]} - \dots \quad (66)$$

The diagrams are given with with corresponding signs and prefactors. All higher-order terms in the expansion have a prefactor of unity. The diagrams look like ladders, with an additional Green function connecting the left and rightmost vertices to close the diagram. Here the rules of the diagrammatic perturbation theory are crucial, because they allow us to derive expressions for every diagram in this infinite partial series without actually carrying out the expansion. To sum the infinite series in a practical way, we take a detour and first sum all the ladder diagrams without the closing Green function (see Fig. 4). Applying the rules of perturbation theory and taking into account all possible spin configurations, we can obtain the following Bethe-Salpeter equation

$$\tilde{I}_{\mathbf{q}\nu\nu'\omega}^{\sigma\sigma\sigma'\sigma'} = \gamma_{\nu\nu'\omega}^{\sigma\sigma\sigma'\sigma'} - \frac{T}{N} \sum_{\mathbf{k}''\nu''\sigma''} \gamma_{\nu\nu''\omega}^{\sigma\sigma\sigma''\sigma''} \tilde{G}_{\mathbf{k}''+\mathbf{q}\nu''+\omega} \tilde{G}_{\mathbf{k}''\nu''} \tilde{I}_{\mathbf{q}\nu''\nu'\omega}^{\sigma''\sigma''\sigma'\sigma'}, \quad (67)$$

$$\tilde{I}_{\mathbf{q}\nu\nu'\omega}^{\sigma\bar{\sigma}\bar{\sigma}\sigma} = \gamma_{\nu\nu'\omega}^{\sigma\bar{\sigma}\bar{\sigma}\sigma} - \frac{T}{N} \sum_{\mathbf{k}''\nu''} \gamma_{\nu\nu''\omega}^{\sigma\bar{\sigma}\bar{\sigma}\sigma} \tilde{G}_{\mathbf{k}''+\mathbf{q}\nu''+\omega} \tilde{G}_{\mathbf{k}''\nu''} \tilde{I}_{\mathbf{q}\nu''\nu'\omega}^{\sigma\bar{\sigma}\bar{\sigma}\sigma}. \quad (68)$$

Here we have omitted spin labels on the Green functions to emphasize that we consider the paramagnetic state. The negative sign arises because we have a closed loop in the diagram. It is easy to see that by repeatedly inserting the left-hand side into the right, we successively generate the sum over all ladder diagrams. This is illustrated in the left of Fig. 4.

Spin seems to play a particular role here. We have two equations which differ only in the spin labels. The first equation (67) actually corresponds to two coupled equations, one for each of the signs of  $\sigma = \pm 1/2$ . Apparently it mixes different spin components of the vertex (there is a sum over spins), while the second does not. To understand this, we observe that each vertex  $\gamma$  has an incoming and outgoing line on the left, as well as on the right. If we interpret an arrow pointing to the right as a propagating particle, the arrow to the left is a propagating hole. When we read the diagram from left to right,  $\gamma$  hence describes scattering of particle-hole pairs (the same is true for processes from top to bottom).  $\gamma_{\nu\nu'\omega}^{\sigma\sigma\sigma'\sigma'}$  hence describes a particle with spin  $\sigma$

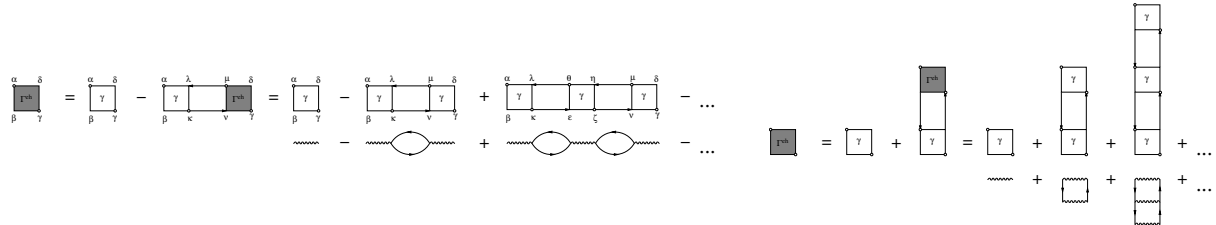


**Fig. 4:** Left: Bethe-Salpeter equation in the horizontal electron-hole channel and the first terms in the infinite series it generates. Right: Vertical channel. Diagrams obtained when the vertex  $\gamma$  is replaced by the Hubbard interaction  $U$  (depicted by a wiggly line) are also indicated.

and a hole with spin  $\bar{\sigma} = -\sigma$  entering from the left which scatter into a particle with spin  $\sigma'$  and a hole with spin  $-\sigma'$ . The energy of the pair is  $\omega$  and is conserved in the scattering process. So is the  $z$ -component of the spin:  $\sigma - \sigma = \sigma' - \sigma' = 0$ . However the total spin is not. By forming the linear combinations  $\gamma_{\nu\nu'\omega}^{d(m)} = \gamma_{\nu\nu'\omega}^{\uparrow\uparrow\uparrow\uparrow} (-)^m \gamma_{\nu\nu'\omega}^{\uparrow\uparrow\downarrow\downarrow}$ , the two equations decouple. We may say the scattering processes occur in different 'channels' which each correspond to a definite value of the total spin  $S$  of the particle hole pair. The plus sign corresponds to the density channel, which can be made plausible by forming the expectation value  $\langle n_{\sigma} n_{\uparrow} \rangle + \langle n_{\sigma} n_{\downarrow} \rangle = \langle n_{\sigma} n \rangle$ , while the minus signs relates to the spin channel, as can be seen from  $\langle n_{\sigma} n_{\uparrow} \rangle - \langle n_{\sigma} n_{\downarrow} \rangle = \langle n_{\sigma} S_z \rangle$ . The latter therefore corresponds to a total spin of  $S = 1$ , while the former has  $S = 0$ . With the same reasoning as above we see that the second equation (68) describes scattering of particle hole pairs with projections  $S_z = \sigma + \sigma = \pm 1$ , so that  $S = 1$ . We have found all spin states of the particle hole pair:  $S = 0, S_z = 0$  and  $S = 1, S_z = 0, \pm 1$ . In the paramagnetic case, the results cannot depend on the spin projection and we have found the useful identity  $\gamma_{\nu\nu'\omega}^{\uparrow\uparrow\uparrow\uparrow} - \gamma_{\nu\nu'\omega}^{\uparrow\uparrow\downarrow\downarrow} = \gamma_{\nu\nu'\omega}^{\uparrow\downarrow\downarrow\uparrow}$ . We have just performed a spin-diagonalization, after which the equations can be written in the form

$$\tilde{\Gamma}_{\mathbf{q}\nu\nu'\omega}^{\alpha} = \gamma_{\nu\nu'\omega}^{\alpha} - \frac{T}{N} \sum_{\mathbf{k}''\nu''} \gamma_{\nu\nu''\omega}^{\alpha} \tilde{G}_{\mathbf{k}''+\mathbf{q}\nu''+\omega} \tilde{G}_{\mathbf{k}''\nu''} \tilde{\Gamma}_{\mathbf{q}\nu''\nu'\omega}^{\alpha}, \quad (69)$$

where  $\alpha = d(m)$  denotes the density ( $S = 0$ ) or spin ( $S = 1$ ) channel. The physical content of this equation is the repeated scattering of particle-hole pairs which describes collective charge or spin excitations. The self-energy in the ladder approximation describes effects due to scattering of electrons and these bosonic excitations.

We can solve this equation simply by matrix inversion when viewing the convolution of Green functions as a matrix in  $\nu$  and  $\nu'$

$$[\tilde{\Gamma}_{\mathbf{q}\omega}^{\alpha}]_{\nu\nu'}^{-1} = [\gamma_{\omega}^{\alpha}]_{\nu\nu'}^{-1} + (T/N) \sum_{\mathbf{k}} \tilde{G}_{\mathbf{k}+\mathbf{q}\nu+\omega} \tilde{G}_{\mathbf{k}\nu} \delta_{\nu\nu'}. \quad (70)$$

We can do this independently for fixed  $\mathbf{q}$ ,  $\omega$  and  $S$ , which are precisely the quantum numbers of the particle-hole pair and which are conserved in scattering processes.

From the left part of Fig. 4 it would seem that we can obtain the self-energy by simply adding a closing line on the vertex  $\tilde{\Gamma}^{eh}$ . However we observe a problem here: the second-order contribution would miss the factor  $1/2$  expected from the diagrammatic rules.

A more systematic way to obtain the ladder self-energy is the Schwinger-Dyson equation (SDE)

$$\Sigma^{\text{LDFA}} = - \text{[Diagram 1]} - \frac{1}{2} \text{[Diagram 2]} \quad (71)$$

It connects the self-energy to the exact two-particle vertex. Here we construct an approximation to the vertex via the Bethe-Salpeter equations. However, approximating it as  $\tilde{\Gamma} \approx \tilde{\Gamma}^{eh}$  with the horizontal series shown in the left of Fig. 4, we would miss the entire series of vertical diagrams

shown on the right. If the interaction were of Hubbard type, it would be obvious from the figure that the corresponding diagrams are all valid contributions to the vertex which should be taken into account. Both series are in fact the diagrams generated by the well-known fluctuation exchange approximation (FLEX) [16].

On the other hand, if we replace the fully antisymmetric box by wiggly interaction lines,

$$\gamma_{1234} \rightarrow -U(\delta_{12}\delta_{34} - \delta_{14}\delta_{32}), \quad \begin{array}{c} 1 \quad 4 \\ \square \quad \gamma \\ 2 \quad 3 \end{array} = \begin{array}{c} \text{wavy line} \\ \text{---} \end{array} - \begin{array}{c} \text{wavy line} \\ \text{---} \end{array},$$

we see that already the series in the left of Fig. 4 generates all FLEX diagrams. It is hence plausible that  $\tilde{I}^{\text{eh}}$  and  $\tilde{I}^{\text{v}}$  give the same contribution to the self-energy. We approximate the vertex as  $\tilde{I} \approx \tilde{I}^{\text{eh}} + \tilde{I}^{\text{v}} - \gamma$ , where we subtract  $\gamma$  once because it appears in both series for  $\tilde{I}^{\text{eh}}$  and  $\tilde{I}^{\text{v}}$ . Inserting  $\tilde{I}$  into the SDE yields the LDFA self-energy

$$\tilde{\Sigma}_{\mathbf{k}\nu} = -\frac{T^2}{N^2} \sum_{\mathbf{k}'\mathbf{q}} \sum_{\nu'\omega} A_\alpha \gamma_{\nu\nu'\omega}^\alpha \tilde{G}_{\mathbf{k}+\mathbf{q}\nu+\omega} \tilde{G}_{\mathbf{k}'+\mathbf{q}\nu'+\omega} \tilde{G}_{\mathbf{k}'\nu'} \left( \tilde{I}_{\nu'\nu\omega}^{\text{h},\alpha} - \frac{1}{2} \gamma_{\nu'\nu\omega}^\alpha \right). \quad (72)$$

Here  $A_d = 1$ , and  $A_m = 3$  accounts for the degeneracy ( $S_z = 0, \pm 1$ ) of the magnetic  $S = 1$  channel. The two equal contributions from  $\tilde{I}^{\text{eh}}$  and  $\tilde{I}^{\text{v}}$  have canceled the prefactor  $1/2$  of the second diagram in the SDE, Eq. (71). The double counting correction  $\gamma$  in  $\tilde{I}$  attains a factor  $1/2$  and provides the correct prefactor of the second-order contribution in Eq. (66).

Fig. 5 shows results obtained within the ladder approximation for the two-dimensional Hubbard model. Fig. 5 (a) shows the static ( $\omega = 0$ ), homogeneous ( $\mathbf{q} = 0$ ) spin susceptibility computed from the vertex. In DMFT the response to a homogeneous field increases as moments form with decreasing temperature. After a similar increase in LDFA, neighboring spins start to couple antiferromagnetically. Hence the temperature of the downturn marks the effective exchange energy scale. We can see that the ladder approximation agrees well with Quantum Monte Carlo (QMC) results within error bars. We can therefore be confident that we have included the dominant contributions. Conversely, the entire series of diagrams made up by terms of the form of diagram (f) describing particle-particle scattering that we have neglected apparently plays only a minor role in this regime. We can further see a significant size dependence, indicating that the self-energy corrections are truly long-ranged.

In DMFT the susceptibility diverges at the antiferromagnetic wave vector  $\mathbf{q} = (\pi, \pi)$  (not shown). We can view the Bethe-Salpeter equation as a generalization of a geometric series  $\sum_{n=0}^{\infty} q^n = 1/(1-q)$ , where the matrix  $(T/N) \sum_{\mathbf{k}\nu} \gamma_{\nu\nu'\omega}^\alpha \tilde{G}_{\mathbf{k}+\mathbf{q}\nu+\omega} \tilde{G}_{\mathbf{k}\nu} \delta_{\nu\nu'}$  plays the role of  $q$ . The divergence hence appears when the leading eigenvalue of this matrix approaches 1. Here it has physical significance and indicates a second-order transition to the antiferromagnetic Néel state as indicated by the vertical line. It is clearly an artifact of the mean-field approximation, because the Mermin-Wagner theorem forbids breaking of a continuous symmetry in two dimensions [17].

In LDFA, we account for the long-range fluctuations that are essential to the proof of the theorem and which destroy the spurious long-range order. To obtain a finite result in LDFA even

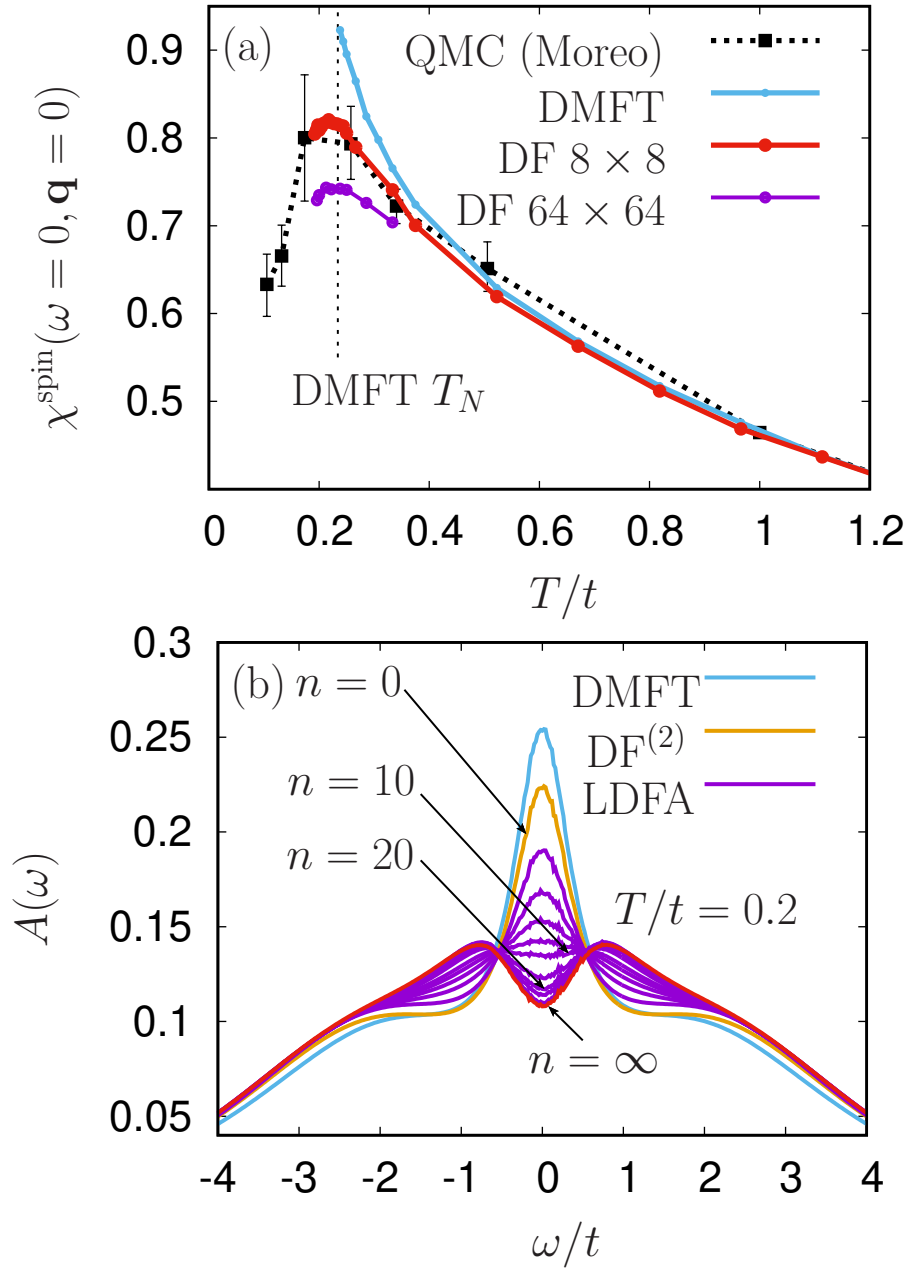


**Fig. 5:** (a) Temperature dependence of the static homogeneous susceptibility for  $U/t = 4$  and different temperatures. (b) Local density of states in DMFT,  $DF^{(2)}$  and different orders of the ladder approximation. All orders contribute to the formation of a pseudogap.

though the series diverges in DMFT is possible by computing the self-energy from Green functions which are self-consistently renormalized by the self-energy itself. Below the DMFT Néel temperature, this requires a regularization procedure [18].

Fig. 5 (b) shows the local density of states. In DMFT we see the quasi-particle peak and broad Hubbard bands. In the second-order approximation, the spectral weight at the Fermi level is reduced. By iterating the Bethe-Salpeter equation, we can compute the results to successively higher orders. Apparently all orders of the perturbation series contribute to the result. Instead of a quasi-particle peak, the LDFA spectral function exhibits a pseudogap.

## 5 Summary and outlook

In just two examples we have seen that diagrammatic extensions of DMFT can introduce highly non-trivial effects beyond DMFT and remedy artifacts of the mean-field approximation in particular in low dimensions. They can give qualitatively different and even quantitative results. At the same time, the diagrammatic approach allows us to isolate the dominant contributions and provides us with intuition on the underlying microscopic processes.

In the last ten years of their development, diagrammatic extensions of DMFT have been applied to a variety of systems and scenarios. They have been used to describe unconventional superconductivity in the Kondo lattice model, magnetism in frustrated systems, disordered, inhomogeneous and non-equilibrium systems and even quantum critical behavior in the Hubbard and Falicov-Kimball models. First simple applications to materials have emerged. New methods based on different functionals and the fermion-boson vertices and extensions to cluster- and extended DMFT have been developed. The diagram series has been sampled using diagrammatic Monte Carlo techniques [19, 20] and even more advanced diagrammatic approximations like the parquet equations have been considered. All these developments are summarized in Ref. [6]. For many of the applications the unique ability of the methods to simultaneously describe the strong local dynamical correlations and extended critical fluctuations is crucial. Diagrammatic extensions of DMFT provide a complementary viewpoint to results obtained within other approaches. Most notably within cluster DMFT approaches, in which all diagrams to the self-energy are summed within the range of the comparatively small clusters [21].

The approaches continue to be developed. Recently more fundamental questions are being investigated. For example how to construct conserving approximations when the approximations are made two-particle self-consistent [22], the role of the self-consistency condition in dual fermion [23, 24], or the role of three-particle vertices [25] in dual fermion and D $\Gamma$ A.

Hopefully this introduction will inspire work in two important research directions: i) the combination of diagrammatic extensions with the functional renormalization group and ii) a merger with density-functional theory to arrive at a quantitative theory of correlated materials.



## References

- [1] N.F. Mott, Rev. Mod. Phys. **40**, 677 (1968)
- [2] G.R. Stewart, Rev. Mod. Phys. **56**, 755 (1984)
- [3] E. Dagotto, Rev. Mod. Phys. **66**, 763 (1994)
- [4] A. Georges, G. Kotliar, W. Krauth, and M.J. Rozenberg, Rev. Mod. Phys. **68**, 13 (1996)
- [5] W. Metzner and D. Vollhardt, Phys. Rev. Lett. **62**, 324 (1989)
- [6] G. Rohringer, H. Hafermann, A. Toschi, A.A. Katanin, A.E. Antipov, M.I. Katsnelson, A.I. Lichtenstein, A.N. Rubtsov, and K. Held, Rev. Mod. Phys. **90**, 025003 (2018)
- [7] A. Georges and G. Kotliar, Phys. Rev. B **45**, 6479 (1992)
- [8] E. Gull, A.J. Millis, A.I. Lichtenstein, A.N. Rubtsov, M. Troyer, and P. Werner, Rev. Mod. Phys. **83**, 349 (2011)
- [9] J.W. Negele and H. Orland: *Quantum Many-Particle Systems* (Perseus books, 1998)
- [10] A. Toschi, A.A. Katanin, and K. Held, Phys. Rev. B **75**, 045118 (2007)
- [11] H. Kusunose, J. Phys. Soc. Jpn. **75**, 054713 (2006)
- [12] A.N. Rubtsov, M.I. Katsnelson, and A.I. Lichtenstein, Phys. Rev. B **77**, 033101 (2008)
- [13] G. Li, Phys. Rev. B **91**, 165134 (2015)
- [14] N. Hugenholtz, Physica **23**, 481 (1957)
- [15] H. Park, K. Haule, and G. Kotliar, Phys. Rev. Lett. **101**, 186403 (2008)
- [16] N.E. Bickers, D.J. Scalapino, and S.R. White, Phys. Rev. Lett. **62**, 961 (1989)
- [17] N.D. Mermin and H. Wagner, Phys. Rev. Lett. **17**, 1133 (1966)
- [18] J. Otsuki, H. Hafermann, and A.I. Lichtenstein, Phys. Rev. B **90**, 235132 (2014)
- [19] S. Isakov, A.E. Antipov, and E. Gull, Phys. Rev. B **94**, 035102 (2016)
- [20] J. Gukelberger, E. Kozik, and H. Hafermann, Phys. Rev. B **96**, 035152 (2017)
- [21] T. Maier, M. Jarrell, T. Pruschke, and M.H. Hettler, Rev. Mod. Phys. **77**, 1027 (2005)
- [22] F. Krien, E.G.C.P. van Loon, H. Hafermann, J. Otsuki, M.I. Katsnelson, and A.I. Lichtenstein, Phys. Rev. B **96**, 075155 (2017)
- [23] E.G.C.P. van Loon, M.I. Katsnelson, preprint arXiv:1805.08572 (2018)

- [24] T. Ribic, P. Gunacker, preprint arXiv:1805.10996 (2018)
- [25] T. Ribic, P. Gunacker, S. Isakov, M. Wallerberger, G. Rohringer, A.N. Rubtsov, E. Gull, and K. Held, Phys. Rev. B **96**, 235127 (2017)

# **13 Dynamical Mean-Field and Dynamical Cluster Approximation Based Theory of Superconductivity**

Thomas A. Maier  
Oak Ridge National Laboratory  
Oak Ridge, Tennessee

## **Contents**

<b>1</b>	<b>Introduction</b>	<b>2</b>
<b>2</b>	<b>Dynamical mean-field theory and dynamical cluster approximation</b>	<b>4</b>
2.1	Preliminary remarks . . . . .	4
2.2	General framework for the normal state . . . . .	5
2.3	Nambu-Gorkov formalism . . . . .	7
2.4	Pair-field susceptibility . . . . .	10
<b>3</b>	<b>Superconductivity in the 2D Hubbard model</b>	<b>14</b>
3.1	Attractive Hubbard model . . . . .	14
3.2	Repulsive Hubbard model . . . . .	17
3.3	Extended Hubbard model . . . . .	24
<b>4</b>	<b>Summary and concluding remarks</b>	<b>26</b>

# 1 Introduction

The collective behavior of electrons in solids gives rise to a range of different emergent phenomena, including magnetism, the fractional quantum Hall effect, and superconductivity. Of these, superconductivity is perhaps the most fascinating state that has captivated generations of physicists over more than a century. When cooled below a critical temperature  $T_c$ , superconductors exhibit conductance without resistance, the property that underlies most applications of superconductors, including power transmission and generation as well as medical applications. A second and equally important effect observed in superconductors is the complete expulsion of an external magnetic field during its transition to the superconducting state (the Meissner-Ochsenfeld effect). This repulsion of magnetic fields can be stronger than gravity which leads to levitation, the most fascinating manifestation of superconductivity. Fundamentally, it implies that the electrons in superconductors behave collectively.

Conceptually, two main ingredients, illustrated in Fig. 1, are necessary to understand the superconducting state [1]: (1) Electrons form boson-like Cooper pairs driven by a net attractive interaction; (2) These Cooper pairs condense into a coherent macroscopic quantum state analogous to a Bose-Einstein condensate. The energy required to break up the pairs (also called energy gap) suppresses the scattering processes from defects and impurities that would otherwise give rise to electrical resistance in normal conductors.

*But why would two negatively charged electrons, which repel each other because of the Coulomb repulsion, would be attracted to form pairs?* For conventional superconductors, which include many elemental metals such as Hg, Al, and Nb, the attractive force that binds the electrons arises from the interaction between the negatively charged electrons and the positively charged ions. The distortion of the ion lattice left behind by the motion of an electron attracts a second electron and thus results in an effective attractive interaction between the electrons. This attraction is local in space, resulting in an  $s$ -wave structure of the Cooper pair wave-function and thus an isotropic  $s$ -wave gap in momentum space. But since the ion dynamics is slow compared

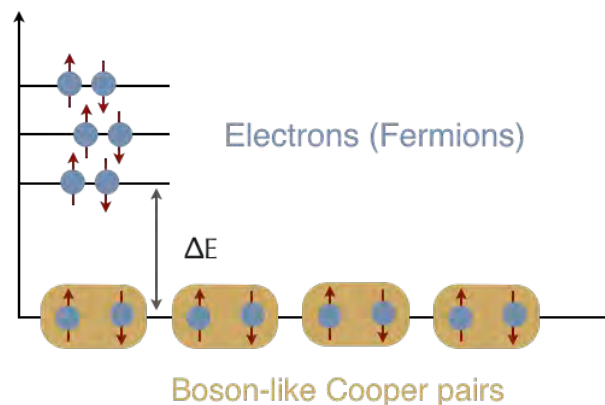


**Fig. 1: Main conceptual ingredients of the BCS theory of superconductivity:** (1) Through a net attractive interaction, electrons form Cooper pairs and (2) the Cooper pairs become phase coherent and condense into a single macroscopic quantum state. The binding energy  $\Delta E$  required to break up a pair suppresses the scattering processes that lead to resistance.

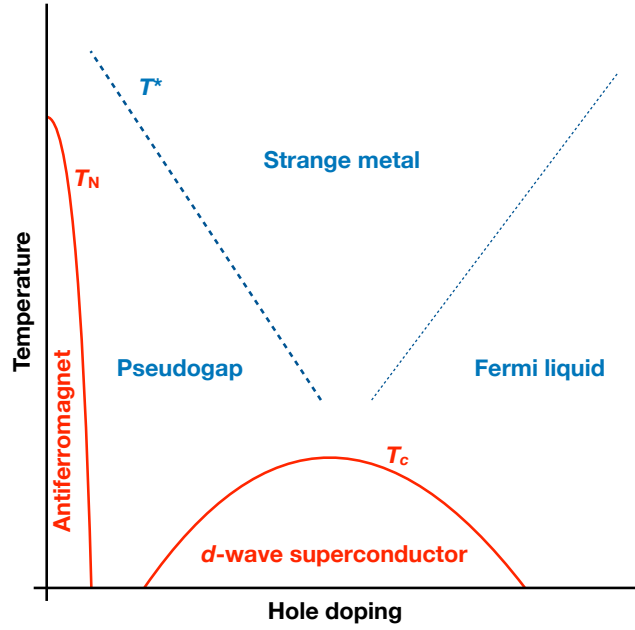


**Fig. 2: Schematic temperature-doping phase diagram of the cuprate high-temperature superconductors:** *The d-wave superconducting state below the critical temperature  $T_c$  emerges upon hole doping of the antiferromagnetic parent compound. Upon cooling, it arises from a normal state that hosts a pseudogap at low doping, where an energy gap is present in the electronic excitations, or a strange metal non-Fermi liquid phase at higher doping. BCS theory is not adequate to describe this situation and non-perturbative approaches are necessary to accurately treat the electron-electron correlations that give rise to these phases.*

to the electrons, it is strongly retarded in time, i.e., active at long time scales, where the effectively instantaneous Coulomb repulsion can be overcome. These concepts are well described and understood within a rigorous theoretical foundation, the BCS (Bardeen-Cooper-Schrieffer) theory [2, 1], and its extension, the Migdal-Eliashberg theory [3, 4].

Superconductivity in heavy fermion materials, copper-oxygen, and iron-based materials and other related compounds, however, is thought to arise from a different mechanism than the electron-phonon mechanism [5]. While the two main conceptual ingredients of BCS theory, i.e., the formation of Cooper pairs and their condensation into a macroscopic quantum state, still hold, the pairing mechanism that leads to the attraction of electrons is believed to be different from the electron-phonon mechanism. Because of the strong local Coulomb repulsion in these systems, local  $s$ -wave pairing is energetically unfavorable and the Cooper pair wave function is found to have a different symmetry; in the cuprates, for example, the pairs are bound in a  $d_{x^2-y^2}$ -wave state, in which the pair wave function changes sign in momentum space and which corresponds to pair formation on nearest-neighbor atom positions in the crystal lattice. Similarly, in the iron-based superconductors, the pairs are believed to form an extended, sign changing  $s$ -wave state, in which the local amplitude is strongly reduced. As we will see, such a pair structure with a sign change indicates that the pairing interaction is actually repulsive in momentum space, in marked contrast to the conventional electron-phonon case. It is therefore generally accepted that pairing in these “unconventional” superconductors has a different

origin, and most likely arises from the strong magnetic interactions or fluctuations between the electron spins that result in an antiferromagnetic phase in the undoped parent compounds. Moreover, BCS theory assumes that the superconducting state is created from a normal metallic Fermi liquid state with well defined quasiparticles. In contrast, the normal state in many unconventional superconductors is everything but normal (see Fig. 2). Strong electron-electron correlations in these systems often lead to non-Fermi liquid behavior and BCS theory is not adequate. One instead needs a non-perturbative approach that can handle the strong correlations and which does not assume a Fermi liquid normal state as a starting point. Dynamical mean-field theory (DMFT) [6] and the dynamical cluster approximation (DCA) [7] provide such a tool, which allows us to study how superconductivity emerges in systems where the normal state behavior is governed by strong electron correlations.

These lecture notes are concerned with such unconventional systems, in which superconductivity arises from the strong local Coulomb repulsion between the electrons. Given that superconductivity requires electrons to form pairs, this seems like a paradox. The goal of this lecture is to demonstrate how DMFT and DCA calculations have helped us resolve this paradox. Following a pedagogical discussion of the DMFT and DCA frameworks to study superconductivity, we highlight a set of applications that showcase the ability of these approaches to provide important insight. In this lecture we assume a basic familiarity with BCS, DMFT, and DCA theory.

## 2 Dynamical mean-field theory and dynamical cluster approximation

### 2.1 Preliminary remarks

To keep things simple, we will focus most of these lecture notes on one of the simplest models of correlated electron systems, the single-band Hubbard model [8]. Its Hamiltonian

$$H = \sum_{ij,\sigma} t_{ij} c_{i\sigma}^\dagger c_{j\sigma} + U \sum_i n_{i\uparrow} n_{i\downarrow} \quad (1)$$

is divided into a non-interacting part  $H_0$  given by the first term and an interacting part  $H_{\text{int}}$  given by the second term. Here  $c_{i\sigma}^{(\dagger)}$  destroys (creates) an electron on site  $i$  with spin  $\sigma$  and  $n_{i\sigma} = c_{i\sigma}^\dagger c_{i\sigma}$  is the corresponding number operator. The first ( $H_0$ ) term describes the hopping of electrons between sites  $i$  and  $j$  with amplitude  $t_{ij}$ , and the second ( $H_{\text{int}}$ ) term raises the energy by the Coulomb repulsion  $U$  when two electrons with opposite spin reside on the same site. If not otherwise noted, we consider the sites in this model to form a two-dimensional (2D) square lattice with a hopping  $t_{ij} = -t$  if  $i$  and  $j$  are nearest-neighbor sites. Despite its simplicity, this model is commonly believed to provide a description of the generic physics of the cuprate high-temperature superconductors [9], in which photoemission experiments find a single electronic band crossing the Fermi level.

The single-particle dynamics of the Hubbard Hamiltonian at finite temperatures is described by the thermodynamic Green function and its Fourier-transform to Matsubara frequencies and

momentum space

$$G_{ij,\sigma} = - \left\langle T_\tau c_{i\sigma}(\tau) c_{j\sigma}^\dagger \right\rangle \quad (2)$$

$$G_{ij,\sigma}(i\omega_n) = \int_0^\beta d\tau e^{i\omega_n \tau} G_{ij,\sigma}(\tau), \quad \omega_n = (2n+1)\pi T \quad (3)$$

$$G_\sigma(\mathbf{k}, i\omega_n) \equiv \langle \langle c_{\mathbf{k}\sigma}; c_{\mathbf{k}\sigma}^\dagger \rangle \rangle_{i\omega_n} = \frac{1}{N} \sum_{ij} e^{i\mathbf{k}(\mathbf{r}_i - \mathbf{r}_j)} G_{ij,\sigma}(i\omega_n). \quad (4)$$

Here  $\tau$  is the imaginary time,  $T_\tau$  the time ordering operator,  $\beta = 1/T$  the inverse temperature and  $\omega_n = (2n+1)\pi T$  are the fermionic Matsubara frequencies. For problems with translational symmetry in space and time, the Green function becomes diagonal in momentum  $\mathbf{k}$  and frequency  $i\omega_n$  as stated in Eqs. (3) and (4). The Green function  $G_0$  of the non-interacting system, i.e.  $H = H_0$ , is given by

$$G_0(\mathbf{k}, i\omega_n) = \frac{1}{i\omega_n + \mu - \varepsilon_{\mathbf{k}}}, \quad (5)$$

where  $\mu$  is the chemical potential and  $\varepsilon_{\mathbf{k}}$  the dispersion, obtained from a Fourier-transform of the hopping  $t_{ij}$ . For our 2D model with only nearest neighbor hopping  $t$ , we have

$$\varepsilon_{\mathbf{k}} = -2t(\cos k_x + \cos k_y) \quad (6)$$

with  $\mathbf{k} = (k_x, k_y)$ . Finally, the Dyson equation

$$G(\mathbf{k}, i\omega_n) = \frac{1}{G_0^{-1}(\mathbf{k}, i\omega_n) - \Sigma(\mathbf{k}, i\omega_n)}. \quad (7)$$

defines the self-energy  $\Sigma(\mathbf{k}, i\omega_n)$  as the difference between the (inverse) non-interacting Green function  $G_0$  and the fully renormalized Green function  $G$  and thus describes the effects of the interaction term  $H_{\text{int}}$  on the single-particle dynamics.

## 2.2 General framework for the normal state

Calculating the Green function  $G$  and self-energy  $\Sigma$  in the thermodynamic limit is prohibitively expensive as the problem size grows exponentially in the number of degrees of freedom (sites in the Hubbard model). The DMFT and DCA approaches reduce this complexity by representing the infinite-size system by a reduced-size cluster, and use coarse-graining in momentum space to retain information about the degrees of freedom (sites) not contained on the cluster [7]. In DMFT the cluster consists only of a single site, called the impurity site, while in DCA the cluster has several sites. The size of the cluster is controlled by the way the momentum space is coarse-grained. Fig. 3 shows several examples starting from the single-site ( $N_c = 1$ ) DMFT impurity. The DCA is obtained for  $N_c > 1$ . It reduces to the DMFT for  $N_c = 1$  and approaches the exact result for  $N_c \rightarrow \infty$ . Because the DCA includes the DMFT as a limiting case, we restrict the following discussion to the DCA.

The first Brillouin zone is split into  $N_c$  patches of equal size. As illustrated in Fig. 3, each patch is represented by a cluster momentum  $\mathbf{K}$  at its center. The basic assumption of the

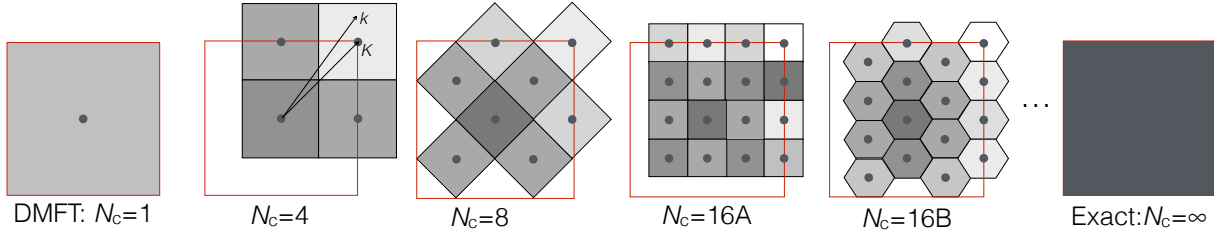


**Fig. 3: Coarse-graining of momentum space:** At the heart of the DCA (and DMFT) methods is a partitioning of the first Brillouin zone into  $N_c$  patches over which the Green function is coarse-grained (averaged) to represent the system by a reduced number of  $N_c$  “cluster” degrees of freedom. The bulk degrees of freedom not included on the cluster are taken into account as a mean-field. For  $N_c = 1$ , the dynamical mean-field approximation is recovered, while for  $N_c \rightarrow \infty$ , one obtains the exact result. For a given cluster size  $N_c$ , one can have different locations and shapes of the coarse-graining patches, as illustrated for  $N_c = 16A$  and  $16B$ .

approximation is that the self-energy is only weakly momentum dependent (or purely local in DMFT), so that its momentum dependence is well represented by the coarse-grid of cluster momenta  $\mathbf{K}$ , i.e.,

$$\Sigma(\mathbf{k}, i\omega_n) \simeq \Sigma_c(\mathbf{K}, i\omega_n) \text{ (in DCA) or } \Sigma(\mathbf{k}, i\omega_n) \simeq \Sigma_{ii}(i\omega_n) \text{ (in DMFT)}. \quad (8)$$

Here,  $\Sigma_c(\mathbf{K}, i\omega_n)$  is the self-energy of a cluster of size  $N_c$ , and  $\Sigma_{ii}(i\omega_n)$  that of a single-site impurity in DMFT. One then sets up an effective cluster problem to calculate  $\Sigma_c(\mathbf{K}, i\omega_n)$  or  $\Sigma_{ii}(i\omega_n)$ . To this end, the Green function is coarse-grained over the DCA patches (or the full Brillouin zone in DMFT)

$$\bar{G}(\mathbf{K}, i\omega_n) = \frac{N_c}{N} \sum_{\mathbf{k} \in \mathcal{P}_{\mathbf{K}}} G(\mathbf{k}, i\omega_n) = \frac{N_c}{N} \sum_{\mathbf{k} \in \mathcal{P}_{\mathbf{K}}} \frac{1}{i\omega_n - \varepsilon_{\mathbf{k}} + \mu - \Sigma_c(\mathbf{K}, i\omega_n)}, \quad (9)$$

where  $\mathcal{P}_{\mathbf{K}}$  is the patch centered at  $\mathbf{K}$  containing  $N/N_c$  momenta  $\mathbf{k}$ . Note that in DMFT, the sum runs over the full Brillouin zone and the coarse-grained Green function reduces to the local Green function. Given  $\bar{G}$  and  $\Sigma_c$ , one can then set up an algorithm, such as, for example, the quantum Monte Carlo (QMC) algorithms discussed in Refs. [10, 11], to calculate the cluster Green function. The non-interacting part of the cluster problem is defined by the cluster-excluded Green function

$$\mathcal{G}(\mathbf{K}, i\omega_n) = (\bar{G}^{-1}(\mathbf{K}, i\omega_n) + \Sigma_c(\mathbf{K}, i\omega_n))^{-1}, \quad (10)$$

where the cluster self-energy has been added to avoid double counting. While  $\mathcal{G}(\mathbf{K}, i\omega_n)$  is the Green function of a cluster of size  $N_c$ , note that the remaining lattice degrees of freedom are encoded in  $\mathcal{G}$  through the use of the coarse-grained Green function  $\bar{G}$ . Together with the interacting part of the Hamiltonian, one then sets up the action for the effective cluster problem, which reads after Fourier-transform to real space

$$S[\phi^*, \phi] = - \int_0^\beta d\tau \int_0^\beta d\tau' \sum_{ij, \sigma} \phi_{i\sigma}^*(\tau) \mathcal{G}_{0,ij,\sigma}(\tau - \tau') \phi_{j\sigma}(\tau) + \int_0^\beta d\tau \sum_i U \phi_{i\uparrow}^*(\tau) \phi_{i\uparrow}(\tau) \phi_{i\downarrow}^*(\tau) \phi_{i\downarrow}(\tau). \quad (11)$$



Here  $\phi$  and  $\phi^*$  are the Grassmann variables corresponding to the operators  $c$  and  $c^\dagger$ , respectively. From this the cluster Green function

$$G_{c,ij,\sigma}(\tau - \tau') = \frac{1}{Z} \int \mathcal{D}[\phi^* \phi] \phi_{i\sigma}(\tau) \phi_{j\sigma}^*(\tau') e^{-S[\phi^*, \phi]}, \quad (12)$$

with

$$Z = \int \mathcal{D}[\phi^* \phi] e^{-S[\phi^*, \phi]} \quad (13)$$

the partition function, is evaluated and used to determine the cluster self-energy

$$\Sigma_c(\mathbf{K}, i\omega_n) = \mathcal{G}_0^{-1}(\mathbf{K}, i\omega_n) - G_c^{-1}(\mathbf{K}, i\omega_n). \quad (14)$$

Then, using this new result for  $\Sigma_c(\mathbf{K}, i\omega_n)$  in Eq. (9), these steps are iterated to convergence. We note that this DCA algorithm was recently extended into the DCA<sup>+</sup> method [12] through the inclusion of a self-energy  $\Sigma(\mathbf{k}, i\omega_n)$  with continuous momentum  $\mathbf{k}$  dependence that replaces the piecewise constant self-energy  $\Sigma_c(\mathbf{K}, i\omega_n)$  in the coarse-graining step, while leaving the cluster problem unchanged. This has the benefit that results depend less on the shape of the cluster that is being used.

## 2.3 Nambu-Gorkov formalism

In this section we generalize the DCA (and DMFT) formalism to perform calculations in the symmetry broken superconducting state. This phase is signaled by an order parameter that describes the finite expectation value for the creation of a pair of electrons in time-reversed momentum states

$$\Delta_{\mathbf{k}} = \langle c_{\mathbf{k}\uparrow} c_{-\mathbf{k}\downarrow} \rangle \neq 0 \text{ for some } \mathbf{k}. \quad (15)$$

Here we restrict the discussion to spin singlet pairs and note that  $\Delta_{\mathbf{k}}$  can only be finite for a grand canonical ensemble in which the particle number is not fixed. This is not a problem for DMFT or DCA, since these approaches are formulated for the grand canonical ensemble. The momentum structure of  $\Delta_{\mathbf{k}}$  determines the symmetry of the superconducting state. Examples are  $\Delta_{\mathbf{k}} \propto 1$  (*s*-wave),  $\cos k_x + \cos k_y$  (extended *s*-wave),  $\cos k_x - \cos k_y$  (*d*<sub>x<sup>2</sup>-y<sup>2</sup>-wave),  $\sin k_x \sin k_y$  (*d*<sub>xy</sub>-wave) or  $a \sin k_x + b \sin k_y$  (*p*-wave). Because  $\Delta_{\mathbf{k}}$  is finite in the superconducting phase, one has, in addition to the normal Green function</sub>

$$G(\mathbf{k}, i\omega_n) = \langle \langle c_{\mathbf{k}\uparrow}; c_{\mathbf{k}\uparrow}^\dagger \rangle \rangle_{i\omega_n} \quad (16)$$

a finite anomalous Green function

$$F(\mathbf{k}, i\omega_n) = \langle \langle c_{\mathbf{k}\uparrow}; c_{-\mathbf{k}\downarrow} \rangle \rangle_{i\omega_n}. \quad (17)$$

Using the concept of Nambu spinors [1]

$$\Psi_{\mathbf{k}}^\dagger = \left( c_{\mathbf{k}\uparrow}^\dagger, c_{-\mathbf{k}\downarrow} \right), \quad \Psi_{\mathbf{k}} = \begin{pmatrix} c_{\mathbf{k}\uparrow} \\ c_{-\mathbf{k}\downarrow}^\dagger \end{pmatrix} \quad (18)$$

one then defines the Green function matrix in Nambu space [1]

$$\mathbf{G}(\mathbf{k}, i\omega_n) = \langle \langle \Psi_{\mathbf{k}}; \Psi_{\mathbf{k}}^\dagger \rangle \rangle_{i\omega_n} = \begin{pmatrix} G(\mathbf{k}, i\omega_n) & F(\mathbf{k}, i\omega_n) \\ F^*(\mathbf{k}, -i\omega_n) & -G^*(\mathbf{k}, i\omega_n) \end{pmatrix}, \quad (19)$$

which contains information about both the normal and the anomalous Green function. Note that the  $\mathbf{G}$  matrix contains only two independent matrix elements  $G$  and  $F$ . The elements in the second row are related to those in the first row by general symmetry relations for Green functions. In the presence of an external pairing field  $\eta(\mathbf{k}) = \eta'(\mathbf{k}) + i\eta''(\mathbf{k})$ , which couples to  $c_{-\mathbf{k}\downarrow}c_{\mathbf{k}\uparrow}$ , the non-interacting part of the Hubbard Hamiltonian becomes

$$H_0 = \sum_{\mathbf{k}} \Psi_{\mathbf{k}}^\dagger \left( \epsilon_{\mathbf{k}} \sigma_3 - \eta'(\mathbf{k}) \sigma_1 + \eta''(\mathbf{k}) \sigma_2 \right) \Psi_{\mathbf{k}}, \quad (20)$$

where the  $\sigma_i$  are the Pauli spin matrices

$$\sigma_0 = \begin{pmatrix} 1 & 0 \\ 0 & 1 \end{pmatrix}, \sigma_1 = \begin{pmatrix} 0 & 1 \\ 1 & 0 \end{pmatrix}, \sigma_2 = \begin{pmatrix} 0 & -i \\ i & 0 \end{pmatrix}, \sigma_3 = \begin{pmatrix} 1 & 0 \\ 0 & -1 \end{pmatrix}. \quad (21)$$

With this, the lattice Green function in the superconducting state becomes

$$\mathbf{G}(\mathbf{k}, i\omega_n) = \left( i\omega_n \sigma_0 - (\epsilon_{\mathbf{k}} - \mu) \sigma_3 - \eta'(\mathbf{k}) \sigma_1 - \eta''(\mathbf{k}) \sigma_2 - \Sigma_c(\mathbf{K}, i\omega_n) \right)^{-1} \quad (22)$$

with the cluster self-energy matrix

$$\Sigma_c(\mathbf{K}, i\omega_n) = \begin{pmatrix} \Sigma_c(\mathbf{K}, i\omega_n) & \phi_c(\mathbf{K}, i\omega_n) \\ \phi_c^*(\mathbf{K}, -i\omega_n) & -\Sigma_c^*(\mathbf{K}, i\omega_n) \end{pmatrix}. \quad (23)$$

Here, the diagonal parts  $\Sigma_c(\mathbf{K}, i\omega_n)$  describe the usual quasiparticle renormalization, while the off-diagonal parts  $\phi_c(\mathbf{K}, i\omega_n)$  contain information about the momentum and frequency dependence of the pairing state. As in the normal state, the coarse-grained Green function

$$\bar{\mathbf{G}}(\mathbf{K}, i\omega_n) = \frac{N_c}{N} \sum_{\mathbf{k} \in \mathcal{P}_{\mathbf{K}}} \mathbf{G}(\mathbf{k}, i\omega_n) = \begin{pmatrix} \bar{G}(\mathbf{K}, i\omega_n) & \bar{F}(\mathbf{K}, i\omega_n) \\ \bar{F}^*(\mathbf{K}, -i\omega_n) & -\bar{G}^*(\mathbf{K}, i\omega_n) \end{pmatrix} \quad (24)$$

is then used to calculate the corresponding non-interacting (cluster-excluded) Green function matrix

$$\mathcal{G}_0(\mathbf{K}, i\omega_n) = (\bar{\mathbf{G}}^{-1}(\mathbf{K}, i\omega_n) + \Sigma_c(\mathbf{K}, i\omega_n))^{-1}. \quad (25)$$

To calculate  $\Sigma_c(\mathbf{K}, i\omega_n)$ , an effective cluster model is set up using  $\mathcal{G}_0$  together with the interaction  $U$

$$\begin{aligned} S[\Psi^*, \Psi] = & - \int_0^\beta d\tau \int_0^\beta d\tau' \sum_{ij} \Psi_i^\dagger(\tau) \mathcal{G}_{0,ij}(\tau - \tau') \Psi_j(\tau') \\ & + \frac{U}{2} \int_0^\beta d\tau \sum_i [\Psi_i^\dagger(\tau) \sigma_3 \Psi_i(\tau)] [\Psi_i^\dagger(\tau) \sigma_3 \Psi_i(\tau)], \end{aligned} \quad (26)$$

where the  $\Psi_i^\dagger$  and  $\Psi_i$  are spinors  $\Psi_i^\dagger = (\phi_{i\uparrow}^*, \phi_{i\downarrow})$  of Grassmann variables  $\phi_{i\sigma}^\dagger$  and  $\phi_{i\sigma}$  which generate coherent states corresponding to the fermionic operators  $c_{i\sigma}^\dagger$  and  $c_{i\sigma}$ , respectively. From this, the cluster Green function

$$\mathbf{G}_{c,ij}(\tau - \tau') = \frac{1}{Z} \int \mathcal{D}[\Psi^* \Psi] \Psi_i(\tau) \Psi_j(\tau') e^{-S[\Psi^*, \Psi]} \quad (27)$$

where

$$Z = \int \mathcal{D}[\Psi^* \Psi] e^{-S[\Psi^*, \Psi]} \quad (28)$$

is the partition function, is calculated using a cluster solver algorithm, such as e.g., a QMC algorithm [13] or a non-crossing approximation (NCA) [14], and used to determine the cluster self-energy

$$\Sigma_c(\mathbf{K}, i\omega_n) = \mathcal{G}_0^{-1}(\mathbf{K}, i\omega_n) - \mathbf{G}_c^{-1}(\mathbf{K}, i\omega_n). \quad (29)$$

Then, just as in the normal state, using this new result for  $\Sigma_c(\mathbf{K}, i\omega_n)$  in Eq. (22), steps (22) to (29) are iterated to self-consistency. After convergence, the superconducting order parameter

$$\bar{\Delta}(\mathbf{K}) = \frac{N_c}{N} \sum_{\mathbf{k} \in \mathcal{P}_K} \langle c_{\mathbf{k}\uparrow} c_{-\mathbf{k}\downarrow} \rangle = \bar{F}(\mathbf{K}, \tau = 0) \quad (30)$$

is calculated from the coarse-grained anomalous Green function  $\bar{F}$ .

Two notes are in order:

- Usually one is interested in an instability to a superconducting phase in the absence of an external pair-field, i.e., spontaneous  $U(1)$  gauge symmetry breaking. In this case, the calculation is initialized with a finite pair-field  $\eta(\mathbf{k})$  with a given momentum structure. After the first few iterations, the pair-field is switched off, and the system relaxes. If the calculation converges to a finite order parameter  $\bar{\Delta}(\mathbf{K})$ , the system is in the superconducting phase, otherwise it is in the normal state.
- The symmetry of the superconducting order is given by the momentum structure of the coarse-grained  $\bar{\Delta}(\mathbf{K})$  and therefore restricted by the cluster size and geometry. In the case of the DMFT, when  $N_c = 1$ ,  $\bar{\Delta}(\mathbf{K}) = \bar{\Delta}$  is local, and therefore only superconducting states with a local contribution such as  $s$ -wave or extended  $s$ -wave can be described. Larger clusters are necessary to describe order parameters with a symmetry less than the lattice symmetry. For example, a  $2 \times 2$  cluster is the smallest cluster to describe phases with a  $d_{x^2-y^2}$ -wave symmetry which transforms according to  $\cos k_x - \cos k_y$ .

As a typical example of such a calculation, Fig. 4 shows DCA results from Ref. [14] for the superconducting state of a 2D Hubbard model with  $U = 12t$  and electron filling  $\langle n \rangle = 0.81$  for a temperature  $T = 0.05t$ . These results were obtained with a non-crossing approximation to solve the DCA effective cluster problem on an  $N_c = 4$  site  $2 \times 2$  cluster [15]. One sees that the anomalous Green function  $\bar{F}(\mathbf{K}, \omega) \equiv \bar{G}_{12}(\mathbf{K}, i\omega_n)$  is finite, switches sign between  $\mathbf{K} = (\pi, 0)$  and  $(0, \pi)$ , and vanishes for  $\mathbf{K} = 0$  and  $(\pi, \pi)$ . This is exactly what one expects for

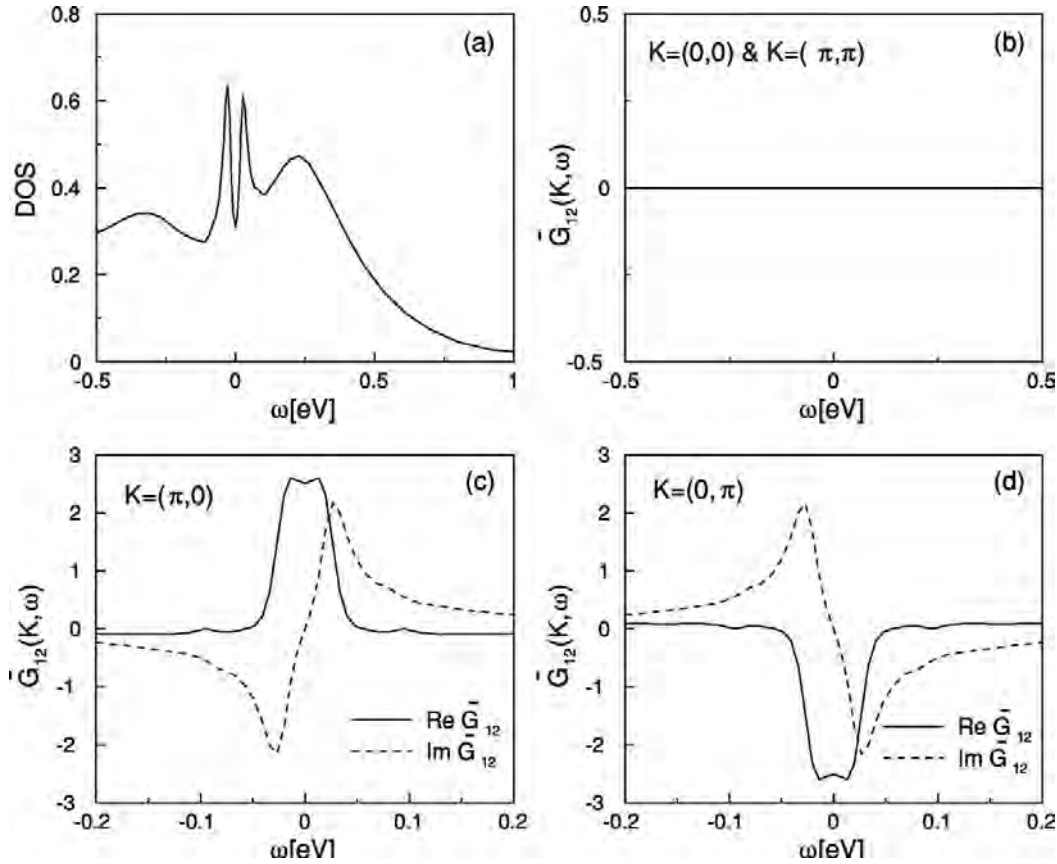


**Fig. 4:  $d$ -wave superconducting state in a 2D Hubbard model: DCA/NCA calculation for an  $N_c = 4$  site  $2 \times 2$  cluster.** Density of states near the chemical potential (a), and coarse-grained anomalous Green function  $\bar{G}_{12}(\mathbf{K}, i\omega_n \rightarrow \omega + i\delta) \equiv \bar{F}(\mathbf{K}, \omega + i\delta)$  (b), (c), and (d) for a system with electron filling  $\langle n \rangle = 0.81$ , temperature  $T = 0.05t$  and Coulomb repulsion  $U = 12t$  for the different cluster momenta  $\mathbf{K}$ . Figure from [14].

a  $d_{x^2-y^2}$ -wave order parameter that transforms according to  $\Delta(\mathbf{k}) \propto \cos k_x - \cos k_y$ . Since the DCA patches about  $\mathbf{K} = 0$  and  $(\pi, \pi)$  contain equal parts of positive and negative contributions of  $\Delta(\mathbf{k})$ , the coarse-grained result averaged over these patches vanishes, while  $\Delta(\mathbf{k})$  has the same sign over each of the patches centered at  $(\pi, 0)$  and  $(0, \pi)$  and switches sign between them. The superconducting gap that arises from the finite pair amplitude is reflected in the density of states (DOS) shown in the upper left panel, where the lower Hubbard subband of the full spectrum is shown.

## 2.4 Pair-field susceptibility

An alternative way to identify an instability towards a superconducting phase (or any symmetry broken phase for that matter) is to calculate the response of the system to an applied field (pair-field in the case of superconductivity), i.e., the susceptibility, and then extrapolate that response to the limit of a vanishing field. Spontaneous symmetry breaking occurs when the susceptibility diverges in that limit.

### General formalism

In linear response theory, the superconducting response to an external pair-field  $\eta_\alpha$ , where  $\alpha$  specifies the symmetry ( $s$ -wave,  $d$ -wave, etc.), is given by the pair-field susceptibility

$$P_\alpha(T) = \int_0^\beta d\tau \langle \Delta_\alpha(\tau) \Delta_\alpha^\dagger(0) \rangle \quad (31)$$

since the pair-field  $\eta_\alpha$  couples to the pairing operator

$$\Delta_\alpha^\dagger = \frac{1}{\sqrt{N}} \sum_{\mathbf{k}} g_\alpha(\mathbf{k}) c_{\mathbf{k}\uparrow}^\dagger c_{-\mathbf{k}\downarrow}^\dagger, \quad (32)$$

and we are interested in the response  $\Delta_\alpha$  of the system to the pair-field. Here  $g_\alpha(k)$  is the form-factor corresponding to the symmetry of interest, i.e.,  $g_d(\mathbf{k}) = \cos k_x - \cos k_y$  for a  $d_{x^2-y^2}$  state, for example. Instead of calculating the correlation function in Eq. (31) directly, the pair-field susceptibility may be calculated within the formalism described in then previous section 2.3. This is done by keeping the external pair-field  $\eta_\alpha$  finite throughout the calculation and measuring the order parameter  $\Delta_\alpha$  at convergence. If this is done for a number of different magnitudes of the external field  $\eta_\alpha$ , one has information on the  $\eta_\alpha$  dependence of the order parameter  $\Delta_\alpha(\eta_\alpha)$ . The pair-field susceptibility  $P_\alpha$  may then be extracted from the limit of vanishing pair-field as  $P_\alpha = \left. \frac{d\Delta_\alpha(\eta_\alpha)}{d\eta_\alpha} \right|_{\eta_\alpha \rightarrow 0}$ .

Alternatively, one may calculate the correlation function in Eq. (31) directly in the normal state of the system. This does not require the Nambu-Gorkov formalism discussed in Sec. 2.3, i.e., the calculation may be carried out in the normal state. What is required, however, is a calculation of the 4-point two-particle Green function [10]

$$G_{2,\sigma_1 \dots \sigma_4}(x_1, x_2; x_3, x_4) = -\langle T_\tau c_{\sigma_1}(x_1) c_{\sigma_2}(x_2) c_{\sigma_3}^\dagger(x_3) c_{\sigma_4}^\dagger(x_4) \rangle, \quad (33)$$

where the combined index  $x_i = (\mathbf{X}_i, \tau_i)$  has both spatial  $\mathbf{X}_i$  and imaginary time  $\tau_i$  coordinates. Fourier-transforming on both the space and time variables gives  $G_{2,\sigma_1 \dots \sigma_4}(k_4, k_3; k_2, k_1)$  with  $k = (\mathbf{k}, i\omega_n)$ . From this, one may then calculate the pair-field susceptibility as

$$P_\alpha(T) = \frac{T^2}{N^2} \sum_{\mathbf{k}, \mathbf{k}'} g_\alpha(\mathbf{k}) G_{2,\uparrow\downarrow\uparrow}(k, -k, -k', k') g_\alpha(\mathbf{k}'). \quad (34)$$

The way  $G_2$  is calculated in the DCA algorithm is similar to the way  $G$  is calculated at the single-particle level. Just as the Dyson equation (7) relates the Green function to the self-energy, the Bethe-Salpeter equation (BSE) relates  $G_2$  to the irreducible particle-particle vertex function  $\Gamma^{\text{pp}}(k, -k; -k', k')$ . It reads

$$\begin{aligned} G_{2,\uparrow\downarrow\uparrow}(k, -k, -k', k') &= G_\uparrow(k) G_\downarrow(-k) \delta_{k,k'} + \frac{T}{N} \sum_{\mathbf{k}''} G_\uparrow(k) G_\downarrow(-k) \\ &\times \Gamma^{\text{pp}}(k, -k, -k'', k'') G_{2,\uparrow\downarrow\uparrow}(k'', -k'', -k', k') \end{aligned} \quad (35)$$

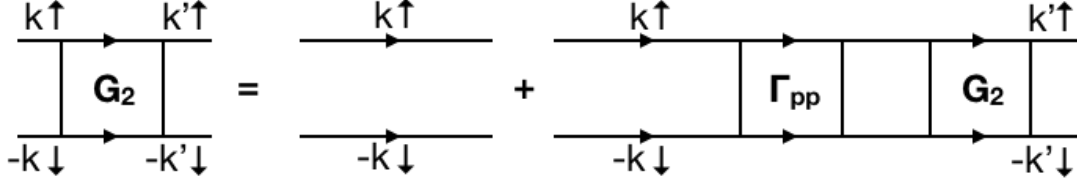


**Fig. 5: Feynman diagrams for the Bethe-Salpeter equation:** The two-particle Green function  $G_2$  in the particle-particle channel on the left hand side has a bare contribution (first diagram on the right-hand side) that describes the propagation of a pair of electrons in time-reversed momentum and spin states, and a vertex contribution (second diagram) that describes the (repeated) scattering of the pair due to the interactions in the Hamiltonian.

and is schematically shown in Fig. 5. This equation describes the propagation of a pair of electrons in time-reversed momentum and spin states and the repeated scattering of this pair due to the Coulomb term in the Hamiltonian.

Just as the self-energy  $\Sigma(\mathbf{k}, i\omega_n)$  is approximated by the cluster self-energy  $\Sigma_c(\mathbf{K}, i\omega_n)$ , the irreducible vertex function  $\Gamma^{\text{pp}}$  is approximated by the corresponding cluster irreducible vertex function [10]

$$\Gamma^{\text{pp}}(k, -k, -k', k') \approx \Gamma_c^{\text{pp}}(K, -K, -K', K'), \quad (36)$$

where  $K = (\mathbf{K}, i\omega_n)$  and  $K' = (\mathbf{K}', i\omega_{n'})$ . Just as the self-energy, the cluster irreducible vertex  $\Gamma_c^{\text{pp}}$  is determined from the solution of the cluster problem, i.e., by calculating the cluster two-particle correlation function

$$G_{2c, \uparrow\downarrow\uparrow}(K, -K, -K', K') = G_{c, \uparrow}(K) G_{c, \downarrow}(-K) \delta_{K, K'} + \frac{T}{N_c} \sum_{K''} G_{c, \uparrow}(K) G_{c, \downarrow}(-K) \quad (37)$$

$$\times \Gamma_{c, pp}(K, -K, -K'', K'') G_{2c, \uparrow\downarrow\uparrow}(K'', -K'', -K', K').$$

Defining  $[\mathbf{G}_{2c}]_{K, K'} \equiv G_{2c, \uparrow\downarrow\uparrow}(K, -K, -K', K')$ ,  $[\mathbf{G}_{2c}^0]_{K, K'} = G_{c, \uparrow}(K) G_{c, \downarrow}(-K) \delta_{K, K'}$  and  $[\Gamma_c^{\text{pp}}]_{K, K'} = \frac{T}{N_c} \Gamma_c^{\text{pp}}(K, -K, -K', K')$ , and writing Eq. (37) in matrix notation in  $K, K'$ , one then has

$$\Gamma_{c, pp} = [\mathbf{G}_{2c}^0]^{-1} - [\mathbf{G}_{2c}]^{-1}. \quad (38)$$

Using the cluster vertex  $\Gamma_c^{\text{pp}}(K, -K, -K', K')$  in the BSE for the lattice  $G_2$ , one can then calculate the coarse-grained two-particle Green function for the lattice

$$\bar{G}_{2, \uparrow\downarrow\uparrow}(K, -K, -K', K') = \frac{N_c^2}{N^2} \sum_{\mathbf{k} \in \mathcal{P}_K} \sum_{\mathbf{k}' \in \mathcal{P}_{K'}} G_{2, \uparrow\downarrow\uparrow}(\mathbf{k}, -\mathbf{k}, -\mathbf{k}', \mathbf{k}') \quad (39)$$

$$= \bar{G}_{2, \uparrow\downarrow}^0(K) \delta_{K, K'} + \frac{T}{N_c} \sum_{K''} \bar{G}_{2, \uparrow\downarrow}^0(K)$$

$$\times \Gamma_c^{\text{pp}}(K, -K, -K'', K'') \bar{G}_{2, \uparrow\downarrow\uparrow}(K'', -K'', -K', K').$$

with the coarse-grained bare propagator

$$\bar{G}_{2, \uparrow\downarrow}^0(K) = \frac{N_c}{N} \sum_{\mathbf{k} \in \mathcal{P}_K} G_{\uparrow}(\mathbf{k}) G_{\downarrow}(-\mathbf{k}). \quad (40)$$

Here we used the fact the cluster vertex  $\Gamma_c^{\text{pp}}(K, -K, -K', K')$  only depends on the cluster momenta  $\mathbf{K}$  and  $\mathbf{K}'$  so that the sum over  $\mathbf{k}''$  in Eq. (35) can be partially carried out over the patches. The coarse-grained  $G_2$  may then be inserted into Eq. (34) to obtain

$$P_\alpha(T) = \frac{T^2}{N_c^2} \sum_{K, K'} \bar{g}_\alpha(\mathbf{K}) \bar{G}_{2, \uparrow\downarrow\uparrow}(K, -K, -K', K') \bar{g}_\alpha(\mathbf{K}'), \quad (41)$$

where we have separately coarse-grained the form factor  $\bar{g}_\alpha(\mathbf{K}) = N_c/N \sum_{\mathbf{k} \in \mathcal{P}_K} g_\alpha(\mathbf{k})$ . Note that one can also take into account the full  $\mathbf{k}$  dependence of  $g_\alpha(\mathbf{k})$  by using the modified algorithm discussed in Ref. [10].

### Bethe-Salpeter eigenvalues and eigenfunctions

Writing Eq. (39) in matrix form

$$\bar{\mathbf{G}}_2 = [\mathbb{1} - \bar{\mathbf{G}}_{2, \uparrow\downarrow}^0 \mathbf{\Gamma}_c^{\text{pp}}]^{-1} \bar{\mathbf{G}}_{2, \uparrow\downarrow}^0 = \bar{\mathbf{G}}_{2, \uparrow\downarrow}^0 [\mathbb{1} - \mathbf{\Gamma}_c^{\text{pp}} \bar{\mathbf{G}}_{2, \uparrow\downarrow}^0]^{-1} \quad (42)$$

we see that a divergence in  $\bar{\mathbf{G}}_2$  occurs when the term in brackets vanishes. Eq. (42) can be recast in terms of the left ( $\Phi_\alpha^L$ ) and right eigenvectors ( $\Phi_\alpha^R$ ) of the “pairing matrix”  $\mathbf{\Gamma}_c^{\text{pp}} \bar{\mathbf{G}}_{2, \uparrow\downarrow}^0$ , where, for example,  $\Phi_\alpha^R$  is determined from [16]

$$-\frac{T}{N_c} \sum_{K'} \Gamma_{c, pp}(K, K') \bar{G}_{2, \uparrow\downarrow}^0(K') \phi_\alpha^R(K') = \lambda_\alpha \phi_\alpha^R(K). \quad (43)$$

By transforming the term in brackets in Eq. (42) onto this eigenbasis of the pairing matrix, one can write Eq. (42) as

$$G_{2, \uparrow\downarrow\uparrow}(K, K') = \bar{G}_{2, \uparrow\downarrow}^0(K) \sum_\alpha \frac{\phi_\alpha^R(K) \phi_\alpha^L(K')}{1 - \lambda_\alpha}. \quad (44)$$

Since the pair-field susceptibility is given by Eq. (41), we see that a superconducting instability occurs when the leading eigenvalue  $\lambda_\alpha$  becomes equal to one, and the symmetry of the corresponding state is determined by the momentum and frequency structure of  $\phi_\alpha^R(K)$  and  $\phi_\alpha^L(K)$ . This approach is in many ways more powerful than calculating the response function directly, because here, one does not have to assume a given form factor  $g_\alpha(\mathbf{k})$  and therefore cannot “miss” the structure of the dominant correlations.

We note the similarity of Eq. (43) to the familiar BCS gap equation

$$-\frac{1}{N} \sum_{\mathbf{k}'} \frac{V(\mathbf{k}, \mathbf{k}') \tanh\left(\frac{\beta}{2} E_{\mathbf{k}'}\right) \Delta(\mathbf{k}')}{2E_{\mathbf{k}'}} = \Delta(\mathbf{k}'), \quad (45)$$

where  $V(\mathbf{k}, \mathbf{k}')$  is the pairing interaction, which is essentially given by the low frequency limit of  $\Gamma^{\text{pp}}(k, k')$ ,  $E_{\mathbf{k}}$  the Bogoliubov quasiparticle energy that is encoded in the Green function  $G(\mathbf{k})$ , and  $\Delta(\mathbf{k})$  the superconducting energy gap. In fact, Eq. (45) is derived from a Bethe-Salpeter equation in the superconducting state analogous to the normal state equation (43) under a number of simplifying assumptions. Hence, we see that the leading eigenvector  $\phi_{\text{lead}}(K) \equiv \phi_{\text{lead}}^R(K)$  is the normal state analog to the superconducting gap  $\Delta(\mathbf{k})$ . Close to the transition at  $T = T_c$ , they are equivalent.

### 3 Superconductivity in the 2D Hubbard model

We now demonstrate how the DMFT and DCA approaches have been used to investigate unconventional superconductivity in the simplest model of correlated electron systems, the 2D Hubbard model given by the Hamiltonian in Eq. (1) on a square lattice. We start by discussing the attractive model, which has  $U < 0$ , and then turn to the repulsive model with  $U > 0$ . While the former should be viewed as a toy model to study pairing, the latter has been studied extensively in the context of the high- $T_c$  cuprates.

#### 3.1 Attractive Hubbard model

The Hamiltonian of the attractive Hubbard model is given by the Hamiltonian in Eq. (1) with an attractive local Coulomb interaction  $U < 0$ . Since the Coulomb interaction between electrons is repulsive, i.e. positive, the negative  $U$  interaction should be considered an effective interaction that may result from integrating out other degrees of freedom, such as phonons in the case of the BCS model. In contrast to this case, however, the interaction  $U$  is an instantaneous static interaction without frequency dependence. Since the interaction between the electrons is explicitly attractive, this model provides an interesting toy model and testbed to study the superconducting phase transition as a function of the electron filling  $\langle n \rangle$  and interaction strength  $|U|/t$ .

In fact, this problem has been studied extensively in the literature (see, e.g., Ref. [17] and references therein). As this model does not suffer from the usual fermionic negative sign problem, large scale quantum Monte Carlo simulations have been used to study the temperature versus  $|U|$  phase diagram. One generally finds a finite temperature phase transition to a superconducting phase at finite doping  $\langle n \rangle < 1$ , while at half-filling  $\langle n \rangle = 1$ , this phase is suppressed to zero temperature by its degeneracy (due to particle-hole symmetry) with a charge-density wave (CDW) phase. As one moves away from half-filling, CDW correlations are suppressed and the superconducting  $T_c$  rises sharply. Since the pairing interaction  $U$  between electrons is local, one finds that the superconducting phase has  $s$ -wave symmetry, i.e., the Cooper pairs forming this state are local.

Because we are in 2D, for which the Mermin-Wagner theorem [18] forbids a finite temperature transition to a phase in which a continuous symmetry is broken, such as the  $U(1)$  gauge symmetry that is broken in the superconducting phase, the instability instead is a Kosterlitz-Thouless (KT) transition [19,20] to a superconducting state in which the correlations decay algebraically. DMFT and DCA calculations, however, do not obey the Mermin-Wagner theorem. They neglect the long range, beyond mean-field fluctuations that lead to the destruction of long-range order at finite temperature, the fundamental reason for this theorem. Due to their mean-field character, DMFT and DCA instead display mean-field type transitions. In DCA calculations, however, non-local fluctuations are taken into account up to the size of the cluster, and one may see KT behavior in a finite region above  $T_c$ , where the correlations are limited in range to within the cluster. Close to  $T_c$ , when the correlation length exceeds the cluster size, however, the KT behavior changes over to mean-field behavior.



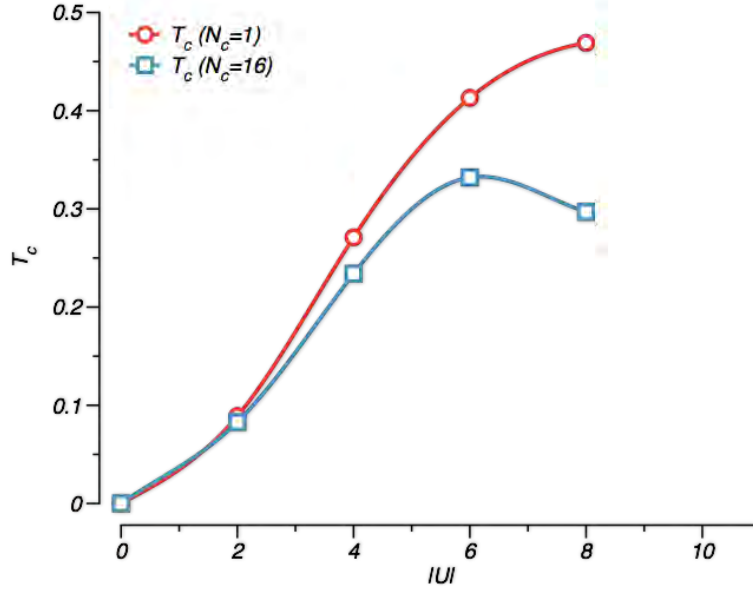


**Fig. 6: Superconductivity in the attractive Hubbard model:** Transition temperature  $T_c$  in the negative  $U$  Hubbard model versus  $|U|$  at a filling of  $\langle n \rangle = 0.85$  calculated with DCA/QMC.  $T_c$  keeps rising with  $|U|$  in the DMFT ( $N_c = 1$ ) limit, while non-local fluctuations on the  $4 \times 4$ -cluster DCA calculation start suppressing  $T_c$  at larger  $|U|$ .

Fig. 6 shows the results of single-site DMFT ( $N_c = 1$ ) and  $4 \times 4$ -site DCA ( $N_c = 16$ ) calculations of  $T_c$  in an attractive Hubbard model with nearest-neighbor hopping  $t$  and electron filling  $\langle n \rangle = 0.85$ . Here  $T_c$  for the  $s$ -wave superconducting state was determined from the temperature  $T$  at which leading eigenvalue  $\lambda_s(T)$  of the Bethe-Salpeter equation (43) crosses one. We see that in both cases,  $T_c$  initially rises with increasing  $|U|$ . This is expected, since the increasing pair binding energy  $\sim |U|$  leads to an increasing energy reduction associated with forming a superconducting phase, so that it occurs at higher temperatures.

At larger  $|U|$ , however, one observes different behavior: While  $T_c$  keeps rising for  $N_c = 1$ , it already starts to level off a bit. For  $N_c = 16$ , one even sees non-monotonic behavior, where  $T_c$  falls again after reaching a maximum for  $|U| \sim 6t$ . How can we understand this behavior, given the fact that with increasing  $|U|$ , the pair-binding energy keeps increasing? This behavior is known as the BCS-BEC crossover [21], where BEC stands for Bose-Einstein condensation. For small attractive interactions  $U$ , the physics is well described by BCS theory. The Cooper pairs are weakly bound and their size, determined by the superconducting coherence length  $\sim 1/|U|$ , is large. Therefore, the pairs have large spatial overlap, and as soon as they form, they become phase coherent. In contrast, in the large  $|U|$  regime, the pairs are tightly bound and much more local objects. Hence, they have a harder time to become phase coherent, since the phase of individual pairs can fluctuate more easily. In this case, even though the pair-binding energy is large,  $T_c$  is suppressed, since phase coherence does not set in until lower temperatures are reached. DMFT only describes the spatially local aspect of this physics, i.e., phase fluctuations in time. Instead, the finite size clusters in the DCA also know about the spatial aspect of this physics, i.e., phase fluctuations of local pairs on different sites. This explains why  $T_c$  is reduced in the 16-site cluster relative to the single-site results.

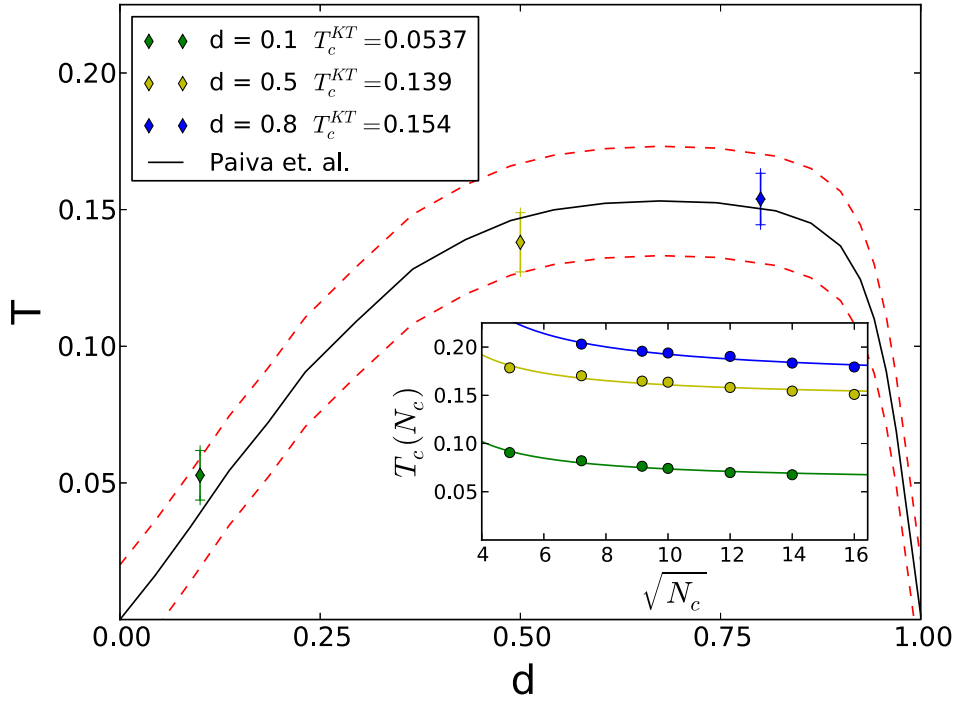


**Fig. 7: Kosterlitz-Thouless transition temperature in the attractive Hubbard model:**  $T_c^{KT}$  for different electron densities  $d = \langle n \rangle$  for  $U = -4t$  calculated with  $DCA^+/QMC$ . The results were obtained by calculating  $T_c(N_c)$  from the leading ( $s$ -wave) eigenvalue of the Bethe-Salpeter equation for different cluster sizes  $N_c$  and extrapolating the results to the exact  $N_c \rightarrow \infty$  limit, where they compare well with finite size lattice DQMC calculations by Paiva *et al.* Figure from [22].

In fact, for even larger clusters one would expect  $T_c$  to drop even more. An example of this is shown in Fig. 7, which displays the results of a  $DCA^+$  calculation of  $T_c$  versus electron filling  $d \equiv \langle n \rangle$  for  $U = -4$ . The inset shows the linear cluster size ( $\sqrt{N_c}$ ) dependence of  $T_c$  for different  $\langle n \rangle$ , and one sees that  $T_c$  keeps dropping with increasing cluster size. For a filling of  $\langle n \rangle = 0.8$ , close to the filling used in Fig. 6, we see that  $T_c \sim 0.25$  for  $U = -4$  drops to  $\sim 0.15$  in the infinite cluster size limit. Here,  $T_c(N_c)$  was again determined from  $\lambda_s(T_c(N_c)) = 1$  and the (exact) infinite cluster size limit  $T_c(N_c \rightarrow \infty) \equiv T_{KT}$  is obtained from fitting the  $T_c(N_c)$  curves with the expected KT behavior [19, 20]

$$T_c(N_c) = T_{KT} + \frac{A}{[B + \log(\sqrt{N_c})]^2}. \quad (46)$$

Here, we have assumed that the transition at finite  $N_c$  occurs at the temperature  $T_c(N_c)$ , at which the superconducting correlation length reaches the linear cluster size. The log arises from the fact that this correlation length has an exponential temperature dependence in the KT case.

The main panel in Fig. 7 shows  $T_c$  for different  $\langle n \rangle$  determined this way. Also shown are results from finite size lattice determinant QMC calculations by Paiva *et al.* (solid black curve) [17]. We see that the  $DCA^+$  results agree very well with those of Paiva *et al.*, showing that the DCA approximation and the procedures used to determine  $T_c$  provide reliable results.

### 3.2 Repulsive Hubbard model

We now turn to the 2D repulsive Hubbard model. Its Hamiltonian is given by Eq. (1) with  $U > 0$ . Unlike the attractive model, there is no explicitly attractive interaction in this model that could lead to superconductivity. Rather, the only interaction that is present is repulsive. Nevertheless, this model has been investigated extensively in the context of superconductivity, because it is commonly believed to provide a generic and the simplest description of the physics of cuprate high-temperature superconductors [9].

So how can a model with only a repulsive interaction have a superconducting instability? Various cluster DMFT and DCA studies have been concerned with addressing this question. Since the local Coulomb repulsion  $U$  in this model is large (a realistic description of the cuprates requires  $U/t \gtrsim 6$ ), an  $s$ -wave superconducting state, in which the electrons are paired on the same site, is energetically unfavorable. Rather, one expects a state in which the electrons are paired on different sites. Since DMFT can only describe local order parameters, it is not adequate to study superconductivity in this model. Rather, one needs to use cluster extensions of DMFT, and here we focus on DCA studies of this problem.

#### Superconducting instability

If the Hubbard model is supposed to describe the cuprate high-temperature superconductors, then it should have a superconducting instability to a  $d_{x^2-y^2}$ -wave state with a  $\cos k_x - \cos k_y$  momentum structure. By Fourier-transforming to real space, we see that in this state, the electrons are paired on nearest-neighbor sites with a  $d_{x^2-y^2}$  phase (+1 along  $\pm x$  and -1 along  $\pm y$ ). Thus, one needs at least a 4-site  $2 \times 2$  cluster to describe this state. The earliest DCA calculations of this problem were therefore done for a  $2 \times 2$  cluster. The left panel in Fig. 8 shows the temperature versus doping  $\delta = 1 - \langle n \rangle$  phase diagram of the 2D Hubbard model with  $U/t = 8$  that resulted from this DCA  $N_c = 4$  study [23]. And indeed, it has an extended  $d_{x^2-y^2}$ -wave superconducting phase at finite doping  $\delta$  below the critical temperature  $T_c$ . Here  $T_c$  is the temperature  $T$  where the pair-field susceptibility in Eq. (41),  $P_d(T)$ , with a  $d_{x^2-y^2}$ -wave form factor  $g_d(\mathbf{K}) = \cos K_x - \cos K_y$  diverges.

In addition, the phase diagram has an antiferromagnetic phase below the Néel temperature  $T_N$ . This phase transition was determined in an analogous manner to that for the superconducting phase, by calculating the spin susceptibility  $\chi_s(\mathbf{Q}, T) = \sum_{ij} e^{i\mathbf{Q}(\mathbf{x}_i - \mathbf{x}_j)} \int_0^\beta d\tau \langle \mathcal{T}_\tau S_i^z(\tau) S_j^z(0) \rangle$  for  $\mathbf{Q} = (\pi, \pi)$ , where  $S_i^z = (c_{i\uparrow}^\dagger c_{i\uparrow} - c_{i\downarrow}^\dagger c_{i\downarrow})/2$  is the usual  $z$ -component of the spin operator. This is done in the same manner as for the pair-field susceptibility, i.e., within the framework described in Sec. 2.4, by calculating the irreducible vertex (in the spin  $S = 1$  particle-hole channel) from the corresponding cluster susceptibility, and then using this vertex in the Bethe-Salpeter equation for the lattice susceptibility  $\chi_s(\mathbf{Q}, T)$  [10]. Even though the Mermin-Wagner theorem (see discussion in Sec. 3.1) does not allow for an antiferromagnetic phase at finite  $T$  in the purely 2D model, the mean-field character of the DCA leads to this phase transition at finite  $T$ . In the real cuprate materials, it is the coupling between the copper-oxygen planes that stabilizes this transition at finite  $T$ .

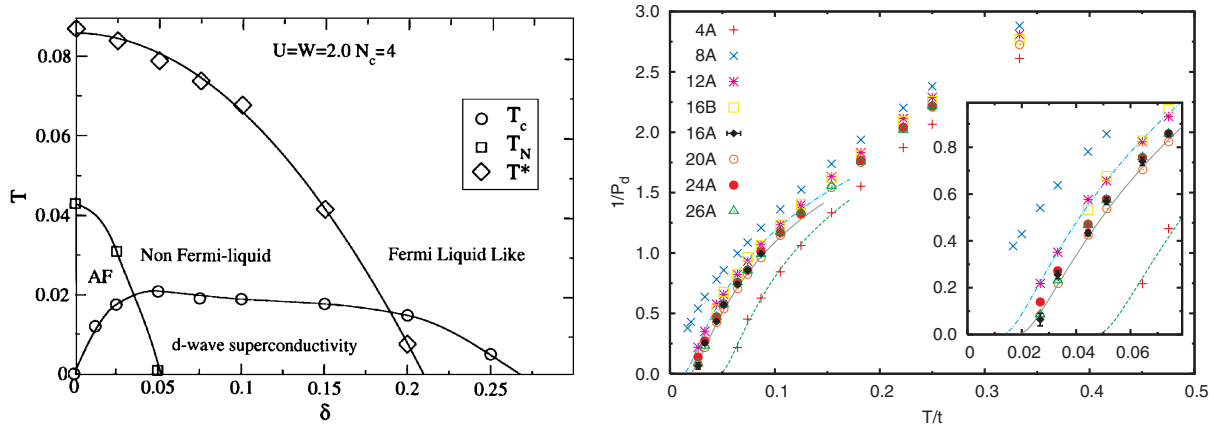


**Fig. 8: D-wave superconductivity in the 2D repulsive Hubbard model:** *Left panel:* The temperature  $T$  versus doping  $\delta = 1 - \langle n \rangle$  phase diagram calculated with DCA/QMC for a  $2 \times 2$  cluster with  $U = 8t$  has an antiferromagnetic phase near half-filling below  $T_N$ , a d-wave superconducting phase at finite doping below  $T_c$ , and pseudogap behavior in the normal state below  $T^*$ . *Right panel:* Temperature dependence of the inverse pair-field susceptibility  $1/P_d(T)$  calculated with DCA/QMC for different cluster sizes for  $U = 4t$  and  $\langle n \rangle = 0.9$ .  $T_c$  is only weakly dependent on cluster size  $N_c$  when  $N_c \gtrsim 12$ . Figures from [23] (left) and [24] (right).

The phase diagram also displays a line labeled  $T^*$ . This line does not indicate a phase transition. Rather, it indicates the temperature below which the bulk spin susceptibility  $\chi_s(\mathbf{Q} = 0, T)$  starts to drop when the system is further cooled. This exotic behavior is very different from the Pauli susceptibility of a normal metal, which is basically independent of temperature at low  $T$ . The downturn in  $\chi_s(\mathbf{Q} = 0, T)$  signals the opening of a pseudogap in the low energy spin excitations, which is also observed in various measurements in the cuprates [25]. In addition, at the same temperature  $T^*$ , the single-particle spectral function  $A(\mathbf{k}, \omega) = -\text{Im} G(\mathbf{k}, \omega + i\delta)/\pi$  starts to show a pseudogap, i.e., a partial suppression of spectral weight at the Fermi level  $\omega = 0$ . This is also observed in photoemission experiments in the cuprates, and provides evidence that not only the spin degree of freedom, but electronic excitations in general are suppressed at low energies. Thus, just like in the real materials, superconductivity in the Hubbard model emerges from an exotic state, which is very different from a normal metal.

Coming back to superconductivity, the question arises of what happens to the phase transition in more accurate calculations employing larger clusters when longer-ranged fluctuations are taken into account. Just like for the attractive Hubbard model, where the critical temperature is found to drop in larger clusters because of the inclusion of spatial phase fluctuations (see previous Sec. 3.1), we would expect  $T_c$  to fall when larger clusters are used. Does  $T_c$  go to zero or will it remain finite in the exact infinite size cluster limit? This question was first addressed with the larger cluster DCA calculations [24] of the pair-field susceptibility in a Hubbard model with  $U = 4t$  and  $\langle n \rangle = 0.9$  shown in the right panel of Fig. 8. Here, the temperature dependence of the inverse pair-field susceptibility  $1/P_d(T)$  is plotted for a number of different cluster sizes and shapes (indicated by the letters 'A' and 'B' following the cluster size, see Ref. [24]), and the lines are fits to the exponential KT behavior one expects in two

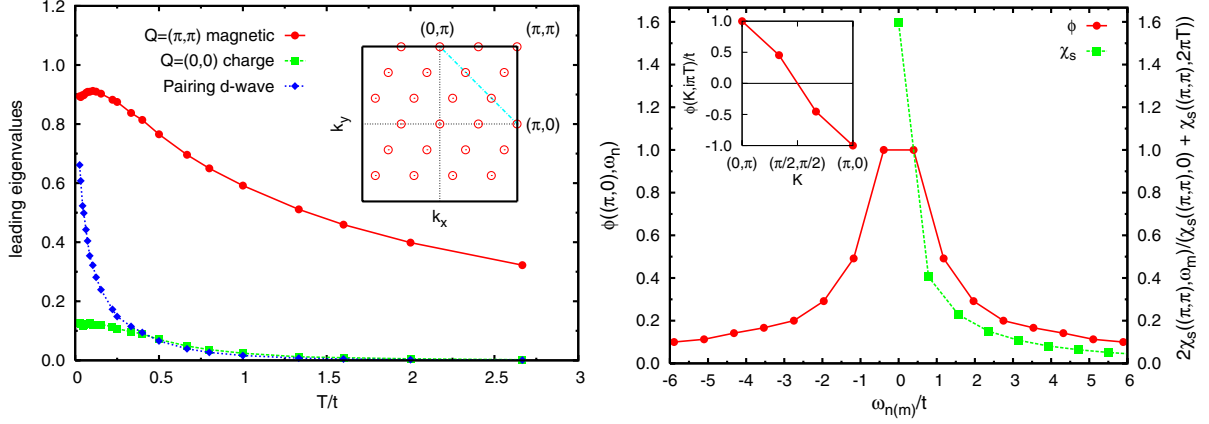


**Fig. 9: Dominant correlations in the 2D repulsive Hubbard model:** DCA/QMC results for a 24-site cluster with  $U = 4t$  and  $\langle n \rangle = 0.85$ . Left panel: Leading eigenvalues of the Bethe-Salpeter equation (43) in different channels. The  $\mathbf{Q} = 0$  pairing eigenvalue has  $d_{x^2-y^2}$ -wave symmetry and increases towards one at low temperatures. The  $\mathbf{Q} = (\pi, \pi)$  magnetic eigenvalue dominates but saturates at low temperatures, and the  $\mathbf{Q} = 0$  charge eigenvalue remains small. The inset shows the position of the cluster momenta  $\mathbf{K}$  in the 24-site cluster. Right panel: The frequency  $\omega_n = (2n + 1)\pi T$  dependence of the (normalized) leading  $d_{x^2-y^2}$ -wave pairing eigenvector  $\phi_d(\mathbf{K}, \omega_n)$  for  $T = 0.125t$  reflects the  $\omega_m = 2m\pi T$  dependence of the (normalized) antiferromagnetic spin susceptibility  $\chi_s(\mathbf{Q} = (\pi, \pi), \omega_m)$ . The inset shows the  $d_{x^2-y^2}$ -wave  $\cos K_x - \cos K_y$  momentum dependence of  $\phi_d(\mathbf{K}, \omega_n = \pi T)$  along the dashed line shown in the left inset. Figure from [26].

dimensions, i.e.,  $P_d(T) \sim \exp[2B/\sqrt{T - T_c}]$ . We see that  $1/P_d(T)$  goes to zero, i.e.,  $P_d(T)$  diverges, at a temperature  $T_c(N_c)$  for most clusters, with the 4-site cluster clearly showing the largest  $T_c \approx 0.05t$ . As expected, for larger clusters  $T_c$  falls but is stabilized when  $N_c \gtrsim 12$ , for which  $T_c \approx 0.02t$ . More recent calculations [22] using the DCA<sup>+</sup> extension were able to go to even larger clusters, and found similar results with similar  $T_c$  in the large cluster limit. These calculations were also done for larger  $U = 7t$ , for which a larger  $T_c \approx 0.05t$  was found. These calculations have thus provided evidence that the doped 2D Hubbard model has a  $d$ -wave superconducting instability at finite temperatures.

### Pairing mechanism

So far, the calculations we have discussed are “numerical experiments”, i.e., they show that a model, despite the presence of only repulsive interactions, can have a superconducting ground state, but do not give an answer to the question of what causes it. Unlike real experiments, however, we can directly analyze the effective interaction that gives rise to superconductivity in this model, i.e., the irreducible particle-particle vertex  $\Gamma^{pp}(K, K')$  that enters the Bethe-Salpeter equation (43) for the pair-field susceptibility. This vertex describes the scattering of a pair of electrons with momenta and spins  $(\mathbf{k} \uparrow, -\mathbf{k} \downarrow)$  to a pair of electrons with  $(\mathbf{k}' \uparrow, -\mathbf{k}' \downarrow)$  (see Fig. 5). As discussed in Sec. 2.4, we can also study the leading eigenvalue and -vector of the Bethe-Salpeter equation and thus obtain new insight into this question.

The left panel of Fig. 9 shows the temperature dependence of the leading eigenvalue  $\lambda_d(T)$  of the particle-particle Bethe-Salpeter equation (43) for  $U = 4t$ ,  $\langle n \rangle = 0.85$ , calculated with DCA in the 24-site cluster shown in the inset [26]. As one sees from the blue curve, it rises sharply at low temperatures and approaches one, consistent with the divergence in the pair-field susceptibility. One can also construct similar Bethe-Salpeter equations for the charge and magnetic particle-hole channels. The leading eigenvalues for these channels are shown in red ( $\mathbf{Q} = (\pi, \pi)$  magnetic) and green ( $\mathbf{Q} = 0$  charge). We see that the magnetic eigenvalue is initially dominant, approaches one, but then saturates at values smaller than one at low temperatures. The leading eigenvalue in the charge channel, in contrast, remains small over the entire temperature range. From this, we can conclude that antiferromagnetic and superconducting correlations are the dominant correlations in the system.

The momentum dependence of the eigenvector  $\phi_d(\mathbf{K}, \omega_n)$  corresponding to the leading pairing eigenvalue along the dashed line in the inset of the left panel is shown in the inset of the right panel. We see that it has a  $d_{x^2-y^2}$ -wave  $\cos K_x - \cos K_y$  dependence. We note that in contrast to the calculation of the pair-field susceptibility, where a  $d$ -wave form factor is assumed, here this comes out naturally. The Matsubara frequency dependence of the pairing eigenfunction  $\phi_d(\mathbf{K}, \omega_n)$  is shown in the main right panel and compared with the frequency dependence of the  $\mathbf{Q} = (\pi, \pi)$  magnetic susceptibility  $\chi_s(\mathbf{Q}, \omega_m)$ . From this we see that (1) the pairing is retarded, i.e., frequency dependent, and (2) the pairing dynamics reflects that of the antiferromagnetic spin fluctuations.

We can also study the momentum and frequency dependence of  $\Gamma^{\text{pp}}(\mathbf{K}, \omega_n, \mathbf{K}', \omega_{n'})$  directly. Its momentum dependence is shown for three different temperatures in Fig. 10. We see that  $\Gamma^{\text{pp}}(\mathbf{K}, \mathbf{K}')$  is peaked at large momentum transfer  $\mathbf{K} - \mathbf{K}' = (\pi, \pi)$ , and this peak increases in size as the temperature is lowered. This mirrors the growth of the antiferromagnetic spin fluctuations with decreasing temperature, as seen in the plot of  $\chi_s(\mathbf{Q} = (\pi, \pi), \omega_m = 0)$  in the same figure.

Interestingly, we see that the pairing interaction  $\Gamma^{\text{pp}}$  in momentum space is positive, that is, repulsive! One may then ask: How does a repulsive interaction give rise to pairing? The answer lies in its momentum structure. If we look at the Bethe-Salpeter equation (43), or its simpler version, the BCS gap equation (45), we see that for an interaction  $V(\mathbf{k}, \mathbf{k}') \equiv V$  that does not depend on momentum, a non-trivial solution  $\Delta(\mathbf{k}) \neq 0$  only exists if  $V < 0$ . This follows from the minus sign on the left hand side and the fact that the other terms under the sum are all positive. This is the case for the conventional BCS superconductors or the attractive Hubbard model discussed in Sec. 3.1, for which  $V < 0$  and the gap equation gives an  $s$ -wave gap  $\Delta(\mathbf{k}) \equiv \Delta$  without momentum dependence.

In contrast, the pairing interaction we find for the Hubbard model is positive and has momentum dependence. In particular, it increases with increasing momentum transfer  $\mathbf{k} - \mathbf{k}'$ . The Fermi surface of the doped Hubbard model is schematically shown in the right panel of Fig. 11. It is similar to that of the hole-doped cuprates. The pairing interaction  $V(\mathbf{k}, \mathbf{k}')$  scatters a pair with momenta  $(\mathbf{k}, -\mathbf{k})$  to a pair with momenta  $(\mathbf{k}', -\mathbf{k}')$  for  $\mathbf{k}$  and  $\mathbf{k}'$  near the Fermi surface and this scattering is strongest for a momentum transfer of  $\mathbf{k} - \mathbf{k}' = (\pi, \pi)$ . If the pairing gap  $\Delta(\mathbf{k}')$



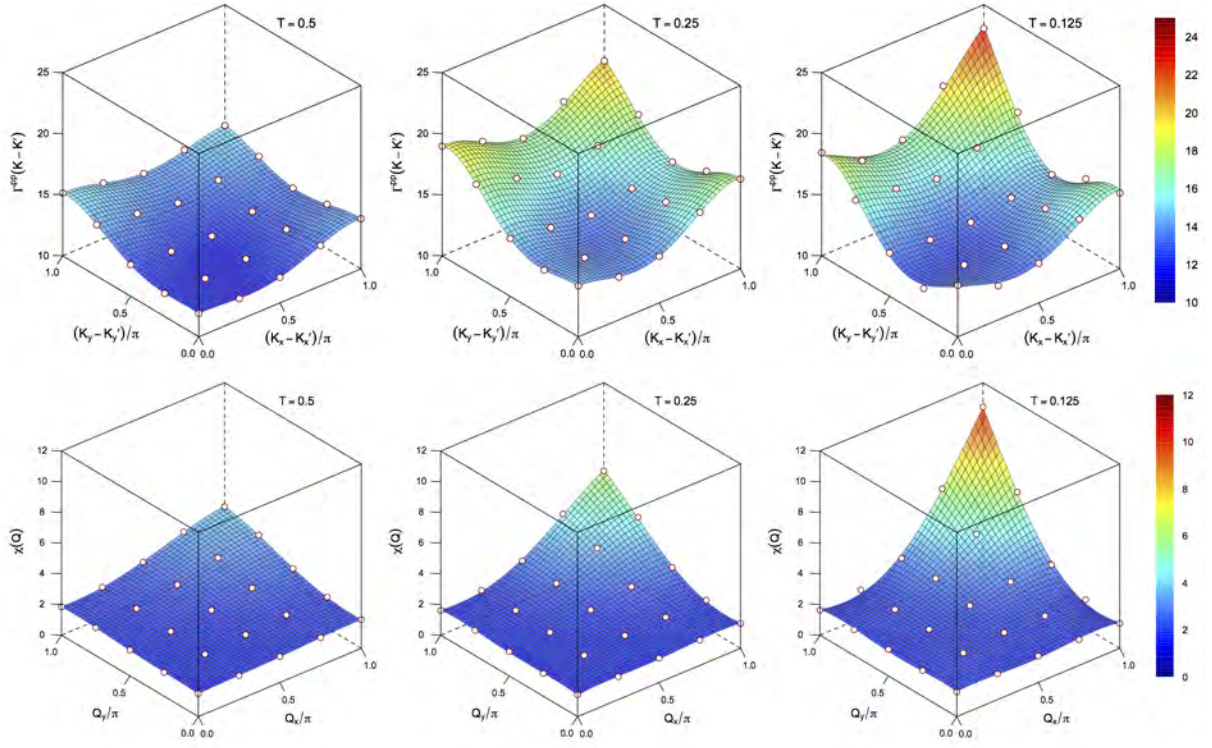


**Fig. 10: Momentum structure of the pairing interaction in the 2D Hubbard model:** *Top panel:*  $\mathbf{K} - \mathbf{K}'$  dependence of  $\Gamma^{\text{pp}}(\mathbf{K}, \mathbf{K}')$  for  $\omega_n = \omega_{n'} = \pi T$  calculated with DCA/QMC for a Hubbard model with  $U = 4t$  and  $\langle n \rangle = 0.85$  on a  $4 \times 4$  cluster for different temperatures. *Lower panel:*  $\mathbf{Q}$ -dependence of the spin susceptibility  $\chi_s(\mathbf{Q}, \omega_m = 0)$  for the same parameters. Both quantities display a similar increase near  $(\pi, \pi)$  as the temperature is lowered. Figure from [5].

is positive for  $\mathbf{k}' = (\pi, 0)$ , and  $V(\mathbf{k} - \mathbf{k}')$  predominantly scatters pairs from  $\mathbf{k}' = (\pi, 0)$  to  $\mathbf{k} = (0, \pi)$ , the gap equation has a non-trivial ( $\Delta(\mathbf{k}) \neq 0$ ) solution if  $\Delta(\mathbf{k}) < 0$  for  $\mathbf{k} = (0, \pi)$ . This is the case for a  $d_{x^2-y^2}$ -wave gap  $\Delta(\mathbf{k}) \sim \cos k_x - \cos k_y$ , which changes sign between  $\mathbf{k} = (\pi, 0)$  and  $(0, \pi)$ . Hence, the  $d_{x^2-y^2}$ -wave momentum structure of the gap arises naturally from a pairing interaction that is repulsive in momentum space and peaked at large momentum transfer. In fact a superconducting gap that changes sign on the Fermi surface generally signals a non-BCS like repulsive pairing interaction and therefore is taken as evidence for the presence of unconventional superconductivity [5].

How a repulsive pairing interaction that is peaked at  $(\pi, \pi)$  can lead to pairing can also be seen by Fourier-transforming the interaction  $\Gamma^{\text{pp}}(\mathbf{K}, \mathbf{K}')$  to real space, according to

$$\Gamma^{\text{pp}}(\ell_x, \ell_y) = \sum_{\mathbf{K}, \mathbf{K}'} e^{i\mathbf{K}\ell} \Gamma^{\text{pp}}(\mathbf{K}, \mathbf{K}') e^{i\mathbf{K}'\ell}, \quad (47)$$

for  $\omega_n = \omega_{n'} = \pi T$ . Here,  $\Gamma^{\text{pp}}(\ell_x, \ell_y)$  is the strength of the  $\omega_n = \omega_{n'} = \pi T$  pairing interaction between a singlet pair formed with one electron at the origin and the other at site  $(\ell_x, \ell_y)$ . It is shown in the right panel of Fig. 11. We see that this interaction is strongly repulsive for on-site

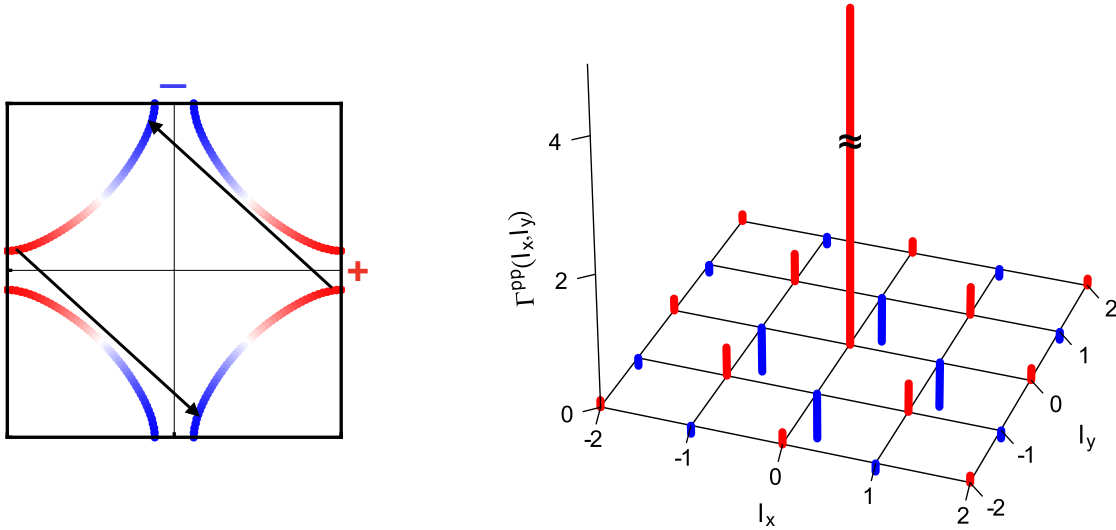


**Fig. 11: D-wave pairing from repulsive interactions:** *Left panel:* Sketch of how repulsive scattering at large momentum transfer gives rise to  $d_{x^2-y^2}$ -wave pairing for the Fermi surface of a hole-doped Hubbard model. For this case, a gap that changes sign between the regions near  $(\pi, 0)$  and  $(0, \pi)$  satisfies the BCS gap equation (45). *Right panel:* Real space Fourier-transform  $\Gamma^{\text{pp}}(\ell_x, \ell_y)$ , Eq. (47), of the pairing interaction  $\Gamma^{\text{pp}}(\mathbf{K}, \mathbf{K}')$  for  $\omega_n = \omega_{n'} = \pi T$  shown in Fig. 10 for  $T = 0.125t$ . Here red (blue) bars indicate positive (negative) values of  $\Gamma^{\text{pp}}(\ell_x, \ell_y)$  and the length of the bars corresponds to its magnitude. The pairing interaction is strongly repulsive for on-site pairs, but attractive when the electrons forming the pair sit on nearest-neighbor sites. Figure from [5].

pairs, but attractive (negative) if the electrons are on nearest-neighbor sites. At longer distances, the interaction keeps oscillating but falls off rapidly with distance.

We have seen that the momentum and frequency structure of the pairing interaction given by the irreducible particle-particle vertex  $\Gamma^{\text{pp}}(\mathbf{k}, \omega_n, \mathbf{k}', \omega_{n'})$  reflects that of the spin fluctuations described by the spin susceptibility  $\chi_s(\mathbf{q}, \omega_m)$ . In fact, from weak coupling theory, one expects that

$$\Gamma^{\text{pp}}(\mathbf{k}, \omega_n, \mathbf{k}', \omega_{n'}) \approx \frac{3}{2} \bar{U}^2 \chi_s(\mathbf{k} - \mathbf{k}', \omega_n - \omega_{n'}), \quad (48)$$

where  $\bar{U}$  is a coupling constant. This form of the pairing interaction is only approximate, i.e., it only accounts for a subset of the Feynman diagrams that enter  $\Gamma^{\text{pp}}$ . However, DCA studies have found that other contributions, such as the charge fluctuations, are negligible [16]. Hence, this approximate form has been shown to give a very good approximation of the “exact” DCA vertex  $\Gamma^{\text{pp}}$  and thus the resulting eigenvalues and -vectors of the Bethe-Salpeter equation, and therefore  $T_c$  [27]. One then speaks of a spin-fluctuation pairing interaction, in which the pairing is mediated by the exchange of (antiferromagnetic) spin fluctuations [5]. In contrast to the electron-phonon interaction, however, in this case the electrons that are being paired provide their own pairing glue, i.e., there are no separate degrees of freedom such as the phonons in conventional superconductors that mediate the pairing. Thus, it is not possible to separately tune the degrees of freedom that are being paired and the degrees of freedom that mediate the pairing. This makes it difficult to optimize  $T_c$ . One may see this by using a separable



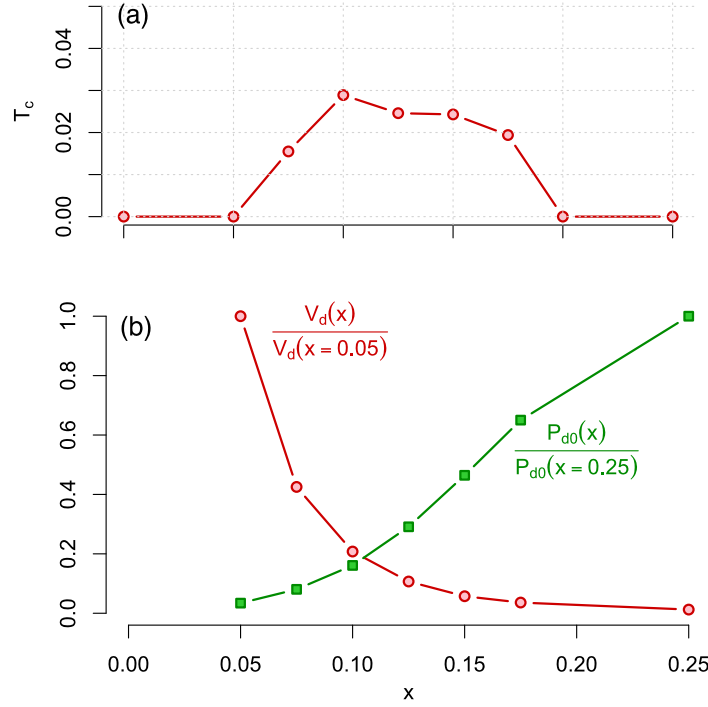


**Fig. 12: Dome-shaped structure of the superconducting phase:** *Top panel:* Superconducting  $T_c$  versus doping  $x$  in the 2D Hubbard model with  $U = 8t$  calculated with DCA/QMC for an 8-site cluster. *Bottom panel:* Normalized interaction strength  $V_d$  and intrinsic pair-field susceptibility  $P_{d,0}$  versus doping  $x$  for  $T = 0.125t$ . The dome-like shape arises from competing trends in these two quantities as the doping varies. Figure from [28].

approximation for  $\Gamma^{\text{pp}}$  [26],

$$\Gamma^{\text{pp}}(K, K') \approx -V_d \phi_d(K) \phi_d(K'), \quad (49)$$

which becomes valid close to  $T_c$  when the  $d$ -wave eigenvalue  $\lambda_d$  is well separated from other eigenvalues. With this, the Bethe-Salpeter equation (43) for the  $d$ -wave eigenvalue becomes

$$V_d(T) P_{d,0}(T) \approx \lambda_d \quad (50)$$

with the “intrinsic”  $d$ -wave pair-field susceptibility  $P_{d,0}(T) = T/N_c \sum_K \phi_d^2(K) \bar{G}_{2,\uparrow\downarrow}^0(K)$ . The doping  $x = 1 - \langle n \rangle$  dependence of  $P_{d,0}(T)$  and  $V_d(T)$  extracted from  $V_d = \lambda_d/P_{d,0}$  via Eq. (50) is shown in the bottom panel of Fig. 12 together with the  $x$ -dependence of  $T_c$ . From this we see that the doping  $x$ , as a tuning parameter, has opposite effects on the strength of the pairing interaction  $V_d$  and the intrinsic pair-field susceptibility  $P_{d,0}$ , and thus  $T_c$  as seen in the top panel: With decreasing  $x$ ,  $V_d$  rises, but  $P_{d,0}$  falls, and the opposite behavior is observed with increasing  $x$ . The increase in  $V_d$  as half-filling ( $x = 0$ ) is approached can be understood from the increase in the strength of the spin-fluctuations. The reason that this increase does not lead to an increase in  $T_c$  is that, at the same time,  $P_{d,0}$  is suppressed. This can be understood from a reduction in the quasiparticle weight as the Mott state is approached. The interplay of the pairing strength  $V_d$  and the intrinsic pair-field susceptibility  $P_{d,0}$  and their opposite doping dependence lead to the dome-shaped  $T_c$  seen in the top panel of Fig. 12.

### 3.3 Extended Hubbard model

In the conventional electron-phonon mechanism of superconductivity, retardation is a necessary ingredient in order to overcome the repulsive effect of the Coulomb interaction. In the Hubbard model, as well as in the cuprates, however, the  $d$ -wave structure of the Cooper pair wave function completely avoids the strongly repulsive effect of the local Coulomb  $U$ , because the electrons making up the pair sit on nearest-neighbor sites. Retardation is therefore not a necessary ingredient in this case. From the strong frequency dependence of the  $d$ -wave eigenvector shown in Fig. 9, however, we see that the pairing is nevertheless retarded on a scale set by the dynamics of the spin fluctuations.

The situation changes when an additional nearest-neighbor Coulomb repulsion

$$V \sum_{\langle ij \rangle, \sigma\sigma'} n_{i\sigma} n_{j\sigma'} \quad (51)$$

is considered and added to the Hubbard Hamiltonian in Eq. (1). The idea is that in realistic systems, the Coulomb repulsion is hardly screened to a purely local interaction, but has an additional short-ranged contribution. The resulting extended Hubbard model has recently been studied with DCA to examine the effect of  $V$  on  $d$ -wave superconductivity [29]. For  $d$ -wave pairs, where the electrons sit on neighboring sites,  $V$  is expected to have detrimental effects on superconductivity.

This is seen in the plot of  $T_c$  versus the strength of  $V$  shown in Fig. 13. These results were obtained from  $2 \times 2$ -cluster DCA calculations of the leading  $d$ -wave eigenvalue for the extended Hubbard model for  $U = 7t$  and  $\langle n \rangle = 0.9$ . Although, as expected,  $T_c$  is reduced with increasing  $V$ , this decrease is rather modest, even up to relatively large values of  $V$  close to  $U/2$ . Why is  $d$ -wave superconductivity so robust with respect to a nearest-neighbor Coulomb repulsion  $V$ , which, in a static picture, will strongly reduce the binding energy of a  $d$ -wave pair and thus should rapidly suppress  $T_c$ ? A clue lies in the frequency dependence of the pairing interaction.

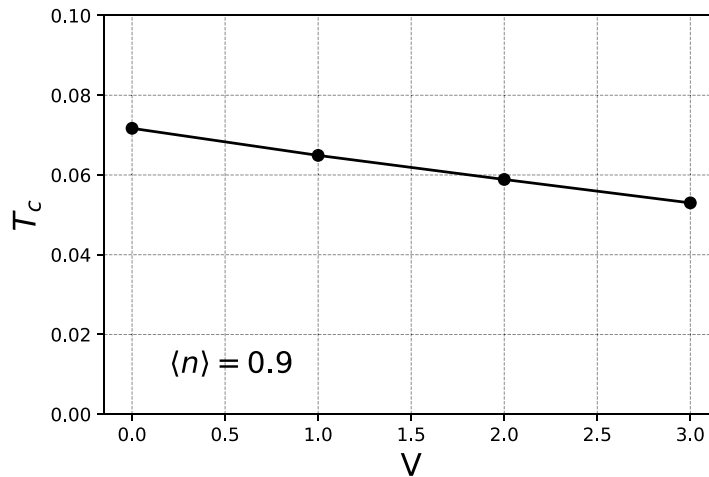


**Fig. 13: Resilience of  $d$ -wave pairing to a nearest-neighbor Coulomb repulsion: DCA/QMC  $2 \times 2$ -cluster results for  $T_c$  versus the nearest-neighbor Coulomb repulsion  $V$  in an extended 2D Hubbard model with  $U = 7t$  and  $\langle n \rangle = 0.9$ . Figure from [29].**

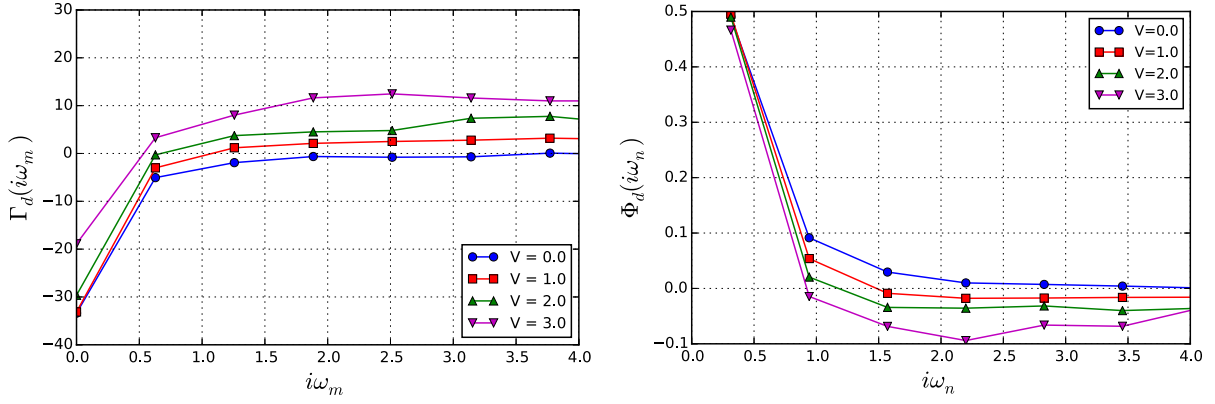


**Fig. 14: The role of retardation in the pairing mechanism:** *Left panel:* DCA/QMC  $2 \times 2$ -cluster results for the  $d$ -wave projected pairing interaction  $\Gamma_d(i\omega_m = i\omega_n - i\omega_{n'})$  with  $\omega_{n'} = \pi T$  versus  $\omega_m$  for different values of  $V$  for  $\langle n \rangle = 0.9$  and  $T = 0.1t$ .  $\Gamma_d$  is attractive at low frequencies and for finite  $V$  turns repulsive at higher frequencies. *Right panel:* Frequency dependence of the leading  $d$ -wave eigenvector  $\phi_d(\mathbf{K}, \omega_n)$  for  $\mathbf{K} = (\pi, 0)$  for different values of  $V$ . The sign change in  $\phi_d(\mathbf{K}, \omega_n)$  reduces the repulsive effect of  $V$  and thus stabilizes  $d$ -wave superconductivity. Figure from [29].

Fig. 14 shows a plot of the  $d$ -wave projected pairing interaction

$$\Gamma_d(\omega_m = \omega_n - \omega_{n'}) = \frac{\sum_{\mathbf{K}, \mathbf{K}'} g_d(\mathbf{K}) \Gamma^{\text{pp}}(\mathbf{K}, \omega_n, \mathbf{K}', \omega_{n'}) g_d(\mathbf{K}')}{\sum_{\mathbf{K}} g_d^2(\mathbf{K})}. \quad (52)$$

Here  $g_d(\mathbf{K}) = \cos K_x - \cos K_y$  and  $\omega_{n'} = \pi T$ . For  $V = 0$ , we see that  $\Gamma_d(\omega_m)$  is negative over the whole frequency range. In other words, the pair scattering is attractive in the  $d$ -wave channel, as we know from the previous results for the standard model without  $V$ . When  $V$  is turned on, we see that  $\Gamma_d(\omega_m)$  remains attractive at low frequencies, but then turns repulsive at higher frequencies. This reflects the fact that  $V$  is repulsive in the  $d$ -wave channel.

The dynamics of  $\Gamma_d(\omega_m)$  is similar to that of the conventional electron-phonon superconductors, which is attractive at low frequencies due to the electron-phonon interaction, and repulsive at high frequencies due to the Coulomb repulsion. The effect of this sign change on the  $d$ -wave pairing eigenvector is shown in the right panel of Fig. 14, where the frequency dependence of  $\phi_d(\mathbf{K}, \omega_n)$  is plotted for different values of  $V$ . As seen before in Fig. 9, for  $V = 0$ , it rapidly falls to zero. For finite  $V$ , however, we see that  $\phi_d(\mathbf{K}, \omega_n)$  changes sign and turns negative at high frequencies, reflecting the sign change in the  $d$ -wave pairing interaction  $\Gamma_d(i\omega_m)$ . Thus, just as  $\phi_d(\mathbf{K}, \omega_n)$  changes sign in  $\mathbf{K}$  to adapt to the repulsive nature of the pairing interaction at large momentum transfer,  $\phi_d(\mathbf{K}, \omega_n)$  also changes sign in frequency to adapt to the repulsive tail of the pairing interaction due to the Coulomb  $V$ . Therefore, just as in the electron-phonon case, retardation is important and necessary to protect the  $d$ -wave pairs from the repulsive effects of the (nearest-neighbor) Coulomb interaction.

## 4 Summary and concluding remarks

In these lecture notes, we have described how one can study superconductivity within the DMFT and DCA frameworks and how these approaches have been used to provide new insight into the nature of the pairing mechanism that leads to superconductivity in Hubbard models. As with other ordered states, there are always two alternative methods to determine a possible phase transition to a symmetry broken state within a mean-field approach like DMFT and DCA. The first option is to extend the algorithm to account for a finite order parameter that describes the symmetry broken state (anomalous propagator  $\langle c_{\mathbf{k}\uparrow} c_{-\mathbf{k}\downarrow} \rangle$  in the case of superconductivity), and start the calculation with a finite field that couples to the order parameter. This field is then switched off after a few iterations and the calculation relaxes to either a state with order or without. One may also keep the field turned on during the full calculation, carry out calculations for different field strengths, and then calculate the response (susceptibility) to the field from the derivative of the order parameter with respect to the field. The transition temperature  $T_c$  is then obtained from the temperature where the susceptibility diverges. The second option is to carry out the usual normal state calculation in the absence of order or an external field, but instead calculate the susceptibility directly from the 4-point correlation function constructed from the order parameter. Since both DMFT and DCA approaches are thermodynamically consistent [7], both calculations will give identical results for the susceptibility and therefore  $T_c$ .

We have also seen that DMFT and DCA are powerful approaches to study superconductivity in Hubbard models. DMFT, due to its local nature, can only describe superconducting phases with order parameters that have a local contribution, such as  $s$ -wave. Applied to the attractive Hubbard model, it allows to study  $s$ -wave superconductivity, which is expected in the doped model due to its on-site attractive pairing potential  $U < 0$ . While it captures the rise of  $T_c$  with increasing  $|U|$ , DCA calculations employing larger clusters are needed to describe the downturn of  $T_c$  at large  $|U|$  due to phase fluctuations.

For the repulsive Hubbard model,  $s$ -wave pairing is energetically unfavorable and therefore DMFT is not an adequate approach. DCA calculations employing a  $2 \times 2$  cluster are the simplest possible calculations to study the  $d_{x^2-y^2}$ -wave pairing state that is expected for this model, which offers the most basic description of the cuprate high-temperature superconductors. And indeed, such  $2 \times 2$ -cluster DCA calculations have found properties reminiscent of the real materials, including antiferromagnetic,  $d$ -wave superconducting, and pseudogap behavior. DCA calculations also find that superconductivity remains stable in larger cluster calculations, providing evidence that the doped 2D Hubbard model does have a finite temperature  $d$ -wave superconducting transition.

Finally, we have seen that one can go beyond these numerical experiments and use these approaches to get insight into the mechanism that leads to pairing in these systems. Unlike real experiments, these calculations can be used to directly analyze the momentum and frequency structure of the pairing interaction. For the simple Hubbard model, one finds that it reflects the momentum structure of the spin fluctuations, and one speaks of a spin-fluctuation pairing interaction. Just as in the conventional electron-phonon case, this interaction is retarded on a scale

set by the dynamics of the antiferromagnetic spin fluctuations. While this retardation is not needed to overcome the local Coulomb repulsion in the simple Hubbard model, we have seen that it is essential in making the  $d$ -wave pairing state resilient to an additional nearest-neighbor Coulomb repulsion.

Because of the difficulty associated with solving the DMFT impurity or DCA cluster problem, most applications of these approaches in the field of superconductivity have been concerned with single-band Hubbard models. Additional orbital degrees of freedom must, however, be included in more complex models if one wants to study most materials other than the cuprates, such as, for example, the iron-based superconductors. While this remains a challenging but desirable task for the long term, more immediate progress may be made with simple toy models, such as the bilayer Hubbard model studied in Ref. [30], that have some overlap with the physics of the real materials.

## Acknowledgments

I would like to acknowledge the close collaboration I have enjoyed with D.J. Scalapino and the many useful discussions and joint work with U. Hähner, M. Jarrell, M. Jiang, J. Keller, T. Pruschke, T.C. Schulthess and P. Staar. Support from the Center for Nanophase Materials Sciences is also acknowledged, which is a Department of Energy (DOE) Office of Science User Facility. Some of the material presented in these lecture notes was supported by the DOE Office of Science, Office of Advanced Scientific Computing Research, Scientific Discovery through Advanced Computing (SciDAC) program.

## References

- [1] J. Schrieffer: *Theory of Superconductivity* (Perseus Books, Reading, 1993)
- [2] J. Bardeen, L.N. Cooper, and J.R. Schrieffer, Phys. Rev. **108**, 1175 (1957)
- [3] A.B. Migdal, Sov. Phys. JETP **34**, 1438 (1958)
- [4] G.M. Eliashberg, Soviet Physics JETP-USSR **11**, 696 (1960)
- [5] D.J. Scalapino, Rev. Mod. Phys. **84**, 1383 (2012)
- [6] A. Georges, W. Krauth, and M. Rozenberg, Rev. Mod. Phys. **68**, 13 (1996)
- [7] T. Maier, M. Jarrell, T. Pruschke, and M. Hettler, Rev. Mod. Phys. **77**, 1027 (2005)
- [8] J. Hubbard, Proc. Royal. Soc. London **276**, 238 (1963)
- [9] P.W. Anderson, Science **235**, 1196 (1987)
- [10] M. Jarrell, T. Maier, C. Huscroft, and S. Moukouri, Phys. Rev. B **64**, 195130 (2001)
- [11] E. Gull, A.J. Millis, A.I. Lichtenstein, A.N. Rubtsov, M. Troyer, and P. Werner, Rev. Mod. Phys. **83**, 349 (2011)
- [12] P. Staar, T. Maier, and T.C. Schulthess, Phys. Rev. B **88**, 115101 (2013)
- [13] A. Lichtenstein and M. Katsnelson, Phys. Rev. B **62**, R9283 (2000)
- [14] T. Maier, M. Jarrell, T. Pruschke, and J. Keller, Phys. Rev. Lett. **85**, 1524 (2000)
- [15] T. Maier, M. Jarrell, T. Pruschke, and J. Keller, Eur. Phys. J. B **13**, 613 (2000)
- [16] T.A. Maier, M.S. Jarrell, and D.J. Scalapino, Phys. Rev. Lett. **96**, 047005 (2006)
- [17] T. Paiva, R.R. dos Santos, R. Scalettar, and P. Denteneer, Phys. Rev. B **69**, 184501 (2004)
- [18] N. Mermin and H. Wagner, Phys. Rev. Lett. **17**, 1133 (1966)
- [19] J. Kosterlitz, J. Phys. C **7**, 1046 (1973)
- [20] J. Kosterlitz and D. Thouless, J. Phys. C **6**, 1181 (1973)
- [21] Q. Chen, J. Stajic, S. Tan, and K. Levin, Phys. Rep. **412**, 1 (2005)
- [22] P. Staar, T. Maier, and T.C. Schulthess, Phys. Rev. B **89**, 195133 (2014)
- [23] M. Jarrell, T. Maier, M.H. Hettler, and A. Tahvildarzadeh, Europhys. Lett. **56**, 563 (2001)
- [24] T.A. Maier, M. Jarrell, T.C. Schulthess, P.R.C. Kent, and J.B. White, Phys. Rev. Lett. **95**, 237001 (2005)

- [25] M.R. Norman, D. Pines, and C. Kallin, *Adv. Phys.* **54**, 715 (2005)
- [26] T.A. Maier, M. Jarrell, and D. Scalapino, *Phys. Rev. B* **74**, 094513 (2006)
- [27] T.A. Maier, A. Macridin, M. Jarrell, and D.J. Scalapino, *Phys. Rev. B* **76**, 144516 (2007)
- [28] T.A. Maier, *J. Supercond. Nov. Magn.* **25**, 1307 (2012)
- [29] M. Jiang, U.R. Hähner, T.C. Schulthess, and T.A. Maier, *Phys. Rev. B* **97**, 184507 (2018)
- [30] T. Maier and D. Scalapino, *Phys. Rev. B* **84**, 180513(R) (2011)





# 14 Quantum Criticality and Superconductivity in Diagrammatic Extensions of DMFT

Karsten Held

Institute of Solid State Physics, TU Wien

1040 Vienna, Austria

## Contents

<b>1</b>	<b>Introduction</b>	<b>2</b>
<b>2</b>	<b>Synopsis: Dynamical vertex approximation</b>	<b>3</b>
<b>3</b>	<b>Criticality in the <math>3d</math> Hubbard model</b>	<b>5</b>
<b>4</b>	<b>Quantum criticality in the <math>3d</math> Hubbard model</b>	<b>8</b>
<b>5</b>	<b>Quantum criticality in the <math>2d</math> periodic Anderson model</b>	<b>11</b>
<b>6</b>	<b>Superconductivity in the <math>2d</math> Hubbard model</b>	<b>15</b>
<b>7</b>	<b>Conclusion and outlook</b>	<b>20</b>

# 1 Introduction

Dynamical mean field theory (DMFT) [1, 2] has been a breakthrough for describing electronic correlations in models [3] and – in combination with density functional theory – even in actual materials [4–6]. This breakthrough has been brought about since DMFT includes a major part of the electronic correlations, namely the local ones. On the other hand, the arguably most fascinating physical phenomena such as (quantum) criticality, high-temperature superconductivity and vertex corrections to the conductivity rely on non-local correlations.

Hence, in recent years these non-local correlations have been at the focus of the methodological development. There are two routes that include the local DMFT correlations but also incorporate non-local correlations beyond. On the one hand there are cluster extensions of DMFT, which take instead of the single site of DMFT a cluster of lattice sites that is embedded in a dynamical mean field. This way correlations within the cluster are taken into account. For a review see [7] and for a pedagogical introduction see the lecture by Th. Maier in this School.

Because of numerical limitations the size of the cluster is, however, limited to about  $10 \times 10$  lattice sites and even less in the case of realistic multi-orbital calculations. This is sufficient to describe short range correlations; and indeed cluster extensions of DMFT have been highly successful for describing pseudogaps and  $d$ -wave superconductivity in the two-dimensional ( $2d$ ) Hubbard model. However long-range correlations as they occur for example in the vicinity of a phase transition cannot be described in this way.

For including short- and long-range correlations on an equal footing, in recent years, diagrammatic extensions of DMFT have been developed. This development started with the dynamical vertex approximation (D $\Gamma$ A) [8] and the dual fermion (DF) approach [9], continuing with a plethora of further approaches [10–13]. All of these approaches take a local two-particle vertex as a starting point and from this construct the local DMFT correlations as well as non-local correlations beyond. The difference lies in the details: which vertex is taken, by which Green functions these are connected, and which Feynman diagrams are considered. For a review, see [14]. Successes of these diagrammatic extensions of DMFT include the calculation of critical exponents in the Hubbard [15, 16] and Falicov-Kimball model [17], quantum criticality in the  $3d$  Hubbard [18] and  $2d$  periodic Anderson model [19], the suppression of antiferromagnetism by spin fluctuations in the  $3d$  and  $2d$  Hubbard model [20, 15, 21], the fate of the Mott-Hubbard metal-insulator transition for the  $2d$  Hubbard model [22], pseudogaps [23, 20, 11, 24, 25, 12] and superconductivity [21, 26] in the  $2d$  Hubbard model.

In the following we first give a brief synopsis of the D $\Gamma$ A approach in Section 2, for further reading see the Lecture Notes [27] and the review [14]. For an introduction to the DF approach we refer the reader to the Chapter by H. Hafermann in these Lecture Notes, as well as to [14]. The main focus of the present Lecture Notes is on physical results, starting with the critical and quantum critical properties of the  $3d$  Hubbard model in Section 3 and 4, respectively. The quantum critical properties of the  $2d$  periodic Anderson model are discussed in Section 5, before we turn to superconductivity in the  $2d$  Hubbard model in Section 6. Finally, Section 7 provides a brief summary and outlook.

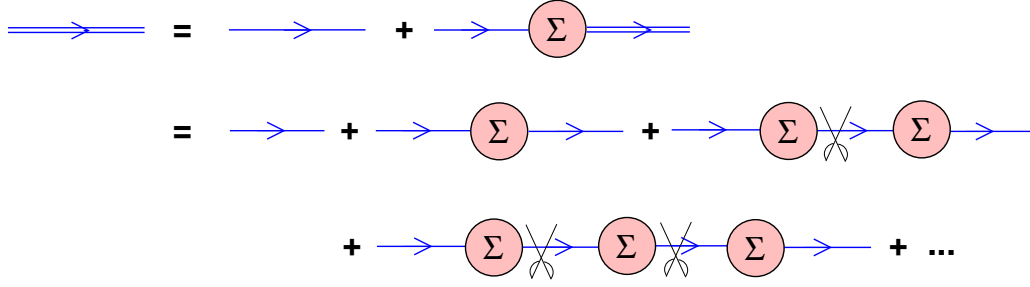


**Fig. 1:** Dyson equation connecting Green function and self energy. The pair of scissors indicates that these diagrams are one-particle reducible (i.e., cutting one  $G_0$  line separates the Feynman diagram into two parts). From [27].

## 2 Synopsis: Dynamical vertex approximation

The basic idea of the dynamical vertex approximation (D $\Gamma$ A) is a resummation of Feynman diagrams, not in order-by-order of the Coulomb interaction as in conventional perturbation theory, but in terms of their locality. That is, we assume the fully irreducible  $n$ -particle vertex to be local and from this building block we construct further diagrams and non-local correlations. The first level ( $n = 1$ ) is then just the DMFT which corresponds to all local Feynman diagrams for the self-energy  $\Sigma$ . Note that  $\Sigma$  is nothing but the fully irreducible  $n = 1$ -particle vertex. One particle-irreducibility here means that cutting one Green function line does not separate the Feynman diagram into two pieces. Indeed, such reducible diagrams must not be included in the self-energy since it is exactly these diagrams that are generated from the Dyson equation which resolved for  $G$  reads

$$G_{\nu\mathbf{k}} = (1/G_{0,\nu\mathbf{k}} - \Sigma_{\nu\mathbf{k}})^{-1} \quad (1)$$

for momentum  $\mathbf{k}$ , Matsubara frequency  $\nu$  and non-interacting Green function  $G_{0,\nu\mathbf{k}}$ . For an illustration, see Fig. 1, which also explicitly shows how one-particle reducible diagrams are generated through the Dyson equation; and hence must not be contained in the  $\Sigma$ -diagrams

On the next level, for  $n = 2$ , we assume the locality of the two-particle fully irreducible vertex  $\Lambda$ . That is cutting two Green function lines does not separate the diagram into two pieces. There is a set of exact equations, coined parquet equations [28–30, 14], that allows us to calculate from a given  $\Lambda$  the full vertex, self-energy, and Green function as well as the irreducible vertices  $\Gamma_\ell$  in three different channels  $\ell$ .

For understanding how these irreducible vertices  $\Gamma_\ell$  and  $\Lambda$  come about, we consider in Fig. 2 the parquet decomposition of the full vertex  $F$  into the fully irreducible vertex  $\Lambda$  and those parts that are two-particle reducible. There are three distinct such reducible parts  $\Phi_\ell$ , since say leg 1 may stay connected with leg 2, 3, or 4 when cutting two Green function lines as indicated in Fig. 2. The irreducible vertex is just the complement:  $\Gamma_\ell = F - \Phi_\ell$ . The three possible channels  $\ell$  are denoted as particle-hole ( $ph$ ), transversal particle-hole ( $\overline{ph}$ ) and particle-particle ( $pp$ ) channel. It is important to note that each reducible diagram is contained in one and only one of these channels.<sup>1</sup>

<sup>1</sup>One can easily show that otherwise cutting lines would result in a diagram with one incoming and two outgoing lines, which is not possible because of the conservation of (fermionic) particles.

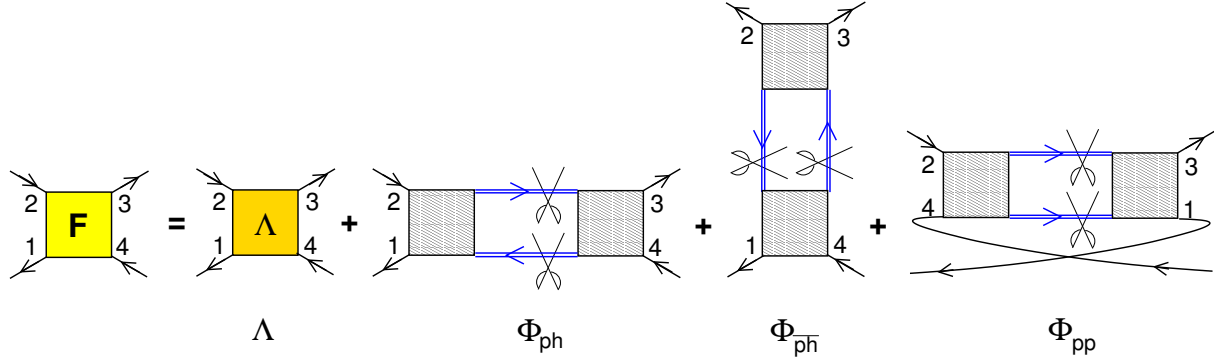


**Fig. 2:** Parquet decomposition of the full (reducible) vertex  $F$  into the fully irreducible vertex  $\Lambda$  and two-particle reducible diagrams  $\Phi_r$  in the three channels. The two pairs of scissors indicate the reducibility of the three  $\Phi_\ell$ 's. From [27].

There is a set of 6 “parquet” equations: (1) the actual parquet equation (Fig. 2); (2-4) the Bethe-Salpeter equation in the three channels (in the following we only reproduce the  $ph$  channel<sup>2</sup> with  $r \in \{d, s\}$  for a symmetric/antisymmetric spin combination)<sup>3</sup>

$$F_{r, \mathbf{k} \mathbf{k}' \mathbf{q}}^{\nu \nu' \omega} = F_{r, ph, \mathbf{k} \mathbf{k}' \mathbf{q}}^{\nu \nu' \omega} + \sum_{\mathbf{k}_1 \nu_1} \Gamma_{ph, r, \mathbf{k} \mathbf{k}_1 \mathbf{q}}^{\nu \nu_1 \omega} G_{\mathbf{k}_1 \nu_1} G_{(\mathbf{k}_1 + \mathbf{q})(\nu_1 + \omega)} F_{r, \mathbf{k}_1 \mathbf{k}' \mathbf{q}}^{\nu_1 \nu' \omega}; \quad (2)$$

the (5) Dyson Eq. (1); and (6) the Schwinger-Dyson equation which in a four vector notation  $k = (\nu, \mathbf{k})$  reads

$$\Sigma_k = -U \sum_{k', q} (F_c^{k, k' q} - F_s^{k, k' q}) G_{k+q} G_{k'} G_{k'+q} \quad (3)$$

and connects  $\Sigma$  and  $F$  (here for a single-orbital and local interaction  $U$ ).<sup>4</sup> This set of 6 parquet equations allows us to determine the six quantities  $F$ ,  $\Phi_r$ ,  $\Sigma$ , and  $G$  if we know  $\Lambda$  — or if we approximate it by a local  $\Lambda$  in D $\Gamma$ A. This local  $\Lambda$  can be calculated by solving an Anderson impurity model, similar as in DMFT but on the two-particle level.

In principle, one can then further turn to the  $n = 3$ -particle level etc.; and for  $n \rightarrow \infty$  D $\Gamma$ A recovers the exact solution. As a matter of course determining the  $n=3$ -particle vertex becomes already cumbersome. But it may serve at least for estimating the error if one is truncating the scheme at the two-particle vertex level. Such an error estimate has been done already for the DF approach [31]. A similar calculation for D $\Gamma$ A is more difficult because one first needs to determine the  $n=3$ -particle fully irreducible vertex, whereas the DF approach is based on the full vertex  $F$ , which is readily obtained from continuous-time quantum Monte-Carlo simulations [32–34], but a diagrammatically less compact object.

Let us finally mention a simplified ladder D $\Gamma$ A scheme. Here, instead of a local  $\Lambda$ , one starts with a local  $\Gamma_{ph}$  and  $\Gamma_{ph}^-$  and uses the Bethe-Salpeter ladder Eq. (2) in these channel to obtain

<sup>2</sup>The frequency-momentum convention is such that the four legs in Fig. 2 have frequency-momentum  $k_1 = k$ ,  $k_4 = k'$ ,  $k_2 = k + q$ , and, because of energy-momentum conservation,  $k_3 = k' + q$ .

<sup>3</sup>We assume a proper normalization of the momentum and frequency sums with respect to the number of  $\mathbf{k}$ -points and  $\beta$ , i.e.,  $\sum_{\mathbf{k}} 1 = 1$  and  $\sum_{\nu} \hat{=} \frac{1}{\beta} \sum_{\nu}$ .

<sup>4</sup>There is an additional Hartree(-Fock) term not shown.

*F.* This way, fluctuations in the particle-particle (Cooperon) channels are neglected. But if we are close to half-filling, or, more specifically, if no superconducting fluctuations nor weak localization is to be expected, the dominant non-local correlations are included in this simplified ladder D $\Gamma$ A. The advantage is that if we do not couple the ladders through the parquet equations, the ladder only depends on a single frequency-momentum  $q$  instead of three  $(q, k, k')$ . Hence numerically much lower temperatures (finer frequency grids) and much larger momentum grids are feasible. Going further into details would require a chapter on its own, and we refer the reader to [14] and for a pedagogical introduction of D $\Gamma$ A to [27]; for properties of the local two-particle vertex cf. [35].

### 3 Criticality in the 3d Hubbard model

Let us start with the Hamiltonian of the Hubbard model

$$\mathcal{H} = -t \sum_{ij, \sigma} c_{i\sigma}^\dagger c_{j\sigma} + U \sum_i n_{i\uparrow} n_{i\downarrow}, \quad (4)$$

consisting of two terms: a nearest-neighbor hopping amplitude  $t$  and a local Coulomb repulsion  $U$ . Here  $c_{i\sigma}^\dagger$  ( $c_{i\sigma}$ ) creates (annihilates) an electron on site  $i$  with spin  $\sigma$ , and  $n_{i\sigma} = c_{i\sigma}^\dagger c_{i\sigma}$ .

For the study of critical properties in the paramagnetic phase, in particular the behavior of the susceptibility<sup>5</sup>  $\chi$  and the correlation length  $\xi$  is relevant. In the vicinity of the critical temperature  $T_c$ , the diverging behavior of  $\chi$  and  $\xi$  is described by critical exponents  $\gamma$  and  $\nu$ , respectively

$$\chi_{\mathbf{Q}}^{\omega=0} \sim (T - T_c)^{-\gamma}; \quad (6)$$

$$\xi \sim (T - T_c)^{-\nu}. \quad (7)$$

Here, the static ( $\omega = 0$ ) susceptibility is taken for that momentum  $\mathbf{q} = \mathbf{Q}$  at which the first divergence occurs at  $T_c$ , signaling the emergence of, e.g., ferromagnetic,  $\mathbf{Q} = (0, 0, \dots)$ , or antiferromagnetic,  $\mathbf{Q} = (\pi, \pi, \dots)$ , order.

In practice the D $\Gamma$ A (or DF) susceptibility is calculated from the full two-particle vertex which describes the connected part of the two-particle Green function. The latter term (often referred to as vertex corrections) in turn together with the disconnected “bubble” diagram yields the susceptibility.<sup>6</sup> This full two-particle vertex includes non-local correlation effects, while the irreducible vertex acting as a building block is local in D $\Gamma$ A.

<sup>5</sup>For the sake of completeness, let us define  $\chi$  as the Fourier-transform of the spin-spin correlation function from imaginary time  $\tau$  and lattice sites  $\mathbf{R}$  to frequency  $\omega$  and momentum  $\mathbf{q}$  ( $\beta = 1/T$ : inverse temperature)

$$\chi_{\mathbf{q}}^{\omega} = \int_0^{\beta} d\tau \sum_{\mathbf{R}} \langle S_{\mathbf{R}}^z(\tau) S_{\mathbf{0}}^z(0) \rangle e^{-i\mathbf{q}\mathbf{R}} e^{i\omega\tau}. \quad (5)$$

<sup>6</sup>Note that the DMFT calculation of the susceptibility takes the local irreducible vertex in the particle-hole channel and from this constructs the particle-hole ladder [3]. The difference to the ladder D $\Gamma$ A or DF is that the connecting Green functions are recalculated self-consistently or, to mimic this self-consistency effect, a Moriyasque  $\lambda$ -correction is employed, see [14, 20, 27, 36]. Further, the transversal particle-hole channel is taken into account on an equal footing. In parquet D $\Gamma$ A, additionally, particle-particle vertex corrections couple into the particle-hole and transversal particle hole channel.

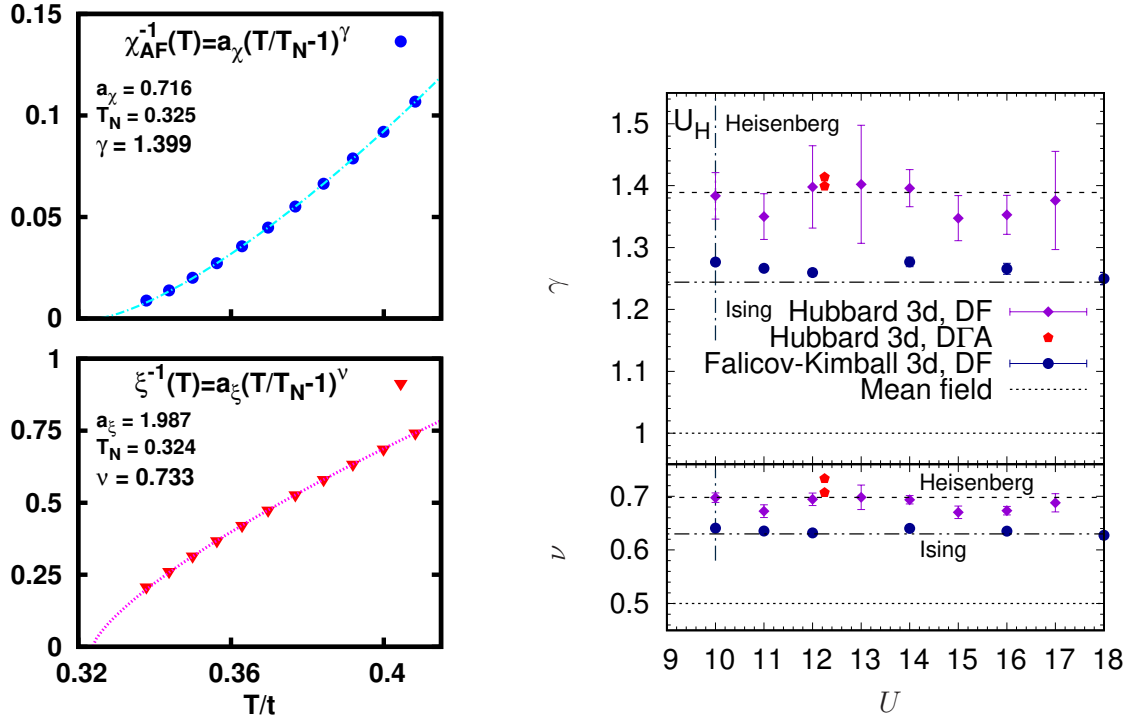


**Fig. 3:** Left: Inverse antiferromagnetic susceptibility  $\chi_{\mathbf{Q}=(\pi,\pi,\pi)}^{-1}$  (top) and correlation length  $\xi^{-1}$  (bottom) as a function of temperature  $T$  for the 3d Hubbard model at half-filling and  $U \approx 12.2t$  in D $\Gamma$ A. Right: Extracted critical exponents obtained in D $\Gamma$ A (from the fits in the left panel) and DF (also for the Falicov-Kimball model) compared to mean-field, 3d Heisenberg and 3d Ising critical exponents. From Refs. [14–16].

That is, if we plot the susceptibility  $\chi_{\mathbf{q}}^{\omega=0}$  as a function of momentum  $\mathbf{q}$ , it has a maximum at a certain  $\mathbf{q} = \mathbf{Q}$  of value  $\chi_{\mathbf{Q}}^{\omega=0}$ . The width around this maximum on the other hand is given by the inverse correlation length  $\xi^{-1}$  according to the Ornstein-Zernike [37] relation

$$\chi_{\mathbf{q}}^{\omega=0} \sim \frac{1}{(\mathbf{q} - \mathbf{Q})^2 + \xi^{-2}}. \quad (8)$$

This relation was found to hold even in a quite large  $\mathbf{q}$ -region around the maximum  $\mathbf{Q}$  so that, in practice,  $\xi$  is actually obtained from a fit according to Eq. (8).

Fig. 3 (left panels) plots the thus obtained D $\Gamma$ A susceptibility and correlation length as a function of temperature. There is a clear deviation from a mean-field behavior [ $\gamma = 1$ ,  $\nu = 0.5$ , see Fig. 4 (a)]. For the temperatures of Fig. 3 (left),  $\gamma \approx 1.4$ ,  $\nu \approx 0.7$  is obtained from the indicated numerical fit [15], with the error bar in Fig. 3 (right) corresponding to the deviation to a second fit omitting one temperature point. Within the error bars, this agrees with the critical exponents obtained for the Heisenberg model [ $\gamma \approx 1.39$ ,  $\nu \approx 0.705$ , see Fig. 4 (b)] for large scale simulations [38]. Indeed universality tells us that the two models should have the same critical exponents since the dimension is the same (3d), as is the symmetry of the order parameter:  $O(3)$  since we have rotational symmetry as regards the possible orientation of the ordered magnetic moment.

Let us also note that the two exponents are connected through the Fisher relation [39] as

$$\gamma/\nu = 2 - \eta \quad (9)$$

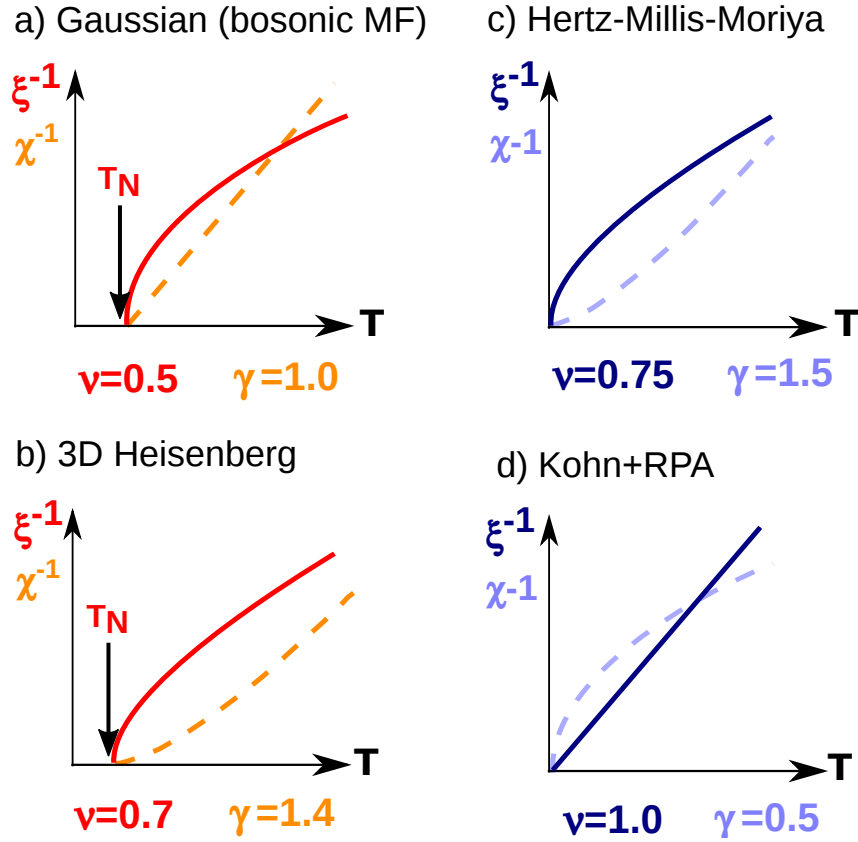


**Fig. 4:** Inverse susceptibility  $\chi^{-1}$  and correlation length  $\xi^{-1}$  as a function of temperature  $T$ . Left: Classical critical point with a finite critical temperature  $T_N$ , comparing a) Gaussian fluctuations and b) the 3d Heisenberg model. Right: Quantum critical point with a phase transition at  $T = 0$ , comparing c) conventional Hertz-Millis-Moriya theory and d) the Kohn-line universality class. From Ref. [18].

with the critical exponent  $\eta$  describing the decay of spatial correlations at  $T = T_c$ . The exponent  $\eta$  vanishes above the upper critical dimension, and is typically very small  $\eta \approx 0$  in 3D and even in 2D. Hence, we will further consider  $\eta = 0$  in these Lecture Notes.

While the deviation from mean-field exponents is obvious, one should always keep in mind that the fitting procedure to extract critical exponents from numerical as well as from experimental data has a large degree of uncertainty [40, 41]. Further there is, necessarily, some distance of the numerical data to the critical temperature.<sup>7</sup> Hence “last minute” changes of the curvature in the immediate vicinity of the critical temperature might be missed in a numerical fit. For the attractive Hubbard model, whose superconducting phase transition out of half-filling should have the universality class of the  $XY$  model, it was found [42] that the critical exponents might also be consistent with  $\gamma = 2$ ,  $\nu = 1$  close to  $T_c$ . At the same time, other groups obtained the same critical 3d Heisenberg exponents using the DF approach [16], and different ones for the Falicov-Kimball model [17]. which has an Ising universality class, see Fig. 3 (right panel).

<sup>7</sup>As the correlation length keeps increasing to thousands and ten thousands of lattice sites, we need a larger and larger numerical resolution in Fourier, i.e.  $\mathbf{k}$ , space. Doing reliable calculations significantly closer to  $T_c$  than shown is hardly possible.

## 4 Quantum criticality in the 3d Hubbard model

A quantum critical point (QCP) is a critical point at zero temperature,  $T = 0$ . In this case, besides the classical fluctuations with long-range correlations in space, an additional dimension, time, becomes relevant. At any finite temperature, these correlations in time are not relevant since they are cut-off at a scale  $\beta = 1/T$ . Maybe one can best understand this in imaginary time  $\tau$  as it is restricted to the interval  $\tau \in [0, \beta]$ .

For a classical critical point at finite  $T$ , the correlation length in time will hence eventually exceed  $\beta = 1/T$  if we are close enough to the phase transition. At this point, correlations in time are cut off, and not relevant any longer close enough to the phase transition. Consequently, the critical exponents are only determined by the number  $d$  of spatial dimensions and the symmetry of the order parameter.

This changes for a quantum phase transition at  $T = 0$ . Here, also a divergent correlation length in time becomes relevant. The effective dimension is hence  $d_{\text{eff}} = d + z$ . With the above argument, one might assume one extra dimension, i.e.,  $z = 1$ . However, fluctuations in time can also lead to other values of the dynamical critical exponent  $z$ . This is because the spatial correlation length diverges as  $\xi \sim T^{-\nu}$  at a QCP whereas the correlation length in time behaves as  $\xi_\tau \sim T^{-z\nu}$ . Depending on the kind of ordering and the dimension,  $z$  may vary. For example, we have  $z = 1$  for an insulating and  $z = 2$  for a metallic antiferromagnetic QCP. For a review see [43].

The standard theory for quantum critical points and exponents is the Hertz-Millis-Moriya theory [44–46], based on weak coupling ladder diagrams in a perturbative renormalization group. Experimentally, on the other hand, quantum criticality is best studied in heavy fermion systems. That is, in strongly correlated electron systems with  $f$ -electrons for which a weak coupling theory is certainly not sufficient. This has led to different proposals and further theories. One theory that takes strong electronic correlations into account and the breakdown of the  $f$ -electron Fermi surface is the so-called local quantum criticality, see e.g. [47]. This theory is based on the extended DMFT [48, 49] which considers the local correlations and self-energy emerging from non-local interactions, here considered to arise from non-local spin fluctuations.

Diagrammatic extensions of DMFT such as the D $\Gamma$ A take both kinds of physics into account: similar diagrams as in Hertz-Millis-Moriya theory but with the local vertex instead of a bare interaction as a starting point so that DMFT effects of strong correlations are automatically included; and they inherently allow us to describe breakdowns of Fermi surfaces as well.

Let us now turn to quantum criticality in the 3d Hubbard model. Because of perfect nesting we have an antiferromagnetic ground state for all interactions  $U$  at half-filling. Thus, we need to find another way to realize a quantum critical point. One possibility is to dope the system as shown in Fig. 5. With doping the antiferromagnetic order is suppressed so that we eventually arrive at a quantum critical point (QCP) at  $n \approx 0.8$ . A further complication arises however: The second order phase transition is only towards a commensurate Néel antiferromagnetic ordering with wave vector  $\mathbf{Q} = (\pi, \pi, \pi)$  close to half filling (open triangles in Fig. 5). With further doping and at the QCP it is towards an incommensurate antiferromagnetic ordering with  $\mathbf{Q} =$



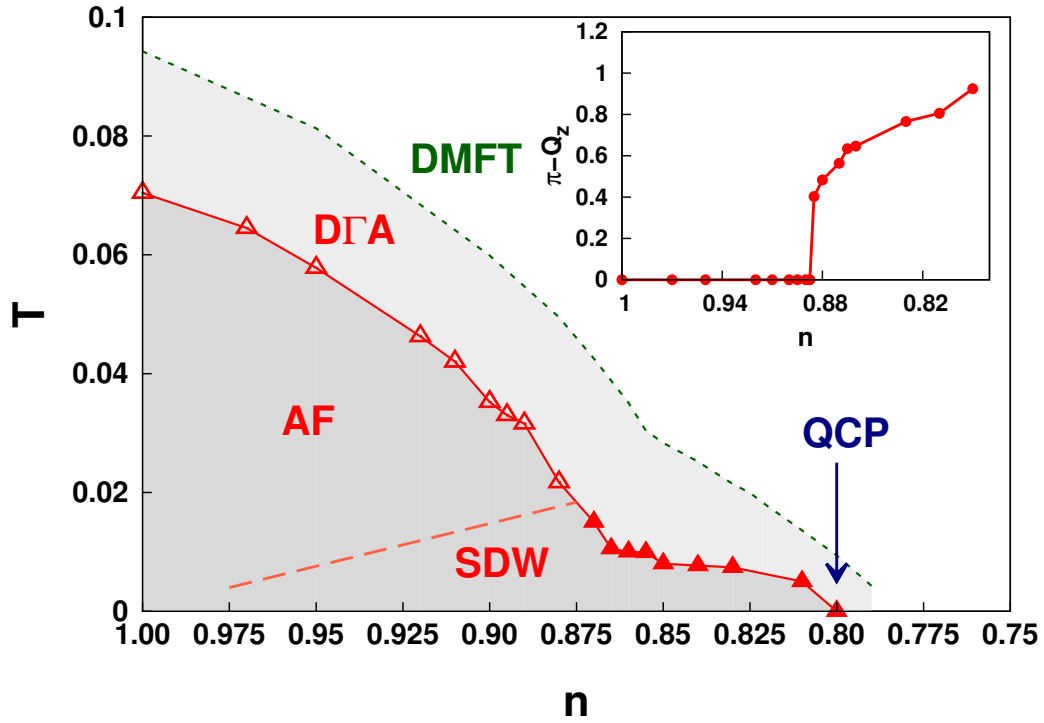


**Fig. 5:** Phase diagram of the 3d Hubbard model at  $U = 4\sqrt{6}t \approx 9.8t$ , showing the antiferromagnetic critical temperature as a function of electron filling  $n$  in DMFT (green dashed line) and DΓA (red triangles). Inset: The antiferromagnetic ordering wave vector  $\mathbf{Q}$  is commensurate with  $Q_z = \pi$  (open triangles in the main panel) around half-filling and incommensurate with  $Q_z < \pi$  ordering at larger doping (full triangles in the main panel). The dashed line of the main panel indicates the possible crossover between commensurate and incommensurate  $Q_z$  in the ordered phase. From Ref. [18].

$(\pi, \pi, \pi - \delta)$  (filled triangles in Fig. 5). Besides this interesting aspect of the changing  $\mathbf{Q}$  vector (cf. inset of Fig. 5), we also see that the spin fluctuations taken into account in the DΓA suppress the critical temperature compared to the DMFT solution.

In Fig. 6 we study the critical exponents again for both, the susceptibility  $\chi$  and correlation length  $\xi$ . For  $n = 1$  and  $n = 0.87$  we are far away from the QCP in Fig. 5, and within the numerical error bars our fit suggests the classical critical exponents of the Heisenberg model ( $\nu \approx 0.7$ ,  $\gamma \approx 1.4$ ). The dopings  $n = 0.805$  and  $n = 0.79$  are just below and above the QCP in Fig. 5. Here, the critical exponent for the correlation length  $\xi$  clearly shows a different exponent; within the error bars we obtain  $\nu \approx 1$ . Only at the lowest temperature there is a deviation to a smaller  $\xi^{-1}$  for  $n = 0.805$ , signaling the eventual finite-temperature antiferromagnetic phase transition as we are still to the left of the QCP in Fig. 6. At  $n = 0.79$ , on the other hand, we are to the right of the QCP. That is, eventually the correlation length must saturate because of the paramagnetic ground state. Indeed, here the value at the lowest  $T$  in Fig. 6 indicates a deviation to a larger  $\xi^{-1}$ .

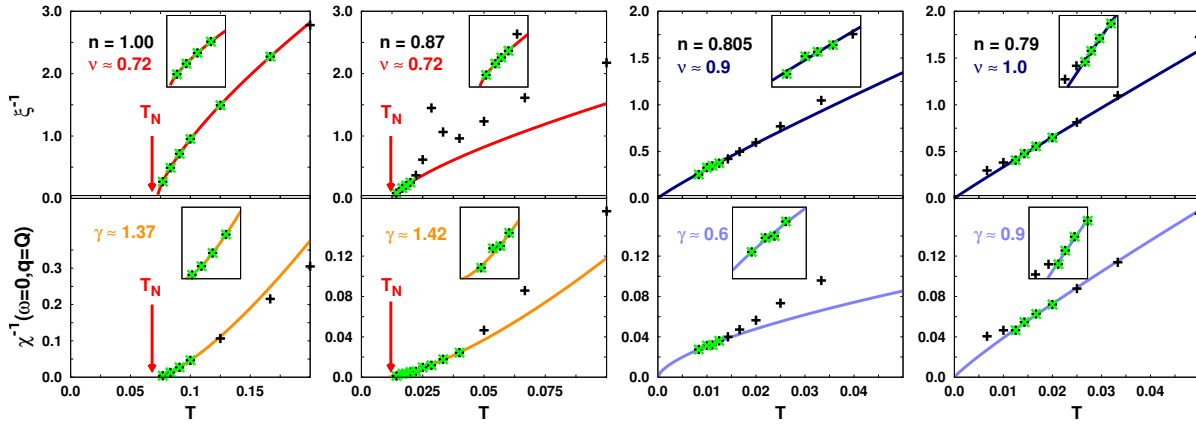


**Fig. 6:** Inverse correlation length ( $\xi^{-1}$ , upper panels) and susceptibility ( $\chi^{-1}$ , lower panels) vs.  $T$  in D $\Gamma$ A for different  $n$ . Solid lines: fits for extracting the critical exponents  $\gamma$  and  $\nu$  from the green points. Insets: zoom in to the lowest temperature points. From Ref. [18].

The result  $\nu \approx 1$  was quite a surprise at first. Since our effective dimensions is  $d_{\text{eff}} = d + z = 3 + 2 > 4$  we are above the upper critical dimension four<sup>8</sup> and one should expect the behavior of a bosonic mean-field theory with  $\nu = (d + z - 2)/(2z) = 3/4$  according to Hertz-Millis-Moriya theory, see Fig. 4c). By analytical calculations in the random phase approximation (RPA) it was shown [18] that one obtains the exponents of a different universality class instead. This is caused by peculiarities of the Fermi surface. More specifically, there are Kohn-lines on the Fermi surface of the doped Hubbard model which are separated by an incommensurate wave vector and have opposite Fermi velocities, see Fig. 7. These lines give rise to the so-called Kohn anomalies in the phonon spectrum [50] if we take phonons and the electron-phonon coupling into account.

In the case of a QCP they give rise to particularly strong transversal spin fluctuations which eventually lead to the exponents  $\nu = 1$  and  $\gamma = 0.5$ , see Fig. 4d) [18]. Note, that their ratio ( $\nu = 2\gamma$ ) is just the opposite, as to be expected from the Fisher relation Eq. (9) which for  $\eta \approx 0$  yields  $\nu = \gamma/2$ . While the numerical error bar for determining  $\gamma$  in Fig. 6 is considerably larger than for  $\nu$ ,<sup>9</sup> it is save to say that also numerically  $\nu > \gamma$  in D $\Gamma$ A instead of the expected behavior  $\nu = \gamma/2 < \gamma$  without Kohn lines.

In case of a finite temperature classical critical point, the Kohn anomalies are not relevant because the Fermi surface effect is broadened out by a finite self-energy at the Fermi energy. If we add a finite next-nearest neighbor hopping  $t'$  on the other hand, there are no full Kohn lines any longer. But individual Kohn points with opposite Fermi velocities still occur quite generically. We expect such points to lead to a further, different, universality class for the critical exponents ( $\gamma = \nu = 1$ ).

<sup>8</sup>The marginal case of  $d_{\text{eff}} = 4$  requires special considerations.

<sup>9</sup>as can be seen from the somewhat different fitted values for  $n = 0.805$  and  $n = 0.79$

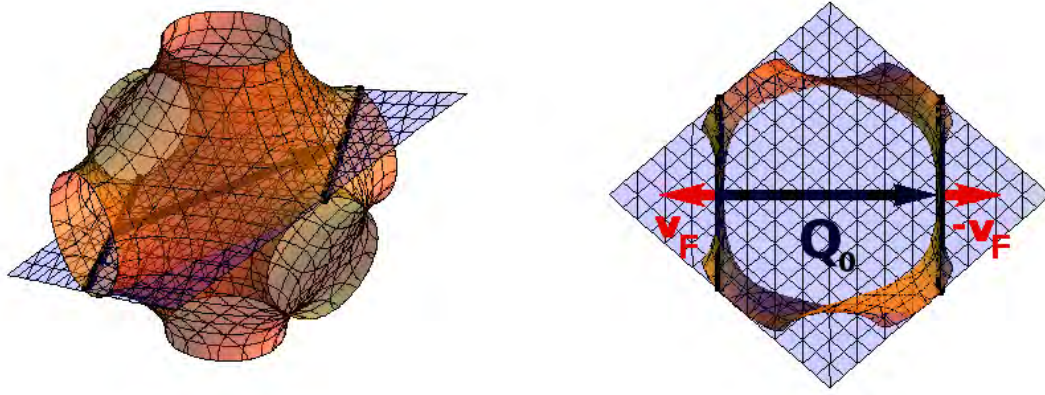


**Fig. 7:** Left: Visualization of the parallel Kohn lines (black lines) on the Fermi surface of the 3d Hubbard model with nearest neighbor hopping. Right: Two-dimensional cut as indicated in the left panel, showing the connecting wave vector  $Q_0$  (black arrow) and the opposite Fermi velocities  $v_F$  (red arrows). From Ref. [18].

## 5 Quantum criticality in the 2d periodic Anderson model

With the additional dimensions  $z$  brought about by the temporal correlations, it is not that simple to remain below the upper critical dimension  $d = 4$ . Hence, we next study the 2d case and another model, the periodic Anderson model (PAM)

$$\mathcal{H} = \sum_{\mathbf{k},\sigma} \varepsilon_{\mathbf{k}} d_{\mathbf{k}\sigma}^\dagger d_{\mathbf{k}\sigma} + \varepsilon_f \sum_{i\sigma} f_{i\sigma}^\dagger f_{i\sigma} + U \sum_i n_{f,i\uparrow} n_{f,i\downarrow} + V \sum_{i,\sigma} (d_{i\sigma}^\dagger f_{i\sigma} + f_{i\sigma}^\dagger d_{i\sigma}). \quad (10)$$

This Hamiltonian can be considered as the simplest model for an  $f$ -electron system where we have two different kinds of electrons: Localized  $f$ -electrons with creation (annihilation) operators  $f_{i\sigma}^\dagger$  ( $f_{i\sigma}$ ), and  $n_{f,i\sigma} = f_{i\sigma}^\dagger f_{i\sigma}$ . These interact by a local Coulomb repulsion  $U$  and feel a local one-particle potential  $\varepsilon_f$ . Further, there are itinerant  $d$ -electrons [ $d_{i\sigma}^\dagger$  ( $d_{i\sigma}$ )] with hopping  $t$  from site to site, or alternatively with an energy-momentum dispersion relation  $\varepsilon_{\mathbf{k}}$ . Finally, there is a hybridization  $V$  between both kinds of electrons. The difference to the single impurity Anderson model is that there is not only a single site of interaction but a periodic array of sites. If we consider the strong coupling limit  $U \gg V$  of the periodic Anderson model in the particle-hole symmetric case of half-filling ( $\mu = 0$ ,  $\varepsilon_f = -U/2$ ), we have an average filling of one  $f$ - and  $d$ -electron per site. Because of the strong interaction, the  $f$ -sites are single-occupied, i.e., they can be considered as a spin. In second order perturbation theory there is a coupling  $J = 4 V^2/U$  between this localized spin and the spin-operator for the conduction electrons. That is, we can map the periodic Anderson model onto a Kondo lattice model in the strong coupling limit.

This Kondo lattice model and hence the periodic Anderson model has two competing phases: On the one hand there is the Kondo effect that we also know from the (single-site) Kondo model. At high temperatures, we have free spins and a Curie susceptibility  $\chi \sim T^{-1}$ . Below the Kondo temperature,  $T_K$  an additional Abrikosov-Suhl resonance develops at the Fermi energy, and the

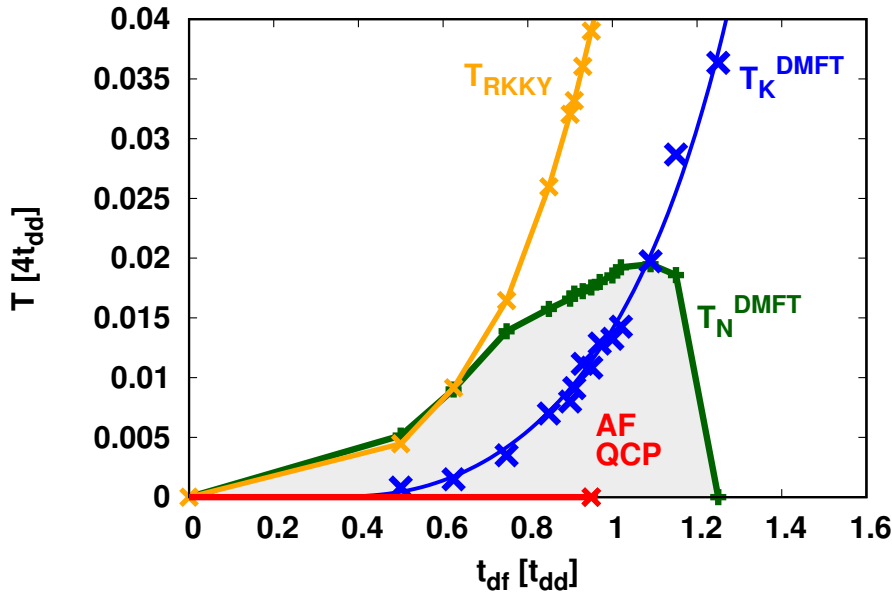


**Fig. 8:** Phase diagram temperature  $T$  vs. hybridization  $t_{df} \equiv V$  of the 2d half-filled periodic Anderson model at  $U = 4t_{dd}$  (nearest-neighbor d-d hopping). The figure shows the antiferromagnetic transition line in DMFT (green) and DΓA (red), the DMFT Kondo-temperature  $T_K^{\text{DMFT}}$  (blue), and  $T_{\text{RKKY}}$  (yellow). From [19].

spin is screened. In the particle-hole symmetric case of half-filling, this Kondo resonance is however somewhat special: We have a renormalization of the following (non-interacting) situation: There is a flat  $f$ -band at the Fermi energy  $E_F$  in the middle of the dispersive conduction band. If we now switch on the hybridization a gap opens at the band crossings at  $E_F$ . This hybridization gap at  $E_F$  leads to an insulator not only for the non-interacting model, but also if we have a renormalized picture thereof due to the Kondo effect. This phase is hence called a Kondo insulator.

For the (single-site) Kondo model

$$T_K \sim e^{-1/(2\rho(0)J)} \quad (11)$$

with non-interacting density of states  $\rho(0)$  [51], and also for the PAM we get a Kondo temperature of similar magnitude, in particular an exponential scaling; see e.g. [52] for DMFT calculations revealing an actually somewhat enhanced  $T_K$  in the PAM.

Competing with the Kondo effect is a magnetic phase. For understanding this magnetic ordering, we can envisage the magnetic Ruderman-Kittel-Kasuya-Yosida (RKKY) coupling in perturbation theory: An  $f$ -electron spin is coupling with amplitude  $J$  to the conduction electrons. These are however not immobile and carry the spin information to neighboring sites with an amplitude given by the (non-interacting) susceptibility  $\chi_0$ . On another site, the conduction electron couples again with the localized  $f$ -spin on that site, so that we altogether get the following coupling strength or critical temperature for the magnetic ordering:

$$T_{\text{RKKY}} \sim J^2 \chi_{0,\mathbf{Q}}^{\omega=0}. \quad (12)$$

In our case, the maximal coupling is for the antiferromagnetic wave vector  $\mathbf{Q} = (\pi, \pi)$  and this magnetic ordering opens a gap at  $\varepsilon_F$  so that we have an insulating antiferromagnetic phase.

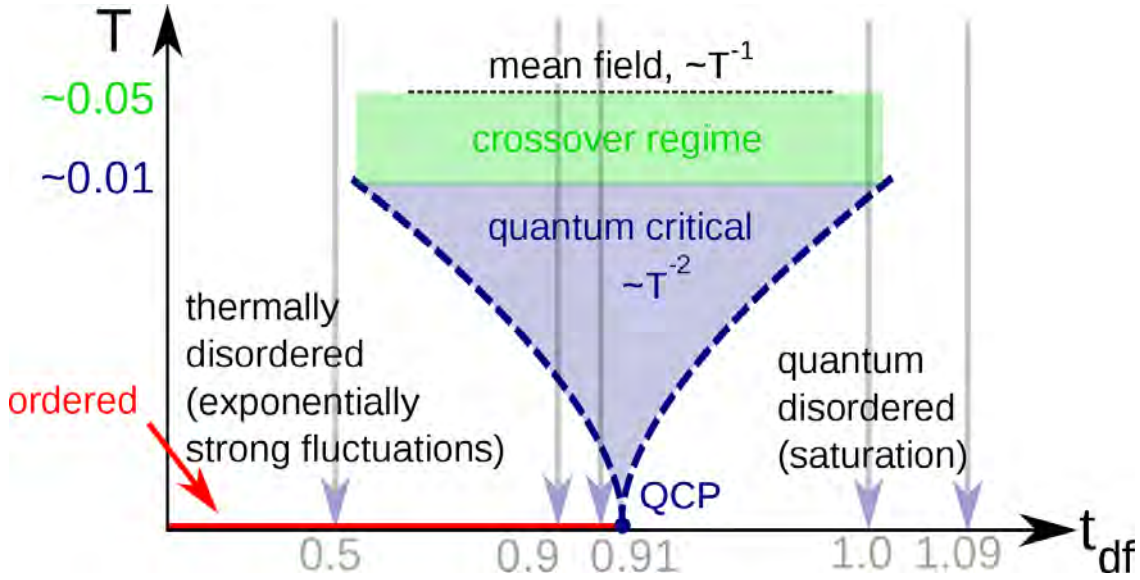


**Fig. 9:** Schematics of the quantum critical region with a scaling  $\chi \sim T^{-2}$  above the quantum critical point of Fig. 8. From [19].

Since  $T_K$  is exponentially small for small  $J$ , cf. Eq. (11),  $T_{RKKY} > T_K$  and we get an antiferromagnetic insulator at small  $J$ . But with increasing  $J$ , at some point the Kondo effect wins, and there is a phase transition to a Kondo insulator without long-range order at  $T_K \approx T_{RKKY}$ . Plotting  $T_{RKKY}$  and  $T_K$  vs.  $V$ , one obtains the famous Doniach [53] phase diagram.

In Fig. 8, we show the corresponding phase diagram as obtained using DMFT<sup>10</sup> and DΓA. Note that in DMFT,  $T_{RKKY} \sim J^2 \sim V^4$  only holds for small  $V$ ; for larger values of  $V$  this second order result is no further applicable. If the DMFT Kondo temperature<sup>11</sup>  $T_K$  becomes of the order of the DMFT antiferromagnetic ordering temperature, antiferromagnetism breaks down, and we have a Kondo insulator instead at a finite critical  $V_c$ . That is, we have a quantum critical point between a Kondo insulator at large  $V$  and an antiferromagnetic insulator at small  $V$ .

The DΓA phase diagram in Fig. 8 is distinctively different. Non-local correlations, i.e., specifically antiferromagnetic spin fluctuations, suppress the antiferromagnetic ordering. Since we are in  $2d$ , this suppression is particularly strong and DΓA respects the Mermin-Wagner theorem [55]: long-range antiferromagnetic order only survives at  $T = 0$ .<sup>12</sup> Nonetheless, we have a QCP which we further analyze in the following.

Above the QCP, there is a quantum critical region where exponents of the susceptibility and correlation length are governed by the QCP, i.e., temporal fluctuations are relevant, see Fig. 9. For the QCP of a  $2d$  antiferromagnetic insulator we expect the same exponents as for the  $2d$  Heisenberg model, i.e.,  $\chi \sim T^{-2}$ ,  $\gamma = 2$  (and with Eq. (9)  $\nu = \gamma/2 = 1$  for  $\eta \approx 0$ ) [56]. In contrast, for high temperatures we expect the Curie behavior  $\chi \sim T^{-1}$  for free spins.

<sup>10</sup>For the DMFT phase diagram of the Kondo lattice model see [54].

<sup>11</sup>determined from the maximum of the local susceptibility as a function of  $T$

<sup>12</sup>Cf. [20] for the fulfillment of the Mermin-Wagner theorem for the  $2d$  Hubbard model in DΓA.

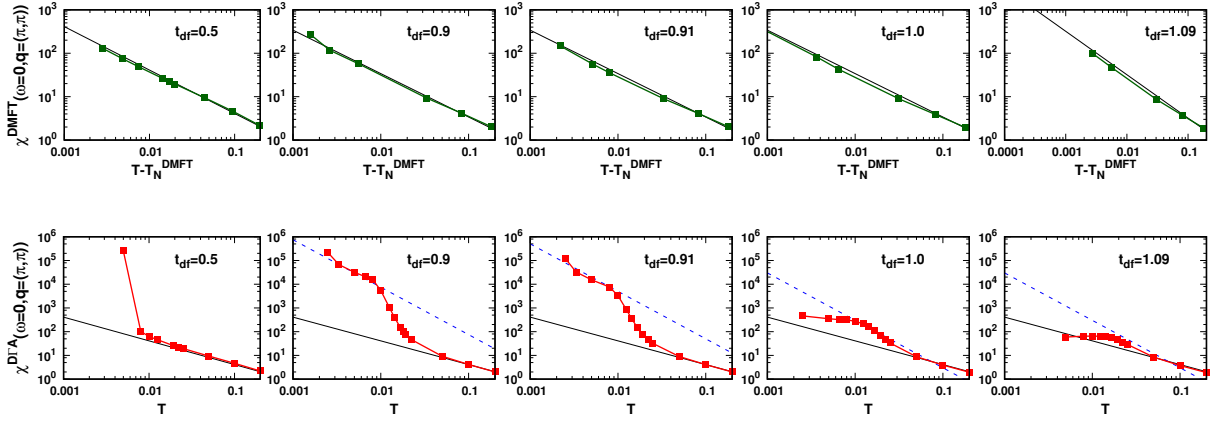


**Fig. 10:** Magnetic susceptibilities vs. temperature on a double logarithmic plot in DMFT (top panels, green) and D $\Gamma$ A (bottom panels, red) for different hybridization strengths  $t_{df} = V$ . The black solid and blue dotted lines indicate a  $\chi \propto T^{-1}$  and  $\chi \propto T^{-2}$  behavior, respectively. From [19].

The behavior of the susceptibility  $\chi \sim T^{-\gamma} \sim T^{-2}$  and related correlation length  $\xi \sim T^{-\nu} \sim T^{-1}$  in the quantum critical region can be rationalized as follows: First, the conjectured mapping onto a non-linear  $\sigma$  model [57] and quantum Monte Carlo data for the Heisenberg model [58] suggest a dynamical critical exponent  $z = 1$ . Further, in the quantum critical region, temperature sets a cut-off  $1/T$  to the correlation length in time:  $\xi_\tau \lesssim 1/T$ . Finally with  $\xi \sim T^{-\nu}$  and  $\xi_\tau \sim T^{-z\nu}$ , we have  $\xi \sim \xi_\tau^{1/z} \sim T^{-1}$  for  $z = 1$ .

Fig. 10 shows that D $\Gamma$ A is indeed able to resolve such a complex behavior and the quantum critical exponent  $\gamma = 2$  with a crossover towards  $\gamma = 1$  at high temperatures. DMFT does not include spatial correlations and hence shows a  $\chi \sim T^{-1}$  (i.e.,  $\gamma = 1$ ) behavior in the whole temperature range.

For low  $T$  and  $V < V_C$  eventually antiferromagnetic order sets in. While true long range antiferromagnetic order only sets in at  $T = 0$ , we have already an exponentially large correlation length and susceptibilities at finite  $T$ . These will eventually dominate, setting an end to the quantum critical region. Indeed for such parameters the D $\Gamma$ A results of Fig. 10 show a deviation to even larger susceptibilities at the lowest temperature.

For low  $T$  and  $V > V_C$ , on the other hand, eventually a Kondo insulating phase develops (quantum disordered phase in Fig. 9). Because this is a gapped (renormalized) band insulator with a hybridization gap, we expect that here the susceptibility eventually vanishes. Indeed for such parameters the D $\Gamma$ A results of Fig. 10 show a deviation to smaller susceptibilities at lower temperatures. A full suppression of the susceptibility because of the Kondo gap was only found at larger  $V$  (not shown); but it is also expected at  $t_{df} = V = 1.09$  but only for even lower temperatures.



## 6 Superconductivity in the 2d Hubbard model

In this section we would like to leave the question of critical exponents behind and discuss instead the prospects of superconductivity in the 2d Hubbard model. There are different ways how superconductivity might arise. But non-local correlations are the key; DMFT cannot describe  $d$ -wave superconductivity. One possibility is through antiferromagnetic spin fluctuations. These do not only lead to a pseudogap in diagrammatic extensions of DMFT [23, 20, 25] but may also act as a pairing glue for superconductivity [59].

Since antiferromagnetic spin fluctuations emerge from the particle-hole channel and superconductivity is an instability of the particle-particle channel,<sup>13</sup> one needs in principle the parquet equations for describing this interplay. The drawback is that solving these equations requires a much larger effort than solving the ladder equation in a specific channel. This restricts the available temperature range, and even if it is called “high-temperature” superconductivity the typical  $T_c$  is still quite low compared to room temperature. We will later present such parquet D $\Gamma$ A calculations, but here the lowest possible temperatures are actually not low enough to unambiguously identify a phase transition into a superconducting phase. Such parquet D $\Gamma$ A can yield, however, the leading superconducting instability and the trend that superconductivity prevails over antiferromagnetism for large enough dopings.

Before turning to these parquet results, let us instead first discuss a poor man’s variant of such a parquet equation [60]. Here, from a local vertex  $\Gamma_{\sigma\sigma'}^{\nu,\nu',\omega}$ , irreducible in the particle-hole channel, first the non-local vertex  $F_{\sigma\sigma'}^{k,k',q}$  is calculated via the Bethe-Salpeter ladder in the particle-hole and transversal particle-hole channel. This  $F$  includes spin-fluctuation; and is in turn also used to calculate  $\Sigma_k$ . Up to this point it is a conventional ladder D $\Gamma$ A calculation.

But in the next step we use this  $F$  to calculate a non-local vertex irreducible in the particle-particle channel:  $\Gamma_{pp}^{k,k',q=0} \equiv F_{k',-k,k-k'} - \Phi_{pp}^{\nu,\nu',\omega=0}$ , where all particle-particle reducible diagrams  $\Phi_{pp}$  of  $F$  are subtracted and again a four-vector notation is used. With this  $\Gamma_{pp}$  we solve the particle-particle ladder or the simplified linearized gap (Eliashberg) equation

$$\lambda v_k = - \sum_{k'} \Gamma_{pp}^{k,k',q=0} G_{k'} G_{-k'} v_{k'}, \quad (13)$$

where  $\lambda$  and  $v_k$  are the eigenvalue and eigenvector in the particle-particle channel, respectively. This is like a single parquet step, where we insert one channel (the particle-hole and transversal particle-hole) into another (the particle-particle). In a full parquet we would also turn back from the particle-particle to the particle-hole channel.

Physically Eq. (13) is akin to the standard random phase approximation (RPA) ladder which yields

$$\chi = \chi_0 / (1 + U \chi_0) \quad (14)$$

but with the momentum and frequency dependent  $\Gamma_{pp}^{k,k',q=0}$  instead of  $U$ . If the leading eigenvalue  $\lambda$  of  $-U \chi_0$  [or here of  $-\Gamma_{pp} \chi_0$ ] approaches one [ $\lambda \rightarrow 1$ ], Eq. (14) diverges and superconductivity sets in.

---

<sup>13</sup>also coined Cooperon channel

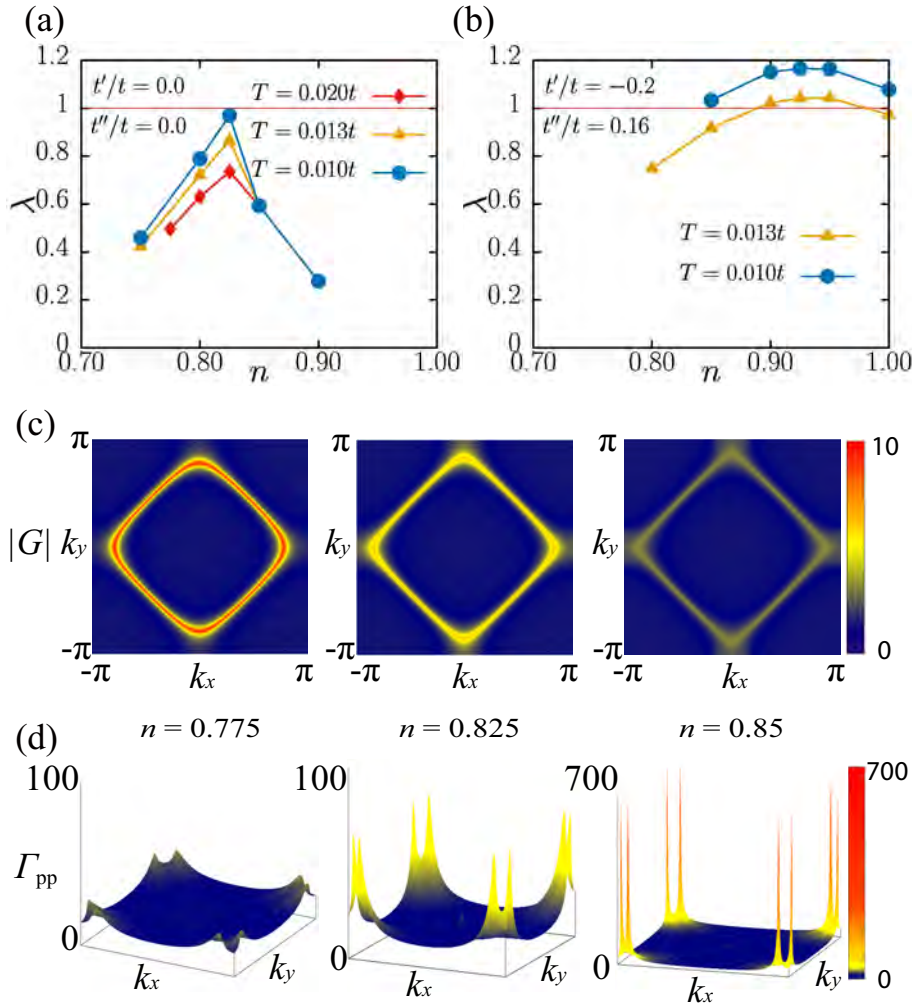


**Fig. 11:** Leading  $d$ -wave eigenvalue  $\lambda$  against band filling  $n$  for  $U = 6t$ ,  $T/t = 0.010, 0.013, 0.020$  with (a)  $t' = t'' = 0$  and (b)  $t'/t = -0.20$ ,  $t''/t = 0.16$ . (c) Momentum dependence of the Green function  $|G_{\pi/\beta, \mathbf{k}}|$ , and (d) the pairing interaction vertex  $\Gamma_{pp, \mathbf{Q}=(\pi, \pi)}$  for  $n = 0.775$  (overdoped),  $0.825$  (optimally doped), and  $0.85$  (underdoped), at  $T/t = 0.02$  and further parameters as in (a). From [60].

Fig. 11 shows the leading superconducting eigenvalue which is of  $d$ -wave symmetry and approaching  $\lambda = 1$  at  $T_c \lesssim 0.01t$  for nearest-neighbor hopping ( $t$ ) only [Fig. 11(a)]. At this  $T_c$  the superconducting susceptibility diverges. If next- ( $t'$ ) and next-next-nearest neighbor hoppings ( $t''$ ) are included with parameters adjusted to the bandstructure of Hg-based cuprates we get a somewhat larger  $T_c \approx 0.015t$  [Fig. 11(b)]. If we translate this into Kelvin, by taking a typical hopping parameter  $t \approx 0.45$  eV, this corresponds to  $T_c \approx 50 - 80$  K for a filling of  $n = 0.80 - 0.95$ . These are very reasonable  $T_c$  values for cuprates, in particular if one takes into account that no further optimization with respect to  $t'$  and  $t''$  has been done.

Fig. 11 also reveals a superconducting dome. This is the consequence of two opposing effects: On the one hand, stronger antiferromagnetic spin fluctuations towards half-filling increase the superconducting pairing glue  $\Gamma_{pp}^{k, k', q=0}$  in Fig. 11(d) so that  $T_c$  would increase towards half-filling. But at the same time the spin-fluctuations suppress the Green function which also enters



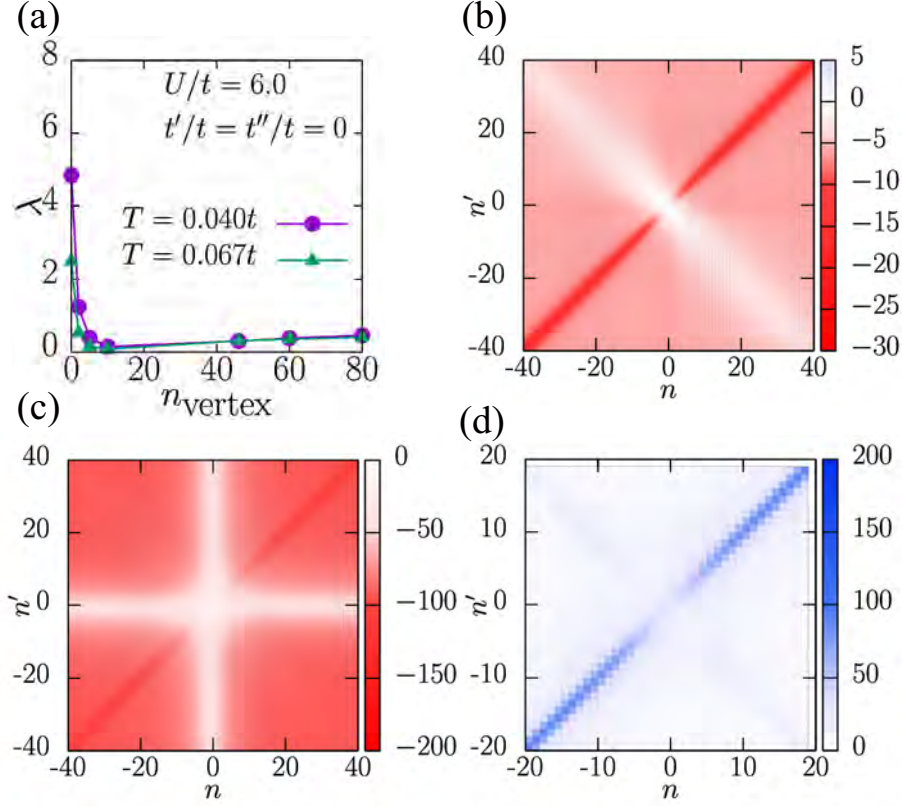


**Fig. 12:** (a) Eigenvalue  $\lambda$  against the frequency range  $n_{\text{vertex}}$  over which the local vertex structure of in the magnetic channel  $\Gamma_m(\nu_n, \nu_{n'}, \omega = 0)$  (shown in panel b) is considered. (c) Full vertex  $F_m, \mathbf{Q}=(\pi, \pi)(\nu_n, \nu_{n'}, \omega = 0)$  and (d) pairing interaction  $\Gamma_{pp, \mathbf{Q}=(\pi, \pi)(\nu_n, \nu_{n'}, \omega = 0)$ . The parameters are:  $U = 6t, t' = t'' = 0, n = 0.825$  and  $T/t = 0.040, 0.067$ . From [60].

in the Eliashberg Eq. (13). Eventually this leads even to the development of a pseudogap, but for the parameters of Fig. 11(c) only a suppression of  $|G_k|$  towards half-filling is visible. This Green function effect suppresses  $T_c$ . The balance of both effects yields the dome-like structure. A superconducting dome has also been reported in e.g. [61, 62, 26, 63], but not in the dual-fermion approach [64, 21] or in Ref. [65].

Kitatani *et al.* [60] were further able to point out that the dynamics of the vertex, i.e., its frequency structure plays a pivotal role for  $T_c$ . That is, the vertex dynamics suppresses  $T_c$  by one order of magnitude. Without this suppression room temperature superconductivity would be possible.

Fig. 12(b) shows the local vertex  $\Gamma_m$  that serves as starting point for the D $\Gamma$ A calculation. Clearly, it is suppressed at the lowest frequencies. This low frequency suppression is also seen in the non-local full vertex  $F_m, \mathbf{Q}$  that is calculated from  $\Gamma_m$  and shown in Fig. 12(c). That is, antiferromagnetic spin fluctuations are suppressed for small frequencies. Not surprisingly also the superconducting pairing glue, i.e., the non-local vertex irreducible in the particle-particle channel in Fig. 12(d) is suppressed.

Fig. 12(a) shows the values of the superconducting eigenvalue  $\lambda$  that we had without this suppression of the vertex. More precisely, the  $\lambda$  that we would have if we replaced the local vertex of Fig. 12(b) by its static limiting value  $\Gamma_m^{\nu_n, \nu_{n'}, \omega=0} = -U$  for Matsubara frequencies  $|\nu_n|, |\nu_{n'}|, |\omega| > n_{\text{vertex}}$ . For  $n_{\text{vertex}} = 0$ , we have  $\Gamma_m^{\nu_n, \nu_{n'}, \omega=0} = -U$  at all frequencies and an order of

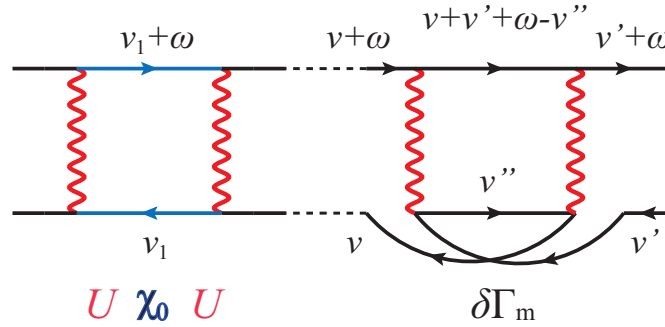


**Fig. 13:** Left part of the diagram: a typical RPA ladder diagram in the particle-hole channel with building block  $U$  (red wavy line) and  $\chi_0$  (two blue Green functions with fermionic frequencies  $\nu_1$  and  $\nu_1 + \omega$ ). Right part of the diagram: Local (second-order) vertex correction  $\delta\Gamma_m$  with a particle-particle bubble. From [60].

magnitude larger  $\lambda$  in Fig. 12(a); for  $n_{\text{vertex}} \rightarrow \infty$  we recover the proper D $\Gamma$ A result. Not only  $\lambda$  is enhanced but along with it also  $T_c$  from about 0.01t to 0.13t.

In this situation it is imperative to identify the physical processes that are responsible for the suppression of  $\Gamma_m$  in Fig. 12(b). Analyzing diagrams order by order, Kitatani *et al.* [60] found that already the second order particle-particle diagram as displayed in Fig. 13 (right part) is the main driving force for the suppression of  $\Gamma_m$  in Fig. 12(b). From Fig. 13 we also see that the particle-particle bubble becomes maximal for  $\nu + \nu' + \omega \approx 0$ . Note that  $\omega = 0$  in Fig. 12(b), so that the suppression is maximal at  $\nu = -\nu'$  in Fig. 12(b). These particle-particle screening processes explain the substantial suppression of the local  $\Gamma_m$  and hence of antiferromagnetic spin fluctuations and the superconducting pairing glue  $\Gamma_{pp}$  for lowest frequencies.

Having identified this oppressor of high temperature superconductivity, a screening of antiferromagnetic spin fluctuations by local particle-particle bubbles, gives us some hope to find new ways of enhancing  $T_c$ , possibly to room temperature and beyond. However, this is only the first step, getting rid of (a large) particle-particle screening is not at all trivial, and remains a challenge for the future.

## Superconductivity in parquet D $\Gamma$ A

Finally, we would like to turn to the more complete parquet D $\Gamma$ A. As already mentioned, this means that we have to do calculations at higher temperatures, considerably above  $T_c$ . Fig. 14 shows the parquet D $\Gamma$ A result for a filling  $n = 0.85$  where we have  $d$ -wave superconductivity in Fig. 12. Indeed, in this parameter range Kauch *et al.* find that  $d$ -wave superconductivity is the leading instability in the (superconducting) particle-particle channel, seemingly surpassing the magnetic instability at lower temperatures. For this doping, the magnetic susceptibility is still peaked at  $\mathbf{Q} = (\pi, \pi)$  in Fig. 14 (left). This antiferromagnetic wave vector  $\mathbf{Q} = (\pi, \pi)$  naturally connects the positive [at  $\mathbf{k} = (\pm\pi, 0)$ ] and negative [at  $\mathbf{k} = (0, \pm\pi)$ ] regions of the superconducting  $d$ -wave eigenvector in Fig. 14 (middle panels), as is needed for the Eliashberg Eq. (13) to realize an eigenstate for a repulsive interaction. Fig. 14 (right) displays the same

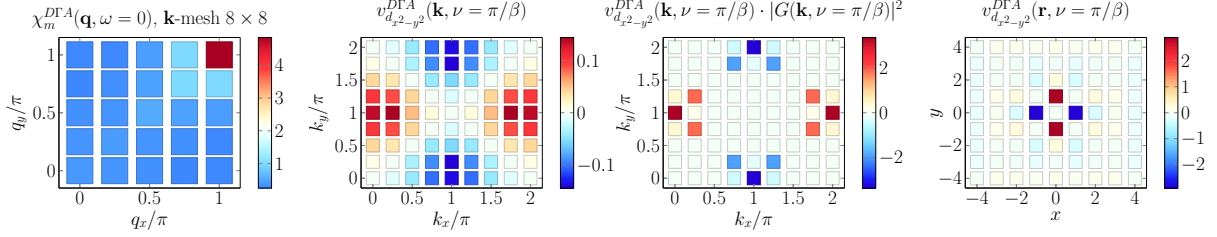


**Fig. 14:** Left: Magnetic susceptibility  $\chi_m(\mathbf{q}, \omega = 0)$  vs.  $q_x$  and  $q_y$  at  $U = 4t$ ,  $\beta = 20/t$ ,  $n = 0.85$  as obtained from parquet D $\Gamma$ A with an  $8 \times 8$  cluster. Left-middle: Eigenvector  $v_{d_{x^2-y^2}}(\mathbf{k}, \nu = \pi/\beta)$  corresponding to the dominant eigenvalue in the particle-particle channel. Right-middle: Projection of  $v_{d_{x^2-y^2}}(\mathbf{k}, \nu = \pi/\beta)$  onto the Fermi surface as obtained by multiplying with  $|G|^2$  at the lowest Matsubara frequency. Right: Eigenvector  $v_{d_{x^2-y^2}}(\mathbf{r}, \nu = \pi/\beta)$  Fourier-transformed to lattice space (in units of lattice vector  $a = 1$ ). From [66].

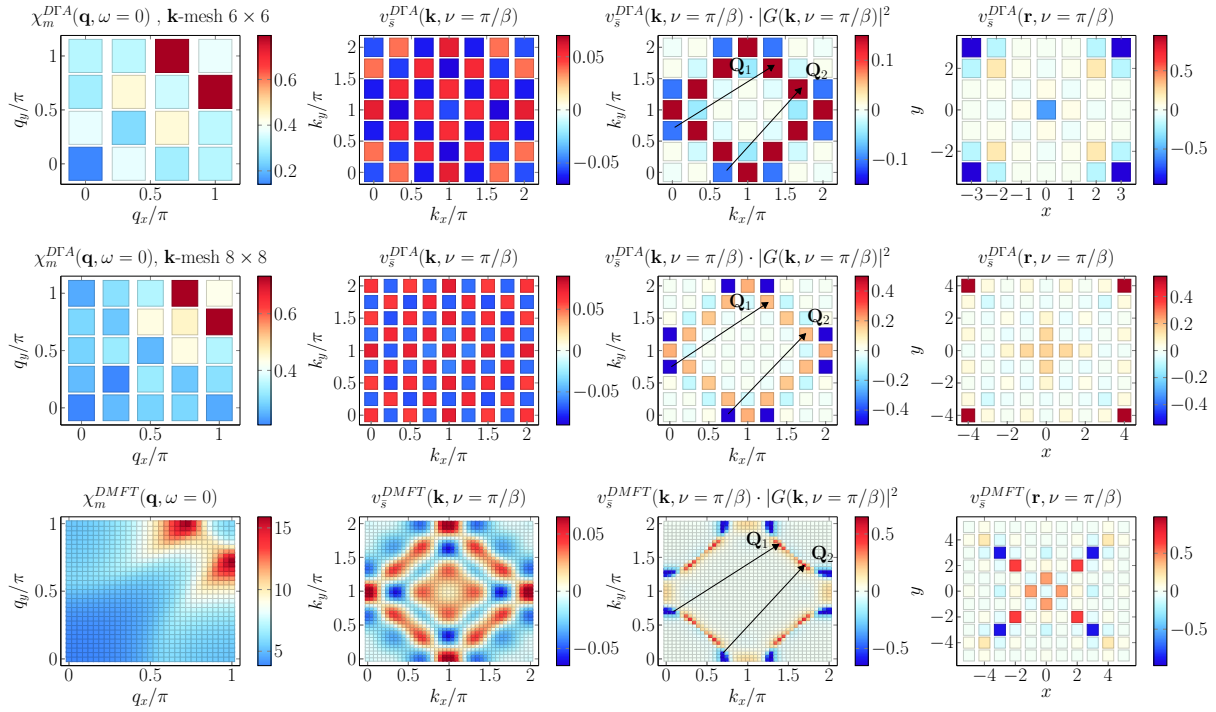
superconducting eigenvector in real space, showing that the eigenvector describes a nearest-neighbor plus-minus structure, i.e.,  $d_{x^2-y^2}$ , alternation.

Fig. 15 shows the same kind of analysis but now deeply in the overdoped regime, i.e., for  $n = 0.72$ . Here, the magnetic susceptibility is peaked at an incommensurate wave vector  $\mathbf{Q}_1 = (\pi + \delta, \pi)$  [and symmetrically related  $\mathbf{Q}_2 = (\pi, \pi + \delta)$  etc.] similar as in Fig. 5 for the 3d Hubbard model. For the finite momentum clusters of parquet D $\Gamma$ A,  $\delta$  can, as a matter of course, only take values congruent with the momentum grid. In this incommensurate case, the leading superconducting eigenvalue is not  $d$ -wave anymore but a higher-order  $\bar{s}$ -wave.

Fig. 15 (left-middle) shows the momentum dependence of this  $\bar{s}$ -wave, which becomes more obvious if we project onto the Fermi surface (right-middle). Because of the incommensurability,  $\mathbf{Q}_1$  does not link the antinodal points  $(0, \pm\pi)$  and  $(\pm\pi, 0)$  any longer as for  $n = 0.85$  in Fig. 14. Instead  $\mathbf{Q}_1$  and  $\mathbf{Q}_2$  connect the points of the Fermi surface which are close to the antinodal points  $(0, \pm\pi)$  and  $(\pm\pi, 0)$  and have a large negative component of the eigenvector  $v_{\bar{s}}$  to points that are in-between the nodal and antinodal point on the Fermi surface and have a large positive component of the eigenvector  $v_{\bar{s}}$ , see the  $\mathbf{Q}_1$  and  $\mathbf{Q}_2$  arrows in Fig. 15. In other words, the incommensurate antiferromagnetic ordering is not compatible with  $d$ -wave superconductivity any longer, but requires an even more complex  $\mathbf{k}$ -dependence of the order parameter (eigenvector for  $\lambda = 1$ ). This complex  $\mathbf{k}$ -dependence is dominated by terms  $\cos(nk_x) \cos(nk_y)$  with  $n = 3, 4$ .

Fig. 15 (right) shows the eigenvector contributions in real space. This Figure makes clear why we call it an  $s$ -wave: all neighbors of the same shell of neighbors contribute with the same sign. In contrast, in Fig. 14 we have an alternating ( $d$ -wave) sign. Further, in Fig. 15 (right) it is not a next-nearest or local  $s$ -wave component that dominates. Instead the leading contribution stems from a relative lattice vector further away along the diagonal [ $\mathbf{R} = (n, n)$  with  $n = 3, 4$  in Fig. 15 (right)]. Kauch *et al.* hence coin it higher-order  $\bar{s}$ -wave: If we expand the angular dependence of  $v_{\bar{s}}$  in terms of  $s$ ,  $d$ -wave etc. it is an angular  $s$ -wave<sup>14</sup>; but it is of higher order

<sup>14</sup>More precise (but less common) would be to call it a  $a_{1g}$ -wave because the eigenvector belongs to this irreducible representation of the square lattice symmetry; there is no continuous rotational symmetry as  $s$ -wave might suggest.



**Fig. 15:** Parquet  $D\Gamma A$  for a  $6 \times 6$  (top) or  $8 \times 8$  (middle) cluster, and simplified calculation on a larger cluster with DMFT susceptibility as a starting point (bottom). Left column: Magnetic susceptibility  $\chi_m(\mathbf{q}, \omega = 0)$  vs.  $q_x$  and  $q_y$  at  $U = 5t$ ,  $\beta = 15/t$ ,  $n = 0.72$ . Left-middle column: Eigenvector  $v_{\bar{s}}(\mathbf{k}, \nu = \pi/\beta)$  corresponding to the dominant eigenvalue in the particle-particle channel. Right-middle column: Projection of  $v_{\bar{s}}(\mathbf{k}, \nu = \pi/\beta)$  onto the Fermi surface as obtained by multiplying with  $|G|^2$  at the lowest Matsubara frequency. Right: Eigenvector  $v_{\bar{s}}(\mathbf{r}, \nu = \pi/\beta)$  in real (lattice) space. From [66].

in the radial expansion (couples further away neighbors). How far apart the coupled sites are depends on the specific incommensurable wave vector and is also influenced by the finite cluster size. But the auxiliary calculations, starting from the DMFT susceptibility on a large cluster [Fig. 15 (bottom)] further confirm that such a higher-order  $\bar{s}$ -wave phase naturally develops if the magnetic spin fluctuations are incommensurable.

## 7 Conclusion and outlook

To sum up, we have briefly recapitulated the  $D\Gamma A$  method before reviewing recent highlights obtained with it: the calculation of critical exponents, quantum criticality, and superconductivity. In the following we will focus only on the latter two aspects. Quite generally, the advantage of diagrammatic extensions of  $D\Gamma A$  is that they are able to describe short- and long-range correlations as well as temporal correlations, which become relevant at a quantum critical point. In Section 4, we have seen that particular lines on the Fermi surface of the  $3d$  Hubbard model with nearest-neighbor hopping, so-called Kohn-lines, lead to a new universality class of critical exponents.

For studying a situation with  $d + z < 4$ , in Section 5 we turned to the periodic Anderson model in  $d = 2$  at half-filling. This model describes a phase transition from an antiferromagnetic insulator to a Kondo insulator ( $z = 1$ ). Here a quantum critical region could be identified, where the susceptibility shows a  $\chi \sim T^{-2}$  behavior, whereas at higher temperatures  $\chi \sim T^{-1}$ . For a hybridization strength smaller than the QCP and for temperatures below the quantum critical region we eventually find an even stronger increase of  $\chi$ . This is to be expected since even though there is no long-range antiferromagnetic order for  $T > 0$  there is still an exponentially strong increase of the susceptibility and correlation length at low temperatures. For a hybridization strength larger than the QCP and for temperatures below the quantum critical region we are in the Kondo insulating regime so that eventually  $\chi \rightarrow 0$  because of the (renormalized) single-particle excitation gap.

In Section 6 we turned to superconductivity in the  $2d$  Hubbard model. We find  $d$ -wave superconductivity with a dome-like  $T_c$ -structure as a function of doping and a reasonable  $T_c \approx 50$  K. Most interestingly, an order of magnitude larger  $T_c$ 's, i.e., room temperature superconductivity, would be possible if the vertex would not be screened at low frequencies by particle-particle diagrams. Understanding this suppression of  $T_c$  gives us hope for identifying new routes towards higher  $T_c$ 's. At large doping levels, we find a high-order  $\bar{s}$ -wave superconductivity to be the dominant superconducting channel, which is a natural consequence of having incommensurate antiferromagnetic spin fluctuations.

Up to now, the focus of diagrammatic extensions of DMFT has been on method development and applications to simple models such as the Hubbard, the periodic Anderson, and Falicov Kimball model. As a first step such model calculations are crucial for better understanding physics. In the future we will see many more applications to non-equilibrium and real materials. First realistic materials calculations [67] have already been performed for  $\text{SrVO}_3$  using *ab initio* DGA [67]. This AbinitoDGA (ADGA) code for solving multi-orbital ladder DGA equations including non-local interactions is made available via Gnu Public license [68]. For the model Hamiltonians studied in these lecture notes, instead, the one-orbital ladder DGA code (ladderDGA [69]) with Moriya-esque  $\lambda$  correction and the victory code [70] for solving the parquet equations have been used.

## Acknowledgments

First of all, I would like to thank my close and in many cases long-term co-workers in the research area of diagrammatic extensions of DMFT: A. Galler, P. Gunacker, A. Kauch, J. Kaufmann, A. Katanin, M. Kitatani, G. Li, P. Pudleiner, T. Ribic, G. Rohringer, G. Sangiovanni, T. Schäfer, C. Taranto, P. Thunström, J. Tomczak, A. Toschi, A. Valli, and M. Wallerberger. Without them, the development presented in these Lecture Notes would not have been possible. Secondly I acknowledge financial support by the European Research Council under the European Union's Seventh Framework Program (FP/2007-2013) through ERC Grant No. 306447, and the Austrian Science Fund (FWF) through project P30997.

## References

- [1] W. Metzner and D. Vollhardt, Phys. Rev. Lett. **62**, 324 (1989)
- [2] A. Georges and G. Kotliar, Phys. Rev. B **45**, 6479 (1992)
- [3] A. Georges, G. Kotliar, W. Krauth, and M.J. Rozenberg, Rev. Mod. Phys. **68**, 13 (1996)
- [4] K. Held, I.A. Nekrasov, G. Keller, V. Eyert, N. Blümer, A.K. McMahan, R.T. Scalettar, T. Pruschke, V.I. Anisimov, and D. Vollhardt, Phys. Status Solidi B **243**, 2599 (2006), previously appeared as Psi-k Newsletter No. 56 (April 2003)
- [5] G. Kotliar, S.Y. Savrasov, K. Haule, V.S. Oudovenko, O. Parcollet, and C.A. Marianetti, Rev. Mod. Phys. **78**, 865 (2006)
- [6] K. Held, Adv. Phys. **56**, 829 (2007)
- [7] T.A. Maier, M. Jarrell, T.C. Schulthess, P.R.C. Kent, and J.B. White, Phys. Rev. Lett. **95**, 237001 (2005)
- [8] A. Toschi, A.A. Katanin, and K. Held, Phys. Rev. B **75**, 045118 (2007)
- [9] A.N. Rubtsov, M.I. Katsnelson, and A.I. Lichtenstein, Phys. Rev. B **77**, 033101 (2008)
- [10] G. Rohringer, A. Toschi, H. Hafermann, K. Held, V.I. Anisimov, and A.A. Katanin, Phys. Rev. B **88**, 115112 (2013)
- [11] C. Taranto, S. Andergassen, J. Bauer, K. Held, A. Katanin, W. Metzner, G. Rohringer, and A. Toschi, Phys. Rev. Lett. **112**, 196402 (2014)
- [12] T. Ayrál and O. Parcollet, Phys. Rev. B **92**, 115109 (2015)
- [13] G. Li, Phys. Rev. B **91**, 165134 (2015)
- [14] G. Rohringer, H. Hafermann, A. Toschi, A.A. Katanin, A.E. Antipov, M.I. Katsnelson, A.I. Lichtenstein, A.N. Rubtsov, and K. Held, Rev. Mod. Phys. **90**, 025003 (2018)
- [15] G. Rohringer, A. Toschi, A. Katanin, and K. Held, Phys. Rev. Lett. **107**, 256402 (2011)
- [16] D. Hirschmeier, H. Hafermann, E. Gull, A.I. Lichtenstein, and A.E. Antipov, Phys. Rev. B **92**, 144409 (2015)
- [17] A.E. Antipov, E. Gull, and S. Kirchner, Phys. Rev. Lett. **112**, 226401 (2014)
- [18] T. Schäfer, A.A. Katanin, K. Held, and A. Toschi, Phys. Rev. Lett. **119**, 046402 (2017)
- [19] T. Schäfer, M. Kitatani, A.A. Katanin, A. Toschi, and K. Held, (unpublished) (2018)
- [20] A.A. Katanin, A. Toschi, and K. Held, Phys. Rev. B **80**, 075104 (2009)

- [21] J. Otsuki, H. Hafermann, and A.I. Lichtenstein, Phys. Rev. B **90**, 235132 (2014)
- [22] T. Schäfer, F. Geles, D. Rost, G. Rohringer, E. Arrigoni, K. Held, N. Blümer, M. Aichhorn, and A. Toschi, Phys. Rev. B **91**, 125109 (2015)
- [23] A.N. Rubtsov, M.I. Katsnelson, A.I. Lichtenstein, and A. Georges, Phys. Rev. B **79**, 045133 (2009)
- [24] C. Jung: *Superperturbation theory for correlated fermions*, Ph.D. thesis, University of Hamburg, 2010
- [25] T. Schäfer, A. Toschi, and K. Held, J. Magn. Magn. Mater. **400**, 107 (2016)
- [26] M. Kitatani, N. Tsuji, and H. Aoki, Phys. Rev. B **92**, 085104 (2015)
- [27] K. Held: *Dynamical Vertex Approximation* in E. Pavarini, E. Koch, D. Vollhardt, A.I. Lichtenstein (eds.): *Autumn School on Correlated Electrons. DMFT at 25: Infinite Dimensions Modeling and Simulation*, Vol. 4 (Forschungszentrum Jülich, 2014) [arXiv:1411.5191]
- [28] C. De Dominicis, J. Math. Phys. **3**, 983 (1962)
- [29] C. De Dominicis and P.C. Martin, J. Math. Phys. **5**, 14 (1964)
- [30] N.E. Bickers: *Theoretical Methods for Strongly Correlated Electrons* (Springer-Verlag New York Berlin Heidelberg, 2004), Ch. 6, pp. 237–296
- [31] T. Ribic, P. Gunacker, S. Isakov, M. Wallerberger, G. Rohringer, A.N. Rubtsov, E. Gull, and K. Held, Phys. Rev. B **96**, 235127 (2017)
- [32] E. Gull, A.J. Millis, A.I. Lichtenstein, A.N. Rubtsov, M. Troyer, and P. Werner, Rev. Mod. Phys. **83**, 349 (2011)
- [33] P. Gunacker, M. Wallerberger, E. Gull, A. Hausoel, G. Sangiovanni, and K. Held, Phys. Rev. B **92**, 155102 (2015)
- [34] P. Gunacker, M. Wallerberger, T. Ribic, A. Hausoel, G. Sangiovanni, and K. Held, Phys. Rev. B **94**, 125153 (2016)
- [35] G. Rohringer, A. Valli, and A. Toschi, Phys. Rev. B **86**, 125114 (2012)
- [36] G. Rohringer and A. Toschi, Phys. Rev. B **94**, 125144 (2016)
- [37] L.S. Ornstein and F. Zernike, Proc. Roy. Acad. Amsterdam **17**, 793 (1916)
- [38] C. Holm and W. Janke, Phys. Rev. B **48**, 936 (1993)
- [39] M.E. Fisher, Rep. Prog. Phys. **30**, 615 (1967)

- [40] P. Sémon and A.-M.S. Tremblay, Phys. Rev. B **85**, 201101 (2012)
- [41] N. Goldenfeld: *Lectures On Phase Transition And The Renormalization Group* (CRC Press, 2018)
- [42] L. Del Re, M. Capone, and A. Toschi, arxiv:1805.05194 (2018)
- [43] H. v. Löhneysen, A. Rosch, M. Vojta, and P. Wölfle, Rev. Mod. Phys. **79**, 1015 (2007)
- [44] J.A. Hertz, Phys. Rev. B **14**, 1165 (1976)
- [45] A.J. Millis, Phys. Rev. B **48**, 7183 (1993)
- [46] T. Moriya: *Spin Fluctuations in Itinerant Electron Magnetism* (Springer Verlag, Berlin, Heidelberg, 1985)
- [47] J.-X. Zhu, D.R. Grempel, and Q. Si, Phys. Rev. Lett. **91**, 156404 (2003)
- [48] Q. Si and J.L. Smith, Phys. Rev. Lett. **77**, 3391 (1996)
- [49] R. Chitra and G. Kotliar, Phys. Rev. Lett. **84**, 3678 (2000)
- [50] W. Kohn, Phys. Rev. Lett. **2**, 393 (1959)
- [51] A. Hewson: *The Kondo Problem to Heavy Fermions* (Cambridge University Press, 1993)
- [52] T. Pruschke, R. Bulla, and M. Jarrell, Phys. Rev. B **61**, 12799 (2000)
- [53] S. Doniach, Physica B+C **91**, 231 (1977)
- [54] J. Otsuki, H. Kusunose, and Y. Kuramoto, Phys. Rev. Lett. **102**, 017202 (2009)
- [55] N.D. Mermin and H. Wagner, Phys. Rev. Lett. **17**, 1307 (1966)
- [56] S. Chakravarty, B.I. Halperin, and D.R. Nelson, Phys. Rev. Lett. **60**, 1057 (1988)
- [57] A.V. Chubukov, S. Sachdev, and J. Ye, Phys. Rev. B **49**, 11919 (1994)
- [58] M. Troyer, M. Imada, and K. Ueda, J. Phys. Soc. Jpn **66**, 2957 (1997)
- [59] D.J. Scalapino, Rev. Mod. Phys. **84**, 1383 (2012)
- [60] M. Kitatani, T. Schäfer, H. Aoki, and K. Held, arXiv:1801.05991 (2018)
- [61] B. Kyung, J.-S. Landry, and A.-M.S. Tremblay, Phys. Rev. B **68**, 174502 (2003)
- [62] T. Maier, M. Jarrell, T. Pruschke, and M.H. Hettler, Rev. Mod. Phys. **77**, 1027 (2005)
- [63] J. Vučičević, T. Ayral, and O. Parcollet, Phys. Rev. B **96**, 104504 (2017)



- [64] H. Hafermann, M. Kecker, S. Brener, A.N. Rubtsov, M.I. Katsnelson, and A.I. Lichtenstein, *J. Supercond. Nov. Magn.* **22**, 45 (2009)
- [65] W. Metzner, M. Salmhofer, C. Honerkamp, V. Meden, and K. Schönhammer, *Rev. Mod. Phys.* **84**, 299 (2012)
- [66] A. Kauch, F. Hörbinger, G. Li, and K. Held, (unpublished) (2018)
- [67] A. Galler, P. Thunström, P. Gunacker, J.M. Tomczak, and K. Held, *Phys. Rev. B* **95**, 115107 (2017)
- [68] A. Galler, P. Thunström, J. Kaufmann, M. Pickem, J.M. Tomczak, and K. Held, [arXiv:1710.06651](https://arxiv.org/abs/1710.06651) (2017)
- [69] G. Rohringer, A. Katanin, T. Schäfer, A. Hausoel, K. Held, and A. Toschi, [github.com/ladderDGA](https://github.com/ladderDGA) (2018)
- [70] G. Li, A. Kauch, P. Pudleiner, and K. Held, [arXiv:1708.07457](https://arxiv.org/abs/1708.07457) (2017)



# 15 Correlated Electrons out of Equilibrium: Non-Equilibrium DMFT

Martin Eckstein

University of Erlangen-Nürnberg

91058 Erlangen

## Contents

<b>1</b>	<b>Introduction</b>	<b>2</b>
<b>2</b>	<b>The Keldysh formalism</b>	<b>4</b>
2.1	Two-time Green functions and electronic structure . . . . .	4
2.2	The Keldysh contour . . . . .	7
2.3	Kadanoff-Baym equations . . . . .	12
2.4	Steady-state formalism . . . . .	16
<b>3</b>	<b>Non-equilibrium dynamical mean-field theory</b>	<b>16</b>
3.1	The dynamical mean-field formalism . . . . .	16
3.2	Impurity solvers . . . . .	19
<b>4</b>	<b>Photo-doping the Mott insulator</b>	<b>24</b>
4.1	Paramagnetic Mott insulator . . . . .	24
4.2	Dynamics of the antiferromagnetic Mott insulator . . . . .	28
<b>5</b>	<b>Outlook and further questions</b>	<b>32</b>

# 1 Introduction

The conventional way to manipulate materials properties involves changes of external parameters such as pressure or magnetic fields on time scales which are slow compared to the intrinsic relaxation times in the solid. The theoretical understanding of condensed matter phases can therefore largely be build on the assumption that solids are locally in thermal equilibrium at all times. This has changed with the availability of femtosecond laser pulses, which can be used to excite a system and probe its dynamics before the return to equilibrium [1]. Such experiments have opened a new field of research in condensed matter physics with many facets:

- **Time-resolved spectroscopy:** Femtosecond pulses are available in a wide frequency range, including the THz, infra-red, visible, or X-ray domain. One can therefore make both excitation and probe selective to certain degrees of freedom, and thus observe in real time how energy is passed on after an excitation. For example, electronic relaxation processes can be revealed by measuring the population dynamics in the conduction band using time-resolved photoemission spectroscopy, or one can distinguish charge-density waves of lattice or electronic origin by how fast they can be quenched [2].
- **Materials design out of equilibrium:** Other than thermal excitation, which typically results in a suppression of all ordered states, a sufficiently strong ultra-short excitation can enhance electronic orders or reveal collective phases which are not represented in the equilibrium phase diagram. This is, in particular, relevant if the equilibrium phase diagram results from competing effects. For example, signatures of light-induced superconductivity have been observed in various materials [3,4], electronic excitation can enhance the order parameter in an exciton condensate [5], and changes of the electron population can close the gap in  $\text{VO}_2$  [6]. In a number of cases femtosecond excitation eventually results in hidden states, i.e., long-lived metastable states with new types of magnetic and orbital order, which are entirely inaccessible along thermodynamic pathways [7, 8].
- **Dynamical stabilization:** Dynamical stabilization implies the modification of properties *while* a system is driven by an external perturbation. Experimentally established is the technique of nonlinear phononics [9], by which the lattice structure is deformed transiently along the coordinates of phonons which couple anharmonically to selectively excited modes. More generally, when a system with some nonlinearity, which may be the interaction or the dependence of the dispersion  $\varepsilon(\mathbf{k})$  on  $\mathbf{k}$ , is periodically driven, its period-averaged dynamics and can be understood in terms of a so-called Floquet Hamiltonian, which can qualitatively differ from the un-driven Hamiltonian [10]. Examples include band-structure control (e.g., the generation of topologically nontrivial bands by circularly polarized light [11]), or a manipulation of low energy Hamiltonians (superconducting pairing [12, 13], spin-exchange [14]). While the latter has been demonstrated in cold atoms [15], a potential application of this so-called Floquet engineering to real solids hinges on the question of heating.

- **Strong-field physics:** On the femtosecond timescale, a solid can endure external fields of the order volts per lattice constant, which would lead to an immediate breakdown of the material in the steady state. Such fields can be used to drive coherent non-equilibrium dynamics, in which electrons explore a sizeable fractions of the Brillouin zone, leading to phenomena like high-harmonic generation in solids [16].

A challenge for the investigation of non-equilibrium states in solids is that many fundamental concepts of condensed matter physics rely on thermal equilibrium. An important example is the electronic structure itself. Quasi-particles in correlated systems may become ill-defined by a non-equilibrium excitation which involves a substantial population of states far from the Fermi surface. In this limit, even a theoretical approach based on kinetic equations, which provides an intuitive rate-equation for the time-dependent population of electrons in a given (“rigid”) band structure, becomes questionable. Below we will describe how real-time Green functions give an interpretation of the electronic structure in non-equilibrium states. Another fundamental question is how fast and whether an interacting system *thermalizes* after a perturbation [17]. In many cases, the energy deposited by a laser in the electronic system would imply electronic temperatures large enough to melt, rather than enhance, various orders. However, beyond a description based on a Boltzmann equation the understanding of thermalization is not obvious. In general, thermalization can be delayed by the presence of a gap. In the strongly interacting Hubbard model, thermalization after an sudden turn-on of the interaction can happen on the ultra-fast time-scale of the inverse hopping, but only in a narrow regime of interactions [18]. Ideal integrable model systems never thermalize, and even though such models hardly find an exact representation in condensed matter, the vicinity to an integrable point can result in a two-stage relaxation where the earlier stage (pre-thermalization) is governed by the integrable dynamics [19] and can feature long-range order even when the final thermal state does not. In these notes we attempt an understanding of the many-body dynamics in solids from a model perspective. For a general discussion, let us take the Hubbard model as a paradigmatic example

$$H(t) = - \sum_{ij,\sigma} v_{ij}(t) c_{i\sigma}^\dagger c_{j\sigma} + U \sum_i c_{i\uparrow}^\dagger c_{i\uparrow} c_{i\downarrow}^\dagger c_{i\downarrow}. \quad (1)$$

Here,  $c_{i\sigma}^\dagger$  ( $c_{i\sigma}$ ) create (annihilate) an electron with spin  $\sigma$  at site  $i$  of a crystal lattice,  $v_{ij}$  is the hopping matrix element, and electrons interact via a local Coulomb interaction  $U$ . Taking this model (or its multi-orbital variants) as a faithful representation of the electronic properties, we can ask how the state of the system evolves from a given initial state, which is usually the thermal ensemble for the Hamiltonian  $H(0)$ . Time-dependent electromagnetic fields (the laser excitation) are most easily included by a Peierls substitution, which introduces the vector potential  $\mathbf{A}(\mathbf{r}, t)$  as a phase factor in the hopping matrix elements,

$$v_{ij}(t) = v_{ij} \exp\left(-\frac{ie}{\hbar} \int_{\mathbf{R}_i}^{\mathbf{R}_j} d\mathbf{r} \cdot \mathbf{A}(\mathbf{r}, t)\right), \quad (2)$$

and adds a scalar potential term  $e \sum_{i\sigma} \Phi(\mathbf{R}_i, t) c_{i\sigma}^\dagger c_{i\sigma}$  to the Hamiltonian ( $e$  is the charge of an electron). When we are interested in the action of optical or THz fields, the wavelength is

much longer than the lattice spacing, and the field can be approximated as space-independent, with  $\mathbf{E}(t) = -\partial_t \mathbf{A}(t)$  and  $\Phi = 0$ . Including electric fields in multi-band models is more subtle, because the Peierls substitution does not describe inter-band dipole couplings or Stark shifts of the Wannier orbitals. We also note that the Hamiltonian (1) describes only electronic motion, while in a solid also the lattice dynamics does play a role at longer times. Unless we are interested in a specific response such as a deformation of the lattice, we may account for this by including the phonons as a dissipative environment (heat bath), which is relatively straightforward in the Keldysh formalism used below. In many cases of interest, however, only short times are of interest, on which electrons may safely be considered as an isolated system.

The Keldysh formalism provides the framework to discuss many-body physics for transient and steady-state non-equilibrium situations (diagrammatic perturbation theory, path integrals). All diagrammatic approximations, such as perturbation theory, GW, etc., can be reformulated in the time-domain, by replacing imaginary-time arguments and frequencies by times on a more general real-time contour, only the numerical evaluation of the resulting equations in real-time is far more costly, as discussed below. Regarding correlated materials, dynamical mean-field theory (DMFT) [20] and its extensions present a very versatile approach to obtain the electronic structure even from first principles, as discussed in previous lectures of this series [21]. Like any other many-body formalism based on imaginary time, DMFT can be reformulated for the real-time dynamics, as noted first in [22, 23]. Although the evaluation of the DMFT equations is more challenging (in particular the solution of the auxiliary impurity problem), non-equilibrium DMFT has since then been applied to a wide range of topics [24], including the dynamics after quenches and dynamical phase transitions in various ideal model systems, the study of photo-induced dynamics in Mott insulators, the understanding of light-induced phases (manipulation of magnetic interactions, light-induced superconductivity, hidden states with spin and orbital order), the investigation of strong-field phenomena in correlated systems such as the dielectric breakdown and high-harmonic generation, and the properties of periodically driven states (Floquet engineering).

In these notes we explain the foundations of non-equilibrium DMFT in the Keldysh formalism, and then discuss the photo-induced dynamics in Mott insulators to illustrate the approach.

## 2 The Keldysh formalism

This section presents a brief summary on the Keldysh formalism. For an in-depth introduction we refer to standard textbooks, e.g., [25, 26].

### 2.1 Two-time Green functions and electronic structure

The Keldysh formalism is based on Green functions  $G(i, t, j, t')$ , that describe the propagation of particles and holes between orbitals  $i, j$  and times  $t, t'$ . It is convenient to start from the

following electron and hole propagators, as introduced by Kadanoff and Baym,

$$G_{\mathbf{k}}^<(t, t') = +i\langle c_{\mathbf{k}}^\dagger(t')c_{\mathbf{k}}(t) \rangle \quad (3)$$

$$G_{\mathbf{k}}^>(t, t') = -i\langle c_{\mathbf{k}}(t)c_{\mathbf{k}}^\dagger(t') \rangle. \quad (4)$$

Here  $c_{\mathbf{k}}^\dagger$  and  $c_{\mathbf{k}}$  denote creation and annihilation operators for an electron in a single-particle orbital  $\mathbf{k}$ . (Only momentum  $\mathbf{k}$  is shown for simplicity of notation, but spin or orbital indices may easily be added.) The time-dependence of the operators is understood in the Heisenberg picture, and  $\langle \cdots \rangle = \text{Tr}(\rho_0 \cdots)/Z$  is an average using the density matrix of the initial state. These Green functions describe the propagation of an additional electron or hole on top of the many-body state, and therefore contain the full information on all single-particle observables. In the following we discuss their properties in equilibrium states, so-called non-equilibrium steady states, and a general time-evolving state:

- **Equilibrium:** In equilibrium, translational invariance in time implies that the propagators (3) and (4) depend only on the time-difference, and one can introduce the Fourier transform  $G(\omega) = \int dt e^{i\omega t} G(t, 0)$ . A straightforward expansion of the Green functions in (many-body) energy eigenstates leads to the relations

$$G_{\mathbf{k}}^<(\omega) = 2\pi i A_{\mathbf{k}}(\omega) f(\omega) \quad \equiv \quad 2\pi i N_{\mathbf{k}}^<(\omega), \quad (5)$$

$$G_{\mathbf{k}}^>(\omega) = -2\pi i A_{\mathbf{k}}(\omega)[1 - f(\omega)] \quad \equiv \quad -2\pi i N_{\mathbf{k}}^>(\omega). \quad (6)$$

Here we have introduced the (many-body) spectral function  $A_{\mathbf{k}}(\omega)$ , which is defined in terms of the retarded Green function as

$$A_{\mathbf{k}}(\omega) = -\frac{1}{\pi} \text{Im} \int dt e^{i(\omega+i0)t} G_{\mathbf{k}}^R(t), \quad (7)$$

$$G_{\mathbf{k}}^R(t - t') = \theta(t - t') (G_{\mathbf{k}}^>(t - t') - G_{\mathbf{k}}^<(t - t')). \quad (8)$$

The equations show that equilibrium states are characterized by the spectral function only, which contains information about the band structure, including the position of the bands, and the lifetime of quasiparticles. The occupation (which is, e.g., measured in photo-emission) is linked to the spectrum by a *universal occupation function*  $f(\omega)$  which only depends on temperature.

- **Non-equilibrium steady states:** An important application of the Keldysh formalism is to study non-equilibrium steady states. When the system is simultaneously subject to a time-independent perturbation and coupled to external reservoirs (e.g., metallic leads with a voltage bias), we can assume that any transients after the initial switch-on of the perturbation decay with time, until energy (particle) absorption from the perturbation is balanced by dissipation into the bath. The system then resides in a steady state in which all correlation functions are translationally invariant in time, but yet the system is not in a thermal equilibrium state: We have  $G_{\mathbf{k}}^<(\omega) = 2\pi i A_{\mathbf{k}}(\omega) F_{\mathbf{k}}(\omega)$  and  $G_{\mathbf{k}}^>(\omega) = -2\pi i A_{\mathbf{k}}(\omega)(1 - F_{\mathbf{k}}(\omega))$  like in Eqs. (5) and (6) with a positive definite spectral function  $A_{\mathbf{k}}(\omega)$  and occupation function  $F_{\mathbf{k}}(\omega)$ , but  $F_{\mathbf{k}}$  is not given by the Fermi function.

- **Transient time-evolution:** In a time-evolving state, time-translational invariance is lost, so that both spectral and occupation functions depend on two time-arguments separately. It is still often convenient to introduce a partial frequency dependence: A symmetric choice is the *Wigner transform* for a function  $X(t, t')$ , with an average time  $t_{av} = (t + t')/2$  and a relative time  $t_{rel} = t - t'$ , and a Fourier transform with respect to  $t_{rel}$ ,

$$X(t_{av}, \omega) = \int dt_{rel} e^{i\omega t_{rel}} F(t_{av} + t_{rel}/2, t_{av} - t_{rel}/2). \quad (9)$$

One may introduce Wigner transforms  $G^{<, >}(t, \omega)$ , or equivalently time-dependent occupation functions and spectral functions. In fact, a quantum Boltzmann equation [26] is an equation of motion for a time-dependent occupation function, often supplemented with the approximation that the spectrum takes a given form. However, in a situation where both the spectrum and the occupation change at the same pace, as can easily be the case for the ultra-fast dynamics in strongly correlated condensed matter systems, the separation of spectrum and occupation becomes somewhat arbitrary. An exception is the dynamics governed by non-interacting or mean-field Hamiltonians, where in the absence of external fields the spectrum is given by the eigenvalues of a single-particle Hamiltonian, and the occupation by the corresponding expectation values of the one-particle density matrix.

### Probabilistic interpretation of real-time Green functions

We can illustrate the meaning of the propagators  $G^{\gtrless}$  by their relation to a time-resolved electron removal and addition experiment, such as photoemission spectroscopy. In a time- and angle-resolved photoemission experiment, one measures the probability that an electron is emitted under the action of a short probe pulse, as a function of the photo-electron energy  $E$  and the photo-electron momentum  $\mathbf{k}_e$ . An idealized description is obtained by adding a term  $S(t - t_p) e^{i\Omega(t - t_p)} f^\dagger c_{\mathbf{k}} + h.c.$  to the Hamiltonian which allows a transition to an outgoing state  $f$ . The signal is the change of  $\langle f^\dagger f \rangle$  during a pulse. Here  $\Omega$  is the photon energy, and  $S(t - t_p)$  is the time profile of the probe pulse, which is centered around a given time  $t_p$ . With respect to real photo-emission, this formulation makes three approximations: (i) the sudden approximation, which assumes that there is no interaction between the electrons in the solid and in the outgoing state  $f$ , (ii) a classical approximation of the light pulse, and (iii) a simplistic treatment of the transition matrix elements. These approximations are, however, the same as those usually made to get a rough interpretation of photo-emission results in equilibrium in terms of the occupied spectrum  $A_{\mathbf{k}}(\omega) f(\omega)$ . The signal can be obtained using time-dependent perturbation theory in the light-matter coupling [27], leading to (to leading order in  $S$ )

$$I_{\mathbf{k}}(E, t_p) = \int dt dt' e^{iE(t - t')} (-i) G_{\mathbf{k}}^<(t_p + t, t_p + t') S(t) S(t')^*. \quad (10)$$



To further illustrate Eq. (10), one can consider a Gaussian probe profile  $S(t) = \exp(-t^2/2\Delta t^2)$  with duration  $\Delta t$ , and transform Eq. (10) to a mixed time-frequency representation

$$I_{\mathbf{k}}(E, t_p) \propto \int d\omega dt N^<(t_p + t, E + \omega) e^{-\frac{t^2}{2\Delta t^2}} e^{-\omega^2 \Delta t^2}. \quad (11)$$

Here  $N_{\mathbf{k}}^<(t, \omega) = G_{\mathbf{k}}^<(t, \omega)/(2\pi i)$  is related to the Wigner transform (9) of the Green function, in analogy to Eq. (5). In equilibrium we have  $N_{\mathbf{k}}^<(\omega) = A_{\mathbf{k}}(\omega)f(\omega)$ , so that long pulses imply the usual interpretation of the photoemission spectrum in terms of the occupied density of states, while Eq. (11) shows that in a transient state  $N_{\mathbf{k}}^<(t, \omega)$  gives the probability distribution to remove a particle with energy  $\hbar\omega$  and momentum  $\mathbf{k}$  from the system *at time*  $t$  after averaging over a filter  $e^{-\frac{t^2}{2\Delta t^2}} e^{-\omega^2 \Delta t^2}$  which satisfies the energy-time uncertainty  $\Delta t \Delta\omega = 1$  [28, 29].

### Fluctuation-dissipation theorem

Equations (5) and (6) provide a fermionic variant of the fluctuation-dissipation theorem, which holds more generally for any observable. The *response* of an observable  $X$  to an external force is given by the Kubo formula  $\chi(t-t') = -i\theta(t-t')\langle[X(t), X(t')]\rangle$ , while  $C^>(t-t') = -i\langle X(t)X(t')\rangle$  correspond to the fluctuations. Again, in equilibrium all correlation functions depend on time-difference only, and an eigenstate representation yields

$$C^<(\omega) = 2ib(\omega) \text{Im} \chi(\omega + i0), \quad (12)$$

where  $b(\omega) = 1/(e^{\beta\omega} - 1)$  is the Bose function. This is the fluctuation-dissipation theorem, which states that the imaginary part of the response function, which describes energy dissipation, is related to the power spectrum of the fluctuations. If  $X$  is a collective excitation, such as the displacement field of phonons,  $\text{Im} \chi(\omega)$  and  $C^<(\omega)$  correspond to the spectrum and the occupation of the collective mode, respectively.

The fluctuation-dissipation theorem provides a measurement to decide whether a system is in thermal equilibrium, and to determine the effective temperature of a given subset of degrees of freedom. For example, optical spectroscopy measures the polarization response to long-wavelength electric fields. A full characterization of the non-equilibrium state would require also a measurement of the noise power spectral density of the polarization (or the current). Measuring noise is generally harder than measuring the response, but recent experiments in this direction have extracted current fluctuations from the shot-to-shot variance in the measured intensity of the reflected probe-pulse in a pump-probe experiment [30].

## 2.2 The Keldysh contour

For an isolated system with Hamiltonian  $H(t)$ , the solution of the Schrödinger equation  $i\partial_t|\psi(t)\rangle = H(t)|\psi(t)\rangle$  with initial condition  $|\psi(t_0)\rangle = |\psi_0\rangle$  can be written in terms of the unitary time-evolution operator  $\mathcal{U}(t, t_0)$

$$|\psi(t)\rangle = \mathcal{U}(t, t_0) |\psi_0\rangle, \quad (13)$$

which is defined by the differential equation  $i\partial_t \mathcal{U}(t, t_0) = H(t)\mathcal{U}(t, t_0)$  with initial condition  $\mathcal{U}(t_0, t_0) = 1$ . Formally, the evolution operator can be written as the time-ordered product,

$$\mathcal{U}(t, t') = T_t e^{-i \int_{t'}^t d\bar{t} H(\bar{t})} \quad (\text{for } t > t'), \quad (14)$$

where the *time-ordering operator*  $T_t$  brings operators at later time to the left. The adjoint of (15) is the inverse (backward) time-evolution  $\mathcal{U}(t, t')^\dagger = T_{\bar{t}} e^{+i \int_{t'}^t d\bar{t} H(\bar{t})}$ , where  $T_{\bar{t}}$  is the anti time-ordering operator. The time-ordered exponential can be read as the step-wise time-evolution

$$\mathcal{U}(t, t') \approx e^{-i\delta t H(t-\delta t)} \dots e^{-i\delta t H(t'+2\delta t)} e^{-i\delta t H(t'+\delta t)} e^{-i\delta t H(t')} \quad (\text{for } t > t'), \quad (15)$$

taking the Hamiltonian constant along each infinitesimal interval,  $\mathcal{U}(t+\delta t, t) = e^{-i\delta t H(t)} + \mathcal{O}(\delta t^2)$ . In order to describe the time-evolution of a quantum system, we aim to compute observables or correlation functions of the general form

$$\langle \hat{O}(t) \rangle = \text{Tr} \left( \rho_0 \mathcal{U}(t, t_0)^\dagger \hat{O} \mathcal{U}(t, t_0) \right). \quad (16)$$

Here  $\rho_0$  is the density matrix which defines the state of the system at initial time  $t_0$ . The density matrix  $\rho_0$  provides only the statistical weights of the initial states, while Eq. (16) describes the evolution of an isolated quantum system: If  $\rho_0 = \sum_n w_n |\psi_n\rangle \langle \psi_n|$  is the statistical mixture of states  $|\psi_n\rangle$ , Eq. (16) can be written as

$$\langle \hat{O}(t) \rangle = \sum_n w_n \langle \psi_n(t) | \hat{O} | \psi_n(t) \rangle, \quad (17)$$

where  $|\psi_n(t)\rangle = \mathcal{U}(t, t_0) |\psi_n\rangle$  is obtained by solving the unitary Schrödinger equation with initial condition  $|\psi_n(t_0)\rangle = |\psi_n\rangle$ . In the following, we take  $\rho_0$  to be the Gibbs ensemble with respect to some initial Hamiltonian  $H(0)$ .

The time-ordering in  $\mathcal{U}(t, t_0)$  and the anti-time-ordering in  $\mathcal{U}(t, t_0)^\dagger$  in Eq. (16) can be combined into a single time-ordering along a time contour. The latter extends from  $t_0$  in forward direction and then in backward direction (from now on, we will take  $t_0 = 0$  without loss of generality). Moreover, the thermal density matrix can be written as a time-evolution operator along an imaginary time axis  $[0, -i\beta]$ , so that the three branches can be combined into a single *L-shaped contour*  $\mathcal{C}$ , as depicted in Fig. 1. The order of times is indicated by the arrows in the figure (from earlier to later). We will use the notation  $t >_{\mathcal{C}} t'$  ( $t <_{\mathcal{C}} t'$ ) to denote that  $t$  is later (earlier) on  $\mathcal{C}$  than  $t'$ . Throughout these notes, we will denote a time argument on the upper (lower) branch by  $t_{\pm}$  with  $t \in \mathbb{R}$ , respectively, and a time-argument on the vertical branch by  $-i\tau$  with  $\tau \in [0, \beta]$ . Together with the time-contour we introduce the contour-ordering operator

$$T_{\mathcal{C}} A(t) B(t') = \begin{cases} A(t) B(t') & t >_{\mathcal{C}} t' \\ \xi B(t') A(t) & t' >_{\mathcal{C}} t \end{cases}. \quad (18)$$

The sign  $\xi$  is  $-1$  if the permutation of  $A$  and  $B$  involves an odd number of permutations of fermion creation of annihilation operators, and  $+1$  otherwise. With this the expectation value (16) is written as

$$\langle \hat{O}(t) \rangle = \frac{1}{Z} \text{Tr} \left( T_{\mathcal{C}} e^{-i \int_{\mathcal{C}} d\bar{t} H(\bar{t})} \hat{O}(t_{+}) \right), \quad Z = \text{Tr} \left( T_{\mathcal{C}} e^{-i \int_{\mathcal{C}} d\bar{t} H(\bar{t})} \right), \quad (19)$$

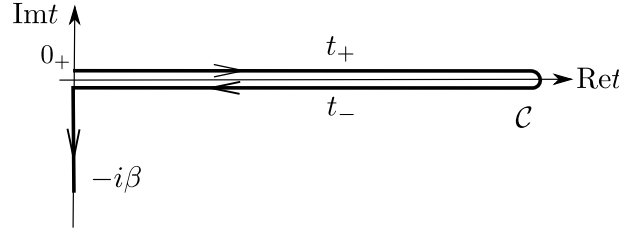


**Fig. 1:** The Keldysh contour  $\mathcal{C}$ , ranging from time 0 to a maximum time  $t_{\max}$ , back to time 0, and finally to  $-i\beta$  on the imaginary-time branch. Times on the upper and lower real-time branch are denoted by  $t_+$  and  $t_-$ , respectively. Both  $t_+$  and  $t_-$  are real, and the index  $\pm$  serves only to distinguish backward and forward time-evolution. The arrows denote the time-ordering along  $\mathcal{C}$  from “earlier” to “later” contour times.

where we have introduced integrals along the time-integrals

$$\int_{\mathcal{C}} dt f(t) = \int_0^{t_{\max}} dt f(t_+) - \int_0^{t_{\max}} dt f(t_-) - i \int_0^{\beta} d\tau f(-i\tau). \quad (20)$$

The electron and hole propagators (3) and (4) appear now naturally as different components of a **contour-ordered Green function**

$$G_{jj'}(t, t') = -i \langle T_{\mathcal{C}} c_j(t) c_{j'}^{\dagger}(t') \rangle. \quad (21)$$

By choosing the time-arguments on the upper and lower branch of the contour, respectively, we recover the lesser and greater Green functions (3) and (4) for  $t, t' > 0$

$$G^<(t, t') = G(t_+, t'_-) \quad \text{and} \quad G^>(t, t') = G(t_-, t'_+). \quad (22)$$

In turn, one can see that  $G^<$  and  $G^>$  suffice to restore the full Green function  $G(t, t')$  on the real-time branches, so that  $G(t, t')$  is equivalent to specifying the single-particle properties at all times. Without proof, we note that the mixed components  $G(\tau, t)$  are one-to-one related to the correlations  $G(t, t')$  with one or two arguments before  $t = 0$ , assuming the system is then in equilibrium.

### Functional integrals and many-body theory

The introduction of the contour allows to repeat one-to-one all steps which lead to the definition of path integrals and perturbation theory in the Matsubara formalism. We can obtain the path integral for the partition function (or rather, any generating function for contour-ordered expectation values) as

$$Z = \text{Tr} (T_{\mathcal{C}} e^{-i \int_{\mathcal{C}} dt H(t)}) = \int \mathcal{D}[\bar{c}, c] e^{iS} \quad (23)$$

$$S = \int_{\mathcal{C}} dt \left( \sum_j \bar{c}_j(t) i \partial_t c_j(t) - H[\bar{c}, c] \right). \quad (24)$$

This expression is understood in the usual way as a continuum limit of a discretized time contour with timesteps  $t_a$ ,  $a = 0, \dots, M$  along the contour ( $t_0 = 0^+$  and  $t_M = -i\beta$ ). Anti-periodic or periodic boundary conditions  $c(t_0) = -c(t_M)$  are implied for bosons and fermions, respectively, and  $j$  labels all orbital degrees of freedom. Note that  $\partial_t$  is the usual time-derivative, not a derivative along the contour direction.

With the general expectation value

$$\langle \dots \rangle_S = Z^{-1} \int \mathcal{D}[\bar{c}, c] e^{iS} \dots, \quad (25)$$

we naturally arrive at the Green function

$$G_{jj'}(t, t') = -i \langle c_j(t) \bar{c}_{j'}(t') \rangle_S. \quad (26)$$

For the action (24), the latter equals the contour-ordered Greens function (21). The (anti)-periodic boundary condition of  $c$  and  $\bar{c}$  imply an (anti)-periodic boundary condition for  $G$ ,

$$G(0_+, t) = \pm G(-i\beta, t), \quad G(t, 0_+) = \pm G(t, -i\beta), \quad (27)$$

where the upper (lower) sign refers to the case where  $c$  and  $c^\dagger$  are Bose (Fermi) operators.

### Equations of motion

The action of the noninteracting problem  $H(t) = \varepsilon(t) c^\dagger c$ ,  $S = \int dt dt' \bar{c}(t) \delta_C(t, t') (i\partial_t - \varepsilon) c(t')$  is a quadratic form, where  $\delta_C(t, t')$  is the delta-function consistent with the contour integral (20). The integrals  $\int_C$  are to be understood as the continuum limit of a discrete form  $S = \sum_{a, a'} \bar{c}_a A_{aa'} c_{a'}$  where  $a, a'$  label all orbital and discrete time indices. Gaussian integration for the discrete action yields  $\sum_b A_{ab} G_{ba'} = \delta_{aa'}$ , i.e.,  $G_{aa'} = -i \langle c_a \bar{c}_{a'} \rangle_S$  and  $A$  are inverse matrices in time. Reinstating the continuum limit, the equation  $A G = 1$  yields the equation of motion for  $G$ ,

$$\int_C d\bar{t} \delta_C(t, \bar{t}) (i\partial_{\bar{t}} - \varepsilon) G(\bar{t}, t') = (i\partial_t - \varepsilon(t)) G(t, t') = \delta_C(t, t'). \quad (28)$$

The “derivation” of this equation has seemingly been a bit too careless, as in contrast to the inverse of the discrete matrix  $A$ , the differential equation (28) does not have a unique solution unless either an initial or boundary condition is specified. However, with the boundary condition (27) the solution is unique. For the equilibrium Green function and the single orbital Hamiltonian  $H = \varepsilon c^\dagger c$ , it is instructive to check that the solution is given by

$$G(t, t') = e^{-i\varepsilon(t-t')} \left( i f(\varepsilon) \theta_C(t', t) - i f(-\varepsilon) \theta_C(t, t') \right), \quad (29)$$

where  $\theta_C(t, t') = 1$  for  $t >_C t'$  and 0 otherwise. The same result is obtained from Eq. (21) and the Heisenberg equation of motion for  $c(t)$  and  $c^\dagger(t)$ .

From now on we use a continuum notation assuming that all operations take place within the space of (anti)-periodic functions. Multiplication of two contour functions corresponds to convolution along  $C$

$$[A * B](t, t') = \int_C d\bar{t} A(t, \bar{t}) B(\bar{t}, t'), \quad (30)$$

$$\Sigma_{j,j}(t,t') = \begin{array}{c} \begin{array}{c} j,t' \quad \quad j,t \\ \text{---} \quad \text{---} \quad \text{---} \quad \text{---} \\ j,t' \quad \quad j,t \end{array} \begin{array}{c} \text{---} \sigma \\ \text{---} \sigma \end{array} \end{array} + \begin{array}{c} \text{---} \\ \text{---} \end{array} + \begin{array}{c} \text{---} \end{array} + \dots$$

$$j',t' \longrightarrow j,t = (G_0)_{j,j'}(t,t') \quad \begin{array}{c} j,t \\ \text{---} \\ j,t \end{array} = U(t)$$

**Fig. 2:** Diagrammatic representation of the local self-energy in the Hubbard model: The noninteracting Green function  $G_{0,jj'}(t, t')$  is represented by a directed line, and the interaction  $U(t)$  is denoted by a dashed line. The first two diagrams are  $\Sigma_{\sigma}^{(2)}(t, t')$  and  $\Sigma_{\sigma}^{(1)}(t, t')$ , the third diagram is a non-skeleton diagram, with a self-energy insertion in one of the  $G_0$ -lines.

and the inverse  $A^{-1}(t, t')$  of a function  $A(t, t')$  is understood as the differential or integral equation  $\int_{\mathcal{C}} d\bar{t} A^{-1}(t, \bar{t}) A(\bar{t}, t') = \int_{\mathcal{C}} d\bar{t} A(t, \bar{t}) A^{-1}(\bar{t}, t') = \delta_{\mathcal{C}}(t, t')$  with the boundary condition (27) (additional matrix multiplication in orbital indices implied).

### Diagrammatic perturbation theory

The construction of diagrammatic perturbation theory does not depend on the time contour, and is formally identical for Matsubara Green functions and contour-ordered Green functions. In particular, perturbation theory is based on the Wick theorem, which states that  $n$ -particle contour-ordered expectation values for a *quadratic action* can be factorized into a determinant of two-point correlation functions (for fermions),  $\langle c_1 \cdots c_n c_n^\dagger \cdots c_1^\dagger \rangle_{S_0} = \det(M)$ ,  $M_{ij'} = \langle c_i c_{j'}^\dagger \rangle_{S_0}$ , (for bosons one would obtain a permanent). Wick's theorem in fact follows as a simple property of Gaussian path integrals.

We can introduce the self-energy  $\Sigma(t, t')$ , which is a function of two times on the contour. It can be expanded in a power series of the Green function, where each term is represented as a Feynman diagram. The topology of the diagrams is the same as in the equilibrium Matsubara formalism, only internal time-integrals in the interpretation of diagrams must be taken over the contour  $\mathcal{C}$  instead of over imaginary time. The relation of non-interacting Green function and the self-energy is therefore given by the Dyson equation

$$G = G_0 + G_0 * \Sigma * G = G_0 + G * \Sigma * G_0 \quad (31)$$

$$\Leftrightarrow G^{-1}(t, t') = G_0^{-1}(t, t') - \Sigma(t, t'). \quad (32)$$

For illustration and later reference, we state the explicit expression of the first and second-order diagram for the self-energy of the Hubbard model, as shown in Fig. 2,

$$\Sigma_{\sigma}^{(1)}(t, t') = U(t) n_{\bar{\sigma}}(t) \delta_{\mathcal{C}}(t, t'), \quad (33)$$

$$\Sigma_{\sigma}^{(2)}(t, t') = U(t) U(t') G_{0\sigma}(t, t') G_{0\bar{\sigma}}(t', t) G_{0\bar{\sigma}}(t, t'). \quad (34)$$

## Self-consistent expansions

The sum of all Feynman diagrams generates  $\Sigma[G_0]$  as a functional of  $G_0$ . One can re-sum this expansion by removing all terms in which the  $G_0$ -lines itself have self-energy insertions (such as the third diagram in Fig. 2), and in turn replace all Green function lines by the full interacting self-energy  $G$ . This results in the so-called skeleton functional  $\Sigma[G]$ . In combination with the Dyson equation Eq. (32), an approximation to the skeleton functional, e.g., the truncation to given order, yields a closed-form non-linear integral-differential equation for  $G$ . Although the skeleton expansion to given order generates an infinite subset of the diagrams of the bare expansion  $\Sigma[G_0]$ , this does not always lead to quantitatively better results. An example is the second order perturbation theory for the impurity problem in DMFT [20], where only the bare expansion can qualitatively recover the Mott transition. However, any truncation of the self-consistent skeleton expansion  $\Sigma[G]$  satisfies conservation laws for energy and particle number, while an approximation to  $\Sigma[G_0]$  does not [31], which is of great importance for the description of non-equilibrium dynamics. If energy is not conserved, the concept of thermalization becomes meaningless, as only the conservation laws fix the statistical properties of a system in thermal equilibrium.

## 2.3 Kadanoff-Baym equations

In this subsection we discuss the numerical solution of the Dyson equation in real time. We consider the standard form, obtained from (32) and the inverse  $G_0^{-1} = \delta_{\mathcal{C}}(t, t')(i\partial_t - h(t))$  (orbital indices can be added easily)

$$(i\partial_t - h(t))G(t, t') - \int_{\mathcal{C}} d\bar{t} \Sigma(t, \bar{t}) G(\bar{t}, t') = \delta_{\mathcal{C}}(t, t'). \quad (35)$$

This equation is a non-Markovian equation of motion for the Green function, where the self-energy takes the role of a memory kernel. To solve the equation one can take an equidistant time grid, with  $M$  time slices along  $\mathcal{C}$ . The operator  $(i\partial_t - h(t))\delta_{\mathcal{C}}(t, t') - \Sigma(t, t')$  can then be written as a  $M$ -dimensional matrix, and the solution for  $G$  becomes a matrix inversion. This scheme, however, does not exploit the possibility to transform Eq. (35) into a step-wise time propagation scheme: Because of the causal nature of the time-evolution, if the solution of Eq. (35) is known for real times  $t, t' \leq n\Delta t$ , it can be extended to the domain  $t, t' \leq (n+1)\Delta t$  without modification of the previous times, even when  $\Sigma$  depends on  $G$  in a non-linear way, e.g., in the form of a perturbative expression  $\Sigma[G]$ . (In general, any functional expression  $\Sigma[G]$  should be causal, such that  $\Sigma(t, t')$  in the domain  $t, t' \leq n\Delta t$  can be determined from  $G$  in the same domain  $t, t' \leq n\Delta t$ .)

One can introduce a parametrization of contour functions which allows to make use of this causality. The values of the contour-ordered function  $G(t, t')$  with  $t$  and  $t'$  on different branches of  $\mathcal{C}$  are not all independent, because the largest real-time argument can be shifted between the

upper to the lower contour branch. For example, for  $t' < t$

$$G(t_+, t'_+) = \frac{1}{Z} \text{Tr} \left( e^{-\beta H(0)} \underbrace{\mathcal{U}(0, t) \mathcal{U}(t, t_{\max})}_{c_-} \underbrace{\mathcal{U}(t_{\max}, t) c \mathcal{U}(t, t') c^\dagger \mathcal{U}(t', 0)}_{c_+} \right) = G(t_-, t'_+). \quad (36)$$

The brackets indicate the part of the contour-ordered operator  $T_C e^{-i \int_C dt H(t)}$  along the upper and lower branch, respectively. Because the time-evolution between  $t$  and  $t_{\max}$  along the upper and lower branch cancel,  $c$  can be shifted between the two branches. The redundancy which follows from Eq. (36) can be resolved in an elegant way, using the so-called Keldysh rotation. Let us first focus only on the real-time branches of  $\mathcal{C}$ : With the two branches, one can start from a parametrization of  $G$  in terms of a  $2 \times 2$  matrix

$$\hat{G}(t, t') \equiv \begin{pmatrix} G(t_+, t'_+) & G(t_+, t'_-) \\ G(t_-, t'_+) & G(t_-, t'_-) \end{pmatrix}, \quad t, t' \in \mathbb{R}. \quad (37)$$

The over-completeness of this representation can be removed by an invertible map (with  $\hat{\tau}_3 = \text{diag}(1, -1)$ )

$$\underline{G}(t, t') \equiv \hat{L} \hat{\tau}_3 \hat{G}(t, t') \hat{L}^\dagger, \quad \text{where } \hat{L} = \frac{1}{\sqrt{2}} \begin{pmatrix} +1 & -1 \\ +1 & +1 \end{pmatrix}. \quad (38)$$

From the rotation we get ( $G_{ab} = G(t_a, t'_b)$  for  $a, b = \pm$ )

$$\begin{aligned} \underline{G}(t, t') &= \frac{1}{2} \begin{pmatrix} (G_{++} - G_{+-} + G_{-+} - G_{--}) & (G_{++} + G_{+-} + G_{-+} + G_{--}) \\ (G_{++} - G_{+-} - G_{-+} + G_{--}) & (G_{++} + G_{+-} - G_{-+} - G_{--}) \end{pmatrix} \\ &= \begin{pmatrix} G^R(t, t') & G^K(t, t') \\ 0 & G^A(t, t') \end{pmatrix}. \end{aligned} \quad (39)$$

The second equality follows from the causality (36). For example, in the  $(1, 0)$ -component we can shift the first time argument between the upper and lower contour for  $t > t'$ , which gives  $\frac{1}{2}(G_{-+} - G_{--} - G_{-+} + G_{--}) = 0$ , while for  $t < t'$  we can shift the second argument, which gives  $\frac{1}{2}(G_{++} - G_{+-} - G_{-+} + G_{--}) = 0$ . In combination,  $\frac{1}{2}(G_{++} - G_{+-} - G_{-+} + G_{--}) = 0$ . The other components follow analogously, using the conventional definition of the retarded, advanced, and Keldysh Green functions

$$G^R(t, t') = \theta(t - t') (G^>(t, t') - G^<(t, t')), \quad (40)$$

$$G^A(t, t') = \theta(t' - t) (G^<(t, t') - G^>(t, t')), \quad (41)$$

$$G^K(t, t') = G^>(t, t') + G^<(t, t'). \quad (42)$$

Using the Keldysh matrices, convolutions greatly simplify: restricted to the real-time branches of  $\mathcal{C}$ , the convolution of two contour functions  $A(t, t')$  and  $B(t, t')$  is given by  $C(t_\alpha, t'_{\alpha'}) = \int d\bar{t} (A(t_\alpha, \bar{t}_+) B(\bar{t}_+, t'_{\alpha'}) - A(t_\alpha, \bar{t}_-) B(\bar{t}_-, t'_{\alpha'}))$ , which can be written in the form

$$\hat{C}(t, t') = \int d\bar{t} \hat{A}(t, \bar{t}) \hat{\tau}_3 \hat{B}(\bar{t}, t'). \quad (43)$$

After the Keldysh rotation this becomes

$$\underline{C}(t, t') \equiv \hat{L} \hat{\tau}_3 \hat{C}(t, t') \hat{L}^\dagger = \int d\bar{t} \hat{L} \hat{\tau}_3 \hat{A}(t, \bar{t}) \hat{L}^\dagger \hat{L} \hat{\tau}_3 \hat{B}(\bar{t}, t') \hat{L}^\dagger = \int d\bar{t} \underline{A}(t, \bar{t}) \underline{B}(\bar{t}, t'), \quad (44)$$

i.e., a simple convolution in real-time with an additional  $2 \times 2$  matrix structure.

Noting that in the  $2 \times 2$  matrix the derivative and delta function are  $i\partial_t \hat{1}$  and  $\delta(t - t') \hat{\tau}_3$ , the Dyson equation becomes, after Keldysh rotation

$$(i\partial_t - h(t)) \underline{G}(t, t') - \int d\bar{t} \underline{\Sigma}(t, \bar{t}) \underline{G}(\bar{t}, t') = \delta(t, t'). \quad (45)$$

Comparing matrix elements on both sides we have equations for the individual components of  $G$ . For illustration, let us take the  $(0, 0)$ -component

$$(i\partial_t - h(t)) G^R(t, t') - \int_{t'}^t d\bar{t} \Sigma^R(t, \bar{t}) G^R(\bar{t}, t') = \delta(t - t'), \quad (46)$$

which must be solved with the initial condition  $G^R(t, t') = 0$  for  $t < t'$ . In these equations we have already taken into account that retarded components vanish for  $t < t'$ , and have restricted the time-arguments accordingly. This has an important consequence: In order to determine  $G^R(t, t')$  in the domain  $t, t' \leq t_{max}$ , also  $G$  and  $\Sigma$  have to be known only for  $t, t' \leq t_{max}$ . Thus one can solve this equation in a time-stepping manner: With the parametrization  $y(s) = G^R(t' + s, t')$ , Eq. (46) can be written as a Volterra integral-differential equation of the second kind,

$$\frac{d}{ds} y(s) = q(s) + p(s)y(s) + \int_0^s d\bar{s} k(s, \bar{s}) y(\bar{s}), \quad (47)$$

taking  $q(s) = 0$ ,  $p(s) = -ih(s)$ ,  $k(s, \bar{s}) = -i\Sigma^R(t' + s, t' + \bar{s})$ . On an equidistant grid  $s \in \{m\Delta t\}$ , using a notation  $y_m = y(m\Delta t)$  etc., with a trapezoidal rule for the integral and a finite difference formula for the differential term, we obtain

$$\frac{y_{n+1} - y_n}{\Delta t} = q_{n+1} + p_{n+1}y_{n+1} + \Delta t \left( \frac{1}{2}y_{n+1} + \sum_{m=1}^n k_{n,m} y_m + \frac{1}{2}y_0 \right). \quad (48)$$

Starting from an initial value  $y_0$  (here,  $y(0) = G^R(t', t') = -i$ ), this equation provides an equation of  $y_{n+1}$  in terms of  $y_m$  for  $m \leq n$ , which can be successively applied for  $n = 1, 2, 3, \dots$  to determine the full function  $y$  (see Fig. 3). In practice, accurate higher order approximations should be used for derivative and integral [32], but the basic strategy of solving the Volterra equation remains the same.

The arguments above can be extended to a causal time-propagation scheme for  $G$  on the full  $L$ -shaped contour. For completeness, we state the parametrization used in the following [33]



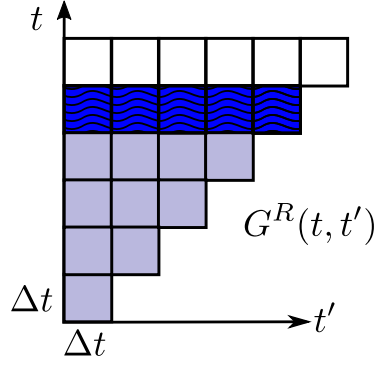


**Fig. 3:** Illustration of the integral equation (46): The hatched region indicates a time-slice  $\{ G^R(n\Delta t, m\Delta t) | m \leq n \}$ . The blue region indicates the values of  $G^R$  entering the evaluation of the derivative  $\partial_t G^R(t, t')$  which is needed to propagate  $G^R$  from a time-slice  $m\Delta t$  to  $(m+1)\Delta t$ .

(for other implementations, see, e.g., [34]):

$$(-\partial_\tau - h(0^-))G^M(\tau) - \int_0^\beta d\bar{\tau} \Sigma^M(\tau - \bar{\tau}) G^M(\bar{\tau}) = \delta(\tau), \quad (49)$$

$$(i\partial_t - h(t)) G^R(t, t') - \int_{t'}^t d\bar{t} \Sigma^R(t, \bar{t}) G^R(\bar{t}, t') = \delta(t - t'), \quad (50)$$

$$(i\partial_t - h(t)) G^{tv}(t, \tau') - \int_0^t d\bar{t} \Sigma^R(t, \bar{t}) G^{tv}(\bar{t}, \tau') = Q^{tv}(t, \tau'), \quad (51)$$

$$(i\partial_t - h(t)) G^<(t, t') - \int_0^t d\bar{t} \Sigma^R(t, \bar{t}) G^<(\bar{t}, t') = Q^<(t, t'), \quad (52)$$

with

$$Q^{tv}(t, \tau') = \int_0^\beta d\bar{\tau} \Sigma^{tv}(t, \bar{\tau}) G^M(\bar{\tau}, \tau'), \quad (53)$$

$$Q^<(t, t') = \int_0^{t'} d\bar{t} \Sigma^<(t, \bar{t}) G^A(\bar{t}, t') - i \int_0^\beta d\bar{\tau} \Sigma^{tv}(t, \bar{\tau}) G^{vt}(\bar{\tau}, t'). \quad (54)$$

Here, the integral limits take into account that retarded functions vanish for  $t < t'$ ,  $X^{vt}(\tau, t) = X(-i\tau, t_\pm)$ . The component with both time arguments on the imaginary branch is the usual initial state Matsubara Green function,  $X(-i\tau, -i\tau') \equiv iX^M(\tau - \tau')$ . These integral equations and the equivalent conjugate equation  $G * G^{-1} = 1$  for the real and imaginary time Green functions are known as Kadanoff-Baym equations [34]. Apparently Eq. (49) for  $G^M$  is decoupled from the other equations. It can be solved in advance to give the Matsubara Green function of the initial equilibrium state, which then enters the other equations in the form of an initial conditions.

If no cutoff to the memory integrals is applied, the required computational resources scale with the number of time-steps  $M$  like  $\mathcal{O}(M^3)$  (CPU time) and  $\mathcal{O}(M^2)$  (memory), which can provide a bottleneck for the simulation, in particular in case of many orbitals.

## 2.4 Steady-state formalism

In a time-translationally invariant non-equilibrium steady state, the Kadanoff-Baym equations can be solved by means of Fourier transform. The imaginary time branch, which corresponds to the initial state correlations, is moved to  $t_0 = -\infty$  and then omitted. The individual components of Eq. (45) become

$$G^R(\omega + i0) = (\omega + i0 - h - \Sigma^R(\omega + i0))^{-1} = G^A(\omega - i0)^\dagger, \quad (55)$$

$$(\omega + i0 - h - \Sigma^R(\omega + i0))G^K(\omega) = \Sigma^K(\omega)G^A(\omega). \quad (56)$$

The second equation can thus be solved as

$$G^K(\omega) = G^R(\omega) \Sigma^K(\omega) G^A(\omega). \quad (57)$$

In practice, one can iteratively solve Eqs. (55) and (57) together with a given approximation  $\Sigma[G]$  for the self-energy, such as Eq. (34): Starting from a given guess for  $\Sigma^R(\omega + i0)$  and  $\Sigma^K(\omega)$ ,  $G^K(\omega)$ ,  $G^R(\omega + i0)$ , and the spectral function  $A(\omega)$  are obtained. A Fourier transform gives  $G^R(t) = -i\theta(t)\int d\omega A(\omega) e^{-i\omega t}$  and  $G^K(t) = \int \frac{d\omega}{2\pi} G^K(\omega) e^{-i\omega t}$ , which are then used to calculate  $\Sigma^R(t)$  and  $\Sigma^K(t)$ , and thus  $\Sigma^R(\omega + i0)$  and  $\Sigma^K(\omega)$ . The procedure is iterated to convergence. Since the components  $A(\omega)$ ,  $\Sigma^K(\omega)$ ,  $G^K(\omega)$  are well localized in frequency, the frequency grid can be kept finite.

The solution of Eq. (57) is not unique for  $\Sigma = 0$ , i.e., for a noninteracting system in isolation from the environment: In this case, Eq. (56) is solved by any ansatz of the form

$$G_0^K(\omega) = G^R(\omega) F(\omega) - F(\omega) G^A(\omega), \quad (58)$$

with an arbitrary (hermitian) distribution function  $F(\omega)$ . This fact just shows that for an isolated noninteracting system any distribution of the single-particle levels provides a possible steady state. By extending the real-time part of the contour to  $(-\infty, \infty)$  the memory on the initial condition has been removed, which thus leaves the steady state undetermined for  $\Sigma^K = 0$ . One can resolve this ambiguity by fixing the distribution function in the solution Eq. (58) of Eq. (56). Mathematically, this is achieved by a choice  $\Sigma^K(\omega) = -i\eta F(\omega)$  with  $\eta \rightarrow 0^+$ , which corresponds to attaching a heat bath to the system with a flat density of states, a given distribution  $F(\omega)$ , and infinitesimal coupling  $\sqrt{\eta}$ . In the steady state the bath determines the distribution function of the system, irrespective of the coupling strength, while the spectral properties of the system are not affected.

## 3 Non-equilibrium dynamical mean-field theory

### 3.1 The dynamical mean-field formalism

DMFT approximates only the spatial correlations in a mean-field manner, but accurately treats local temporal fluctuations. The main approximation is the locality of the self-energy, which becomes exact in the limit of infinite coordination number [35]. The formulation of DMFT

within the Keldysh and the Matsubara framework differs only by the choice of the time contour, and all arguments regarding the derivation of DMFT, such as the cavity method [20] and power counting arguments for the locality of the self-energy, can be transferred one-to-one from imaginary time to  $\mathcal{C}$ . We therefore directly state the final equations, and then proceed to a discussion of their solution, which is in fact very different in real and imaginary time.

For clarity, the DMFT equations in this section are all stated for the single-band Hubbard model in the spin-symmetric phase; orbital indices can easily be added. Within DMFT, the self-energy at a given site  $j$  of the lattice can be obtained from a local model with a general quadratic action

$$S_{\text{imp},j} = \int_{\mathcal{C}} dt dt' \left( \sum_{\sigma} \bar{c}_{\sigma}(t) \mathcal{G}_{j\sigma}^{-1}(t, t') c_{\sigma}(t') - U(t) \bar{c}_{\uparrow}(t) c_{\uparrow}(t) \bar{c}_{\downarrow}(t) c_{\downarrow}(t) \delta_{\mathcal{C}}(t, t') \right), \quad (59)$$

$$\mathcal{G}_j^{-1}(t, t') = (i\partial_t + \mu) \delta_{\mathcal{C}}(t, t') - \Delta_j(t, t'), \quad (60)$$

which describes one site of the lattice embedded in an environment with hybridization function  $\Delta_j(t, t')$ . This is the action of a time-dependent Anderson Impurity Hamiltonian. This action defines the interacting impurity Green function

$$G_{\text{imp},j}(t, t') = -i \langle c(t) \bar{c}(t') \rangle_{S_{\text{imp},j}}. \quad (61)$$

The impurity self-energy is set by the impurity Dyson equation

$$G_{\text{imp},j}^{-1}(t, t') = \mathcal{G}_j^{-1}(t, t') - \Sigma_{\text{imp},j}(t, t'). \quad (62)$$

The impurity self-energy then serves as an approximation for the lattice self-energy,

$$\Sigma_{jj'}(t, t') = \delta_{jj'} \Sigma_{\text{imp},j}(t, t'), \quad (63)$$

and lattice Green functions are obtained by solving the Dyson equation

$$G_{jj'}^{-1}(t, t') = (i\partial_t + \mu) \delta_{\mathcal{C}}(t, t') \delta_{jj'} - \delta_{jj'} \Sigma_{jj}(t, t') - \delta_{\mathcal{C}}(t, t') v_{ij}(t), \quad (64)$$

where  $v_{ij}(t)$  are the hopping matrix elements, which contain the external laser fields, Eq. (2). Finally the equations are closed and the auxiliary quantity  $\Delta_j(t, t')$  can be eliminated when the local lattice Green function  $G_{jj}$  equals the corresponding impurity quantity

$$G_{\text{imp},j}(t, t') \stackrel{!}{=} G_{jj}(t, t'). \quad (65)$$

Equations (59) through (65) provide the closed set of equations for non-equilibrium DMFT.

### Self-consistency scheme without $\Sigma$

In equilibrium, the self-consistent solution of the DMFT equations is usually achieved by an iterative procedure. One can start from a guess for  $\Sigma$ , solve the lattice Dyson equation to obtain  $G_{ii}$ , invert the impurity Dyson equation (62) to get  $\Delta$ , and solve the impurity model with action (59) to get an update for  $\Sigma$ . The same might be done in real time. Although in principle

straightforward matrix equations in time, some of the steps can, however, become numerically unstable, in particular when algorithms are used which are accurate to high-order in the time-step. In particular, given  $G$  and  $\Delta$  one cannot easily solve Eq. (62) for the self-energy. We therefore explain how the self-consistency cycle can be reformulated, avoiding the explicit use of the self-energy. (The following steps are presented for a spatially homogeneous state, where  $\varepsilon_{\mathbf{k}}(t)$  is the Fourier transform of  $v_{ij}(t)$ , and  $\sum_{\mathbf{k}} G_{\mathbf{k}}$  is the local Green function. We define the sum to be normalized,  $\sum_{\mathbf{k}} = 1$ .)

- (1) Given  $\Delta$ ,  $G_{\text{imp}}$  is calculated, Eq. (61). This is the main step of the algorithm, which requires the solution of a many-body problem out of equilibrium (Sec. 3.2).
- (2) A function  $Z$  with  $Z^{-1}(t, t') = (i\partial_t + \mu) \delta_C(t, t') - \Sigma(t, t')$  is obtained by solving the integral equation  $Z + G_{\text{imp}} * \Delta * Z = G_{\text{imp}}$ .
- (3) For each  $\mathbf{k}$ , we determine  $G_{\mathbf{k}}$  from the integral equation  $Z + Z * \varepsilon_{\mathbf{k}} * G_{\mathbf{k}} = G_{\mathbf{k}}$ . (Here  $\varepsilon_{\mathbf{k}}(t, t') \equiv \varepsilon_{\mathbf{k}}(t) \delta_C(t, t')$  is interpreted as diagonal matrix in time.)
- (4) We calculate the sums  $G = \sum_{\mathbf{k}} G_{\mathbf{k}}$ ,  $G_1 = \sum_{\mathbf{k}} \varepsilon_{\mathbf{k}} * G_{\mathbf{k}}$ ,  $G_2 = \sum_{\mathbf{k}} (\varepsilon_{\mathbf{k}} + \varepsilon_{\mathbf{k}} * G_{\mathbf{k}} * \varepsilon_{\mathbf{k}})$ , and obtain  $\Delta$  from the integral equation  $\Delta + G_1 * \Delta = G_2$ .

These equations are obtained directly by summing the lattice Dyson equation over  $\mathbf{k}$  and comparing to the impurity Dyson equation. Steps (2)–(4) require the solution of linear equations on  $\mathcal{C}$  of the form  $(1 + F) * X = Q$ , with a kernel  $F$  and a source term  $Q$ . Such equations reduce to stable second-order Volterra equations in time [32, 33]. Because all these steps are causal (the solution in some domain  $t, t' \leq t_0$  can be determined from the input in the same domain  $t, t' \leq t_0$ ) the real-time DMFT equations can be propagated step by step in time.

We finally note that, while in equilibrium momentum sums can be rewritten in terms of integrals over the density of state,  $\sum_{\mathbf{k}} = \int d\varepsilon D(\varepsilon)$  with  $D(\varepsilon) = \sum_{\mathbf{k}} \delta(\varepsilon - \varepsilon_{\mathbf{k}})$ , this is not necessarily possible when  $\varepsilon_{\mathbf{k}}$  is time-dependent, because in this case  $G_{\mathbf{k}}(t, t')$  depends on  $\mathbf{k}$  not only via a single number such as the unperturbed  $\varepsilon_{\mathbf{k}}^0$  [e.g., with a vector-potential  $\mathbf{A}(t)$ , Eq. (2) implies  $\varepsilon_{\mathbf{k}}(t) = \varepsilon_{\mathbf{k}+e\mathbf{A}(t)}$ ].

## Bethe lattice

The solution of an integral equation for each  $\mathbf{k}$ , i.e., step (3) in the self-consistency above, can be numerically costly. For predictions of DMFT which should be generic for any lattice, one can therefore use the so-called Bethe lattice, which leads to a closed-form self-consistency. This is also common in equilibrium DMFT, but with a slight variation even electric fields can naturally be included: The Bethe lattice is a graph with coordination number  $Z$ , but no loops. As for any tight-binding model, the electric field is defined on the links  $(ij)$  of the graph by means of the Peierls phase  $e^{\pm i\phi_{ij}(t)}$ , so that  $\phi_{ij}(t) = eaA_{ij}(t)$ , where  $aA_{ij}(t)$  is the projection of the vector potential along the bond. To have a divergence-less field on this graph, each site should simply have equally many bonds with a field pointing inwards and pointing outwards.

In general, a formal closed form self-consistency is obtained from the cavity construction [20] (integrating out the rest of the lattice), which gives

$$\Delta_j(t, t') = \sum_{j_1, j_2} v_{j, j_1}(t) G_{j_1, j_2}^{[j]}(t, t') v_{j_2, j}(t'). \quad (66)$$

Here  $G_{j_1, j_2}^{[j]}$  is the Green function of the lattice where site  $j$  is excluded. On a lattice without loops, only terms  $j_1 = j_2$  remain, and in the limit of infinite coordination we then have  $G_{j_1, j_1}^{[j]}(t, t') = G_{j_1, j_1}(t, t')$ . With half of the hoppings having a phase  $e^{i\phi(t)}$  and  $e^{-i\phi(t)}$ , respectively, and rescaling  $v \sim v_*/\sqrt{Z}$  for  $Z \rightarrow \infty$ , a closed-form self-consistency

$$\Delta(t, t') = \frac{v_*^2}{2} \left( e^{i\phi(t)} G(t, t') e^{-i\phi(t')} + e^{-i\phi(t)} G(t, t') e^{i\phi(t')} \right) \quad (67)$$

is obtained for a translationally invariant state.

### 3.2 Impurity solvers

The most challenging part of the DMFT equations is the solution of the auxiliary problem, i.e., the determination of the Green function (61) from the action (59) with a given hybridization function  $\Delta(t, t')$ . It can be shown that the action (59) describes a time-dependent Anderson impurity Hamiltonian. However, for one reason or the other, it often turns out to be substantially harder to determine the time-evolving non-equilibrium state of a system than determining the equilibrium state. An example are matrix-product states (MPS): While a MPS representation is efficient for ground states which satisfy an area-law entanglement, the time-propagated state can often not be represented efficiently, leading to an exponential increase of computational resources with the simulated time. Quantum Monte Carlo techniques face a different problem with the same devastating effect: Even when a sign-problem can be avoided in equilibrium (imaginary time), summing up all phases in non-equilibrium leads to an exponentially small average sign. It appears that the problem of time-evolution in many body systems is a challenge, although this may seem at odds with the fact that the final state (after thermalization) is again simple. So far, all impurity solvers are therefore restricted to either short times, or rely on approximations which work in certain regimes of parameter space only.

#### Weak-coupling expansions of the self-energy

In equilibrium and for the half-filled single-band Hubbard model, second-order perturbation theory (iterated perturbation theory, IPT) extrapolates between weak and strong coupling when it is formulated in terms of the bare Green function (60), and qualitatively reproduces the metal-insulator transition [20]. In non-equilibrium, IPT has so far remained restricted to the weak-coupling regime, because the non-conserving nature of the bare expansion can lead to artifacts in the time-evolution [33]. Apart from that, weak-coupling approximations are easy to implement, cf. Eq. (34), and numerically relatively cheap.

## Quantum Monte Carlo techniques

In equilibrium, quantum Monte Carlo (QMC) can give numerically exact results at nonzero temperature [36]. QMC stochastically sums the perturbation expansion in the hybridization function or the interaction to all orders. In real-time, the contributions to the perturbation expansion become complex-valued, which results in a dynamical sign problem and limits a straight-forward real-time generalization of the imaginary-time QMC to short times. There are interesting and fundamental problems to be studied in the short-time dynamics, such as dynamical phase transitions [18], but in order to study the photo-induced dynamics in most materials few hopping times are often not yet sufficient. Recent developments which indicate ways to overcome the dynamical sign-problem [37] have not been tested in the context of non-equilibrium DMFT.

## Hamiltonian representation of the impurity problem

If one can find a finite system which can accurately reproduce a given hybridization function  $\Delta(t, t')$ , the Green function can be determined from a numerical solution of the time-dependent Schrödinger equation, such as using matrix product states and the density matrix renormalization group [38]. It can be shown that a general action with hybridization  $\Delta(t, t')$  is indeed representable by an Anderson impurity model in the most simple geometry, i.e., a star-geometry where the impurity site is coupled to bath sites but there is no link between the bath sites [39]. In this representation, the number of bath orbitals which are needed increases with the simulated time, leading a exponential increase of the computation time. So far, this approach has been used only for the special situation in which the initial state consists of a lattice of uncoupled sites (this is a quench situation which can be realized in cold atoms), but in principle more general initial states can be included. A different representation has been derived for the steady state, using an impurity model in which the bath-sites are coupled to dissipative Lindblad terms [40]. In general, the numerical effort in the Hamiltonian-based techniques increases exponentially with the number of orbitals, which limits the frequency resolution in the steady state and the accessible times in the real-time formalism.

## Perturbation theory in the hybridization function

A systematic expansion in  $\Delta(t, t')$ , with the atomic limit as zeroth order, is expected to work well in the Mott phase, it can be formulated for an arbitrary local part of the Hamiltonian (multi-orbital Hubbard models, electron-phonon interactions), and one can re-sum the terms of the expansion in such a way that the theory becomes conserving. In particular the lowest order (the so called non-crossing approximation, NCA) has been used extensively to study the dynamics of Mott insulators within DMFT. In the following we summarize the equations for the NCA. The technical details of this expansion on the Keldysh contour are explained in Ref. [41] and Ref. [24], to which we also refer for a list of early references related to the use of the expansion as an impurity solver for DMFT and cluster DMFT in equilibrium.

In the hybridization expansion one splits the action  $S$  into the local part  $S_{at} = \int_{\mathcal{C}} dt H_{at}(t)$ , where the atomic Hamiltonian  $H_{at}$  contains the local interaction, and the hybridization  $S_{\Delta}$ . The latter can have a very general form, such as

$$S_{\Delta} = - \sum_{\gamma} \int_{\mathcal{C}} dt_1 dt_2 \bar{\phi}_{\gamma}(t) \Delta_{\gamma}(t, t') \psi_{\gamma}(t'), \quad (68)$$

where  $\gamma$  sums over all hybridization channels, and  $\psi$  and  $\bar{\phi}$  are quite general operators. In the single impurity Anderson model, e.g.,  $\gamma \equiv \sigma$ ,  $\bar{\phi}_{\gamma} \equiv \bar{c}_{\sigma}$ ,  $\psi_{\gamma} \equiv c_{\sigma}$ , but the general formulation also allows for inter-orbital hybridizations in multi-band systems with spin-orbital indices  $a, a'$ , such as  $\sum_{a,a'} \int_{\mathcal{C}} dt_1 dt_2 \bar{c}_a(t) \Delta_{aa'}(t, t') c_{a'}(t')$ , where  $\gamma \equiv (a, a')$ , anomalous hybridizations in superconducting systems,  $\int_{\mathcal{C}} dt_1 dt_2 [c_{\uparrow}(t) \Delta_{cc}(t, t') c_{\downarrow}(t') + \bar{c}_{\downarrow}(t) \Delta_{\bar{c}\bar{c}}(t, t') \bar{c}_{\uparrow}(t')]$ , retarded density-density interactions  $\sum_{\sigma\sigma'} \int_{\mathcal{C}} dt_1 dt_2 n_{\sigma}(t) V_{\sigma\sigma'}(t, t') n_{\sigma'}(t')$  (here  $\bar{\phi}_{\sigma\sigma'} \equiv \bar{c}_{\sigma} c_{\sigma'}$  and  $\psi_{\sigma\sigma'} \equiv \bar{c}_{\sigma'} c_{\sigma}$ ), or electron-phonon interactions ( $\psi = c_{\sigma} b, c_{\sigma} \bar{b}$  etc., acting in a local space of electrons and phonons).

The hybridization expansion is formulated in terms of propagators of the many-body states  $|\alpha\rangle$  of the isolated impurity. For example, for the single-impurity model, these are the Fock-states  $|0\rangle, c_{\uparrow}^{\dagger}|0\rangle, c_{\downarrow}^{\dagger}|0\rangle, c_{\uparrow}^{\dagger}c_{\downarrow}^{\dagger}|0\rangle$ . In the hybridization expansion, we introduce bare propagators  $g_{\alpha\alpha'}(t, t')$  and renormalized propagators  $\mathcal{G}_{\alpha,\alpha'}(t, t')$ , which capture the propagation from state  $\alpha'$  to  $\alpha$  along the forward direction on  $\mathcal{C}$ . The zeroth order propagators are just the time-evolution operators of the atomic Hamiltonian

$$g_{\alpha,\alpha'}(t, t') = -i \langle \alpha | T_{\mathcal{C}} e^{-i \int_{\mathcal{C}, t'}^t d\bar{t} H_{at}(\bar{t})} | \alpha' \rangle \quad \text{for } t >_{\mathcal{C}} t', \quad (69)$$

$$g(t, t') = i g(t, 0_+) \xi g(-i\beta, t') \quad \text{for } t <_{\mathcal{C}} t'. \quad (70)$$

The second line specifies how to “glue” together propagators along the open end of the contour ( $g$  is understood as a matrix in  $\alpha, \alpha'$ ), such that the evolution direction is always in forward direction along  $\mathcal{C}$ : For  $t <_{\mathcal{C}} t'$ , the propagation from  $t'$  to  $t$  along  $\mathcal{C}$  involves a propagation to the end  $-i\beta$  of  $\mathcal{C}$ , and then a propagation from  $0_+$  to  $t$  (see Fig. 4a). The matrix  $\xi_{\alpha\alpha'} = \delta_{\alpha\alpha'} (-1)^{n_{\alpha}^F}$ , where  $n_{\alpha}^F$  is the number of Fermions in  $|\alpha\rangle$ , is introduced for convenience so that  $g$  satisfies the boundary condition (27) for bosons and fermions if there is an even and odd number of fermions in  $\alpha$ , respectively. (Note that  $g$ , and later  $\mathcal{G}$  are at least block-diagonal with respect to the Fermion number, i.e.,  $\xi$  commutes with  $\mathcal{G}$ ).

The renormalized propagators  $\mathcal{G}(t, t')$  simply include all hybridization events between  $t'$  and  $t$  in forward direction along  $\mathcal{C}$ . When the time-evolution operator  $e^{iS_{at}+iS_{\Delta}}$  is expanded in  $S_{\Delta}$ , these terms can be represented intuitively as diagrams as shown in Fig. 4c. All diagrams can be re-summed into a Dyson series, which takes the form

$$\mathcal{G} = g + g \odot \Sigma \odot \mathcal{G}, \quad (71)$$

where  $\Sigma$  (also a matrix in  $\alpha$ ) contains all topologically connected hybridization diagrams, and the convolution  $\odot$  is understood as a time-ordered convolution along forward direction on  $\mathcal{C}$

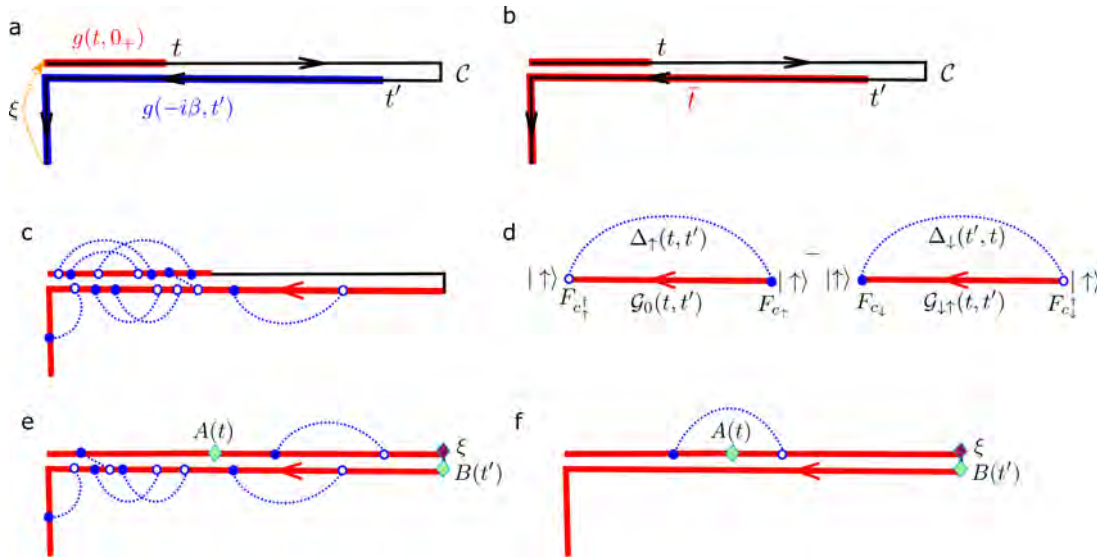


**Fig. 4:** Illustration of the hybridization expansion: (a) gluing together time-evolution operators along the contour in a cyclic fashion. (b) The integration range of the convolution  $\odot$  along  $C$ , cf. Eqs. (72) and (73) (c) Diagrams contributing to  $\mathcal{G}$ , where the blue dotted lines represent  $\Delta(t, t')$ , the open/filled lines are the vertex operators  $F_\psi, F_{\bar{\psi}}$ , and the red lines represent  $g$  (d) The diagrams for the NCA self-energy  $\Sigma_{|\uparrow\rangle}$  in the single-impurity Anderson model. (e) Diagrams for the correlation function  $\langle A(t)B(t') \rangle_S$  without (e) and with (f) vertex corrections.

(Fig. 4b):

$$[A \odot B](t, t') = \int_{C: t >_C \bar{t} >_C t'} d\bar{t} A(t, \bar{t}) B(\bar{t}, t') \quad \text{for } t >_C t' \quad (72)$$

$$[A \odot B](t, t') = \int_{C: -i\beta >_C \bar{t} >_C t'} d\bar{t} A(t, \bar{t}) B(\bar{t}, t') + \int_{C: t >_C \bar{t} >_C 0_+} d\bar{t} A(t, \bar{t}) B(\bar{t}, t') \quad \text{for } t <_C t'. \quad (73)$$

Such time-ordered convolutions naturally appear in the expansion of the time-evolution operator. In practice, using the differential equation for the evolution operator one can solve the Dyson equation (71) as an integral-differential equation

$$(i\partial_t - H_{at})\mathcal{G}(t, t') - [\Sigma \odot \mathcal{G}](t, t') = 0, \quad (74)$$

to be solved with the initial condition  $\mathcal{G}(t_-, t_+) = -i$ , and the boundary condition (27). By construction, the trace

$$Z = \text{Tr} (\xi i\mathcal{G}(t_+, t_-)) \quad (75)$$

is the partition function. In the following, we assume that  $Z = 1$ , which can always be achieved by adding a suitable constant to  $H_{at}$ .  $R = \xi i\mathcal{G}(t_+, t_-)$  is the reduced density matrix on the impurity,  $R_{\alpha\alpha'} = \text{Tr}_{\text{bath}}[|\alpha'\rangle\langle\alpha|]$ , so that all local observables on the impurity are obtained from

$$\langle \hat{O} \rangle = \text{Tr} (\xi i\mathcal{G}(t_+, t_-) \hat{O}), \quad (76)$$

once the propagators  $\mathcal{G}$  are known.



In the non-crossing approximations, one considers only hybridization diagrams without crossings (also crossings between lines of different flavor  $\Delta_\gamma$  are excluded). This can be understood as a leading order expansion in the self-consistent diagrammatic expansion which can be derived from a Luttinger-Ward functional and thus leads to a conserving approximation. The diagrams have a simple form, where for each channel  $\gamma$  in Eq. (68) one adds two diagrams for the two directions of  $\Delta$ ,

$$\Sigma(t, t') = \sum_{\gamma} i \left( \Delta_{\gamma}(t, t') F_{\bar{\phi}_{\gamma}}(t) \mathcal{G}(t, t') F_{\psi_{\gamma}}(t') + P_{\gamma} \Delta_{\gamma}(t', t) F_{\psi_{\gamma}}(t) \mathcal{G}(t, t') F_{\bar{\phi}_{\gamma}}(t') \right), \quad (77)$$

where  $(F_A)_{\alpha\alpha'} = \langle \alpha | A | \alpha' \rangle$  is the matrix representation of the vertex operators  $A = \psi_{\gamma}, \bar{\phi}_{\gamma}$ , and  $P_{\gamma} = -1$  if  $\psi_{\gamma}$  and  $\bar{\phi}_{\gamma}$  are fermionic operators. These diagrams have an intuitive interpretation, where the vertex operators corresponds to a simultaneous transition between a many-body state on the impurity and a transition in the bath. For example, the first diagram in Fig. 4d shows the emission of an electron with spin  $\uparrow$  in the bath, causing a transition of the impurity state from  $|\uparrow\rangle$  to  $|0\rangle$ . The electron then propagates in the bath and is later reabsorbed.

Finally, in addition to observables (76) one needs contour-ordered two-point correlation functions  $\langle T_{\mathcal{C}} A(t) B(t') \rangle_S$ . The operators can simply be inserted as additional vertices on the contour. The general diagrammatic series contains the bare term

$$\langle T_{\mathcal{C}} A(t) B(t') \rangle_S = - \text{Tr} \left( \xi \mathcal{G}(t', t) F_A(t) \mathcal{G}(t, t') F_B(t') \right). \quad (78)$$

One may check the consistency of this term with Eq. (76) (using  $\mathcal{G}(t_-, t_+) = -i$ )

$$\begin{aligned} \langle T_{\mathcal{C}} A(t_-) B(t_+) \rangle_S &= - \text{Tr} \left[ \xi \mathcal{G}(t_+, t_-) F_A \mathcal{G}(t_-, t_+) F_B \right] = i \text{Tr} \left[ \mathcal{G}(t_+, t_-) \xi F_{AB} \right] \stackrel{(76)}{=} \langle A(t) B(t) \rangle \\ \langle T_{\mathcal{C}} A(t_+) B(t_-) \rangle_S &= - \text{Tr} \left[ \xi \mathcal{G}(t_-, t_+) F_A \mathcal{G}(t_+, t_-) F_B \right] = i \text{Tr} \left[ \xi F_A \mathcal{G}(t_+, t_-) F_B \right] = \\ &= i \text{Tr} \left[ \mathcal{G}(t_+, t_-) F_B \xi F_A \right] = \pm i \text{Tr} \left[ \mathcal{G}(t_+, t_-) F_B F_A \xi \right] = \pm \langle B(t) A(t) \rangle. \end{aligned}$$

Here we have used that the matrix  $\xi$  commutes with  $\mathcal{G}$ , because the evolution conserves the Fermion parity, and it commutes (anti-commutes) with the matrix  $F_X$  if  $X$  is a Bose (Fermi) operator. One can also verify Eq. (78) in the atomic limit, using Eqs. (69) and (70). Eq. (78) is used in the NCA impurity solver to measure the impurity Green function. Equations (74), (77), and (78) thus provide the complete set of equations for the most general multi-orbital NCA. The equations have a matrix structure with the Fock-space dimension of the impurity, but symmetries usually render these equations block-diagonal, at least in the fermion parity, and for non-superconducting states also in the particle number.

We note that in general the expectation value  $\langle T_{\mathcal{C}} A(t) B(t') \rangle_S$  contains diagrams which correspond to vertex corrections of the operators  $A$  and  $B$ , see Fig. 4e and f. Even within NCA, some of these diagrams are generated if the correlation function  $\langle T_{\mathcal{C}} A(t) B(t') \rangle_S$  is calculated by explicitly taking a derivative of the NCA solution to  $\langle B(t') \rangle_S$  with respect to a source field that couples to  $A(t)$ . Such an explicit measurement, which includes the vertex corrections, can be useful for the calculation of susceptibilities within NCA. For the measurement of the Green function within the DMFT cycle, one sticks to Eq. (78), which gives a consistent approximation.

## 4 Photo-doping the Mott insulator

The Mott transition, at which electrons get localized due to the Coulomb interaction, is one of the hallmarks of strong electronic correlations in solids. In contrast to a band-insulator with filled or empty bands, electrons in the Mott insulator still have active spin and orbital degrees of freedom, which can result in complex phases with magnetic and orbital order. Short-ranged magnetic and orbital correlations, on the other hand, may induce interactions between doped electrons and holes, and thus give rise to yet new states such as superconductivity. The development of DMFT has been instrumental in the understanding of the Mott transition [21], and it is therefore a natural application of the non-equilibrium extension of DMFT to analyze the dynamics of Mott insulators after various excitation protocols.

### 4.1 Paramagnetic Mott insulator

The most straightforward way to excite a Mott insulator is a short electric field pulse of frequency  $\Omega \approx U$ . This generates charge excitations in the paramagnetic Mott insulator, i.e. doubly occupied and empty sites. The properties of such a photo-excited state and its thermalization have been analyzed in Ref. [42]. Figure 5a) shows the time-evolution of the double occupancy  $d(t) = \langle n_{\uparrow}(t)n_{\downarrow}(t) \rangle$  during and after the excitation. These results have been obtained for the Bethe lattice and the NCA impurity solver, using a single-cycle electric-field pulse. Setting the bandwidth  $W = 4$  fixes the energy- and timescale ( $\hbar = 1$ ). (The results in [42] have been obtained for the hyper-cubic lattice using the hybridization expansion up to third order. They are qualitatively similar to the results shown here.)

The double occupancy increases during the pulse, and subsequently shows an exponential relaxation to a new final value. Thermalization would imply that the properties of the system eventually approach the properties of a system in equilibrium, at a temperature  $T_f$  such that the total energy equals the thermal energy expectation value  $E_{th}(T_f)$  at temperature  $T_f$ ,  $\langle H(t) \rangle \equiv E_{tot} \stackrel{!}{=} E_{th}(T_f)$ . (Note that the system is treated in isolation from environment, so that the total energy is conserved after the excitation. We can determine  $T_f$  from a comparison to independent equilibrium simulations, and then compute the thermal expectation value  $d_{th}(T_f)$  for the different values of  $U$  in Fig. 5. A fit of the form

$$d(t) = d_{th}(T_f) + A \exp(-t/\tau), \quad (79)$$

(see black dashed lines) shows that the evolution of  $d(t)$  is compatible with thermalization of the electronic system. The timescales, however, strongly depend on  $U$ , and range from few hopping times in the correlated metal ( $U = 2.5$ ), to  $\tau > 1000$  in the Mott phase ( $U = 6$ ). Empirically, the dependence of the thermalization times on  $U$  can be described by the exponential dependence  $\tau(U) \sim \exp \left[ \alpha \frac{U}{v_*} \log \left( \frac{U}{v_*} \right) \right]$ , with some numerical constant  $\alpha$  (blue dashed line in Fig. 5b). This result has an interpretation in terms of a bottleneck due to the inefficient transfer of a large energy quantum of order  $U$  into many single-particle excitations [43]. The exponential dependence was first measured in a system of ultra-cold atoms [43]. In solids, the life-times

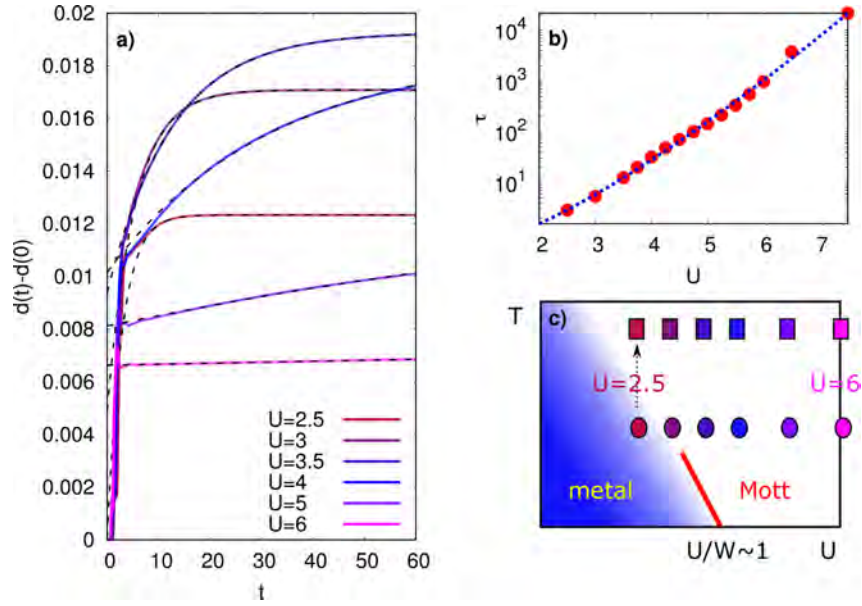


**Fig. 5:** a) Evolution of the double occupancy in the Hubbard model on the Bethe lattice during and after a single-cycle pulse of duration  $2\delta t$  with  $\delta t = 2\pi/\Omega$  and  $\Omega = U$ , i.e.,  $A(t) = A_0 e^{-4(t-\delta t)^2/\delta t^2} \sin(t-\delta t)\Omega$  for  $0 \leq t \leq 2\delta t$  in Eq. (67). The initial temperature is  $T = 0.2$ , initial states correspond to values of  $U$  in the metal-insulator crossover and in the Mott state, as schematically shown by the circle symbols in panel c). Square symbols in c) show the state after thermalization ( $T_f \approx 0.5$  for all curves). Dashed lines in a) are exponential fits, see Eq. (79). b) Symbols: Relaxation times  $\tau$ , obtained from the fits (79).

of photo-excited carriers in Mott insulators can indeed range to thousands of hopping times (picoseconds), but the decay mechanism may involve other degrees of freedom: Spin-fluctuations have been discussed as a possible mechanism for the doublon decay in cuprates [44,45], while in organic materials there are molecular vibrations at relatively high energies  $\omega_0$ , opening the possibility for a multi-phonon decay at a timescale governed by  $U/\omega_0$  rather than  $U/W$  [46,47].

### Thermalization of small-gap Mott insulators

We now focus on the regime of small  $U$ , where rapid thermalization is observed in the double occupancy. We can identify the thermalization also in the relaxation of the spectral function and the occupation function, see Fig. 6. In the Figure, the spectral function and occupation function have been obtained by the backward Fourier transform with cutoff  $s_{max}$

$$A(\omega, t) = -\frac{1}{\pi} \text{Im} \int_0^{s_{max}} ds G^R(t, t-s) e^{i\omega s} \quad (80)$$

$$N^<(\omega, t) = -\frac{1}{\pi} \text{Im} \int_0^{s_{max}} ds G^<(t, t-s) e^{i\omega s}. \quad (81)$$

(The Wigner transform, or a photoemission spectrum (10) would look similar.) Both spectral function and occupation function become independent of  $t$  within a few hopping times, comparable to the relaxation time  $\tau$  of the double occupancy. At the latest time  $t = 18$ , we find

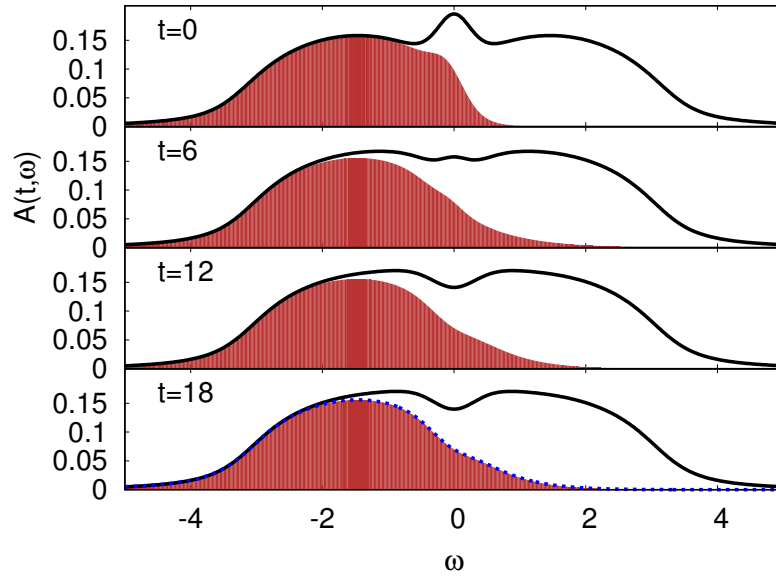


**Fig. 6:** *a) Spectral function, Eq. (80), for  $U = 2.5$ ,  $\beta = 5$  and the same excitation protocol as in Fig. 5, plotted for different times  $t$ . The shaded region shows the occupation function, Eq. (81), for the same parameters. The blue dotted line for  $t = 18$  shows  $A(t, \omega)f(\omega, T_f)$ , where  $T_f = 1/1.967$  is determined from the total energy.*

the fluctuation theorem satisfied in the form  $N^<(\omega) = A(\omega) f(\omega, T_f)$ , with the temperature  $T_f = 1/1.967$  is obtained from the total energy. This confirms that, regarding the single-particle properties, the system indeed thermalizes on the timescale of few hoppings.

A rapid thermalization of a small-gap Mott insulator is in agreement with early time-resolved photoemission measurements on the Mott insulator 1T-TaS<sub>2</sub> [48]. At the shortest measurable times, the spectrum of the photo-excited system resembles that of a Mott insulator at electronic temperatures of the order of the gap, where thermal effects lead to a filling in of states in the gap. In spite of some naive expectation, rapid thermalization of a strongly correlated system is far from obvious: Already the analysis above predicts a rather sensitive dependence of the thermalization time on the gap, and also model studies for an interaction quench in the Hubbard model [18] show thermalization within timescales of the order of the bandwidth only in a narrow interaction regime. Most importantly, thermalization in a strongly correlated system cannot directly be understood from a simple Boltzmann equation. The latter would only describe the evolution of the occupation function, while thermalization in the correlated system implies that also the spectral function is modified. In Fig. 6, e.g., the spectral function completely changes during the evolution: In the initial state ( $\beta = 5$ ) there is still a reminiscence of the quasiparticle peak, while in the final state at high electronic temperature the system resides in a bad-metallic state, with a pseudo-gap instead of the quasiparticle peak.

In view of this, it is reassuring that recently also a successful comparison between theory and experiment of time-dependent features of the thermalization could be achieved [49]. A refined analysis of the photoemission spectroscopy in 1T-TaS<sub>2</sub> shows the transient emergence and decay of the population in the upper Hubbard band. Such a reduction of the occupied weight in the upper band should happen along with the electronic thermalization if the system is slightly hole-

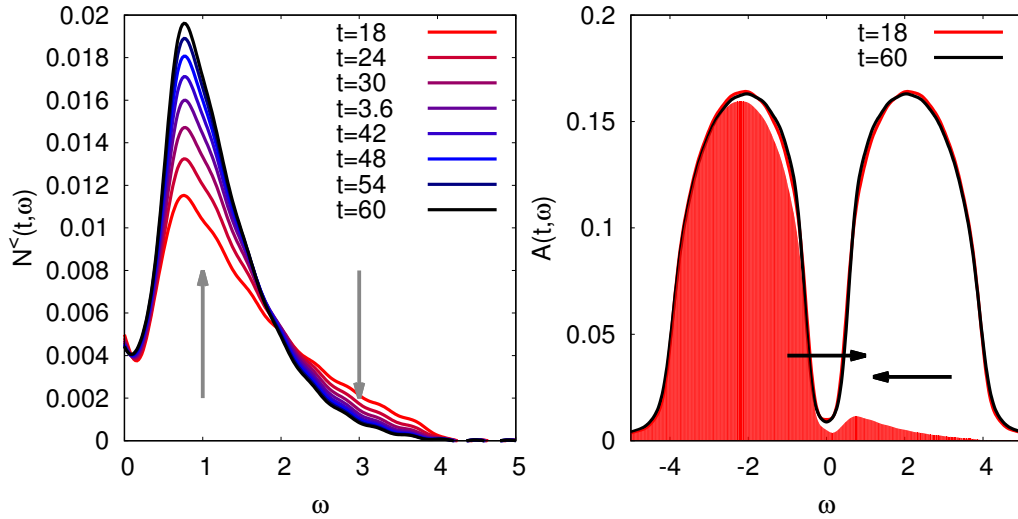


**Fig. 7:** *a)* Occupation function, Eq. (81), for  $U = 4$  and the same excitation protocol as in Fig. 5, plotted for different times  $t$ . The arrows indicate increase and decrease of weight at low and high energies, respectively. *b)* Spectral function, Eq. (80), for the same parameters. The arrows indicate an energy-conserving redistribution of occupied weight, as approximately described by a local Boltzmann equation (see text).

doped. Since the laser transfers population both within the Hubbard bands and to higher and lower bands other than the valence band, the filling in the valence band may change during the excitation. In spite of the extremely sensitive dependence of thermalization timescales on the model parameters, the observed experimental bound for this timescale is consistent with DMFT results [49].

### Impact ionization

In Fig. 5 one can see that the double occupancy increases during the thermalization after the pulse. This implies that the kinetic energy of the photo-excited state is initially too high, and kinetic energy from one or more charge excitations is used to generate *additional doublons*. This process is similar to an Auger process in atomic physics, or *impact ionization* in semiconductors [50]. The process is visible also in the evolution of the occupation function (Fig. 7a). The occupied density of states (81) in the upper Hubbard band shows an increase of the weight at small energies, which *exceeds* the decrease at high energies. This phenomenology is clearly distinct from intra-band relaxation via spins and phonons, where the total weight remains constant while it is redistributed from higher to lower energies.

Naively one can argue that a doublon with high kinetic energy (represented by occupied density of states in the upper part of the upper Hubbard band) undergoes a scattering process with a “particle in the lower band” leading to one additional hole (unoccupied weight in the lower Hubbard band) and two doublons with low kinetic energy (occupied density of states in the lower part of the upper Hubbard band), as indicated by the arrows in Fig. 7b. In the ideal case, when the relaxation of each doublon from the high-energy window generates precisely one doublon-hole pair, one would expect the increase of the weight at low energies to be larger

by a factor *three* than the decrease at high energies, a quantitative estimate which works rather well for small gap Mott insulators [50]: In the present case, the increase of weight from  $t = 18$  to  $t = 60$  in the interval  $0.5 \leq \omega \leq 2$  is larger by approximately a factor 3.1 than the decrease in the interval  $2 \leq \omega \leq 4$ .

The argument presented above seemingly relies on a scattering of quasiparticles (doublons) with a well-defined energy, as described by a Boltzmann equation. The success of such an argument may come as a surprise, as the energy of a doublon is not really well-defined, and the width of the peaks in the momentum-resolved spectral  $A_k(\omega)$  function is of order one. However, one can reformulate the scattering argument on the basis of a local time-dependent occupation function defined by  $G^<(\omega, t) = 2\pi i A(\omega, t) F(\omega, t)$ , putting it on more rigorous grounds [51]: Under the assumption that (i), the spectral function  $A(\omega)$  is more or less time-independent, which is justified numerically for weakly excited paramagnetic Mott insulators (compare the spectra at the earliest and later time in Fig. 7b), and (ii), that the distribution function  $F(\omega, t)$  evolves slowly compared to the inverse bandwidth, one can argue that the non-equilibrium DMFT dynamics of  $F$  is given by a local Boltzmann equation

$$\begin{aligned} \partial_t F(\omega_1, t) = & \alpha \int d\omega_2 d\omega_3 d\omega_4 A(\omega_2) A(\omega_2) A(\omega_4) \delta(\omega_1 + \omega_2 - \omega_3 - \omega_4) \times \\ & \times \left( F(\omega_3) F(\omega_4) (1 - F(\omega_1)) (1 - F(\omega_2)) - F(\omega_1) F(\omega_2) (1 - F(\omega_4)) (1 - F(\omega_3)) \right), \end{aligned}$$

where  $\alpha$  is a phenomenological parameter. This equation indeed describes energy-conserving scattering processes as shown in Fig. 7b, even though the individual doublons do not have well-defined energies.

Impact ionization processes are interesting in the context of photo-voltaic devices: Usually, a photon creates a single charge excitation, which then quickly relaxes to the bottom of the band due to scattering with phonons. The usable energy per photon is therefore not given by  $\hbar\omega$ , but only by the gap  $\Delta$ . However, if impact ionization is faster than such intra-band relaxation processes, the final state can have *two or more* electrons at the energy  $\Delta$ . DMFT shows that impact ionization processes in small-gap Mott insulators indeed can occur on a time-scale much faster than typical electron-phonon relaxation times. However, as seen below, short-range spin fluctuations in Mott insulators can provide another fast intra-band relaxation mechanism, so that it remains to be seen to what extent impact ionization plays an important role in real Mott materials.

## 4.2 Dynamics of the antiferromagnetic Mott insulator

At half-filling and on a bipartite lattice, the Hubbard model shows an extended antiferromagnetic phase at low temperature. At weak coupling this phase is well described as a Slater mean-field antiferromagnet, while for large  $U$  the Heisenberg model is the limiting description. Several works on DMFT have focused on the melting or partial melting of this phase after photo-excitation or quenches of the interaction. After quenches around large  $U$  (Heisenberg regime), there is a threshold of the quench amplitude  $\Delta U$  beyond which the order rapidly melts [52].

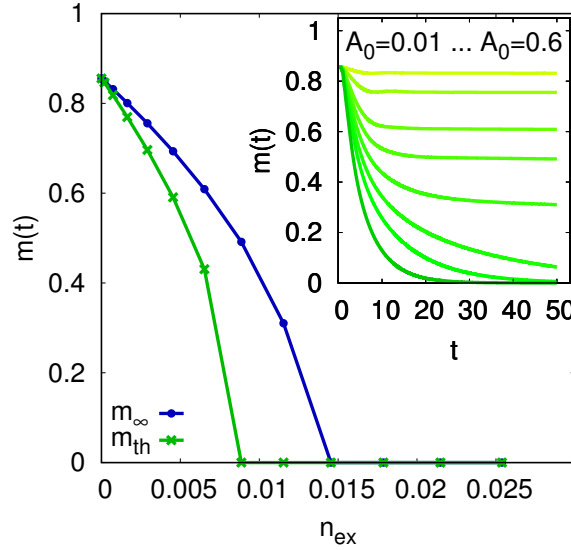


**Fig. 8:** *Inset: Antiferromagnetic order parameter  $m(t)$  in the Hubbard model on the Bethe lattice ( $U = 5$ ,  $\beta = 20$ ), after excitation with a single-cycle electric field pulse. The different curves correspond to different excitation densities (pulse amplitudes  $A_0$ ) up to  $n_{ex} \approx 0.025$ . Main plot: Extrapolated value  $m_\infty$ , obtained by fitting the curves in the inset with  $m(t) = m_\infty + Ae^{-\gamma t}$  for  $t \geq 15$ .  $m_{th}$  is the order parameter after thermalization.*

A critical slowdown  $1/\tau \sim |\Delta U - \Delta U_c|$  is observed, where  $\Delta U_c$  is the critical quench amplitude for melting the antiferromagnetic phase. (A similar non-thermal critical behavior is also found after quenches at small interaction [53].) While this reminds of a second-order phase transition, the melting of the anti-ferromagnetism after the quench is a *non-thermal* process: Like the paramagnetic Mott insulator, the antiferromagnetic Mott state thermalizes only on times which are exponentially large in  $U/W$ . The ordered state can thus prevail even when the energy after the quench is higher than the energy of the half-filled system *above* the Néel temperature. Instead, the threshold for the melting is set by the number of excited doublons after the quench, i.e., the occupied weight in the upper Hubbard band.

The non-thermal melting can also be seen after excitation with a short pulse: Like in the paramagnetic phase at large  $U$ , a pulse leads to an increase of the double occupancy which does not thermalize within the simulated time of  $\sim 100$  hoppings. Figure 8 shows the time-evolution of the antiferromagnetic order parameter  $m(t) = \langle c_{j\uparrow}^\dagger c_{j\uparrow} - c_{j\downarrow}^\dagger c_{j\downarrow} \rangle_j$  on  $A$ -sublattice in the Hubbard model on the Bethe lattice after excitation with an electric field pulse:  $m(t)$  saturates to a finite value for excitation densities  $n_{ex} \lesssim 0.015$ , while complete melting of long-range order is observed for  $n_{ex} \gtrsim 0.015$ , with a relatively sharp threshold of the final value  $m_\infty$  as a function of the excitation density. The corresponding value of the order parameter in the thermalized state, which would be reached after thermalization,  $m_{th}(n_{ex})$ , is always lower than the value of  $m_\infty$  in the photo-excited state. The intermediate state is expected to relax only on the exponentially long timescale of doublon-hole recombination.

The non-thermal melting of the antiferromagnetic order can be understood in terms of a hole which is moving in the antiferromagnetic spin background and thus induces a spin-flip in every hopping process [54]. Because each spin-flip increases the energy in the magnetic sector by



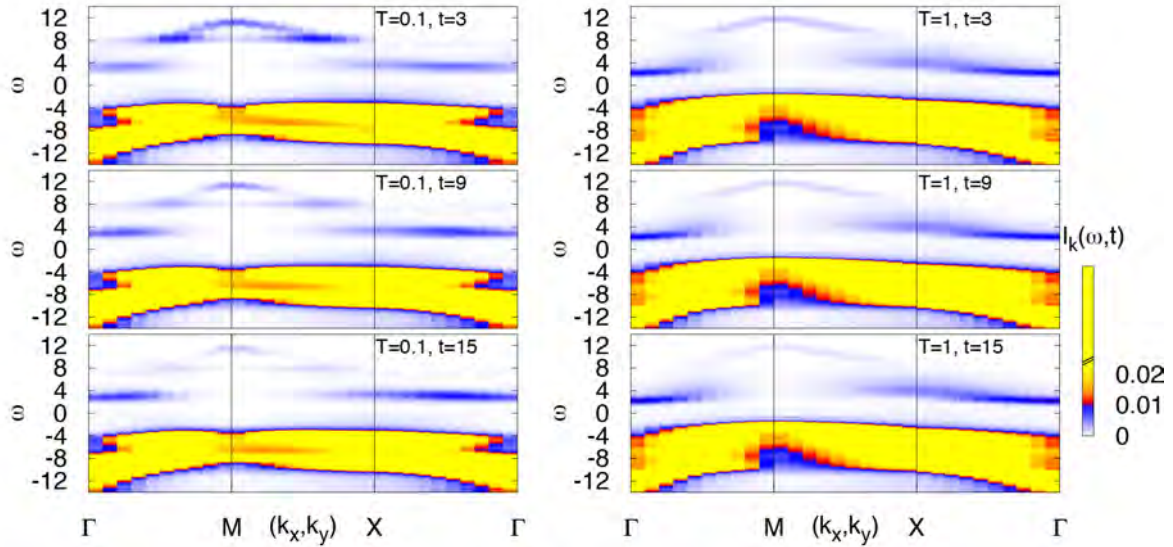


**Fig. 9:** Simulated time-resolved photo-emission spectrum in a two-dimensional Mott insulator (Hubbard model,  $U = 12$ ) after a transfer of population to the upper Hubbard band. (Dynamical cluster approximation with a  $2 \times 2$  cluster and an NCA impurity solver.) At high temperature (right) the relaxation of weight within the upper band becomes slower, because the spins are already thermally disordered ( $T \gtrsim J_{ex}$ ) and cannot take up more energy. Adapted from Ref. [55].

an amount of the order of the exchange energy  $J_{ex} \sim v_*^2/U$ , this implies an ultra-fast transfer of kinetic energy from photo-doped electrons to the spins, and thus an ultra-fast mechanism for intra-band relaxation. A rapid energy transfer to spins is even possible in the paramagnetic phase, where spins have no long-range order, but are short-ranged and short-lived. While short-range fluctuations cannot be captured in single-site DMFT, they have been studied using cluster extensions (the dynamical cluster approximation) [55]. Figure 9 shows a simulated time-resolved photo-emission spectrum in the two-dimensional Hubbard model. One finds a redistribution of the occupied density of states, which happens along with a reduction of short-range spin correlations. Using parameters comparable to cuprates, the relaxation times  $\tau \sim 10\text{--}20$  fs are compatible with the timescales for the initial saturation of the optical response in cuprates after a few-fs laser excitation and with exact-diagonalization results for small clusters in the  $t$ - $J$  model [54].

### The photo-doped state

In the time window between thermalization (on timescales exponentially large on  $U/W$ ) and the relaxation of the kinetic energy by partial melting of spin fluctuations, the electronic system is in an almost steady non-equilibrium state. It turns out that in this steady state only the excitation density  $n_{ex}$  and the antiferromagnetic order parameter  $m_\infty$  remain as the main non-equilibrium control parameters which determine the properties of the system, in analogy to the thermodynamic variables in equilibrium: Firstly, the spectral function of the photo-excited state with given  $n_{ex}$  and  $m_\infty$  matches the spectral function of a chemically doped system with the same order parameter and a density of carriers  $n - 1 = 2n_{ex}$  [52]. This shows that chemically



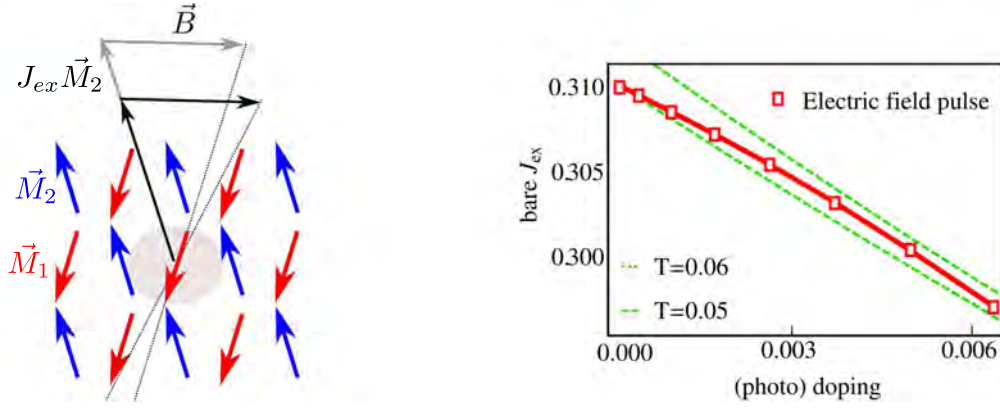


**Fig. 10:** Left: Macro-spin dynamics of the antiferromagnetic order parameter after a photo-doping excitation. In the presence of an external field  $\vec{B}$ , the order parameter  $\vec{M}_1$  on sub-lattice 1 aligns with the effective field  $J_{ex}\vec{M}_2 + \vec{B}$ . If  $J_{ex}$  is modified, a precessional dynamics follows. Right: The exchange interaction extracted from the macro-spin dynamics in the photo-excited system at excitation density  $2n_{ex}$  (red symbols), and from the macro-spin state in a chemically doped system with filling  $n = 1 + 2n_{ex}$  (green lines). Adapted from Ref. [56].

doping  $n - 1$  doublons or holes in equilibrium has a similar effect as photo-exciting the same number of doublons *and* holes, which is why the steady state may be called a photo-doped state. Furthermore, it was shown that also the magnetic exchange interaction  $J_{ex}$  is modified in the photo-excited state due to the presence of mobile carriers [56], to the same extent as by chemical doping. The latter can be seen in a time-resolved precession experiment, Fig. 10. One can analyze the change of  $J_{ex}$  from the global macro-spin dynamics of the antiferromagnetic order parameter after a photo-doping excitation: The dynamics of the sub-lattice magnetization  $\vec{M}_1$  on one of the two sub-lattices of the anti-ferromagnet is determined by the precession of the moment  $\vec{M}_1$  in an effective magnetic field  $\vec{B}_{eff} = J_{ex}\vec{M}_2 + \vec{B}$  given by the exchange coupling to the other sub-lattice and the external field,

$$\frac{d}{dt}\vec{M}_1 = (J_{ex}\vec{M}_2 + \vec{B}) \times \vec{M}_1, \text{ and } 1 \leftrightarrow 2. \quad (82)$$

In equilibrium, the static external field implies a canted anti-ferromagnetic state (Fig. 10). If the photo-doping modifies the effective parameter  $J_{ex}$ , spins are no longer aligned with  $\vec{B}_{eff}$  and start to precess. From the precession dynamics, which can be obtained from the DMFT solution of the photo-excited Hubbard model, one can thus read off  $J_{ex}$ . As shown in Fig. 10, one finds an exchange interaction which is different from the equilibrium state of the half-filled model, but roughly equals the value obtained in an equilibrium state with the same density of carriers  $n - 1 = 2n_{ex}$  [56].

### Multi-orbital systems

The previous analysis shows that photo-doping provides an ultra-fast way to manipulate materials properties. The photo-doped state in the single-band anti-ferromagnet is controlled (after some primary electronic relaxation) by a single control parameter  $n_{ex}$ . This may be expected from the simplicity of the model, which has only a single band and is particle-hole symmetric,

such that hole-doping, electron doping, and photo-doping have a similar effect. In more complex models, in particular those involving more than one orbital, there is a large playground to manipulate the occupations of different types of doubly occupied and multiply occupied states [57] and use this to modify the effective interactions which govern spin and orbital order. A recent investigation of photo-doping in the two-orbital Hubbard model at quarter filling has revealed a possible path to reach hidden states by photo-doping [58]: For one electron in two degenerate orbitals of  $e_g$  symmetry, the Hubbard model features both spin and orbital order in equilibrium, analogous to the order in  $\text{KCuF}_3$  [59]. Photo-excitation is followed by non-thermal melting, which results in a transient reduction of the two orders. In contrast to the effect of heating, however, the magnetic order melts consistently slower than the orbital order. The photo-doped state therefore has an intrinsically different spin-orbital order from the equilibrium state, and the coupling between the two order parameters leads to a ferro-orbital state, which can otherwise not be established in the equilibrium phase diagram.

## 5 Outlook and further questions

In these notes we have presented the theoretical basis for a description of correlated electron systems out of equilibrium using non-equilibrium DMFT. These lecture notes do not represent a review of non-equilibrium DMFT. For example, a large field of research which has been left out includes the so-called Floquet engineering of Hamiltonians by periodic driving [10], where DMFT provides a framework to study directly the driven dissipative state [13]. Rather than listing all this work, we end this lecture with a loose list of questions and topics which remain open for further research:

- **Multi-orbital effects:** Many correlated materials have more than one active orbital, so that their physics is governed by the interplay of orbital order, spin-order, and the strong coupling to the lattice. In such systems, intertwined order parameters allow to steer a system along nontrivial pathways into novel transient or hidden phases, or dynamically stabilize non-equilibrium states, such as already seen in Ref. [58]. Some interesting directions to be explored further, such as photo-induced metal-insulator transitions have already been demonstrated within the Gutzwiller approximation [60]. The investigation of multi-orbital effects within DMFT is clearly only at the beginning.
- **Long term steady states:** Non-equilibrium steady states have so far been used to investigate driven steady states (e.g., to discuss current-induced phase transitions [61]). An interesting open question is whether one can design an approximate non-equilibrium steady state description of pre-thermalized or photo-doped states in correlated systems.
- **Impurity solvers:** There are currently no non-perturbative impurity solvers which work at long times. While NCA can be applied very flexibly within the Mott phase, it becomes increasingly inaccurate for correlated metallic phases. An interesting perspective

is given by the application of the non-perturbative methods (QMC [37] and Hamiltonian-based solvers [39]), which currently seem to be too expensive for the long-term transient dynamics, to explore the non-equilibrium steady states.

- Role of non-local correlations:** DMFT assumes a spatially local self-energy. One might wonder whether the local approximation, though correct in the limit of taking the coordination number  $Z$  to infinity at a fixed length of the time contour, would miss qualitatively important effects for finite-dimensional systems. Most likely, the long-time limit and the  $Z \rightarrow \infty$  limit do not commute, i.e., even in highly coordinated systems at some timescale there may be effects which have a qualitative influence on the dynamics that is not captured by DMFT. This includes the influence of short-range fluctuations on the relaxation dynamics, such as discussed around Fig. 9, or the feedback of collective excitations on the non-equilibrium dynamics. These effects may be investigated to first approximation using diagrammatic approximations such as GW or FLEX.
- Non-local interactions, screening, and the path towards an ab-initio description:** An important consequence of non-local interactions is the feedback of the long-range Coulomb interaction on the parameters of the model Hamiltonians via dynamical screening. For large excitation densities, or interactions involving many bands, one can expect a sizeable renormalization of the Hubbard  $U$  via screening, which may even close a Mott gap. A possible way to include these effects is via the extended DMFT formalism [62]. The question of screening is also closely related to the possible ab-initio determination of model parameters. Other than in equilibrium, an ab-initio formalism comparable to density functional theory is less developed. The combination of a non-equilibrium Green function approach such as DMFT with a density-functional approach suffers from the double counting problem, which is unresolved in equilibrium. An interesting perspective is therefore the combination of non-equilibrium GW with DMFT [63], which can be formulated in a consistent functional language. The main challenge in this direction is, again, the solution of the resulting impurity problem with retarded interactions which can currently only be solved in the limited parameter regime accessible by NCA.

## Acknowledgements

I acknowledge funding from the ERC via starting grant No. 716 648.

## References

- [1] C. Giannetti, M. Capone, D. Fausti, M. Fabrizio, F. Parmigiani, and D. Mihailovic, *Adv. Phys.* **65**, 58 (2016)
- [2] T. Rohwer *et al.*, *Nature* **471**, 490 (2011)
- [3] D. Fausti, R.I. Tobey, N. Dean, S. Kaiser, A. Dienst, M.C. Hoffmann, S. Pyon, T. Takayama, H. Takagi, A. Cavalleri, *Science* **331**, 189 (2011)
- [4] Mitrano *et al.*, *Nature* **530**, 461 (2016)
- [5] S. Mor *et al.*, *Phys. Rev. Lett.* **119**, 086401 (2017)
- [6] D. Wegkamp *et al.*, *Phys. Rev. Lett.* **113**, 216401 (2014)
- [7] H. Ichikawa *et al.*, *Nat. Mater.* **10**, 101 (2011)
- [8] L. Stojchevska, I. Vaskivskiy, T. Mertelj, P. Kusar, D. Svetin, S. Brazovskii, and D. Mihailovic, *Science* **344**, 177 (2014)
- [9] M. Först, C. Manzoni, S. Kaiser, Y. Tomioka, Y. Tokura, R. Merlin, and A. Cavalleri, *Nat. Phys.* **7**, 854 (2011)
- [10] M. Bukov, L. D'Alessio, and A. Polkovnikov, *Adv. Phys.* **64**, 139 (2015)
- [11] T. Oka and H. Aoki, *Phys. Rev. B* **79**, 081406(R) (2009)
- [12] M. Knap, M. Babadi, G. Refael, I. Martin, and E. Demler, *Phys. Rev. B* **94**, 214504 (2016)
- [13] Y. Murakami, N. Tsuji, M. Eckstein, and Ph. Werner, *Phys. Rev. B* **96**, 045125 (2017)
- [14] J.H. Mentink, K. Balzer, and M. Eckstein, *Nat. Commun.* **6**, 6708 (2015)
- [15] F. Görg, M. Messer, K. Sandholzer, G. Jotzu, R. Desbuquois, and T. Esslinger, *Nature* **553**, 481 (2018)
- [16] O. Schubert *et al.* *Nat. Photonics* **8**, 119 (2014)
- [17] A. Polkovnikov, K. Sengupta, A. Silva, and M. Vengalattore, *Rev. Mod. Phys.* **83**, 863 (2011)
- [18] M. Eckstein, M. Kollar, and Ph. Werner, *Phys. Rev. Lett.* **103**, 056403 (2009)
- [19] M. Kollar, F.A. Wolf, and M. Eckstein, *Phys. Rev. B* **84**, 054304 (2011)
- [20] A. Georges, G. Kotliar, W. Krauth, and M.J. Rozenberg, *Rev. Mod. Phys.* **68**, 13 (1996)
- [21] E. Pavarini, E. Koch, D. Vollhardt, and A. Lichtenstein (eds.): *DMFT at 25: Infinite Dimensions, Modeling and Simulation* Vol. 4 (Forschungszentrum Jülich, 2014)

- [22] P. Schmidt, and H. Monien, arXiv:cond-mat/0202046.
- [23] J.K. Freericks, V.M. Turkowski, and V. Zlatić, Phys. Rev. Lett. **97**, 266408 (2006)
- [24] H. Aoki, N. Tsuji, M. Eckstein, M. Kollar, T. Oka, and Ph. Werner, Rev. Mod. Phys. **86**, 779 (2014)
- [25] A. Kamenev, *Field Theory of Non-Equilibrium Systems* (Cambridge University Press, 2011)
- [26] H. Haug, and A. Jauho, *Quantum Kinetics in Transport and Optics of Semiconductors* (Springer, 2008)
- [27] J.K. Freericks, H.R. Krishnamurthy, and Th. Pruschke, Phys. Rev. Lett. **102**, 136401 (2009)
- [28] M. Eckstein and M. Kollar, Phys. Rev. B **78**, 245113 (2008)
- [29] F. Randi, D. Fausti, and M. Eckstein, Phys. Rev. B **95**, 115132 (2017)
- [30] F. Randi, M. Esposito, F. Giusti, F. Parmigiani, O. Misochko, D. Fausti, and M. Eckstein, arXiv:1705.08523 (to appear in Phys. Rev. Lett.)
- [31] G. Baym and L.P. Kadanoff, Phys. Rev. **124**, 287 (1961)
- [32] H. Brunner and P.J. van der Houwen, *The Numerical Solution of Volterra Equations* (Elsevier, 1986)
- [33] M. Eckstein, M. Kollar, and Ph. Werner, Phys. Rev. B **81**, 115131 (2010)
- [34] M. Bonitz (edt.), *Progress in Nonequilibrium Green's Functions* (World Scientific, Singapore, 2000)
- [35] W. Metzner and D. Vollhardt, Phys. Rev. Lett. **62**, 324 (1989)
- [36] E. Gull, A.J. Millis, A. Lichtenstein, A.N. Rubtsov, M. Troyer, and Ph. Werner, Rev. Mod. Phys. **83**, 349 (2011)
- [37] G. Cohen, E. Gull, D.R. Reichman, and A.J. Millis, Phys. Rev. Lett. **115**, 266802 (2015)
- [38] F.A. Wolf, I.P. McCulloch, and U. Schollwöck, Phys. Rev. B **90**, 235131 (2014)
- [39] Ch. Gramsch, K. Balzer, M. Eckstein, and M. Kollar, Phys. Rev. B **88**, 235106 (2013)
- [40] E. Arrigoni, M. Knap, and W. von der Linden, Phys. Rev. Lett. **110**, 086403 (2013)
- [41] M. Eckstein and Ph. Werner, Phys. Rev. B **82**, 115115 (2010)
- [42] M. Eckstein and Ph. Werner, Phys. Rev. B **84**, 035122 (2011)

- [43] N. Strohmaier, D. Greif, R. Jördens, L. Tarruell, H. Moritz, T. Esslinger, R. Sensarma, D. Pekker, E. Altman, and E. Demler, *Phys. Rev. Lett.* **104**, 080401 (2010)
- [44] Z. Lenarčič and Peter Prelovšek, *Phys. Rev. B* **90**, 235136 (2014)
- [45] H. Okamoto, T. Miyagoe, K. Kobayashi, H. Uemura, H. Nishioka, H. Matsuzaki, A. Sawa, and Y. Tokura, *Phys. Rev. B* **82**, 060513(R) (2010)
- [46] M. Mitrano *et al.*, *Phys. Rev. Lett.* **112**, 117801 (2014)
- [47] Z. Lenarčič, M. Eckstein, and Peter Prelovšek, *Phys. Rev. B* **92**, 201104(R) (2015)
- [48] L. Perfetti, P.A. Loukakos, M. Lisowski, U. Bovensiepen, H. Berger, S. Biermann, P.S. Cornaglia, A. Georges, and M. Wolf, *Phys. Rev. Lett.* **97**, 067402 (2006)
- [49] M. Ligges *et al.*, *Phys. Rev. Lett.* **120**, 166401 (2018)
- [50] Ph. Werner, K. Held and M. Eckstein, *Phys. Rev. B* **90**, 235102 (2014)
- [51] M. Wais, M. Eckstein, R. Fischer, P. Werner, M. Battiato, and K. Held, arXiv:1806.02570.
- [52] Ph. Werner, N. Tsuji, and M. Eckstein, *Phys. Rev. B* **86**, 205101 (2012)
- [53] N. Tsuji, M. Eckstein, and Ph. Werner, *Phys. Rev. Lett.* **110**, 136404 (2013)
- [54] S. Dal Conte *et al.*, L. Vidmar, *et al.*, *Nat. Phys.* **11**, 421 (2015)
- [55] M. Eckstein and Ph. Werner, *Sci. Rep.* **6**, 21235 (2016)
- [56] J.H. Mentink and M. Eckstein, *Phys. Rev. Lett.* **113**, 057201 (2014)
- [57] H.U.R. Strand, D. Golež, M. Eckstein, and Ph. Werner, *Phys. Rev. B* **96**, 165104 (2017)
- [58] J. Li, H.U.R. Strand, P. Werner, and M. Eckstein, arXiv:1806.01567.
- [59] E. Pavarini, E. Koch, and A.I. Lichtenstein, *Phys. Rev. Lett.* **101**, 266405 (2008)
- [60] M. Sandri and M. Fabrizio, *Phys. Rev. B* **91**, 115102 (2015)
- [61] A. Matthies, J. Li, and M. Eckstein, arXiv1804.09608.
- [62] D. Golez, M. Eckstein, and Ph. Werner, *Phys. Rev. B* **92**, 195123 (2015)
- [63] D. Golez, L. Boehnke, H. Strand, M. Eckstein, and Philipp Werner, *Phys. Rev. Lett.* **118**, 246402 (2017)

# Index

## A

analytic continuation, 11.3  
Anderson molecule, 7.7, 7.37  
angle-resolved photoemission, 4.9  
antiferromagnetism, 14.5, 14.8, 14.11  
atomic-sphere approximation (ASA), 2.8  
atomic-sphere truncation, 7.19  
attractive Hubbard model, 13.14  
auxiliary-field QMC, 10.2  
average spectrum method, 11.20

## B

band magnetism, 2.20  
Bayes' theorem, 11.10  
Baym-Kadanoff functional, 6.12  
BCS theory, 13.3  
Bernoulli polynomials, 11.7  
Bethe lattice, 4.5, 15.18  
Bethe-Salpeter equation, 12.24, 13.11, 14.4  
bit, 11.29  
Boltzmann equation, 15.28  
Brinkman-Rice transition, 1.11

## C

$\text{Ca}_2\text{RuO}_4$ , 7.28  
canonical bands, 2.9  
cellular dynamical mean-field theory, 5.23  
central limit theorem, 11.8  
cluster algorithms, 10.3  
cluster extensions of DMFT, 5.2  
cluster perturbation theory (CPT), 5.14  
coherent potential approximation, 1.12, 1.19  
coherent state path integrals, 12.7  
cold atoms in optical lattices, 1.22  
constrained LDA (cLDA), 3.4  
constrained RPA (cRPA), 3.9  
continuous-time interaction expansion, 10.2  
continuous-time quantum Monte Carlo, 9.3, 9.26  
contour-ordered Green function, 15.9  
conventional superconductors, 13.3  
correlated materials, 1.22

correlated subspace, 6.11  
correlation energy, 1.3, 1.15  
critical exponents, 14.5, 14.11  
crystal field, 6.18, 7.23  
cuprates, 13.4

## D

*d*-wave superconductivity, 5.28, 13.20  
default model, 11.17  
density-functional theory (DFT), 2.2, 6.6  
density-matrix renormalization group, 9.18  
DFT+DMFT, 1.22–1.26, 6.11, 7.15  
diagrammatic collapse, 1.13–1.15  
diagrammatic extensions of DMFT, 12.12, 14.2, 14.3  
discrepancy principle, 11.16  
discrete Fourier transformation, 5.7  
double counting, 6.16, 7.17, 7.33  
downfolding, 7.17  
dual fermions, 12.13  
dual functions, 11.6  
duality transformations, 10.3  
dynamical cluster approximation, 5.24, 13.5  
dynamical mean-field theory (DMFT), 1.19–1.22, 4.13, 5.3, 6.8, 7.12, 9.2, 9.25, 12.4, 13.5, 14.2  
dynamical vertex approximation, 12.12, 14.3  
Dyson equation, 1.20, 4.8, 4.10, 4.14, 7.6, 14.3

## E

electronic correlations, 1.4, 1.21, 1.25  
Eliashberg equation, 14.15  
entangled bands, 3.12  
entanglement, 9.10  
entropy, 11.29  
Euler polynomials, 11.6  
extended Hubbard model, 13.24

## F

Falicov-Kimball model, 1.16

- Fe (iron), 1.2, 1.22, 1.24–1.26
- Fermi surface, 2.28
- ferromagnetism, 1.2, 1.23
- fluctuation exchange approximation (FLEX), 12.26
- fluctuation-dissipation theorem, 15.7
- force theorem, 2.16
- functional integral, 11.20
  
- G
- gamma process, 11.22
- Grassmann algebra, 10.13, 12.7
- Green function, 3.19, 12.4
  - Matsubara, 11.4, 12.4
  - retarded, 11.4
- Gutzwiller
  - approximation, 1.10
  - density-functional theory, 1.14
  - wave function, 1.10–1.13
  
- H
- Hartree mean-field theory, 1.8–1.9
- Hartree-Fock, 6.3
- Heisenberg insulator, 5.26
- hidden state, 15.32
- Hubbard  $U$ , 3.3
- Hubbard bands, 4.9, 5.12
- Hubbard dimer, 7.5
- Hubbard model, 1.3–1.6, 1.8–1.9, 1.15, 4.2, 12.3, 13.4, 14.5, 14.8, 14.15
- Hubbard-I approximation, 5.21
- Hund’s rules, 2.6
- hybrid molecular dynamics, 10.3
- hybridization function, 7.6
  
- I
- ill-posed problem, 11.2
- impact ionization, 15.27
- impurity solver, 9.2
  - multiband, 9.21
  - real time, 9.4, 9.21
- infinite dimensions, 1.6, 1.13, 4.2, 4.5
- inverse photoemission spectroscopy, 5.9
  
- K
- Kadanoff-Baym equations, 15.15
- Kanamori Hamiltonian, 9.22
- Karush-Kuhn-Tucker conditions, 11.27
  
- Keldysh
  - contour, 15.8
  - formalism, 15.4
  - rotation, 15.13
- Kohn lines, 14.10
- Kohn-Sham equations, 6.7
- Kosterlitz-Thouless transition, 13.14
- Kullback-Leibler divergence, 11.31
  
- L
- $\text{La}_2\text{CuO}_4$ , 3.15
- Landau Fermi liquid, 4.9
- Langevin molecular dynamics, 10.3
- lattice Green function, 1.17, 1.20
- lattice QMC approach, 5.11
- lattice stability, 1.25
- LDA+DMFT, 7.12, 7.15
- least-squares (LS)
  - non-negative (NNLS), 11.27
- Lehmann representation, 4.7
- linear response, 3.7, 3.19
- local Dyson equation, 7.6
- local propagator, 1.19–1.21
- local vs. nonlocal correlations, 5.11
- local-density approximation, 6.7
- localization of the basis, 7.19
  
- M
- mass renormalization, 2.28
- matrix product operators (MPO), 9.18
- matrix product states (MPS), 9.5, 9.11
- matrix truncation, 9.14
- Matsubara Green function, 4.6
- maximum entropy method, 11.17
  - Bryan, 11.19
  - classic, 11.19
  - historic, 11.18
- maximum likelihood estimator, 11.10
- mean-field theory, 1.6–1.9, 1.19, 5.3, 6.10
- Mermin-Wagner theorem, 12.26
- metal-insulator transition, 6.18
- mixing, 6.10
- model building, 7.17
- Mott metal-insulator transition, 1.12, 1.21, 4.9, 4.17, 4.19, 5.26, 7.12
- muffin-tin orbitals, 2.7
- multi-orbital Hubbard models, 7.15
- multiplets, 7.23



## N

Nambu-Gorkov formalism, 13.7  
non-crossing approximation, 15.20  
non-negative least-squares, 11.12  
non-spherical Coulomb terms, 7.33  
normal distribution, truncated, 11.32

## O

orbital degeneracy, 7.25  
orbital order, 7.25  
orbital polarization, 6.19

## P

pair-field susceptibility, 13.10  
pairing mechanism, 13.19  
parquet equation, 14.4, 14.18  
path integral, 4.13, 11.20  
Pauli Hamiltonian, 2.5  
periodic Anderson model, 14.11  
periodic CPT, 5.18  
periodic system of the elements, 2.2  
periodization schemes, 5.16  
periodized cellular DMFT, 5.23  
perturbation theory, 12.6, 12.9  
    diagrammatic, 12.6  
    dual, 12.16  
phonons, 1.25  
photo-doping, 15.31  
photoemission spectroscopy, 5.9  
Picard plot, 11.14  
projected-local orbitals, 6.13

## Q

quantum critical point, 14.8, 14.13  
quantum criticality, 14.8, 14.11  
quasi-Newton scheme, 6.11

## R

random phase approximation (RPA), 3.8  
real time evolution, 9.15, 9.21  
reciprocal lattice, 5.5  
reference system, 5.14  
regularization, 11.13  
renormalization group, 11.25  
Ritz variational principle, 6.4  
ruthenates, 7.28

## S

scaling, 1.8, 1.13, 4.3

Schwinger-Dyson equation, 12.25

screened Coulomb interaction, 3.6

screening, 3.5

self-consistency, 4.15, 6.2, 7.12

self-energy, 1.13, 1.16–1.19, 1.21, 4.8,  
12.17

    atomic, 4.9

    Hubbard dimer, 7.6

    local, 4.13, 7.6, 7.8

self-energy-functional theory, 5.24

Shannon entropy, 11.29

sign problem, 10.4

single-electron Green function, 5.9

single-impurity Anderson model, 1.18,  
4.15, 5.22

singular value decomposition (SVD), 9.7,  
11.10

skeleton expansion, 4.11, 4.14, 4.19

skeleton functional, 15.12

Slater determinant, 6.3

Slater insulator, 5.28

Slater-Kanamori parametrization, 6.16

slave-boson mean-field theory, 1.12, 1.14

spectral function, 4.7, 11.3

spin-density functional theory, 2.20

spin-orbit interaction, 2.5, 7.29

Sr<sub>2</sub>RuO<sub>4</sub>, 7.28

SrMnO<sub>3</sub>, 9.27

SrVO<sub>3</sub>, 3.12, 9.26

Stoner theory, 2.20

Su-Schrieffer-Heeger model, 10.2

superconductivity, 14.15

superexchange mechanism, 5.12

superlattice, 5.5

## T

thermalization, 15.24

Tikhonov regularization, 11.14

time-resolved photo-emission spectroscopy,  
15.6

Trotter Suzuki approximation, 9.15

## U

ultrafast spectroscopy, 15.2

unconstrained gauge theories, 10.5

unconventional superconductors, 13.4

upper Hubbard band, 9.26

## V

$V_2O_3$ , 6.18

van-Hove singularities, 2.36

variational cluster approximation, 5.25

vertex, 14.2, 14.17

vison, 10.6

Volterra equation, 15.14

## W

Wannier functions, 3.11, 6.14, 7.18

Weiss field, 7.13

Weiss mean-field theory, 1.7–1.8, 1.15

Wick rotation, 11.3

## Y

$YTiO_3$ , 7.23

## Z

$Z_2$  lattice gauge theories, 10.2





1. **The LDA+DMFT approach to strongly correlated materials**  
Lecture Notes of the Autumn School 2011 Hands-on LDA+DMFT  
edited by E. Pavarini, E. Koch, D. Vollhardt, A. Lichtenstein (2011), 420 pages  
ISBN 978-3-89336-734-4
2. **Correlated Electrons: From Models to Materials**  
Lecture Notes of the Autumn School on Correlated Electrons 2012  
edited by E. Pavarini, E. Koch, F. Anders, and M. Jarrell (2012), 450 pages  
ISBN 978-3-89336-796-2
3. **Emergent Phenomena in Correlated Matter**  
Lecture Notes of the Autumn School on Correlated Electrons 2013  
edited by E. Pavarini, E. Koch, and U. Schollwöck (2013), 520 pages  
ISBN 978-3-89336-884-6
4. **DMFT at 25: Infinite Dimensions**  
Lecture Notes of the Autumn School on Correlated Electrons 2014  
edited by E. Pavarini, E. Koch, D. Vollhardt, A. Lichtenstein (2014), 450 pages  
ISBN 978-3-89336-953-9
5. **Many-Body Physics: From Kondo to Hubbard**  
Lecture Notes of the Autumn School on Correlated Electrons 2015  
edited by E. Pavarini, E. Koch, and P. Coleman (2015), 500 pages  
ISBN 978-3-95806-074-6
6. **Quantum Materials: Experiments and Theory**  
Lecture Notes of the Autumn School on Correlated Electrons 2016  
edited by E. Pavarini, E. Koch, J. van den Brink, G. Sawatzky (2016), 420 pages  
ISBN 978-3-95806-159-0
7. **The Physics of Correlated Insulators, Metals, and Superconductors**  
Lecture Notes of the Autumn School on Correlated Electrons 2017  
edited by E. Pavarini, E. Koch, R. Scalettar, and R. Martin (2017), 450 pages  
ISBN 978-3-95806-224-5
8. **DMFT: From Infinite Dimensions to Real Materials**  
Lecture Notes of the Autumn School on Correlated Electrons 2018  
edited by E. Pavarini, E. Koch, A. Lichtenstein, D. Vollhardt (2018), 480 Pages  
ISBN 978-3-95806-313-6